AN ABSTRACT OF THE THESIS OF

Fu-Lung Chang for the degree of Doctor of Philosophy in Atmospheric Sciences presented on August 5, 1997.

Title: Properties of Low-Level Marine Clouds as Deduced from Advanced Very High Resolution Radiometer Satellite Observations

Redacted for privacy

Abstract Approved: ______________

James A. Coakley, Jr.

A radiation model was developed for retrieving cloud visible optical depth, droplet effective radius, and cloud top emission temperature using AVHRR satellite observations at 0.63, 3.7, and 11 μm. The model was used to determine the sensitivity of the retrieved properties to various approximations often employed in such retrievals. Droplet effective radius appears to be the most sensitive to the commonly used approximations. Cloud properties retrieved using a 16-stream scheme were within ±5% of those retrieved using a 148-stream scheme. Cloud properties retrieved using double Henyey-Greenstein phase functions were within ±10% of those retrieved using Mie scattering. The retrieved cloud properties were used to investigate biases that arise when partly cloudy pixels were assumed to be overcast and biases that arise due to oblique satellite view angles. On average, cloud visible optical depths retrieved for partly cloudy pixels were 40–60% of those retrieved for overcast pixels. Likewise, cloud liquid water paths were 30–50%, droplet effective radii were 1–3 μm smaller, and cloud top emission temperatures were 2–4K larger. Cloud visible optical depths retrieved at 60° satellite zenith angles were 60–70% of those retrieved at nadir. The retrieved droplet effective radii and cloud top emission temperatures varied little with changing satellite zenith angle. For March 1989, cloud optical depths and cloud emission temperatures retrieved for pixels overcast by single-layer, low-level clouds were negatively correlated. Cloud optical depth, liquid water path, and droplet effective radius were positively correlated with the sea surface-cloud top temperature difference.

The retrieved cloud properties were also compared for the spatial coherence, CLAVR (Clouds from AVHRR), and a threshold method based on International Satellite Cloud Climatology Project procedures. For regions containing single-layered cloud systems, fractional cloud cover and cloud brightness temperatures derived by the ISCCP-like threshold method were systematically larger than those derived by the spatial coherence method, whereas cloud reflectivities were systematically smaller. Cloud reflectivities and brightness temperatures derived by CLAVR and the spatial coherence method were in better agreement.

©Copyright by Fu-Lung Chang,

August 5, 1997

All Rights Reserved

Properties of Low-Level Marine Clouds as Deduced from Advanced Very High Resolution Radiometer Satellite Observations

by

Fu-Lung Chang

A THESIS

submitted to

Oregon State University

in partial fulfillment of
the requirements for the
degree of

Doctor of Philosophy

Presented August 5, 1997

Commencement June 1998

Doctor of Philosophy thesis of Fu-Lung Chang presented on August 5, 1997

APPROVED:

Redacted for privacy

Major Professor, representing Atmospheric Sciences

Redacted for privacy

Dean of College of Oceanic and Atmospheric Sciences

Redacted for privacy

Dean of Graduate School

I understand that my thesis will become part of the permanent collection of Oregon State University libraries. My signature below authorizes release of my thesis to any reader upon request.

Fu-Lung Chang

Fu-Lung Chang, Author

ACKNOWLEDGMENTS

I wish to express my deep thanks to my major Professor, James A. Coakley, Jr., for his invaluable guidance, generous support, and constant encouragement during my research into this dissertation. He patiently guided my research and allowed it to flourish. Working with a unique individual like him, I have learned how to regroup when confronted by seemingly insurmountable obstacles, to procede calmly to solutions overcoming these obstacles. To all his efforts and extensive review of the dissertation, I owe him a great debt of gratitude.

I also wish to thank Drs. Jeffrey Barnes, Terence Brown, Steven Esbensen, Walter Rudd, Ted Strub, and Michael Unsworth for examining the dissertation and serving as my committee members. Many thanks also go to Drs. Dudley Chelton, Norman Loeb, Xijian Lin, Steve Platnick, and Mr. Nathaniel Plant for their helpful discussions during the development of the dissertation, to Dr. Gang Luo for help reading the CLAVR Phase II Data, to Guy Boulanger for help on processing the March 1989 AVHRR data, to David Simas and John Wong for their assistance on computer programming and software utilization, and to the staff and students in Atmospheric Sciences for providing me such a wonderful research environment.

I am grateful for the steady funding which supported my research. This work was first supported by a grant from the NOAA Climate and Global Change Program (grant NA16RC0450–02) and then by funding provided by the National Science Foundation Science and Technology Center grant to the Scripps Institution of Oceanography Center for Clouds, Chemistry and Climate (C^4).

Finally, I wish to express gratitude to my lovely wife, Shu-Wei Wang, for her understanding and support. I am glad to share the success of this dissertation with her.

TABLE OF CONTENTS

Page

Chapter 1 Motivation and Overview 1

1.1 Background 1

1.2 Motivation 3

1.3 Rationale 5

1.4 Outline of the dissertation 7

Chapter 2 Cloud Detection Using the Spatial Coherence, CLAVR, and an ISCCP-Like Threshold Method 10

2.1 Introduction 10

2.2 Data analysis 13

2.3 Comparison of cloud-free properties derived by CLAVR and the spatial coherence method 26

2.4 Comparison of cloud properties derived by the spatial coherence, CLAVR, and ISCCP-like threshold methods 33

2.5 Implications of differences between the spatial coherence, CLAVR, and ISCCP-like threshold analyses 43

Chapter 3 The Radiation Model and Cloud Property Retrievals Using Mie and Double Henyey-Greenstein Phase Functions 46

3.1 Introduction 46

3.2 Cloud radiation model 49

3.3 Atmospheric gaseous absorption and scattering 96

3.4 The iterative cloud property retrieval scheme 102

3.5 Validating and comparing the retrieved cloud properties 109

3.6 Sensitivity studies for cloud property retrievals 114

TABLE OF CONTENTS (Continued)

Page

Chapter 4 Effects of Partly Cloudy Pixels and Satellite Zenith Angles on Cloud Properties Retrieved from Satellite Observations 126

4.1 Introduction 126

4.2 Cloud property retrieval procedures 128

4.3 Frequency of occurrence for single-layered, low-level cloud systems 144

4.4 Low-level cloud visible optical depths, droplet effective radii, and cloud top emission temperatures for overcast and partly cloudy pixels 147

4.5 Effects of satellite zenith angle on retrieved cloud properties 158

4.6 Simulation studies for the effects of partly cloudy pixels 173

Chapter 5 Dependence of Cloud Visible Optical Depth on Cloud Top, Atmospheric, and Sea Surface Temperatures 185

5.1 Introduction 185

5.2 Cloud optical depth feedback 187

5.3 ISCCP low-level cloud visible optical depths and temperatures 189

5.4 Variations of cloud visible optical depth with cloud top and 740-mb atmospheric temperatures 195

5.5 Variations of cloud visible optical depth with sea surface temperature 233

5.6 Implications of the negative relationship between cloud visible optical depth and cloud top emission temperature 234

Chapter 6 Relationships between Cloud Liquid Water Path, Visible Optical Depth, Droplet Effective Radius, and Sea Surface-Cloud Top Temperature Difference 254

6.1 Introduction 254

TABLE OF CONTENTS (Continued)

Page

6.2 Low-level cloud liquid water paths 257

6.3 Effects of partly cloudy pixels on cloud liquid water path and droplet effective radius 264

6.4 Relationships between cloud visible optical depth, droplet effective radius, and cloud liquid water path 269

6.5 Variations of cloud liquid water path and droplet effective radius with cloud top emission temperature 285

6.6 Variations of cloud liquid water path and droplet effective radius with sea surface-cloud top temperature difference 295

6.7 The role of cloud vertical thickness in determining cloud liquid water path, optical depth, and droplet radius 296

Chapter 7 Concluding Remarks: Summary and Future Studies 312

7.1 Cloud detection 312

7.2 Cloud property retrievals 315

7.3 Properties of low-level marine clouds 318

Bibliography 322

Appendix Procedures for constructing the spatial coherence cloud mask 332

LIST OF FIGURES

Figure Page

2.1 NOAA-11 AVHRR 4-km GAC data for (a) 11 μm and (b) 0.63 μm 16

2.2 Local means and standard deviations of 11-μm radiances (mWm^{-2}sr^{-1}cm) 17

2.3 Spatial coherence analysis for the data shown in Figure 2.1 19

2.4 Same as Figure 2.2, except that the results are for the CLAVR analysis ... 22

2.5 Pixel-scale cloud cover frcation obtained for the data shown in Figure 2.1 23

2.6 Cloud-free (a) 0.63-μm reflectivity (%) and (b) 11-μm brightness temperature (K) obtained by CLAVR and by the spatial coherence method 27

2.7 Same as Figure 2.1, except that the images are for the Atlantic ocean off the coast of Angola 28

2.8 (a) Spatial coherence analysis and (b) CLAVR analysis for the data shown in Figure 2.7 29

2.9a Cloud-free 11-μm brightness temperatures and 0.63-μm reflectivities and satellite zenith angles obtained by the spatial coherence and CLAVR analyses 30

2.9b Same as Figure 2.9a, except that the results are for the upper half of the images shown in Figure 2.7 31

2.10 (a) Spatial coherence and (b) CLAVR analysis of 2 × 2 pixel arrays 32

2.11 Overcast 0.63-μm reflectivities for 250-km-scale regions 35

2.12 Same as Figure 2.11, except that each point represents a 60-km-scale regions 36

2.13 Same as Figure 2.11, except for overcast 11-μm brightness temperatures .. 37

2.14 Same as Figure 2.13, except that each point represents a 60-km-scale regions 38

LIST OF FIGURES (Continued)

Figure Page

2.15 Same as Figure 2.11, except for fractional cloud cover 41

2.16 Same as Figure 2.15, except that each point represents a 60-km region 42

3.1 Optical properties for water droplets 54

3.2 Standard gamma size distributions for droplet effective radii 4, 10, and 28 μm 55

3.3 Same as Figure 3.1, except for gamma size distributions 56

3.4 Logrithmic-10 values of Mie and DHG phase functions for $\lambda = 0.614$ μm 57

3.5 Same as Figure 3.4, except for $\lambda = 3.749$ μm 58

3.6 Same as Figure 3.4, except for $\lambda = 10.81$ μm 59

3.7 Truncated and the actual expressions of Mie and DHG phase functions for $\lambda = 0.614$ μm and $r_{eff} = 10$ μm 60

3.8 Contour plot for χ^2 statistic 63

3.9 Parameters g, g_1, g_2, and b as a function of droplet effective radius 64

3.10 Contour plots of $h^0(\mu, -\mu_o)$ for $\lambda = 0.614$ μm and $r_{eff} = 10$ μm 68

3.11 Same as Figure 3.10, except for $h^1(\mu, -\mu_o)$ 69

3.12 Same as Figure 3.10, except for $\lambda = 3.749$ μm 70

3.13 Same as Figure 3.12, except for $h^1(\mu, -\mu_o)$ 71

3.14 Polar plots of $R(\tau_c; \mu_o, \mu, \phi - \phi_o)$ for $\lambda = 0.614$ μm, $r_{eff} = 10$ μm, $\tau_c = 1$, and $\theta_o = 5.9^\circ$ 76

3.15 Same as Figure 3.14, except for $\tau_c = 8$ 77

3.16 Same as Figure 3.14, except for $\tau_c = 64$ 78

LIST OF FIGURES (Continued)

Figure Page

3.17 Same as Figure 3.14, except for θ_o = 63.1° 79

3.18 Same as Figure 3.14, except for τ_c = 8 and θ_o = 63.1° 80

3.19 Same as Figure 3.14, except for τ_c = 64 and θ_o = 63.1° 81

3.20 Same as Figure 3.14, except for λ = 3.749 μm, r_{eff} = 4 μm, τ_c = 8 82

3.21 Same as Figure 3.20, except for r_{eff} = 10 μm 83

3.22 Same as Figure 3.20, except for r_{eff} = 28 μm 84

3.23 Same as Figure 3.20, except for θ_o = 63.1° 85

3.24 Same as Figure 3.20, except for r_{eff} = 10 μm and θ_o = 63.1° 86

3.25 Same as Figure 3.20, except for r_{eff} = 28 μm and θ_o = 63.1° 87

3.26 $R(\tau_c; \mu_o, \mu, \phi - \phi_o)$ as functions of cloud visible optical depth and droplet effective radius for λ = 0.614 μm and (θ_o,θ,$\phi - \phi_o$) = (63.1°,56.8°,0°) 89

3.27 Same as Figure 3.26, except for $\phi - \phi_o$ = 90° 90

3.28 Same as Figure 3.26, except for $\phi - \phi_o$ = 180° 91

3.29 Same as Figure 3.26, except for λ = 3.749 μm 92

3.30 Same as Figure 3.26, except for λ = 3.749 μm and $\phi - \phi_o$ = 90° 93

3.31 Same as Figure 3.26, except for λ = 3.749 μm and $\phi - \phi_o$ = 180° 94

3.32 $R(\tau_c; \mu_o, \mu, \phi - \phi_o)$ as a function of satellite zenith angle for λ = 0.614 μm 100

3.33 Same as Figure 3.32, except for λ = 3.749 μm 101

3.34 Reflected radiances calculated for AVHRR channels 1 and 3 104

LIST OF FIGURES (Continued)

Figure Page

3.35 Retrievals of (a) cloud visible optical depth, (b) droplet effective radius, and (c) cloud top emission temperature 107

3.36 Solar zenith, satellite zenith, and relative azimuth angles for the retrievals shown in Figure 3.35 108

3.37 Differences (current – Platnick and Twomey) in cloud visible optical depth, droplet effective radius, and cloud top emission temperature as functions of satellite zenith angle and cloud visible optical depth 111

3.38 Same as Figure 3.36, except that each point represents a case drawn from 60-km regions observed by NOAA-11 AVHRR over the Pacific ocean during March 1989 112

3.39 Retrievals of (a) cloud visible optical depth, (b) droplet effective radius, and (c) cloud top emission temperature for cases with viewing geometries shown in Figure 3.38 113

3.40 Same as Figure 3.39, except that retrievals were obtained using Mie 32-stream and Mie 16-stream schemes 119

3.41 Same as Figure 3.39, except that retrievals were obtained using surface reflectances of zero and 6% 120

3.42 Same as Figure 3.39, except that retrievals were obtained using NOAA-11 and NOAA-12 filter functions 121

3.43 Same as Figure 3.39, except that retrievals were obtained using no iteration and using the iterative scheme 122

3.44 Same as Figure 3.39, except that retrievals were obtained with and without gaseous absorption in the cloud layer 123

3.45 AVHRR channel-3 reflection functions and cloud vertical thickness 124

3.46 Same as Figure 3.39, except that retrievals were obtained using standard midlatitude summertime atmosphere and TOVS derived atmospheric temperature and humidity profiles 125

LIST OF FIGURES (Continued)

Figure Page

4.1 Schematic plot of daytime ascending passes for NOAA-11 AVHRR polar orbiting satellite 130

4.2 Spatial coherence analysis of 2 × 2 GAC pixel arrays 131

4.3 Contour plot of monthly-mean sea surface temperatures (K) 134

4.4 Sea surface temperatures as a function of satellite zenith angle 135

4.5 Monthly-mean sea surface temperatures obtained with Kratz's model (solid) and McMillin-Crosby's empirical equation (dashed) 136

4.6 Frequency distributions of single-layered cloud systems for 60-km-scale regions 141

4.7 Frequency of occurrence (%) for overcast and partly cloudy pixels 142

4.8 Frequency of occurrence for the single-layered, low-level cloud systems 143

4.9 Cloud visible optical depths for single-layered, low-level clouds for March 1989 over the Pacific ocean 149

4.10 Cloud visible optical depths for overcast and partly cloudy pixels drawn from the same 60-km region 150

4.11 Same as Figure 4.9, except for cloud droplet effective radii (μm) 152

4.12 Same as Figure 4.10, except for cloud droplet effective radii (μm) 153

4.13 Same as Figure 4.9, except for cloud top emission temperatures (K) 154

4.14 Same as Figure 4.10, except for cloud top emission temperatures (K) 155

4.15 Same as Figure 4.9, except for sea surface-cloud top temperature differences 156

4.16a Cloud visible optical depths and satellite zenith angles for pixels overcast by single-layered, low-level clouds 160

LIST OF FIGURES (Continued)

Figure Page

4.16b Same as Figure 4.16a, except for cloud droplet effective radii (μm) 161

4.16c Same as Figure 4.16a, except for cloud top emission temperatures (K) 162

4.17 Same as Figure 4.16a, except for solar zenith angles of the observations . 163

4.18 Number of pixels overcast by single-layered, low-level clouds as a function of satellite zenith angle 164

4.19 Same as Figure 4.16a, except for the sea surface-cloud top temperature differences (K) 165

4.20 Monthly-mean cloud top emission temperatures (K) obtained using Kratz's model and McMillin-Crosby's equation for the sea surface temperature 166

4.21 Retrieved (thin) and corrected (dashed) monthly-mean cloud visible optical depths for pixels overcast by single-layered, low-level clouds 167

4.22a Monthly-mean droplet effective radii (μm) obtained with retrieved (solid) and corrected (dashed) cloud visible optical depths 168

4.22b Same as Figure 4.22a, except for cloud top emission temperatures (K) 169

4.23a Monthly-mean cloud visible optical depths for March 1989 for the Pacific ocean 174

4.23b Same as Figure 4.23a, except for cloud droplet effective radii (μm) 175

4.23c Same as Figure 4.23a, except for cloud top emission temperatures (K) 176

4.24a Differences (partly cloudy – overcast) in cloud visible optical depth (dashed), droplet effective radius (thick), and cloud top emission temperature (thin) as a function of cloud cover fraction 177

4.24b Same as Figure 4.24a, except for a cloud visible optical depth of 12 178

4.25 Frequency distribution of mean fractional cloud cover (%) for partly cloudy pixels 181

LIST OF FIGURES (Continued)

Figure Page

4.26 (a) 0.63-μm reflectance (%) and (b) 3.75-μm radiance (mWm^{-2}sr^{-1}cm) for partly cloudy pixels 182

5.1 Cloud visible optical depths, cloud top emission temperatures (K), and cloud cover fractions (%) for partly cloudy pixels assumed to be overcast 190

5.2 Latitudinal distribution of low-level cloud visible optical depth for ISCCP and overcast pixels 193

5.3 Same as Figure 5.2, except for cloud top emission temperatures (K) 194

5.4 Cloud visible optical depths and cloud top emission temperatures (K) for pixels overcast by single-layered, low-level clouds 197

5.5 $d(TAU)/d(TC)$ and monthly-mean cloud top emission temperatures for observations shown in Figure 5.4 198

5.6 Cloud visible optical depths and cloud top emission temperatures for pixels overcast by single-layered, low-level clouds 201

5.7 Latitudinal distribution of $d(TAU)/d(TC)$ for observations shown in Figure 5.6 202

5.8 Same as Figure 5.4, except that observations are for pixels that were partly covered by the single-layered, low-level clouds 206

5.9 Same as Figure 5.6, except that observations are for pixels that were partly covered by the single-layered, low-level clouds 207

5.10 Same as Figure 5.5, except for $d\ln(TAU)/d(TC)$ 208

5.11 Same as Figure 5.10, except that observations are for pixels that were partly covered by the single-layered, low-level clouds 209

5.12 Same as Figure 5.7, except for $d\ln(TAU)/d(TC)$ 210

5.13 Same as Figure 5.12, except that observations are for pixels that were partly covered by the single-layered, low-level clouds 211

LIST OF FIGURES (Continued)

Figure Page

5.14 Cloud visible optical depths for pixels that were overcast and partly covered by the single-layered, low-level clouds 212

5.15 Correlation coefficients of cloud visible optical depths for the overcast and partly cloudy pixels obtained from the day-to-day variations shown in Figure 5.14 213

5.16 Same as Figure 5.14, except for cloud top emission temperatures (K) 214

5.17 Same as Figure 5.15, except that the correlation coefficients are for the cloud top emission temperatures shown in Figure 5.16 215

5.18 Same as Figure 5.14, except for cloud droplet effective radii (μm) 216

5.19 Same as Figure 5.15, except that the correlation coefficients are for the cloud droplet effective radii shown in Figure 5.18 217

5.20 Cloud visible optical depths for pixels that were overcast and partly covered by the single-layered, low-level clouds 218

5.21 Correlation coefficients of cloud visible optical depths for the overcast and partly cloudy pixels obtained from the longitudinal variations shown in Figure 5.20 219

5.22 Same as Figure 5.20, except for cloud top emission temperatures (K) 220

5.23 Same as Figure 5.21, except that the correlation coefficients are for the cloud top emission temperatures shown in Figure 5.20 221

5.24 Same as Figure 5.20, except for cloud droplet effective radii (μm) 222

5.25 Same as Figure 5.21, except that the correlation coefficients are for the cloud droplet effective radii shown in Figure 5.24 223

5.26 Same as Figure 5.4, except that the visible optical depths and cloud temperatures are obtained by ISCCP for low-level clouds 224

LIST OF FIGURES (Continued)

Figure Page

5.27 Same as Figure 5.5, except that $d(TAU)/d(TC)$ and the monthly-mean cloud temperatures are for the ISCCP low-level clouds shown in Figure 5.26 225

5.28 Same as Figure 5.6, except that the visible optical depths and cloud temperatures were obtained by ISCCP for low-level clouds 226

5.29 Same as Figure 5.7, except that the values of $d(TAU)/d(TC)$ are for the ISCCP low-level clouds shown in Figure 5.28 227

5.30 Same as Figure 5.4, except for cloud visible optical depth and 740-mb atmospheric temperature 228

5.31 Same as Figure 5.5, except for $d(TAU)/d(TA740)$ and the monthly-mean 740-mb atmospheric temperatures shown in Figure 5.30 229

5.32 Same as Figure 5.6, except for cloud visible optical depth and 740-mb atmospheric temperature 230

5.33 Same as Figure 5.7, except for $d(TAU)/d(TA740)$ shown in Figure 5.32 231

5.34 Same as Figure 5.4, except for cloud visible optical depth and sea surface temperature 238

5.35 Same as Figure 5.5, except for $d(TAU)/d(SST)$ and the monthly-mean sea surface temperatures shown in Figure 5.34 239

5.36 Same as Figure 5.6, except for cloud visible optical depth and sea surface temperature 240

5.37 Same as Figure 5.7, except for $d(TAU)/d(SST)$ shown in Figure 5.36 241

5.38 Same as Figure 5.4, except for cloud visible optical depth and cloud cover fraction for pixels that were partly covered by single-layered, low-level clouds 242

LIST OF FIGURES (Continued)

Figure Page

5.39 Same as Figure 5.5, except for $d(TAU)/d(CCF)$ and the monthly-mean cloud cover fraction for the partly cloudy pixels shown in Figure 5.38 243

5.40 Same as Figure 5.6, except for cloud visible optical depth and cloud cover fraction for pixels that were partly covered by single-layered, low-level clouds 244

5.41 Same as Figure 5.7, except for $d(TAU)/d(CCF)$ for the partly cloudy pixels shown in Figure 5.40 245

5.42 Same as Figure 5.4, except for cloud top emission temperature and cloud cover fraction for pixels that were partly covered by single-layered, low-level clouds 246

5.43 Same as Figure 5.5, except for $d(TC)/d(CCF)$ and the monthly-mean cloud cover fraction for the partly cloudy pixels shown in Figure 5.42 247

5.44 Same as Figure 5.6, except for cloud top emission temperature and cloud cover fraction for pixels that were partly covered by the single-layered, low-level clouds 248

5.45 Same as Figure 5.7, except for $d(TC)/d(CCF)$ for the partly cloudy pixels shown in Figure 5.44 249

5.46 Same as Figure 5.4, except for cloud visible optical depth and sea surface-cloud top temperature difference 250

5.47 Same as Figure 5.5, except for $d(TAU)/d(\Delta T)$ and the monthly-mean sea surface-cloud top temperature differences shown in Figure 5.46 251

5.48 Same as Figure 5.6, except for cloud visible optical depth and sea surface-cloud top temperature difference 252

5.49 Same as Figure 5.7, except for $d(TAU)/d(\Delta T)$ shown in Figure 5.48 253

LIST OF FIGURES (Continued)

Figure Page

6.1 Cloud liquid water paths for single-layered, low-level clouds for March 1989 over the Pacific ocean 259

6.2 Cloud liquid water paths (g/m^2) for the overcast and partly cloudy pixels drawn from the same 60-km region 260

6.3 Cloud liquid water paths as a function of satellite zenith angle 261

6.4 Monthly-mean cloud liquid water paths (g/m^2) for pixels overcast and partly covered by single-layered, low-level clouds 262

6.5a Same as Figure 5.4, except for cloud liquid water path and cloud cover fraction for pixels that were partly covered by single-layered, low-level clouds 265

6.5b Same as Figure 5.6, except for cloud liquid water path and cloud cover fraction for pixels that were partly covered by single-layered, low-level clouds 266

6.6a Same as Figure 5.4, except for cloud droplet effective radius and cloud cover fraction for pixels that were partly covered by single-layered, low-level clouds 268

6.6b Same as Figure 5.6, except for cloud droplet effective radius and cloud cover fraction for pixels that were partly covered by single-layered, low-level clouds 269

6.7 Same as Figure 5.4, except for cloud visible optical depth and cloud droplet effective radius 271

6.8 Same as Figure 5.5, except for $d(TAU)/d(REFF)$ and the monthly-mean cloud droplet effective radii shown in Figure 6.7 272

6.9 Same as Figure 5.6, except for cloud visible optical depth and cloud droplet effective radius 273

6.10 Same as Figure 5.7, except for $d(TAU)/d(REFF)$ shown in Figure 6.9 274

LIST OF FIGURES (Continued)

Figure | Page

6.11a Longitudinal variations of monthly-mean cloud visible optical depth (dashed) and cloud droplet effective radius (solid) for the north Pacific ocean between 7.5°N and 45°N 275

6.11b Same as Figure 6.11a, except for the south Pacific ocean between 12.5°S and 50°S 276

6.12 Same as Figure 5.4, except for cloud visible optical depth and cloud liquid water path 277

6.13 Same as Figure 5.5, except for $d(TAU)/d(LWP)$ and the monthly-mean cloud liquid water paths shown in Figure 6.12 278

6.14 Same as Figure 5.6, except for cloud visible optical depth and cloud liquid water path 279

6.15 Same as Figure 5.7, except for $d(TAU)/d(LWP)$ shown in Figure 6.14 280

6.16 Same as Figure 5.4, except for cloud liquid water path and cloud droplet effective radius 281

6.17 Same as Figure 5.5, except for $d(LWP)/d(REFF)$ and the monthly-mean cloud droplet effective radii shown in Figure 6.16 282

6.18 Same as Figure 5.6, except for cloud liquid water path and cloud droplet effective radius 283

6.19 Same as Figure 5.7, except for $d(LWP)/d(REFF)$ shown in Figure 6.18 284

6.20 Same as Figure 5.4, except for cloud liquid water path and cloud top emission temperature 287

6.21 Same as Figure 5.5, except for $d(LWP)/d(TC)$ and the monthly-mean cloud top emission temperatures shown in Figure 6.20 288

6.22 Same as Figure 5.6, except for cloud liquid water path and cloud top emission temperature 289

LIST OF FIGURES (Continued)

Figure Page

6.23 Same as Figure 5.7, except for $d(LWP)/d(TC)$ shown in Figure 6.22 290

6.24 Same as Figure 5.4, except for cloud droplet effective radius and cloud top emission temperature 291

6.25 Same as Figure 5.5, except for $d(REFF)/d(TC)$ and the monthly-mean cloud top emission temperatures shown in Figure 6.24 292

6.26 Same as Figure 5.6, except for cloud droplet effective radius and cloud top emission temperature 293

6.27 Same as Figure 5.7, except for $d(REFF)/d(TC)$ shown in Figure 6.26 294

6.28 Same as Figure 5.4, except for cloud liquid water path and sea surface-cloud top temperature difference 297

6.29 Same as Figure 5.5, except for $d(LWP)/d(\Delta T)$ and the monthly-mean sea surface-cloud top temperature differences shown in Figure 6.28 298

6.30 Same as Figure 5.6, except for cloud liquid water path and sea surface-cloud top temperature difference 299

6.31 Same as Figure 5.7, except for $d(LWP)/d(\Delta T)$ shown in Figure 6.30 300

6.32 Same as Figure 5.4, except for cloud droplet effective radius and sea surface-cloud top temperature difference 301

6.33 Same as Figure 5.5, except for $d(REFF)/d(\Delta T)$ and the monthly-mean sea surface-cloud top temperature differences shown in Figure 6.32 302

6.34 Same as Figure 5.6, except for cloud droplet effective radius and sea surface-cloud top temperature difference 303

LIST OF FIGURES (Continued)

Figure Page

6.35 Same as Figure 5.7, except for $d(REFF)/d(\Delta T)$ shown in Figure 6.34 304

6.36a Monthly-mean sea surface-cloud top temperature differences (K) for March 1989 for the Pacific ocean 307

6.36b Same as Figure 6.36a, except for cloud liquid water path (g/m^2) 308

6.36c Same as Figure 6.36a, except for cloud visible optical depth 309

6.36d Same as Figure 6.36a, except for cloud droplet effective radius (μm) 310

6.36e Same as Figure 6.36a, except for cloud top emission temperature (K) 311

LIST OF TABLES

Table Page

2.1 Number of 250-km regions identified as being cloud-free, covered by a single-layered cloud system, or covered by more complex clouds 20

2.2 Number of 60-km regions identified as being cloud-free, overcast, or partially cloud-covered 20

3.1 Cloud visible optical depths and cloud droplet effective radii (μm) 50

3.2 Spectral range, response function, solar constant, and index of refraction for water 51

3.3 Plane-parallel atmospheric model and standard midlatitude summertime atmosphere 95

3.4 Atmospheric absorbing and scattering components in each sub-channel ... 97

4.1 Cloud-free and overcast cloud properties together with locations and sun-earth-satellite viewing geometry 139

4.2 Cloud properties for partly cloudy pixels, assumed to be overcast 140

4.3 Monthly-mean cloud visible optical depths, droplet effective radii (μm), cloud top emission temperatures (K), and cloud top altitudes (km) 151

5.1 Index numbers, locations, $d(TAU)/d(TC)$, monthly-mean cloud visible optical depths, cloud top emission temperatures, numbers of days, correlation coefficients ρ, and whether the correlation is significant at the 90% confidence level 199

5.2 Index numbers, latitudes, $d(TAU)/d(TC)$, monthly-mean cloud visible optical depths, cloud top emission temperatures, numbers of $2.5° \times 2.5°$ samples, effective numbers of independent samples, correlation coefficients ρ, and whether the correlation is significant at the 90% confidence level 200

6.1 Monthly-mean cloud liquid water paths (g/m^2) 263

Properties of Low-Level Marine Clouds as Deduced from Advanced Very High Resolution Radiometer Satellite Observations

Chapter 1
Motivation and Overview

1.1 Background

Clouds influence the climate primarily through their effect on the earth's radiation budget. Their effect on the shortwave radiation leads to cooling; their effect on the longwave radiation leads to warming (Hartmann and Short, 1980; Ramanathan et al., 1989; Harrison et al., 1990; Arking, 1991). At short wavelengths, clouds reflect a large portion of the incident solar radiation back to space and reduce the solar energy absorbed by the earth. This cooling effect, known as the albedo effect, increases the global albedo of the earth from a clear sky value of about 15% to the observed value of roughly 30%.

At long wavelengths, clouds absorb and re-emit radiation. Since temperatures in the atmosphere generally decrease with altitude, the cloud top temperature is usually lower than the temperature of the underlying surface. As clouds are nearly opaque to longwave radiation, the outgoing longwave emission for overcast conditions is generally less than that for cloud-free conditions. As a result, clouds reduce the outgoing longwave radiation at the top of the atmosphere and increase the longwave radiation absorbed within and below the cloud layer. This heating effect is the well-known greenhouse effect.

In the past two decades, the climate change expected from the buildup of atmospheric trace gases has spawned a great number of studies attempting to predict the future climate. Whether the earth's climate is following a warming trend and whether the cloud feedback effect will diminish or enhance the warming are debatable. Numerous climate models, e.g., radiative-convective models (RCMs) and general circulation models (GCMs), have long been used to simulate the earth's atmosphere and to improve understanding of the climate and climate change. Nevertheless, while these studies have established beyond doubt that clouds play a major role in the earth's radiation balance, they have also demonstrated that the parameterization of cloud properties for use in climate models is a formidable problem. By comparing results obtained from 19 GCMs, Cess et al. (1990) showed that the GCMs agree well when effects due to clouds are neglected, but they produce tremendous differences when the cloud effects are included.

Recently, the role of clouds in earth's climate has been characterized in terms of "cloud radiative forcing" — the change to the earth's radiation budget brought about by the presence of clouds (Ramanathan et al., 1989). The net forcing is about -15 Wm^{-2} on a global scale. The minus sign indicates that the cooling effect of clouds dominates their heating effect. The magnitude of the forcing is several times the magnitude of the forcing brought about by doubling the atmospheric concentration of CO_2, which is taken to be a reduction in the longwave emission of 4 Wm^{-2} at the tropopause (Ramanathan and Coakley, 1978). Clearly, the effect of clouds is so strong that relatively small changes in cloud properties are likely to significantly influence the earth's radiation budget. Cloud properties that affect the radiation budget are cloud cover fraction, cloud top altitude, cloud liquid/ice water path, and cloud hydrometeor size. By estimating the variation in the cloud radiative forcing to infer the radiative effect of these cloud properties, Coakley (1993) estimated that a change of ~0.04–0.12 in cloud cover fraction, ~600 meters in cloud top altitude, ~10% in cloud liquid/ice water path, or ~10% in cloud hydrometeor size with liquid/ice water path held constant would affect the earth's radiation budget at a level comparable to the radiative impact of a CO_2 doubling. The sensitivity of climate models to these cloud properties has also been documented by Wetherald and Manabe (1984), Roeckner et al. (1987), and Slingo and Slingo (1991), among many others.

1.2 Motivation

This study was originally motivated by Cess et al. (1990) and later by Tselioudis et al. (1992) and Han et al. (1994). Cess et al. performed comparisons of 19 general circulation models and found that the radiative response of these models differed by a factor of three. They attributed most of the differences in the radiative response to differences in the cloud parameterization schemes used in the models. Clearly, the interactions between clouds, earth's radiation budget, and climate are still poorly understood. Reliable long-term observations of cloud properties are needed in order to improve the treatment of clouds in climate models.

Current research efforts have sought to obtain cloud properties from satellite observations. Tselioudis et al. (1992) used one year of ISCCP (International Satellite Cloud Climatology Project) cloud data to derive the global relationship between cloud optical depth and temperature for low-level clouds. They found that an increase in cloud temperature lead to a decrease in cloud optical depth. They suggested that the cloud optical depth feedback would be positive, opposite to the negative cloud optical depth feedback proposed by Somerville and Remer (1984). A positive feedback means that clouds reflect less sunlight as the earth warms. Han et al. (1994) used two years of ISCCP data to derive the near-global (60°S-60°N) distribution of water-cloud droplet effective radius. The results obtained by Tselioudis et al. and by Han et al. may be biased because many pixels identified by ISCCP as being overcast are in fact only partly cloud-covered.

ISCCP cloud properties are obtained through the application of thresholds to satellite imagery data (Rossow and Schiffer, 1991; Rossow and Garder, 1993). Predetermined threshold values are used to divide satellite pixels into three categories: "clear", "cloudy", and "overcast". Pixels falling in the "clear" category are treated as completely cloud-free. Pixels falling in the "cloudy" and "overcast" categories are treated as completely overcast. Radiances observed for the "overcast" pixels are then used to derive cloud properties. On the other hand, common observations of broken cloudy skies lead one to expect that the occurrence of broken clouds on scales that are smaller or comparable to the spatial resolution of imagers providing global coverage (typically 4–8 km) is rather common. When clouds are broken, it seems unlikely that they would align themselves to fall exactly within the footprint of an imager pixel as the satellite flies over. If many of the pixels identified by ISCCP as being overcast are in fact only partly cloud-covered (Wielicki and Parker, 1992; Chang and Coakley, 1993), then many of the properties attributed to clouds in ISCCP cloud data products are probably biased. They are contaminated by the properties of the cloud-free portions of the pixels. Errors associated with threshold estimates of cloud properties may be sizable. The relationship between cloud optical depth and cloud temperature obtained by Tselioudis et al. (1992) and the cloud droplet effective radii obtained by Han et al. (1994) need to be re-examined using pixels that are more likely to be overcast.

For the retrieval of cloud properties, a plane-parallel radiation model is developed. The satellite view angle dependence in the retrieved cloud properties is assessed for pixels that are overcast by single-layered, low-level clouds. The model is used to assess the sensitivity of the retrieved cloud properties to various approximations often employed in such retrievals.

In addition, comparisons are performed for the cloud properties retrieved using the spatial coherence method (Coakley and Bretherton, 1982), CLAVR (Clouds from AVHRR, Stowe et al., 1997), and a threshold method that simulates the ISCCP scheme (Rossow and Garder, 1993). It has been argued that cloud analysis methods are merely used to "define" clouds and therefore differences in the treatment of cloudy pixels may present no more than different ways of "defining" cloud properties (Rossow, 1989). Comparing the results of one method with those of another may be of little relevance unless the different ways of "defining" cloud properties lead to differences in cloud physical quantities — like cloud optical depth, cloud droplet size, cloud altitude, and cloud liquid water path — that might be measured by alternate means.

1.3 Rationale

The dissertation explores the retrieval of cloud properties for single-layered, low-level clouds based on radiances from the NOAA-11 Advanced Very High Resolution Radiometer (AVHRR) for the Pacific ocean during March 1989. The spatial coherence method (Coakley and Bretherton, 1982) and an iterative numerical scheme developed for retrieving cloud properties from satellite observations are employed to derive optical depths, droplet effective radii, emission temperatures, and liquid water paths for these single-layered, low-level clouds. The spatial coherence method identifies cloud systems that form well-defined layers on large spatial scales (100–200 km). Experience with satellite imagery data shows that layered cloud systems are rather common over ocean, e.g., marine stratus and stratocumulus, and they are relatively easily identified (Coakley and Baldwin, 1984). The spatial coherence method uses the pixel-to-pixel variability in the 11-μm radiance field to identify pixels that appear to be completely overcast by clouds in a given layer. Properties of cloud layers are then deduced from the overcast pixels.

Cloud systems are often presumed to obey the physical relationships associated with a plane-parallel, homogeneous cloud. Clearly, single-layered cloud systems are expected to exhibit such a behavior more closely than would more complex cloud systems. Effective properties of layered cloud systems should be more readily measurable than the macrophysical and microphysical properties of individual clouds. Large-scale variations in cloud properties brought about by changes in earth's climate may well be noticed first in layered cloud systems. To understand the role that clouds play in governing the earth's radiation budget and climate, layered cloud systems deserve special attention.

Since light scattering by ice crystals is difficult to model (e.g., Heymsfield and Miloshevich, 1993; Macke, 1993; Macke et al., 1996), the cloud property retrieval scheme used here is developed for water clouds only. The dissertation focuses only on low-level clouds in order to limit effects due to phase changes. Low-level clouds have been shown to have a strong influence on the earth's net radiation balance (Hartmann et al., 1992). These clouds substantially increase the planetary albedo because they have higher reflectivies than does the underlying surface. Low-level clouds also have little influence on the thermal radiation emitted to space because their temperatures are close to the temperatures of the underlying surface. Since their albedo effect dominates, the net effect of these clouds on the earth's radiation budget is negative. They reduce the net radiation balance on a global-annual average basis by about 15 Wm^{-2} (Hartmann et al., 1992). Furthermore, the average amount of low-level clouds is about 29% globally and 34% over ocean (Klein and Hartmann, 1993). With such a high occurrence, the earth's radiation budget is obviously sensitive to changes in the area that they cover and their optical properties.

With regard to cloud property retrievals, an iterative retrieval scheme similar to those used by Han et al. (1994), Platnick and Twomey (1994), and Nakajima and Nakajima (1995), is developed for retrieving cloud optical depths, droplet effective radii, and cloud top emission temperatures from AVHRR radiances observed at 0.63, 3.75, and 11 μm. All previous schemes were applied to cloud-contaminated pixels that included both the partly cloudy and overcast pixels. Here, the retrieval is applied only to overcast pixels. The retrieval scheme explores the use of both Mie theory and a double Henyey-Greenstein phase function to model the scattering by cloud droplets. The correlated k-distribution routines developed by Kratz (1995) for the AVHRR channels are used to account for atmospheric gaseous absorption. Rayleigh scattering is used to account for scattering by molecules.

1.4 Outline of the dissertation

Chapter 2 compares results of the spatial coherence, CLAVR, and an ISCCP-like threshold method. Section 2.1 is an introduction. Section 2.2 briefly describes the three methods. Section 2.3 compares the cloud-free properties derived by the spatial coherence method and CLAVR. Section 2.4 compares the cloud properties derived by all three methods. Section 2.5 discusses the discrepancies found between the three methods. Chapter 3 describes the cloud property retrieval scheme. Section 3.1 is the introduction. Section 3.2 describes the radiative transfer model for the cloud layer. Section 3.3 describes the calculations of atmospheric absorption and scattering. Section 3.4 describes the iterative procedure of the cloud property retrieval scheme. Section 3.5 presents the retrieved cloud properties and the comparison with retrievals obtained using the Platnick-Twomey scheme. Section 3.6 presents the sensitivity of the retrieval scheme to approximations often employed in similar schemes.

Chapter 4 estimates biases in cloud properties retrieved by assuming that partly cloud-covered pixels are due to overcast conditions. Chapter 4 also examines the satellite view angle dependence in the retrieved cloud properties. Section 4.1 is the introduction. Section 4.2 describes the procedures used to retrieve low-level cloud properties from the March 1989 data. Section 4.3 shows the spatial and temporal occurrences of single-layered, low-level cloud systems. Section 4.4 compares low-level cloud properties retrieved from the overcast and partly cloud-covered pixels. Section 4.5 shows the effect of satellite view angle on the retrieved cloud properties. Section 4.6 further investigates the cloud droplet effective radii retrieved from pixels containing broken clouds.

Chapter 5 examines the cloud visible optical depth and temperature relationship for single-layered, low-level cloud systems. Section 5.1 is the introduction. Section 5.2 describes cloud optical depth feedback. Section 5.3 presents ISCCP low-level cloud visible optical depths and temperatures. Section 5.4 presents the variations of cloud visible optical depth with cloud top temperature and 740–mb atmospheric temperature. Section 5.5 presents the variations of cloud visible optical depth with sea surface temperature. Section 5.6 discusses the relationships between cloud visible optical depths and temperatures.

Chapter 6 investigates relationships between cloud visible optical depth, cloud liquid water path, cloud droplet effective radius, and sea surface-cloud top temperature difference for single-layered, low-level cloud systems. Section 6.1 is the introduction. Section 6.2 presents the cloud liquid water paths obtained for the single-layered, low-level systems. Section 6.3 shows the effect of partly cloud-covered pixels on cloud liquid water path and droplet effective radius retrievals. Section 6.4 presents the relationships obtained between cloud visible optical depth, cloud liquid water path, and droplet effective radius. Section 6.5 presents the variations of cloud liquid water path and droplet effective radius with cloud top temperature. Section 6.6 shows the variations of cloud liquid water path and droplet effective radius with sea surface-cloud top temperature difference. Section 6.7 discusses the role of cloud vertical thickness in determining low-level marine cloud liquid water path, optical depth, and droplet effective radius.

Chapter 7 contains concluding remarks.

Chapter 2
Cloud Detection Using the Spatial Coherence, CLAVR, and an ISCCP-Like Threshold Method

2.1 Introduction

Meteorological satellites have made possible global observations of clouds. Many cloud analysis methods have been suggested for the detection of clouds from satellite imagery data (e.g., Coakley and Bretherton, 1982; Rossow et at., 1985; Rossow and Garder, 1993; Stowe et al., 1997). These methods have been used to detect the presence of clouds based on the radiance field of the imagery data and to determine the cloud amount. The radiances for imagery pixels (typically 4–8 km in resolution for global coverage) that are determined to be cloudy are used to derive cloud reflectivities, brightness temperatures, and/or more physical properties, such as optical depth, droplet size, and liquid/ice water path. This chapter focuses on cloud detection and the derivations of fractional cloud cover, reflectivities, and brightness temperatures. The next chapter, presents a radiation model and the retrievals of cloud optical depth, droplet effective radius, and cloud top emission temperature.

In this chapter, the spatial coherence method (Coakley and Bretherton, 1982), CLAVR (Clouds from AVHRR, Stowe et al., 1997), and a threshold method based on ISCCP (International Satellite Cloud Climatology Project) procedures (Rossow and Garder, 1993) for extracting clouds from satellite observations are explored. The three methods were applied to NOAA-11 AVHRR 4-km GAC data taken from oceanic daytime passes to identify pixels that were either cloud-free, overcast, or partially cloud-covered. In the case of ISCCP, pixels are identified as being cloud-free, cloudy, or overcast. The fraction of pixels identified as either cloudy or overcast is taken to be the cloud cover, but only the overcast pixels are used to obtain the cloud properties. Cloud-free properties derived by CLAVR were compared to those derived by the spatial coherence method. Cloud properties and cloud cover fractions were derived for 250-km and 60-km-scale regions containing only single-layered cloud systems and compared for the three methods.

The primary objective of the comparisons is to investigate differences in the cloud properties derived by the three methods. Such comparisons are essential because, first, the cloud properties derived by ISCCP are receiving considerable use in assessments of the effect of clouds on the earth's radiation budget (Hartmann et al., 1992), the relationship between low-level cloud optical depth and temperature (Tselioudis et al., 1992), the global distribution of water-cloud droplet size (Han et al., 1994), and the relationship between cloud droplet size and cloud albedo (Han et al., 1997). In ISCCP, cloud properties are obtained through the application of radiance thresholds (Rossow and Garder, 1993). Threshold methods use predetermined threshold values to distinguish between pixels that are cloud-free and cloud-contaminated. The pixels that are identified as being cloud-contaminated are treated as being completely overcast. These cloud-contaminated pixels are divided into cloudy and overcast pixels by additional threshold. Radiances obtained for these overcast pixels are used to derive cloud properties for ISCCP. As was shown in Coakley and Kobayashi (1989) and in Coakley (1991), properties of broken clouds are distinctly different from those of uniform, overcast clouds. If many of the pixels identified by ISCCP as being overcast were in fact only partly cloud-covered and if these partly cloud-covered pixels were taken to be overcast, many of the properties attributed to clouds in the ISCCP data stream would be biased (Wielicki and Parker, 1992; Chang and Coakley, 1993).

CLAVR is being developed as an operational routine by NOAA/NESDIS (Stowe et al., 1997). Unlike ISCCP, both CLAVR and the spatial coherence method seek to identify pixels that are either cloud-free, overcast, or partly cloud-covered. CLAVR and the spatial coherence method use different approaches to identify cloud-free and overcast pixels. CLAVR bases the identification on a decision-tree procedure which incorporates various thresholds applied to the pixel-scale radiances and to the variability of the radiances in 2×2 arrays of the 4-km GAC pixels. The spatial coherence method employs a cluster scheme to identify overcast or cloud-free 2×2 arrays exhibiting low spatial variability in the 11-μm radiance field and having mean radiances that form relatively tight clusters in the 11-μm radiance domain. The properties of cloud-free regions and the properties of single-layered clouds derived by CLAVR are compared with those derived by the spatial coherence method to assess the performance of CLAVR.

This study focuses on single-layered cloud systems. Such cloud systems are relatively easy to identify from satellite imagery data (Coakley and Bretherton, 1982). Single-layered cloud systems, like marine stratus and stratocumulus often extend over large oceanic regions $\geq (250 \text{ km})^2$. In all cloud retrieval schemes, clouds are assumed to behave like plane-parallel, horizontally homogeneous clouds. Single-layered cloud systems are expected to exhibit such behavior more closely than would more complex cloud systems. This study uses the spatial coherence method to identify the single-layered systems.

2.2 Data analysis

2.2.1 AVHRR GAC data

AVHRR 4-km GAC (Global Area Coverage) data from NOAA-11 is used for this study. The AVHRR imager has five channels at wavelengths of 0.63 (0.58–0.68) μm, 0.89 (0.72–0.98) μm, 3.7 (3.55–3.93) μm, 11 (10.3–11.3) μm, and 12 (11.5–12.5) μm. The instantaneous field of view of each channel is approximately 1.4 milliradians leading to a nadir resolution of 1.1 km for a satellite altitude of 833 km. AVHRR scans perpendicularly to the orbital motion of the NOAA satellite. The scanning rate is 360 scan lines per minute. GAC data is produced by a processor on board the satellite which samples the real-time AVHRR data. Four out of every five samples along the scan line are used to compute an average value, and the data from only every third scan line are processed. The volume of GAC data is much smaller than the volume of the original AVHRR data. The spatial resolution of GAC pixels at nadir is taken to be 4 km (Kidwell, 1991).

One day of AVHRR GAC data obtained on September 6, 1989 was analyzed by NOAA/NESDIS (NOAA National Environmental Satellite Data Information and Service) using CLAVR Phase II algorithm to identify pixels that were either cloud-free, overcast, or mixed (partly cloudy). The amount of the CLAVR Phase II data available for this study is currently limited. The AVHRR satellite orbits the globe approximately 14 times per day. The single day of data covers the entire earth. Only daytime passes over oceanic regions between 55°N-55°S were used for this study. The data was analyzed by the spatial coherence method to identify 60-km-scale regions which contained only single-layered cloud systems. The comparisons of cloud properties derived by the spatial coherence method, CLAVR, and an ISCCP-like threshold method were performed for these single-layered systems.

2.2.2 The spatial coherence analysis

The spatial coherence method (Coakley and Bretherton, 1982) was applied to the September 6, 1989 AVHRR GAC data to identify single-layered clouds over oceans which extended over moderately large regions $\geq (250 \text{ km})^2$. In addition, the regions containing single-layered clouds had overcast and cloud-free pixels that spanned several of the 2×2 pixel arrays somewhere within the region. The spatial coherence method utilizes the local spatial variability of the 11-μm radiance field to identify pixels that are cloud-free and pixels that are overcast by the single-layered cloud system. The radiances associated with cloud-free pixels are emitted primarily from the cloud-free ocean and the radiances associated with the overcast pixels are emitted primarily from the cloud layer. The pixels having radiances which lie between those for the overcast and those for the cloud-free pixels are taken to be partially covered by the single-layered clouds.

Figure 2.1 shows images constructed from the AVHRR 11-μm and 0.63-μm radiances for a geographic region of approximately 2400 km × 2000 km. The region contains 384 × 512 (scan spots × scan lines) of GAC pixels and is obtained from a 5–minute orbital segment over the western Pacific ocean centered at about (25°N, 157°E). The images are constructed so that clouds appear as light objects against the dark ocean background. The purple areas denote regions having low 11-μm emission temperatures (high-level clouds) and large 0.63-μm reflectivities (optically thick clouds).

Figure 2.2a shows the spatial coherence analysis of 2×2 pixel arrays for a typical single-layered cloud system over ocean. The radiances are from Box A in Figure 2.1. The data covers an area of approximately (250 km)^2 and contains 64×64 GAC pixels. The local means and standard deviations of the AVHRR 11-μm radiances are shown for every 2×2 pixel array. Each point in the figure represents an (8 km)^2 portion within the (250 km)^2 area. The points (solid circles) with low standard deviations and relatively large 11-μm local mean radiances (near 105 mWm^{-2}sr^{-1}cm) are associated with the emission from the cloud-free ocean. The pixels that contribute to these points are taken to be cloud-free. The points (crosses) with low standard deviations and relatively small 11-μm local mean radiances (near 20 mWm^{-2}sr^{-1}cm) are associated with the emission for overcast pixels. The pixels that contribute to these points are taken to be overcast. The remaining points (open circles) with larger standard deviations and forming an arch between those cloud-free and overcast pixels are taken to be partially covered by the single-layered cloud system. The spatial coherence method incorporates a clustering scheme to automatically determine the pixel arrays that make up the cloud-free and the overcast feet of the arch. The scheme identifies pixel arrays as cloud-free or overcast if they exhibit locally uniform 11-μm radiances that also form a tight cluster in the domain of the local mean 11-μm radiances (Coakley and Bretherton, 1982).

Figure 2.2b shows a two-layered cloud system which is obtained from square B in Figure 2.1. The spatial coherence analysis shows that the 250-km-scale region appears to contain a low-level system with 11-μm emission near 65 mWm^{-2}sr^{-1}cm and

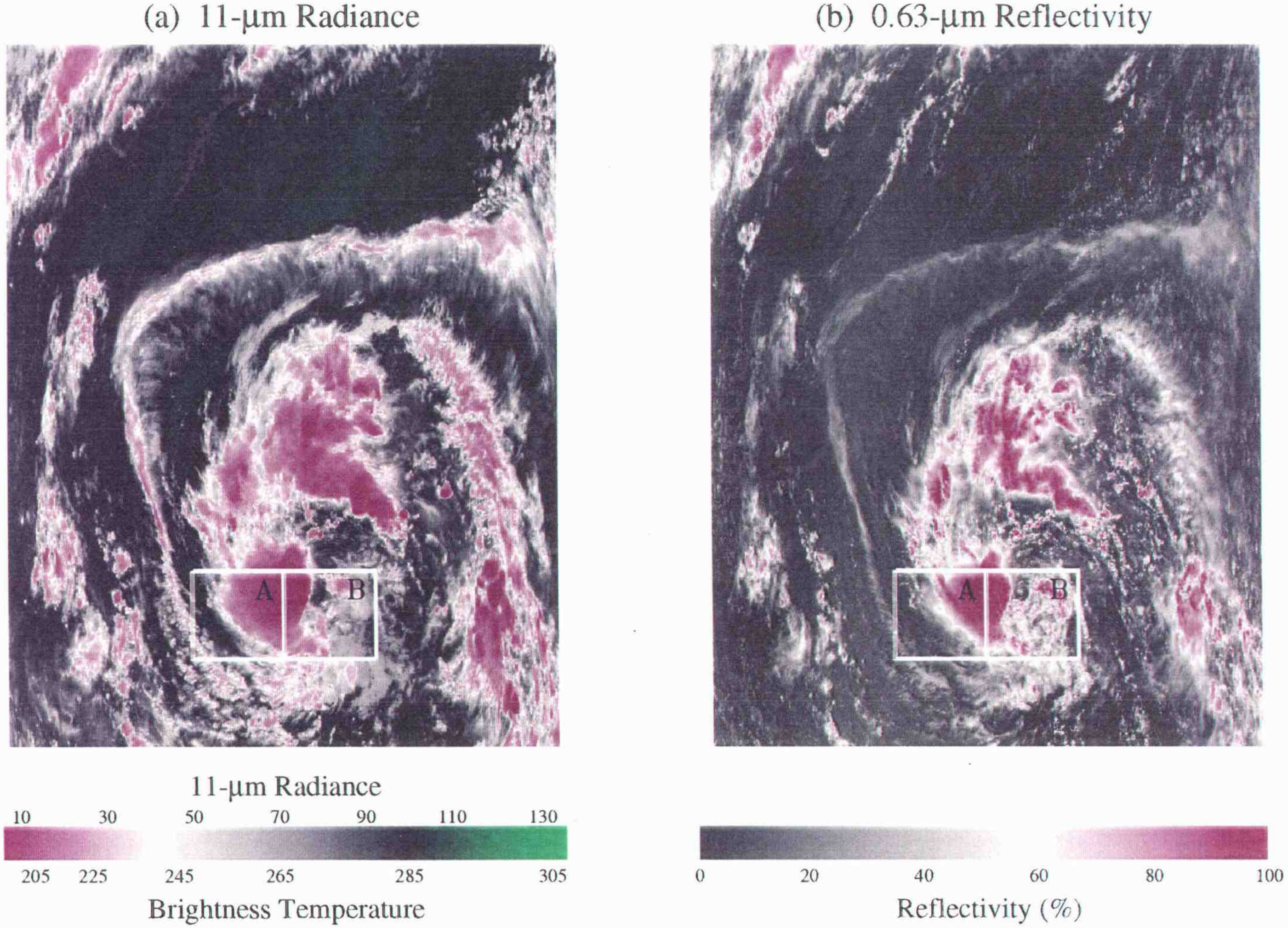
(a) 11-µm Radiance
(b) 0.63-µm Reflectivity
A
B
A
B
11-µm Radiance
10 30 50 70 90 110 130
205 225 245 265 285 305
Brightness Temperature
0 20 40 60 80 100
Reflectivity (%)

Figure 2.1 NOAA-11 AVHRR 4-km GAC data for (a) 11 µm and (b) 0.63 µm. The images are approximately 2400 km x 2000 km (384 x 512 pixels) for September 6 1989 over the Pacific ocean off the coast of Japan. The Boxes indicate 250-km regions.

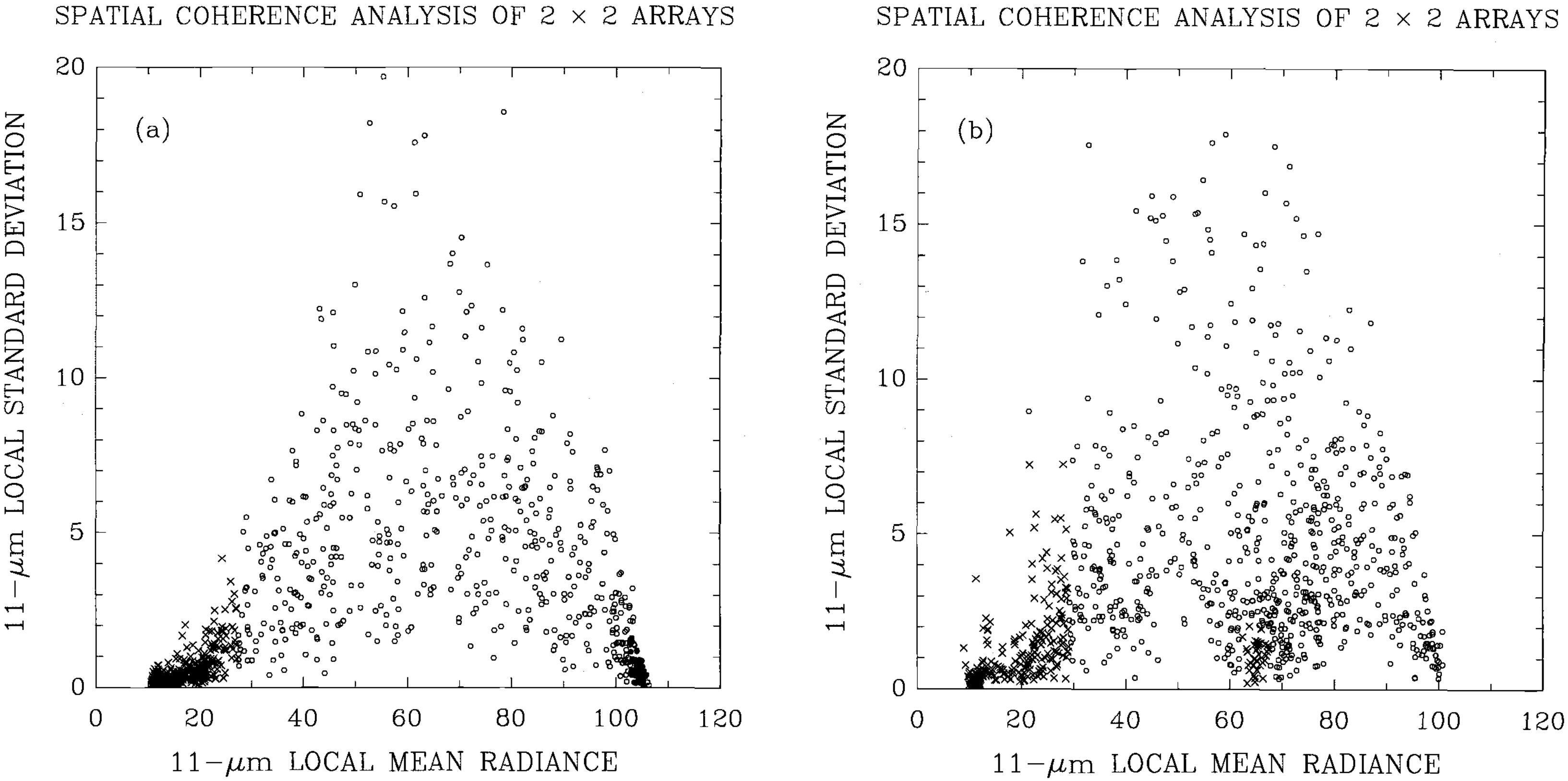

Figure 2.2 Local means and standard deviations of 11-μm radiances (mWm^{-2}sr^{-1}cm). Results were obtained using the spatial coherence method for a 250-km region. Each point gives the local mean and standard deviation for the 4 pixels in a 2 × 2 (scan spots × scan lines) GAC pixel array. Each point represents an (8 km)^2 portion of the (250 km)^2 region. Crosses denote overcast arrays; solid circles denote cloud-free arrays; and open circles denote partly cloud-covered arrays. (a) is for a single-layered system and (b) for a two-layered system.

an upper-level system with 11-μm emission near 20 mWm^{-2}sr^{-1}cm. The upper-level system appears to belong to the cloud system shown in Figure 2.2a. Note that in Figure 2.2b there are not enough pixel arrays to construct a cloud-free foot. The cloud-free radiance for such a region is determined by interpolation from nearby regions which contain pixels that are identified as being cloud-free.

Figure 2.3 shows the results of the spatial coherence analysis for the data shown in Figure 2.1. Figure 2.3a shows the cloud mask constructed based on the spatial coherence analysis. Pixels belonging to local 2 × 2 arrays which emit and reflect spatially uniform radiances are taken to be cloud-free. These cloud-free pixels are shown in ocean blue. Pixels belonging to 2 × 2 arrays which emit spatially uniform 11-μm radiances but exhibit variability in 0.63-μm reflected radiances are taken to be overcast by a layered cloud system. These overcast pixels are shown as "FOOT" in the cloud mask. The color of the "FOOT" pixels denotes their 11-μm brightness temperatures. The rest of the pixels are shown in different colors which indicate the 11-μm brightness temperature associated with the pixel radiance and in different shading which indicates the fractional cloud cover derived for the pixel. Figure 2.3b shows the pixel-scale cloud cover fraction. The procedures used to construct the cloud mask and to derive pixel-scale cloud cover fraction are described in the appendix.

Table 2.1 shows the number of 250-km-scale regions that are identified by the spatial coherence method as containing single-layered cloud systems. The number of 250-km regions that are cloud-free or contain more complex cloud systems are also shown. The table shows that, for this single day of analyzed data, about 4% of the 250-km regions were found to be cloud-free ($A_c < 0.05$) and 26% were found to contain a single-layered cloud system. For the 250-km regions that contained a

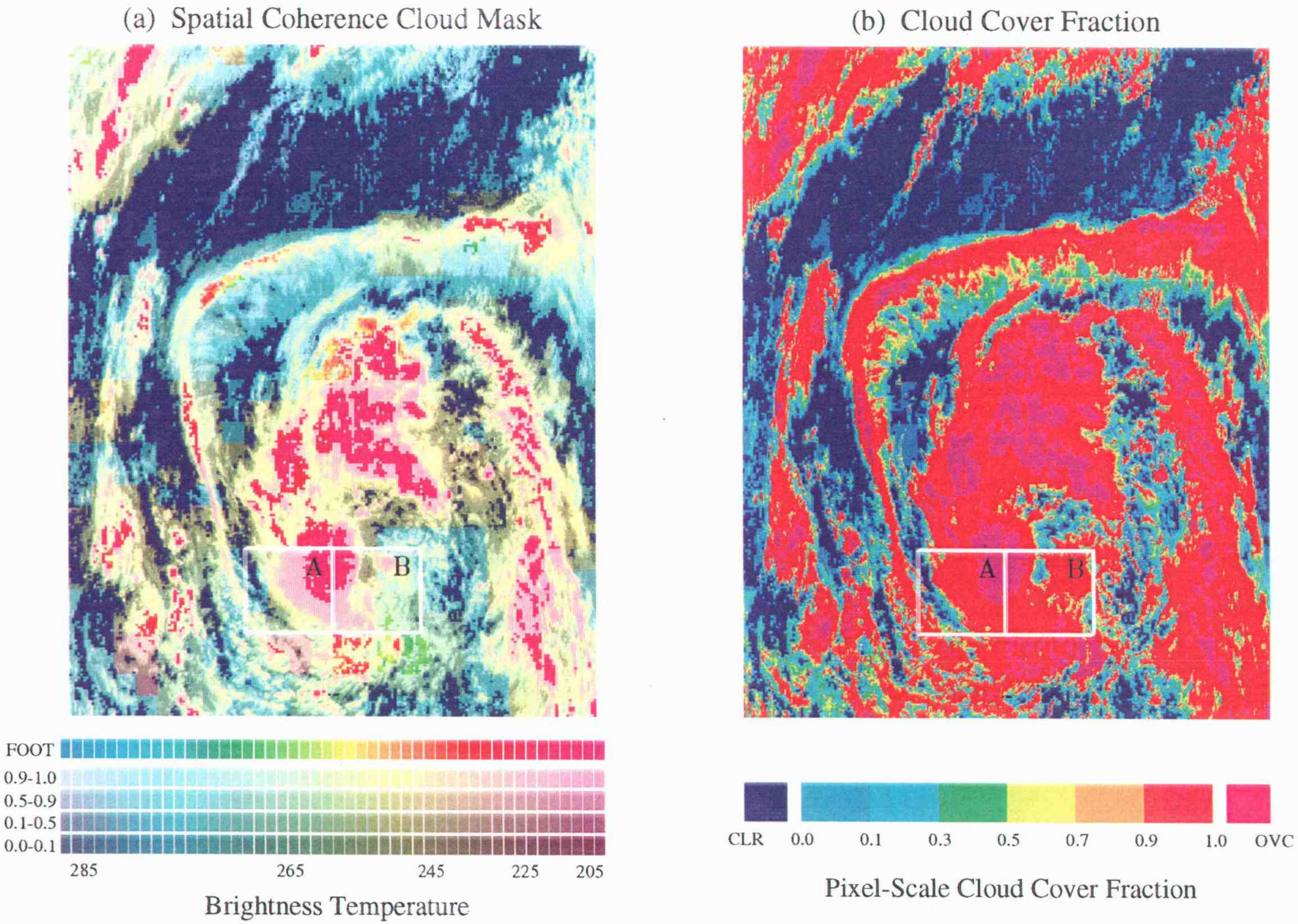
(a) Spatial Coherence Cloud Mask
(b) Cloud Cover Fraction
A
B
A
B
FOOT
0.9-1.0
0.5-0.9
0.1-0.5
0.0-0.1
285
265
245
225
205
Brightness Temperature
CLR
0.0
0.1
0.3
0.5
0.7
0.9
1.0
OVC
Pixel-Scale Cloud Cover Fraction

Figure 2.3 Spatial coherence analysis for the data shown in Figure 2.1. (a) cloud mask and (b) pixel-scale cloud cover fraction.

Table 2.1 Number of 250-km regions identified as being cloud-free, covered by a single-layered cloud system, or covered by more complex clouds.

Cloud-free $A_c < 0.05$	Single-layered $A_c < 0.95$	Single-layered $A_c > 0.95$	More complex $0 \leq A_c \leq 1$
79	538	8	1463

Table 2.2 Number of 60-km regions identified as being cloud-free, overcast, or partially cloud-covered. The 60-km regions were taken from the 250-km regions containing single-layered systems, as shown in Table 2.1.

Cloud-free $A_c < 0.05$	Partly cloud-covered $0.05 \leq A_c \leq 0.95$	Overcast $A_c > 0.95$
946	7153	637

single-layered cloud system, about 98.5% were found to be partially covered by the layered clouds. Furthermore, the 60-km-scale regions which constituted those 250-km regions containing single-layered systems were divided into cloud-free, overcast, and partly cloud-covered categories. Table 2.2 shows the numbers obtained for these three categories. About 11% of the 60-km regions were found to be cloud-free and 7% were found to be overcast. Most of the 60-km regions were partially covered by the layered cloud systems.

2.2.3 CLAVR decision-tree analysis

CLAVR (Clouds from AVHRR) is currently being developed by NOAA/NESDIS as an operational routine for cloud detection and cloud classification using AVHRR data

(Stowe et al., 1997). The September 6, 1989 CLAVR data used in this chapter was analyzed with the CLAVR Phase II algorithm. The CLAVR Phase II algorithm uses all five channels of AVHRR data to detect clouds and then classifies overcast pixels as being covered by either low-, mid-, or high-level clouds (Stowe et el., 1997). The algorithm uses the multispectral radiances, radiance differences, and spatial variations in sequential decision-tree tests. CLAVR, like the spatial coherence method, groups the AVHRR GAC pixels into 2 × 2 pixel arrays. Three different categories: cloud-free, overcast, and mixed, are identified for the 2 × 2 pixel arrays. The rules for identifying these pixels are briefly described as follows:

If all four pixels in the array fail all of the cloud-contamination tests, then all four pixels are labeled as cloud-free (cloud cover fraction = 0). If all four pixels pass at least one of the cloud-contamination tests, then the four pixels are labeled as overcast (cloud cover fraction = 1). If only 1 to 3 pixels pass the cloud-contamination tests, then all four pixels are labeled as mixed and assigned an arbitrary cloud cover fraction of 0.5. If all four pixels that have been identified as being mixed or overcast satisfy a clear restoring test, then these pixels are re-classified as "restored-clear". The specific tests are described in Stowe et al. (1997).

Figure 2.4 shows the CLAVR analysis of the 2 × 2 pixel arrays for the data shown in Figure 2.2. Unlike the spatial coherence method, CLAVR does not use a clustering scheme in the 11-μm radiance domain. A comparison of Figures 2.2 and 2.4 indicates that CLAVR identifies many more pixels as being overcast than does the spatial coherence method. The large fraction of overcast pixels for CLAVR is due to the use of a gross cloud-reflectivity threshold for the visible channel. CLAVR applies relatively stringent spatial-uniformity test to the 11-μm radiance field and as a

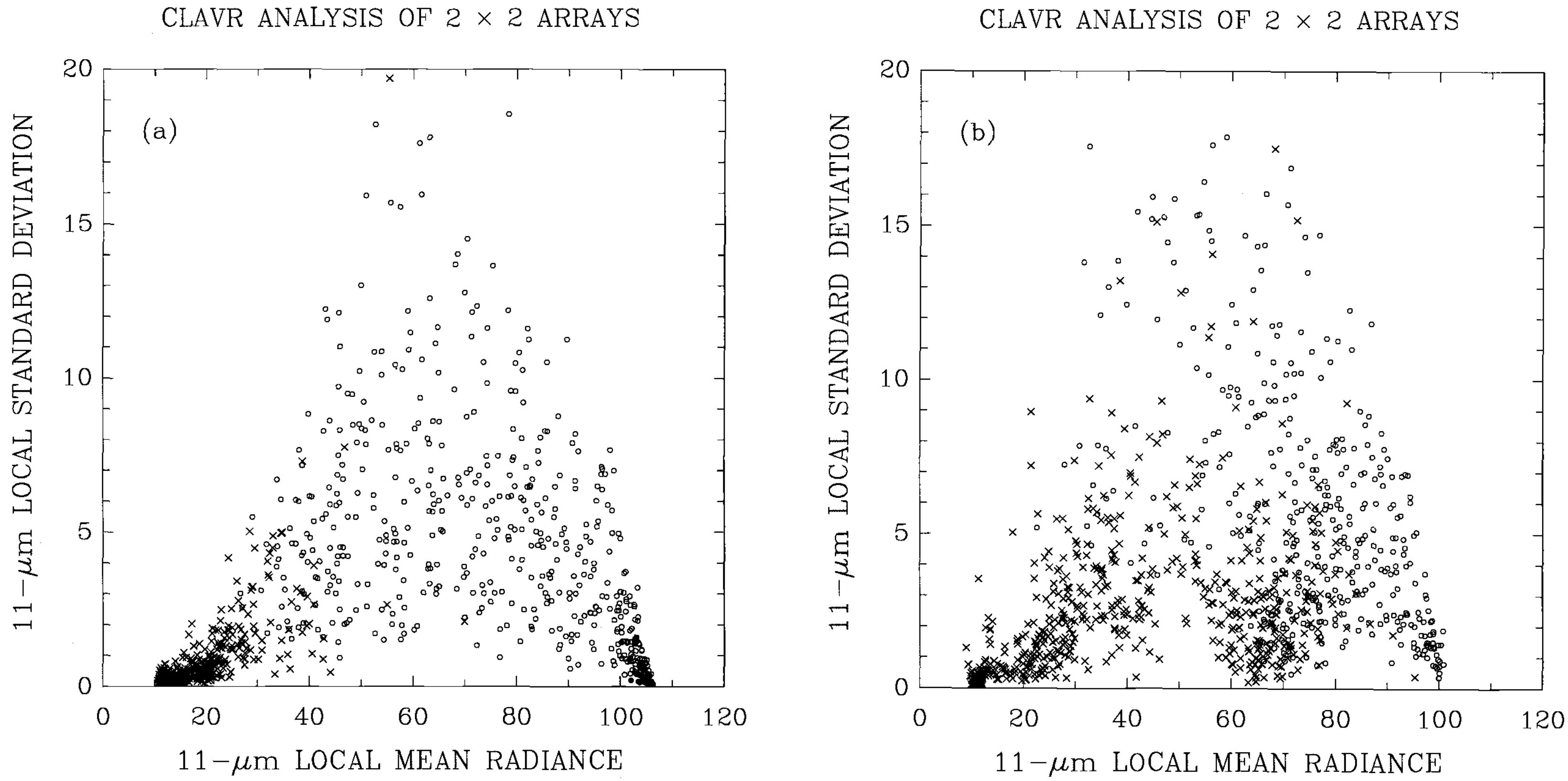

Figure 2.4 Same as Figure 2.2, except that the results are for the CLAVR analysis.

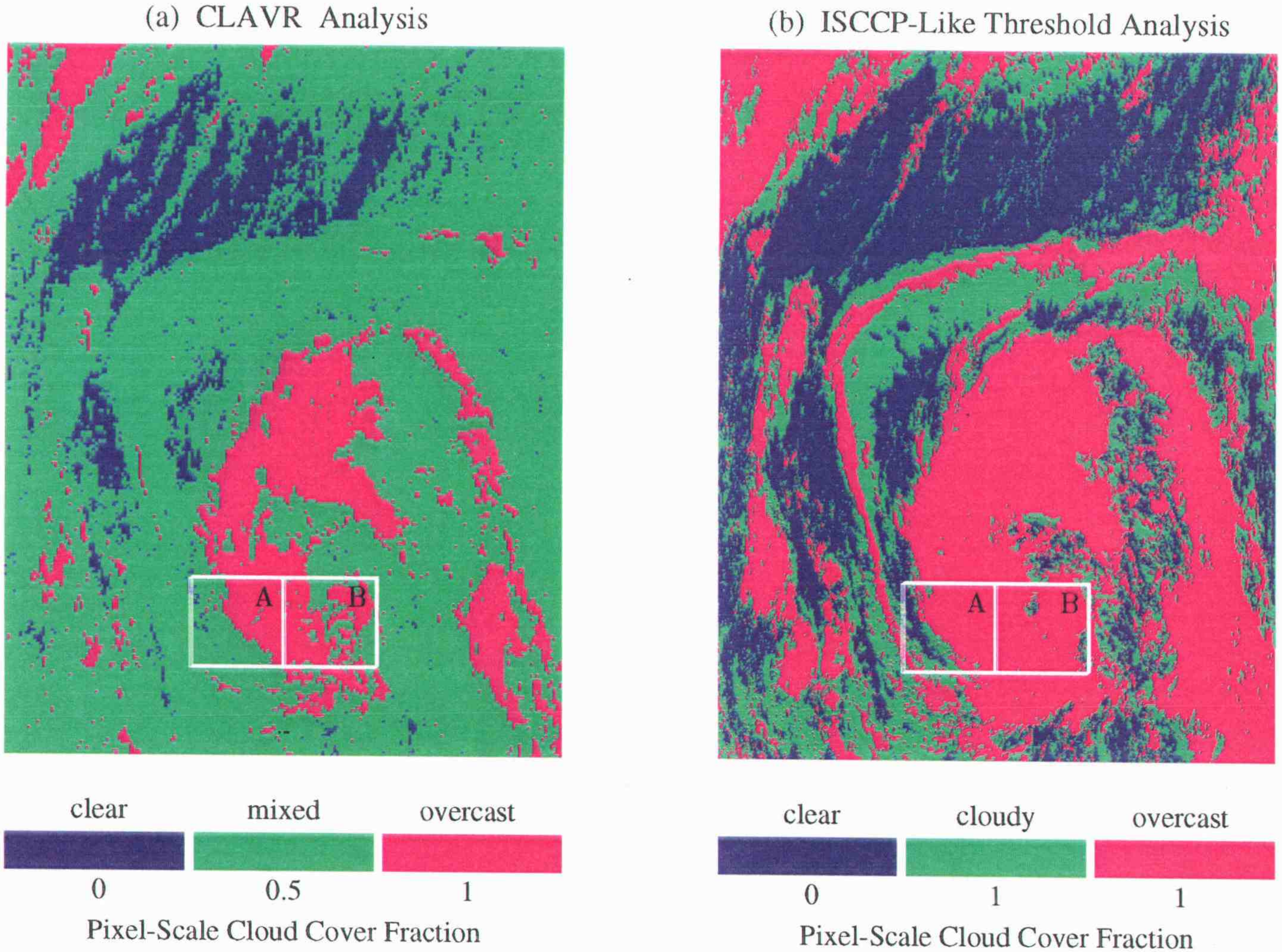
(a) CLAVR Analysis
(b) ISCCP-Like Threshold Analysis
A
B
A
B
clear
mixed
overcast
0
0.5
1
Pixel-Scale Cloud Cover Fraction
clear
cloudy
overcast
0
1
1
Pixel-Scale Cloud Cover Fraction

Figure 2.5 Pixel-scale cloud cover fraction obtained for the data shown in Figure 2.1. (a) CLAVR and (b) ISCCP-like threshold analysis.

result, CLAVR identifies fewer cloud-free pixel arrays than does the spatial coherence method as shown in Figure 2.4a. Figure 2.5a shows results of the CLAVR analysis for the images shown in Figure 2.1. The comparison with Figure 2.3 reveals that CLAVR identifies fewer cloud-free pixels, particularly in regions where broken clouds are extensive.

2.2.4 ISCCP-like threshold analysis

ISCCP was established in July 1983 as part of the World Climate Research Program (WCRP) in order to gain information on global observations of clouds and then to improve the treatment of clouds in climate models (Schiffer and Rossow, 1983). The ISCCP cloud analysis algorithm uses two channels, one visible and one infrared, for cloud detection (Rossow and Schiffer, 1991; Rossow and Garder, 1993). The ISCCP algorithm compares each observed radiance value with a corresponding "clear-sky composite" value. For each pixel, clouds are assumed to be present if the infrared and visible radiances for the pixel differ from the "clear-sky" values by more than the uncertainty in the radiances attributed to the "clear-sky" values. The algorithm is based on the premise that the observed visible and infrared radiances are affected by only two conditions, "cloudy" and "clear," and that the ranges of radiances and their variability associated with these two conditions do not overlap (Rossow and Garder, 1993). A pixel is classified as "cloudy" if either the visible or the infrared radiance is distinct from the corresponding "clear-sky" radiance by an amount larger than the uncertainty in the "clear-sky" radiance. To determine the fractional cloud cover, ISCCP assigns a cloud cover fraction of 1 for the "cloudy" pixels and 0 for the "clear" pixels. Additional thresholds are also applied to pixel radiances to determine pixels that are "definitely" overcast. Radiances of these pixels are then used to derive cloud properties.

A threshold method was developed to simulate the ISCCP scheme. As is done in ISCCP, 0.63-μm reflectivities were first normalized by dividing by the cosine of the solar zenith angle and 11-μm brightness temperatures were corrected for the effect of limb darkening (Rossow and Garder, 1993). Then, a 0.63-μm reflectivity threshold, $R_s + \Delta R_s$, and a 11-μm brightness temperature threshold, $T_s - \Delta T_s$, were used to identify the "cloudy" pixels, as shown in Figure 2.5b, where R_s is the "clear-sky" 0.63-μm reflectivity. T_s is the "clear-sky" 11-μm brightness temperature, and $\Delta R_s = 0.03$ and $\Delta T_s = 2.5$K are the ISCCP threshold values for ocean scenes. A pixel which has either a 0.63-μm reflectivity larger than $R_s + \Delta R_s$ or an 11-μm brightness temperature smaller than $T_s - \Delta T_s$ is taken to be "cloudy" by ISCCP. A pixel which has both a 0.63-μm reflectivity larger than $R_s + 2\Delta R_s$ and an 11-μm brightness temperature smaller than $T_s - 2\Delta T_s$ is taken to be "overcast" by ISCCP. The ISCCP cloud reflectivities and brightness temperatures are derived from the "overcast" pixels. The ISCCP cloud cover fractions are derived by counting both the "cloudy" and "overcast" pixels. The calculation of cloud cover fraction is described in Section 2.4. The cloud-free radiances derived by the spatial coherence method were used to determine the "clear-sky" reflectivities and brightness temperatures. The ISCCP-like threshold method was applied to the September 6, 1989 AVHRR GAC data. Figure 2.5b shows results of the ISCCP-like threshold analysis obtained for the images shown in Figure 2.1. The ISCCP-like threshold method produces far greater fractional cloud cover (the fraction of pixels that are identified as cloudy and overcast) than are produced by either the spatial coherence method or CLAVR.

2.3 Comparison of cloud-free properties derived by CLAVR and the spatial coherence method

Cloud-free 0.63-μm reflectivities and 11-μm brightness temperatures are derived from pixels that are identified as being cloud-free. Figure 2.6 shows a) cloud-free 0.63-μm reflectivities and b) cloud-free 11-μm brightness temperatures derived by the spatial coherence method and CLAVR. Each point gives the average values for the cloud-free pixels obtained within a 60-km-scale region. Only regions for which cloud-free pixels were identified by both the spatial coherence method and CLAVR are shown. The cloud-free 0.63-μm reflectivities and the cloud-free 11-μm brightness temperatures derived by the two methods generally agree, except that many of the cloud-free pixels found by CLAVR have large 0.63-μm reflectivities.

The cause of the large cloud-free reflectivities found by CLAVR is illustrated in Figures 2.7–2.10. Figure 2.7 shows data obtained for the southern Atlantic ocean centered at about (10°W, 20°S). The images, constructed in the same way as those shown in Figure 2.1, show an extensive low-level marine stratus cloud layer which spans more than half of the scene. The low-level stratus exhibits large 0.63-μm reflectivities but exhibits 11-μm brightness temperatures close to those for the underlying sea surfaces. Figure 2.8 shows the spatial coherence and CLAVR analyses for the images. In the figure, the larger grids show 250-km-scale regions and the smaller squares show 60-km-scale regions. Many of the pixels identified by CLAVR as being "clear" (those blue pixels next to the scattered red pixels in Figure 2.8b) are identified as being overcast ("FOOT") by the spatial coherence method. These pixels exhibit high 11-μm brightness temperatures and large 0.63-μm reflectivities.

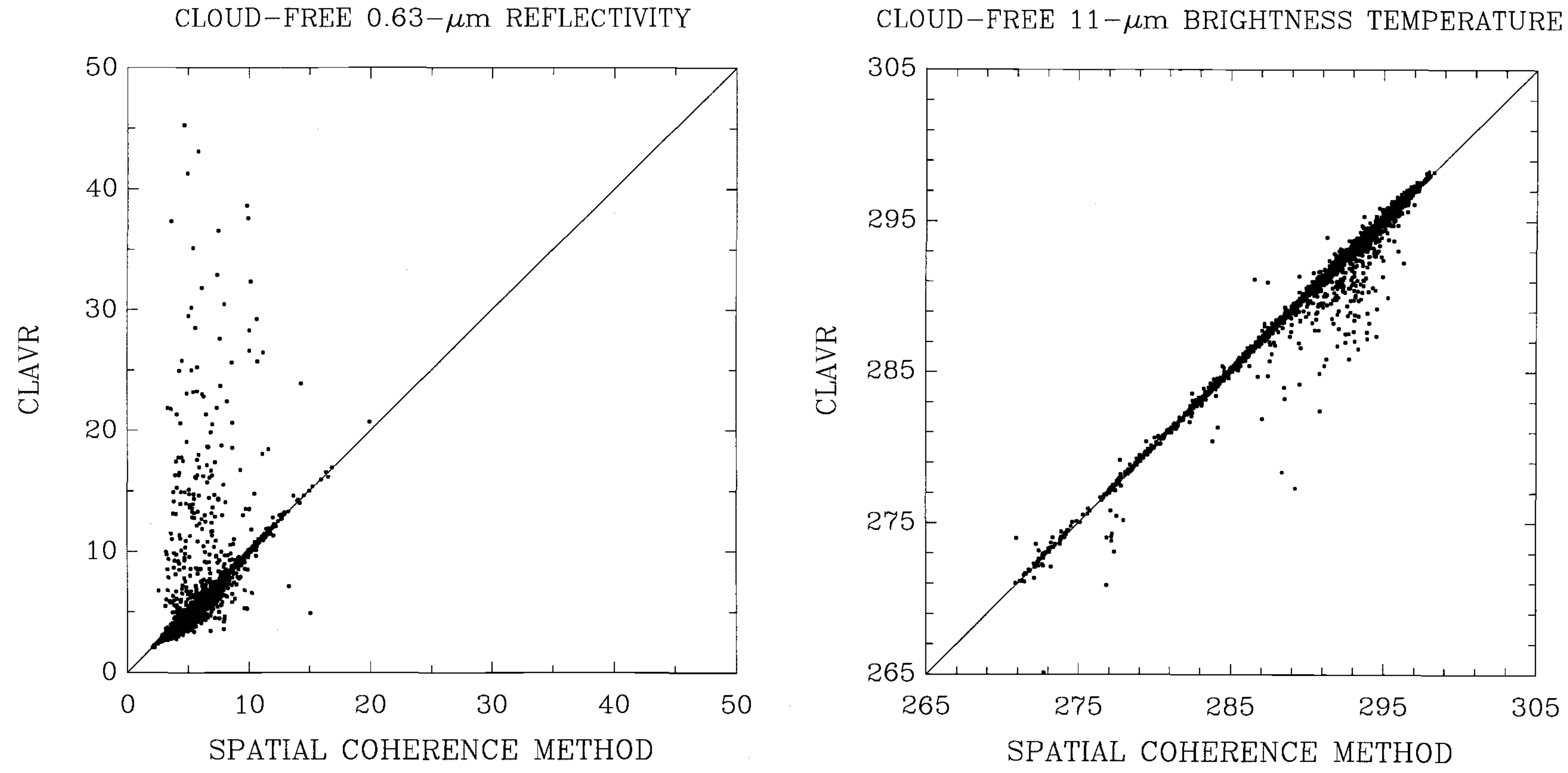

Figure 2.6 Cloud-free (a) 0.63-μm reflectivity (%) and (b) 11-μm brightness temperature (K) obtained by CLAVR and by the spatial coherence method. Each point gives the means of the cloud-free pixels identified by the two methods within a 60-km-scale region.

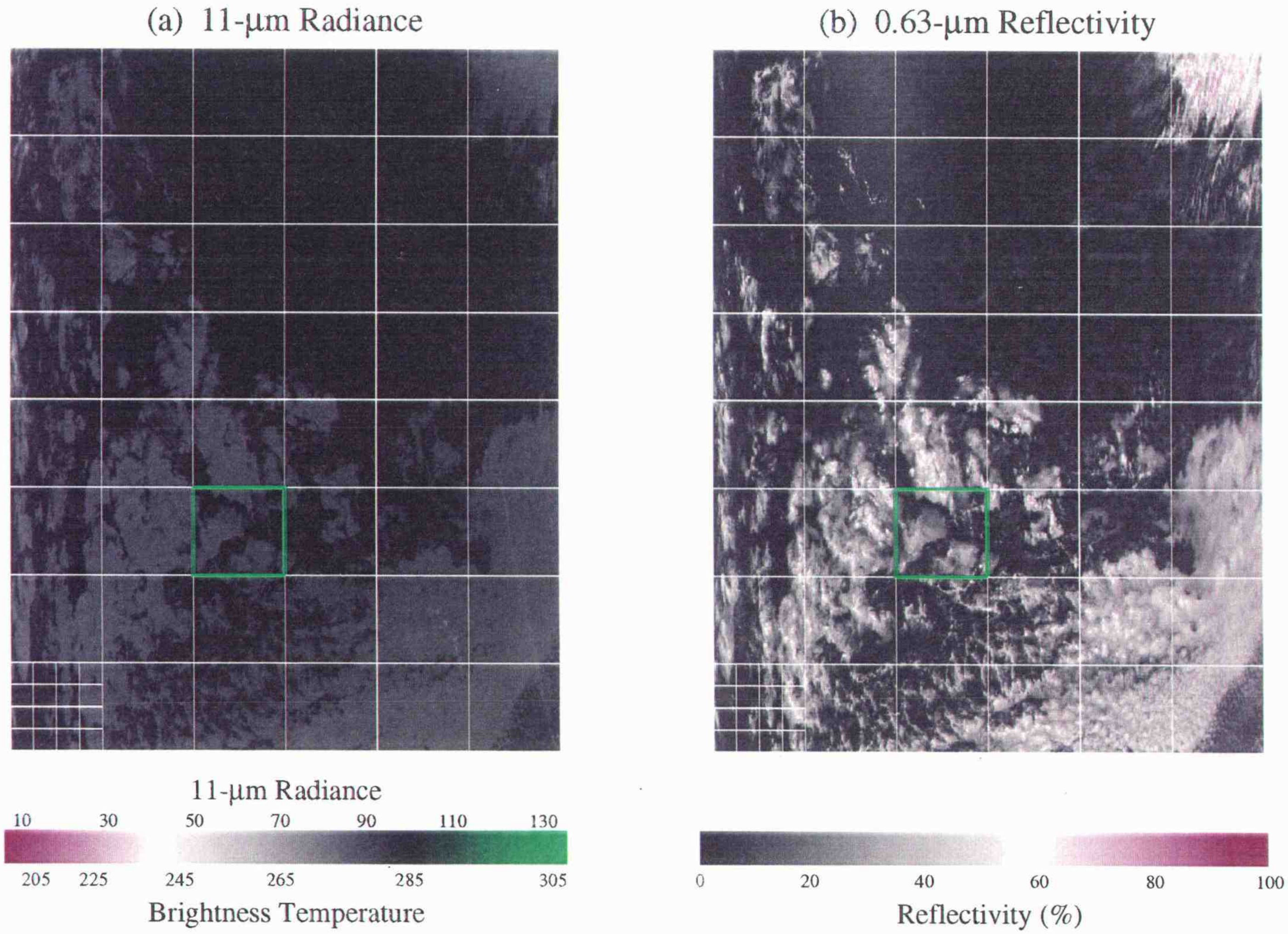
(a) 11-μm Radiance
(b) 0.63-μm Reflectivity
11-μm Radiance
10
30
50
70
90
110
130
205
225
245
265
285
305
Brightness Temperature
0
20
40
60
80
100
Reflectivity (%)

Figure 2.7 Same as Figure 2.1, except that the images are for the Atlantic ocean off the coast of Angola. Smaller squares indicate 60-km-scale regions.

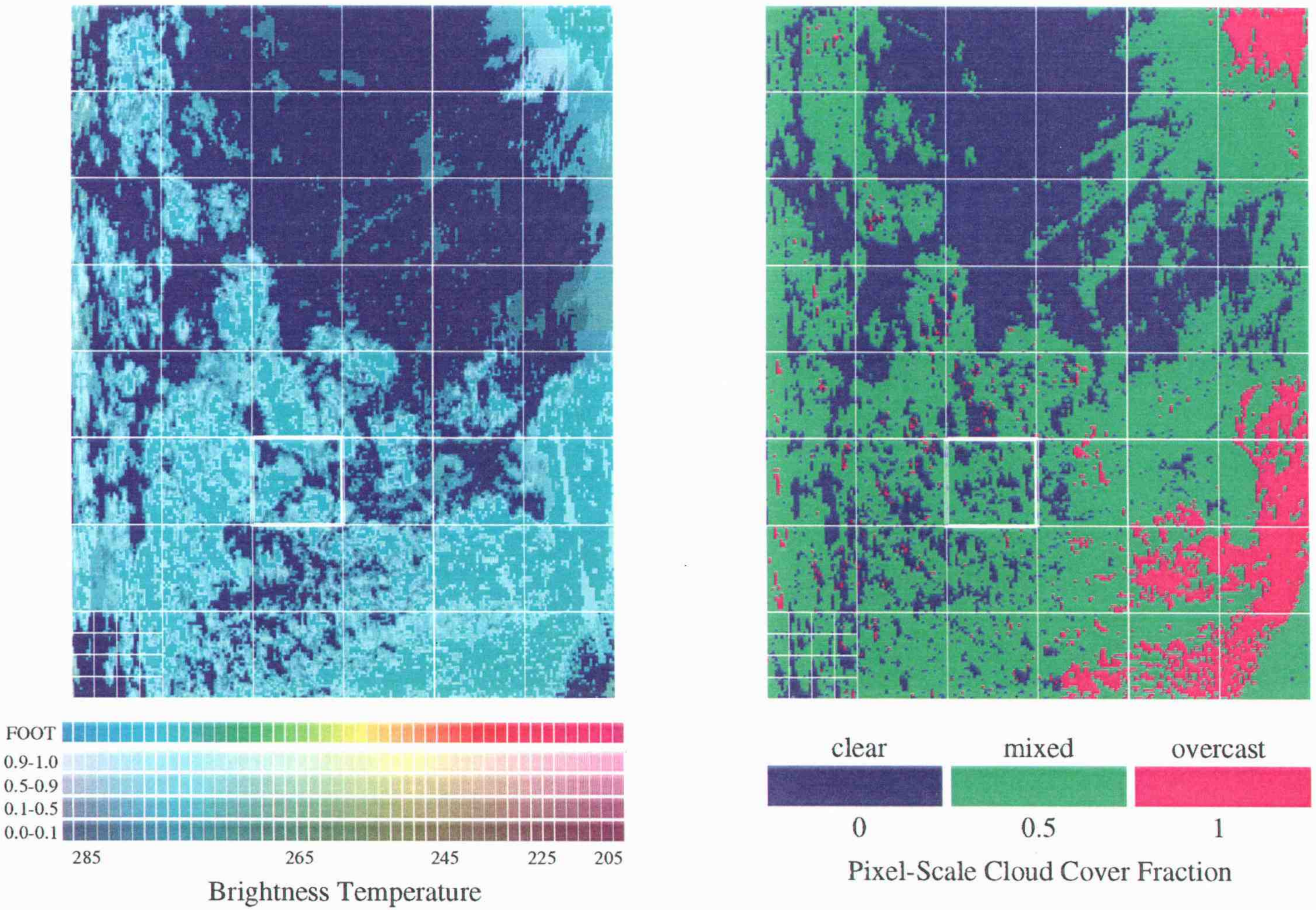

(a) Spatial Coherence Cloud Mask

(b) CLAVR Analysis

FOOT
0.9-1.0
0.5-0.9
0.1-0.5
0.0-0.1
285
265
245
225
205
Brightness Temperature
clear
mixed
overcast
0
0.5
1
Pixel-Scale Cloud Cover Fraction

Figure 2.8 (a) Spatial coherence analysis and (b) CLAVR analysis for the data shown in Figure 2.7.

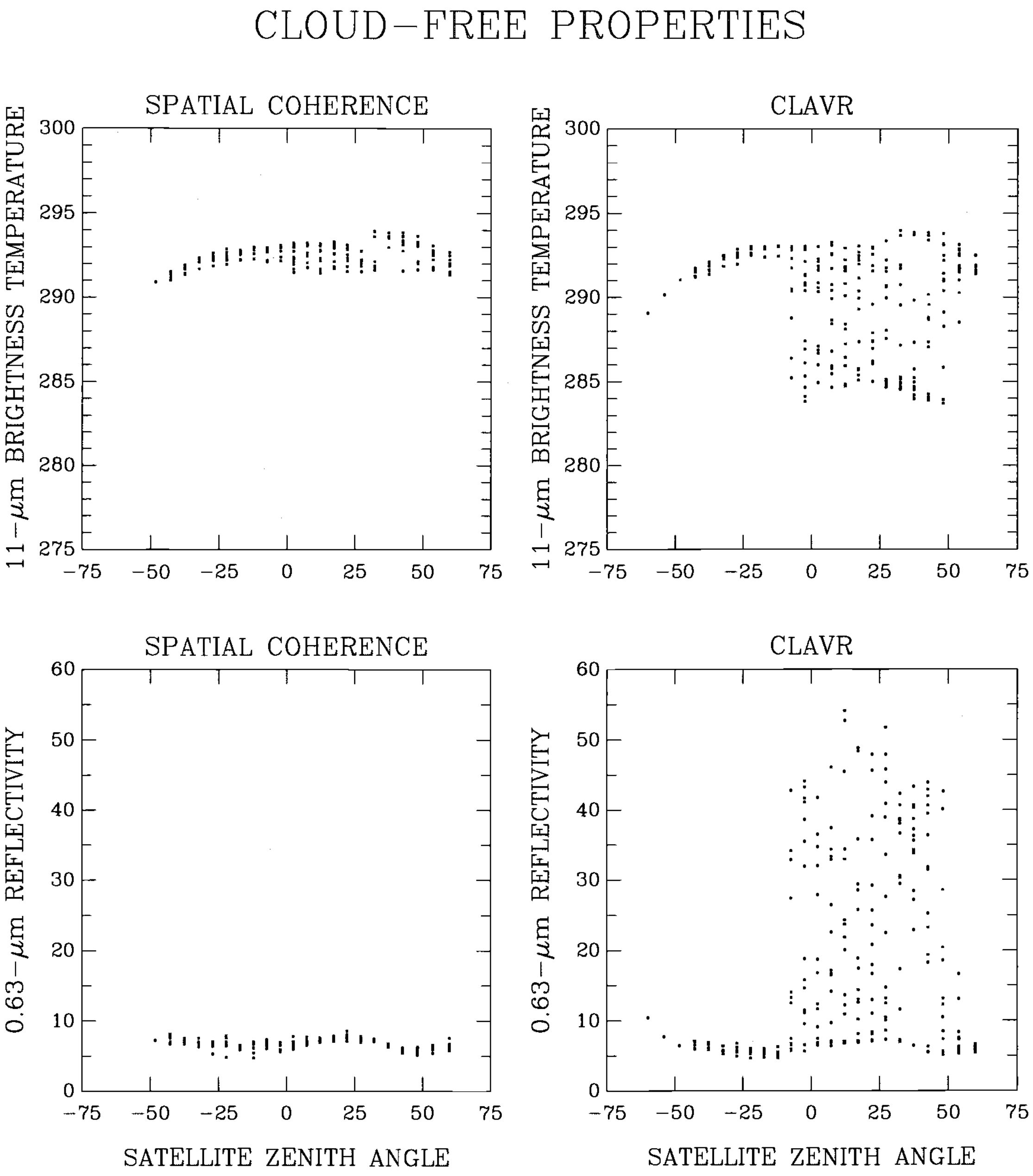

Figure 2.9(a) Cloud-free 11-μm brightness temperatures and 0.63-μm reflectivities and satellite zenith angles obtained by the spatial coherence and CLAVR analyses. Each point gives the mean for a 60-km region. Results obtained for the bottom half of the images shown in Figure 2.7, which contain 24 × 16 60-km regions. Positive satellite zenith angles indicate the direction of forward scattering for reflected sunlight and negative angles indicate the backscattering direction.

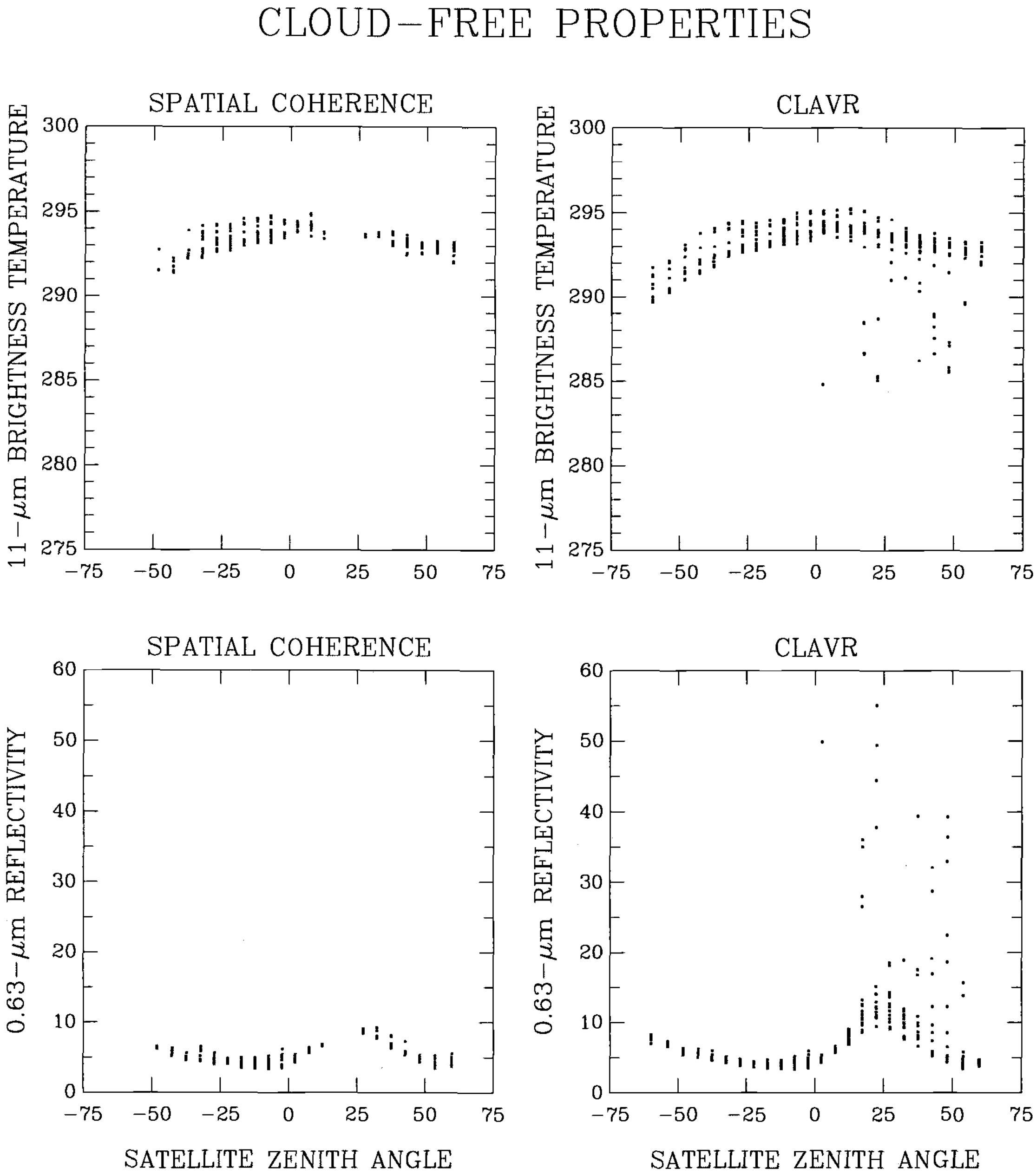

Figure 2.9(b) Same as Figure 2.9a, except that the results are for the upper half of the images shown in Figure 2.7.

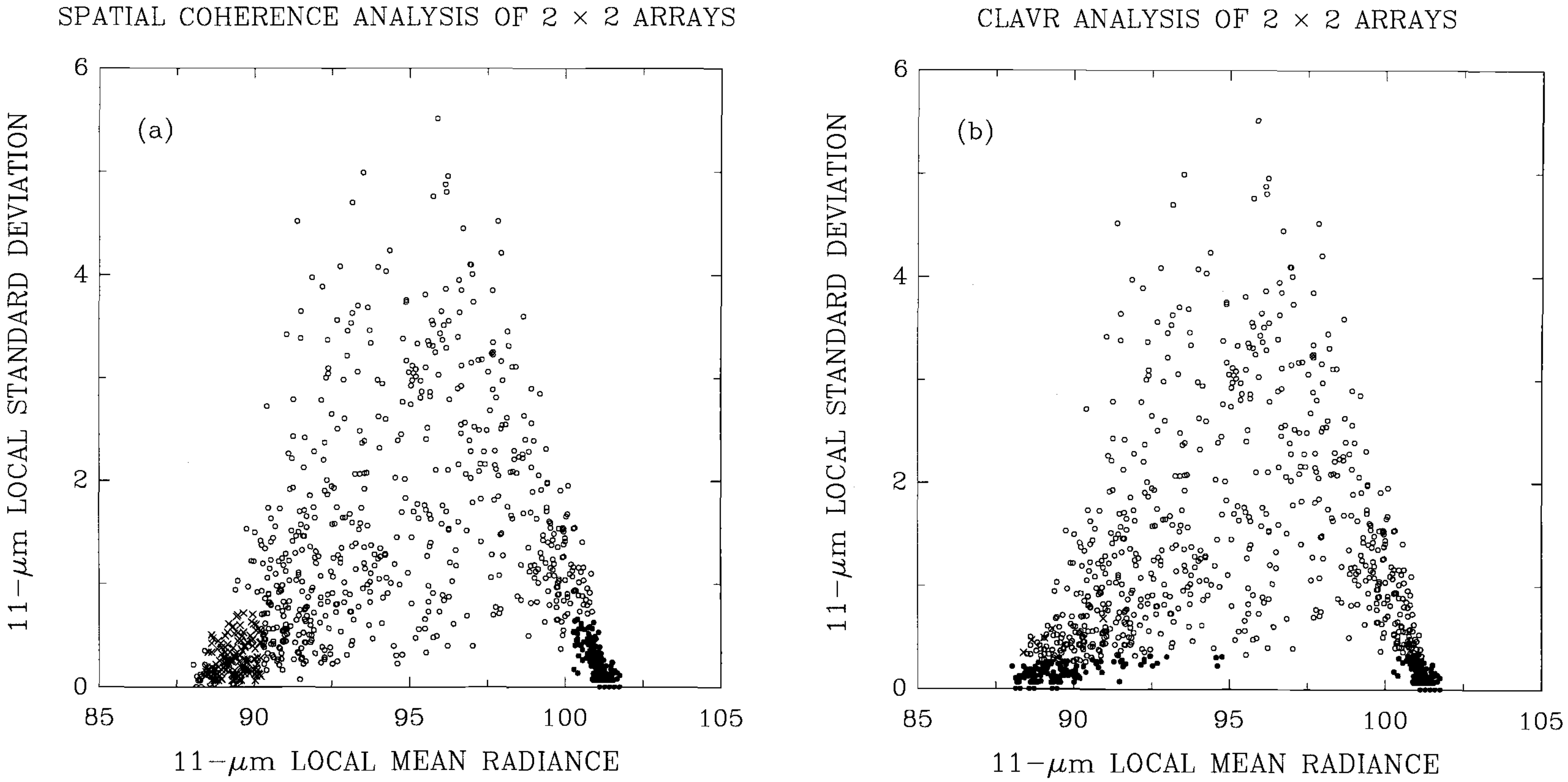

Figure 2.10 (a) Spatial coherence and (b) CLAVR analysis of 2 × 2 pixel arrays. The data is for the 250-km region shown by the green box in Figure 2.7.

Figure 2.9 shows cloud-free 0.63-μm reflectivities and cloud-free 11-μm brightness temperatures as a function of the satellite zenith angle. Figure 2.9a is for the bottom half region shown in Figure 2.7. Figure 2.9b is for the upper half region. Each half region contains 384 × 256 pixels and is divided into 24 × 16 60-km-scale regions. Each 60-km region includes 16 × 16 pixels. In Figure 2.9, each point gives the mean for the cloud-free pixels identified in each 60-km region. The cloud-free reflectivities and brightness temperatures derived by the spatial coherence method appear to cluster together to exhibit a smoothly and slowly varying function of the satellite zenith angle. Unlike the spatial coherence analysis, many of the cloud-free properties derived by CLAVR exhibit relatively large reflectivities and low brightness temperatures. These relatively large reflectivities and low brightness temperatures appear to be cloud-contaminated and are found in regions that CLAVR identifies as being associated with sunglint. Since cloud-free reflectivities can be large in the region of sunglint, the cloud-reflectivity threshold test is bypassed in CLAVR for sunglint regions. Figure 2.10 shows the spatial coherence and CLAVR analyses of 2 × 2 pixel arrays for a sunglint region. The data is for the 250-km region shown by the green square in Figure 2.7. Clearly, a low-level cloud system is shown in the spatial coherence analysis in Figure 2.10a. But, because the 11-μm radiances emitted by the low-level clouds are close to those emitted by the cloud-free ocean, CLAVR fails to identify these pixels as overcast.

2.4 Comparison of cloud properties derived by the spatial coherence, CLAVR, and ISCCP-like threshold methods

Cloud cover fractions and average 0.63-μm reflectivities and 11-μm brightness temperatures for overcast pixels are obtained for both the 250-km and 60-km-scale regions containing single-layered cloud systems. Only 250-km regions that contained cloud-free pixels were considered. The 60-km regions were part of these 250-km regions. Figure 2.11 shows the average 0.63-μm cloud reflectivities for 250-km regions obtained using the three methods. Figure 2.12 shows the averages for 60-km regions. For the ISCCP-like threshold method, the average cloud reflectivities were derived from the "overcast" pixels (pixels have reflectivities and brightness temperatures that pass the double thresholds). The ISCCP-like threshold method produces cloud reflectivities that are systematically smaller than those derived by the spatial coherence method. Cloud reflectivities derived by CLAVR and the spatial coherence method show better agreement. CLAVR tends to produce fewer overcast and cloud-free pixels than does the spatial coherence method. As revealed in Figures 2.8 and 2.10, the fewer overcast and cloud-free pixels result from the restrictive spatial-uniformity threshold, like the threshold applied to 11-μm local standard deviations used in CLAVR. For clouds having large reflectivities, however, CLAVR contains a gross cloud-reflectivity threshold and produces more overcast pixels than does the spatial coherence method. Frequently, partly cloudy pixels have reflectivities that exceed CLAVR's gross cloud-reflectivity threshold test.

Figure 2.13 shows average 11-μm brightness temperatures for overcast pixels within 250-km regions obtained using the spatial coherence, CLAVR, and the ISCCP-like threshold method. Figure 2.14 shows average brightness temperatures for overcast pixels within 60-km regions. Overcast brightness temperatures derived by the ISCCP-like threshold method are systematically higher than those derived by the spatial coherence method and the difference increases as the cloud brightness temperature decreases. Many pixels identified by the ISCCP-like threshold method as being overcast are in fact only partly cloud-covered (Chang and Coakley, 1993). Because

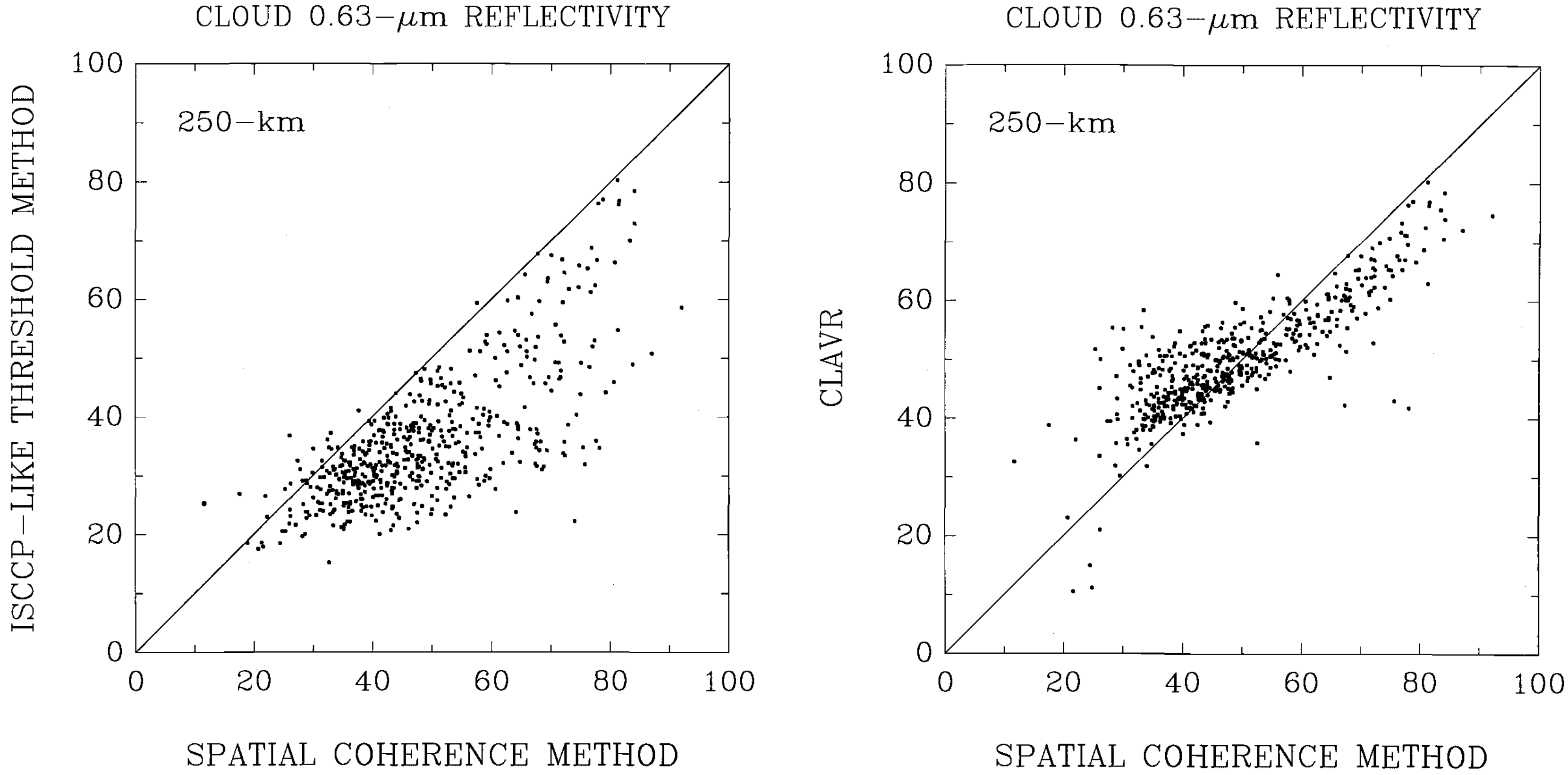

Figure 2.11 Overcast 0.63-μm reflectivities for 250-km-scale regions. (a) ISCCP-like threshold and spatial coherence analysis and (b) CLAVR and spatial coherence analysis.

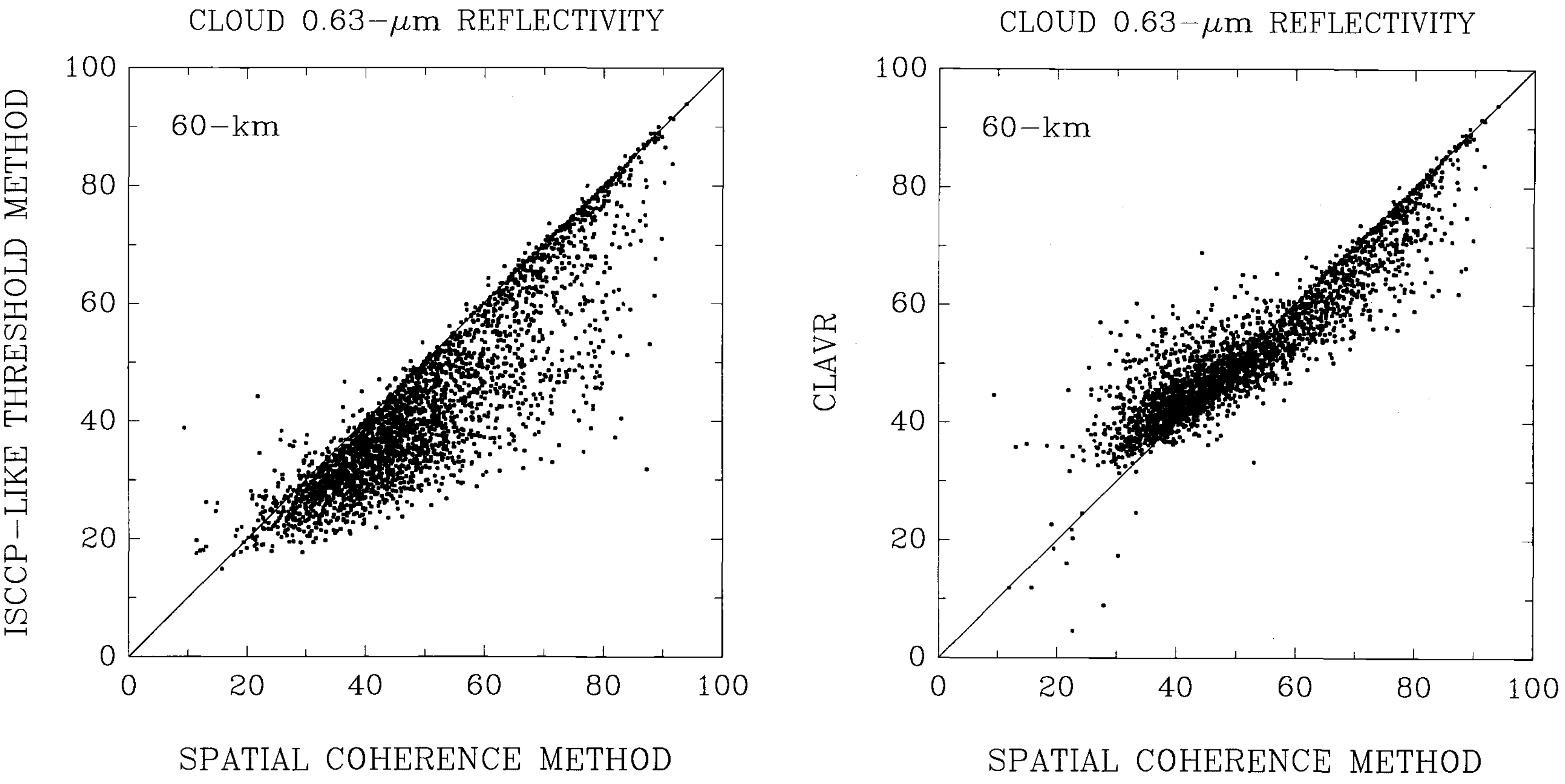

Figure 2.12 Same as Figure 2.11, except that each point represents a 60-km region.

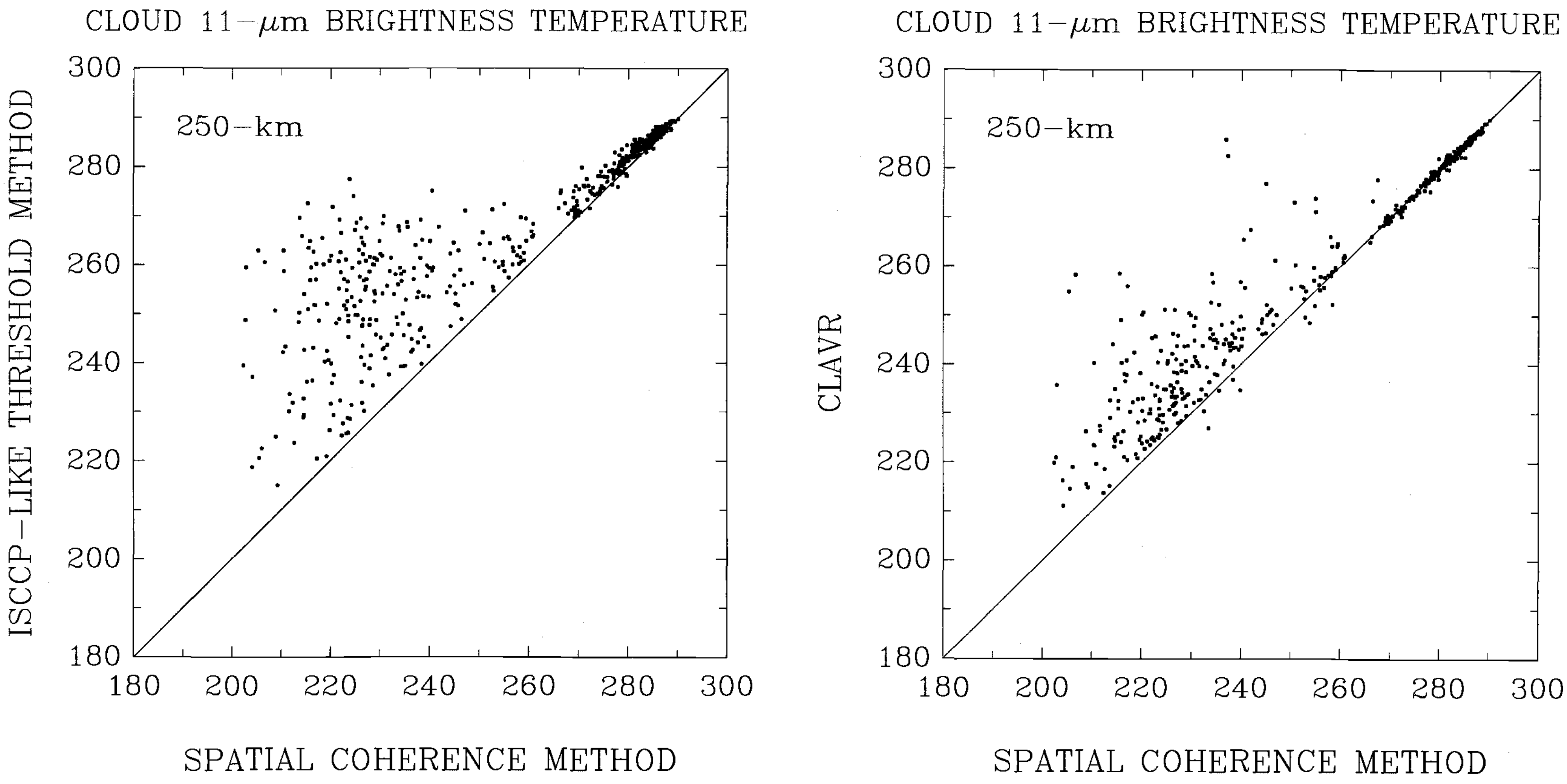

Figure 2.13 Same as Figure 2.11, except for overcast 11-μm brightness temperatures.

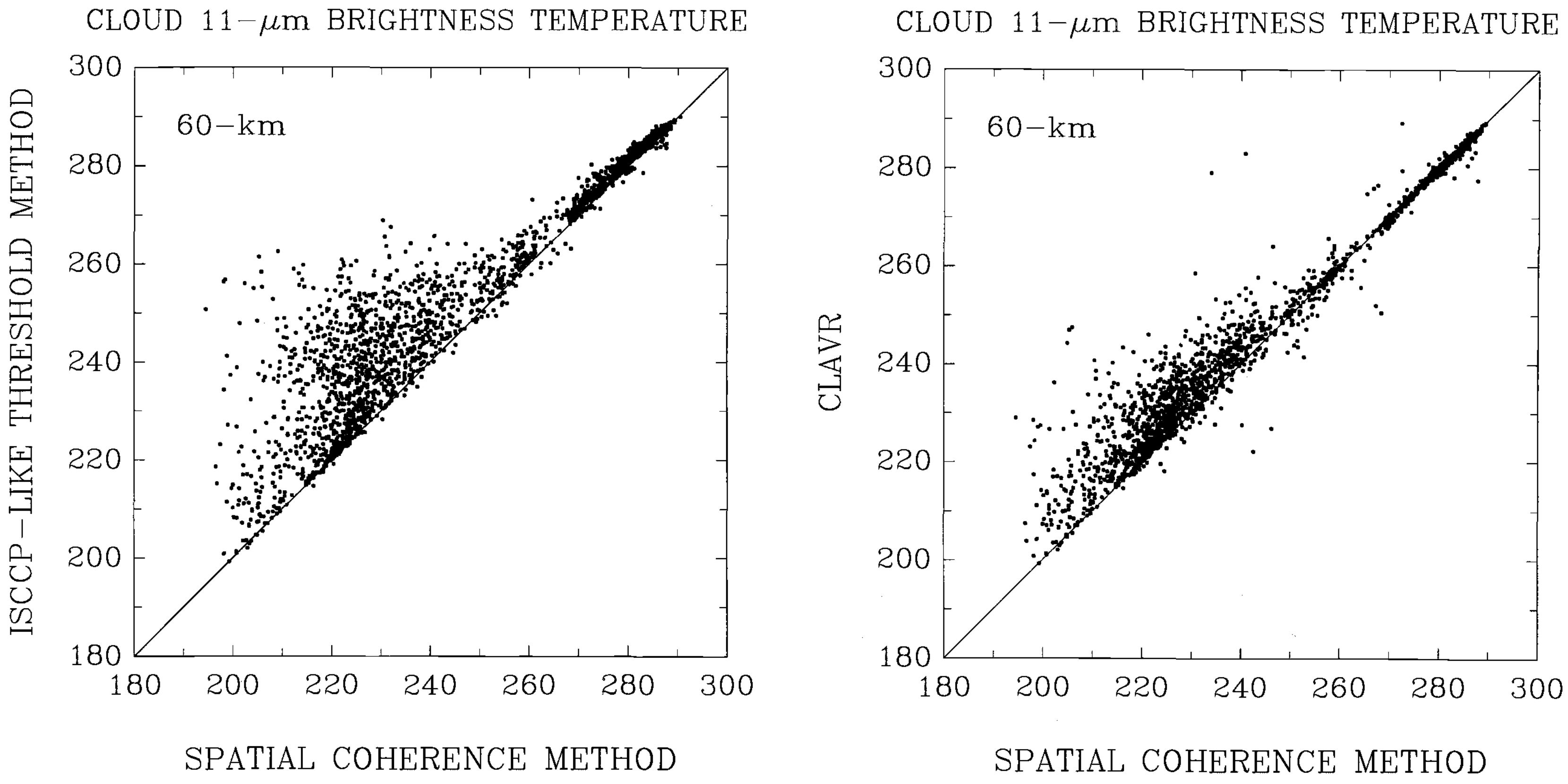

Figure 2.14 Same as Figure 2.13, except that each point represents a 60-km-scale region.

of the contribution by their cloud-free portions, these partly cloud-covered pixels have larger brightness temperatures than do the overcast pixels. As for the CLAVR derived brightness temperatures, they generally agree with those derived by the spatial coherence method. However, for clouds having relatively low temperatures, CLAVR tends to produce higher overcast brightness temperatures than does the spatial coherence method. The higher brightness temperatures result from the partly cloud-covered pixels that passed the gross cloud-reflectivity threshold test.

Figure 2.15 shows fractional cloud cover for the 250-km regions and Figure 2.16 shows fractional cloud cover for the 60-km regions. For single-layered cloud systems, the 250-km and 60-km fractional cloud cover obtained by the spatial coherence method is given by (Coakley and Bretherton, 1982)

$$A_c = \frac{I - I_s}{I_c - I_s}\,, \tag{2.1}$$

where I_s is the average 11-μm radiance observed for cloud-free pixels, I_c is the average 11-μm radiance observed for overcast pixels, and I is the average 11-μm radiance observed for the region.

Unlike the spatial coherence method, both CLAVR and ISCCP obtain the fractional cloud cover by counting pixels. For CLAVR, the fractional cloud cover is taken to be given by (Stowe et al., 1997)

$$A_c = \frac{0.5N_m + N_o}{N}\,, \tag{2.2}$$

where N_m is the number of mixed pixels, N_o is the number of overcast pixels, and N is the total number of pixels within the region. The value 0.5 in the equation is taken to be the average fractional cloud cover for the mixed pixels. For ISCCP, the fractional cloud cover is given by (Rossow and Garder, 1993)

$$A_c = \frac{N_c}{N} \,. \tag{2.3}$$

Here N_c is the total number of cloudy and overcast pixels and N is the total number of pixels.

Figures 2.15 and 2.16 show that the 250-km and 60-km fractional cloud cover obtained by the ISCCP-like threshold method are systematically larger than those obtained by the spatial coherence method. As expected, many of the pixels identified as partly cloud-covered by the spatial coherence method are counted as overcast by the ISCCP-like threshold. The overall mean cloud cover fraction obtained by the ISCCP-like threshold method is ~0.25 larger than that obtained by the spatial coherence method. This finding is similar to that obtained by Chang and Coakley (1993) using only the infrared threshold.

For CLAVR, a fractional cloud cover of 0.5 is frequently obtained. Owing to its restrictive overcast and cloud-free conditions, CLAVR identifies a large fraction of pixels as being partly cloudy ("mixed"). As noted previously by Coakley (1987) and by Chang and Coakley (1993), when a region is mostly cloud-free, the average fractional cloud cover of the partly cloud-covered pixels found within the region is generally small. Conversely, when a region is mostly cloudy, the average fractional cloud cover of the partly cloud-covered pixels is generally large. By assigning 0.5 as the fractional cloud cover for all partly cloud-covered pixels, CLAVR generally produces larger fractional cloud cover than does the spatial coherence method when

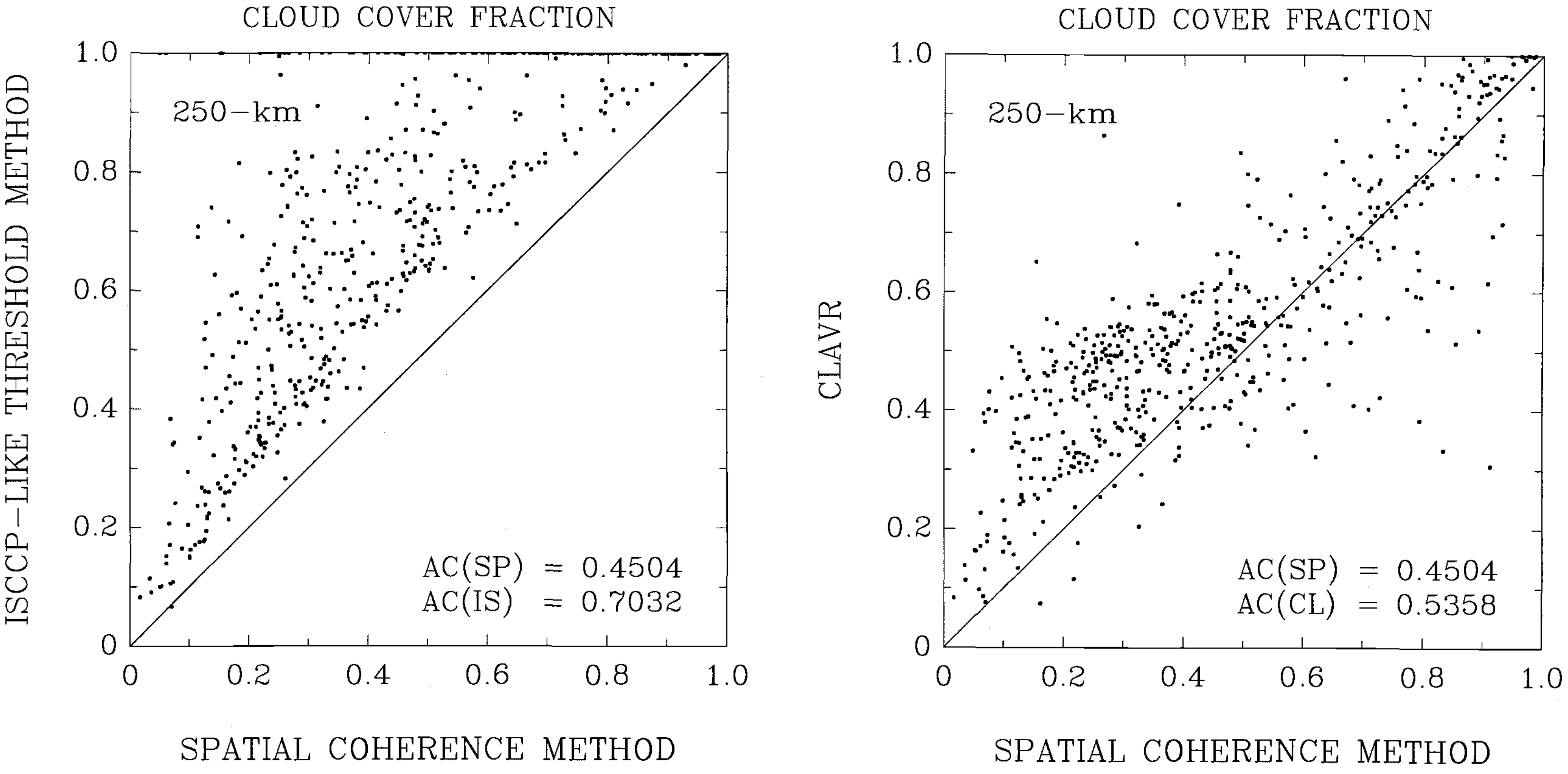

Figure 2.15 Same as Figure 2.11, except for fractional cloud cover. The total average fractional cloud cover is shown in the lower-right corner.

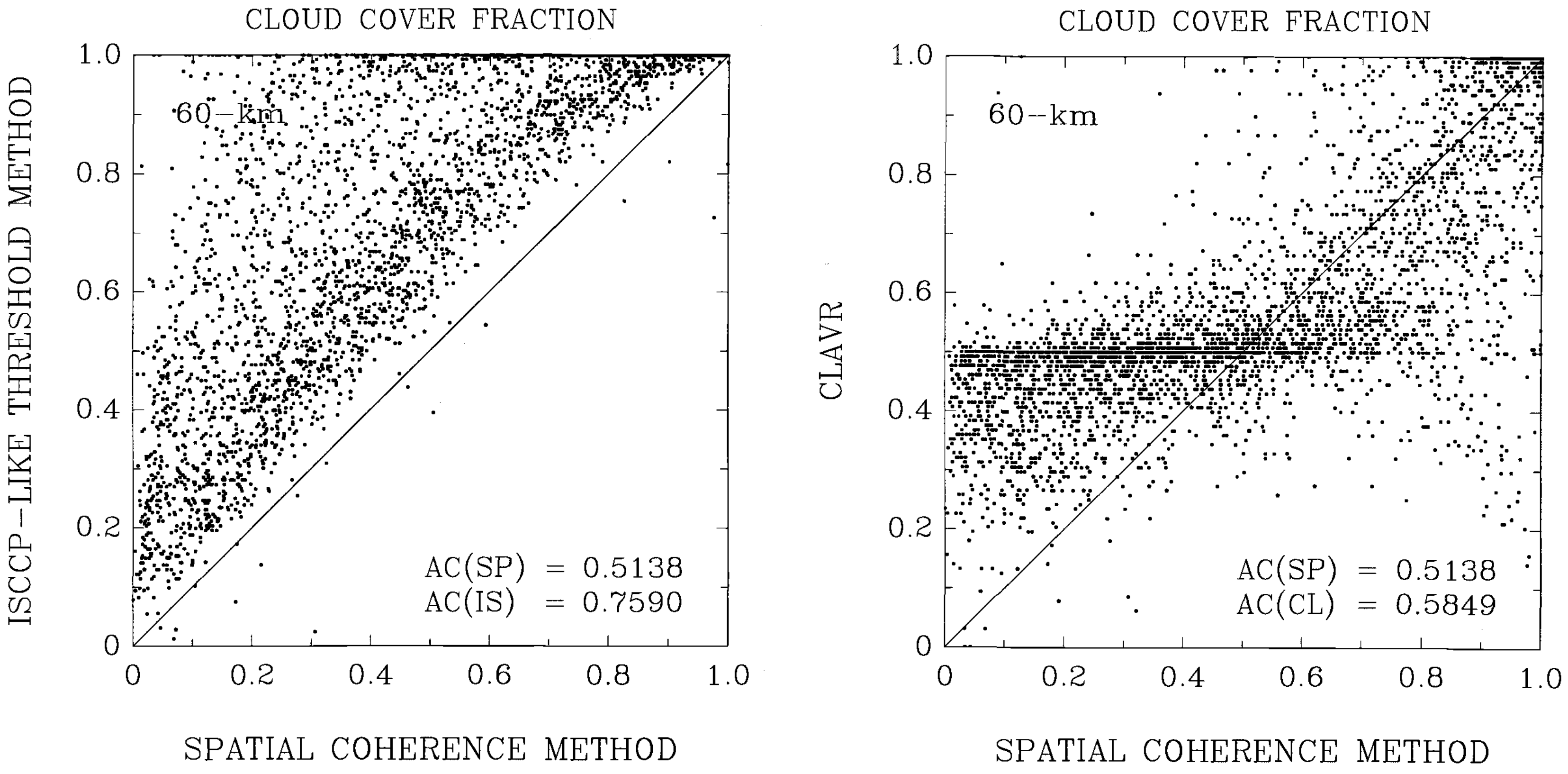

Figure 2.16 Same as Figure 2.15, except that each point represents a 60-km region.

the fractional cloud cover is less than 0.5 and smaller fractional cloud cover when the fractional cloud cover is greater than 0.5.

2.5 Implications of differences between the spatial coherence, CLAVR, and ISCCP-like threshold analyses

For single-layered cloud systems, CLAVR identifies fewer cloud-free pixels than does the spatial coherence method, particularly in regions where broken clouds are extensive. Evidently, CLAVR uses relatively restrictive criteria to identify cloud-free pixels. This finding is consistent with those by Gallegos et al. (1993). Despite differences in the selection of cloud-free pixels between CLAVR and the spatial coherence method, mean 0.63-μm cloud-free reflectivities and mean 11-μm cloud-free brightness temperatures obtained for 60-km regions by the two methods appear to differ little for most of the regions. The mean difference is about 0.5K for the 11-μm cloud-free brightness temperature and about 0.02 for the 0.63-μm cloud-free reflectivities. These differences would give rise to shifts in the NOAA/NESDIS retrievals of sea surface temperature and aerosol optical depth within the uncertainties claimed for these retrievals (Mclain et al., 1985; Rao et al., 1989). In regions of sunglint, large differences in the mean 0.63-μm reflectivities and mean 11-μm brightness temperatures are found between CLAVR and the spatial coherence analyses. Many pixels that are overcast by low-level clouds and exhibit uniform 11-μm radiances close to the 11-μm radiances emitted by the cloud-free ocean are identified as being cloud-free by the CLAVR algorithm. These pixels are probably the "restored-clear" pixels. Improvements are needed in CLAVR's retrieval of cloud-free properties for sunglint regions.

For regions containing clouds with low reflectivities, CLAVR identifies fewer pixels as being overcast than does the spatial coherence method. The smaller number of overcast pixels is due to the relatively restrictive cloud tests used by CLAVR. However, CLAVR identifies more pixels as being overcast when the clouds have large reflectivities. The gross cloud-reflectivity threshold employed by CLAVR often identifies partly cloud-covered pixels as being overcast.

Unlike CLAVR and the spatial coherence method, the ISCCP-like threshold method identifies far more pixels as being overcast. However, partial cloud cover at the 4–8 km pixel-scale is common. Based on analyses of single-layered, marine clouds identified by the spatial coherence method, Chang and Coakley (1993) indicated that as many as $\sim 50\%$ of the 4-km GAC pixels have fractional cloud cover $0.1 < A_c < 0.9$. For 250-km and 60-km regions containing single-layered systems, the fractional cloud cover derived by the ISCCP-like threshold method is systematically larger than those derived by the spatial coherence method; ISCCP overcast reflectivities are systematically smaller than those for the spatial coherence method; and ISCCP overcast brightness temperatures are systematically higher than those for the spatial coherence method. Clearly, whether cloud-contaminated pixels are taken to be overcast or partly cloud-covered alters estimates of fractional cloud cover, cloud reflectivities, and cloud brightness temperatures. Since cloud reflectivities are used to retrieve cloud optical depths and cloud brightness temperatures are used to retrieve cloud top altitudes. The determination of the overcast pixels will alter the retrievals of these cloud properties.

In addition, as shown in Figures 2.15a and 2.16a, the average fractional cloud cover obtained with the ISCCP-like threshold method is about 0.25 larger than that obtained with the spatial coherence method. This difference is larger than the mean bias, $\Delta A_c = \sim 0.15$, reported for the spatial coherence estimates of cloud cover fraction (Wielicki and Parker, 1992; Luo et al., 1994). This mean bias arises from the assumption adopted in the spatial coherence method that clouds are opaque at 11 μm. Luo et al. showed that a substantial fraction of the area covered by cloud edges is semitransparent at 11 μm.

Chapter 3

The Radiation Model and Cloud Property Retrievals Using Mie and Double Henyey-Greenstein Phase Functions

3.1 Introduction

In order to understand the role of clouds in governing the earth's radiative energy balance and their response to anthropogenic influence and climate change, remote sensing schemes have been developed to retrieve cloud amount, cloud optical depth, droplet effective radius, and cloud top emission temperature (Curran and Wu, 1982; Arking and Childs, 1985; Rawlins and Foot, 1990; Nakajima and King, 1990; Platnick and Twomey, 1994; Han et al., 1994). In retrieving these cloud properties, considerable attention has recently been focused on the use of AVHRR data from NOAA polar orbiting satellites (Han et al., 1994; Platnick and Twomey, 1994; Nakajima and Nakajima, 1995; Platnick and Valero, 1995). The instrument provides narrow band observations at five channels (one visible, two near-infrared, and two infrared).

At visible wavelengths, cloud droplets are nonabsorbing. Sunlight penetrates deeply into the cloud and photons undergo many scatterings before they exit the cloud. The radiance reflected by clouds at visible wavelengths depends primarily on cloud optical depth. At near-infrared wavelengths, however, cloud droplets absorb. The absorption cross section scales as the volume of the droplet and the scattering cross section scales as the area of the droplet. The single-scattering albedo thus scales inversely with the droplet radius, so that small droplets scatter larger fractions of the radiation incident upon them than do larger droplets and large droplets absorb larger fractions of the incident radiation than do smaller droplets. Therefore, cloud droplet size can be inferred by examining the cloud reflectance at near-infrared wavelengths.

Aircraft (e.g., Nakajima and King, 1990) and surface based studies (e.g., Twomey and Cocks, 1985) used reflectances observed at 1.6 and 2.2 μm to retrieve cloud droplet effective radius. The retrieved radii, however, were systematically larger than the radii measured *in situ*. The bias in the retrieved droplet radii was thought to be due to "anomalous" cloud absorption (Stephens and Tsay, 1990), but Taylor (1992) showed that the additional absorption may have been due to an underestimate in the absorption by atmospheric gases, both above clouds and in clouds.

In this chapter, a radiation model for retrieving cloud visible optical depths, droplet effective radii, and cloud top emission temperatures from AVHRR data is described. The model employs an iterative retrieval scheme which uses radiances observed at 0.63, 3.7, and 11 μm for the retrievals of cloud visible optical depth, droplet effective radius, and cloud top emission temperature. The retrieval scheme was applied to data for a wide range of sun-earth-satellite viewing geometries. The angular dependence of the retrieved cloud visible optical depths, droplet effective radii, and cloud top emission temperatures was studied and is discussed in the next chapter.

For the radiation model, a 16-stream, adding-doubling, radiative transfer routine was used to calculate radiances at AVHRR channels 1, 3, and 4 for various values of cloud visible optical depths, droplet effective radii, and cloud top altitudes. The model is presented in three sections: 1) cloud radiation model, 2) atmospheric gaseous absorption and scattering, and 3) the iterative cloud property retrieval scheme. The radiation model employs a plane-parallel geometry. In dealing with the scattering of sunlight by cloud particles, both Mie scattering and an analytic double Henyey-Greenstein phase functions were employed. The analytic double Henyey-Greenstein phase function was used to approximate the Mie phase function. Cloud bidirectional reflectivities obtained with the double Henyey-Greenstein phase function were compared with those obtained using the Mie phase function for both conservative (visible) and non-conservative (near-infrared) scattering. The bidirectional reflectivities obtained with the 16-stream, adding-doubling, routine were also compared with those derived using a 148-stream routine to assess the potential biases associated with the 16-stream approximation.

The radiation model was used to generate look-up tables of radiative properties at AVHRR 0.63, 3.7, and 11 μm for sets of cloud visible optical depths and droplet effective radii. These radiances cover the range of the radiances that would be observed by an AVHRR imager. These radiances include components of radiances reflected, emitted, and transmitted by clouds and the atmosphere and radiances reflected and emitted by earth surface. The model calculations were made at a variety of cloud visible optical depths, droplet effective radii, cloud top altitudes, and satellite-earth-sun viewing geometries. AVHRR radiances were then interpreted in terms of cloud visible optical depth, droplet effective radius, and cloud top emission temperature by comparing the observed radiances with the calculated radiances.

Cloud visible optical depths, droplet effective radii, and cloud top emission temperatures were retrieved by applying the current scheme to the NOAA-12 AVHRR 1-km LAC data taken during the Monterey Area Ship Track experiment in June 1994.

These retrievals were compared with those obtained by applying the Platnick and Twomey (1994) retrieval scheme to the same data. Sensitivity studies were performed to assess the effects of various approximations often used in such retrieval schemes. The sensitivity was examined for varying numbers of streams, using a standard atmosphere model to approximate the actual temperature and humidity profiles, fixing cloud top altitudes, neglecting gaseous absorption in clouds, or using different values of surface reflectance. The sensitivity studies were performed by using an ensemble of cloud data obtained from NOAA-11 AVHRR 4-km GAC data for March 1989.

3.2 Cloud radiation model

The retrieval scheme employs a plane-parallel model. A matrix adding-doubling scheme (Grant and Hunt, 1969; Liou, 1980) was used to treat the multiple scattering by clouds. The calculations were initiated using the reflectivities, transmissivities, and emissivities of an optically thin cloud layer. These reflectivities, transmissivities, and emissivities were calculated using the single-scattering approximation (Liou, 1980; Goody and Yung, 1989). The adding-doubling calculations used 16 streams in both the upward and downward directions. The streams were at Gauss quadrature points. The Mie phase function was expanded to 32 terms of the Legendre polynomial series. The delta-M method (Wiscombe, 1977) was employed to treat the forward scattering peak of the phase function. Cloud particles were assumed to be water spheres. Scattering and absorption cross sections were obtained using Mie theory. In addition, analytic double Henyey-Greenstein phase functions were introduced to approximate the Mie phase functions. Computational results of the cloud radiation model obtained using the double Henyey-Greenstein phase functions were compared with those obtained with

Table 3.1 Cloud visible optical depths and cloud droplet effective radii (μm).

Cloud visible optical depths	0.2, 1, 2, 3, 4, 6, 8, 12, 16, 24, 32, 48, 64, 128
Cloud droplet effective radii	2, 3, 4, 5, 6, 8, 10, 12, 14, 16, 18, 20, 24, 28, 32, 40

the Mie phase functions. Also, results calculated using a 148-stream scheme with the associated Legendre expansion to 296 terms for the phase function were obtained and used to assess the errors in the 16-stream model.

The correlated *k*-distribution models developed for the AVHRR channels by Kratz (1995) were used to correct for atmospheric gaseous absorption. Bidirectional reflectivities and transmissivities were calculated for 14 cloud visible optical depths and 16 cloud droplet effective radii, as shown in Table 3.1. Following Kratz, calculations were performed for 11 sub-channels, as shown in Table 3.2. AVHRR channels 1 and 3 are both divided into five sub-channels. As was indicated by Kratz, this subdivision is necessary in order to model variations of the Planck function and the incident solar flux as well as the distribution of molecular absorption and variations in the index of refraction for water within these spectral intervals. The spectral response functions associated with these sub-channels are also from Kratz, as shown in Table 3.2. Cloud emissivities were also calculated for the 14 visible optical depths and the 16 droplet effective radii for the 3.75- and 11-μm channels.

Table 3.2 Spectral range, response function, solar constant, and index of refraction for water.

	Central wavenumber (cm^{-1})	Wavenumber interval (cm^{-1})	Central wavelength (μm)	Wavelength interval (μm)	Spectral response function	Spectral solar constant ($mWm^{-2}cm$)	Index of refraction for water
Channel 1-1	17550	17300-17800	0.570	0.562-0.578	0.34804	55.562	1.333,0.0i
Channel 1-2	16950	16600-17300	0.590	0.578-0.602	0.78896	59.211	1.332,0.0i
Channel 1-3	16300	16000-16600	0.614	0.602-0.625	0.89060	61.123	1.332,0.0i
Channel 1-4	15250	14500-16000	0.656	0.625-0.690	0.96461	64.516	1.331,0.0i
Channel 1-5	13900	13300-14500	0.719	0.690-0.752	0.24758	68.221	1.331,0.0i
Channel 3-1	2817.5	2775-2860	3.549	3.497-3.604	0.62487	17.456	1.392,0.00724i
Channel 3-2	2740	2705-2775	3.650	3.604-3.697	0.96992	16.960	1.378,0.00425i
Channel 3-3	2667.5	2630-2705	3.749	3.697-3.802	0.96178	16.223	1.369,0.00339i
Channel 3-4	2595	2560-2630	3.854	3.802-3.906	0.97803	15.614	1.359,0.00357i
Channel 3-5	2525	2490-2560	3.960	3.906-4.016	0.24603	15.158	1.352,0.00427i
Channel 4	925	880-970	10.81	10.31-11.36			1.164,0.08630i

3.2.1 Optical properties of water droplets

The amount of radiation reflected, transmitted, and emitted by a cloud droplet depends on the droplet's scattering cross section, $\sigma_{sca}(\lambda, r)$, and absorption cross section, $\sigma_{abs}(\lambda, r)$, where λ is the wavelength and r is the droplet radius. The scattering cross section and absorption cross section are proportional to the droplet's geometric cross section. They are given by

$$\sigma_{sca}(\lambda, r) = Q_{sca}(\lambda, r)\pi r^2, \tag{3.1}$$

$$\sigma_{abs}(\lambda, r) = Q_{abs}(\lambda, r)\pi r^2, \tag{3.2}$$

where $Q_{sca}(\lambda, r)$ is the droplet's scattering efficiency and $Q_{abs}(\lambda, r)$ is the absorption efficiency. The scattering and absorption efficiencies were calculated using Mie theory (Bohren and Huffman, 1983). The refractive index for water was obtained from Hale and Querry (1973) for visible wavelengths and from Downing and Williams (1975) for infrared wavelengths. The indices are listed in Table 3.2. Scattering and absorption are accounted for through the commonly used optical parameters, namely, the extinction efficiency, $Q_{ext} = Q_{sca} + Q_{abs}$, the single-scattering albedo, $\omega_0 = Q_{sca}/(Q_{sca} + Q_{abs})$, and the scattering phase function, $P(\cos\Theta)$, where Θ is the scattering angle. The shape of the scattering phase function is characterized by an asymmetry parameter, g, which is given by

$$g = \frac{1}{2}\int_{-1}^{1} P(\cos\Theta)\cos\Theta d\cos\Theta. \tag{3.3}$$

For isotropic scattering, $g = 0$. For forward scattering, as is common in the planetary atmosphere, $g > 0$. Figure 3.1 shows the extinction efficiencies, single-scattering albedos, and asymmetry parameters as functions of droplet radius for radiation at wavelengths, 0.614, 3.749, and 10.81 μm.

In clouds, distributions of various droplet sizes are always encountered. Fortunately, the exact nature of the size distribution is not crucial (Platnick and Valero, 1995) and the scattering and absorption properties of clouds depend largely on the droplet effective radius which is given by

$$r_{eff} = \frac{\int \pi r^3 n(r) dr}{\int \pi r^2 n(r) dr}, \tag{3.4}$$

where $n(r)$ is the size distribution function, $n(r)dr$ is the number of droplets per unit volume with radius between r and $r + dr$. In the radiation model, a gamma distribution (Hansen, 1971) is adopted to represent the droplet size distribution. The gamma distribution is given by

$$n(r) = N \frac{\left(r_{eff} v_{eff}\right)^{(2v_{eff}-1)/v_{eff}}}{\Gamma\left[\left(1 - 2v_{eff}\right)/v_{eff}\right]} r^{(1-3v_{eff})/v_{eff}} e^{-r/(r_{eff} v_{eff})}, \tag{3.5}$$

where $N = \int n(r) dr$ is the total number of droplets per unit volume, Γ is the gamma function, and v_{eff} is the effective variance given by

$$v_{eff} = \frac{\int \left(r - r_{eff}\right)^2 \pi r^2 n(r) dr}{r_{eff}^2 \int \pi r^2 n(r) dr}. \tag{3.6}$$

For most clouds, v_{eff} ranges approximately between 0.1 and 0.2 (Hansen, 1971). As was suggested by Hansen, a value of $v_{eff} = 0.193$ is used here for stratus clouds.

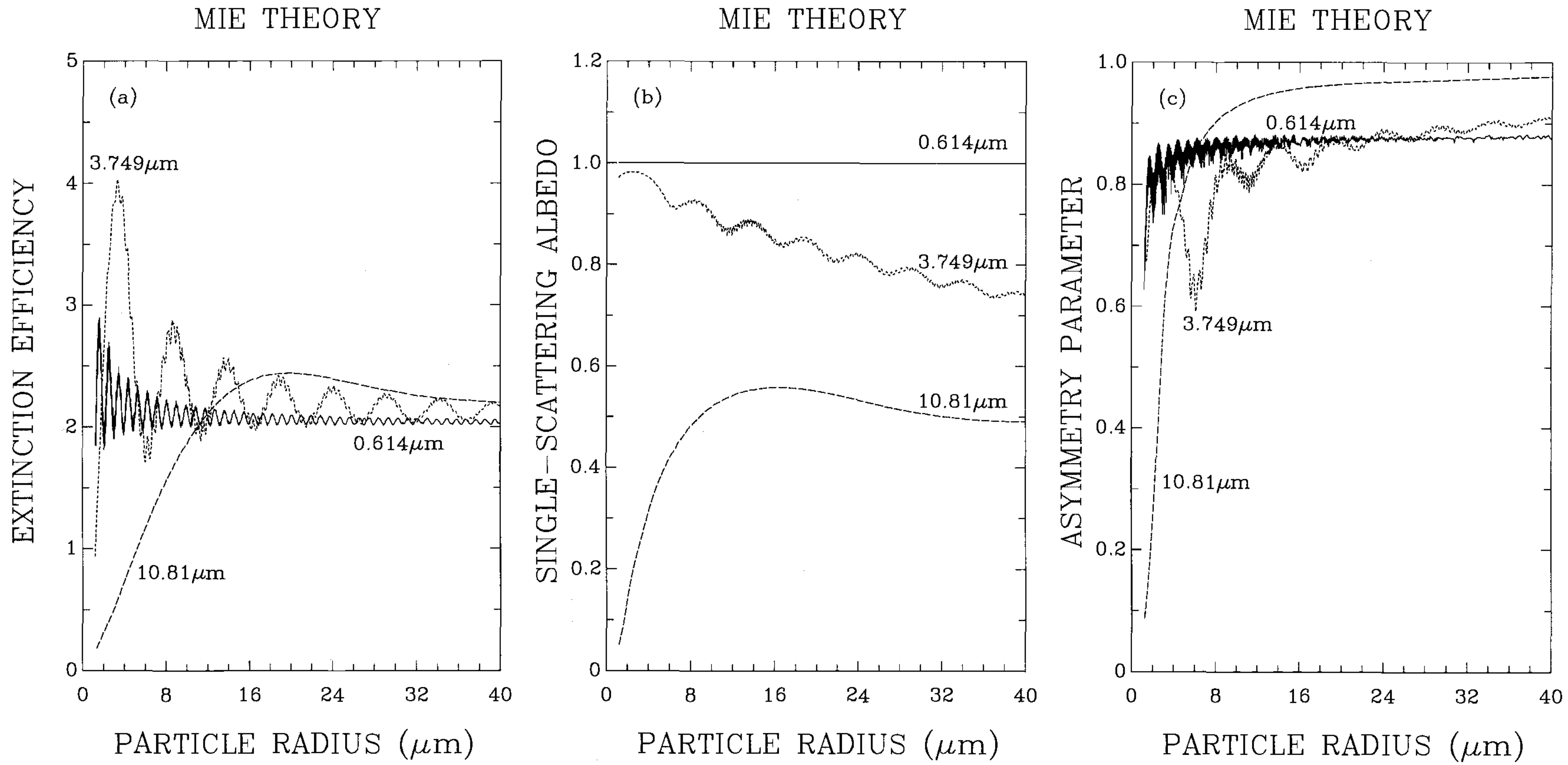

Figure 3.1 Optical properties for water droplets. Results obtained using Mie theory for single droplets at wavelengths 0.613, 3.749, and 10.81 μm. (a) extinction efficiency (b) single-scattering albedo (c) asymmetry parameter.

Figure 3.2 shows the gamma distribution obtained for $r_{eff} = 4$, 10, and 28 μm. The scattering efficiency and the absorption efficiency for droplets distributed over a range of sizes are given by

$$Q_{sca}(\lambda, r_{eff}) = \frac{\int \pi r^2 Q_{sca}(\lambda, r) n(r) dr}{\int \pi r^2 n(r) dr}, \tag{3.7}$$

$$Q_{abs}(\lambda, r_{eff}) = \frac{\int \pi r^2 Q_{abs}(\lambda, r) n(r) dr}{\int \pi r^2 n(r) dr}. \tag{3.8}$$

The extinction efficiency, Q_{ext}, single-scattering albedo, ω_0, and asymmetry parameter, g, for the gamma distribution were calculated for the 16 droplet effective

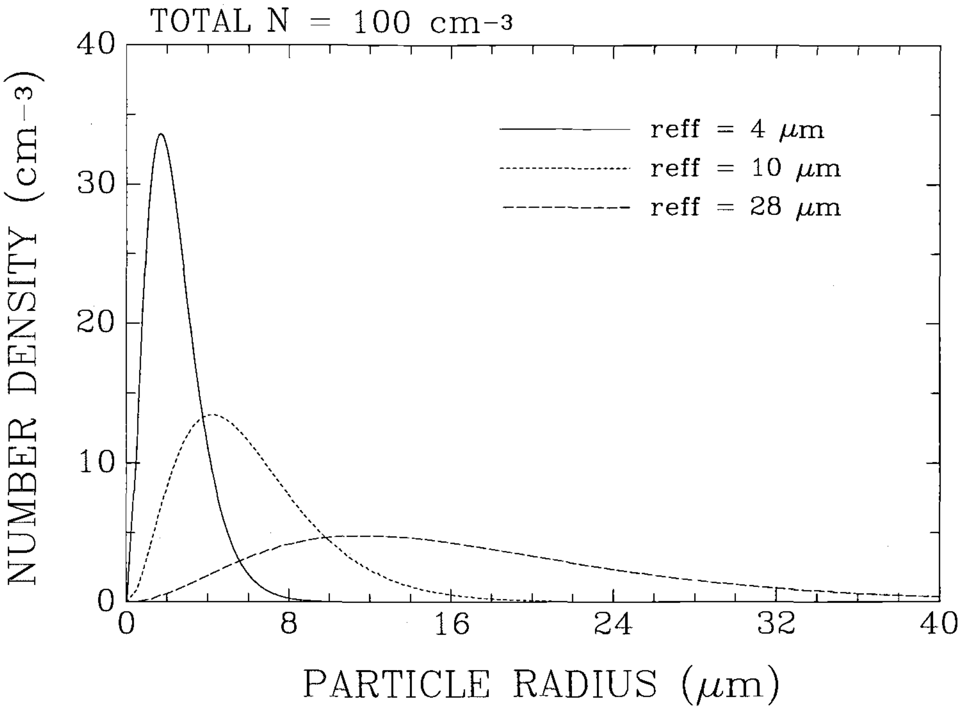

Figure 3.2 Standard gamma size distributions for droplet effective radii 4, 10, and 28 μm.

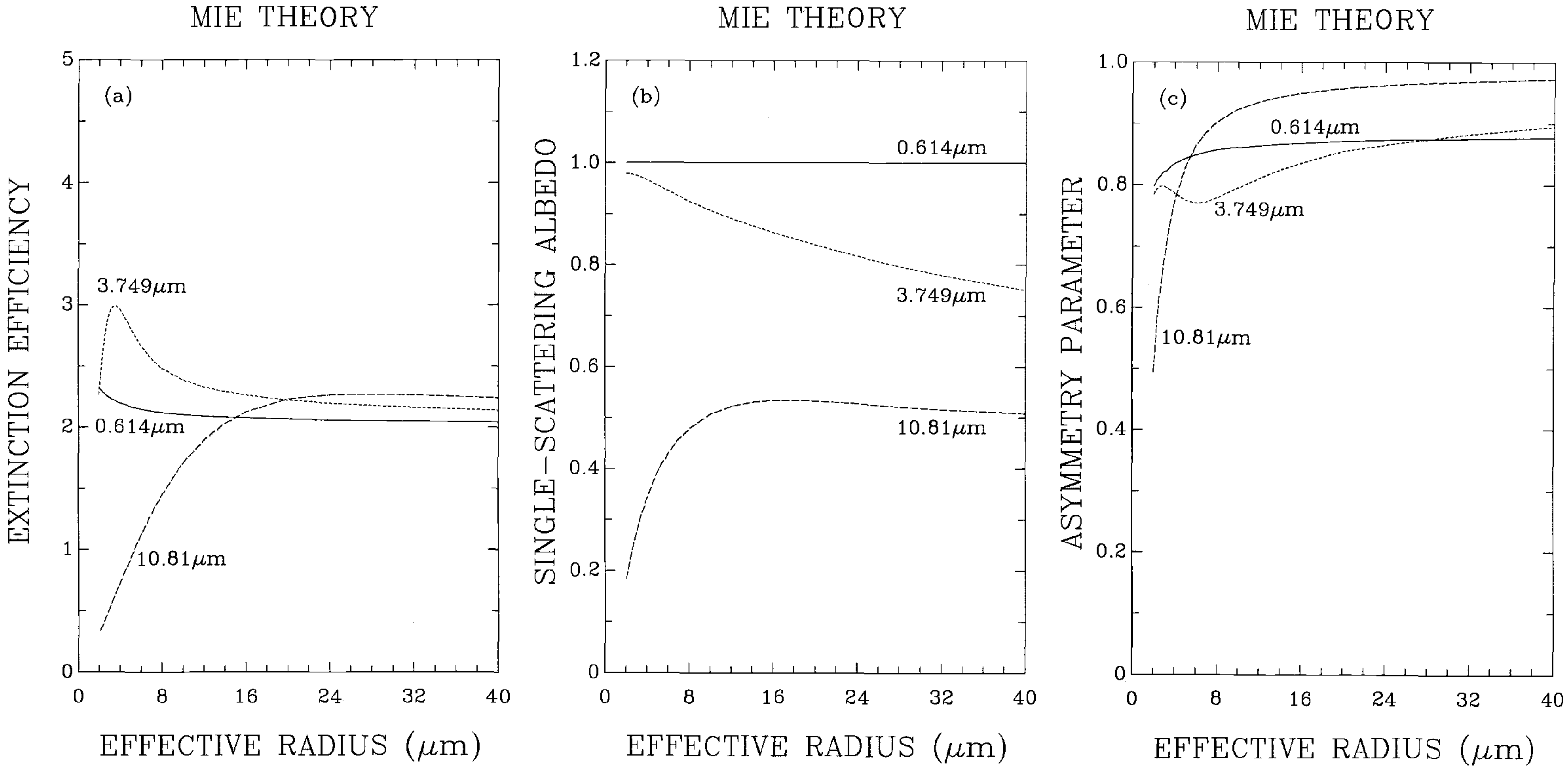

Figure 3.3 Same as Figure 3.1, except for gamma size distributions. An effective variance of $v_{eff} = 0.193$ was used for the gamma size distribution.

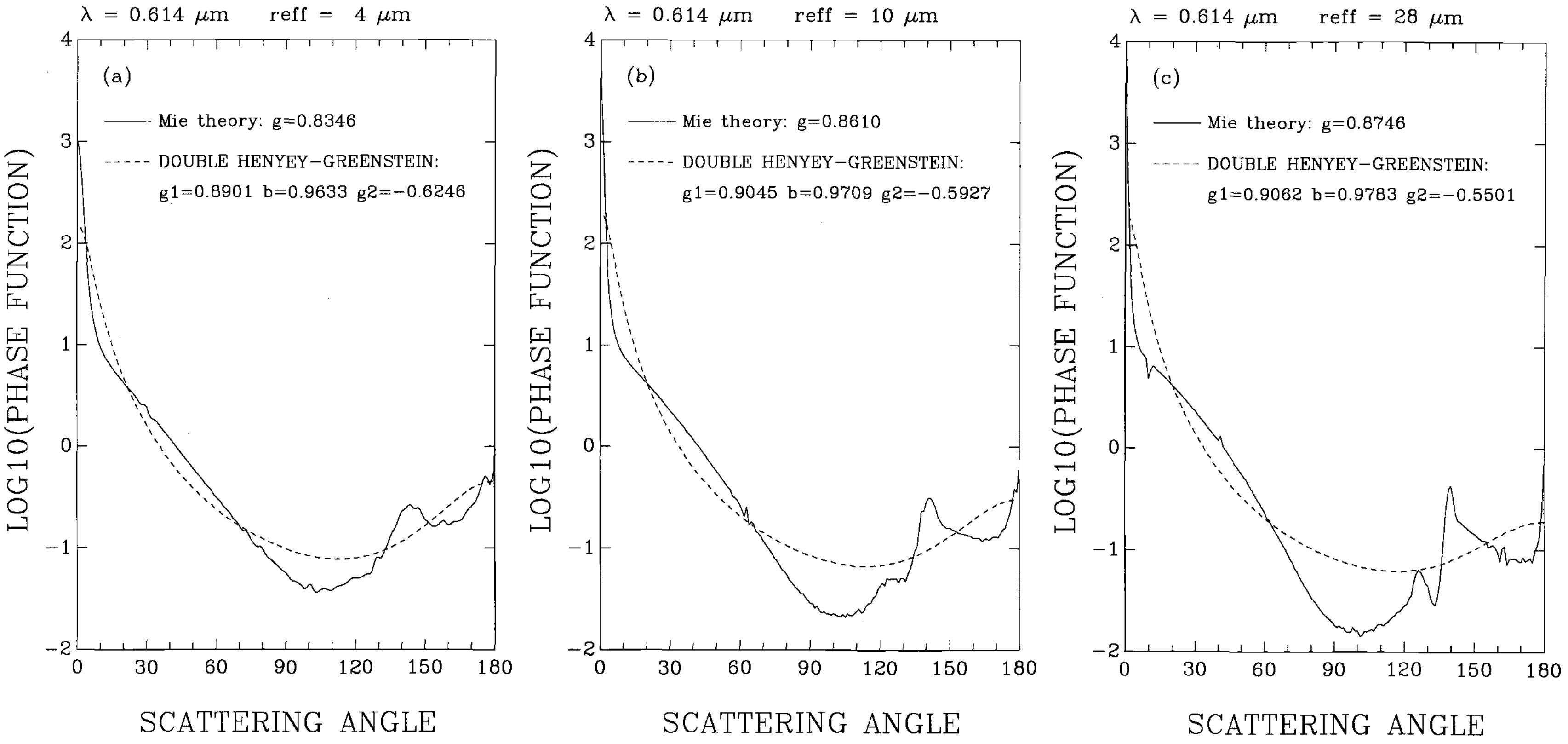

Figure 3.4 Logarithmic-10 values of Mie and DHG phase functions for $\lambda = 0.613\ \mu m$. The asymmetry parameter for Mie and the parameters for DHG phase functions are also given. (a) $r_{eff} = 4\ \mu m$, (b) $r_{eff} = 10\ \mu m$, and (c) $r_{eff} = 28\ \mu m$.

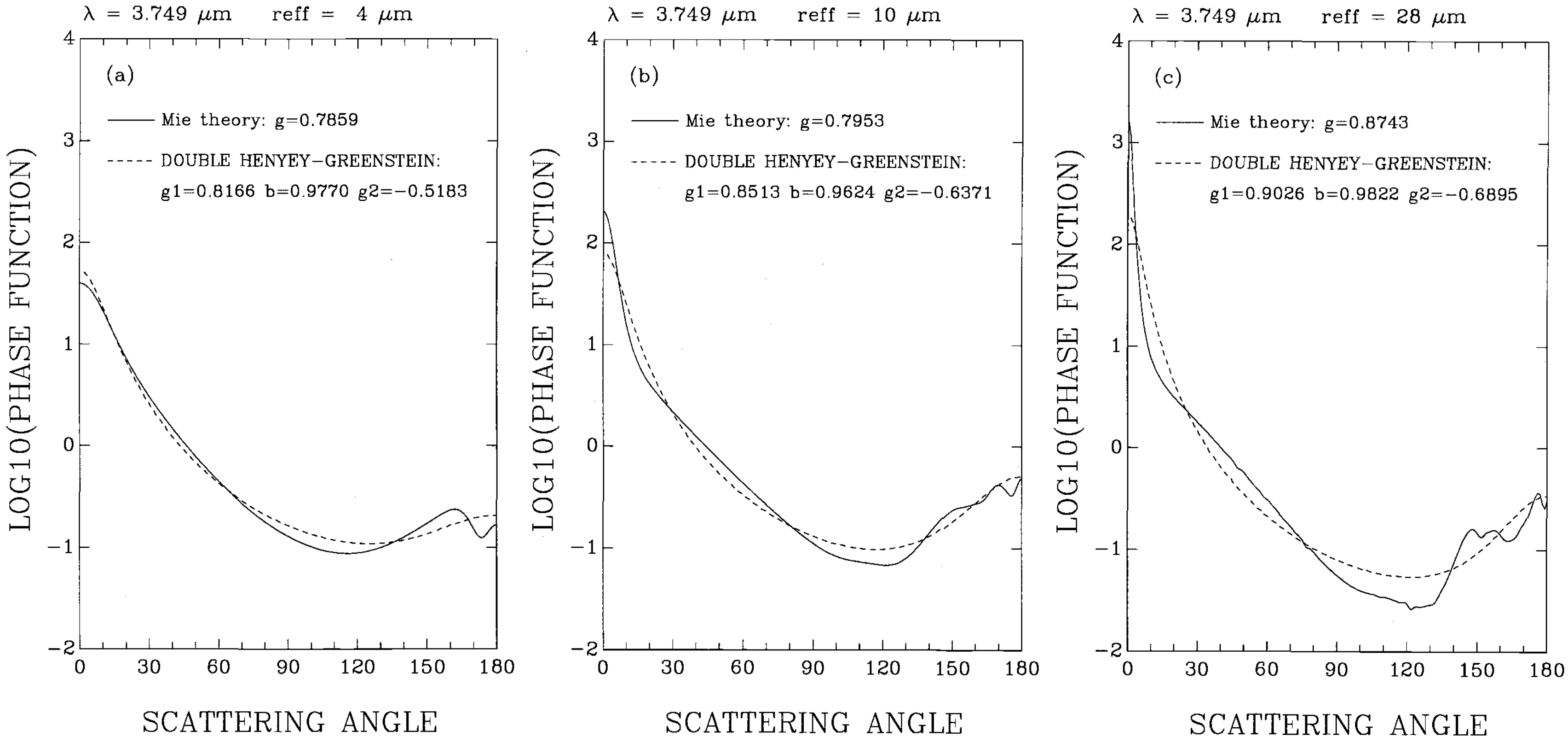

Figure 3.5 Same as Figure 3.4, except for $\lambda = 3.749\ \mu m$.

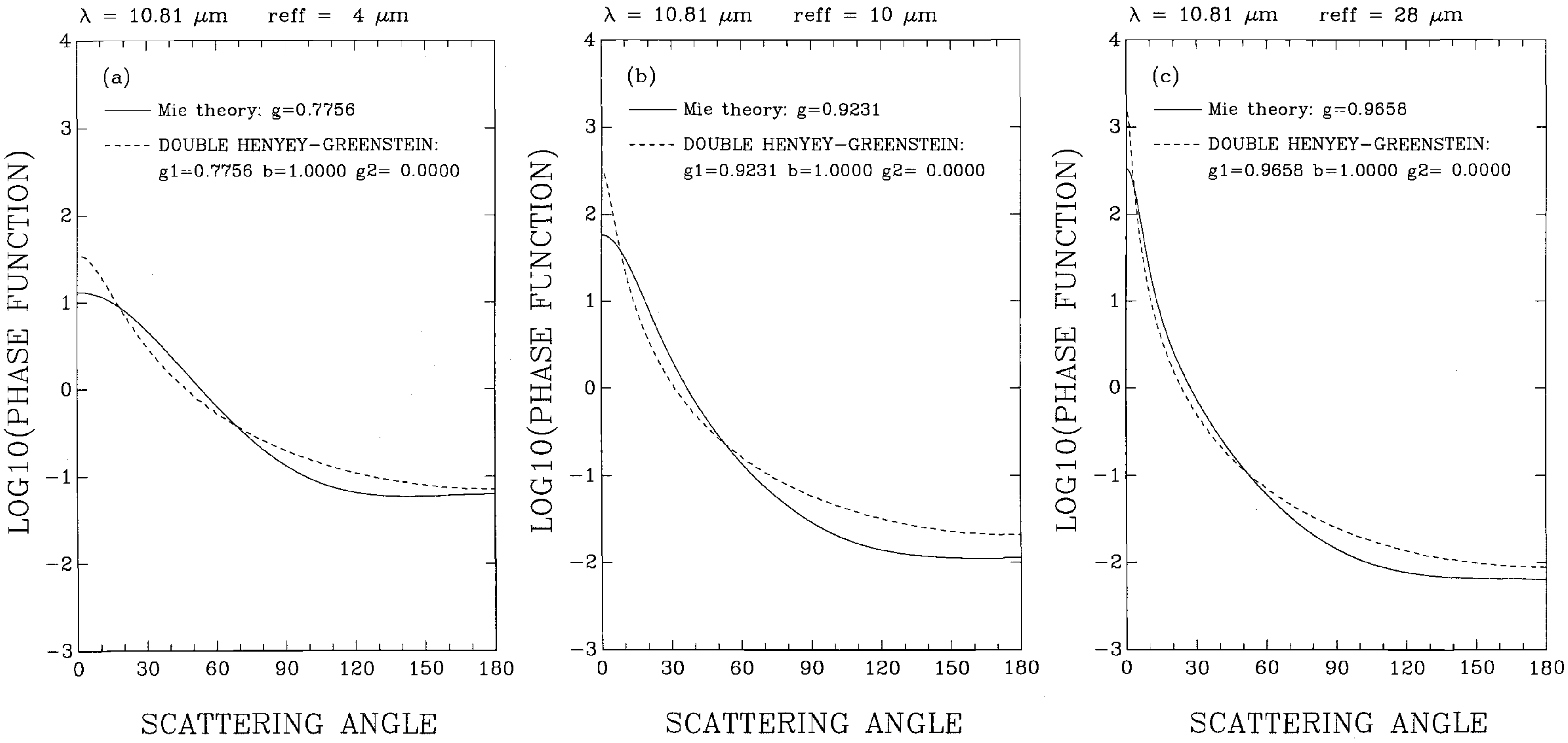

Figure 3.6 Same as Figure 3.4, except for $\lambda = 10.81\ \mu m$.

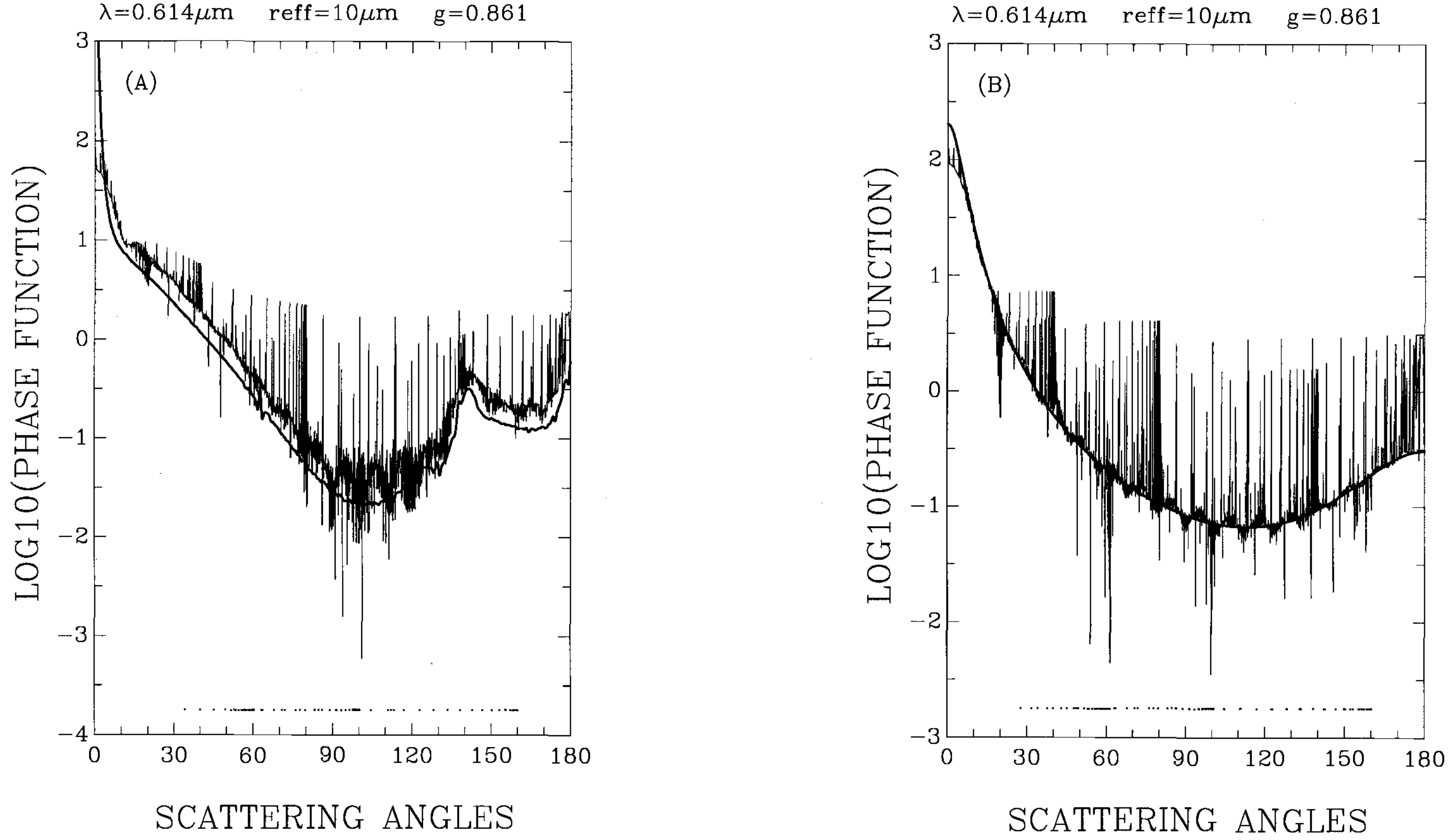

Figure 3.7 Truncated and the actual expressions of Mie and DHG phase functions for $\lambda = 0.614\mu m$ and $r_{eff} = 10\mu m$. The truncated phase functions had 32 terms in the Legendre Polynomial series and 10 terms in the Fourier expansion for the azimuthal components of the phase functions. The values were calculated using 16 streams for both the incident zenith and the scattering zenith angles and 10 relative azimuthal angles. The actual phase functions are shown by thick curves. The dots at the bottom indicate that a negative value in the truncated phase function was found at that scattering angle. (a) Mie phase functions and (b) DHG phase functions.

radii (see Table 3.1) and the 11 wavelengths (see Table 3.2). Figure 3.3 shows these values as a function of the droplet effective radius for wavelengths, 0.614, 3.749, and 10.81 μm.

3.2.2 Mie and double Henyey-Greenstein phase functions

Mie scattering phase functions were also calculated for the 16 droplet effective radii and the 11 wavelengths using the gamma distribution. Figures 3.4-3.6 show examples of the Mie phase functions obtained for wavelengths 0.614, 3.749, and 10.81 μm and for droplet effective radii 4, 10, and 28 μm. The asymmetry parameters associated with these phase functions are also given in the figures. The Mie phase functions are highly anisotropic and are complicated functions of the scattering angle. Such complicated functions require a large number of terms when represented by a series of Legendre Polynomials, which is the common practice in radiative transfer calculations. To simplify the radiative transfer calculations, analytic double Henyey-Greenstein (hereafter referred to as DHG) phase functions were developed and employed to approximate Mie phase functions. Such analytic phase functions can be more easily and accurately expressed in terms of Legendre polynomial series. Figure 3.7 shows the Mie and DHG phase functions calculated for a cloud droplet effective radius of 10 μm at a wavelength of 0.614 μm. The phase functions were calculated for 16 streams in both the upward and downward directions. The Legendre polynomials for the phase functions were truncated at 32 terms. The Fourier expansion for the azimuth component of the phase functions was truncated at 10 terms. The actual phase functions are also plotted. Figure 3.7a show that the truncated Legendre polynomial series for the Mie phase function deviates from the actual phase function. Figure 3.7b shows that the truncated series for the DHG phase function also deviates from the actual phase function.

The widely-used Henyey-Greenstein phase function (Henyey and Greenstein, 1941) is given by

$$P_{\mathrm{HG}}(\cos\Theta; g) = \frac{1-g^2}{\left(1+g^2-2g\cos\Theta\right)^{3/2}}, \tag{3.9}$$

where g is the asymmetry parameter and Θ is the scattering angle. Such a phase function is able to reproduce the forward peak in the Mie phase function quite well, but it fails to capture the upswing in the Mie phase function for backward scattering. This failure is remedied by the DHG phase function which is given by

$$\begin{aligned} P_{\mathrm{DHG}}(\cos\Theta) &= bP_{\mathrm{HG}}(\cos\Theta; g_1) + (1-b)P_{\mathrm{HG}}(\cos\Theta; g_2) \\ &= b\frac{1-g_1^2}{\left(1+g_1^2-2g_1\cos\Theta\right)^{3/2}} + (1-b)\frac{1-g_2^2}{\left(1+g_2^2-2g_2\cos\Theta\right)^{3/2}}, \end{aligned} \tag{3.10}$$

where $0 < g_1 < 1$ characterizes the behavior for forward scattering, $-1 < g_2 < 0$ characterizes the backscattering behavior, and b is a weighting parameter.

The parameters, g_1, g_2, and b, in the DHG phase function are constrained so that, firstly, its asymmetry parameter equals that of the Mie phase function. The relationship between the asymmetry parameter, g, and the parameters, g_1, g_2, and b, is given by

$$g = bg_1 + (1-b)g_2. \tag{3.11}$$

Secondly, the log of the phase function matches the log of the Mie phase function using a least-squares fit over the domain of the scattering angle. The constraints are imposed by minimizing the statistic χ^2 which is given by

$$\chi^2 = \sum_i [\, \ln P_{\mathrm{DHG}}(\cos\Theta_i) - \ln P_{\mathrm{Mie}}(\cos\Theta_i)\,], \tag{3.12}$$

where the summation covers the domain of the scattering angle, $\Theta = 0° - 180°$. Figure 3.8 shows the χ^2 values calculated for $0 < \Delta g_1 < 0.08$ and $-0.8 < g_2 < 0$ for the example of $\lambda = 0.614\ \mu$m and $r_{eff} = 10\ \mu$m, where $\Delta g_1 = g_1 - g$ and

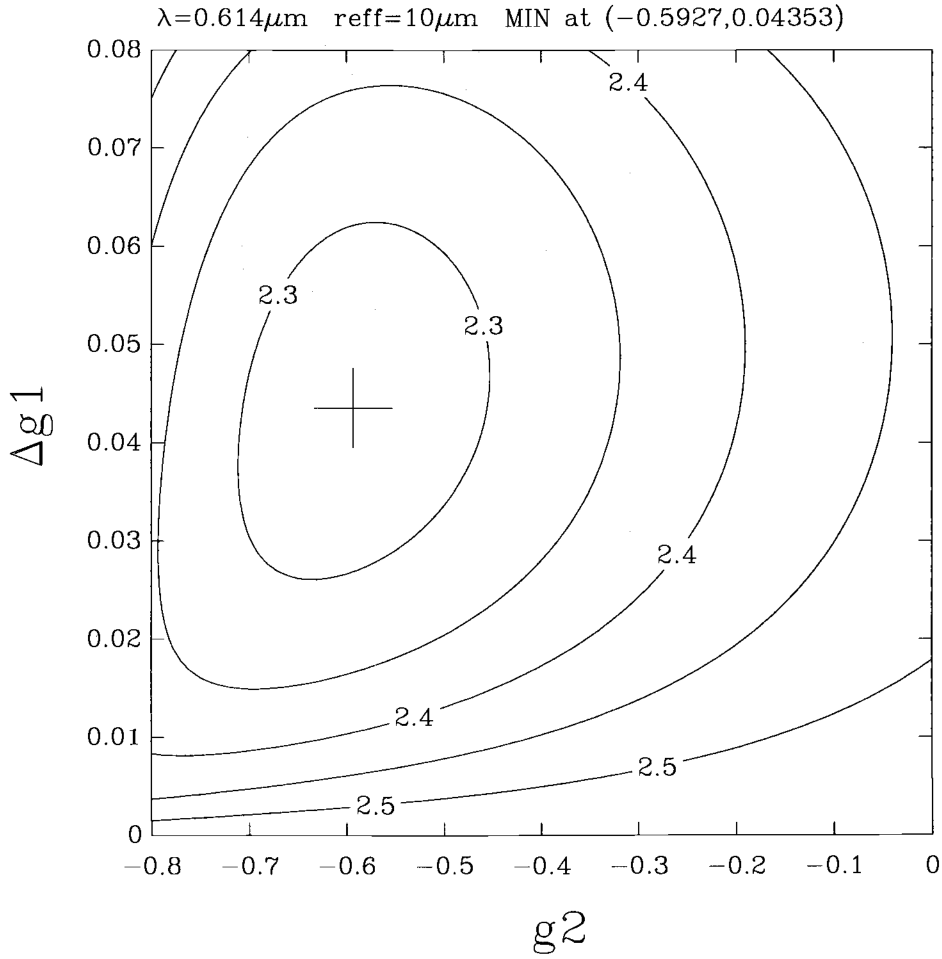

Figure 3.8 Contour plot for χ^2 statistic. Results obtained for $\lambda = 0.614\,\mu m$ and $r_{eff} = 10\,\mu m$. The plus sign indicates the minimum.

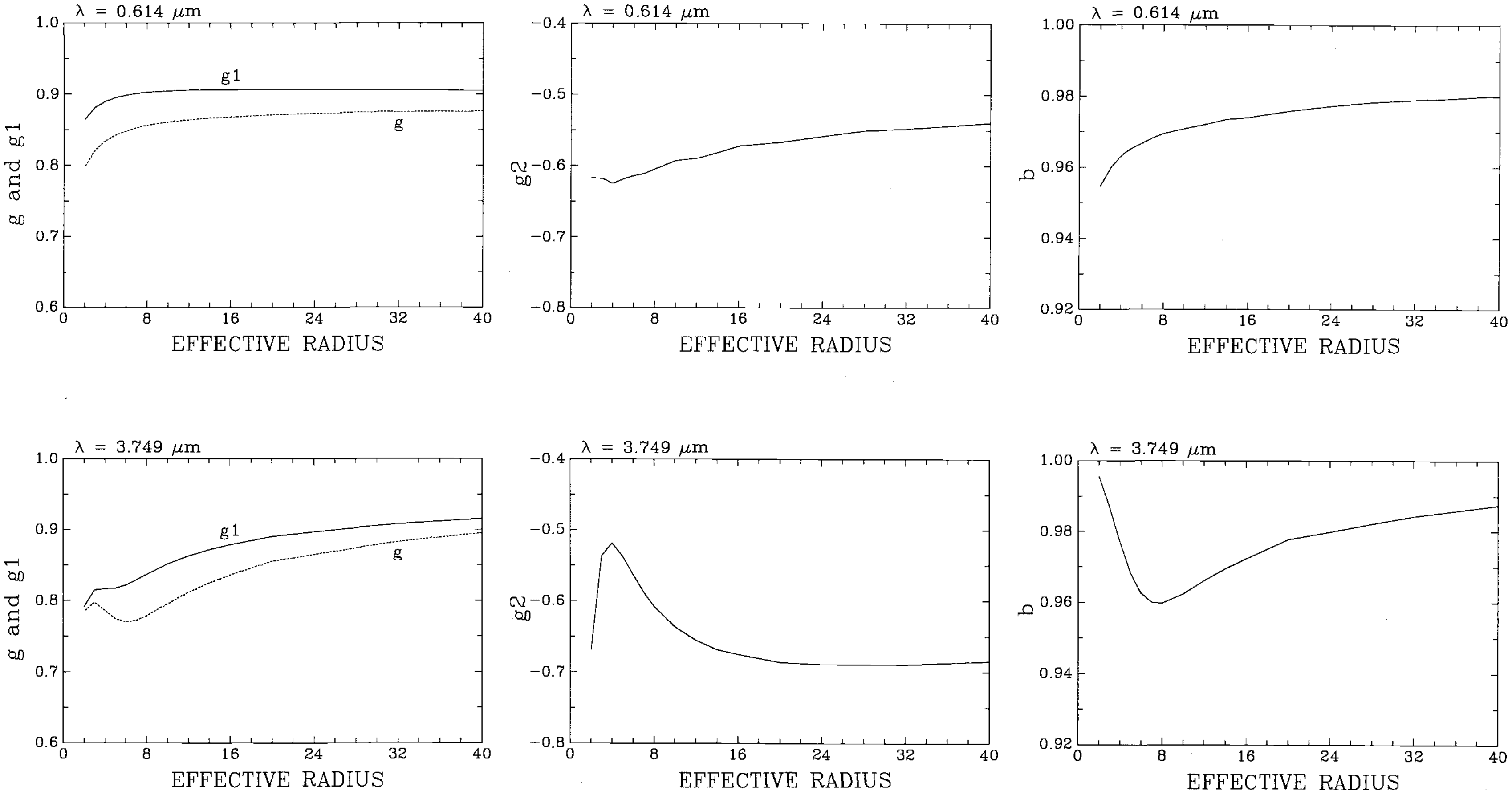

Figure 3.9 Parameters g, g_1, g_2, and b as a function of droplet effective radius. Results obtained for $\lambda = 0.614$ μm (top row) and 3.749 μm (bottom row).

$g = 0.8610$, as shown in Figure 3.4b for $r_{eff} = 10$ μm. The minimum χ^2 is found at $(\Delta g_1, g_2) = (0.04353, -0.5927)$. The DHG phase function shown in Figure 3.4b is given by $g_1 = 0.9045$, $g_2 = -0.5927$, and $b = 0.9709$. Note that the value of b is consistent with the inverse of Eq.(3.11) which gives

$$b = (g - g_2)/(g_1 - g_2)\,. \tag{3.13}$$

Figure 3.9 shows the values of g_1, g_2, and b for wavelengths 0.614 and 3.749 μm at various droplet effective radii. As for 10.81 μm, as is shown in Figure 3.6, $g_1 = g$, $g_2 = 0$, and $b = 1$.

3.2.3 Plane-parallel, radiative transfer calculations

In the radiative transfer calculations, the doubling method was used to calculate reflectivities, transmissivities, and emissivities for clouds with various optical depths. The first step in these calculations is the expansion of the phase function in spherical harmonics. As is often done in radiative transfer calculations (e.g., Liou, 1980; Goody and Yung, 1989), the product of the single-scattering albedo, ω_0, and the phase function, $P(\cos\Theta)$, is expressed by a finite Legendre Polynomial series which is given by

$$\omega_0 P(\cos\Theta) = \sum_{\ell=0}^{L} \mathcal{W}_\ell\, P_\ell(\cos\Theta), \tag{3.14}$$

where $P_\ell(\cos\Theta)$ is the ℓth Legendre polynomial and $\mathcal{W}_\ell$ is the corresponding ℓth expansion coefficient which, in turn, is given by

$$\mathcal{W}_\ell = \frac{(2\ell+1)}{2}\,\omega_0 \int_{-1}^{1} P(\cos\Theta)P_\ell(\cos\Theta)d\cos\Theta. \tag{3.15}$$

For the analytic DHG phase function, $\mathcal{W}_\ell$ is given by

$$\mathcal{W}_\ell = (2\ell+1)\,\omega_o\left[\,bg_1^\ell + (1-b)g_2^\ell\,\right]. \tag{3.16}$$

The second step is the Fourier expansion of the phase function to account for the azimuthal dependence. The scattering angle, Θ, is related to the incident direction (μ', ϕ') and the scattering direction (μ, ϕ) by

$$\cos\Theta = \mu\mu' + \left(1-\mu^2\right)^{1/2}\left(1-\mu'^2\right)^{1/2}\cos\left(\phi-\phi'\right), \tag{3.17}$$

where μ and μ' are the cosine of the zenith angles with respect to the upward normal and ϕ and ϕ' are the azimuth angles. For multiple scattering calculations, it is necessary to transform the reference system from the scattering plane to two vertical planes of the incident and scattering directions. From the addition theorem for spherical harmonics, $\omega_0 P_\ell(\cos\Theta)$ is expanded in a Fourier series as a function of the relative azimuth angle, $\phi - \phi'$. The series is given by

$$\omega_0 P(\cos\Theta) = h^0(\mu,\mu') + 2\sum_{m=1}^{M} h^m(\mu,\mu')\cos m(\phi-\phi'), \tag{3.18}$$

where $h^m(\mu, \mu')$ is given by

$$h^m(\mu,\mu') = \sum_{\ell=m}^{L} \mathcal{W}_\ell \frac{(\ell-m)!}{(\ell+m)!} P_\ell^m(\mu)P_\ell^m(\mu') \tag{3.19}$$

and $P_\ell^m(\mu)$ is the associate Legendre Polynomial. In the numerical calculations, the angular variables, μ and μ' are given at $2K$ discrete Gaussian quadrature points: $0 < \mu_1 < \mu_2 < \cdots < \mu_K < 1$ for the interval [0,1] and $-1 < -\mu_K < -\mu_{K-1} < \cdots < -\mu_1 < 0$ for the interval [-1,0]. Such a discrete scheme is referred to as a K-stream scheme which means there are K streams in both the upward and the downward directions. Here, L is set equal to $2K$ and M is set to equal to 10. As shown by King (1983), the number, M, required in the Fourier expansion of the phase function depends strongly on the incident and scattering geometries. For $M = 10$ and for large optical depths, the results of multiple scattering calculations generally approach within 1% of their asymptotic values.

Figures 3.10-3.13 illustrate examples of the $h^m(\mu, -\mu_o)$ functions obtained for $m = 0$ and 1 for backscattering, where μ and μ_o are both positive with respect to the upward normal direction. In these figures, values of $h^0(\mu, -\mu_o)$ and $h^1(\mu, -\mu_o)$ were calculated at discrete Gauss quadrature points using a 148-stream scheme and a 16-stream scheme. Figures 3.10 and 3.11 show the values for conservative scattering, $\omega_0 = 1$, $\lambda = 0.614\,\mu$m, and $r_{eff} = 10\,\mu$m. Figures 3.12 and 3.13 show the values for non-conservative scattering, $\omega_0 = 0.9065$, $\lambda = 3.749\,\mu$m, and $r_{eff} = 10\,\mu$m. The upper row of figures were obtained using Mie phase functions and the bottom row of figures were obtained using DHG phase functions. As is shown in Figures 3.10 and 3.12, the azimuthally independent function, $h^0(\mu, -\mu_o)$, is positive at all angles. The values at $\mu = 1$ or $\mu_o = 1$ equal to the product of the single-scattering albedo ω_0 and the phase function $P(\cos\Theta)$. This is also true for the forward scattering values, $h^0(-\mu, -\mu_o)$.

Unlike the azimuthally independent function, the azimuth-dependent function, $h^1(\mu, -\mu_o)$, as shown in Figures 3.11 and 3.13, contains both negative and positive

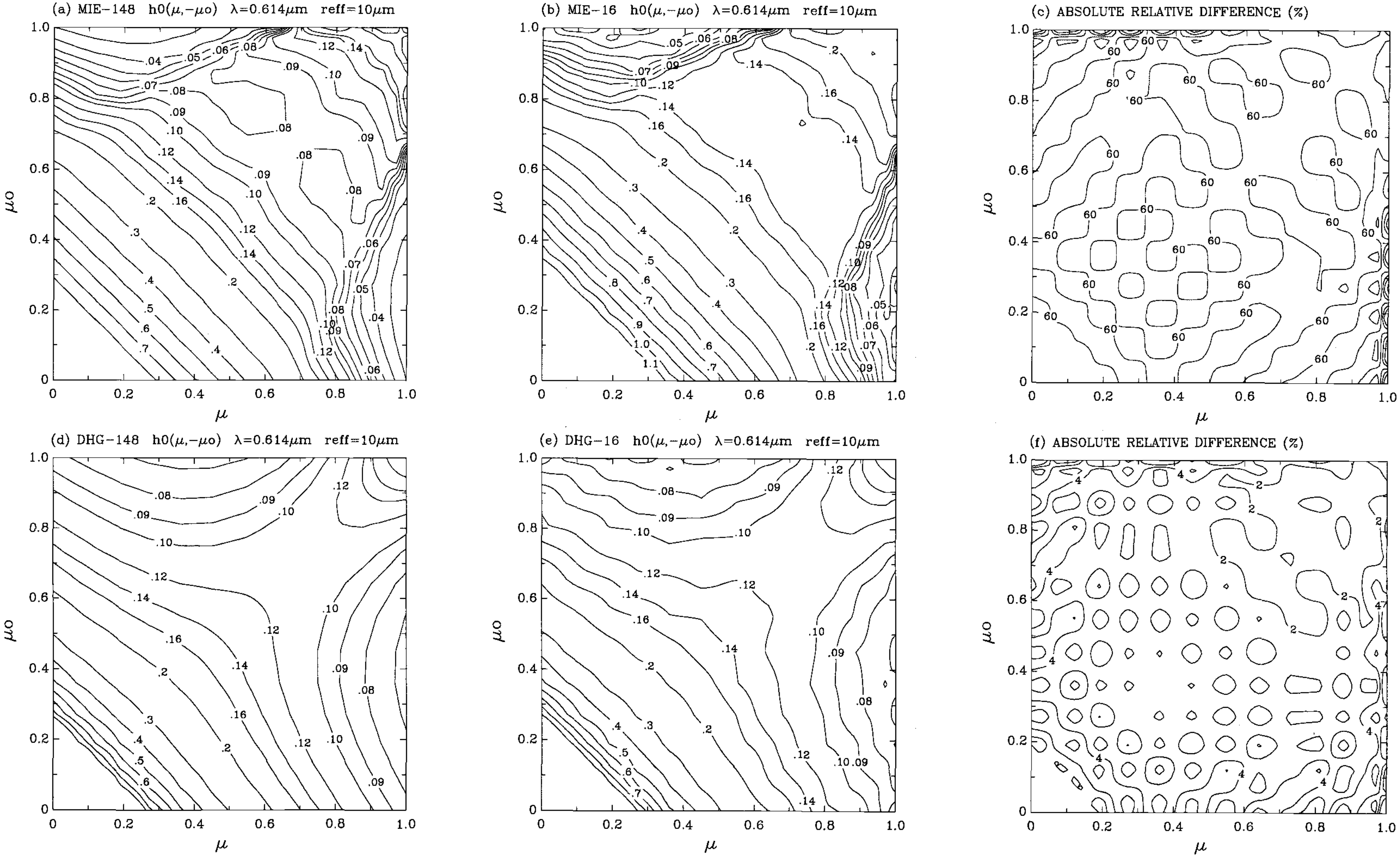

Figure 3.10 Contour plots of $h^0(\mu, -\mu_o)$ for $\lambda = 0.614\ \mu m$ and $r_{eff} = 10\ \mu m$. Results obtained for $0.2 < \mu, \mu_o \leq 1$. (a) Mie 148–stream; (b) Mie 16–stream; (c) absolute relative difference between results shown in (a) and (b); (d) DHG-148 stream; (e) DHG-16 stream; (f) absolute relative difference between results shown in (d) and (e). Differences in (c) and (f) are in percentage.

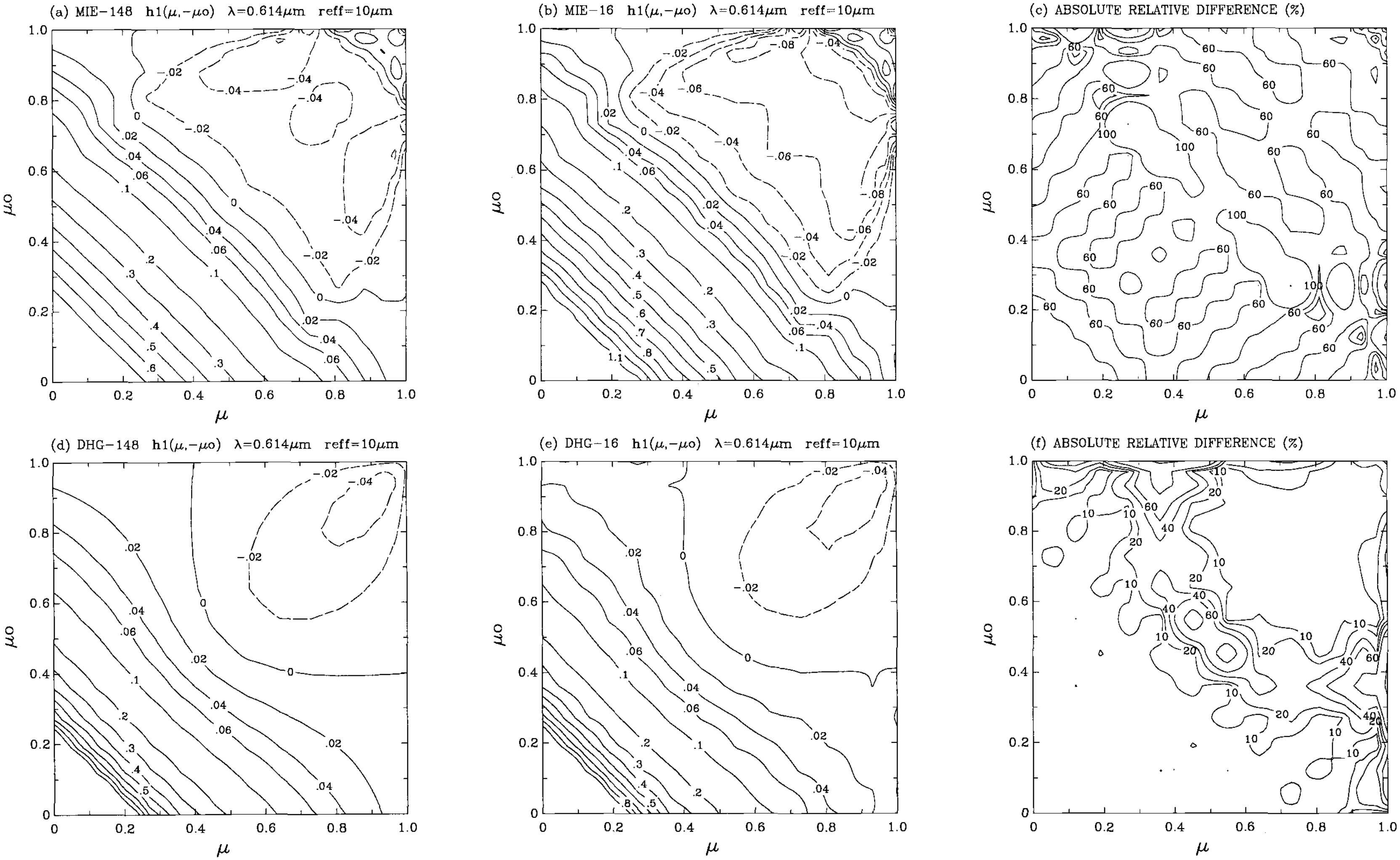

Figure 3.11 Same as Figure 3.10, except for $h^1(\mu, -\mu_o)$.

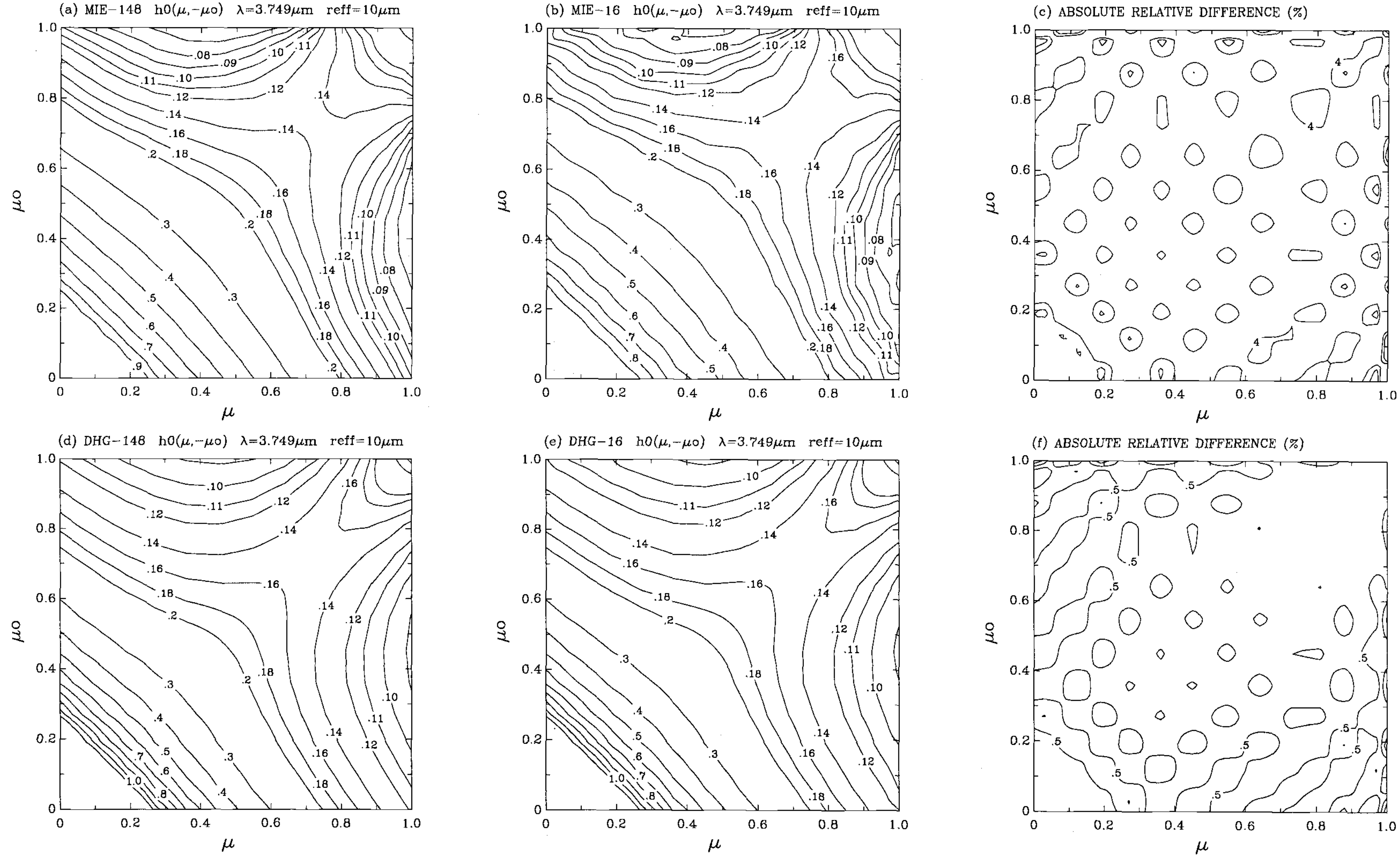
(a) MIE-148 h0(μ,-μo) λ=3.749μm reff=10μm

(b) MIE-16 h0(μ,-μo) λ=3.749μm reff=10μm

(c) ABSOLUTE RELATIVE DIFFERENCE (%)

(d) DHG-148 h0(μ,-μo) λ=3.749μm reff=10μm

(e) DHG-16 h0(μ,-μo) λ=3.749μm reff=10μm

(f) ABSOLUTE RELATIVE DIFFERENCE (%)

Figure 3.12 Same as Figure 3.10, except for λ = 3.749 μm.

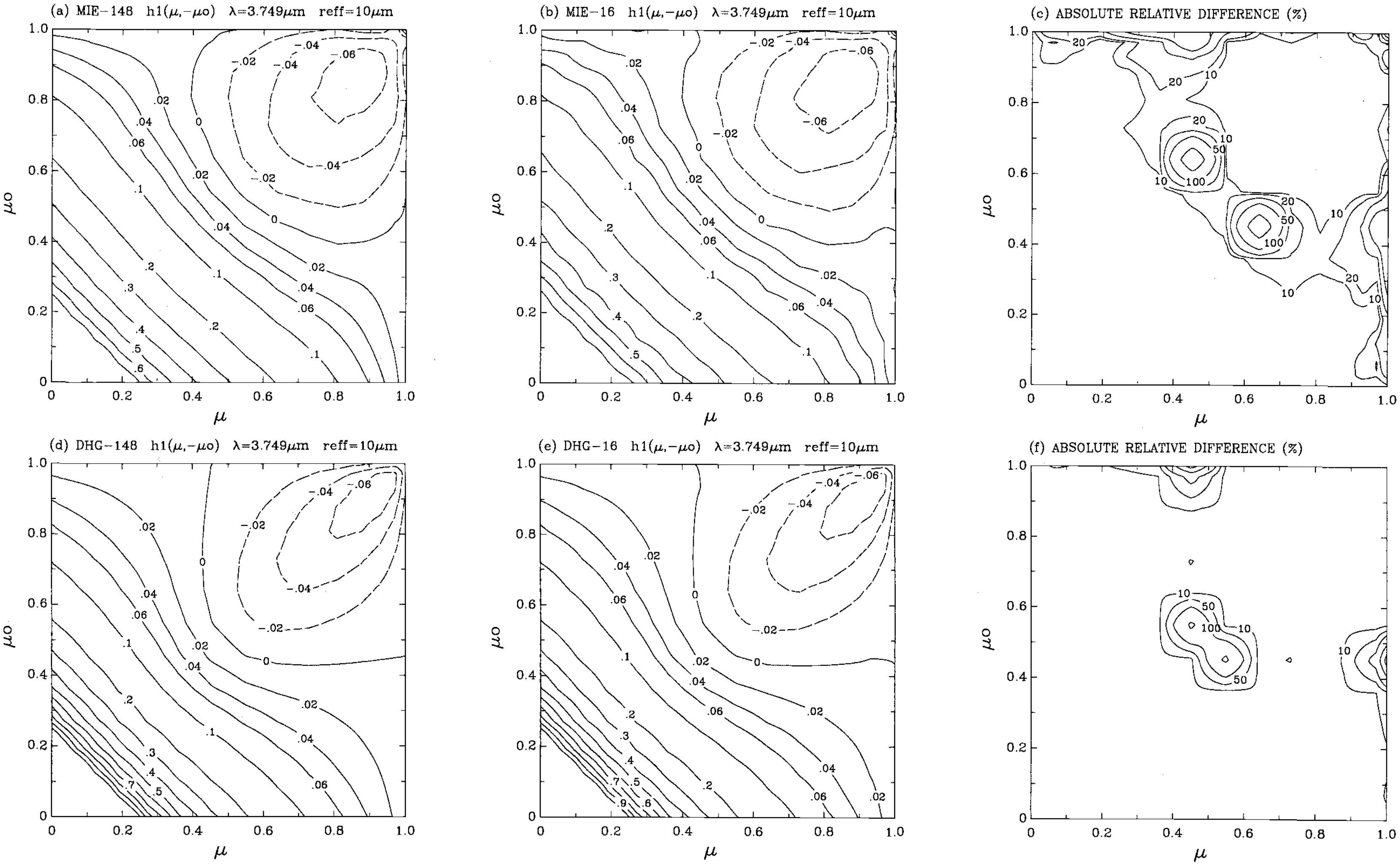

Figure 3.13 Same as Figure 3.12, except for $h^1(\mu, -\mu_o)$.

values. This is true also for the forward scattering, $h^1(-\mu, -\mu_o)$, and for all azimuth-dependent functions ($m > 0$). The large domain of negative values is brought about by the broad minimum in the phase function. As for the values at $\mu = 1$ or $\mu_o = 1$, the azimuth-dependent functions $h^m(\mu, -\mu_o) = 0$ for all $m \geq 0$.

Figures 3.10-3.13 also show the absolute relative differences in the h^m functions between the 148-stream scheme and the 16-stream scheme. These differences are shown in the right columns. The absolute relative difference is taken to be the absolute value of the difference between the 148-stream and the 16-stream schemes divided by the 148-stream and multiplied by 100%. For the conservative cases ($\lambda = 0.614\,\mu$m) calculated using the Mie phase functions, large differences ($> 50\%$) between the 148- and 16-stream schemes are generally found in $h^0(\mu, -\mu_o)$ and $h^1(\mu, -\mu_o)$. For the nonconservative scattering ($\lambda = 3.749\,\mu$m) calculated using the Mie phase functions, much smaller differences ($< 10\%$) are found in $h^0(\mu, -\mu_o)$ and $h^1(\mu, -\mu_o)$, except when $h^1(\mu, -\mu_o)$ approaches zero (note that the relative difference becomes very large as the denominator approaches zero). The smaller differences between the 148- and the 16-stream schemes obtained for $\lambda = 3.749\,\mu$m are because of both a smaller size parameter and a smaller single-scattering albedo for this wavelength as compared to $\lambda = 0.614\,\mu$m. As for the DHG phase functions, values of $h^0(\mu, -\mu_o)$ and $h^1(\mu, -\mu_o)$ show small differences between the 148- and the 16-stream schemes.

Having studied the h^m functions, the next step is to apply the doubling method (e.g., Goody and Yung, 1989) to calculate cloud reflection, transmission, and emission for various cloud visible optical depths. In applying the doubling method, the reflection function, $R(\tau_c; \mu, \mu_o, \phi - \phi_o)$, and transmission function, $T(\tau_c; \mu, \mu_o, \phi - \phi_o)$, are expanded in Fourier series given by

$$R(\tau_c;\mu,\mu_o,\phi-\phi_o) = R^0(\tau_c;\mu,\mu_o) + 2\sum_{m=1}^{M} R^m(\tau_c;\mu,\mu_o)\cos m(\phi-\phi_o), \tag{3.20}$$

$$T(\tau_c;\mu,\mu_o,\phi-\phi_o) = T^0(\tau_c;\mu,\mu_o) + 2\sum_{m=1}^{M} T^m(\tau_c;\mu,\mu_o)\cos m(\phi-\phi_o), \tag{3.21}$$

where τ_c is the cloud visible optical depth, μ is the cosine of the satellite zenith angle θ, μ_o is the cosine of the solar zenith angle θ_o, and $\phi-\phi_o$ is the relative azimuth angle. Note that the actual cloud optical depth is wavelength-dependent. That is,

$$\frac{\tau_{c1}(\lambda_1, r_{eff})}{\tau_{c2}(\lambda_2, r_{eff})} = \frac{Q_{ext1}(\lambda_1, r_{eff})}{Q_{ext2}(\lambda_2, r_{eff})}. \tag{3.22}$$

For each azimuthal component, an optically thin layer of cloud optical depth $\Delta\tau_c$ were used to initiate the doubling procedure. The reflection and transmission functions for this layer were calculated using the single scattering approximation (Liou, 1980; Goody and Yung, 1989). In the single scattering approximation, the reflection and transmission for an optically thin layer, $\Delta\tau_c$, are given in discrete form by

$$R^m(\Delta\tau_c;\mu_i,\mu_j) = \frac{\Delta\tau_c}{4\mu_i\mu_j} h^m(\mu_i,-\mu_j), \tag{3.23}$$

$$T^m(\Delta\tau_c;\mu_i,\mu_j) = e^{-\Delta\tau_c/\mu_i}\delta_{ij} + \frac{\Delta\tau_c}{4\mu_i\mu_j} h^m(\mu_i,\mu_j), \tag{3.24}$$

where δ_{ij} is the Kronecker δ-function, $e^{-\Delta\tau_c/\mu_i}\delta_{ij}$ is the direct transmission, and $i,j = 1,2,\ldots,K$ are at the Gauss quadrature points.

The upwelling radiance, $\mathbf{I}^+$, and downwelling radiance, $\mathbf{I}^-$, are given by

$$\mathbf{I}_0^+ = \mathbf{R}\mathbf{I}_0^- + \mathbf{T}\mathbf{I}_1^+ + \mathbf{E}^+, \tag{3.25}$$

$$\mathbf{I}_1^- = \mathbf{T}\mathbf{I}_0^- + \mathbf{R}\mathbf{I}_1^+ + \mathbf{E}^-, \tag{3.26}$$

where $\mathbf{R}$ is the reflection matrix, $\mathbf{T}$ is the transmission matrix, $\mathbf{E}$ is the emission vector, $\mathbf{I}$ is the radiance vector, 0 indicates the top of the layer, 1 indicates the bottom, + indicates upwelling, and – indicates downwelling. The elements in the vectors, $\mathbf{I}$ and $\mathbf{E}$, and the matrices, $\mathbf{R}$ and $\mathbf{T}$, are values calculated at the Gauss quadrature points. The elements in $\mathbf{R}$, $\mathbf{T}$, and $\mathbf{E}$ are given by

$$\begin{aligned} R_{ij}^m &= 2R^m(\Delta\tau_c; \mu_i, \mu_j)a_j\mu_j \\ &= \frac{a_j\Delta\tau_c}{2\mu_i}h^m(\mu_i, -\mu_j), \end{aligned} \tag{3.27}$$

$$\begin{aligned} T_{ij}^m &= e^{-\Delta\tau_c/\mu_i}\delta_{ij} + 2T^m(\Delta\tau_c; \mu_i, \mu_j)a_j\mu_j \\ &= \left(1 - \frac{\Delta\tau_c}{\mu_i}\right)\delta_{ij} + \frac{a_j\Delta\tau_c}{2\mu_i}h^m(\mu_i, \mu_j), \end{aligned} \tag{3.28}$$

$$\begin{aligned} E_i^m &= (1-\omega_0)\left(1 - e^{-\Delta\tau_c/\mu_i}\right)B(T_c, \lambda) \\ &= (1-\omega_0)\frac{\Delta\tau_c}{\mu_i}B(T_c, \lambda), \end{aligned} \tag{3.29}$$

where a_j is the jth Gauss quadrature weight and $B(T_c, \lambda)$ is the Planck function for temperature T_c and wavelength λ. The reflection, transmission, and emission for a cloud of any optical depth are then obtained through the doubling rules which are given by

$$\mathbf{R}(2\Delta\tau_c) = \mathbf{R}(\Delta\tau_c) + \mathbf{T}(\Delta\tau_c)[1 - \mathbf{R}(\Delta\tau_c)\mathbf{R}(\Delta\tau_c)]^{-1}\mathbf{R}(\Delta\tau_c)\mathbf{T}(\Delta\tau_c), \tag{3.30}$$

$$\mathbf{T}(2\Delta\tau_c) = \mathbf{T}(\Delta\tau_c)[\mathbf{1} - \mathbf{R}(\Delta\tau_c)\mathbf{R}(\Delta\tau_c)]^{-1}\mathbf{T}(\Delta\tau_c), \tag{3.31}$$

$$\mathbf{E}(2\Delta\tau_c) = \mathbf{E}(\Delta\tau_c) + \mathbf{T}(\Delta\tau_c)[\mathbf{1} - \mathbf{R}(\Delta\tau_c)\mathbf{R}(\Delta\tau_c)]^{-1}[\mathbf{1} + \mathbf{R}(\Delta\tau_c)]\mathbf{E}(\Delta\tau_c), \tag{3.32}$$

where **1** is the identity matrix.

Figures 3.14-3.25 show polar plots of the reflection functions $R(\tau_c; \mu, \mu_o, \phi - \phi_o)$ calculated using Mie and DHG phase functions and using 148-stream and 16-stream schemes. Figures 3.14-3.16 show values for $\lambda = 0.614\mu$m, $r_{eff} = 10\mu$m, $\mu_o = 0.9947$ ($\theta_o = 5.9°$), and for cloud visible optical depths, $\tau_c = 1$, 8, and 64. Figures 3.17-3.19 show the same as Figures 3.14-3.16 but for large solar zenith angle $\mu_o = 0.4524$ ($\theta_o = 63.1°$). Figures 3.20-3.22 show values for $\lambda = 3.749$ μm, $\tau_c = 8$, $\mu_o = 0.9947$ ($\theta_o = 5.9°$), and for droplet effective radii, $r_{eff} = 4$, 10, and 28 μm. Figures 3.23-3.25 show the same as Figures 3.20-3.22 but for large solar zenith angle $\mu_o = 0.4524$ ($\theta_o = 63.1°$). The top-row figures were obtained using Mie phase functions. The middle-row figures were obtained using DHG phase functions. Figures 3.14-3.25 were constructed to show results for (a) Mie 148-stream scheme, (b) Mie 16-stream scheme, (c) absolute relative differences between (a) and (b), (d) DHG 148-stream scheme, (e) DHG 16-stream scheme, (f) absolute relative differences between (d) and (e), (g) absolute relative differences between (a) and (d), (h) absolute relative differences between (b) and (e), and (i) absolute relative differences between (a) and (e).

For conservative scattering $\lambda = 0.614$ μm, as shown in Figures 3.14-3.19, the absolute relative differences obtained between the Mie 148- and the Mie 16-stream schemes are generally less than 3%. The absolute relative differences obtained between the DHG 148- and the DHG 16-stream schemes are generally also small. The absolute relative differences obtained between the Mie 148- and the DHG 16-stream schemes

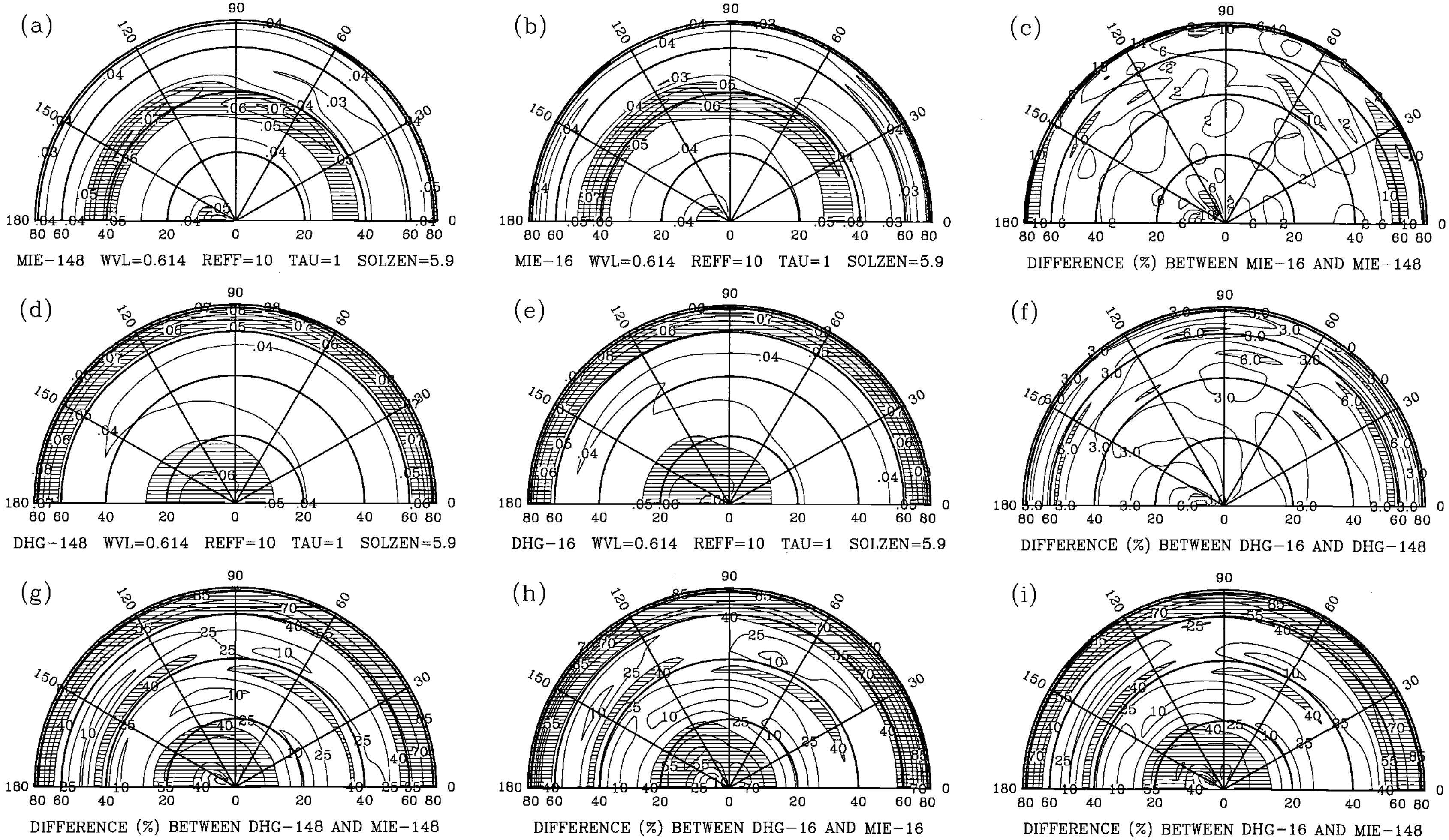

MIE−148 WVL=0.614 REFF=10 TAU=1 SOLZEN=5.9

MIE−16 WVL=0.614 REFF=10 TAU=1 SOLZEN=5.9

DIFFERENCE (%) BETWEEN MIE−16 AND MIE−148

DHG−148 WVL=0.614 REFF=10 TAU=1 SOLZEN=5.9

DHG−16 WVL=0.614 REFF=10 TAU=1 SOLZEN=5.9

DIFFERENCE (%) BETWEEN DHG−16 AND DHG−148

DIFFERENCE (%) BETWEEN DHG−148 AND MIE−148

DIFFERENCE (%) BETWEEN DHG−16 AND MIE−16

DIFFERENCE (%) BETWEEN DHG−16 AND MIE−148

Figure 3.14 Polar plots of $R(\tau_c; \mu_o, \mu, \phi - \phi_o)$ for $\lambda = 0.614\ \mu m$, $r_{eff} = 10\ \mu m$, $\tau_c = 1$, and $\theta_o = 5.9°$. (a) Mie 148–stream; (b) Mie 16–stream; (c) difference between (a) and (b); (d) DHG 148–stream; (e) DHG 16–stream; (f) difference between (d) and (e); (g) difference between (a) and (d); (h) difference between (b) and (e); (i) difference between (a) and (e). The differences are absolute relative differences in percentage.

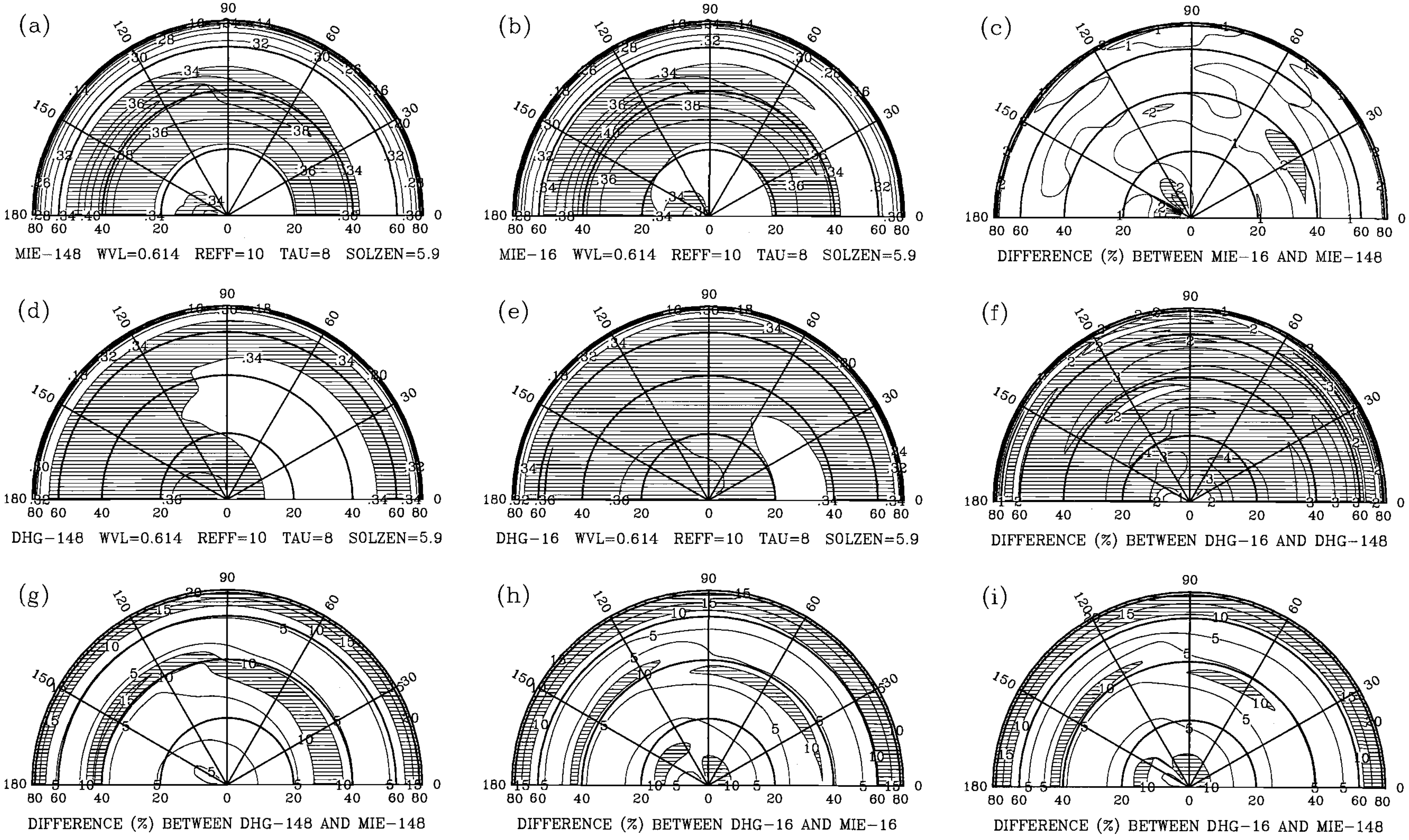

MIE−148 WVL=0.614 REFF=10 TAU=8 SOLZEN=5.9

MIE−16 WVL=0.614 REFF=10 TAU=8 SOLZEN=5.9

DIFFERENCE (%) BETWEEN MIE−16 AND MIE−148

DHG−148 WVL=0.614 REFF=10 TAU=8 SOLZEN=5.9

DHG−16 WVL=0.614 REFF=10 TAU=8 SOLZEN=5.9

DIFFERENCE (%) BETWEEN DHG−16 AND DHG−148

DIFFERENCE (%) BETWEEN DHG−148 AND MIE−148

DIFFERENCE (%) BETWEEN DHG−16 AND MIE−16

DIFFERENCE (%) BETWEEN DHG−16 AND MIE−148

Figure 3.15 Same as Figure 3.14, except for $\tau_c = 8$.

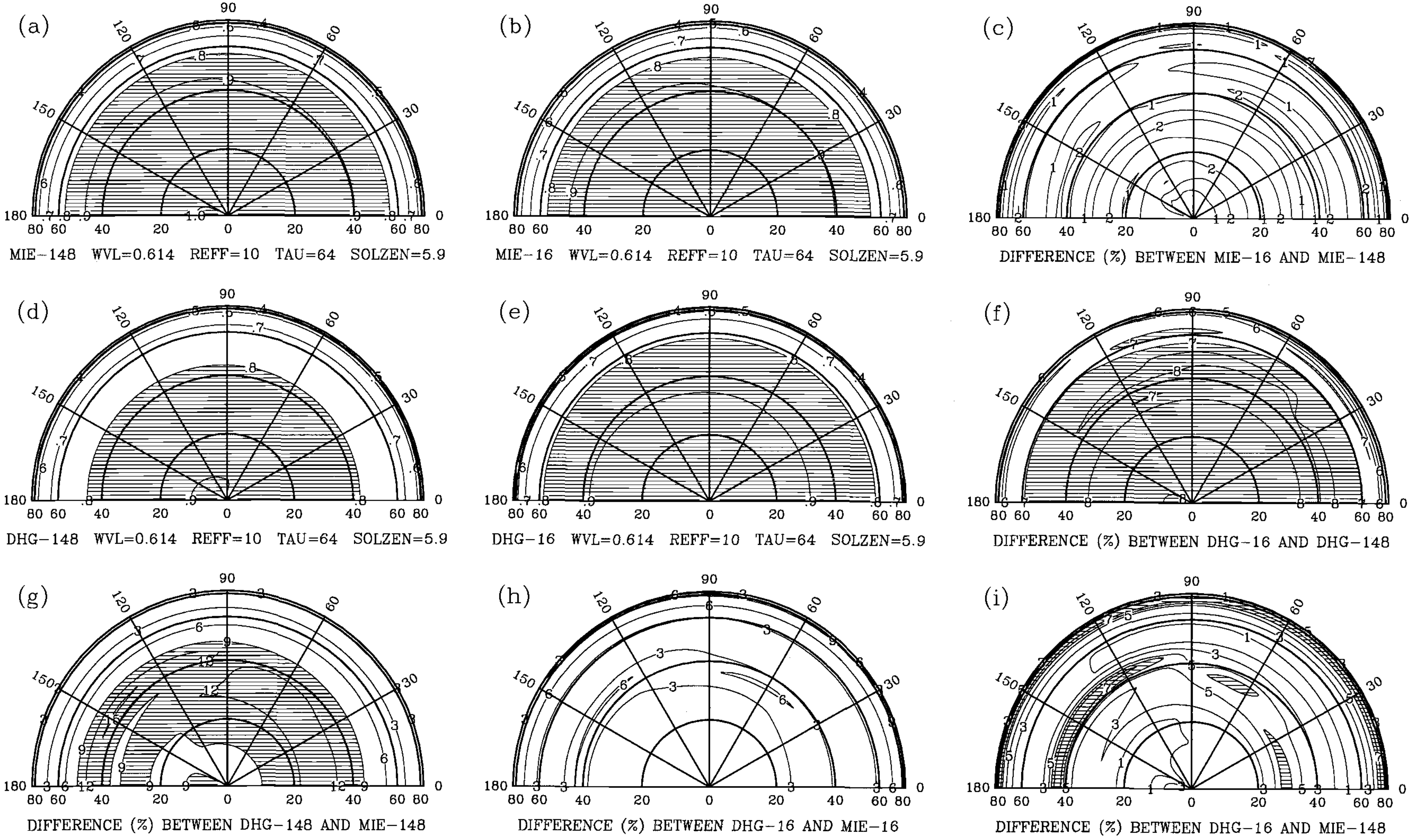

Figure 3.16 Same as Figure 3.14, except for $\tau_c = 64$.

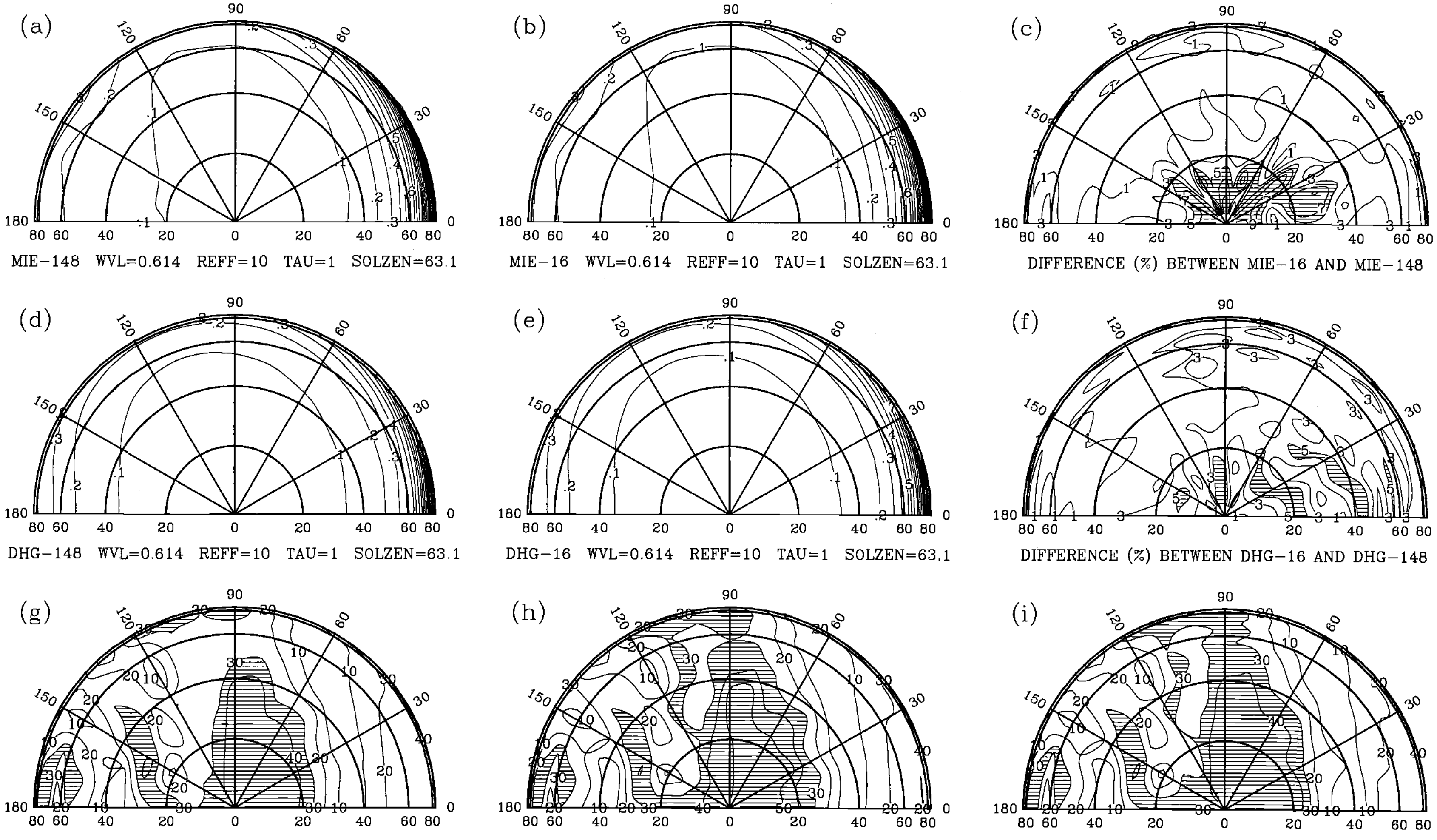

MIE-148 WVL=0.614 REFF=10 TAU=1 SOLZEN=63.1

MIE-16 WVL=0.614 REFF=10 TAU=1 SOLZEN=63.1

DIFFERENCE (%) BETWEEN MIE-16 AND MIE-148

DHG-148 WVL=0.614 REFF=10 TAU=1 SOLZEN=63.1

DHG-16 WVL=0.614 REFF=10 TAU=1 SOLZEN=63.1

DIFFERENCE (%) BETWEEN DHG-16 AND DHG-148

DIFFERENCE (%) BETWEEN DHG-148 AND MIE-148

DIFFERENCE (%) BETWEEN DHG-16 AND MIE-16

DIFFERENCE (%) BETWEEN DHG-16 AND MIE-148

Figure 3.17 Same as Figure 3.14, except for $\theta_o = 63.1°$.

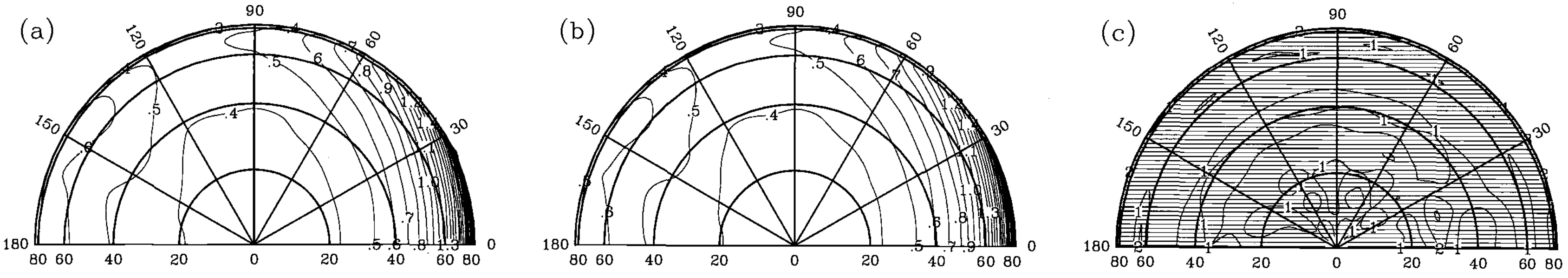

MIE−148 WVL=0.614 REFF=10 TAU=8 SOLZEN=63.1

MIE−16 WVL=0.614 REFF=10 TAU=8 SOLZEN=63.1

DIFFERENCE (%) BETWEEN MIE−16 AND MIE−148

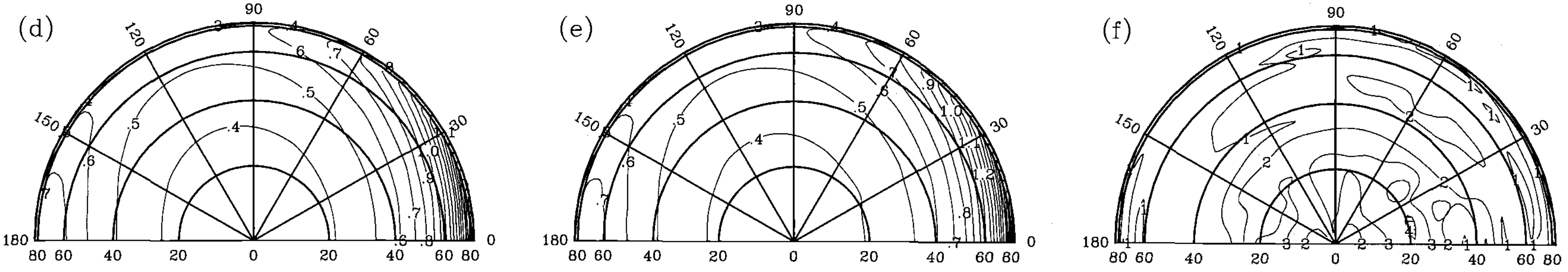

DHG−148 WVL=0.614 REFF=10 TAU=8 SOLZEN=63.1

DHG−16 WVL=0.614 REFF=10 TAU=8 SOLZEN=63.1

DIFFERENCE (%) BETWEEN DHG−16 AND DHG−148

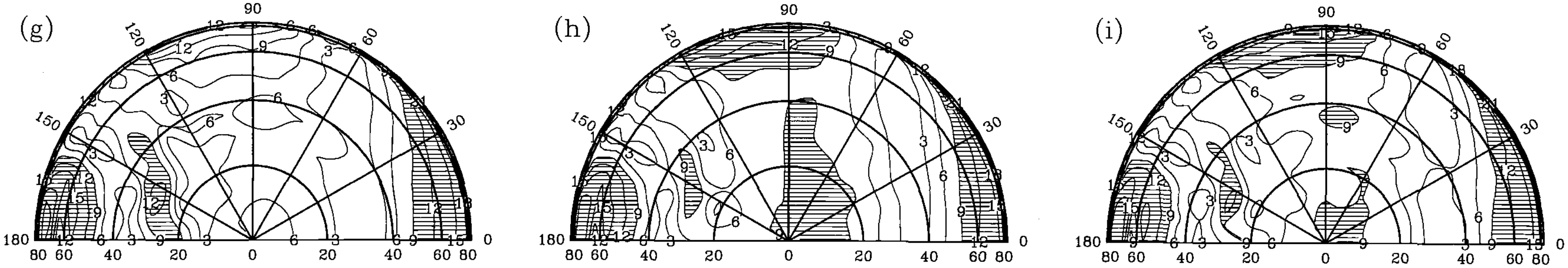

DIFFERENCE (%) BETWEEN DHG−148 AND MIE−148

DIFFERENCE (%) BETWEEN DHG−16 AND MIE−16

DIFFERENCE (%) BETWEEN DHG−16 AND MIE−148

Figure 3.18 Same as Figure 3.14, except for $\tau_c = 8$ and $\theta_o = 63.1°$.

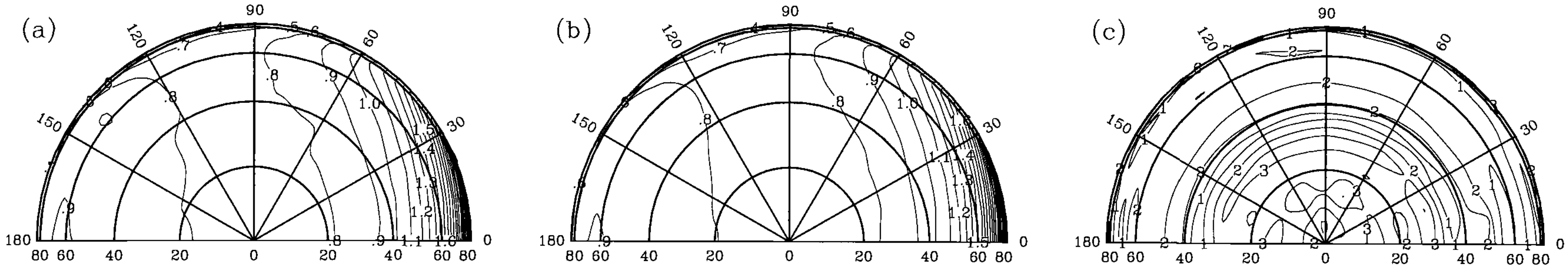

MIE−148 WVL=0.614 REFF=10 TAU=64 SOLZEN=63.1

MIE−16 WVL=0.614 REFF=10 TAU=64 SOLZEN=63.1

DIFFERENCE (%) BETWEEN MIE−16 AND MIE−148

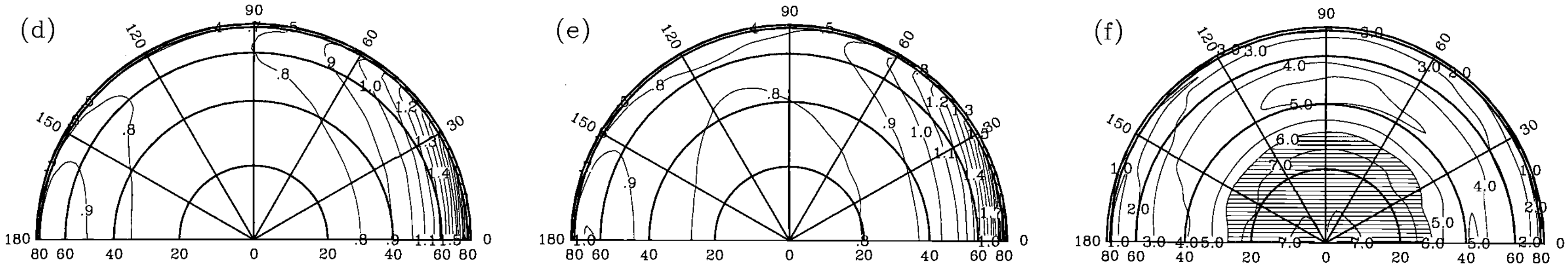

DHG−148 WVL=0.614 REFF=10 TAU=64 SOLZEN=63.1

DHG−16 WVL=0.614 REFF=10 TAU=64 SOLZEN=63.1

DIFFERENCE (%) BETWEEN DHG−16 AND DHG−148

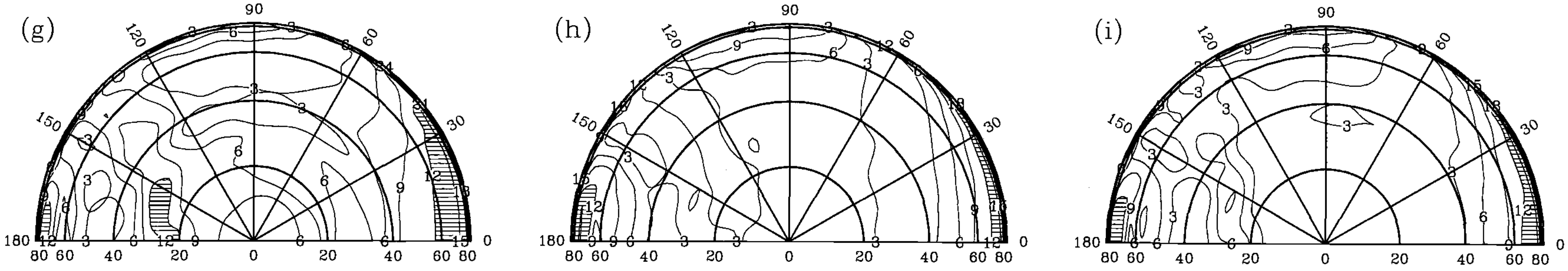

DIFFERENCE (%) BETWEEN DHG−148 AND MIE−148

DIFFERENCE (%) BETWEEN DHG−16 AND MIE−16

DIFFERENCE (%) BETWEEN DHG−16 AND MIE−148

Figure 3.19 Same as Figure 3.14, except for $\tau_c = 64$ and $\theta_o = 63.1°$.

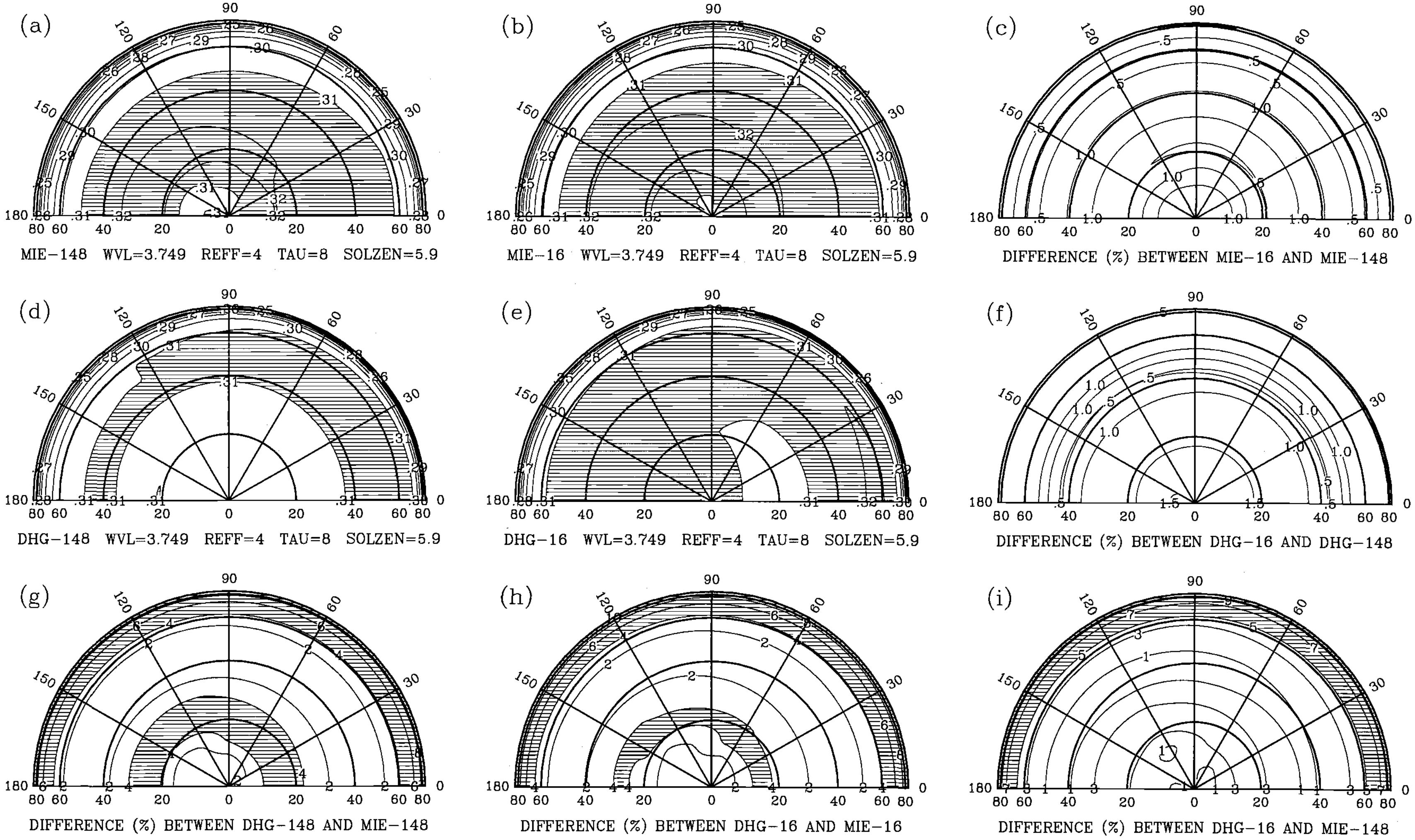

MIE−148 WVL=3.749 REFF=4 TAU=8 SOLZEN=5.9

MIE−16 WVL=3.749 REFF=4 TAU=8 SOLZEN=5.9

DIFFERENCE (%) BETWEEN MIE−16 AND MIE−148

DHG−148 WVL=3.749 REFF=4 TAU=8 SOLZEN=5.9

DHG−16 WVL=3.749 REFF=4 TAU=8 SOLZEN=5.9

DIFFERENCE (%) BETWEEN DHG−16 AND DHG−148

DIFFERENCE (%) BETWEEN DHG−148 AND MIE−148

DIFFERENCE (%) BETWEEN DHG−16 AND MIE−16

DIFFERENCE (%) BETWEEN DHG−16 AND MIE−148

Figure 3.20 Same as Figure 3.14, except for $\lambda = 3.749\ \mu m$, $r_{eff} = 4\ \mu m$, and $\tau_c = 8$.

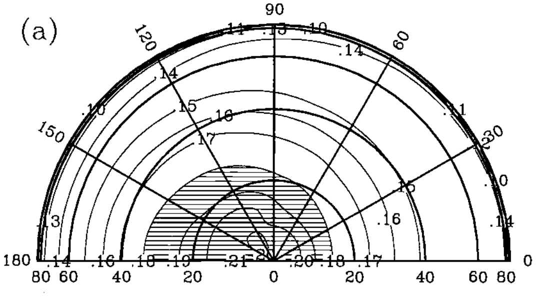

MIE−148 WVL=3.749 REFF=10 TAU=8 SOLZEN=5.9

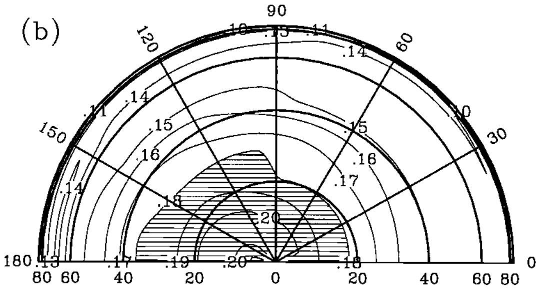

MIE−16 WVL=3.749 REFF=10 TAU=8 SOLZEN=5.9

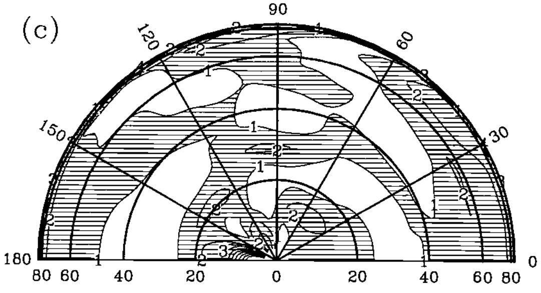

DIFFERENCE (%) BETWEEN MIE−16 AND MIE−148

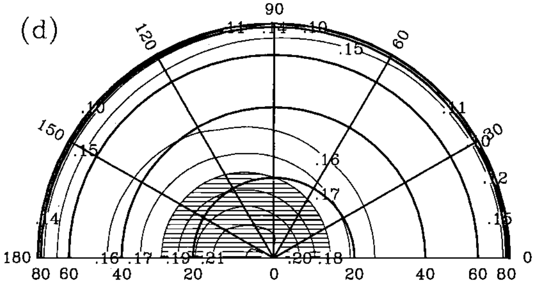

DHG−148 WVL=3.749 REFF=10 TAU=8 SOLZEN=5.9

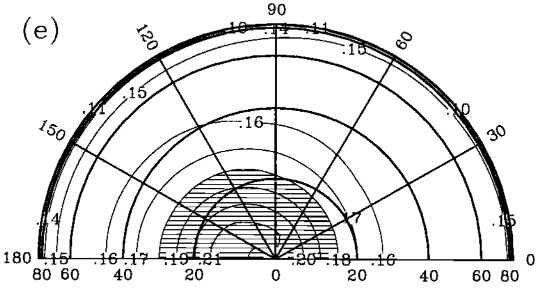

DHG−16 WVL=3.749 REFF=10 TAU=8 SOLZEN=5.9

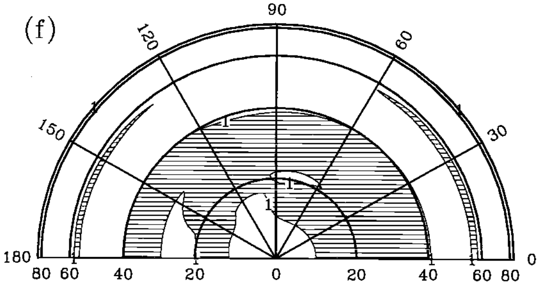

DIFFERENCE (%) BETWEEN DHG−16 AND DHG−148

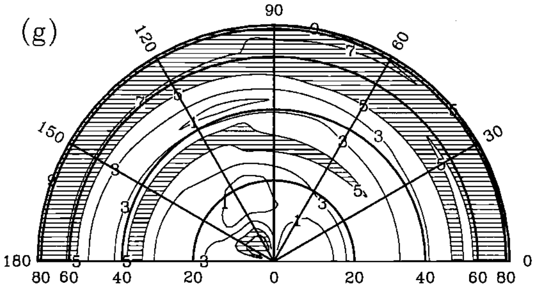

DIFFERENCE (%) BETWEEN DHG−148 AND MIE−148

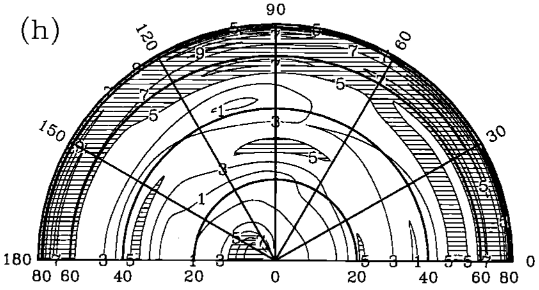

DIFFERENCE (%) BETWEEN DHG−16 AND MIE−16

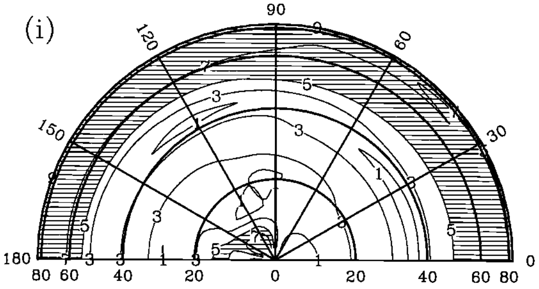

DIFFERENCE (%) BETWEEN DHG−16 AND MIE−148

Figure 3.21 Same as Figure 3.20, except for $r_{eff} = 10\ \mu m$.

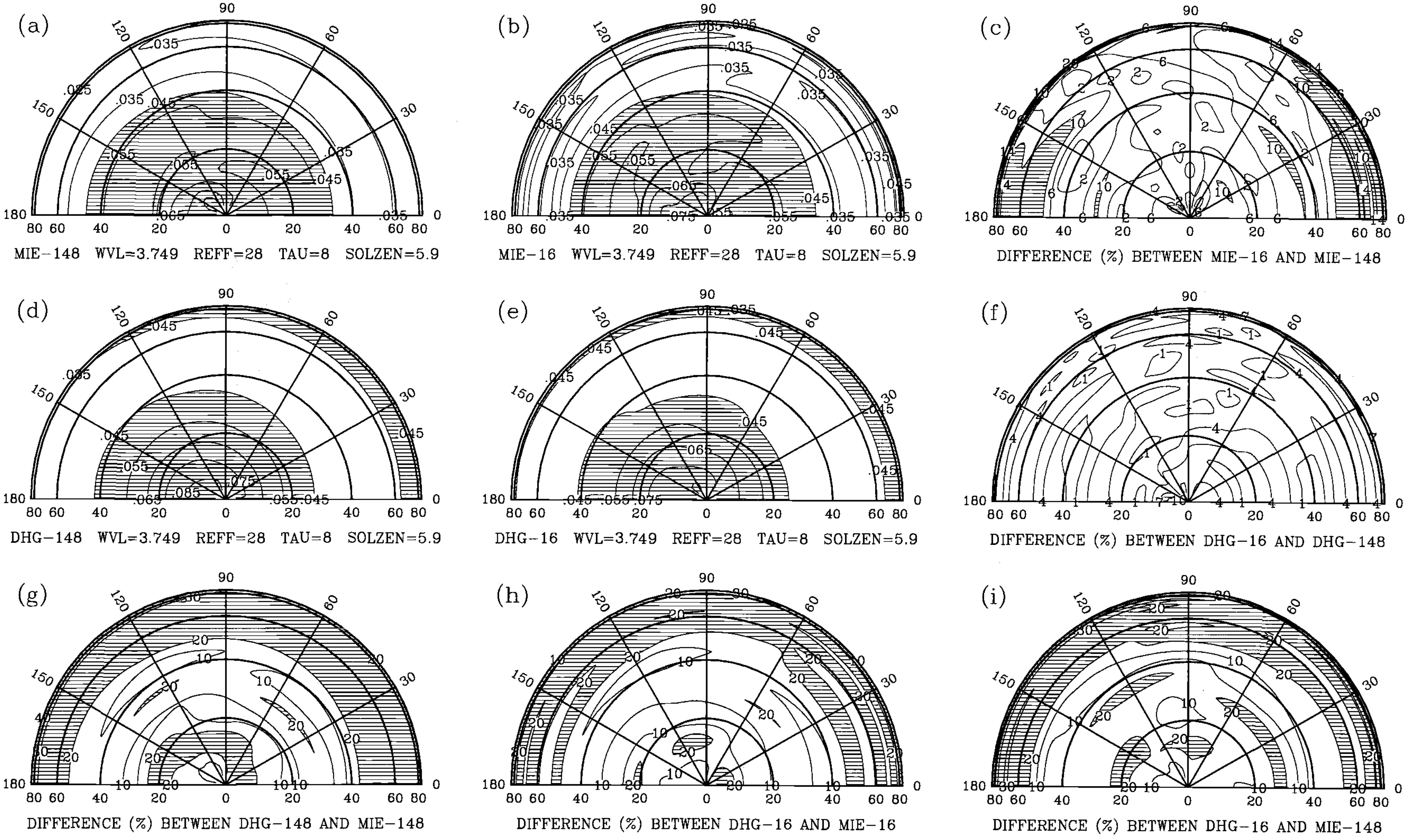

(a) MIE-148 WVL=3.749 REFF=28 TAU=8 SOLZEN=5.9

(b) MIE-16 WVL=3.749 REFF=28 TAU=8 SOLZEN=5.9

(c) DIFFERENCE (%) BETWEEN MIE-16 AND MIE-148

(d) DHG-148 WVL=3.749 REFF=28 TAU=8 SOLZEN=5.9

(e) DHG-16 WVL=3.749 REFF=28 TAU=8 SOLZEN=5.9

(f) DIFFERENCE (%) BETWEEN DHG-16 AND DHG-148

(g) DIFFERENCE (%) BETWEEN DHG-148 AND MIE-148

(h) DIFFERENCE (%) BETWEEN DHG-16 AND MIE-16

(i) DIFFERENCE (%) BETWEEN DHG-16 AND MIE-148

Figure 3.22 Same as Figure 3.20, except for $r_{eff} = 28\ \mu m$.

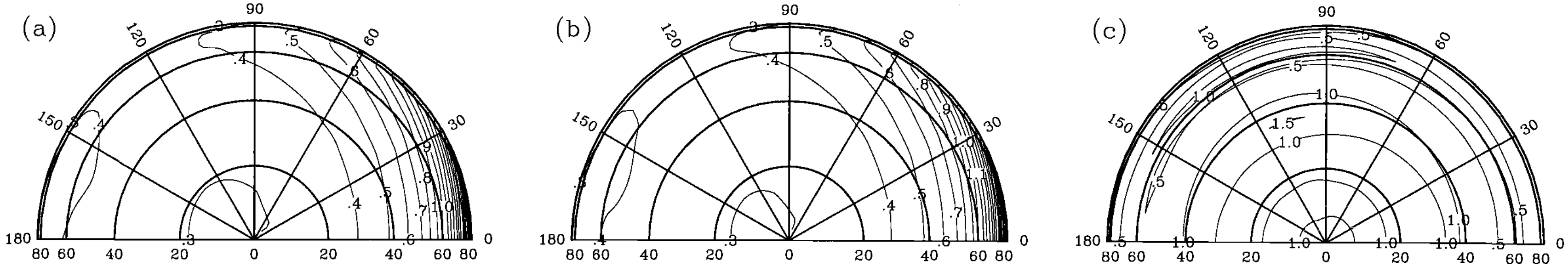

MIE-148 WVL=3.749 REFF=4 TAU=8 SOLZEN=63.1

MIE-16 WVL=3.749 REFF=4 TAU=8 SOLZEN=63.1

DIFFERENCE (%) BETWEEN MIE-16 AND MIE-148

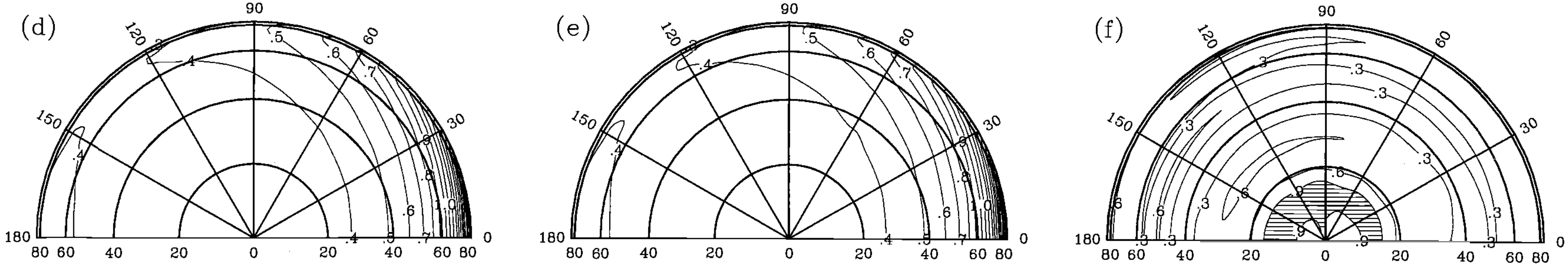

DHG-148 WVL=3.749 REFF=4 TAU=8 SOLZEN=63.1

DHG-16 WVL=3.749 REFF=4 TAU=8 SOLZEN=63.1

DIFFERENCE (%) BETWEEN DHG-16 AND DHG-148

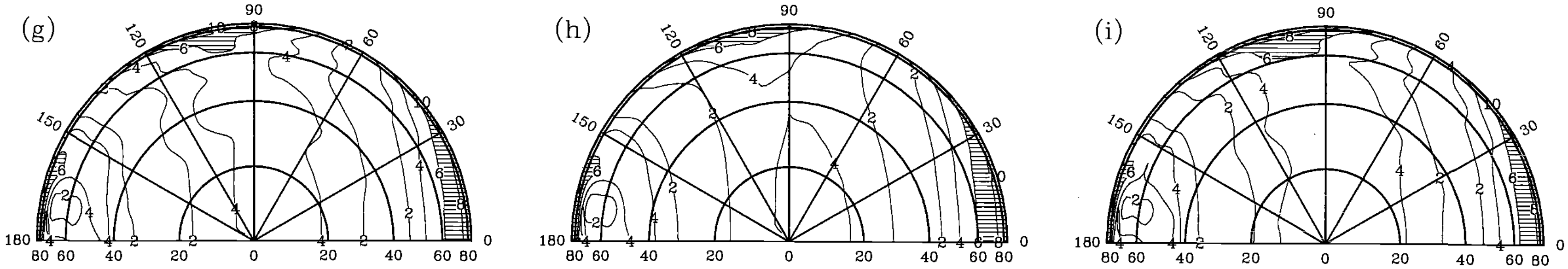

DIFFERENCE (%) BETWEEN DHG-148 AND MIE-148

DIFFERENCE (%) BETWEEN DHG-16 AND MIE-16

DIFFERENCE (%) BETWEEN DHG-16 AND MIE-148

Figure 3.23 Same as Figure 3.20, except for $\theta_o = 63.1°$.

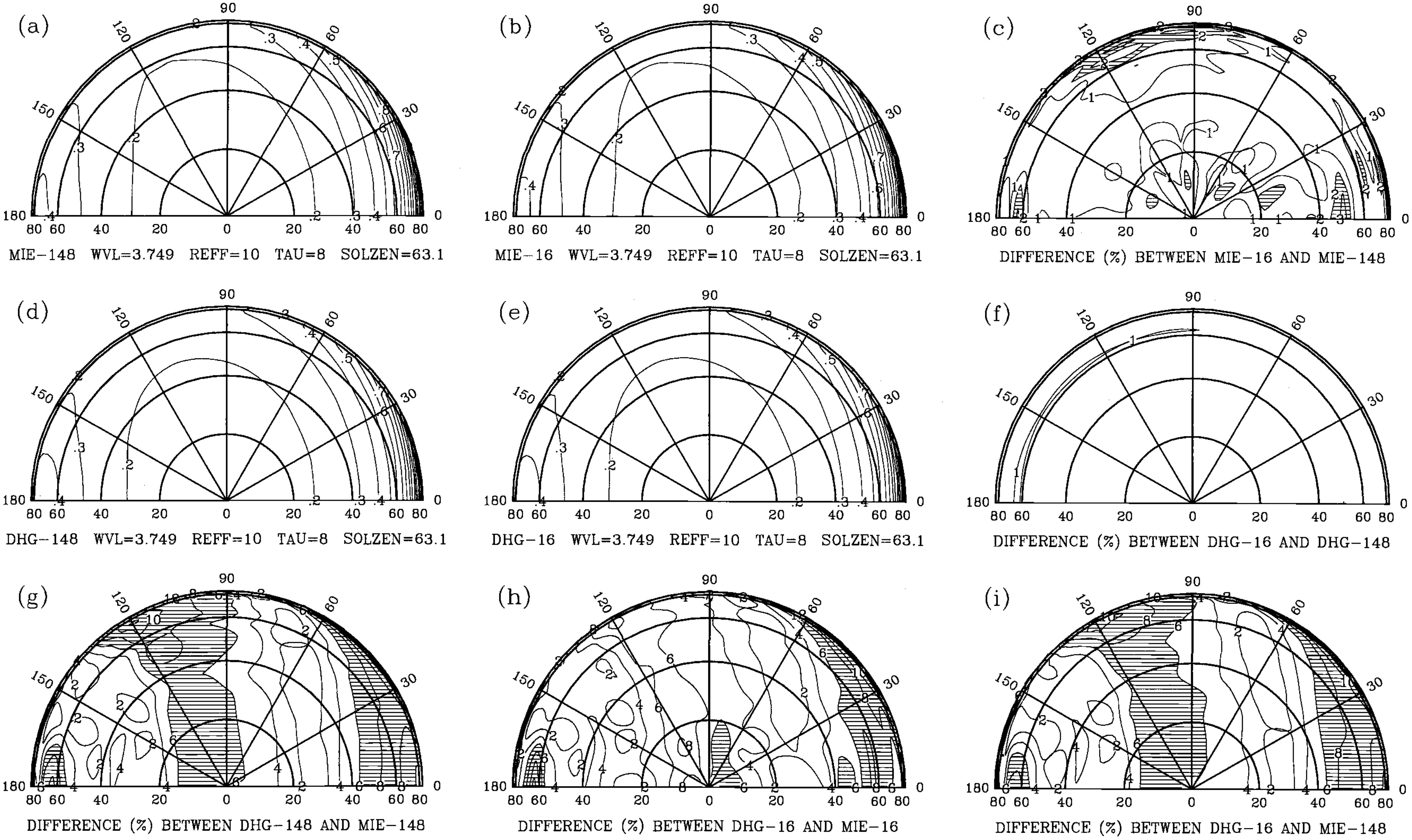

MIE-148 WVL=3.749 REFF=10 TAU=8 SOLZEN=63.1

MIE-16 WVL=3.749 REFF=10 TAU=8 SOLZEN=63.1

DIFFERENCE (%) BETWEEN MIE-16 AND MIE-148

DHG-148 WVL=3.749 REFF=10 TAU=8 SOLZEN=63.1

DHG-16 WVL=3.749 REFF=10 TAU=8 SOLZEN=63.1

DIFFERENCE (%) BETWEEN DHG-16 AND DHG-148

DIFFERENCE (%) BETWEEN DHG-148 AND MIE-148

DIFFERENCE (%) BETWEEN DHG-16 AND MIE-16

DIFFERENCE (%) BETWEEN DHG-16 AND MIE-148

Figure 3.24 Same as Figure 3.20, except for $r_{eff} = 10\ \mu m$ and $\theta_o = 63.1°$.

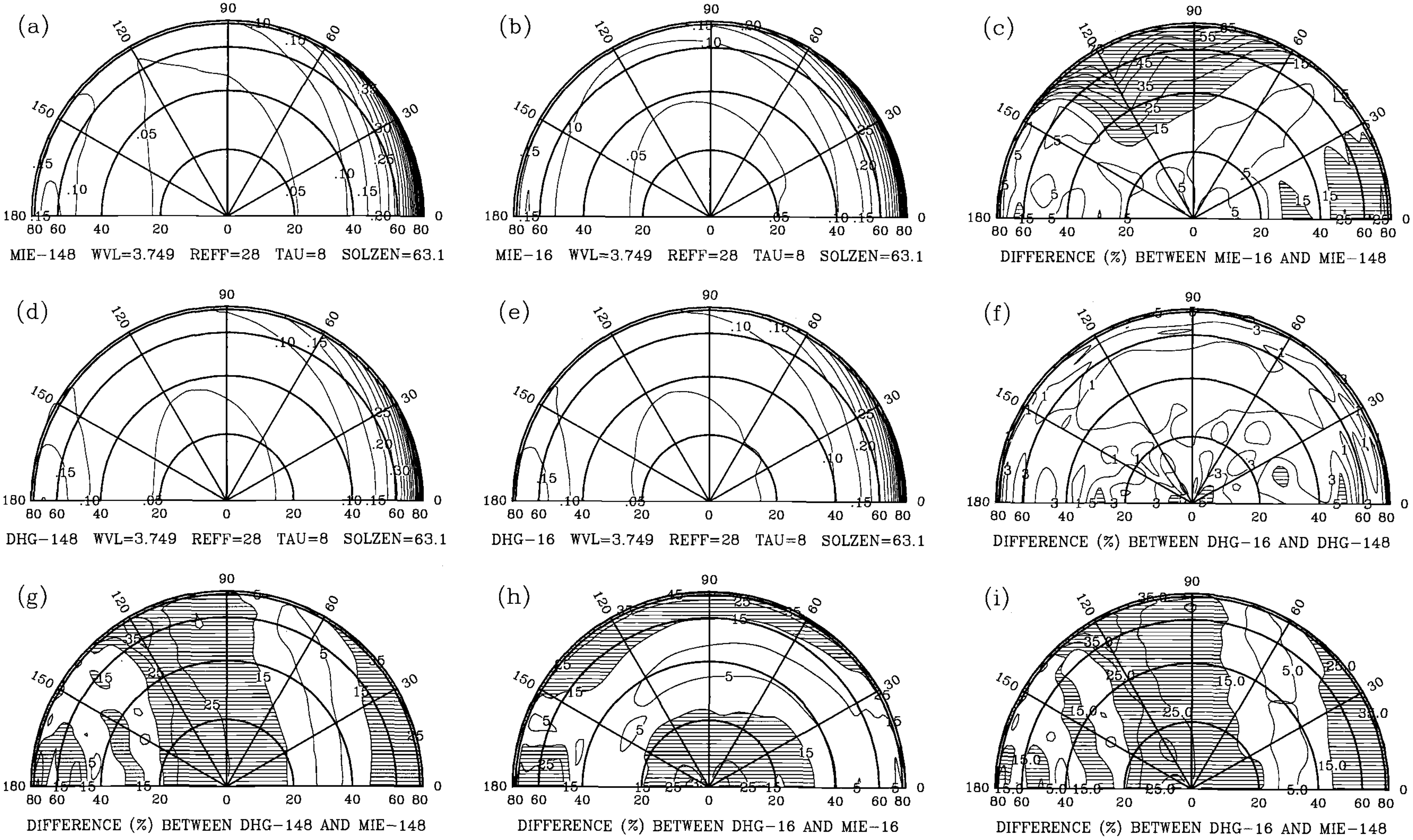

MIE-148 WVL=3.749 REFF=28 TAU=8 SOLZEN=63.1

MIE-16 WVL=3.749 REFF=28 TAU=8 SOLZEN=63.1

DIFFERENCE (%) BETWEEN MIE-16 AND MIE-148

DHG-148 WVL=3.749 REFF=28 TAU=8 SOLZEN=63.1

DHG-16 WVL=3.749 REFF=28 TAU=8 SOLZEN=63.1

DIFFERENCE (%) BETWEEN DHG-16 AND DHG-148

DIFFERENCE (%) BETWEEN DHG-148 AND MIE-148

DIFFERENCE (%) BETWEEN DHG-16 AND MIE-16

DIFFERENCE (%) BETWEEN DHG-16 AND MIE-148

Figure 3.25 Same as Figure 3.20, except for $r_{eff} = 28\ \mu m$ and $\theta_o = 63.1°$.

are generally an order of magnitude larger than those obtained between the Mie 148- and the Mie 16-stream schemes. These differences are largest for the $\tau_c = 1$ case. The findings here suggest that, as compared to the Mie 148-stream scheme, the use of a Mie 16-stream scheme may give rise to biases of a few percent (see sub-figures (c)), whereas the use of a DHG 16-stream scheme may give rise to larger biases of a few tens of percent (see sub-figures (i)).

For the nonconservative scattering $\lambda = 3.749\ \mu$m, as shown in Figures 3.20-3.25, the absolute relative differences obtained between the DHG 148- and the DHG 16-stream schemes are generally less than those obtained between the Mie 148- and the Mie 16-stream schemes. The absolute relative differences obtained between the Mie 148-stream and the DHG 16-stream schemes are similar in magnitude to those obtained between the Mie 148- and the Mie 16-stream schemes. Some differences between the Mie 148- and the Mie 16-stream schemes are larger than 30% for the $r_{eff} = 28\ \mu$m, $\theta = 63.1°$ case. The results suggest that, as compared to the Mie 148-stream scheme, the use of a DHG 16-stream or a Mie 16-stream schemes may give rise to biases of similar magnitude in the retrievals of cloud droplet effective radius. The bias may be less than 10% for $r_{eff} = 10\ \mu$m and may increase with increasing droplet effective radius.

Figures 3.26-3.31 show the reflection functions $R(\tau_c; \mu, \mu_o, \phi - \phi_o)$ as functions of cloud visible optical depth and droplet effective radius for forward scattering ($\theta_o = 63.1°$, $\theta = 56.8°$, $\phi - \phi_o = 0°$), side-scattering ($\theta_o = 63.1°$, $\theta = 56.8°$, $\phi - \phi_o = 90°$), and backscattering ($\theta_o = 63.1°$, $\theta = 56.8°$, $\phi - \phi_o = 180°$). Figures 3.26-3.28 show values for conservative scattering $\lambda = 0.614\ \mu$m and Figures 3.29-3.31 show values for nonconservative scattering $\lambda = 3.749\ \mu$m. Figures 3.26 and 3.27 show

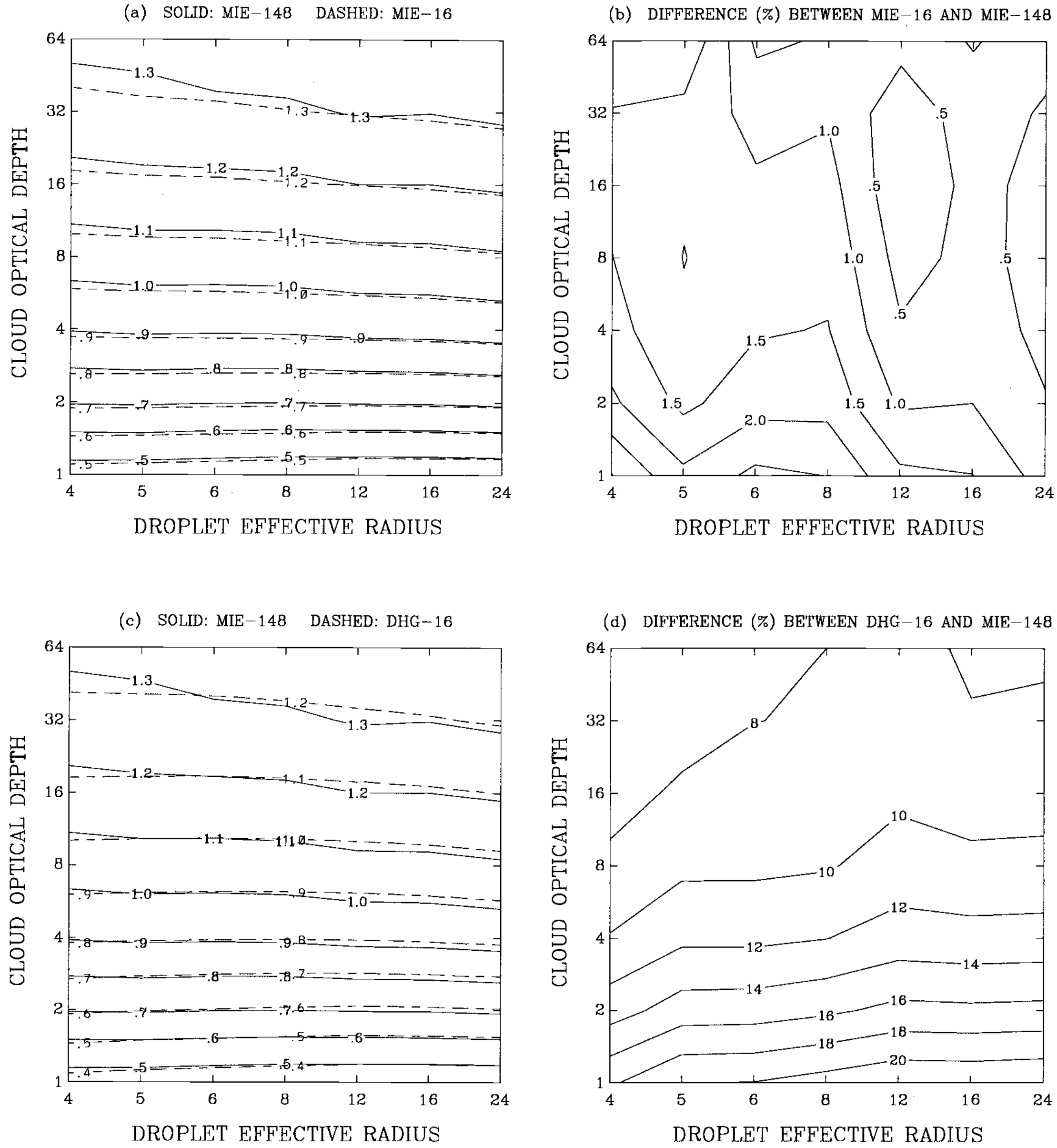
(a) SOLID: MIE-148 DASHED: MIE-16

(b) DIFFERENCE (%) BETWEEN MIE-16 AND MIE-148

(c) SOLID: MIE-148 DASHED: DHG-16

(d) DIFFERENCE (%) BETWEEN DHG-16 AND MIE-148

Figure 3.26 $R(\tau_c; \mu_o, \mu, \phi - \phi_o)$ as functions of cloud visible optical depth and droplet effective radius for $\lambda = 0.614\ \mu m$ and $(\theta_o, \theta, \phi - \phi_o) = (63.1°, 56.8°, 0°)$. (a) Mie 148–stream (solid lines) and Mie 16–stream (dashed lines); (b) absolute relative differences between Mie 148–stream and Mie 16–stream; (c) Mie 148–stream (solid) and DHG 16–stream (dashed); (d) absolute relative differences between Mie 148–stream and DHG 16–stream. Differences in (b) and (d) are in percentage.

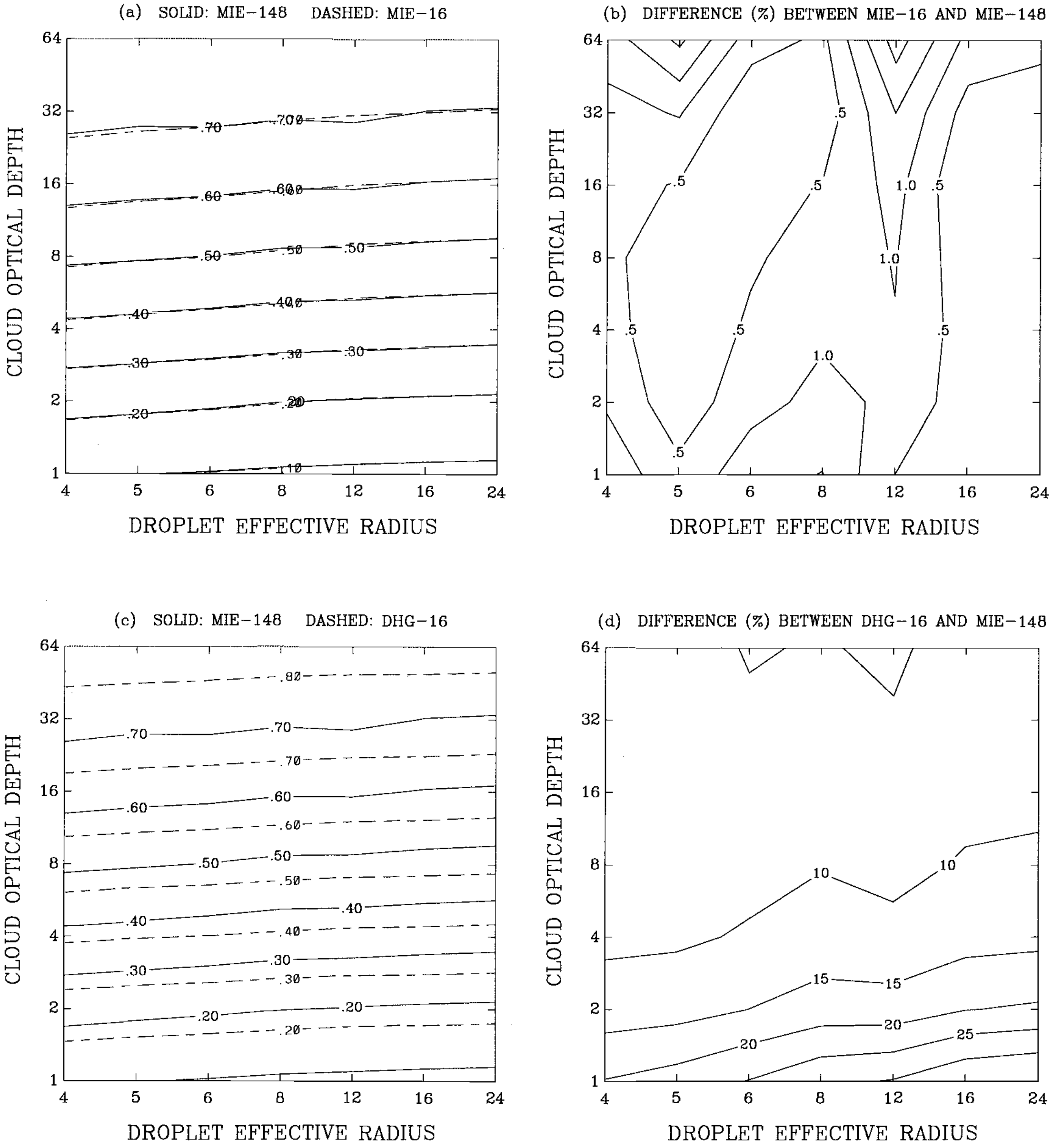

Figure 3.27 Same as Figure 3.26, except for $\phi - \phi_o = 90°$.

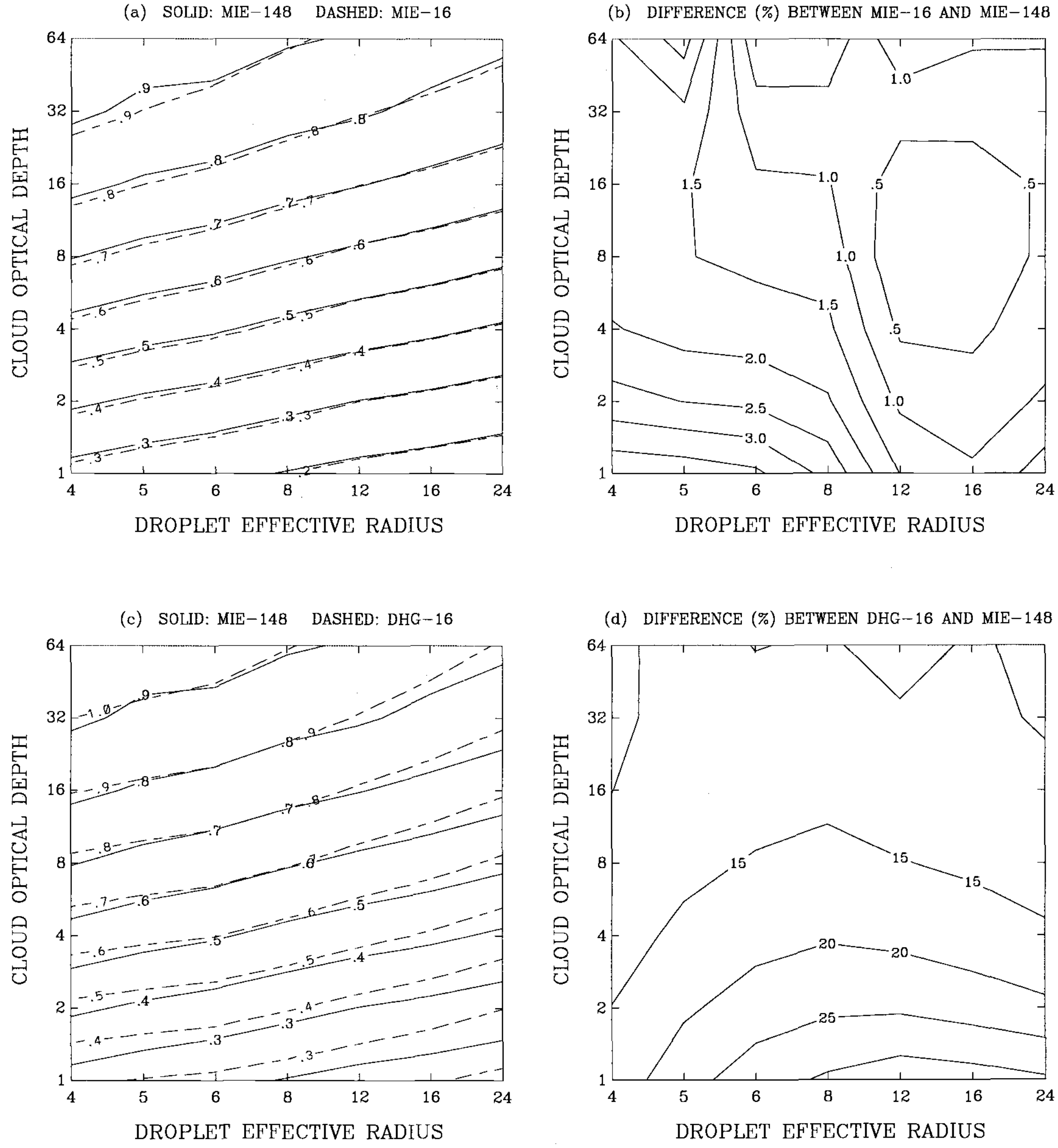

Figure 3.28 Same as Figure 3.26, except for $\phi - \phi_o = 180°$.

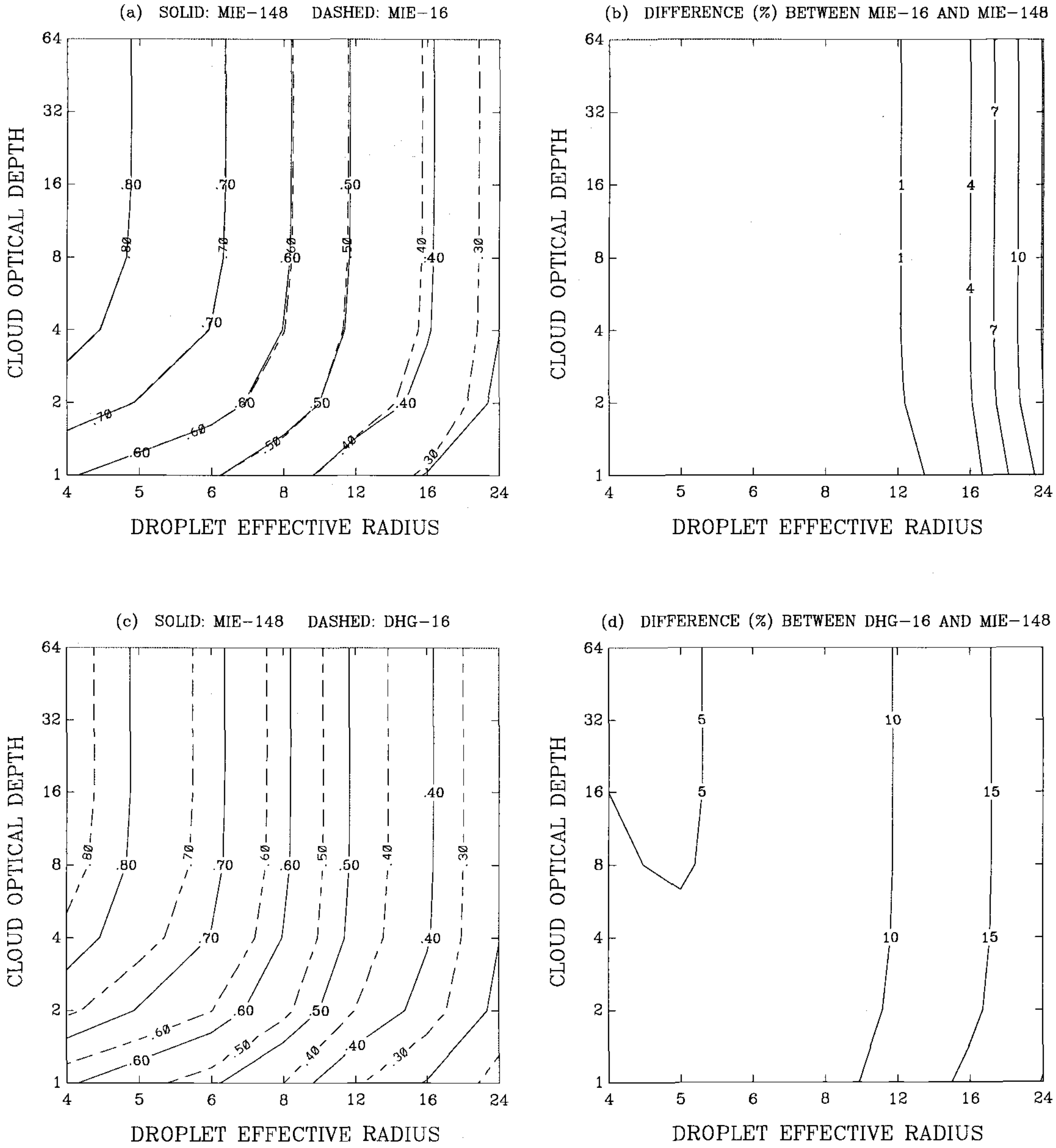

Figure 3.29 Same as Figure 3.26, except for $\lambda = 3.749\ \mu m$.

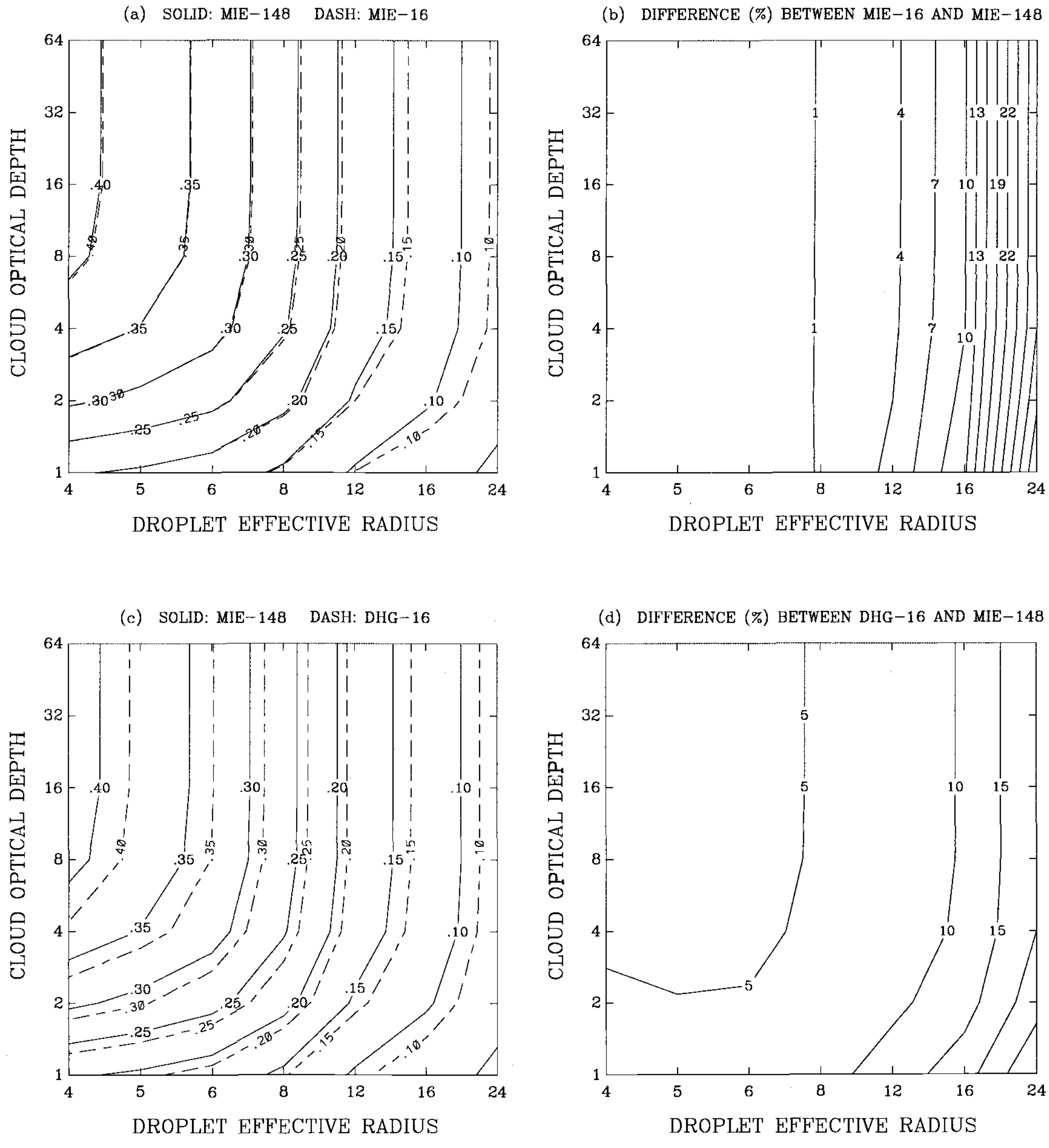
(a) SOLID: MIE-148 DASH: MIE-16

(b) DIFFERENCE (%) BETWEEN MIE-16 AND MIE-148

(c) SOLID: MIE-148 DASH: DHG-16

(d) DIFFERENCE (%) BETWEEN DHG-16 AND MIE-148

Figure 3.30 Same as Figure 3.26, except for $\lambda = 3.749$ μm and $\phi - \phi_o = 90°$.

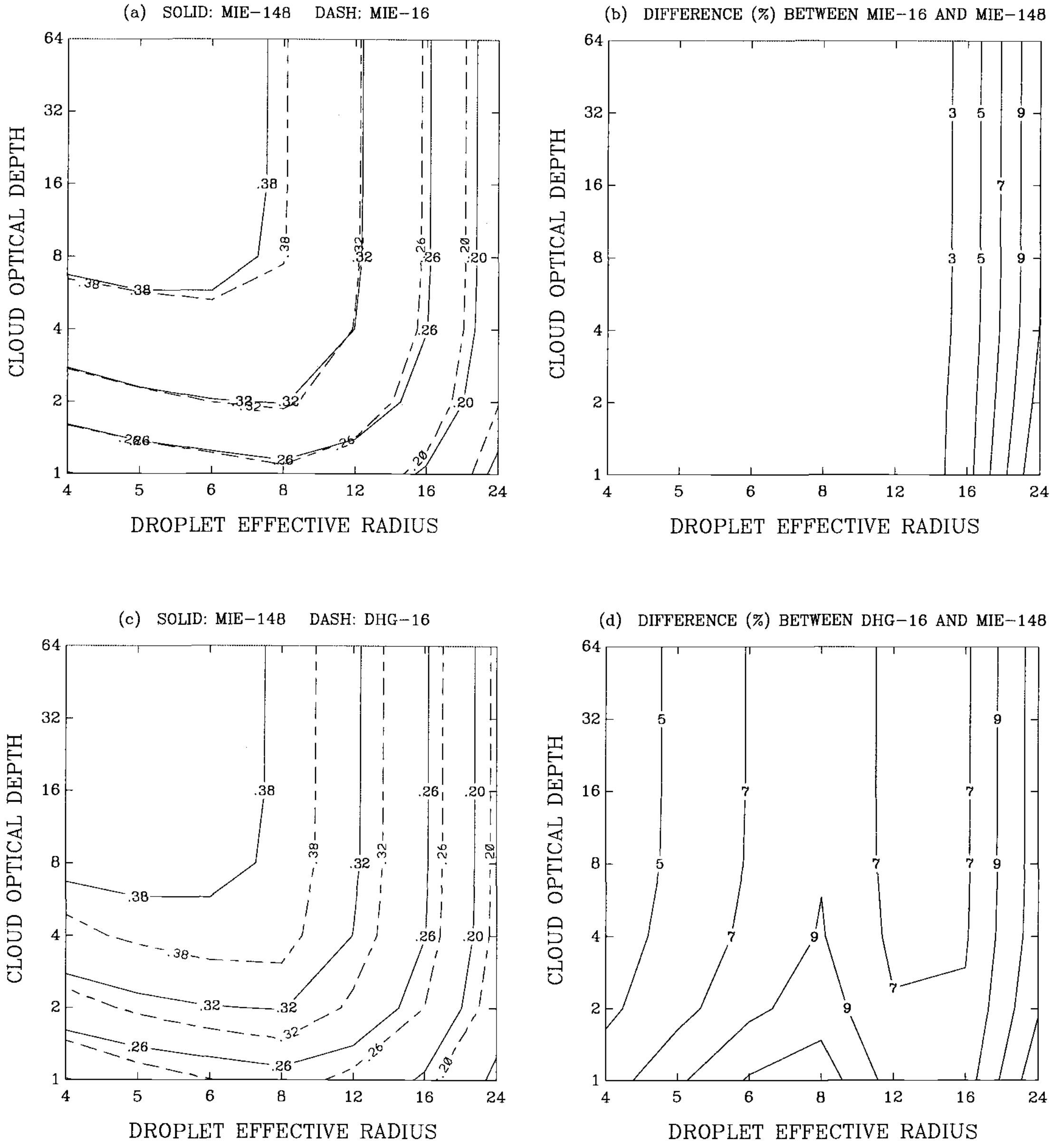

Figure 3.31 Same as Figure 3.26, except for λ = 3.749 μm and $\phi - \phi_o = 180°$.

Table 3.3 Plane-parallel atmospheric model and standard midlatitude summertime atmosphere. U (g/cm^2) is the layer water column amount, U_{oz} (g/cm^2) is the ozone column amount for the whole atmosphere, P (mb) is the pressure, and T (K) is the temperature.

	Ozone layer U_{oz}=0.000686	
		50 km (~ 1 mb)
	$\overline{T} = 222.0$, $\overline{P} = 122.0$, U=0.00115	
T=222.0K		12 km (209.0 mb)
	$\overline{T} = 238.5$, $\overline{P} = 307.6$, U=0.0603	
T=255.0K		7 km (426.1 mb)
	$\overline{T} = 264.0$, $\overline{P} = 522.8$, U=0.2740	
T=273.0K		4 km (628.2 mb)
	$\overline{T} = 279.0$, $\overline{P} = 712.7$, U=0.7300	
T=285.0K		2 km (802.4 mb)
	$\overline{T} = 287.5$, $\overline{P} = 852.3$, U=0.7575	
T=290.0K		1 km (902.2 mb)
	$\overline{T} = 292.0$, $\overline{P} = 957.7$, U=1.165	
T_s=294.0K		0 km (1013.25mb)

that the reflection function at 0.614 μm has a strong dependence on cloud optical depth and a weak dependence on droplet effective radius for the forward and side scattering directions. Figure 3.28 shows that the dependence on droplet effective radius becomes appreciable for the backscattering direction. Figures 3.29 and 3.30 show that the reflection function at 3.749 μm has a strong dependence on droplet effective radius and a weak dependence on cloud optical depth in the forward and side scattering directions. Figure 3.31 shows that, in the backscattering direction, the dependence on droplet effective radius becomes very weak for $r_{eff} < 8$ μm and $\tau_c < 8$.

Figures 3.26-3.28 also show that, for $\lambda = 0.614$ μm, the absolute relative differences obtained between the Mie 148- and the DHG 16-stream schemes are about an order of magnitude larger than those obtained between the Mie 148- and the Mie 16-stream schemes. For $\lambda = 3.749$ μm, as shown in Figures 3.29-3.31, the absolute relative differences obtained for the Mie 148- and the DHG 16-stream schemes are similar to those obtained for the Mie 148- and the Mie 16-stream schemes.

3.3 Atmospheric gaseous absorption and scattering

In retrieving cloud visible optical depths, droplet effective radii, and cloud top emission temperatures from satellite observations, the absorption and scattering effects due to atmospheric molecules must be taken into account. In calculating the atmospheric absorption and scattering, the atmosphere was divided into seven plane-parallel, horizontally and vertically homogeneous layers. The division of the seven layers are given in Table 3.3. Midlatitude summertime atmospheric temperature and humidity profiles and an ozone total column abundance are also shown in the Table

Table 3.4 Atmospheric absorbing and scattering components in each sub-channel.

	H_2O	CO_2	O_3	O_2	CH_4	N_2O	Rayleigh
Channel 1-1	X		X				X
Channel 1-2	X		X				X
Channel 1-3			X				X
Channel 1-4	X		X	X			X
Channel 1-5	X		X	X			X
Channel 3-1	X				X		
Channel 3-2	X				X		
Channel 3-3	X				X		
Channel 3-4	X				X	X	
Channel 3-5	X				X	X	
Channel 4	X	X					

(McClatchey et al., 1972). Absorption due to CO_2, CH_4, N_2O, and O_2 were also calculated using current atmospheric concentrations. Table 3.4 shows which absorbing and scattering components affect each of the AVHRR sub-channels. Note that the calculations neglect the aerosol effect. An inclusion of aerosols will have little change in the retrieved cloud properties because the aerosol optial depth is relatively small as compared to a typical cloud optical depth of 10.

The correlated *k*-distribution model developed by Kratz (1995) for the AVHRR was used to account for atmospheric gaseous absorption. Kratz derived the distribution of absorption coefficients, the k-distribution, so that atmospheric radiative fluxes and heating rates were within 0.5% of those obtained using line-by-line calculations. The correlated k-distribution reduces the burden of multiple scattering calculations, like the adding-doubling calculations, by reproducing the spectral-band absorption without the calculation of absorption in thousands of spectral lines.

The molecular scattering was treated as Rayleigh scattering. The phase function for Rayleigh scattering is given by

$$P(\cos\Theta) = \frac{3}{4}(1 + \cos^2\Theta). \tag{3.33}$$

The scattering cross section for a gas containing N molecules per unit volume is given by

$$N\sigma_{sca} = \frac{24\pi^3}{\lambda^4}\left(\frac{m_s^2 - 1}{m_s^2 + 2}\right)^2 \frac{N}{N_s^2}, \tag{3.34}$$

where m_s is the refractive index of air at standard pressure P_s and temperature T_s, and N_s is the number density at standard pressure and temperature. The refractive index is given by (Elden, 1953)

$$m_s \approx 1 + \left(77.46 + \frac{0.459}{\lambda^2}\right)\frac{P_s}{T_s}10^{-6}, \tag{3.35}$$

where P_s is in millibar, T_s is in K, and λ is in μm.

The cloud layer was inserted into the atmospheric model as a horizontally and vertically homogeneous layer. The cloud layer was assumed to be vertically thin and was placed in one of the atmospheric layers according to the cloud top temperature. In generating tables of radiances observed at the top of the atmosphere, a 16-stream adding routine was used to calculate reflectivities and transmissivities as well as the emission for combinations of layers that scattered, absorbed, and emitted radiation. The adding rules are given for reflectivities and transmissivities by (e.g., Goody and Yung, 1989)

$$\mathbf{R}_{12} = \mathbf{R}_1 + \mathbf{T}_1^*(\mathbf{1} - \mathbf{R}_2\mathbf{R}_1^*)^{-1}\mathbf{R}_2\mathbf{T}_1, \tag{3.36}$$

$$\mathbf{T}_{12} = \mathbf{T}_2(\mathbf{1} - \mathbf{R}_1^*\mathbf{R}_2)^{-1}\mathbf{T}_1, \tag{3.37}$$

$$\mathbf{R}_{12}^* = \mathbf{R}_2^* + \mathbf{T}_2(\mathbf{1} - \mathbf{R}_1^*\mathbf{R}_2)^{-1}\mathbf{R}_1^*\mathbf{T}_2^*, \tag{3.38}$$

$$\mathbf{T}_{12}^* = \mathbf{T}_1^*(\mathbf{1} - \mathbf{R}_2\mathbf{R}_1^*)^{-1}\mathbf{T}_2^*, \tag{3.39}$$

and for emission by

$$\begin{vmatrix} \mathbf{E}_{12}^+ \\ \mathbf{E}_{12}^- \end{vmatrix} = \begin{vmatrix} \mathbf{E}_1^+ \\ \mathbf{E}_2^- \end{vmatrix} + \begin{vmatrix} \mathbf{T}_1^*(\mathbf{1} - \mathbf{R}_2\mathbf{R}_1^*)^{-1}\mathbf{R}_2 & \mathbf{T}_1^*(\mathbf{1} - \mathbf{R}_2\mathbf{R}_1^*)^{-1} \\ \mathbf{T}_2(\mathbf{1} - \mathbf{R}_1^*\mathbf{R}_2)^{-1} & \mathbf{T}_2(\mathbf{1} - \mathbf{R}_1^*\mathbf{R}_2)^{-1}\mathbf{R}_1^* \end{vmatrix} \begin{vmatrix} \mathbf{E}_1^- \\ \mathbf{E}_2^+ \end{vmatrix}, \tag{3.40}$$

where 1 indicates the upper layer, 2 indicates the lower layer, $\mathbf{1}$ is the identity matrix, $\mathbf{R}$ and $\mathbf{T}$ are the reflectivity matrix and the transmissivity matrix for downward radiances, $\mathbf{R}^*$ and $\mathbf{T}^*$ are the reflectivity matrix and transmissivity matrix for upward radiances, $\mathbf{E}^+$ is the upward emission vector, and $\mathbf{E}^-$ is the downward emission vector. The lookup tables of reflectivities, transmissivities, and emission were calculated for 14 cloud optical depths and 16 droplet effective radii, as shown in Table 3.1.

Figures 3.32 and 3.33 show the 0.614- and 3.749-μm reflection functions obtained with and without accounting for the atmospheric absorption and scattering. Thinner curves in the figures are obtained for the no-atmosphere case. Thicker curves are obtained using the midlatitude summertime atmospheric model. The cloud layer was

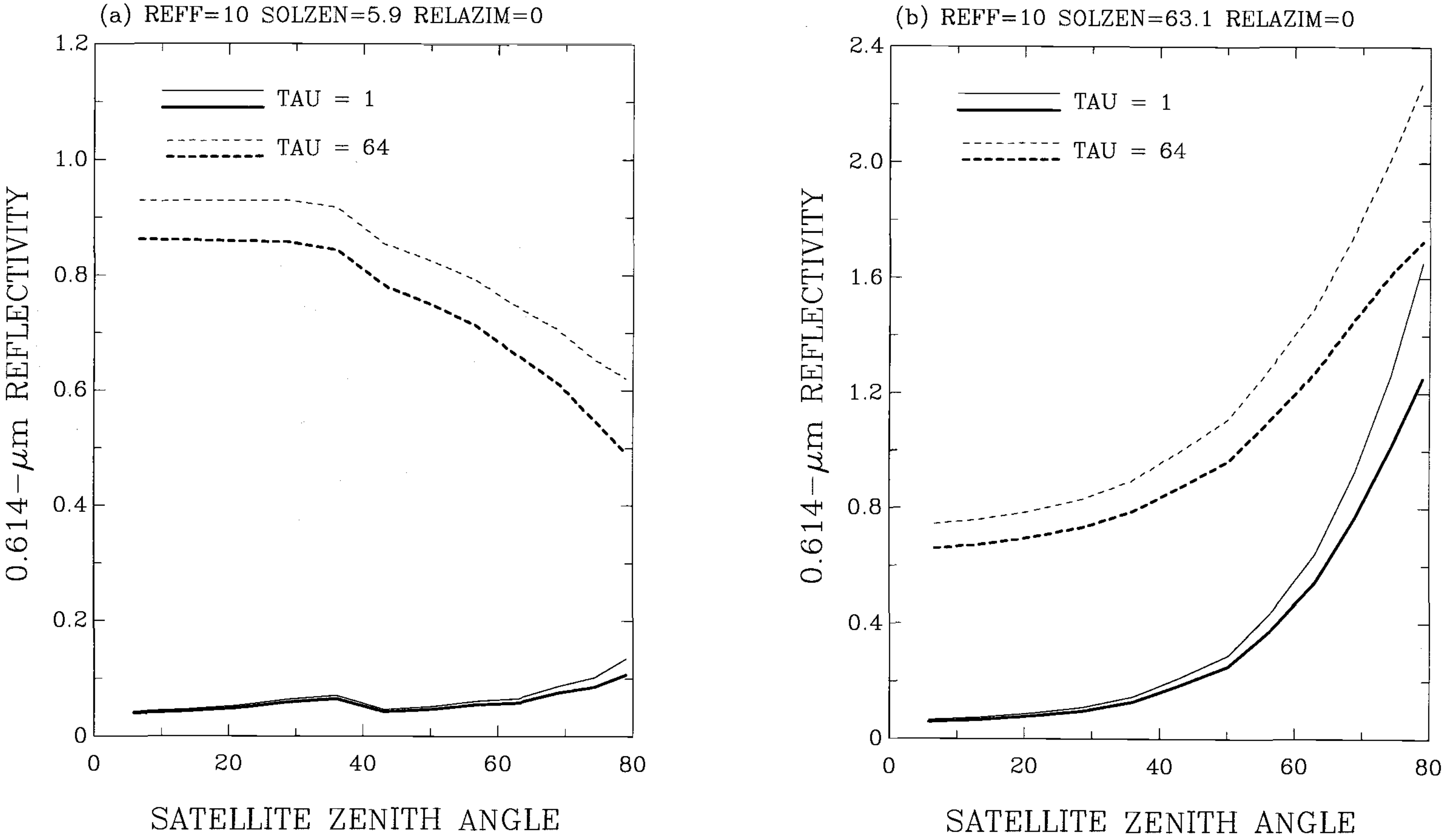

Figure 3.32 $R(\tau_c; \mu_o, \mu, \phi - \phi_o)$ as a function of satellite zenith angle for $\lambda = 0.614\mu m$. Results obtained for $r_{eff} = 10\mu m$, and $\tau_c = 1$ (solid lines) and 64 (dashed lines). Thin curves are for no atmospheric correction and thick curves include the atmospheric correction. (a) $\theta_o = 5.9°$ and (b) $\theta_o = 63.1°$.

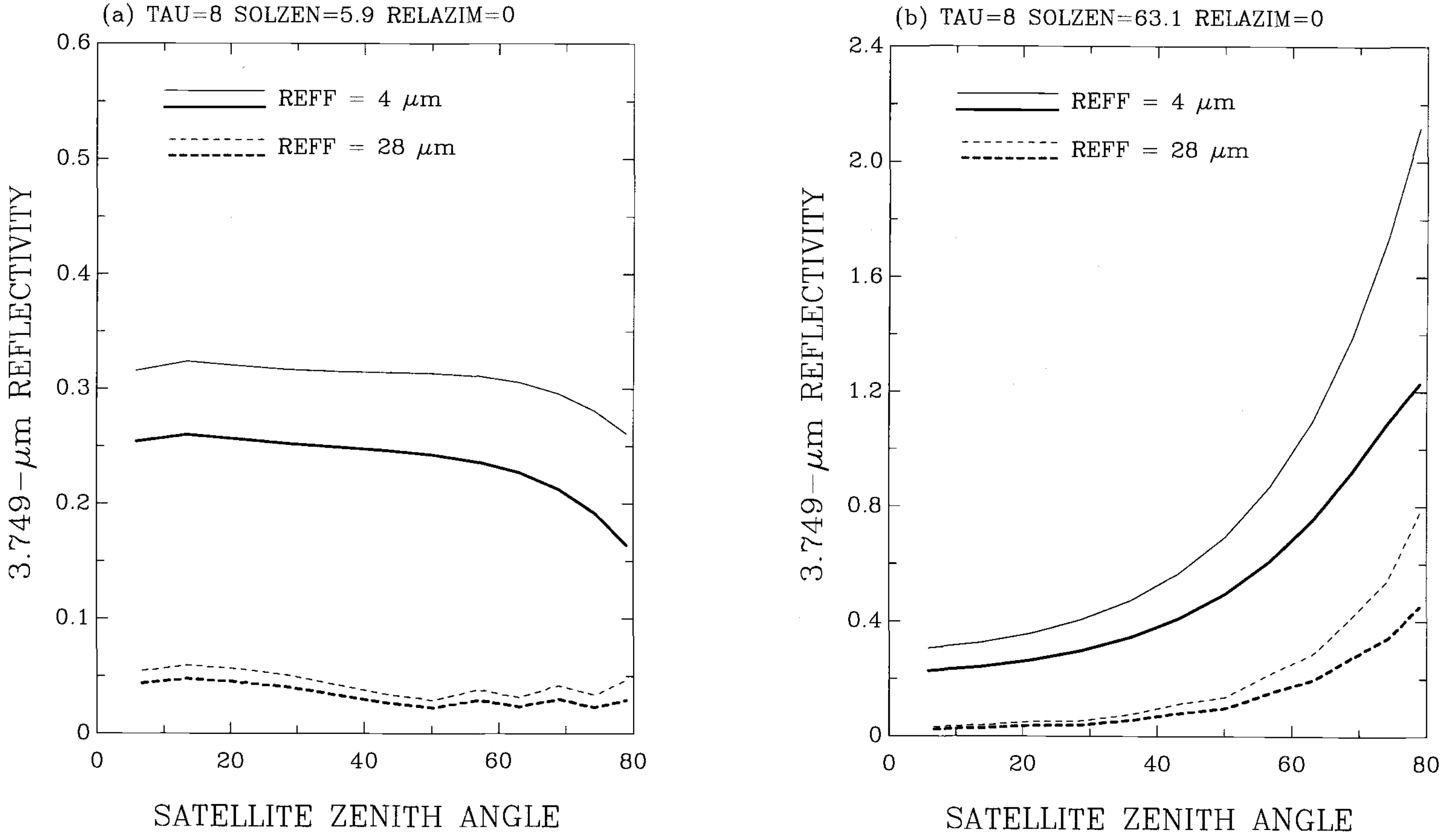

Figure 3.33 Same as Figure 3.32, except for $\lambda = 3.749\ \mu m$. Results obtained for $\tau_c = 8$ and $r_{eff} = 4\ \mu m$ (solid) and $28\ \mu m$ (dashed).

placed at the altitude of 1 km. Figure 3.32 (λ = 0.614 μm), shows that, for solar zenith angle $\theta_o = 5.9°$, the atmospheric absorption reduces the reflected sunlight by $\sim$ 8% when the satellite zenith angle $\theta = 5.9°$ and by $\sim$ 16% when $\theta = 70°$. For $\theta_o = 63.1°$, the atmospheric absorption reduces the reflected sunlight by $\sim$ 20% when $\theta = 70°$. For the 0.614-μm channel, the primary atmospheric absorber is ozone. Figure 3.33 (λ = 3.749 μm), shows that for $\theta_o = 5.9°$, the atmospheric absorption reduces the reflected sunlight by $\sim$ 20% when $\theta = 5.9°$ and by $\sim$ 28% when $\theta = 70°$. For $\theta_o = 63.1°$, the reduction of the reflected sunlight is $\sim$ 38% when $\theta = 70°$. In the 3.749-μm channel, the primary atmospheric absorbers are water vapor and methane.

3.4 The iterative cloud property retrieval scheme

An iterative retrieval scheme was developed and used to retrieve cloud visible optical depths, droplet effective radii, and cloud top emission temperatures for water clouds from AVHRR radiances observed at 0.63, 3.75, and 11 μm (channels 1, 3 and 4). The scheme is similar to that described by Han et al. (1994) except that 1) the retrievals were applied for a wide range of satellite view angles and 2) the retrievals were for pixels identified as being overcast. Han et al. used the pixels identified by the ISCCP threshold method as being overcast, but many of the ISCCP overcast pixels were in fact only partly cloudy. The satellite view angle dependence and the biases in the retrieved cloud properties, which arise when assuming that partly cloudy pixels are overcast, are both examined in the next chapter.

The retrieval scheme compares the AVHRR observed radiances to the radiances calculated by the radiation model. The radiances calculated for AVHRR channels are obtained by summing the radiances calculated for the AVHRR sub-channels weighted by the sub-channel spectral response functions. The reflected radiances for AVHRR channels 1 and 3 are given by

$$I_R(\mu_o, \mu, \phi - \phi_o) = \frac{\sum_j R_{\lambda_j}(\mu_o, \mu, \phi - \phi_o)\mu_o S_{\lambda_j} W_{\lambda_j}}{\sum_j \mu_o W_{\lambda_j}}, \tag{3.41}$$

The emitted radiances for AVHRR channels 3 and 4 are given by

$$I_E(\mu) = \frac{\sum_j E_{\lambda_j}(\mu) W_{\lambda_j}}{\sum_j W_{\lambda_j}}, \tag{3.42}$$

where S_{λ_j} is the solar constant for the spectral interval of sub-channel λ_j and W_{λ_j} is the spectral response function. The spectral solar constant is from Thekaekara (1974) and is given in Table 3.2.

Figure 3.34 shows the reflected radiances ($\mathrm{mWm^{-2}sr^{-1}cm}$) calculated for AVHRR channels 1 and 3. The figure shows the radiances for four sun-earth-satellite viewing geometries: (a) forward scattering, (b) backscattering, (c) side-scattering, and (d) nadir view angle. In the calculations, midlatitude summertime atmospheric temperature and humidity profiles and a Lambertian surface albedo of 0.03 for channel 1 and 0.01 for channel 3 were used. The figure shows results for the Mie 16-stream scheme (solid) and the DHG 16-stream scheme (dashed). The 16 streams were used to ease the computational burden in dealing with the large volume of satellite data.

The Mie 16-stream and the DHG 16-stream schemes differ most in the channel-1 reflected radiances for the forward scattering case. A figure similar to Figure 3.34 was

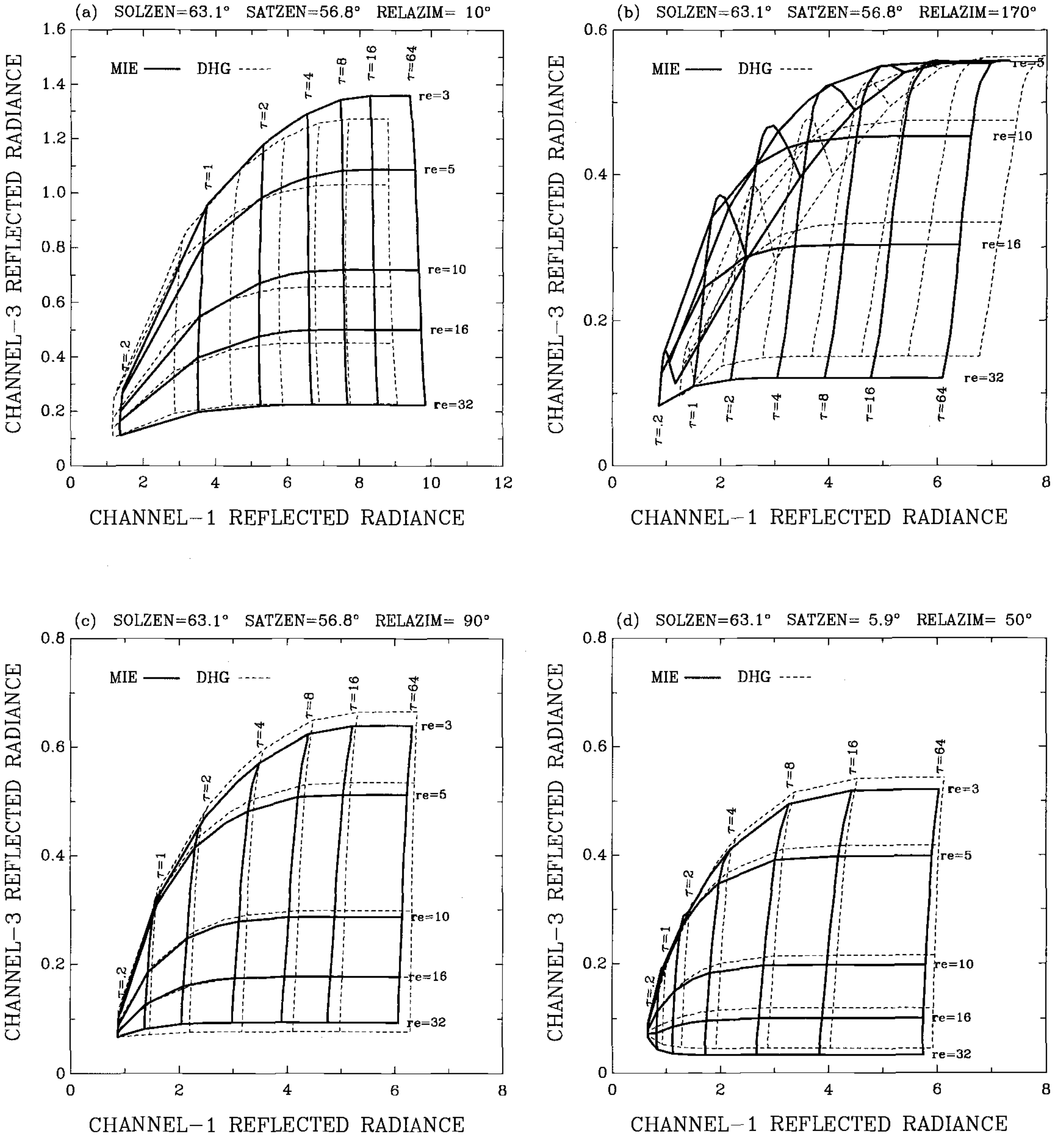

Figure 3.34 Reflected radiances calculated for AVHRR channels 1 and 3. Results obtained for the top of atmosphere using Mie 16–stream (solid lines) and DHG 16–stream (dashed lines) schemes. (a) forward scattering $(\theta_o, \theta, \phi - \phi_o) = (63.1°, 56.8°, 10°)$; (b) backscattering $(\theta_o, \theta, \phi - \phi_o) = (63.1°, 56.8°, 170°)$; (c) side-scattering $(\theta_o, \theta, \phi - \phi_o) = (63.1°, 56.8°, 90°)$; (d) nadir view angle $(\theta_o, \theta, \phi - \phi_o) = (63.1°, 5.9°, 50°)$.

presented by Nakajima and King (1990) for reflected radiances at 0.75 and 2.16 μm. As noted by Nakajima and King, the visible reflected radiance depends primarily on cloud visible optical depth and the near-infrared reflected radiance depends primarily on droplet effective radius. As shown in Figure 3.34, the nearly orthogonal relationship between channel-1 and channel-3 reflected radiances suggests the retrieval of cloud visible optical depths from the channel-1 radiances and the retrieval of droplet effective radii from the channel-3 radiances.

It is worth noting that in the backscattering direction, distinct droplet effective radii may produce the same reflected radiances in channels 1 and 3 when the cloud optical depth is sufficiently small. This double-solution arises because the maximum channel-3 extinction efficiency occurs at $r_{eff} \approx 5\mu$m. For the backscattering directions, the average effective radius was taken to be the retrieved droplet effective radius if double solutions occurred. The double solutions occurred in less than 1% of the March 1989 retrievals for single-layered, low-level clouds over the Pacific ocean.

The retrieval procedures are as follows:

1. Retrieve sea surface temperature using channel-4 radiance observed for cloud-free region,
2. Retrieve cloud optical depth —
   a. Begin with initial values of droplet effective radius $r_{eff} = 10$ μm and cloud top altitude = 1 km.
   b. Generate lookup tables of channel-1 reflected radiances for 14 cloud optical depths.
   c. Compare the AVHRR channel-1 radiance observed for overcast pixels with the

calculated radiances.

d. Interpolate the table values to obtain the visible optical depth.

3. Retrieve cloud top emission temperature —

   a. Generate lookup tables of channel-4 emitted radiances for various cloud top altitudes using the sea surface temperature, effective radius and the visible optical depth retrieved in step 2.
   b. Compare AVHRR channel-4 radiance observed for overcast pixels with the calculated radiances.
   c. Interpolate the table values to obtain the cloud top emission temperature and cloud top altitude.

4. Retrieve droplet effective radius —

   a. Calculate channel-3 emitted radiance using the sea surface temperature, effective radius, the cloud emission temperature retrieved in step 3, and the visible optical depth retrieved in step 2.
   b. Subtract the calculated emitted radiance from the AVHRR channel-3 radiance observed for overcast pixels to obtain the channel-3 reflected radiance.
   c. Interpolate the table values to obtain the droplet effective radius.

5. Repeat steps 2-4 using the new effective radius and cloud top altitude to retrieve new estimates of the cloud visible optical depth, cloud top emission temperature, and droplet effective radius.

6. Stop when the results for the cloud visible optical depth, cloud top emission temperature, and droplet effective radius converge to stable values. The stopping criteria is $\mid \tau_c^{new} - \tau_c^{old} \mid \, < 0.02 \, \tau_c^{old}$.

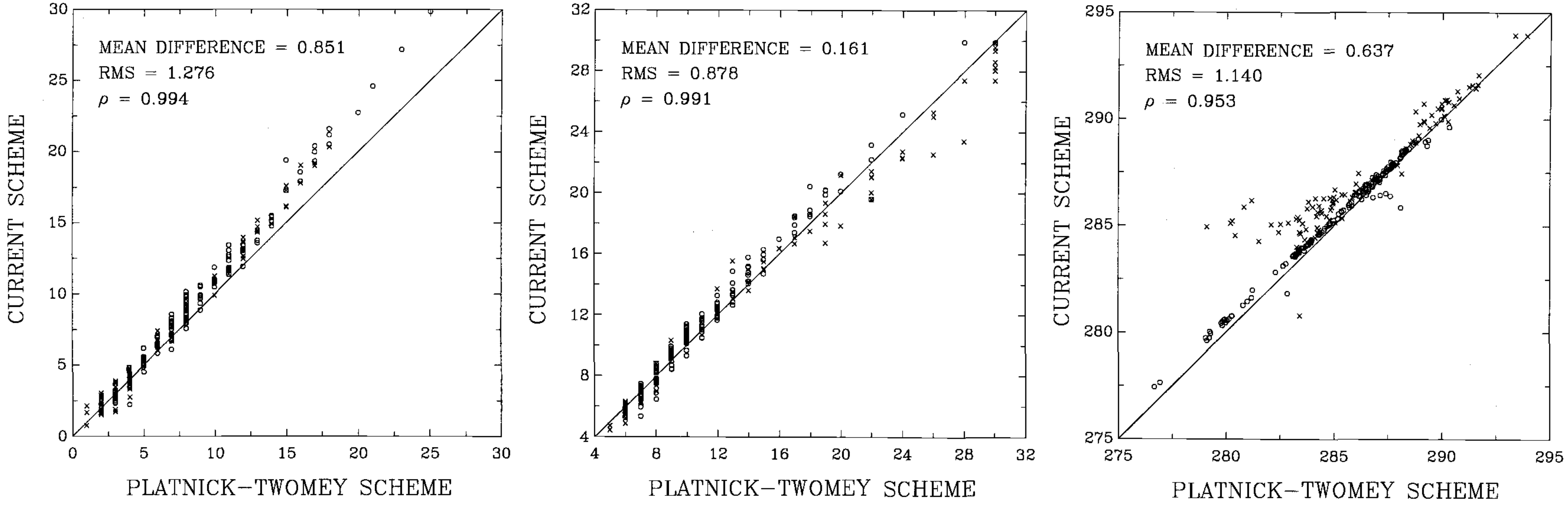

(a) CLOUD VISIBLE OPTICAL DEPTH

(b) DROPLET EFFECTIVE RADIUS

(c) CLOUD TOP EMISSION TEMPERATURE

Figure 3.35 Retrievals of (a) cloud visible optical depth, (b) droplet effective radius, and (c) cloud top emission temperature. Each point represents a NOAA-12 AVHRR 1-km LAC pixel for the MAST experiment in June 1994. Crosses denote satellite zenith angles larger than 40°. ρ is the correlation coefficient.

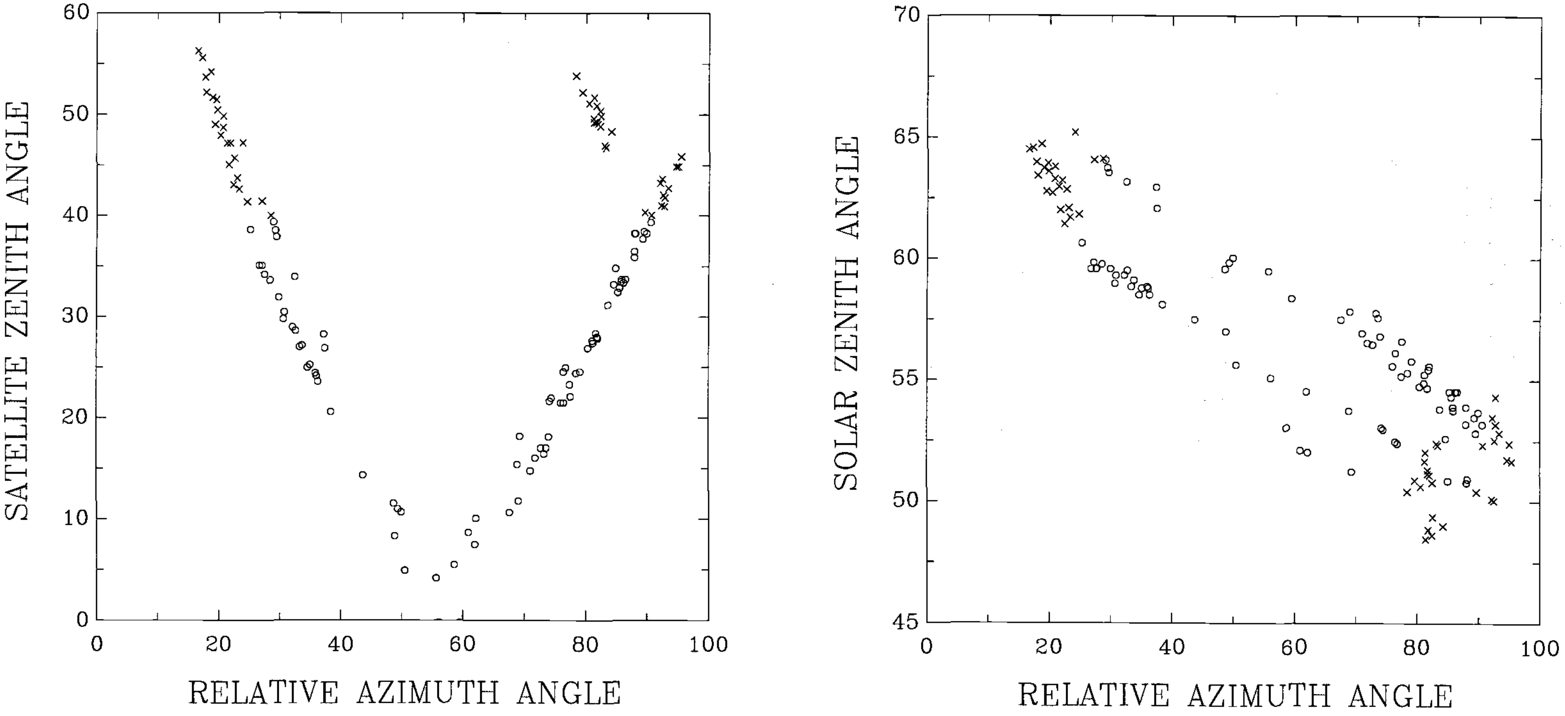

Figure 3.36 Solar zenith, satellite zenith, and relative azimuth angles for the retrievals shown in Figure 3.35.

3.5 Validating and comparing the retrieved cloud properties

3.5.1 Validation of the retrieval scheme

The Mie 16-stream retrieval scheme was applied to NOAA-12 AVHRR 1-km LAC (Local Area Coverage) data obtained during the Monterey Area Ship Track (MAST) experiment in June 1994. The retrieved cloud visible optical depths, droplet effective radii, and cloud top emission temperatures were compared with those retrieved using the Platnick and Twomey (1994) scheme (Dr. Steve Platnick, personal communications). Their scheme had been validated by comparing the retrieved results with the results derived from *in situ* observations obtained with the Particulate Volume Monitor (PVM-100) and Forward Scattering Spectrometer Probe (FSSP-100) on the University of Washington C-131A aircraft (Platnick and Valero, 1995). The retrieved cloud visible optical depths and droplet effective radii lay within the values derived from *in situ* observations. Comparing results obtained using the current scheme with results obtained using other schemes, such as the Platnick-Twomey scheme, tests the performance of the current scheme.

Figure 3.35 shows the comparisons for (a) cloud visible optical depth, (b) droplet effective radius, and (c) cloud top emission temperature. The ensemble of cases shown in the figure were obtained from NOAA-12 AVHRR 1-km LAC (Local Area Coverage) data. The ensemble had satellite zenith angles ranging from 0° to 57°, solar zenith angles ranging from 48° to 65°, and relative azimuth angles ranging from 20° to 100°. These angles are shown in Figure 3.36. The results of the two retrieval schemes track each other. The cloud visible optical depths produced by the current scheme are generally larger than those produced by the Platnick and Twomey scheme. The mean difference (current minus Platnick-Twomey) is 0.85 and the rms difference about the mean is 1.3. The droplet effective radii are on average similar with a mean difference of 0.2 μm and an rms difference about the mean of 0.9 μm. For cloud top emission temperatures, the mean difference is 0.6K and the rms difference about the mean is 1.1K.

Figure 3.37 shows the differences in the retrievals for the two schemes as functions of the satellite zenith angle and cloud visible optical depth. The crosses (×) in the figure indicate that the satellite zenith angle is larger than 40°. The differences in cloud visible optical depth are found to increase with increasing cloud visible optical depths (about 15% for $\tau_c = 20$). No trends are found for the differences in cloud visible optical depths and satellite zenith angles or solar zenith angles. For droplet effective radius, differences larger than $2\,\mu$m are found for satellite zenith angles $> 40°$ and cloud optical depths < 4. For cloud top emission temperatures, large differences are found for satellite zenith angles $> 45°$ and cloud visible optical depths < 4. It is worth noting that for the ensemble of cases studied here most of the small cloud visible optical depths were obtained for pixels having large satellite zenith angles. This satellite zenith angle dependence is examined in the next chapter.

3.5.2 Comparison of Mie and double Henyey-Greenstein retrieval schemes

For the comparisons of cloud visible optical depths, droplet effective radii, and cloud top emission temperatures retrieved using the Mie 16-stream scheme with those retrieved using the DHG 16-stream scheme, over 500 cloud samples taken from NOAA-

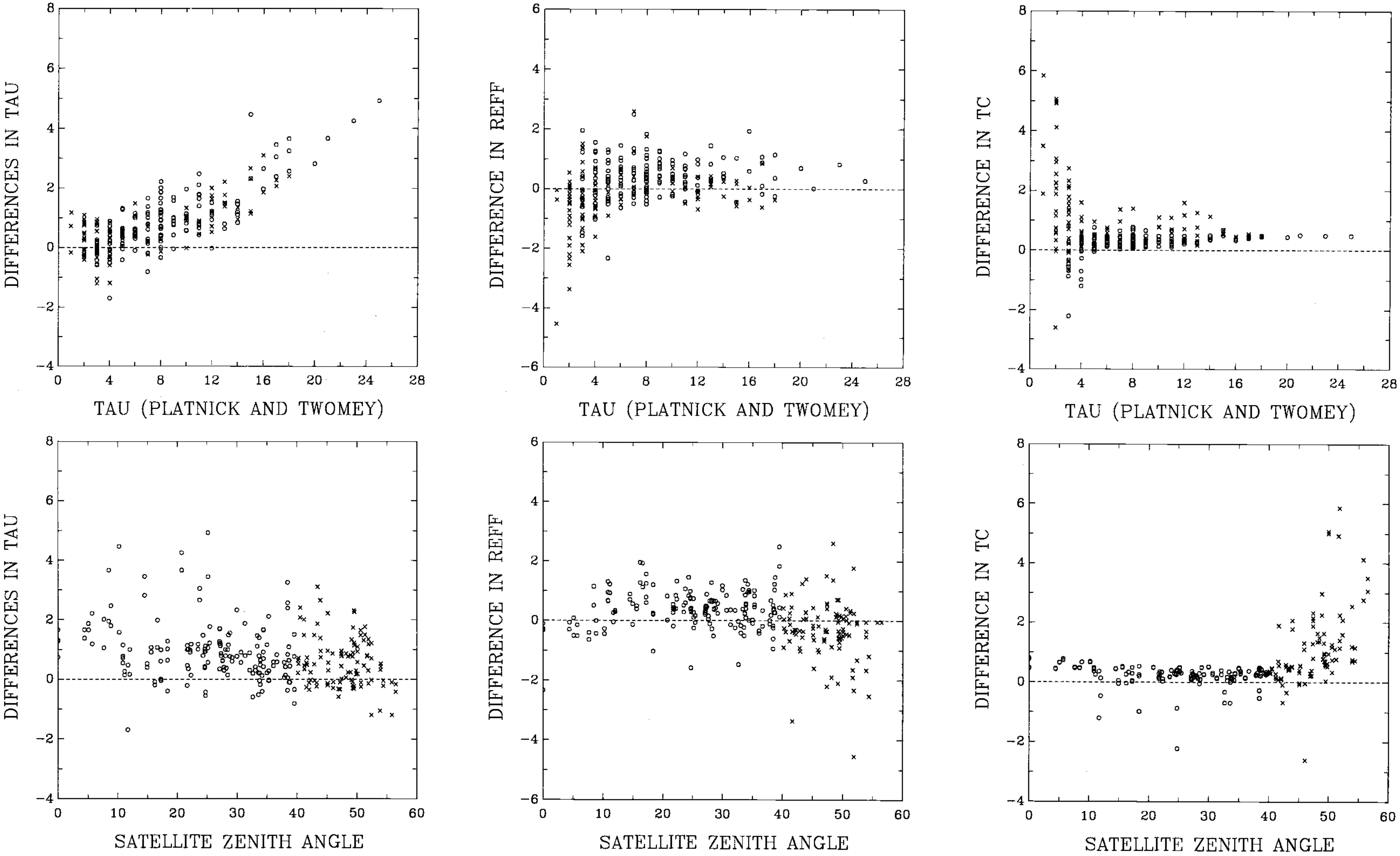

Figure 3.37 Differences (current minus Platnick and Twomey) in cloud visible optical depth, droplet effective radius, and cloud top emission temperature as functions of satellite zenith angle and cloud visible optical depth.

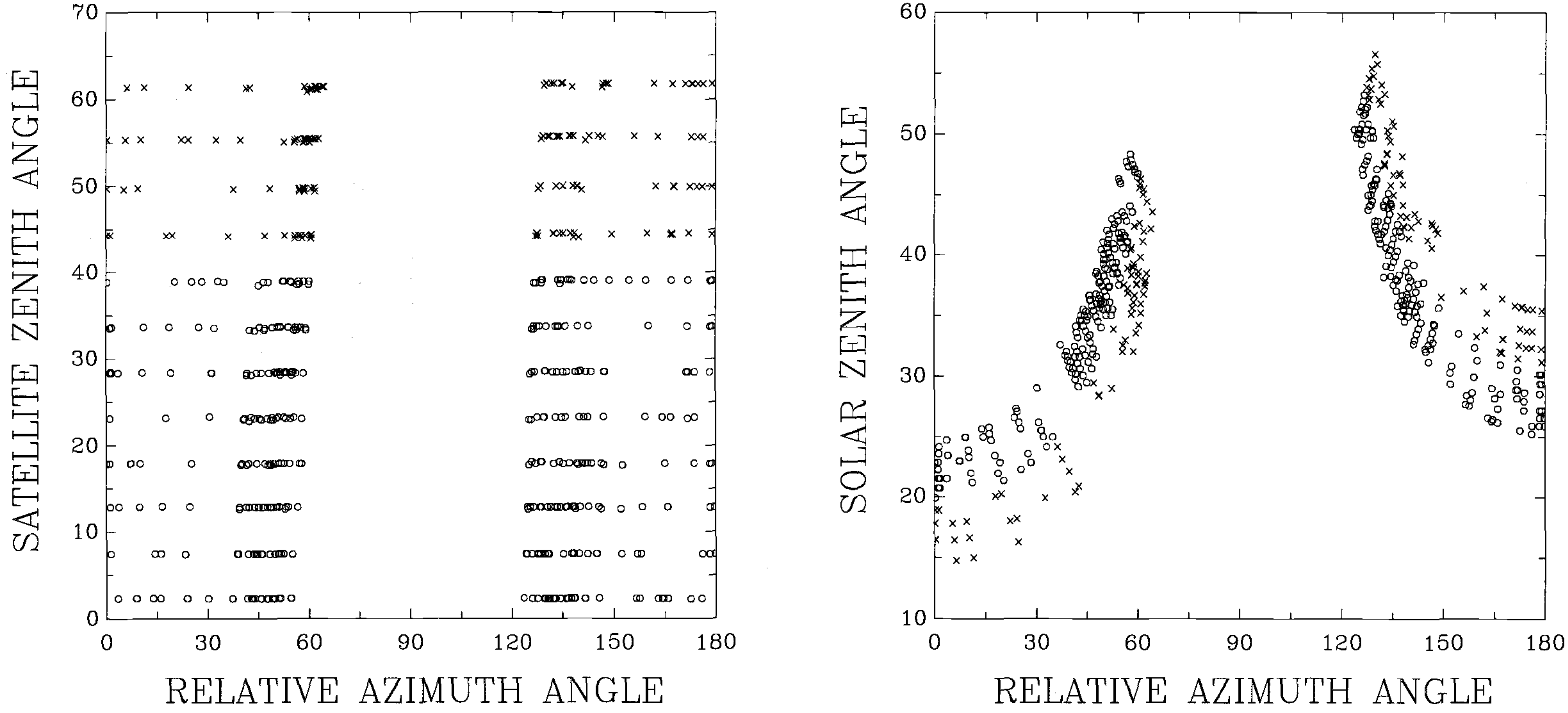

Figure 3.38 Same as Figure 3.36, except that each point represents a case drawn from 60-km regions observed by NOAA-11 AVHRR over the Pacific ocean during March 1989. Crosses denote satellite zenith angles larger than 40°.

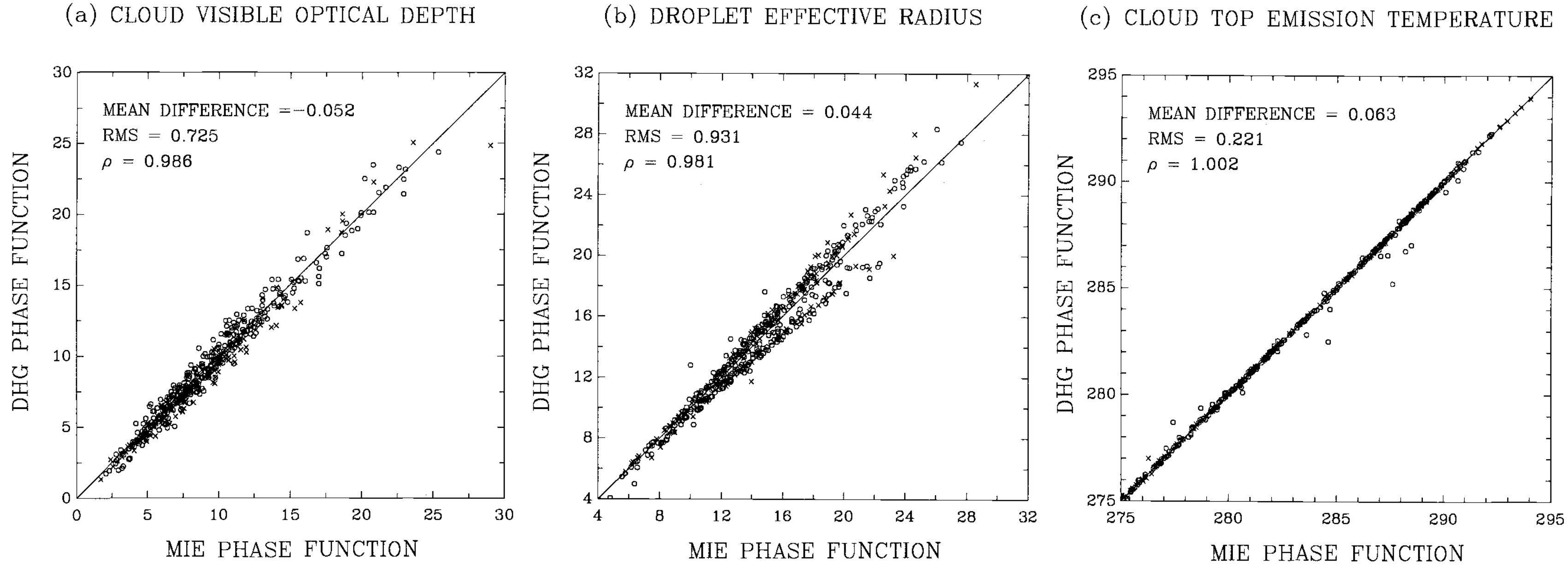

Figure 3.39 Retrievals of (a) cloud visible optical depth, (b) droplet effective radius, and (c) cloud top emission temperature for cases with viewing geometries shown in Figure 3.38. Retrievals obtained using Mie 16–stream and DHG 16–stream schemes. Crosses denote satellite zenith angles larger than 40°. ρ is the correlation coefficient.

11 AVHRR 4-km GAC data were used. The cases were obtained for March 1989 over the Pacific ocean. They cover a wide range of sun-satellite zenith and relative azimuth angles, as shown in Figure 3.38. The radiances for the cases were average values obtained for overcast pixels identified by the spatial coherence method (Coakley and Bretherton, 1982) within 60-km regions. They were restricted to single-layered, low-level cloud systems.

Figure 3.39 shows the retrieved cloud visible optical depths, droplet effective radii, and cloud top emission temperatures for the DHG 16-stream and the Mie 16-stream schemes. The mean difference (DHG minus Mie) is –0.05 for the cloud visible optical depth and is 0.04 μm for the droplet effective radius. The rms difference about the mean is 0.7 for the cloud optical depth and is 0.9 μm for the droplet effective radius. The largest difference for the ensemble is found to be $\sim$ 20% for the cloud visible optical depth and $\sim$ 3 μm for the droplet effective radius. Cloud top emission temperatures show generally good agreement between the two schemes. The mean difference is 0.06K and the rms difference about the mean is 0.2K. The comparisons show that the DHG 16-stream scheme would provide reasonable retrievals of cloud optical depths and droplet effective radii.

3.6 Sensitivity studies for cloud property retrievals

Sensitivity studies were performed using the ensemble described in section 3.5.2. The standard run used a Mie 16-stream iterative retrieval scheme, a Lambertian surface reflectance of 6% for both channels 1 and 3, an instrument filter function derived for NOAA-11 to convert radiances to brightness temperatures, and a midlatitude summertime atmospheric model. Figure 3.40 shows results obtained using a Mie 32-stream scheme and results obtained with the Mie 16-stream scheme. The differences in retrieved cloud visible optical depths and droplet effective radii are generally small. The mean difference (32-stream minus 16-stream) for the cloud visible optical depth is 0.01 and the rms difference about the mean is 0.2. The mean difference for the effective radius is -0.06 μm and the rms difference about the mean is 0.4 μm. The retrieved cloud top emission temperatures for the two are nearly identical.

Figure 3.41 shows results obtained with a surface reflectance of zero and with a Lambertian surface reflectance of 6% for both channels 1 and 3. The use of the 6% surface reflectance reduces the retrieved mean cloud optical depths by 0.7 with an rms difference of 0.7. The changes in the retrieved droplet effective radii and cloud top emission temperatures are generally small.

Figure 3.42 shows the results obtained using NOAA-11 and NOAA-12 instrument filter functions (Kidwell, 1991) for observed radiances in channels 3 and 4. The observed radiances in channels 3 and 4 were converted to brightness temperatures using these instrument filter functions and then converted back to radiances using the Planck functions calculated at the AVHRR sub-channel central wavelengths with the spectral response functions given in Table 3.2. The change in the filter function gives a large mean difference of 2.9 μm in the retrieved droplet effective radius and –1K in the retrieved cloud top emission temperature. The shift in the droplet effective radius is about 2 μm for $r_{eff} = 10$ μm and is about 4 μm for $r_{eff} = 20$ μm.

Figure 3.43 shows results obtained using the iterative scheme and results obtained with no iteration. For no iteration, the cloud visible optical depth was retrieved by assuming a droplet effective radius of $10\ \mu$m and a cloud top altitude of 1 km. The cloud top emission temperature and altitude were retrieved by using the retrieved cloud visible optical depth and a droplet effective radius of 10μm. The droplet effective radius was then retrieved by using the retrieved cloud visible optical depth, cloud top emission temperature and cloud top altitude. The no-iteration scheme gave rise to a mean difference (no-iteration minus iteration) of –0.14 in the cloud visible optical depth, $-0.2\ \mu$m in the droplet effective radius, and 0.05K in the cloud top emission temperature. The rms differences for the three are small. The results show that the retrievals obtained with no iterations are similar to those obtained using the iterative retrieval scheme.

Figure 3.44 shows results obtained with and without effects due to gaseous absorption in the cloud layer. For these calculations, the cloud vertical thickness was computed using the method of Minnis et al. (1992). The vertical thickness is given by

$$\Delta Z = 0.08\tau_c^{1/2} - 0.04 \tag{3.43}$$

with ΔZ in km. The water vapor concentration is calculated using the temperature at the altitude of 1 km. The relative humidity in clouds is taken to be 100%. The differences in the retrieved cloud visible optical depths, droplet effective radii, and cloud top emission temperatures are generally small. A mean difference of 0.3 and an rms difference about the mean of 0.6 are obtained for the retrieved cloud visible optical depths. A mean difference of -0.7μm and an rms difference about the mean of 0.8μm are obtained for the retrieved droplet effective radii. The retrieved cloud top emission temperatures are nearly identical. To further investigate the effect of atmospheric absorption in clouds, Figure 3.45 shows the channel-3 reflection functions obtained for different cloud vertical thicknesses. Values are shown for different cloud droplet effective radii and for (a) nadir viewing, (b) forward scattering, and (c) backscattering angles. The effects of the in-cloud atmospheric gaseous absorption on both channel-1 and channel-3 reflections is generally small for $\Delta Z < 3$ km.

Retrievals were also performed using the atmospheric temperature, humidity, and ozone data derived from the TIROS Operational Vertical Sounder (TOVS) observations in place of the midlatitude summertime atmospheric model. Cloud top altitude was also allowed to vary by comparing the retrieved cloud top emission temperature with the observed TOVS atmospheric temperature profile. The atmospheric transmission and emission above and below the cloud layer were re-calculated during each iteration. Figure 3.46 shows results obtained using the observed and the midlatitude summertime atmospheric profiles. The differences in the retrieved cloud visible optical depths are generally small (< 1) with a mean difference (midlatitude minus observed) of –0.2 and an rms difference about the mean of 0.3. The differences in the retrieved droplet effective radius are generally less than 3 μm. The mean difference is 0.5 μm and the rms difference about the mean is 1.1 μm.

The differences in the retrieved cloud top emission temperatures are larger as cloud top emission temperatures move away from 290K (temperature at 1 km for the midlatitude summertime atmosphere). When cloud top emission temperatures are less than $\sim$ 285K, those obtained with cloud top altitude fixed at 1 km are smaller than those obtained with the retrieved cloud top altitude. Likewise, when cloud top emission temperatures are larger than $\sim$ 290K, those obtained with cloud top altitude fixed at 1 km are larger. Colder temperatures indicate higher altitudes. For clouds having altitudes higher than 1 km, the transmissivity calculated for the atmosphere above 1 km will be smaller than the actual atmospheric transmissivity above the cloud. Consequently, the retrieved cloud top emission temperature will be colder than the actual cloud top temperature. Likewise, for clouds having altitudes lower than 1 km, cloud top emission temperatures retrieved by fixing the cloud tops at 1 km will be warmer than the actual cloud top temperatures.

To summarize, the retrieved cloud droplet effective radius seems to be more sensitive to the commonly used approximations than the retrieved cloud top emission temperature, which in turn is more sensitive than the retrieved cloud visible optical depths.

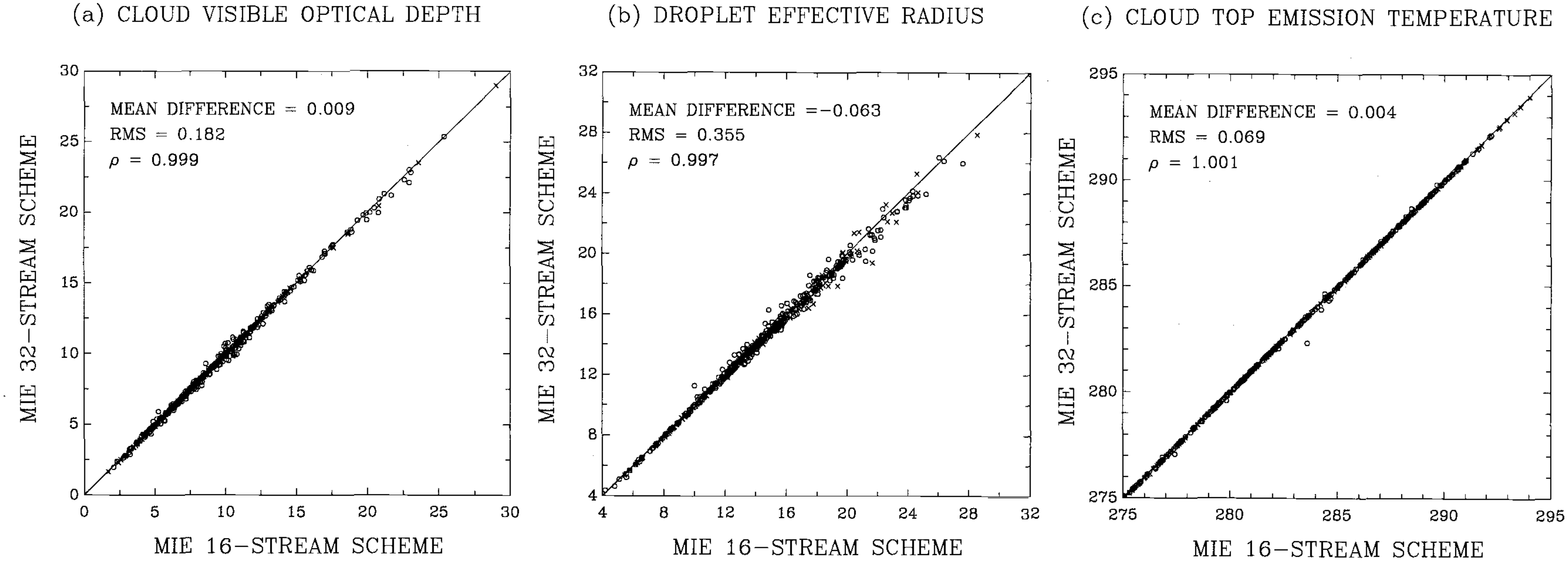
(a) CLOUD VISIBLE OPTICAL DEPTH

(b) DROPLET EFFECTIVE RADIUS

(c) CLOUD TOP EMISSION TEMPERATURE

Figure 3.40 Same as Figure 3.39, except that retrievals were obtained using Mie 32–stream and Mie 16–stream schemes.

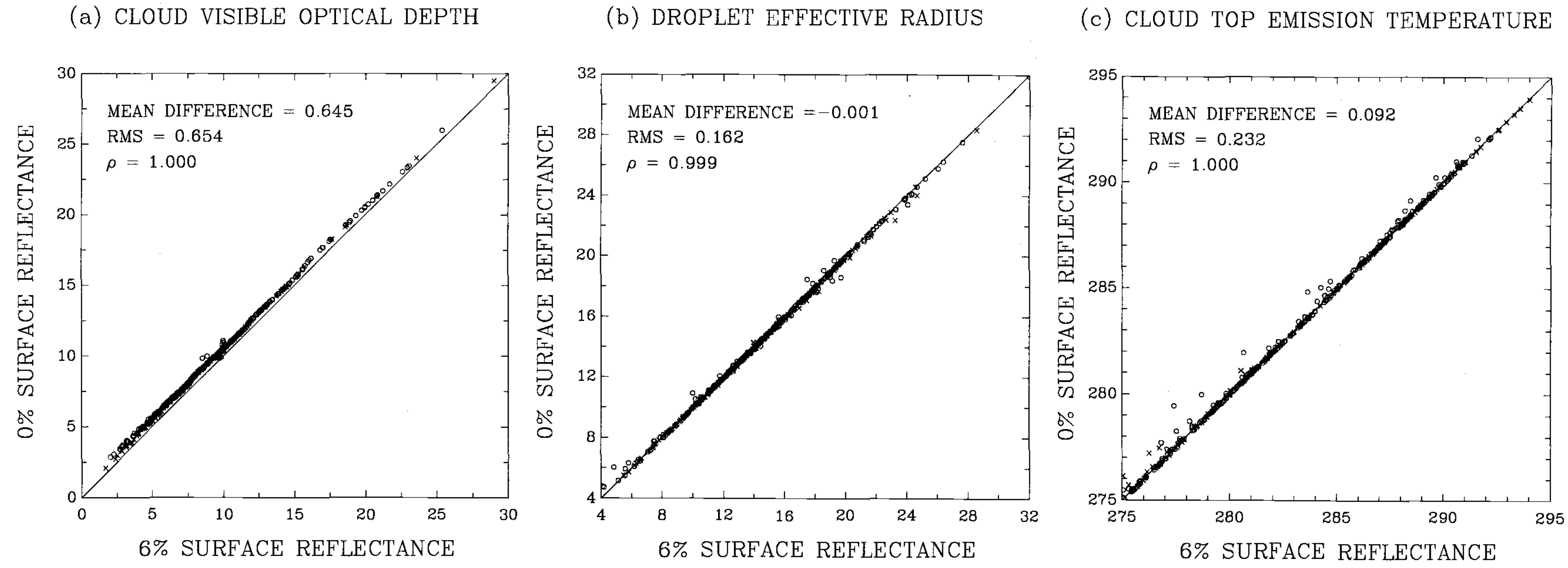

Figure 3.41 Same as Figure 3.39, except that retrievals were obtained using surface reflectances of zero and 6%.

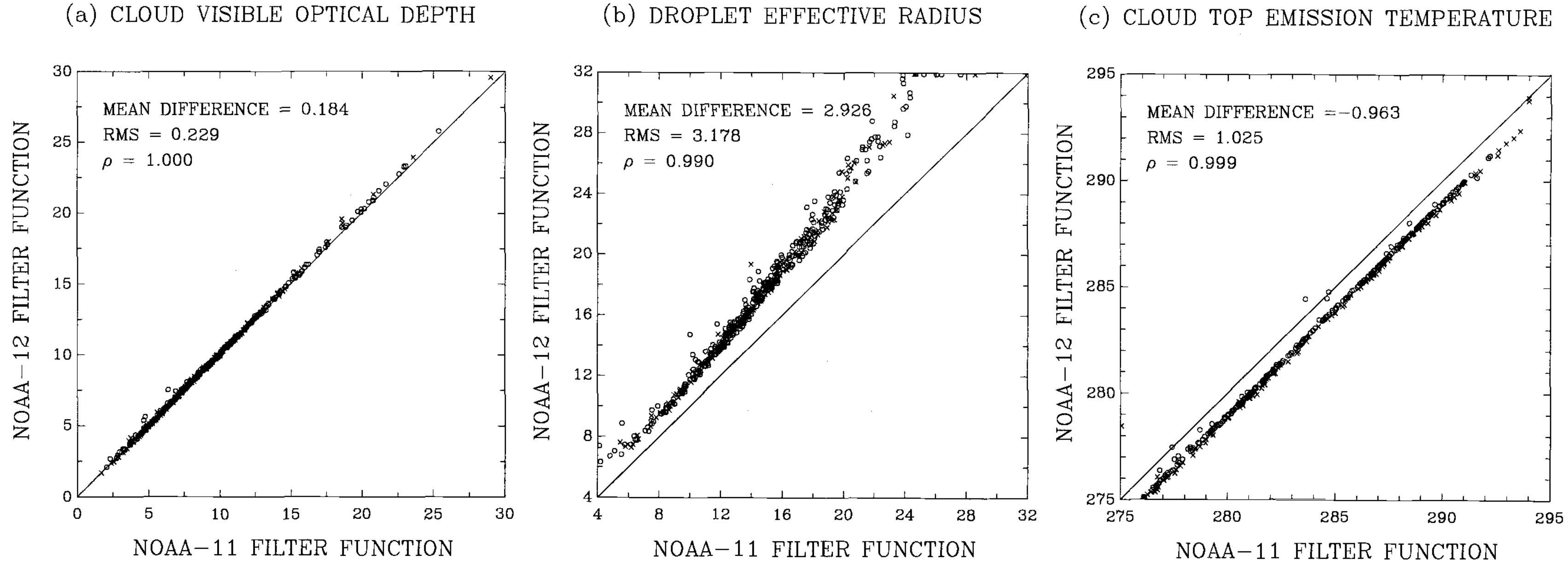

(a) CLOUD VISIBLE OPTICAL DEPTH

(b) DROPLET EFFECTIVE RADIUS

(c) CLOUD TOP EMISSION TEMPERATURE

Figure 3.42 Same as Figure 3.39, except that retrievals were obtained using NOAA-11 and NOAA-12 filter functions.

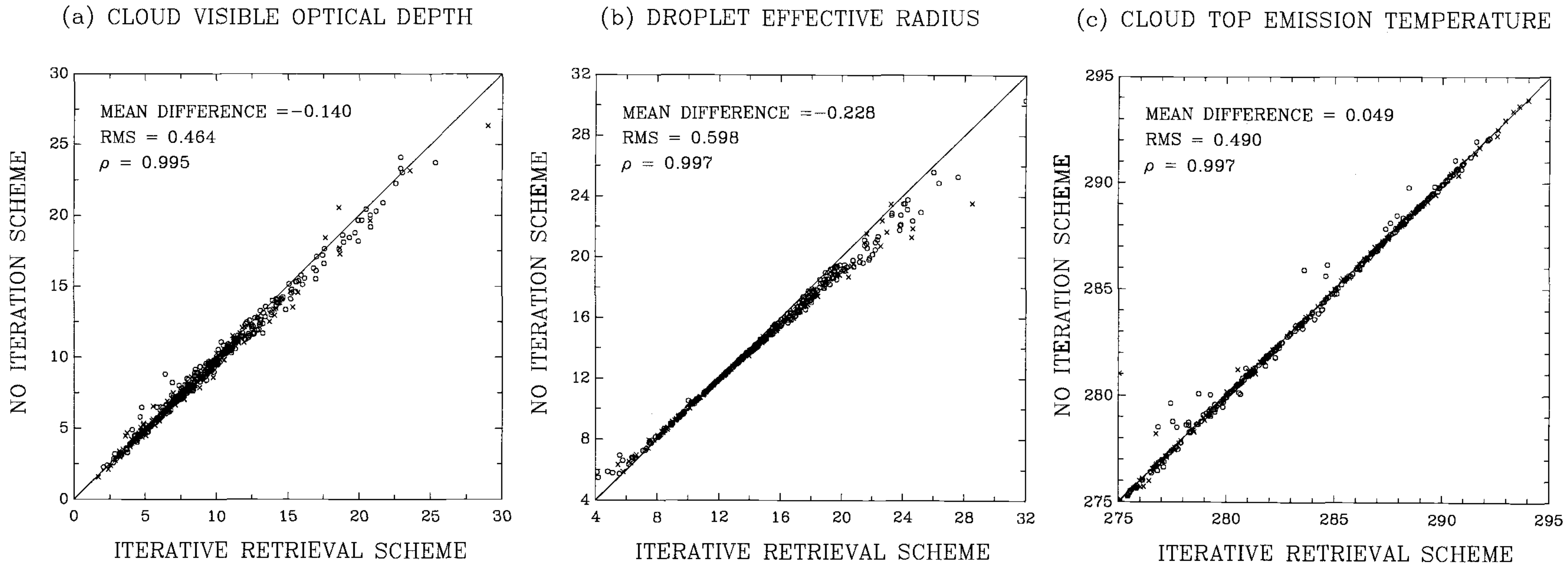

Figure 3.43 Same as Figure 3.39, except that retrievals were obtained using no iteration and using the iterative scheme.

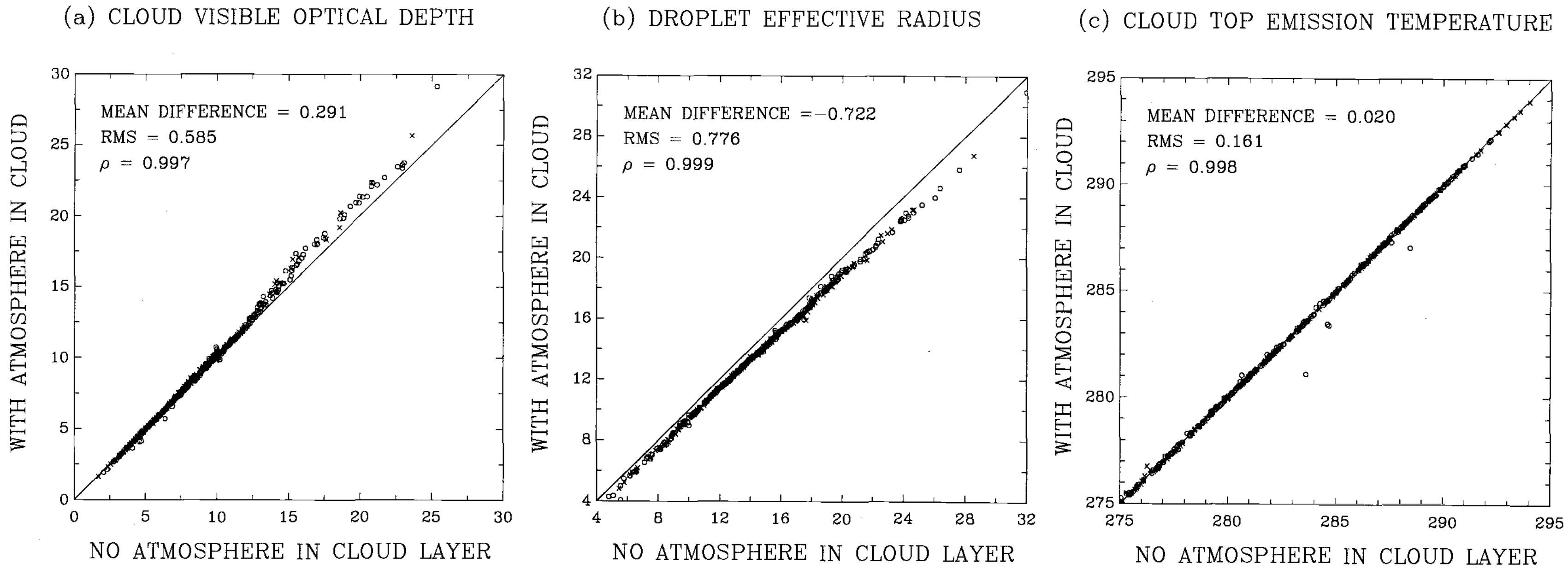

Figure 3.44 Same as Figure 3.39, except that retrievals were obtained with and without gaseous absorption in the cloud layer.

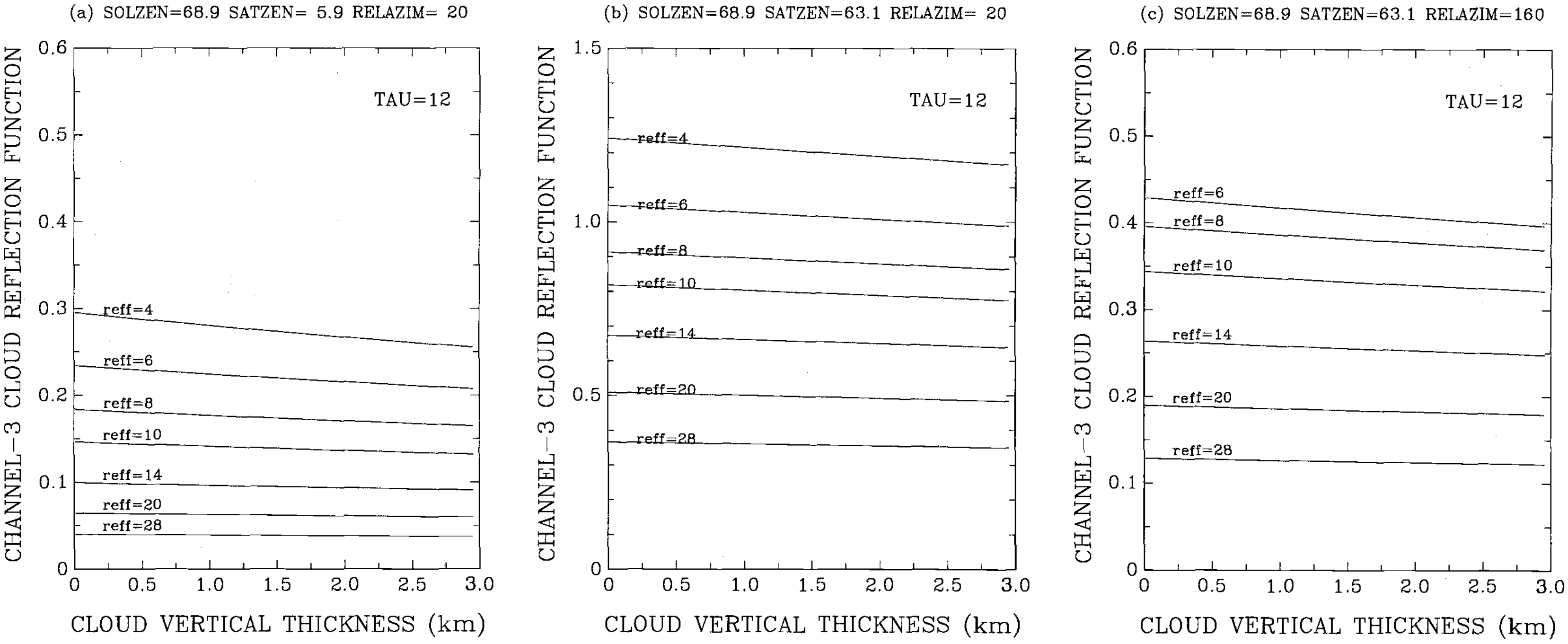

Figure 3.45 AVHRR channel-3 reflection functions and cloud vertical thickness. The atmospheric absorption within the cloud layer is calculated using the Kratz model. A mean temperature of 288K and a mean pressure of 890 mb are used for the cloud layer. Results obtained for $\tau_c = 12$ and various droplet effective radii. (a) nadir view angle $(\theta_o, \theta, \phi - \phi_o) = (68.9°, 5.9°, 20°)$; (b) forward scattering $(\theta_o, \theta, \phi - \phi_o) = (68.9°, 63.1°, 20°)$; (c) backscattering $(\theta_o, \theta, \phi - \phi_o) = (68.9°, 63.1°, 160°)$.

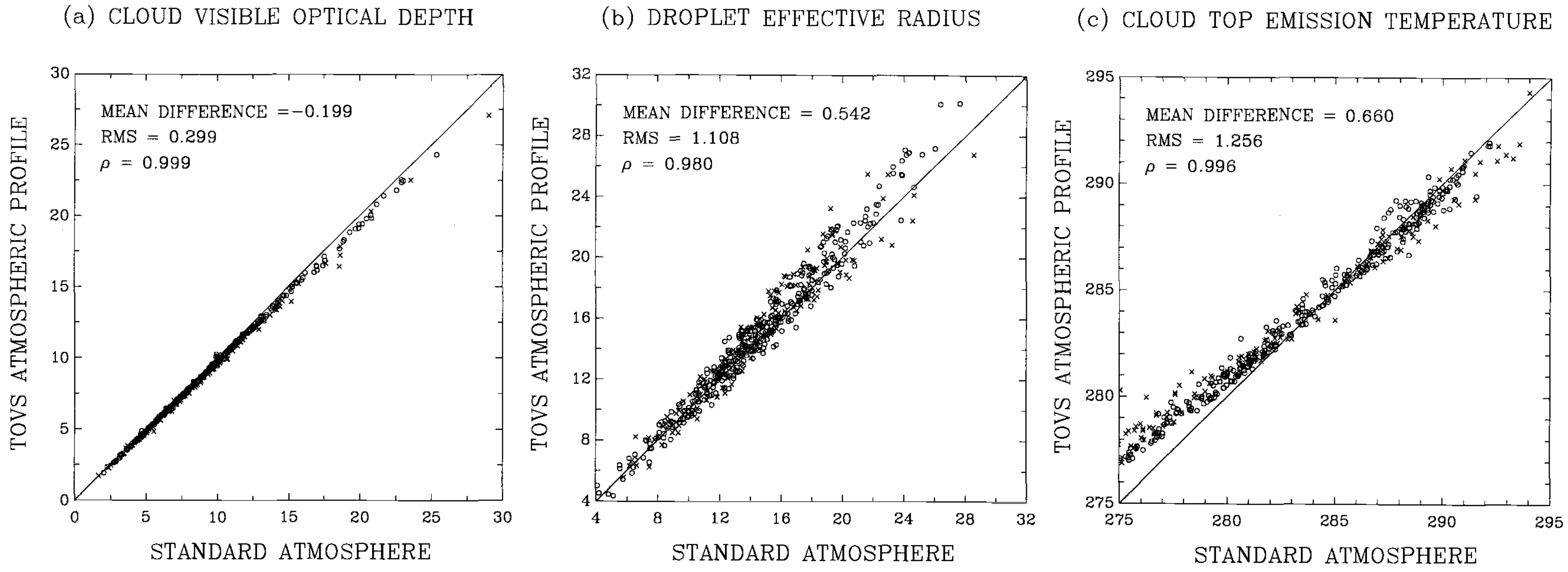

Figure 3.46 Same as Figure 3.39, except that retrievals obtained using standard midlatitude summertime atmosphere and TOVS derived atmospheric temperature and humidity profiles.

Chapter 4
Effects of Partly Cloudy Pixels and Satellite Zenith Angles on Cloud Properties Retrieved from Satellite Observations

4.1 Introduction

The cloud properties derived by ISCCP have received considerable attention. Tselioudis et al. (1992) used one year of ISCCP cloud data to study the visible optical depths of low-level clouds and their relationship to cloud temperatures on a global scale. Han et al. (1994) used two years of ISCCP cloud data to investigate near-global distributions of water-cloud visible optical depths and droplet effective radii. Han et al. used only the pixels observed at near-nadir view angles thereby avoiding any bias introduced by a possible satellite-view-angle dependence, but they and Tselioudis et al. neglected biases which are attributable to partly cloud-covered pixels that were identified as overcast by the ISCCP cloud retrieval procedure. If radiances observed from pixels that are only partly cloud-covered are taken to be due to overcast conditions, then cloud optical depths, droplet effective radii, and cloud top emission temperatures retrieved from these radiances will differ from those retrieved from radiances observed for pixels that are actually overcast. These differences are studied in this chapter.

For regional studies, Platnick and Twomey (1994) applied a retrieval method similar to that described in Chapter 3 to AVHRR data to study the effect of increasing cloud condensation nuclei (CCN) on cloud albedos for marine stratus. Platnick and Valero (1995) applied the same retrieval method to NOAA-12 AVHRR data obtained near the Azores during the Atlantic Stratocumulus Transition Experiment (ASTEX) to retrieve optical depths and droplet effective radii for boundary layer stratocumulus. Nakajima and Nakajima (1995) also performed retrievals of optical depths and droplet effective radii for marine boundary layer clouds using AVHRR data from the First ISCCP Regional Experiment (FIRE) and ASTEX. None of these studies discussed the potential biases in the retrieved cloud properties due to the effect of partly cloudy pixels nor did they explore the dependence of the retrieved properties on satellite zenith angle.

In this chapter, NOAA-11 AVHRR 4-km GAC data for March 1989 for the Pacific ocean is used to retrieve cloud visible optical depths, droplet effective radii, and cloud top emission temperatures. These cloud properties are obtained for 60-km regions containing horizontally uniform, single-layered, low-level clouds. Since the radiation model used here was developed for retrieving properties of water clouds, this study focuses on low-level clouds to avoid effects due to ice. The retrievals were obtained for pixels that were identified as being overcast by single-layered, low-level clouds. Retrievals were also obtained for pixels that were partly covered by the same single-layered, low-level clouds. The spatial coherence method (Coakley and Bretherton, 1982) was used to identify the single-layered, low-level cloud systems and to determine pixels that were overcast and pixels that were only partly cloudy. The radiances observed for the overcast pixels were used in the radiation model, as described in the previous chapter, to retrieve visible optical depths, droplet effective radii, and cloud top emission temperatures for the overcast clouds. The radiances observed for the partly cloudy pixels, as is done in ISCCP, were assumed to be due to overcast conditions and were used to retrieve the cloud properties. The differences in the retrievals for overcast and partly cloudy pixels were assessed.

With regard to the satellite zenith angle dependence, the cloud property retrieval scheme employed here uses the plane-parallel approximation for the radiative transfer calculations. Many theoretical studies have demonstrated that such an approximation may be inappropriate because of irregular cloud shapes and even cloud internal inhomogeneity (Davies, 1978; Welch and Wielicki, 1984; Cahalan et al., 1994; Loeb and Davies, 1996). Recently, by viewing marine stratus and stratocumulus from a wide range of angles using AVHRR GAC data, Loeb and Coakley (1997) showed that plane-parallel radiative transfer calculations fail to model the angular dependence of the reflected sunlight in the forward scattering direction. Their cloud visible optical depths retrieved using the plane-parallel model showed no obvious dependence on satellite zenith angle in the backscattering direction, but in the forward scattering direction a decrease of up to 40% was found in the mean cloud visible optical depths from nadir to oblique zenith angles ($\sim 65°$). In this chapter, the retrieved cloud visible optical depths, droplet effective radii, and cloud top emission temperatures were obtained for satellite zenith angles ranging from nadir to $\sim 60°$. The zenith angle dependence in these retrieved cloud properties was examined for both the forward and backward scattering directions.

4.2 Cloud property retrieval procedures

4.2.1 NOAA-11 AVHRR GAC data

AVHRR 4–km GAC (Global Area Coverage) data obtained by the NOAA-11 satellite for March 1989 for the Pacific ocean was used in this study. The AVHRR has five channels. The central wavelengths of these channels are at approximately 0.63, 0.89, 3.75, 11, and 12 μm. The GAC data was produced by the processor on board the satellite to sample the real-time AVHRR data. Four out of every five samples along the scan line were used to compute an average value and one out of every three scan lines was processed. The volume of GAC data is thus considerably smaller than that of the original AVHRR data. The spatial resolution of the GAC pixels is taken to be 4 km at nadir (Kidwell, 1991).

The AVHRR GAC data was taken from daytime passes over the Pacific ocean between 55°S and 55°N. Figure 4.1 shows examples of the AVHRR satellite overpasses obtained on March 7, 1989. Each pass from 55°S to 55°N is approximately a 30-minute orbital segment. About 140 such 30-minute orbital passes over the Pacific were analyzed in this study to collect information on single-layered, low-level, oceanic clouds. In the data analysis, each of the 30-minute orbital segments was divided into scene scales (roughly 12 scenes), as shown in Figure 4.1. The scene scale covers a geographical area of approximately 2400 km × 1000 km and contains 384 × 256 (scan spots × scan lines) GAC pixels. Each scene was further divided into 60-km-scale regions in the spatial coherence analysis. The 60-km-scale region contains 16 × 16 GAC pixels. Each scene contains 24 × 16 such 60-km regions.

4.2.2 Identification of cloud-free, overcast, and broken-cloudy pixels

The spatial coherence method was employed to identify 60-km regions that contained only single-layered, low-level cloud systems. The method was also used to identify pixels that were either cloud-free, overcast, and partly cloud covered. The

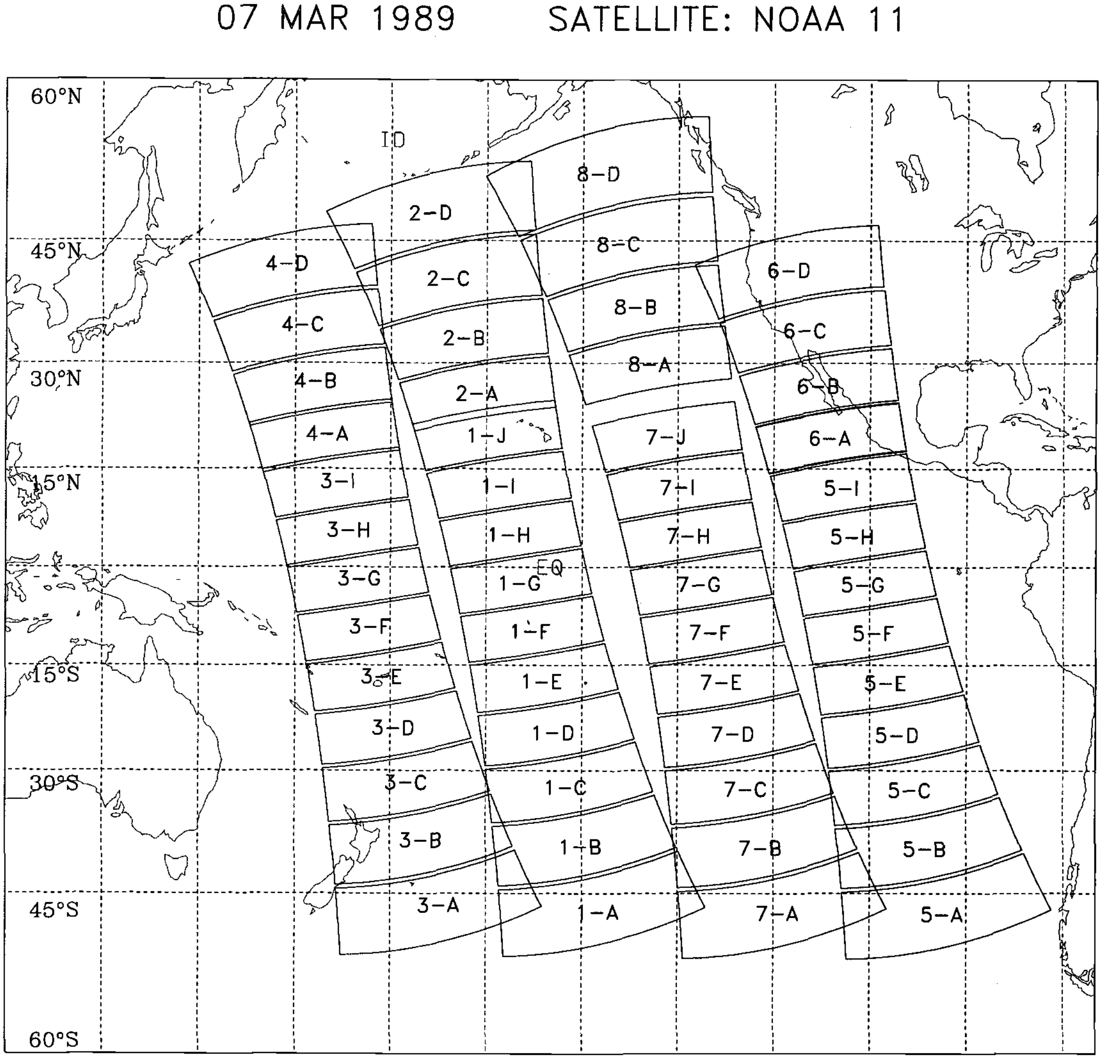
07 MAR 1989 SATELLITE: NOAA 11
60°N
45°N
30°N
15°N
EQ
15°S
30°S
45°S
60°S
ID
2-D
8-D
4-D
2-C
8-C
6-D
4-C
2-B
8-B
6-C
4-B
8-A
2-A
6-B
4-A
1-J
7-J
6-A
3-I
1-I
7-I
5-I
3-H
1-H
7-H
5-H
3-G
1-G
7-G
5-G
3-F
1-F
7-F
5-F
3-E
1-E
7-E
5-E
3-D
1-D
7-D
5-D
3-C
1-C
7-C
5-C
3-B
1-B
7-B
5-B
3-A
1-A
7-A
5-A

Figure 4.1 Schematic plot of daytime ascending passes for NOAA-11 AVHRR polar orbiting satellite. The orbital passes were obtained on March 7, 1989. The boxes represent the scene scale which consists of 384 × 256 (scan spots × scan lines) GAC 4-km pixels.

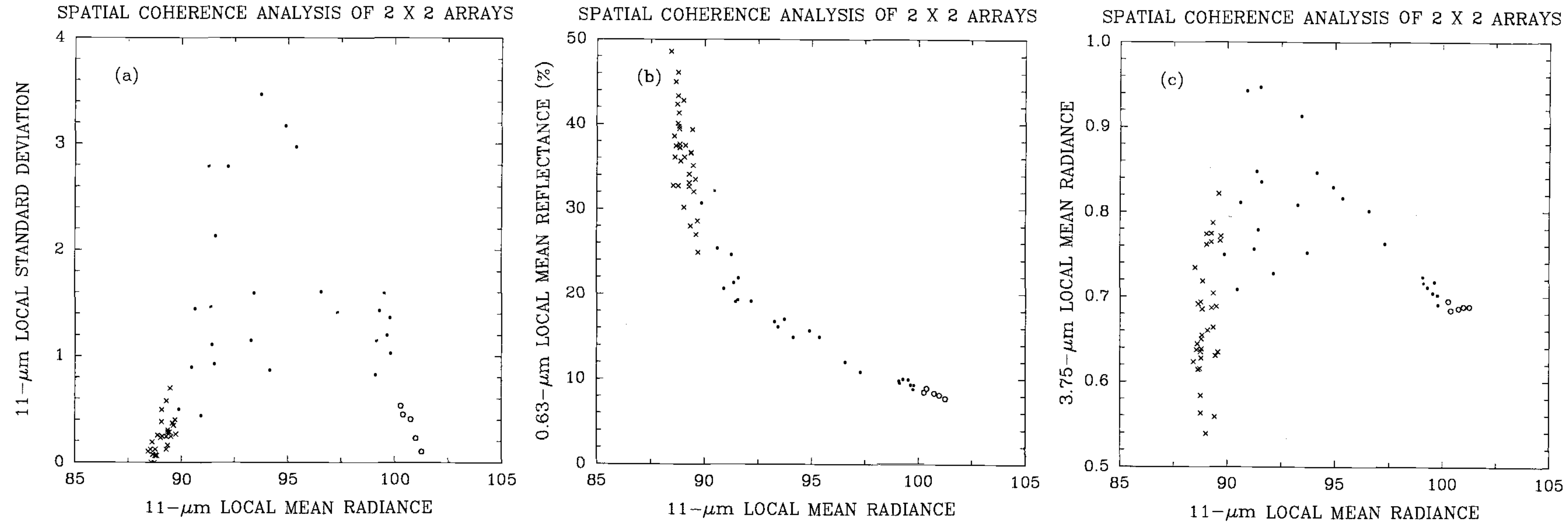

Figure 4.2 Spatial coherence analysis of 2 × 2 GAC pixel arrays. The observations are for a 60-km region drawn from the 250-km region shown in Figure 2.10. Each point represents an (8 km)^2 portion of the (60 km)^2 region. (a) local means and standard deviations of 11-μm radiance (mWm^{-2}sr^{-1}cm) (b) local mean 0.63-μm reflectances and 11-μm radiances (c) local mean 3.75- and 11-μm radiances.

overcast pixels within a 60-km region containing only single-layered clouds emit similar radiances that are attributed to a horizontally uniform cloud layer. The cloud-free pixels also emit similar radiances that are attributed to a uniform underlying sea surface. When a region contains a group of overcast pixels and all other pixels have radiances that lie between those associated with the overcast pixels and those associated with the cloud-free pixels, then the region is presumed to contain a single-layered cloud system. Pixels that are not identified as being either overcast or cloud-free are taken to be partly cloudy.

Figure 4.2a illustrates the spatial coherence analysis of a typical single-layered cloud system. The data shown in the figure is obtained for a 60-km region extracted from the 250-km region that was shown in Figure 2.10a. The single-layered, low-level system covers a large area $>\sim(250 \text{ km})^2$. Figure 4.2a shows the spatial coherence analysis of 2×2 pixel arrays (see Section 2.2.2 for the data analysis). Radiances for the cloud-free pixel arrays are identified by open circles; overcast pixel arrays are identified by crosses, and partly cloudy pixel arrays are identified by dots. Figures 4.2b and 4.2c also show the mean 0.63-μm reflectivities and mean 3.75-μm radiances plotted against the mean 11-μm radiances for the 2×2 arrays. Interestingly, the partly cloudy pixel arrays display considerably larger 3.75-μm radiances, but smaller 0.63-μm reflectivities, than do the overcast pixel arrays. This phenomena was also shown by Coakley and Davies (1986) and by Coakley (1991). They suggested that this phenomena may be explained either by differences in cloud liquid water paths and droplet radii between the cores and the edges of clouds, or by three dimensional radiative transfer effects involving the cloud edges.

4.2.3 Sea surface temperature retrievals

Prior to retrieving cloud properties, sea surface temperatures were retrieved using 11-μm radiances obtained for the pixels that were identified as being cloud-free. Correlated k-distribution routines (Kratz, 1995) together with the atmospheric temperature and humidity profiles obtained from NOAA TIROS Operational Vertical Sounder (TOVS) data were used to correct for atmospheric absorption. Figure 4.3 shows the monthly-mean sea surface temperatures retrieved for March 1989 for the Pacific ocean. The sea surface temperatures show a latitudinal dependence in the midlatitude and subtropical regions. As for the tropics, the sea surface temperatures are rather uniform except that high temperatures are found in the western Pacific, known as the warm pool.

The retrieved sea surface temperatures are also plotted in Figure 4.4 as a function of the satellite zenith angle. The figure shows the monthly means obtained for both northern and southern midlatitudes (35°-55°), subtropics (15°-35°), and tropics (0°-15°). The positive angles indicate the direction of forward scattering for reflected sunlight. Negative angles indicate backscattering. In the figure and others similar to it, the thin error bars in the figure indicate the standard deviations for the variations of the daily means. The thick error bars indicate the 95% confidence intervals of the monthly means and are determined by assuming that the daily mean represents an independent estimate of the monthly mean. The 95% confidence intervals are obtained by

$$\alpha \frac{\sigma}{\sqrt{N}}, \tag{4.1}$$

where σ is the standard deviation of the daily values, N is the number of days for

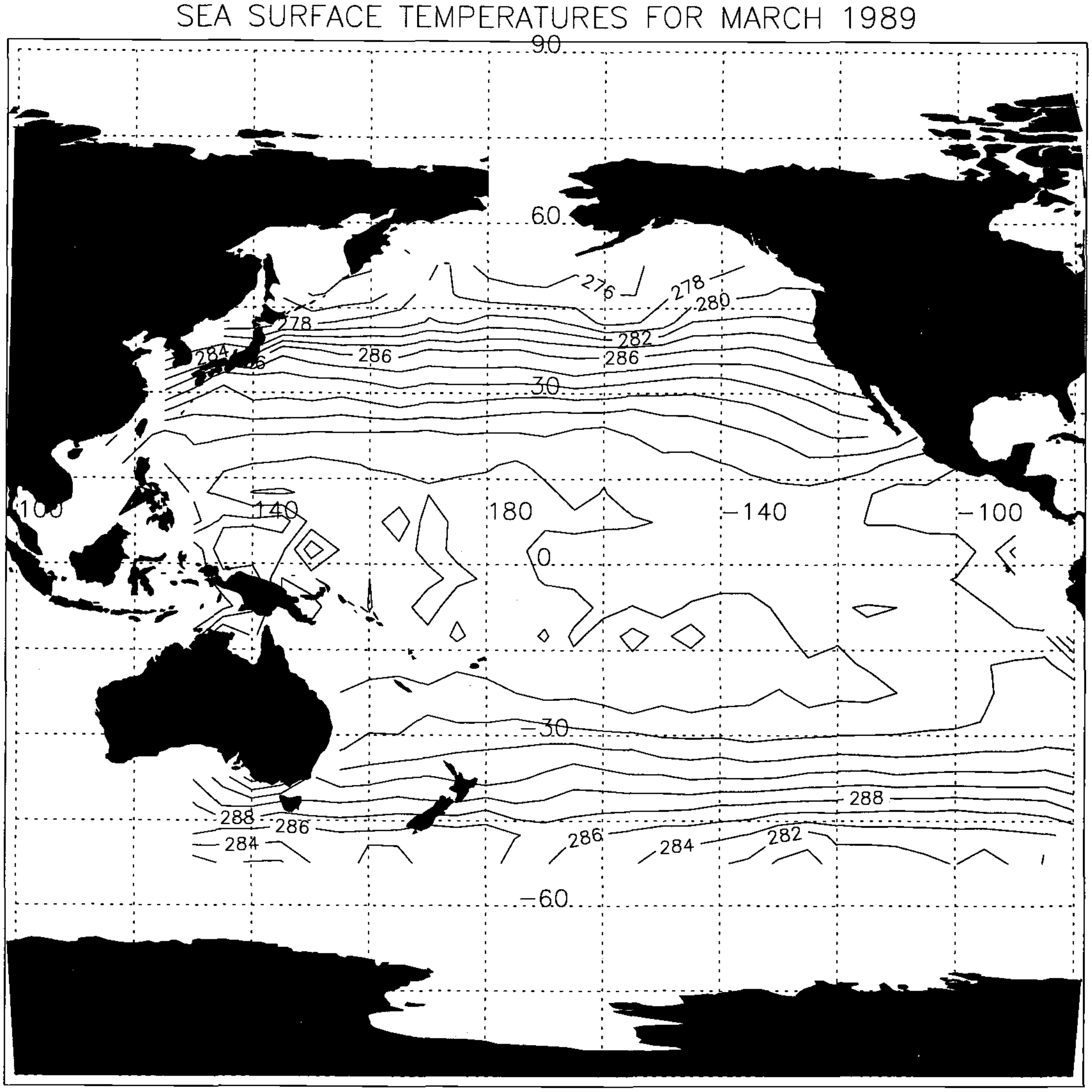
SEA SURFACE TEMPERATURES FOR MARCH 1989
90
60
276
278
280
282
286
278
284
286
30
100
140
180
−140
−100
0
−30
288
288
286
284
286
284
282
−60

Figure 4.3 Contour plot of monthly-mean sea surface temperatures (K). Results retrieved using cloud-free radiances derived by the spatial coherence method. NOAA-11 AVHRR GAC data for March 1989 was used. Kratz's correlated *k*-distribution model was used for atmospheric correction. The contour interval is 2K.

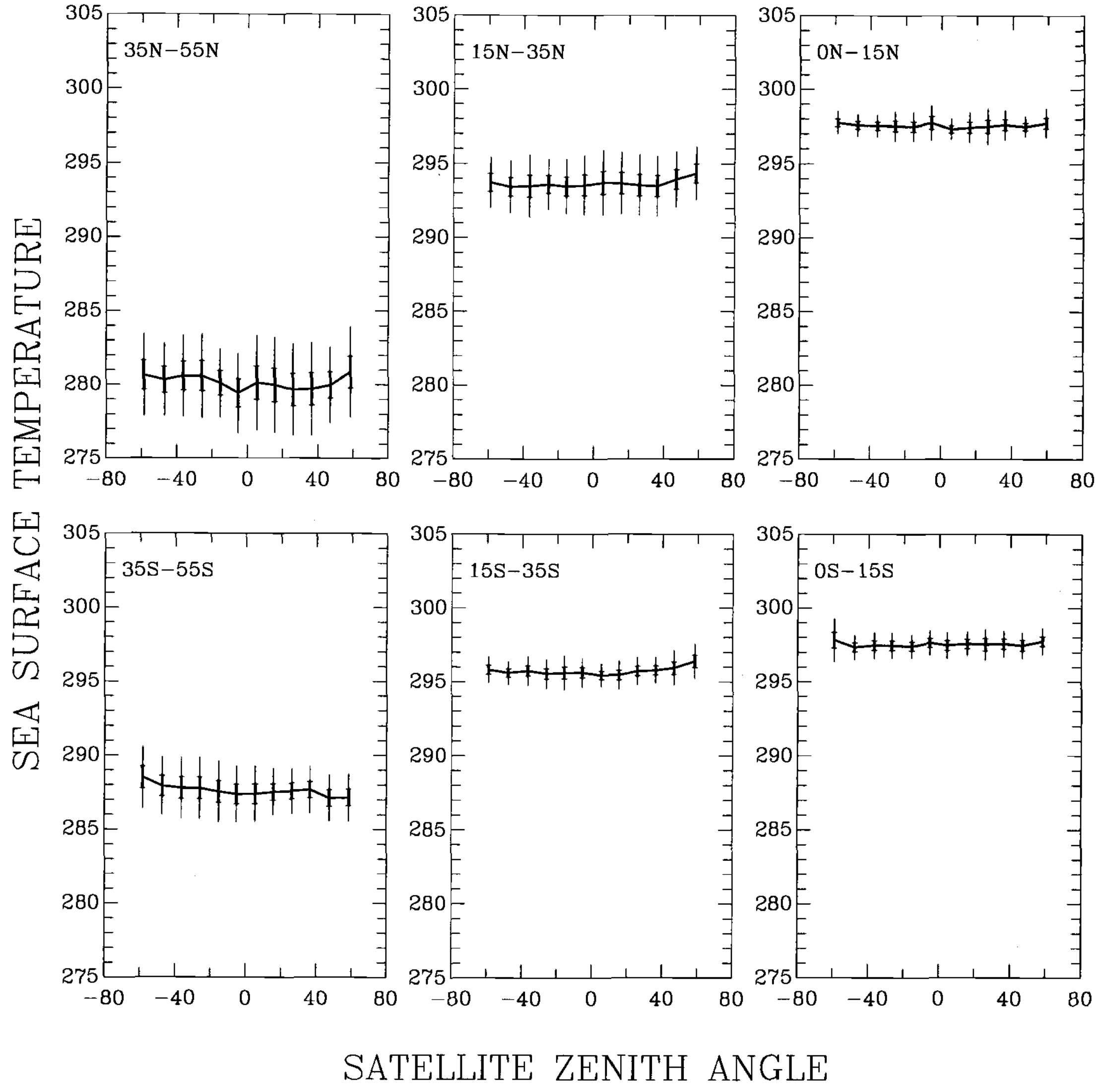

Figure 4.4 Sea surface temperatures as a function of satellite zenith angle. Results derived using Kratz's model and obtained for March 1989 for both northern and southern midlatitudes (35°–55°), subtropics (15°–35°), and tropics (0°–15°). Curves are for the monthly means. Thick bars indicate the 95% confidence intervals for the means. Thin bars represent the standard deviations for the variations of daily means. Negative view angles are for the backward view direction.

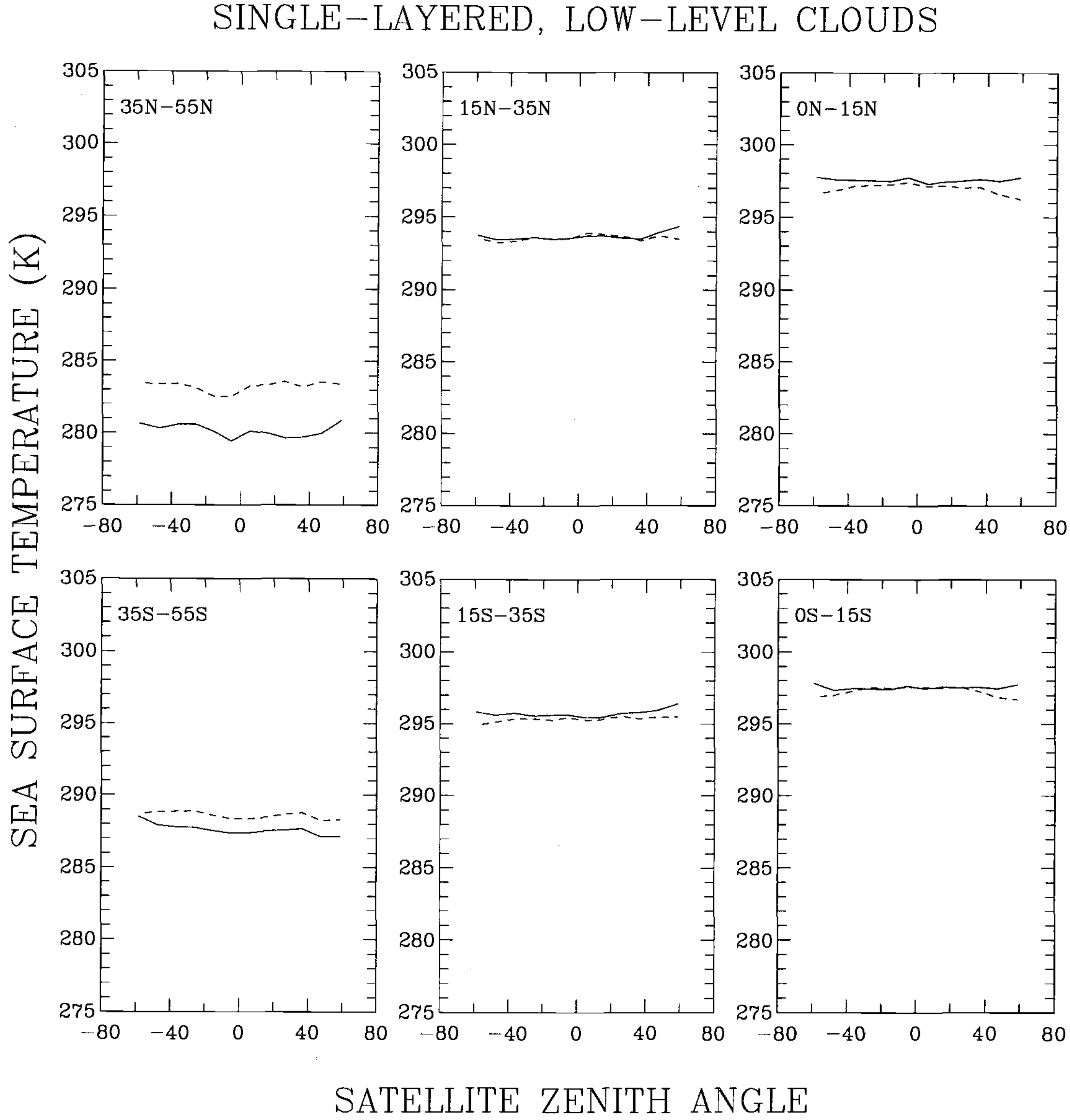

Figure 4.5 Monthly-mean sea surface temperatures obtained with Kratz's model (solid) and McMillin-Crosby's empirical equation (dashed). Results are for March 1989 for both northern and southern midlatitudes (35°–55°), subtropics (15°–35°), and tropics (0°–15°).

which cloud-free observations were obtained, and α is taken to be 1.96, the value for a normal distribution. There appears to be no obvious zenith angle dependence in the retrieved sea surface temperatures.

The sea surface temperatures retrieved using Kratz's correlated *k*-distribution model are also compared with those obtained using the method of McMillin and Crosby (1984). The method is given by the empirical equation,

$$T_{sfc} = c_0 + c_1 T_{ch4} + c_2(T_{ch4} - T_{ch5}), \tag{4.2}$$

where T_{ch4} and T_{ch5} are the AVHRR channel-4 and channel-5 brightness temperatures observed for cloud-free regions and $c_0 = -4.588$, $c_1 = 1.014$, and $c_2 = 2.637$ are derived using the NOAA-7 AVHRR observations. Figure 4.5 shows the monthly-mean sea surface temperatures obtained using Kratz's model and using the empirical equation of McMillin and Crosby. The results for the two methods differ mostly for the midlatitudes. Some differences are also shown for large satellite zenith angles. The sea surface temperatures obtained for the two methods are both used in cloud property retrievals to account for emission from the sea surface. The sensitivity of the retrieved cloud properties to changes in sea surface temperature is examined.

4.2.4 Cloud property retrievals using the iterative retrieval scheme

Radiances observed for overcast pixels, together with the sea surface temperatures retrieved using Kratz's model were used in the radiation model described in Chapter 3 for retrieving cloud properties. Averages of the radiances for the overcast pixels within 60-km regions containing single-layered, low-level systems were used in the retrievals. Similar average radiances were also obtained for the partly cloudy pixels within the 60-km regions. For the retrievals, however, the radiances observed for the partly cloudy pixels were assumed to be due to overcast conditions. The partly cloudy pixels were restricted to regions without sunglint.

Table 4.1 shows an example of the mean radiances for the overcast and cloud-free pixels for 60-km regions. The data in the table was taken on March 6, 1989 for a $\sim(250 \text{ km})^2$ region off the east coast of Japan. The region contains a uniform, single-layered, low-level cloud system and is divided into a 4×4 array of 60-km regions. Each 60-km region consists of 16×16 AVHRR GAC pixels. The mean 0.63, 3.75, and 11-μm radiances and the retrieved cloud visible optical depths, droplet effective radii, and cloud top emission temperatures for overcast pixels are shown in the right column of each box. The left column shows the mean 0.63, 3.75, and 11-μm radiances obtained for cloud-free pixels. The sun-earth-satellite viewing geometry and the location of each 60-km region is also shown in the table. Also, in Table 4.2 the 60-km mean radiances and the retrieved cloud properties for partly cloudy pixels are shown in the left column of each box. The right columns in Table 4.2 are results from simulation studies which are discussed later. Comparing the values for the overcast pixels (Table 4.1, right columns) and those for the partly cloudy pixels (Table 4.2, left columns), it is clear that the 0.63-μm radiances and cloud visible optical depths of the partly cloudy pixels are generally smaller than those of the overcast pixels. The 3.75 and 11-μm radiances and the cloud top emission temperatures obtained for the partly cloudy pixels are generally larger than those obtained for the overcast pixels. The differences are assessed later for the March 1989 data.

Table 4.1 Cloud-free and overcast cloud properties together with locations and sun-earth-satellite viewing geometry. Data obtained on March 6, 1989, for a ~(250 km)^2 region which contained only single-layered, low-level cloud syatems. Each box represents a ~(60 km)^2 region. Left columns give the cloud-free 0.63-μm reflectivity, 3.75-, and 11-μm radiances (mWm^{-2}sr^{-1}cm) obtained by the spatial coherence analysis. Right columns give the overcast 0.63-μm reflectivity, 3.75-, and 11-μm radiances obtained by the spatial coherence analysis along with model retrieved visible optical depth, droplet effective radius, and cloud top emission temperature for the overcast clouds.

(-135.7°,-4.8°) (25.7°,2.6°,174.6°) 0.070 0.361 0.717 0.648 101.5 89.9 9.6 13.5μm 286.6K	(-135.1°,-4.7°) (26.3°,7.8°,174.9°) 0.067 0.374 0.687 0.681 101.5 90.4 9.9 13.8μm 287.1K	(-134.5°,-4.6°) (26.9°,13.0°,175.1°) 0.063 0.303 0.654 0.828 101.6 90.6 7.1 10.8μm 287.1K	(-133.9°,-4.5°) (27.5°,18.2°,175.2°) 0.063 0.288 0.627 0.927 101.6 91.4 6.0 9.0μm 287.6K
(-135.6°,-5.3°) (25.7°,2.6°,173.9°) 0.070 0.441 0.720 0.646 101.3 90.7 12.8 13.1μm 287.5K	(-135.0°,-5.2°) (26.3°,7.8°,174.0°) 0.063 0.344 0.681 0.692 101.5 92.4 9.0 13.2μm 288.7K	(-134.4°,-5.1°) (26.9°,13.0°,173.9°) 0.056 0.216 0.638 0.790 101.7 92.4 4.78 11.0μm 288.4K	(-133.8°,-5.0°) (27.5°,18.3°,174.3°) 0.056 0.276 0.612 0.906 101.7 91.8 5.7 8.6μm 288.1K
(-153.5°,-5.8°) (25.8°,2.6°,172.9°) 0.066 No 0.708 overcast 101.2 pixels	(-134.9°,-5.7°) (26.3°,7.8°,173.0°) 0.057 0.387 0.663 0.677 101.5 92.0 10.5 13.5μm 288.5K	(-134.3°,-5.6°) (26.9°,13.0°,173.0°) 0.040 0.255 0.595 0.776 102.1 92.7 5.9 11.8μm 288.6K	(-133.7°,-5.5°) (27.6°,18.3°,173.2°) 0.040 0.312 0.588 0.866 102.2 92.3 7.2 10.0μm 288.5K
(-135.4°,-62°) (25.8°,2.6°,172.2°) 0.063 No 0.699 overcast 101.2 pixels	(-134.8°,-6.1°) (26.4°,7.8°,172.1°) 0.052 0.429 0.647 0.750 101.4 91.9 11.7 11.3μm 288.5K	(-134.2°,-6.0°) (26.9°,13.0°,172.3°) 0.043 No 0.593 overcast 101.6 pixels	(-133.6°,-5.9°) (27.6°,18.2°,172.5°) 0.040 0.427 0.592 0.803 101.6 90.9 11.1 11.3μm 287.7K

Legend:

(longitude, latitude)
(solar zenith, satellite zenith, relative azimuth)

0.63-μm reflevtivity	0.63-μm reflevtivity
3.75-μm radiance	3.75-μm radiance
11-μm radiance	11-μm radiance
	visible optical depth
	droplet effective radius
	cloud emission temperature

Table 4.2 Cloud properties for partly cloudy pixels, assumed to be overcast. The table shows 0.63-μm reflectivity, 3.75-, and 11-μm radiances obtained for the partly cloudy pixels, along with cloud cover fraction, visible optical depth, droplet effective radius, and cloud top emission temperature. Each box shows results obtained for a (60 km)^2 region. These 60-km regions are the same as those shown in Table 4.1. Left columns show results obtained by the spatial coherence analysis and right columns show results obtained from model simulation which is described in Section 4.6.

0.933		0.854		0.277		0.700	
0.257	0.338	0.248	0.324	0.117	0.106	0.218	0.210
0.652	0.653	0.749	0.682	0.795	0.702	0.901	0.837
90.6	90.6	92.0	92.0	98.6	98.6	94.5	94.5
6.3	8.9	5.8	8.0	2.3	2.1	4.3	4.4
13.7μm	13.6μm	12.1μm	14.0μm	9.5μm	13.5μm	8.9μm	11.2μm
287.0K	287.2K	288.1K	288.4K	295.0K	295.2K	290.2K	290.4K
0.817		0.594		0.527		0.566	
0.243	0.366	0.149	0.217	0.134	0.128	0.187	0.169
0.695	0.660	0.753	0.687	0.878	0.718	0.852	0.778
92.7	92.7	96.1	96.1	96.8	96.8	96.1	96.1
5.9	9.9	3.2	5.2	2.1	2.6	3.6	3.5
12.2μm	13.2μm	11.1μm	14.2μm	5.5μm	12.5μm	9.3μm	12.1μm
288.6K	288.8K	290.7K	291.2K	291.2K	292.1K	291.7K	291.8K
No comparisons because no overcast pixels identified.		0.876		0.659		0.461	
		0.277	0.342	0.144	0.178	0.131	0.160
		0.766	0.675	0.798	0.714	0.835	0.716
		93.2	93.2	95.9	95.9	97.6	97.6
		6.6	9.0	2.9	4.0	2.2	3.5
		11.1μm	13.9μm	10.5μm	14.2μm	7.9μm	15.8μm
		289.3K	289.5K	290.1K	290.7K	291.0K	291.9K
No comparisons because no overcast pixels identified.		0.590		No comparisons because no overcast pixels identified.		0.646	
		0.219	0.265			0.218	0.286
		0.736	0.708			0.801	0.729
		95.8	95.8			94.7	94.7
		5.1	6.5			4.7	6.9
		12.2μm	13.4μm			11.9μm	14.6μm
		291.6K	291.7K			290.0K	290.2K

Legend:

cloud cover fraction for partly cloudy pixels	
0.63-μm reflectivity	0.63-μm reflectivity
3.75-μm radiance	3.75-μm radiance
11-μm radiance	11-μm radiance
visible optical depth	visible optical depth
droplet effective radius	droplet effective radius
cloud emission temperature	cloud emission temperature

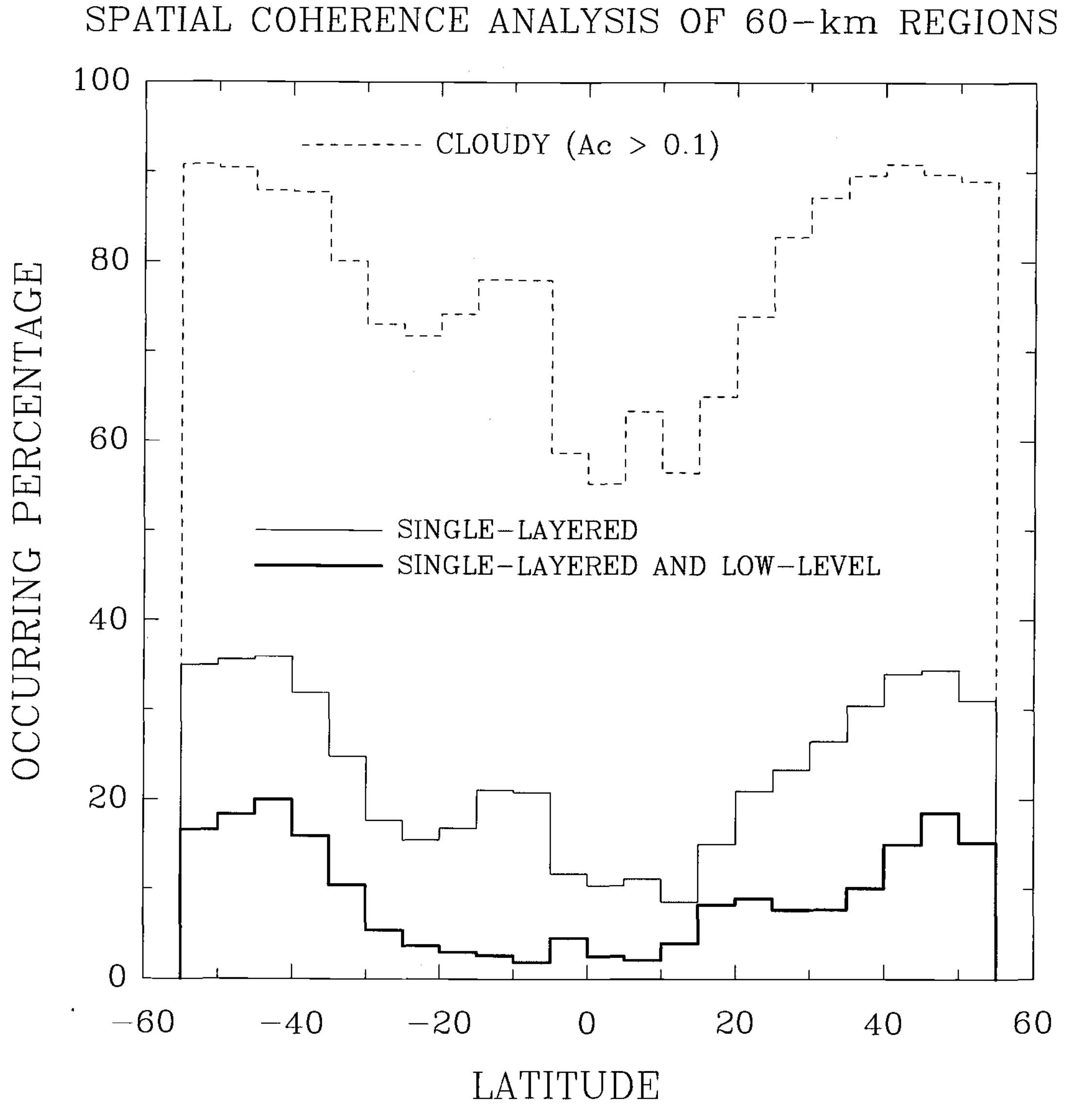

Figure 4.6 Frequency distributions of single-layered cloud systems for 60-km-scale regions. Results obtained for March 1989 over the Pacific ocean. Latitudinal distributions of the frequencies are obtained for 1) cloudy $A_c > 0.1$ (dashed), 2) single-layered (thin), and 3) single-layered, low-level systems (thick).

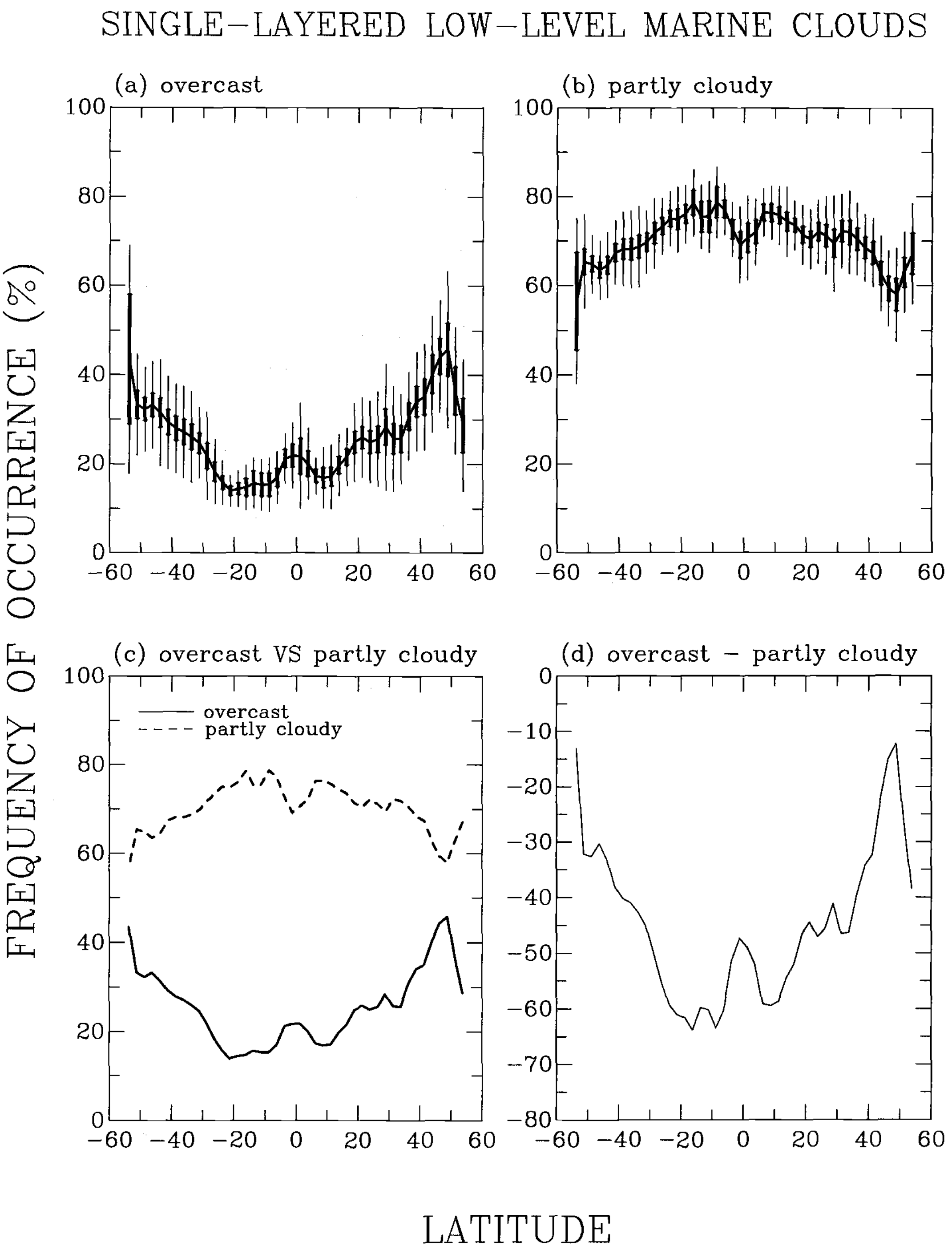

Figure 4.7 Frequency of occurrence (%) for overcast and partly cloudy pixels. Results obtained for single-layered, low-level clouds identified by the spatial coherence method for March 1989 over the Pacific ocean. Curves show the monthly means. Thick bars indicate the 95% confidence intervals for the means and thin bars indicate the standard deviations of the daily means. (a) overcast; (b) partly cloudy; (c) means shown in (a) and (b); (d) differences between the means shown in (c). Negative latitudes are for the south Pacific.

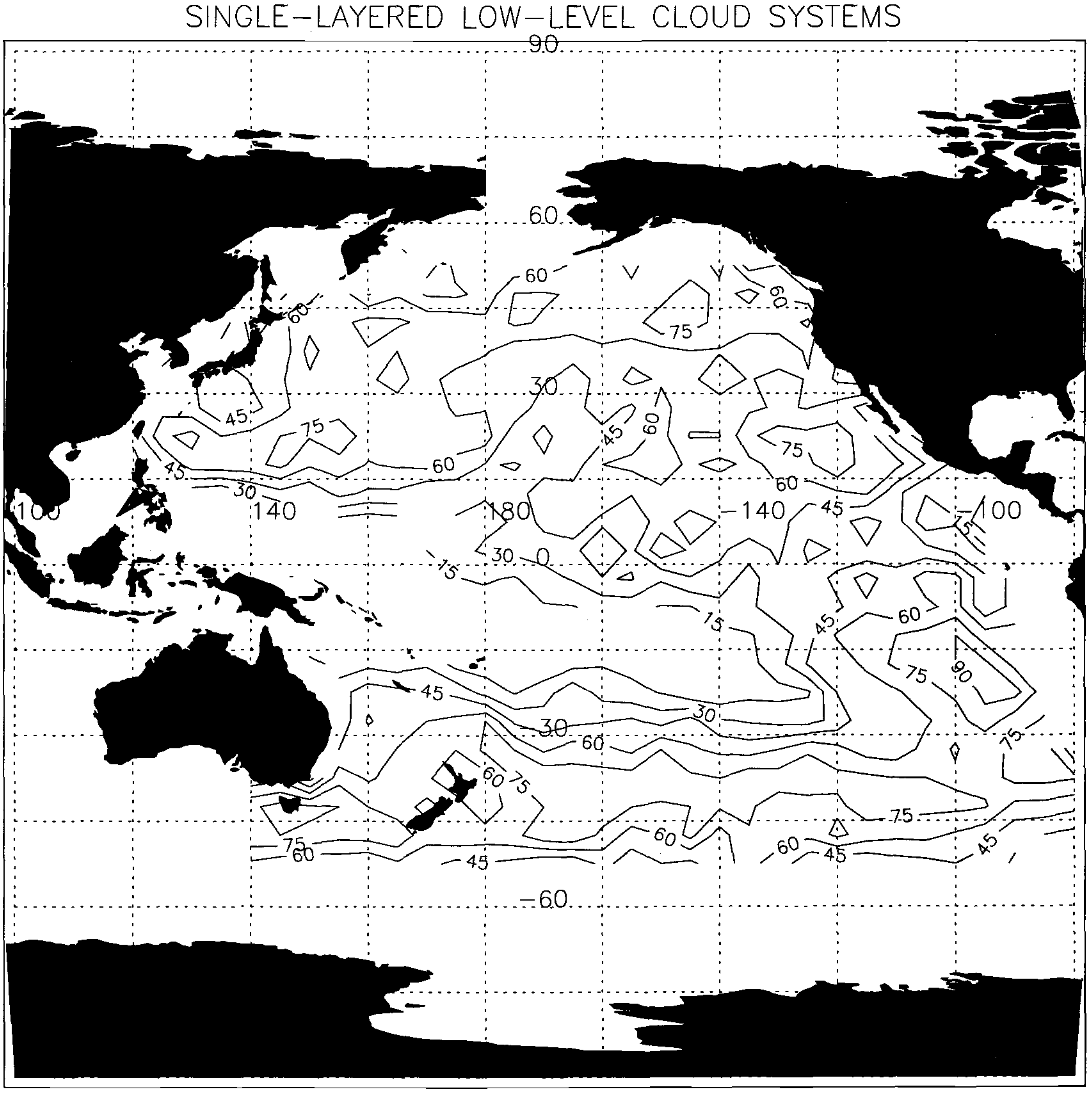

SINGLE-LAYERED LOW-LEVEL CLOUD SYSTEMS

90
60
30
0
-30
-60
100
140
180
-140
-100
15
30
45
60
75
90

Figure 4.8 Frequency of occurrence for single-layered, low-level cloud systems. Contour lines show the fraction (%) of days where single-layered, low-level systems were identified by the spatial coherence method for March 1989. The contour interval is every 15%.

For the retrievals of cloud properties, the atmospheric temperature and humidity profiles together with the ozone column abundance were obtained from the NOAA TIROS Operational Vertical Sounder (TOVS) data. These data are included in the ISCCP C1 data and are given for every 3 hours and for every 2.5° × 2.5° (longitude × latitude) region (Kidwell, 1991). The absorption due to other gases, like CO_2, CH_4, O_2, and N_2O, was calculated using current concentrations in the atmosphere. Scattering by molecules was included. The cloud top altitude was derived by comparing the retrieved cloud top emission temperature to the TOVS temperature profile. The cloud top altitude was allowed to vary during iterations so that atmospheric gaseous absorption and scattering were iteratively calculated for the atmosphere above and below the cloud layer. The 0.63-μm reflectances were calibrated following the method of Rao and Chen (1995). The solar constant was obtained from Thekaekara (1974). No sun-earth distance correction was made because the correction is small for March.

4.3 Frequency of occurrence for single-layered, low-level cloud systems

4.3.1 Frequency distributions of single-layered, low-level cloud systems

A single-layered cloud system is taken to be low-level if the retrieved cloud top emission temperature is larger than the 680-mb atmospheric temperature observed for the region. The 680-mb atmospheric temperature is chosen as it follows the low-level cloud classification used by ISCCP (Rossow and Schiffer, 1991). Figure 4.6 shows the frequency of occurrence for the 60-km regions which contained well-defined, single-layered, low-level clouds. The criteria for determining the well-defined, single-layered cloud systems are described in Chang (1991). The 60-km regions were taken from AVHRR passes (see Figure 4.1) for March 1989. For latitudes between 55°S and 55°N, approximately 80% of the nearly 700,000 60-km regions were found to be cloudy ($A_c > 0.1$). About 30% of the cloudy 60-km regions contained single-layered cloud systems. About 40% of the single-layered clouds were found to be low-level. The frequency of occurrence for single-layered clouds obtained here is smaller than the ~50% obtained by Lin and Coakley (1994) and by Stevermer et al. (1997) because the 60-km regions used here were restricted to be those that made up 250-km regions that contained only single-layered, low-level clouds. The figure also shows the latitudinal distributions of the frequency of occurrence. The single-layered, low-level systems were found primarily at midlatitudes and seldom in the tropic.

4.3.2 Frequency distributions for overcast and partly cloudy pixels

Figure 4.7 shows a) overcast and b) partly cloudy pixel percentages obtained for 60-km regions containing single-layered, low-level cloud systems. The curves in the figure are the monthly means obtained for the 2.5°-latitude band. Thin error bars indicate the standard deviations representing the longitudinal variation of the 2.5° region. Thick error bars indicate the 95% confidence intervals of the means. For 60-km regions containing single-layered, low-level systems with fractional cloud cover $A_c > 0.1$, ~25% of the pixels were found to be overcast and ~70% were partly cloudy. The value of ~70% for partly cloudy pixels is larger than the ~50% reported by Chang and Coakley (1993). The 60-km regions studied here all contained some overcast pixels. As for the study of Chang and Coakley, the 60-km regions were not required to contain overcast pixels so that their cloud-free fractions were larger. In addition, Figure 4.7 shows that higher percentages of partly cloudy pixels were found in low latitudes than in higher latitudes.

4.3.3 Spatial and temporal distributions of single-layered, low-level systems

In order to facilitate the comparison between the cloud properties derived by the spatial coherence method and those derived by ISCCP (presented in the next chapter), the cloud properties derived for the 60-km regions for the March 1989 data were mapped to their corresponding 2.5° × 2.5° (longitude × latitude) geographic regions. The mapping procedure uses the central latitude and longitude of each 60-km region to determine its corresponding 2.5° × 2.5° region. The 2.5°-regional mean is calculated using all 60-km regions falling in the region and weighted by the number of overcast pixels obtained in each 60-km region.

Figure 4.8 shows the fraction of days (%) where a single-layered, low-level system was identified by the spatial coherence method during March 1989. The fraction of days was obtained for every 2.5° × 2.5° region for the Pacific ocean. The observations are for all satellite view angles. The figure shows that single-layered, low-level systems occurred frequently over the Pacific ocean. These single-layered, low-level systems are mostly found meandering through the midlatitudes and eastern Pacific ocean. Regions of low occurrence are found in the western equatorial region and the subtropics of central-southern Pacific ocean. Note that for the regions near the coast of Central and South America, the data analyzed had relatively few satellite passes covering these regions. The findings here agree with the previous results obtained by Klein and Hartmann (1993). Based on annual averages of surface based cloud observations, they found that the largest amounts of stratiform clouds occurred on the east side of the subtropic Pacific and at midlatitudes. The lowest frequencies occurred in the western part of the subtropical ocean and to the west of Hawaii. Deeper convective cumuliform clouds replace the stratiform clouds in these regions (Betts and Rideway, 1989).

4.4 Low-level cloud visible optical depths, droplet effective radii, and cloud top emission temperatures for overcast and partly cloudy pixels

4.4.1 Low-level cloud visible optical depths

Figure 4.9a shows the latitudinal distribution of the zonal-mean cloud visible optical depths obtained for the single-layered, low-level, overcast pixels identified by the spatial coherence method. The monthly means were obtained for every 2.5°-latitude band. Thick error bars indicate the 95% confidence intervals for the monthly means and thin error bars indicate the standard deviations for the longitudinal variations of the 2.5°×2.5°-region monthly means. These results were obtained from observations for which the satellite zenith angle was restricted to be near nadir ($< 25°$). The mean cloud visible optical depths show a minimum near the equator and then increase poleward. The increase from the equator to higher latitudes may be authentic or may be due to a bias resulting from the increase in solar zenith angle from the equator to higher latitudes (Loeb and Davies, 1996). The overall mean cloud visible optical depth obtained for the March 1989, single-layered, low-level, overcast systems is 13.9 for the northern Pacific and 11.9 for the southern Pacific. These numbers are much larger than those obtained by Han et al. (1994), as is shown in Table 4.3. Also, Han et al. showed cloud visible optical depths in the southern hemisphere to be larger than those in the northern hemisphere.

Figure 4.9b shows the cloud visible optical depths for the pixels partly covered by the single-layered, low-level systems. These visible optical depths were obtained by assuming that the partly cloudy pixels were overcast. The overall mean cloud visible optical depth for these partly cloudy pixels is 6.0 for the northern Pacific and 4.5 for the southern Pacific. Figure 4.10a shows the correlations between the cloud visible optical depths obtained for the overcast pixels and those for the partly cloudy pixels, where the two optical depths are drawn from the same 60-km region. The frequency distributions of the visible optical depths for the two are also shown in Figure 4.10b. The cloud visible optical depths obtained for the partly cloudy pixels are systematically smaller than those obtained for the overcast pixels. They are on average $\sim$40-60% of those for the overcast pixels.

4.4.2 Low-level cloud droplet effective radii

Figure 4.11 shows the latitudinal distributions of the zonal-mean cloud droplet effective radii. Relatively small droplet effective radii are found near the equator and high latitudes. Larger droplet effective radii are found in the subtropics. The largest was found in the southern subtropics. The overall mean, low-level, cloud droplet effective radius obtained for the overcast pixels was 13.1μm for the northern Pacific and 14.7μm for the southern Pacific. The finding that the mean low-level cloud droplet effective radius is smaller for the northern Pacific agrees with the previous finding obtained by Han et al. (1994).

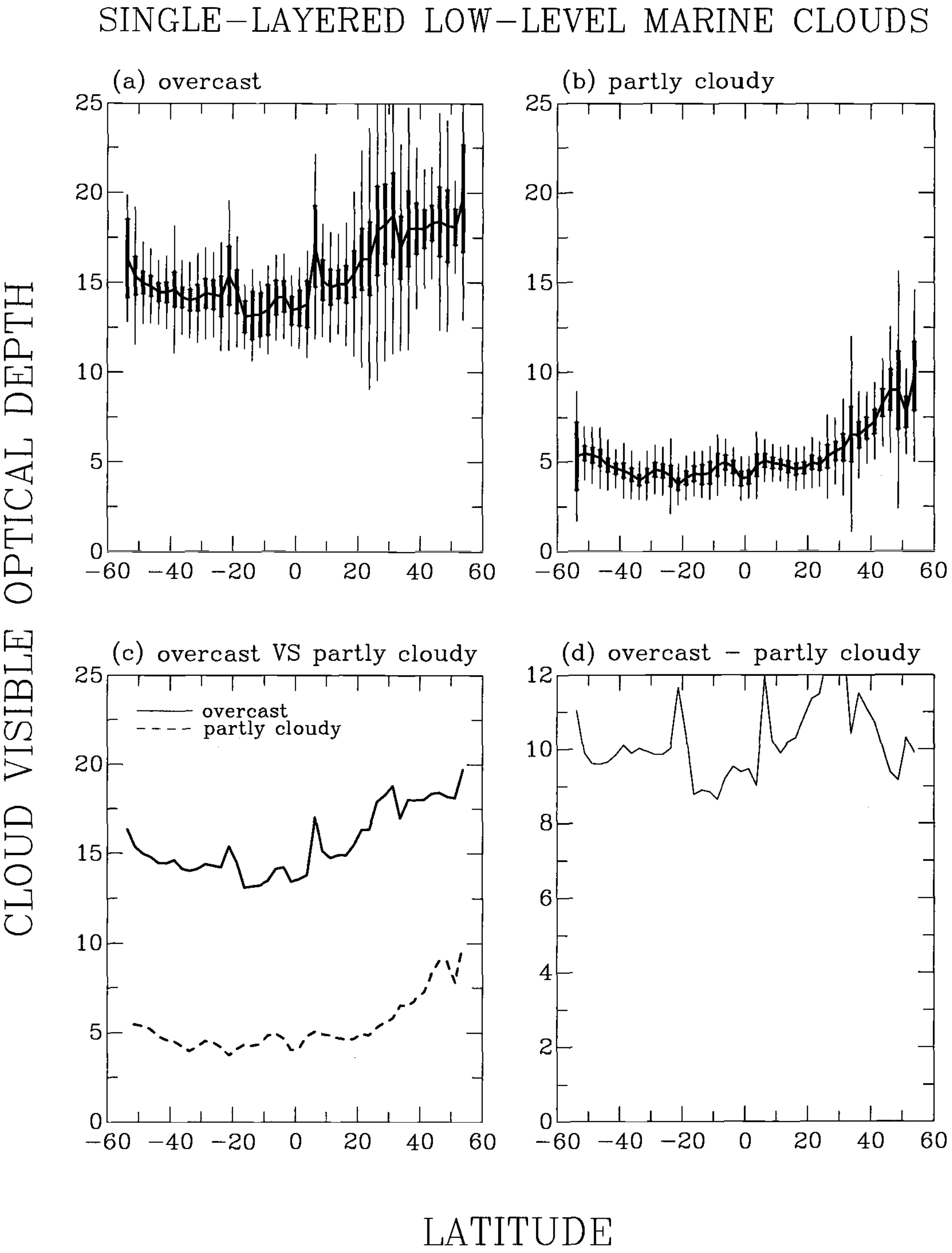

Figure 4.9 Cloud visible optical depths for single-layered, low-level clouds for March 1989 over the Pacific ocean. Observations are restricted to near-nadir satellite view angles. Curves show the monthly means. Thick bars indicate the 95% confidence intervals for the means and thin bars indicate the standard deviations of the daily means. (a) overcast; (b) partly cloudy; (c) means shown in (a) and (b); (d) differences between the means shown in (c). Negative latitudes are for the south Pacific.

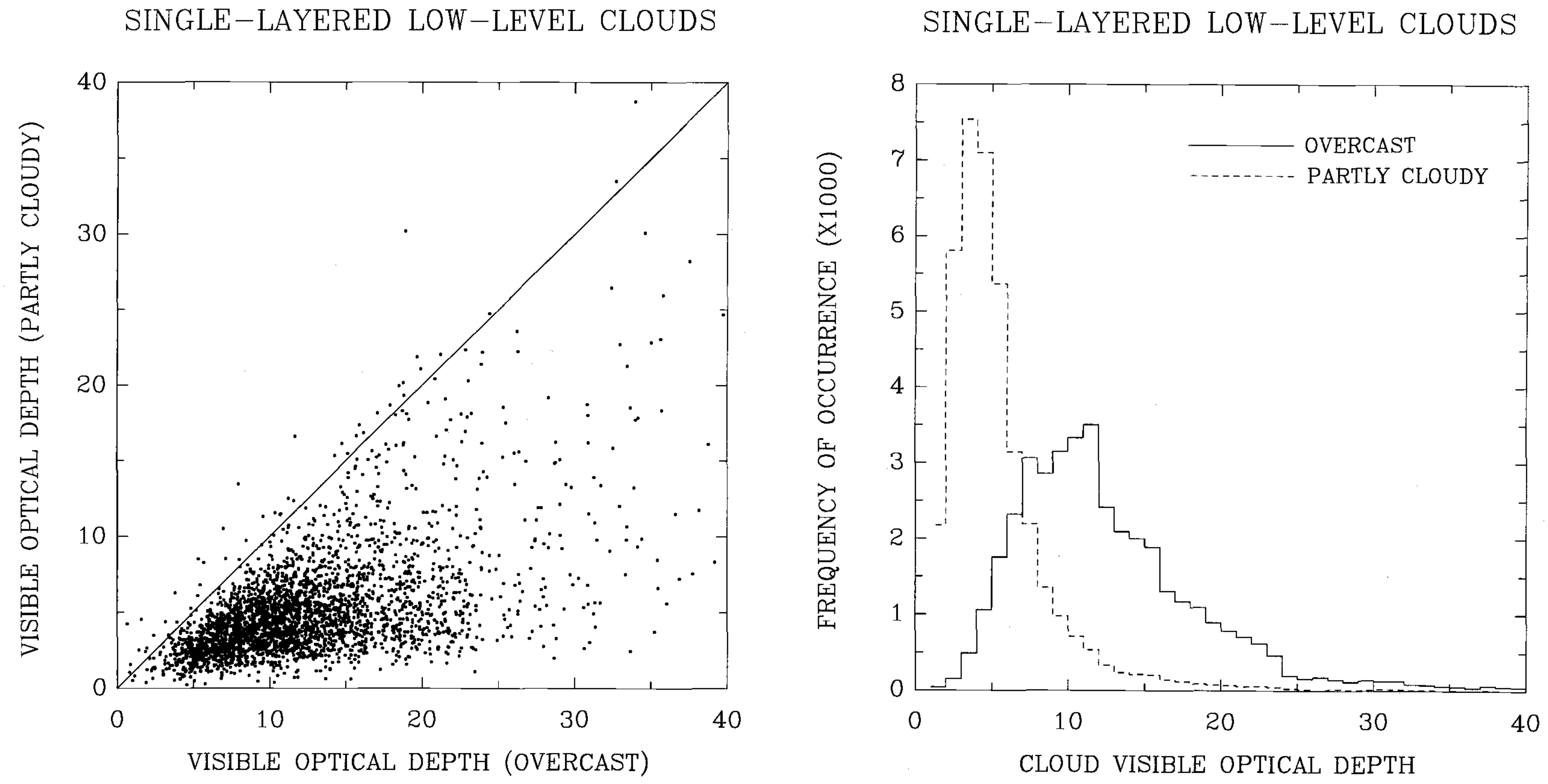

Figure 4.10 Cloud visible optical depths for overcast and partly cloudy pixels drawn from the same 60-km region. Observations are for single-layered, low-level clouds identified by the spatial coherence method for March 1989 over the Pacific ocean. The observations are restricted to near-nadir satellite view angles. (a) overcast and partly cloudy pixels. (b) frequency distributions.

Table 4.3 Monthly-mean cloud visible optical depths, droplet effective radii (μm), cloud top emission temperatures (K), and cloud top altitudes (km). Results obtained for single-layered, low-level, overcast clouds identified by the spatial coherence method for March 1989 over the Pacific ocean. Only near-nadir observations were used. Numbers in the parentheses are obtained for partly cloudy pixels assumed to be overcast. Results obtained by Han et al. (1994) (Table 5 and 6) are also listed for comparison.

	35°N-55°N	15°N-35°N	0°N-15°N	0°S-15°S	15°S-35°S	35°S-55°S
Cloud visible optical depths	17.0 (7.4)	13.9 (5.3)	12.1 (4.9)	10.9 (4.5)	11.7 (4.4)	12.8 (4.6)
	13.9 (6.0)			11.9 (4.5)		
	Han et al.: 5.8 (spring), 6.4 (annual)			Han et al.: 6.8 (spring), 7.4 (annual)		
Droplet effective radii (μm)	11.6 (12.2)	13.3 (11.7)	14.2 (11.5)	14.5 (11.4)	15.9 (13.8)	13.5 (12.9)
	13.1 (11.8)			14.7 (13.0)		
	Han et al.: 12.2 (spring), 11.6 (annual)			Han et al.: 13.1 (spring), 12.6 (annual)		
Cloud top emission temperatures (K)	268.0 (271.1)	281.5 (284.4)	286.8 (289.9)	285.8 (288.3)	283.0 (286.2)	276.3 (279.2)
Cloud top altitudes (km)	1.71 (1.46)	1.72 (1.32)	1.51 (1.10)	1.66 (1.32)	1.78 (1.37)	1.58 (1.25)

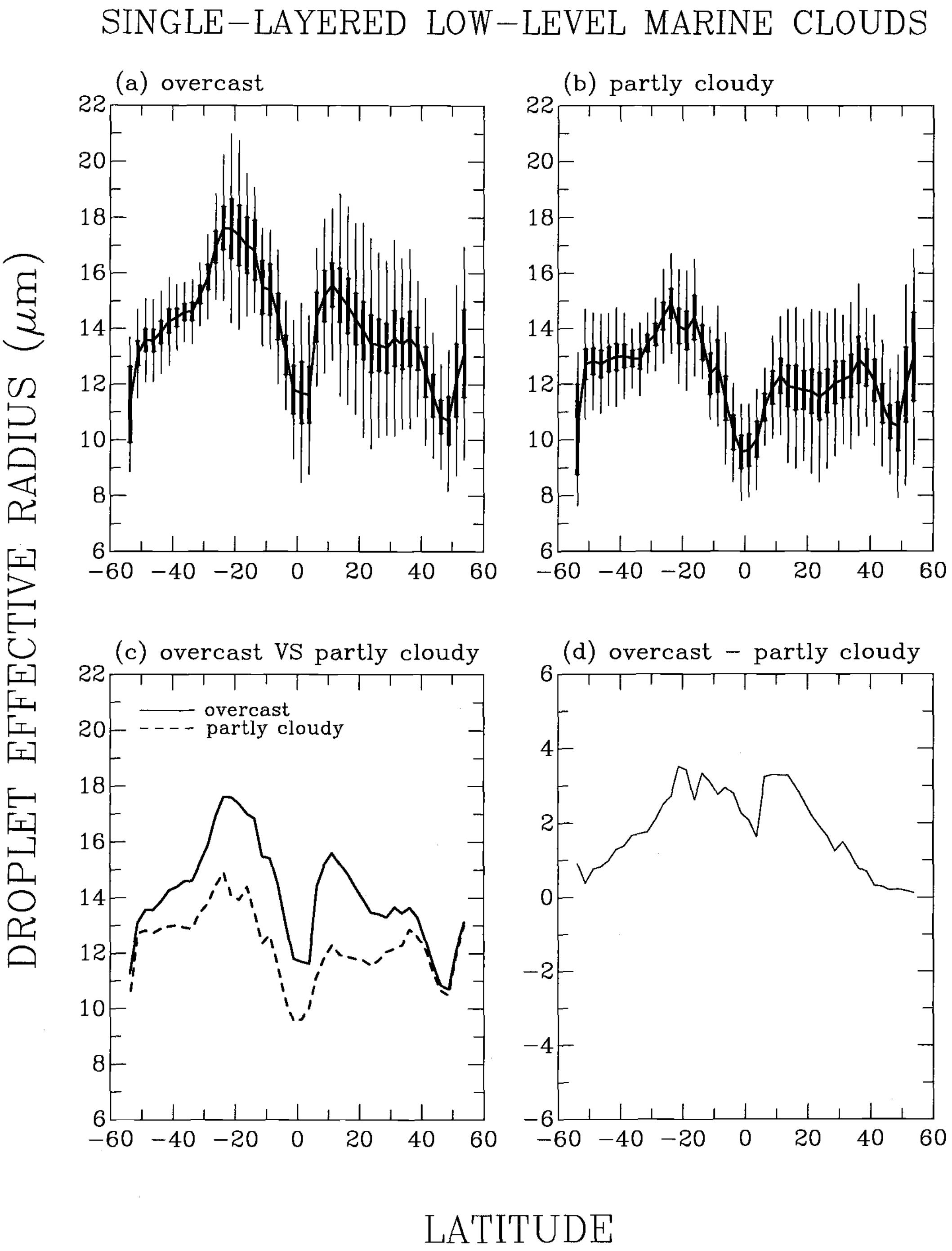

Figure 4.11 Same as Figure 4.9, except for cloud droplet effective radii (μm).

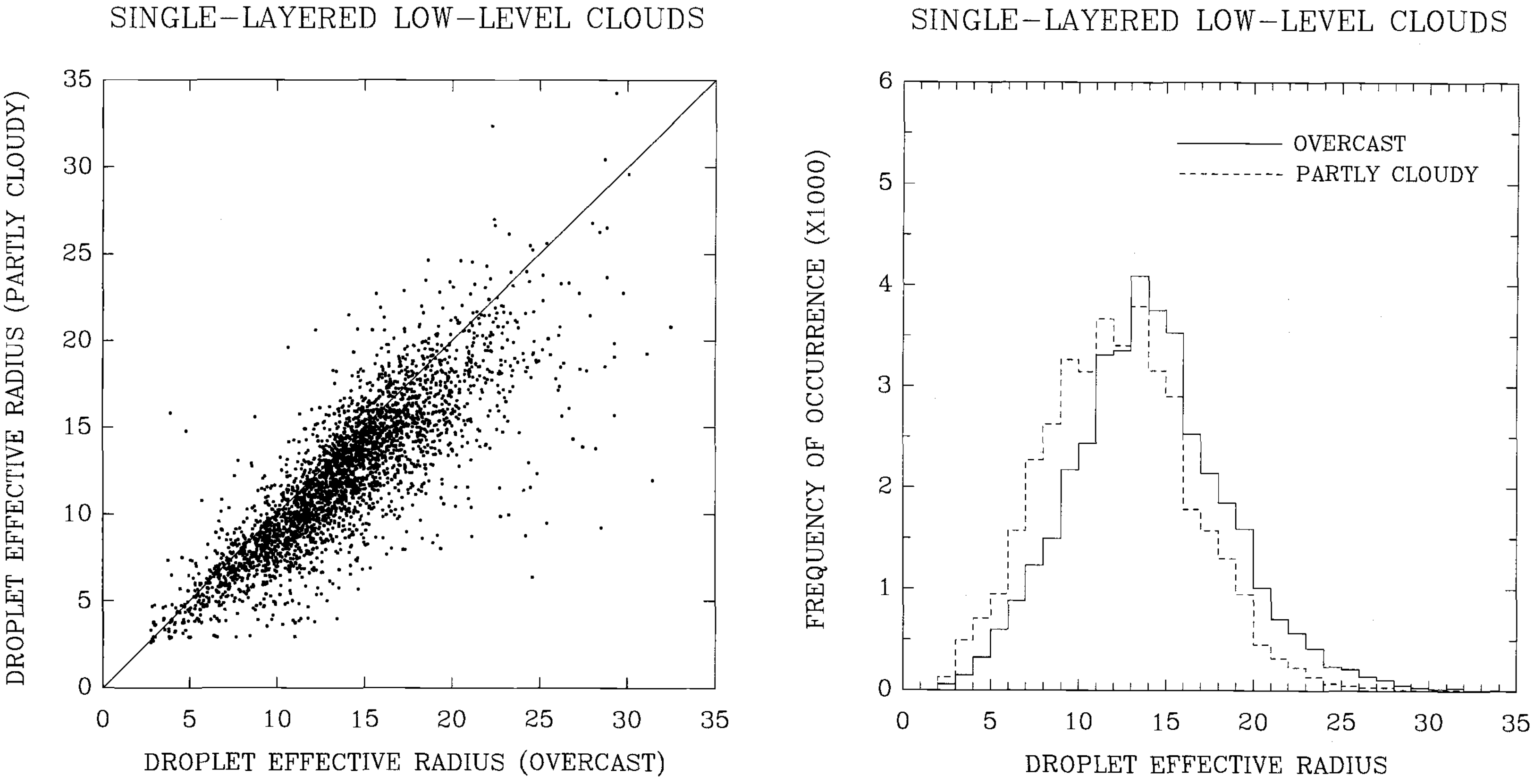

Figure 4.12 Same as Figure 4.10, except for cloud droplet effective radii (μm).

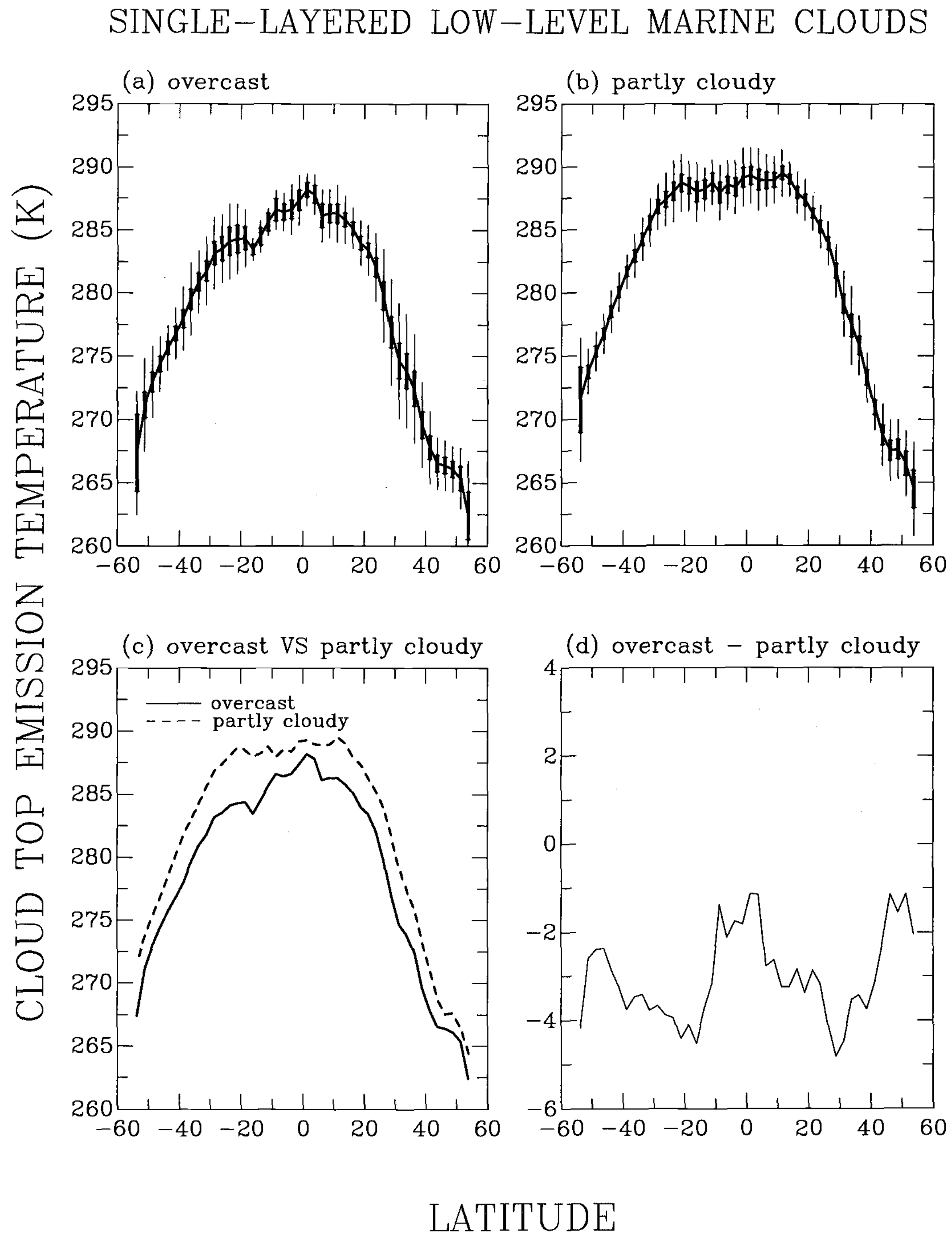

Figure 4.13 Same as Figure 4.9, except for cloud top emission temperatures (K).

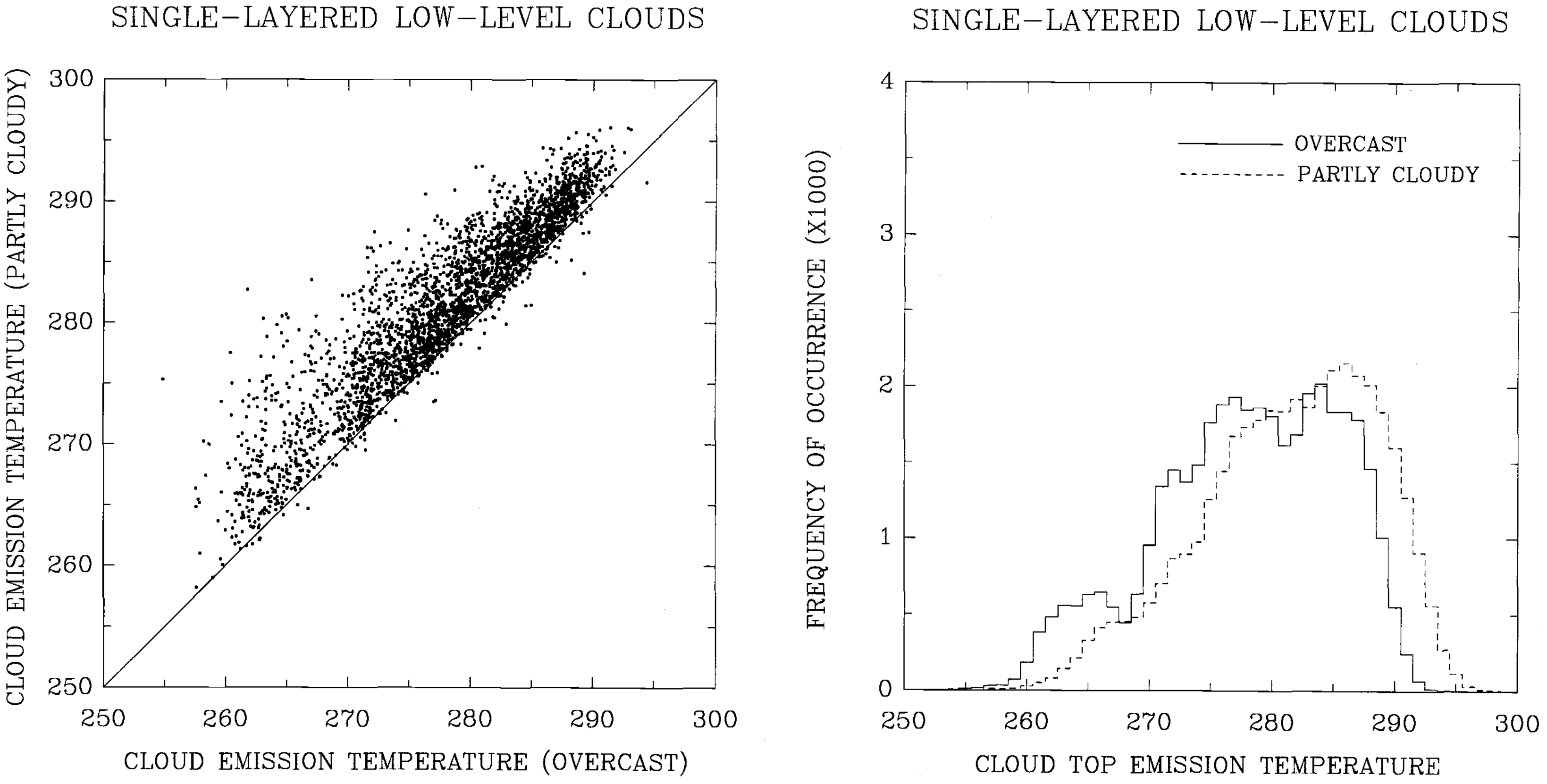

Figure 4.14 Same as Figure 4.10, except for cloud top emission temperatures (K).

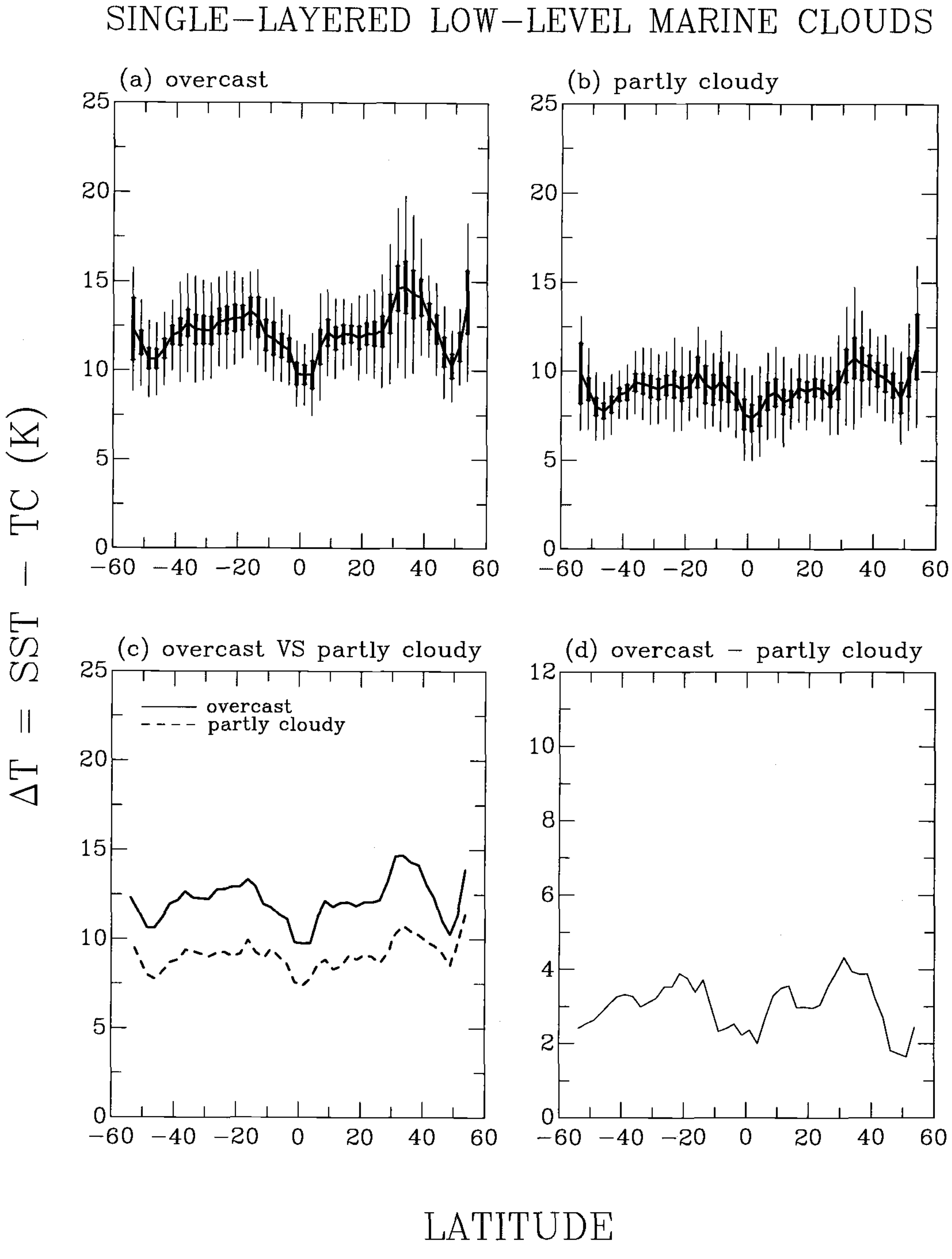

Figure 4.15 Same as Figure 4.9, except for the sea surface-cloud top temperature differences.

For partly cloudy pixels, the overall mean cloud droplet effective radius was 11.8 μm for the northern Pacific and 13.0 μm for the southern Pacific. As is shown in Table 4.3, these cloud droplet effective radii are larger than those obtained by Han et al. (1994). The correlation of the droplet effective radii obtained for overcast and partly cloudy pixels drawn from the same 60-km region is shown in Figure 4.12a. The frequency distributions of the droplet effective radii for the two are shown in Figure 4.12b. The cloud droplet effective radii obtained for the partly cloudy pixels were generally smaller than those for the overcast pixels. The differences in the droplet effective radii between overcast and partly cloudy pixels were on average $\sim 1 - 2\,\mu$m.

4.4.3 Low-level cloud top emission temperatures

Figure 4.13 shows the latitudinal distributions of the zonal-mean cloud top emission temperatures. Figure 4.14a shows the correlation of the cloud top emission temperatures obtained for the overcast and partly cloudy pixels drawn from the same 60-km region. Figure 4.14b shows the frequency distributions of the cloud top emission temperatures for the two. Low-level cloud top emission temperatures are higher at low latitudes and decrease with increasing latitude. The latitudinal variations in cloud top emission temperature are consistent with the latitudinal variations in the sea surface temperature. Figure 4.15 shows the zonal averages of the sea surface-cloud top temperature differences for the single-layered, low-level clouds. The cloud top emission temperatures obtained for the partly cloudy pixels are about 2–4K larger than those obtained for the overcast pixels. The larger cloud top emission temperatures for partly cloudy pixels are due to the additional emission arising from the cloud-free portions of the pixels.

As has been shown in Figures 4.9-4.14, large differences are obtained in the retrieved cloud visible optical depths, droplet effective radii, and cloud top emission temperatures for the overcast and partly cloudy pixels. Such differences suggest that when one retrieves cloud properties from satellite imagery data, the inclusion of partly cloudy pixels will lead to results that are biased. It seems that these biases, as a consequence, would propagate into further errors when one uses these biased cloud properties to study cloud-related issues, such as the low-level cloud optical depth and temperature relationship (Tselioudis et al., 1992). The relationships between low-level cloud properties are re-examined in the next two chapters using pixels that are identified as being overcast.

4.5 Effects of satellite zenith angle on retrieved cloud properties

4.5.1 The dependence of the retrieved cloud properties on satellite zenith angle

Figure 4.16 shows a) cloud visible optical depths, b) droplet effective radii, and c) cloud top emission temperatures retrieved for pixels that were overcast by single-layered, low-level clouds. Here, these cloud properties are plotted as functions of the satellite zenith angle for both the northern and southern midlatitudes, subtropics, and tropics. The monthly mean, 95% confidence interval (thick error bars), and standard deviation of the daily averages (thin error bars) are obtained for every 10° of the satellite zenith angle (12 such 10° bins from –60° to 60°). Again, positive satellite zenith angles are for the forward scattering direction of reflected sunlight and negative angles are for backscattering. The corresponding solar zenith angles are shown in

Figure 4.17. For each regions, the variation in the solar zenith angle is less than 10° for both the forward and backward scattering directions. The effect on the retrieved cloud visible optical depths due to this small variation in the solar zenith angle should be small (Loeb and Coakley, 1997).

Figure 4.16a shows that in the forward scattering direction a decrease of ~30-40% in the mean cloud visible optical depth is obtained for a change in the satellite zenith angle from nadir to 60°. This decrease in the retrieved cloud visible optical depths is observed in all six latitude zones. For backward scattering, a similar decrease is also observed, except for the northern midlatitudes. The decrease obtained here for the forward scattering directions agrees in magnitude with the decrease of 40% in cloud visible optical depth from nadir to ~65° obtained by Loeb and Coakley (1997). Loeb and Coakley, however, found no decrease in the backward scattering direction. The discrepancy may be due to cloud breaks at oblique satellite view angles (Dr. Norman Loeb, personal communication). When clouds are broken by small holes, their visible reflectivities are smaller than those for similar clouds without breaks. Cloud breaks can be easily seen at nadir, but are hidden at oblique view angles. As the spatial coherence method identifies single-layered clouds based on the 11-μm emitted radiance, the hidden cloud breaks, if any, at oblique view angles may go undetected. Figure 4.18 shows the number of pixels overcast by single-layered, low-level clouds as identified by the spatial coherence method. As the pixel-scale spatial resolution increases from about 4-km at nadir to about 12-km for a zenith angle of 60°, the frequency of overcast pixels should decrease (Ye and Coakley, 1996). The nearly constant or slightly increasing number of overcast pixels in the backward scattering direction, as shown in Figure 4.18, may be an indication of the effect of undetected cloud breaks at oblique satellite zenith angles.

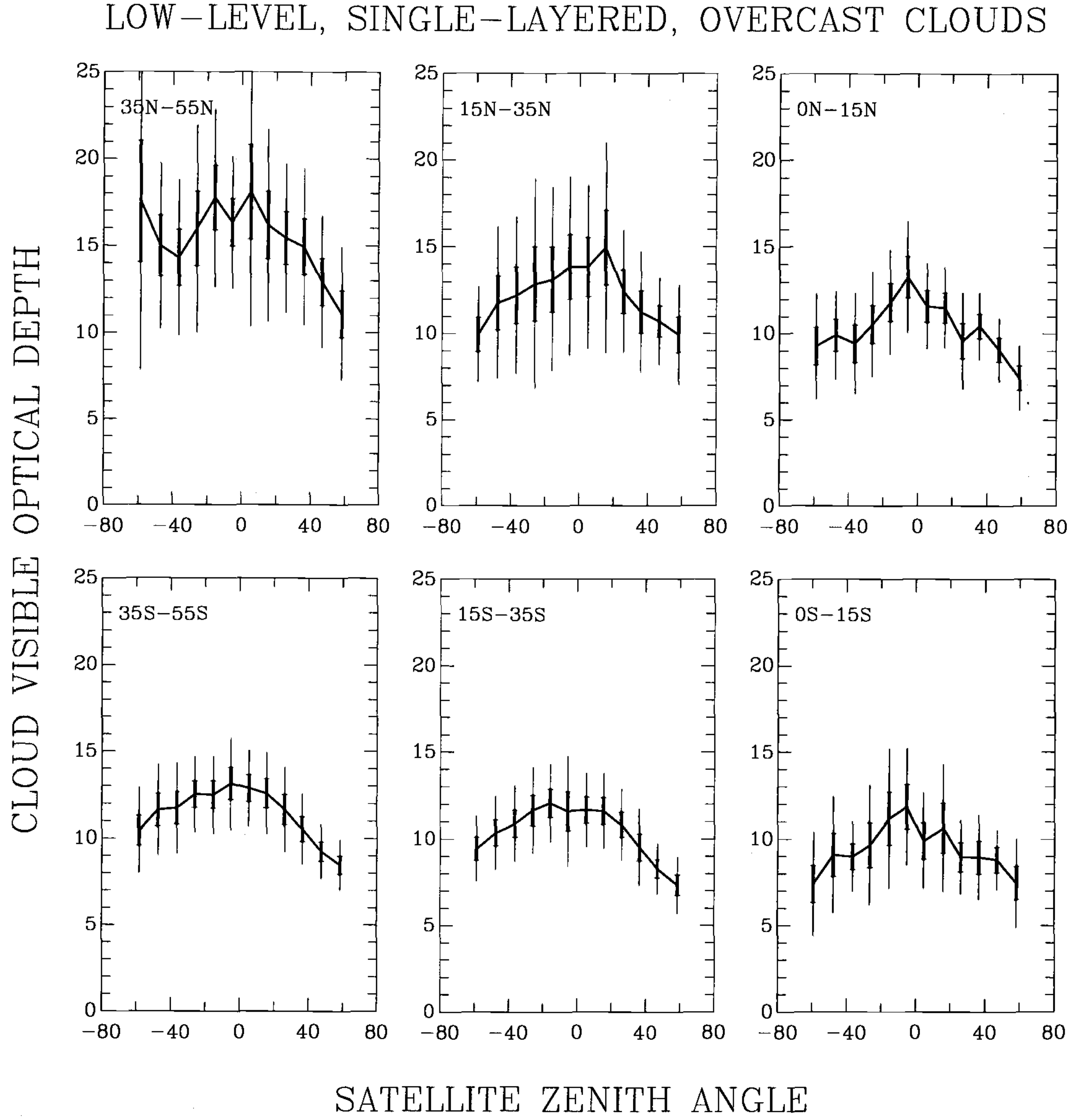

Figure 4.16(a) Cloud visible optical depths and satellite zenith angles for pixels overcast by single-layered, low-level clouds. Observations are for for March 1989 for both northern and southern midlatitudes (35°–55°), subtropics (15°–35°), and tropics (0°–15°). Curves are for the monthly means. Thick bars indicate the 95% confidence intervals for the means. Thin bars represent the standard deviations of the daily means. Negative zenith angles indicate the backward scattering direction.

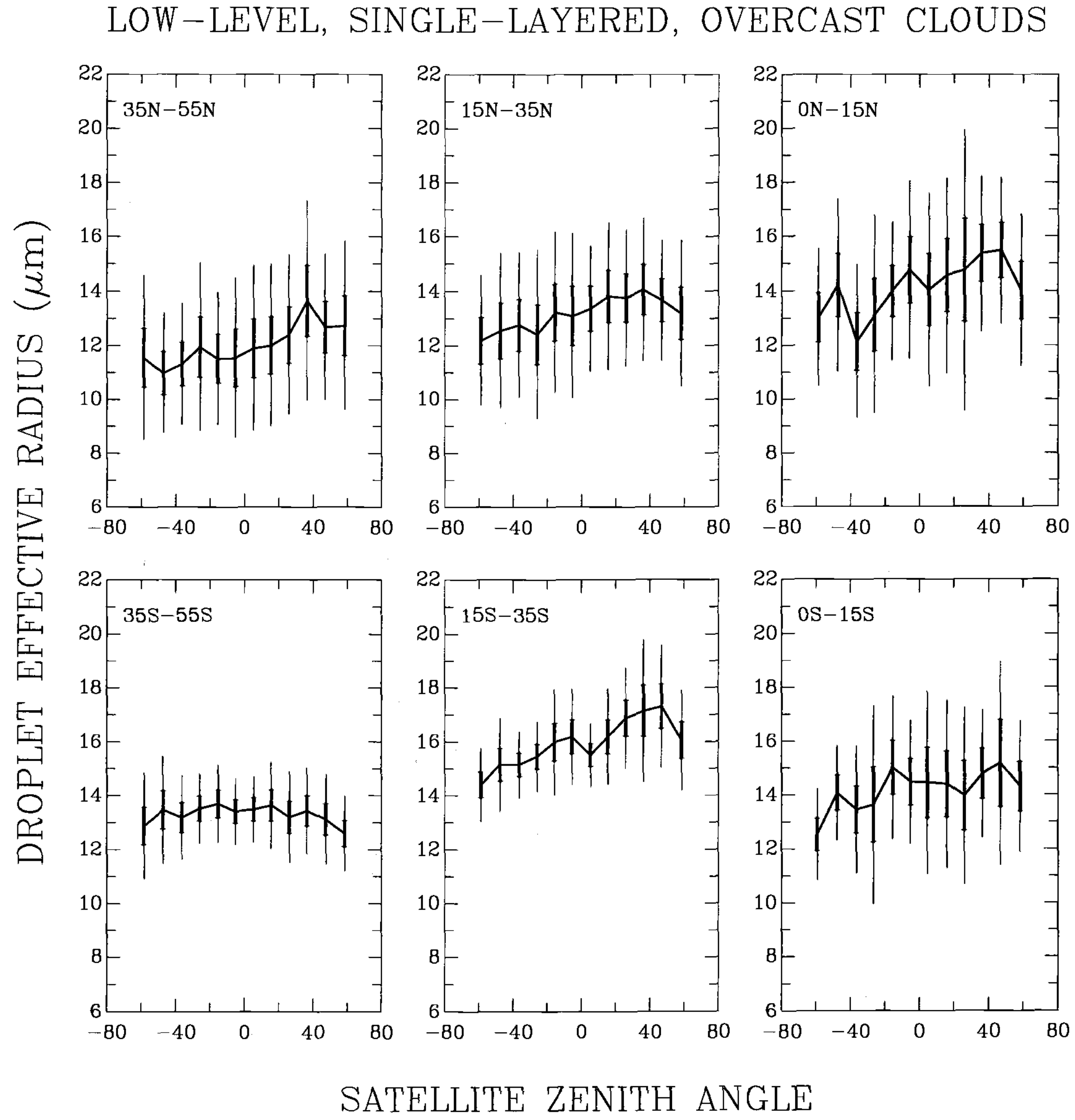

Figure 4.16(b) Same as Figure 4.16a, except for cloud droplet effective radii (μm).

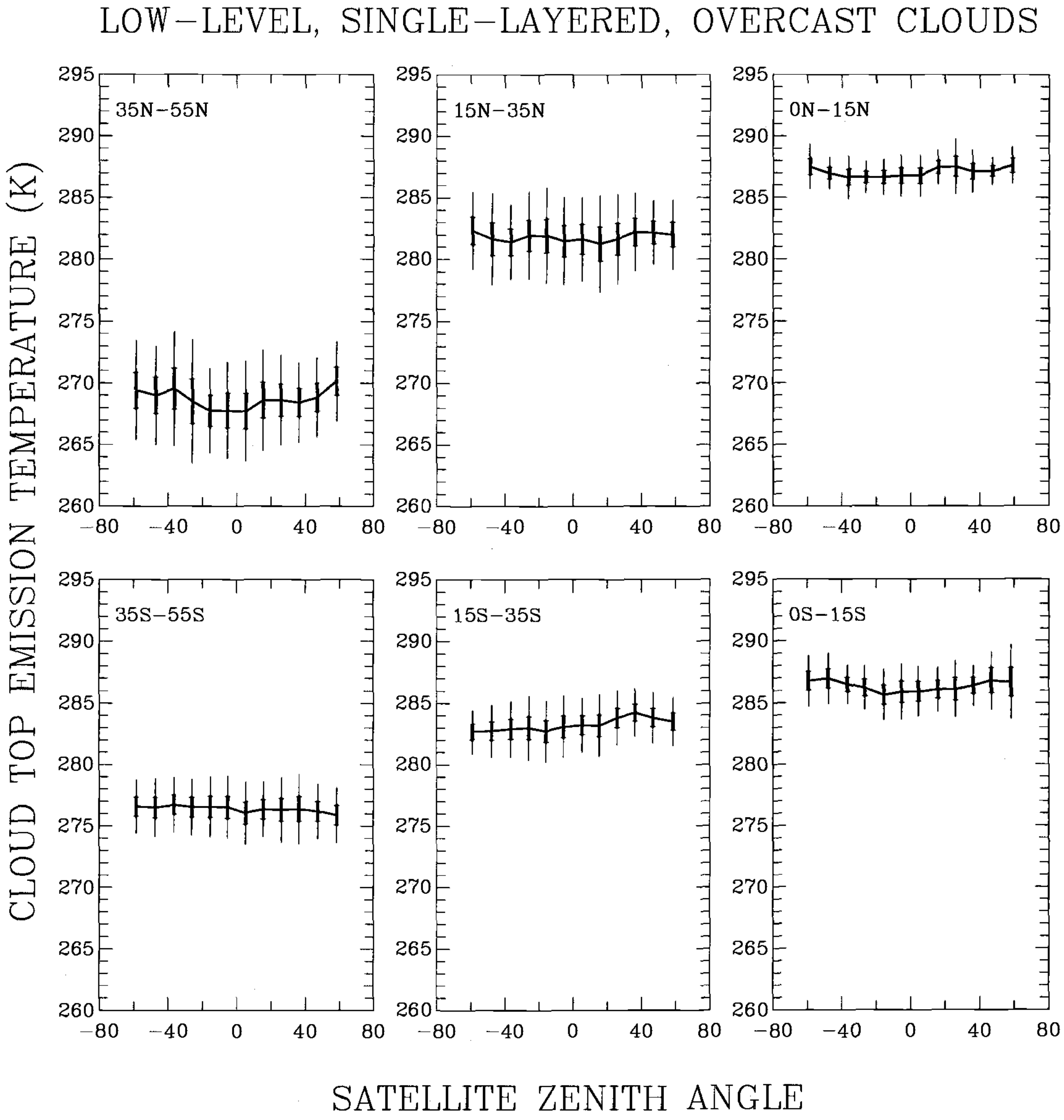

Figure 4.16(c) Same as Figure 4.16a, except for cloud top emission temperatures (K).

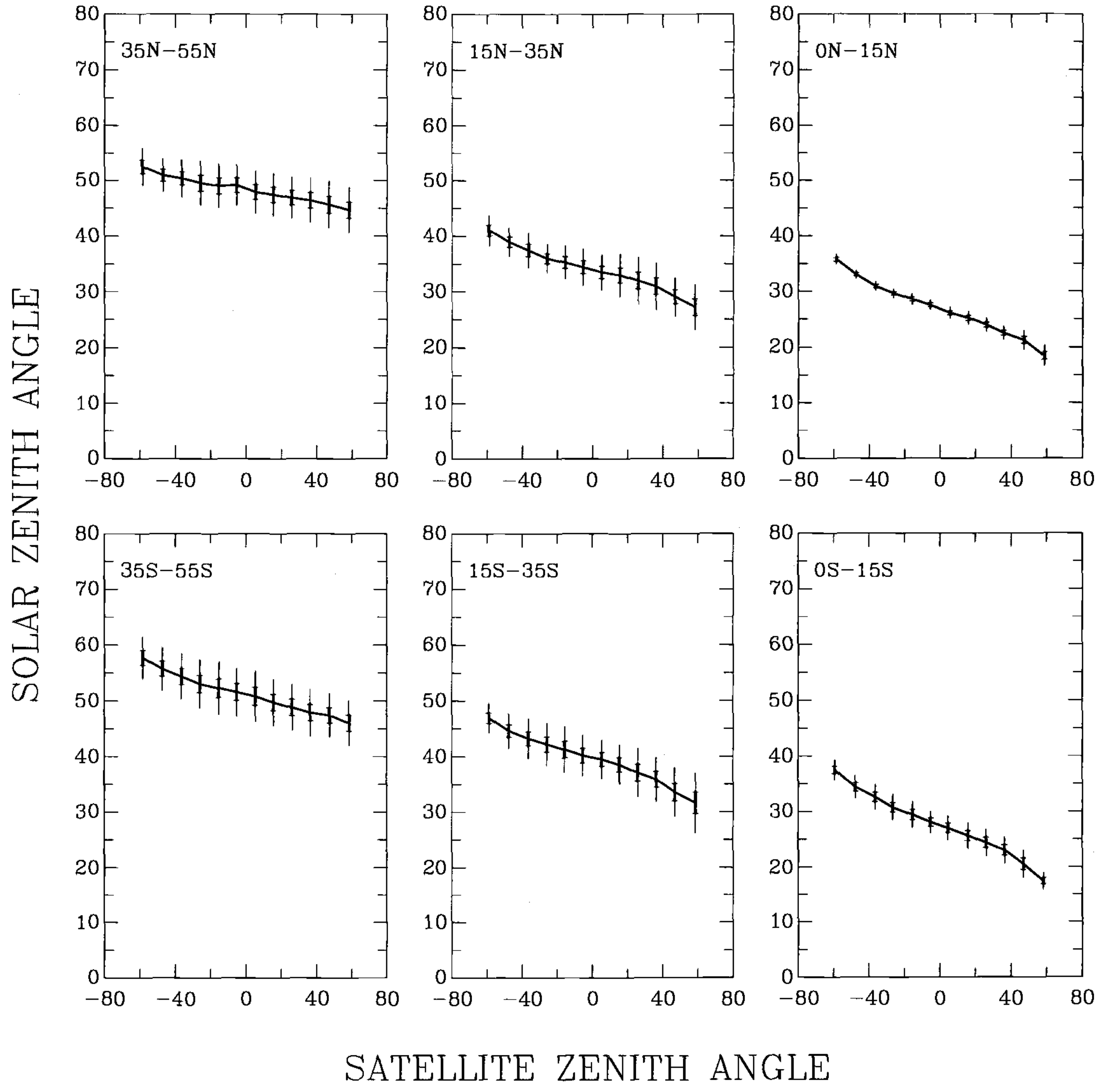

Figure 4.17 Same as Figure 4.16a, except for the solar zenith angles of the observations.

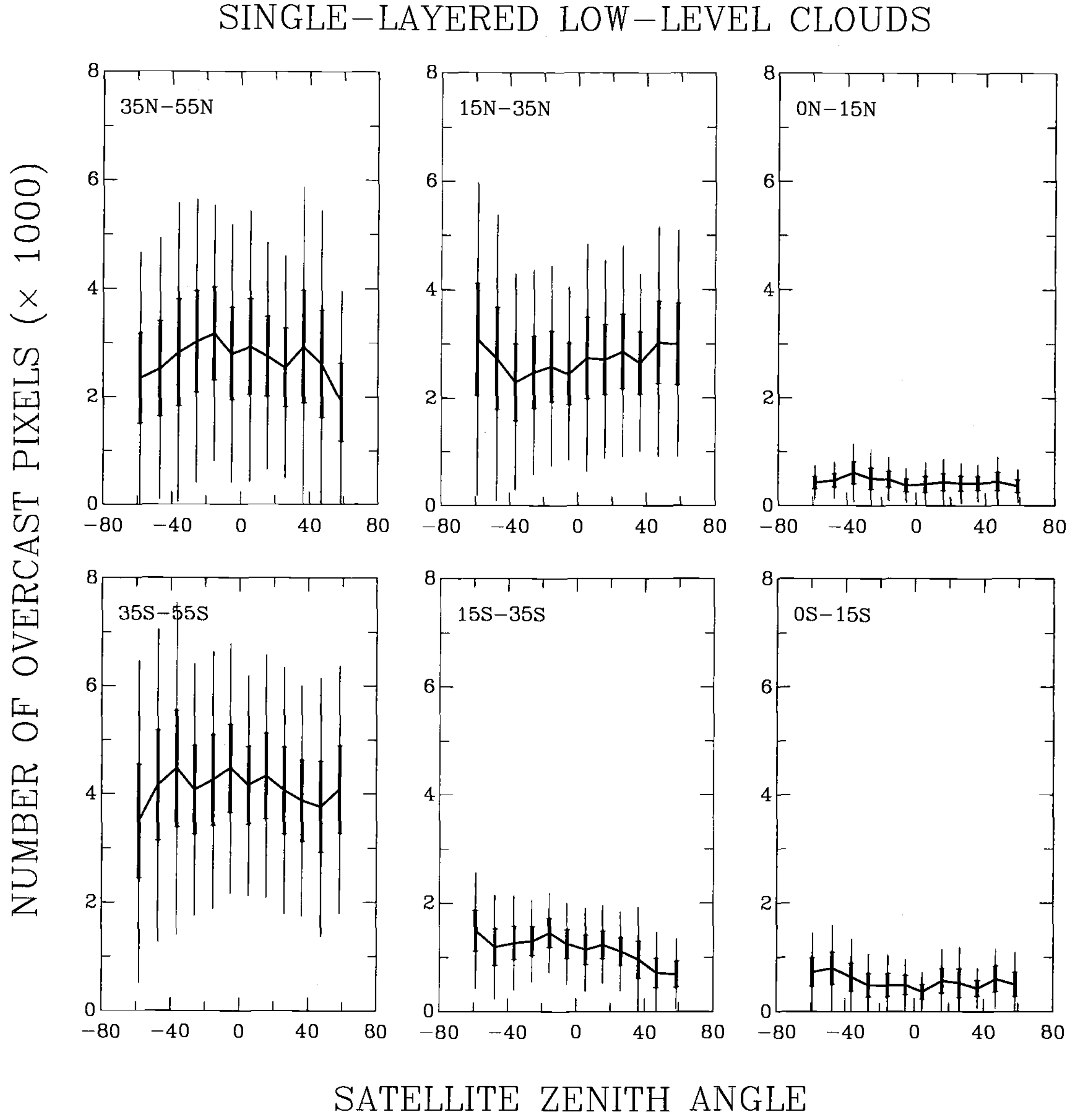

Figure 4.18 Number of pixels overcast by single-layered, low-level clouds as a function of satellite zenith angle. Observations are for March 1989 for both northern and southern midlatitudes (35°–55°), subtropics (15°–35°), and tropics (0°–15°). Curves represent the monthly means of the daily observations. Thin bars represent the standard deviations of the daily observations. Thick bars indicate the 95% confidence intervals of the monthly means.

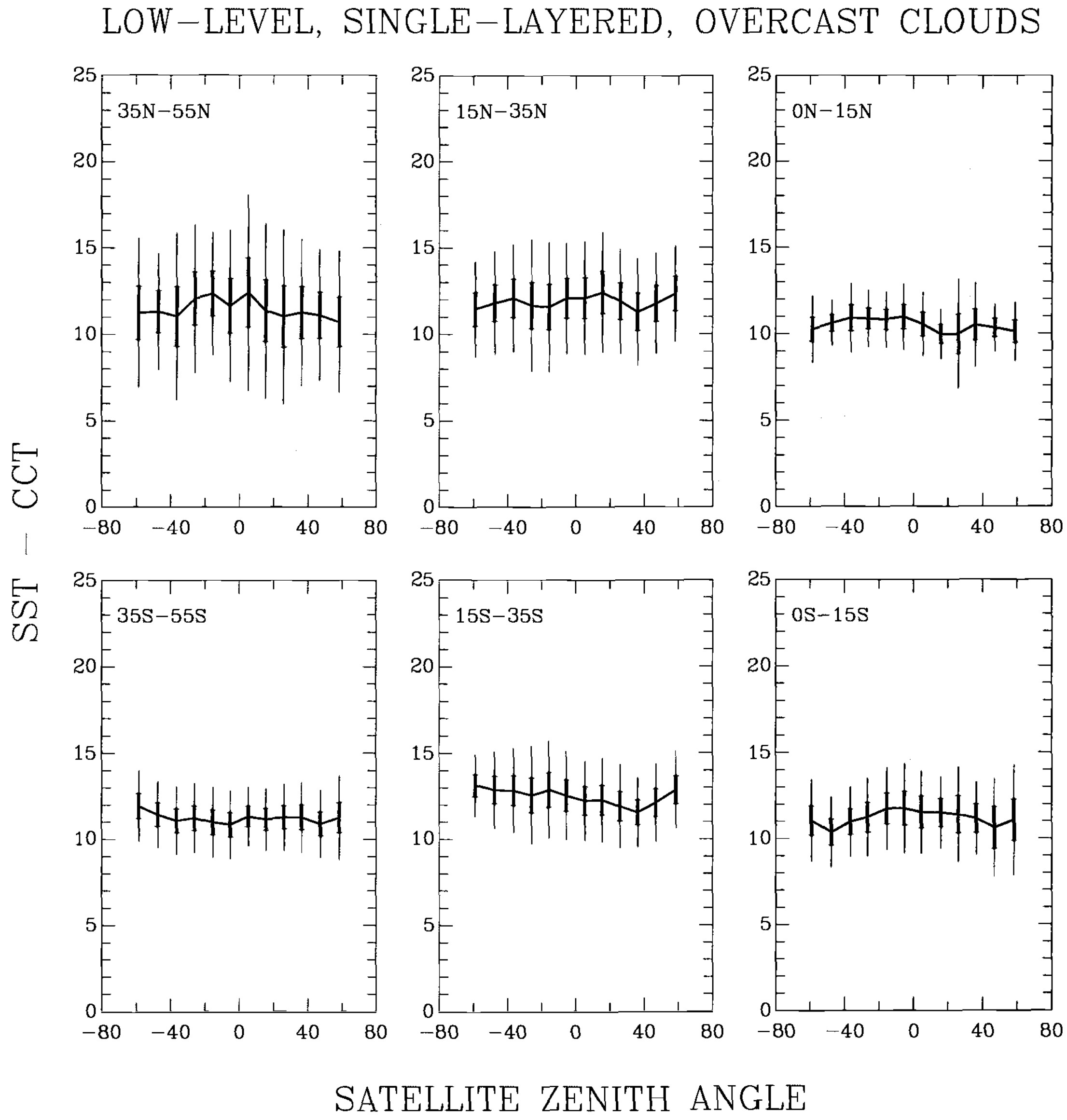

Figure 4.19 Same as Figure 4.16a, except for the sea surface-cloud top temperature differences (K).

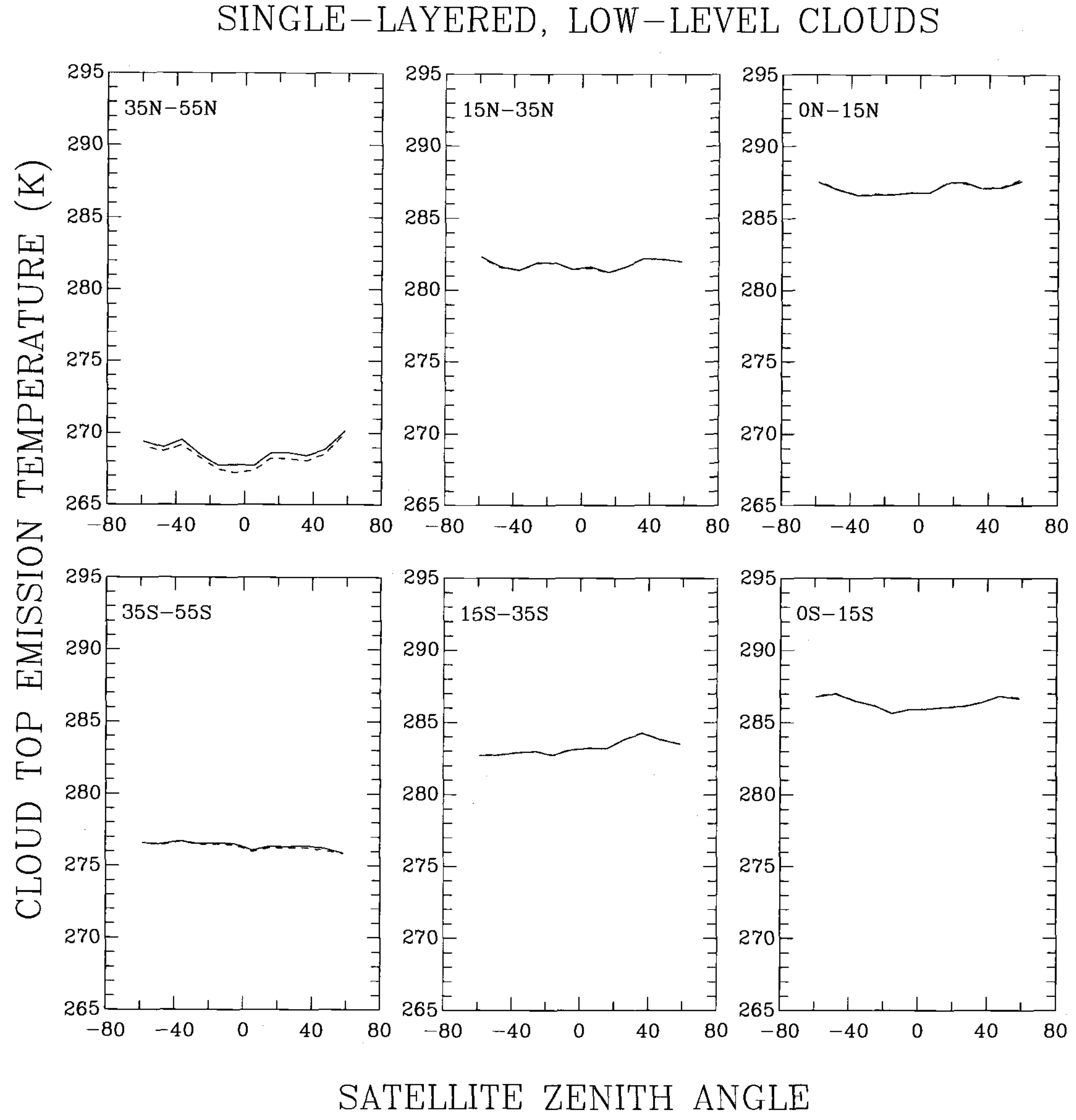

Figure 4.20 Monthly-mean cloud top emission temperatures (K) obtained using Kratz's model (solid) and the McMillin-Crosby equation (dashed) for the sea surface temperatures. Results are for pixels overcast by single-layered, low-level clouds obtained for March 1989 and for both northern and southern midlatitudes (35°–55°), subtropics (15°–35°), and tropics (0°–15°).

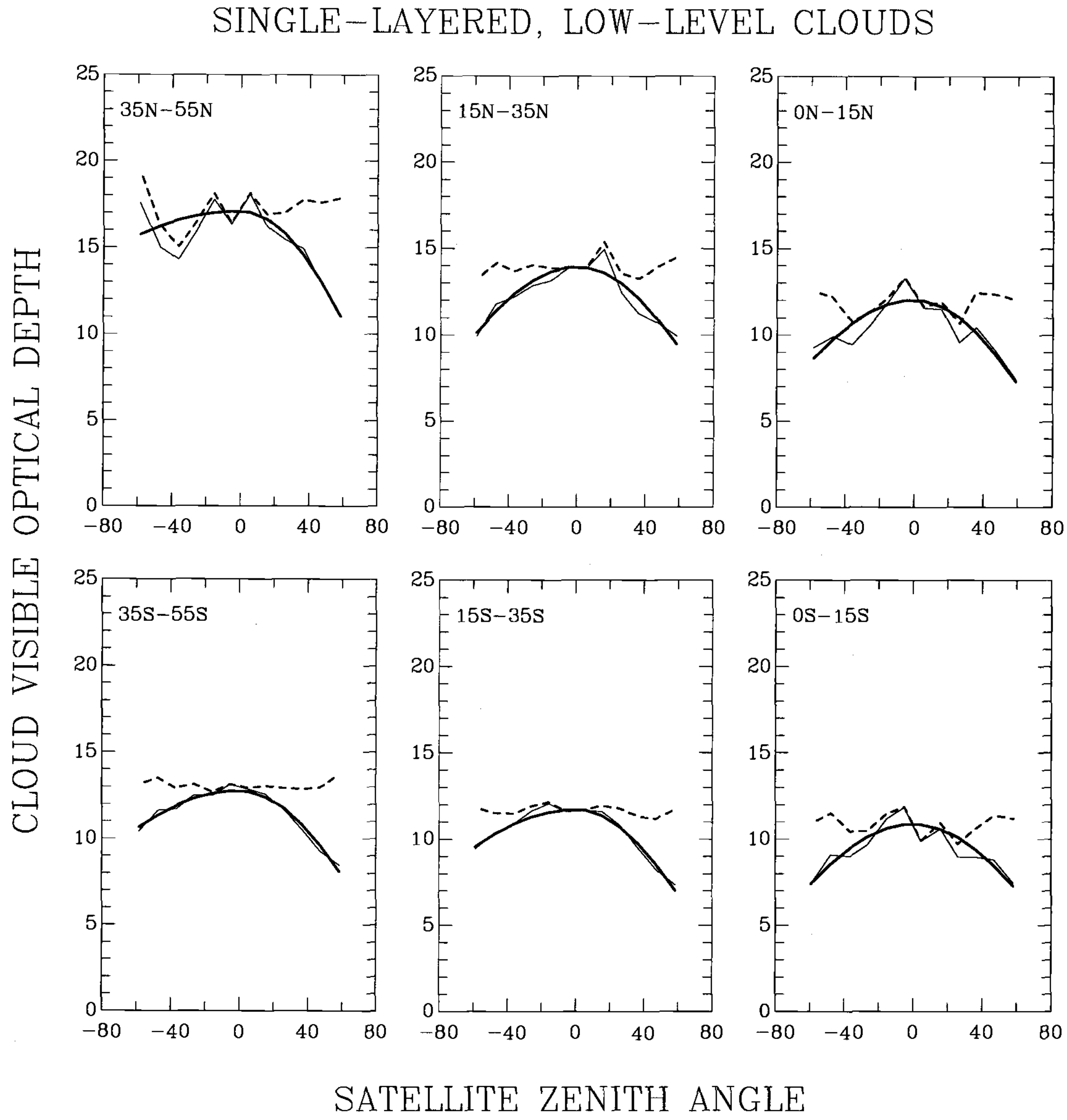

Figure 4.21 Retrieved (thin) and corrected (dashed) monthly-mean cloud visible optical depths for pixels overcast by single-layered, low-level clouds. Dashed curves are obtained by correcting the retrieved cloud visible optical depths for the satellite zenith angle dependence. The procedures are described in the text. Thick curves are the least-squares fits to the retrieved cloud visible optical depths. Thin curves are the same as the monthly means shown in Figure 4.16a.

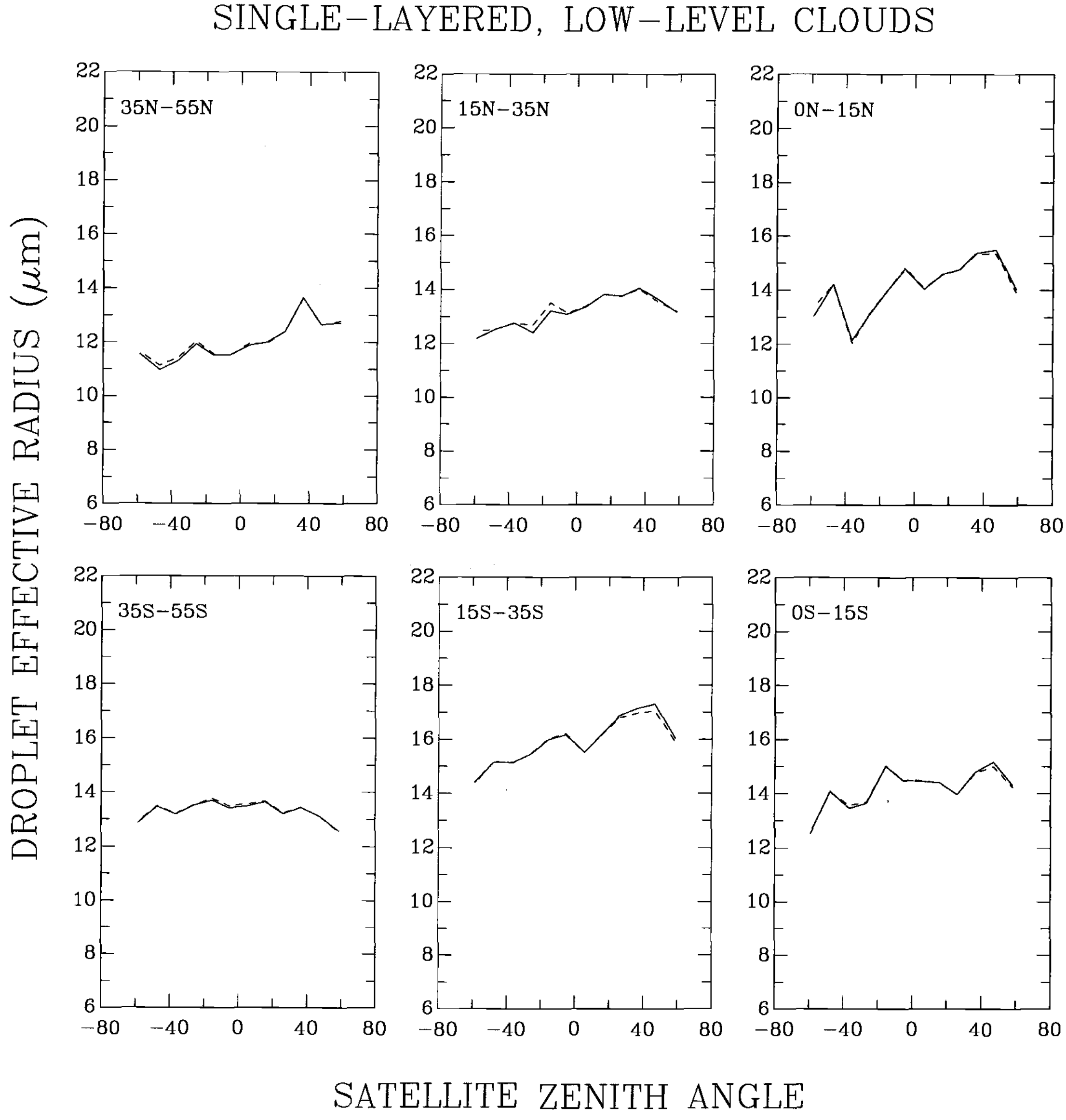

Figure 4.22(a) Monthly-mean cloud droplet effective radii (μm) obtained with retrieved (solid) and corrected (dashed) cloud visible optical depths. Solid curves are the same as the monthly means shown in Figure 4.16b. Dashed curves were obtained with cloud visible optical depths that were corrected for the observed satellite-zenith-angle dependence.

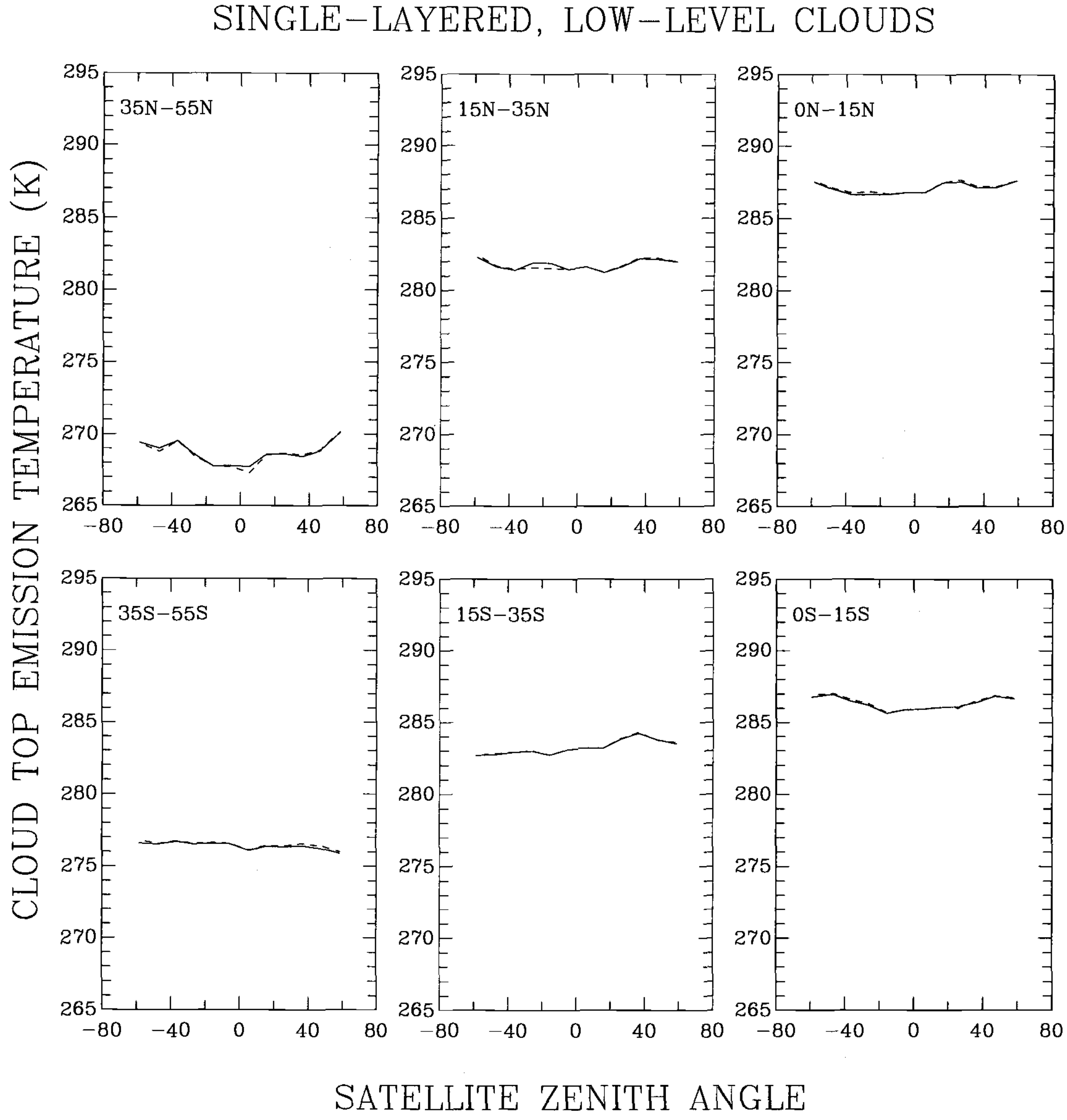

Figure 4.22(b) Same as Figure 4.22a, except for cloud top emission temperatures (K).

Figure 4.16b shows the dependence of cloud droplet effective radius on satellite zenith angle. The retrieved droplet effective radii are on average $\sim 1\ \mu$m larger in the forward scattering direction than in the backward scattering direction. The dependence of droplet effective radius on satellite zenith angle is small in both forward and backward scattering directions. Figure 4.16c shows the satellite zenith angle dependence for the cloud top emission temperature. The retrieved cloud top emission temperatures also show little dependence on the satellite zenith angle. Cloud top emission temperatures obtained for large zenith angles ($>\sim 45°$) are on average 1–2K larger than those obtained for near-nadir zenith angles. Figure 4.19 shows the sea surface-cloud top temperature differences as a function of satellite zenith angle. The sea surface-cloud top temperature differences also show little dependence on the satellite zenith angle.

Table 4.3 also shows the mean cloud visible optical depths, droplet effective radii, and cloud top emission temperatures obtained for both northern and southern midlatitudes, subtropics and tropics. These means are for near-nadir viewing pixels that were overcast by single-layered, low-level clouds. The largest mean cloud visible optical depth and smallest mean droplet effective radius were found in the northern midlatitudes. The largest mean droplet effective radius was found in the southern subtropics. The smallest mean cloud optical depth was found in the tropics. The mean cloud top altitudes for these low-level clouds are also shown in the table. The cloud top altitudes were obtained using the method of Betts et al. (1992). The altitude is given by

$$Z_c = \left(T_{sfc} - T_c\right)/\gamma\,, \tag{4.3}$$

where T_{sfc} is the retrieved sea surface temperature obtained using Kratz's model to account for absorption by atmospheric gaseous, T_c is the retrieved cloud top emission temperature, and $\gamma = 7°/\mathrm{km}$ is the lapse rate. The mean cloud top altitudes for these low-level clouds range from 1.5 to 1.8 km.

The cloud visible optical depths, droplet effective radii, and cloud top emission temperatures shown in Figure 4.16 were retrieved with the sea surface temperatures obtained using Kratz's model for the absorption by atmospheric gaseous. These cloud properties were also retrieved using sea surface temperatures derived from the empirical equation of McMillin and Crosby (1984), Eq. (4.2). Cloud visible optical depths and droplet effective radii retrieved using the two sea surface temperatures were identical. The differences in cloud top emission temperatures for the two were also small and they are shown in Figure 4.20.

In addition, the satellite zenith angle dependence of the retrieved droplet effective radii and cloud top emission temperatures were re-examined by using cloud visible optical depths that were corrected for the satellite zenith angle dependence. The satellite zenith angle dependence of the cloud visible optical depths may have affected the retrieved droplet effective radii and cloud top emission temperatures when using the iterative retrieval scheme. Figure 4.21 shows the corrected cloud visible optical depths (dashed curves). The corrected cloud visible optical depth is given by

$$\tau_c'(\theta) = \frac{\tau_c(\theta)}{\tau_f(\theta)}, \tag{4.4}$$

where θ is the satellite zenith angle, τ_c is the retrieved cloud visible optical depth (thin curves), and τ_f is the least-square fit to the retrieved cloud visible optical depths (thick curves). The least-square fit was obtained using two half-cosine functions to fit the retrieved visible optical depths in both the forward and backward scattering directions. The droplet effective radii and cloud top emission temperatures retrieved using the corrected cloud visible optical depths are shown in Figure 4.22. The results show that the retrieved droplet effective radii and cloud top emission temperatures were not sensitive to such corrections in the cloud visible optical depths.

4.5.2 Differences between overcast and partly cloudy pixels

Figure 4.23 shows the monthly-mean a) cloud visible optical depths, b) droplet effective radii, and c) cloud top emission temperatures as functions of satellite zenith angles for both the overcast (solid curves) and partly cloudy pixels (dashed curves) which were assumed to be overcast. Again, large differences in the cloud properties of overcast and partly cloudy pixels were found at all satellite zenith angles. Figure 4.23a shows that the satellite zenith angle dependence of cloud visible optical depth for the partly cloudy pixels is smaller than that for the overcast pixels. The finding suggests that this angular dependence of cloud visible optical depth may not be found in ISCCP data.

Figure 4.23b shows that occasionally small differences were found between the droplet effective radii for overcast pixels and partly cloudy pixels. In the forward scattering direction, a minimum in the droplet effective radius for partly cloudy pixels was often obtained at satellite zenith angles near 20° for all six latitude zones. The droplet effective radii for partly cloudy pixels were smaller in the forward scattering than in the backscattering direction. Further study is needed to understand why droplet effective radii retrieved for partly cloudy pixels in the forward scattering directions are smaller and why differences between droplet effective radii retrieved for overcast and partly cloudy pixels are relatively small in the backscattering direction.

The mean cloud visible optical depths, droplet effective radii, and cloud top emission temperatures for the partly cloudy pixels at near-nadir are also shown in Table 4.3. The near-global mean, low-level cloud visible optical depths and droplet effective radii obtained by Han et al. (1994) are also listed in the table. Han et al. used only near-nadir ($\theta < 27°$) pixels and reported a mean low-level cloud visible optical depth of 5.8 for Spring and 6.4 for the year for the northern hemisphere oceans and 6.8 for Spring and 7.4 for the year for the southern hemisphere oceans. Their cloud visible optical depths for the northern hemisphere oceans are similar to those obtained here for the partly cloudy pixels. For the southern hemisphere, their values lie between the values obtained for the overcast and partly cloudy pixels. The droplet effective radii for both the northern and southern hemisphere oceans are similar to those obtained here for the partly cloudy pixels.

4.6 Simulation studies for the effect of partly cloudy pixels

4.6.1 Larger droplet sizes retrieved from simulations

In order to understand the effect of partly cloudy pixels on the retrieved cloud visible optical depths, droplet effective radii, and cloud top emission temperatures, simulated radiances were calculated for partly cloudy pixels and used to retrieve the cloud properties. In the simulation, a sea surface temperature of 294K, a standard midlatitude summertime atmospheric profile, and a surface reflectance of 0.03 for

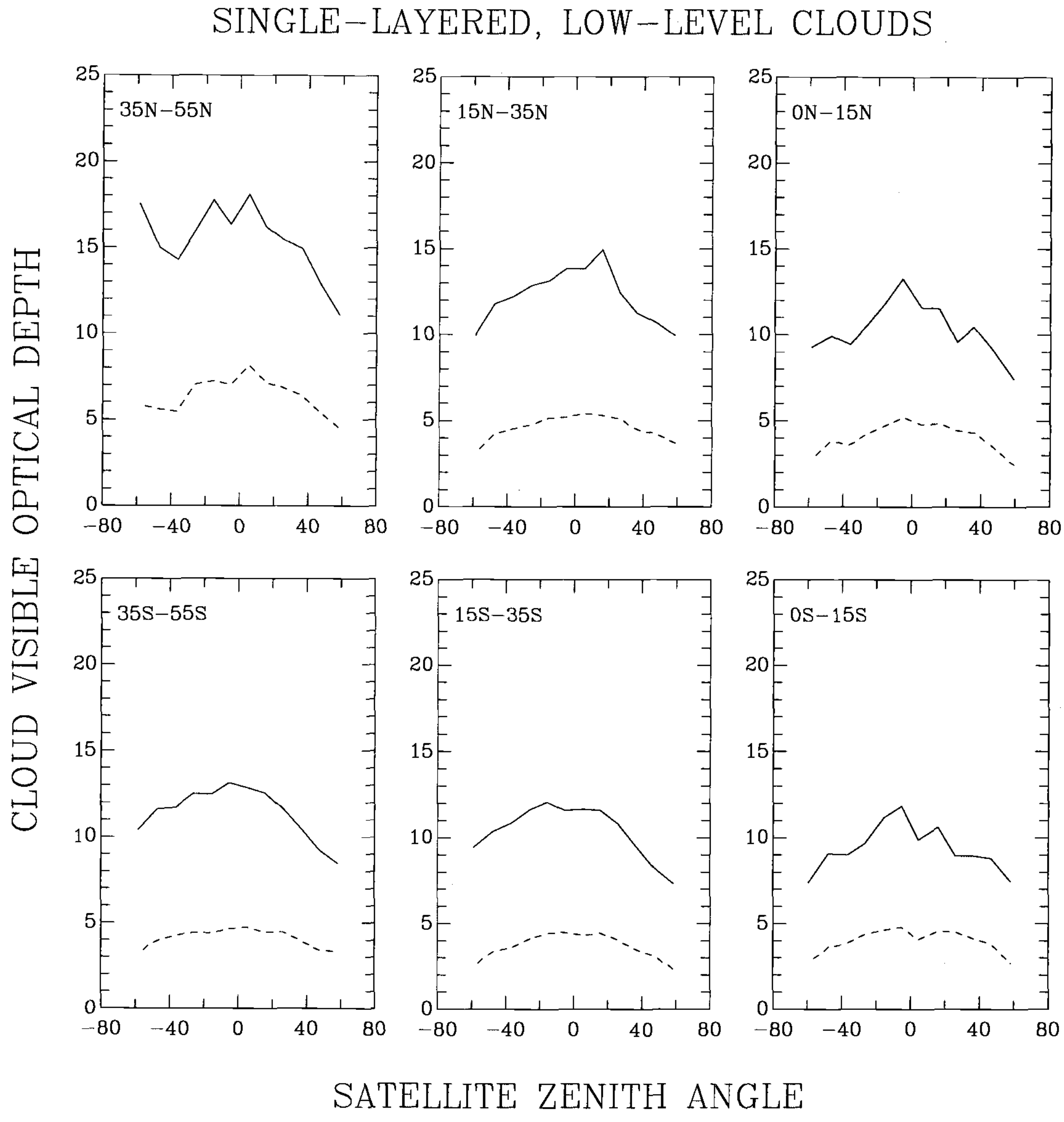

Figure 4.23(a) Monthly-mean cloud visible optical depths for March 1989 for the Pacific ocean. Observations are for single-layered, low-level clouds for both northern and southern midlatitudes (35°–55°), subtropics (15°–35°), and tropics (0°–15°). Solid curves are for overcast pixels; dashed curves are for partly cloudy pixels which were assumed to be overcast.

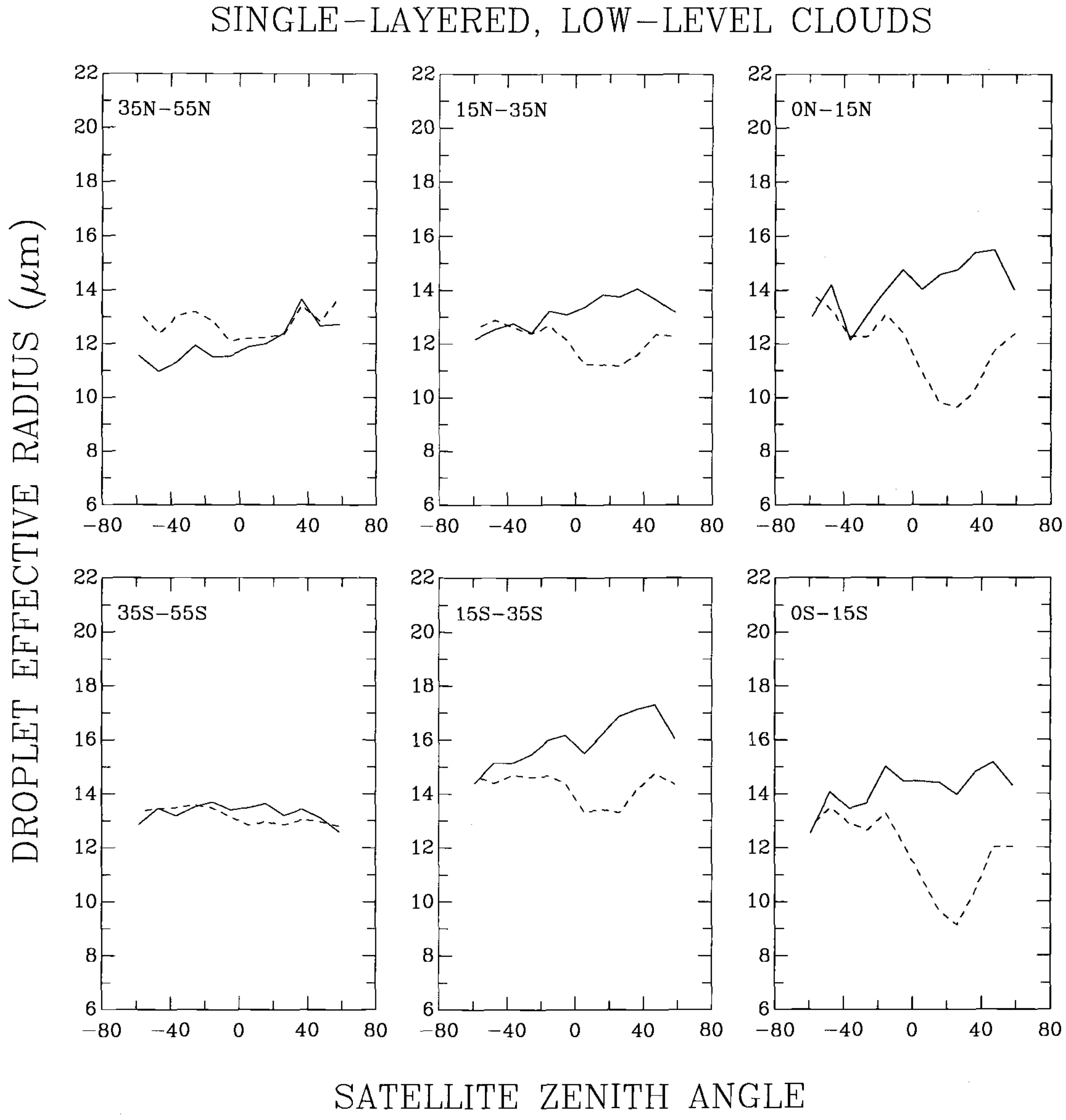

Figure 4.23(b) Same as Figure 4.23a, except for cloud droplet effective radii (μm).

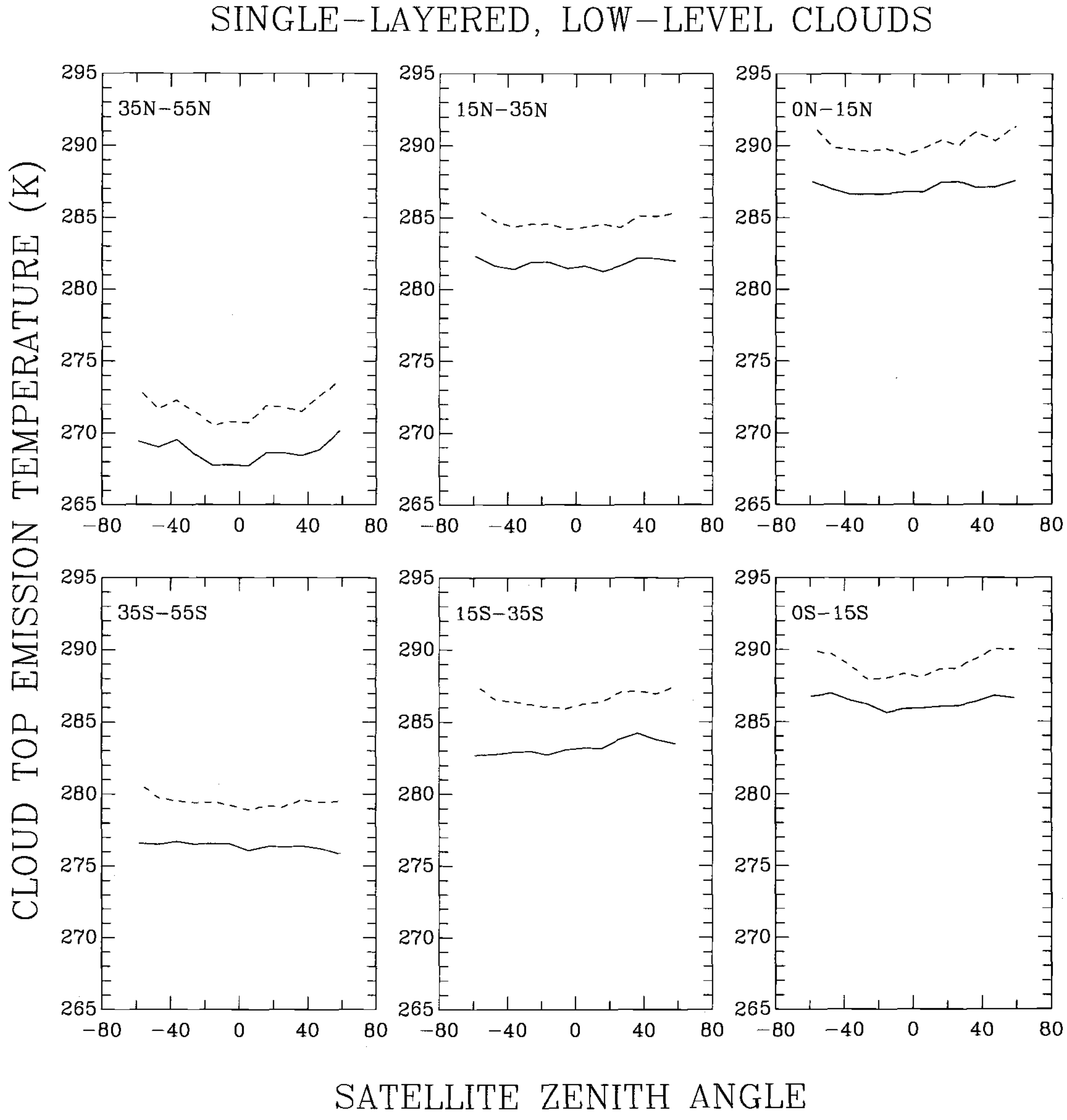

Figure 4.23(c) Same as Figure 4.23a, except for cloud top emission temperatures (K).

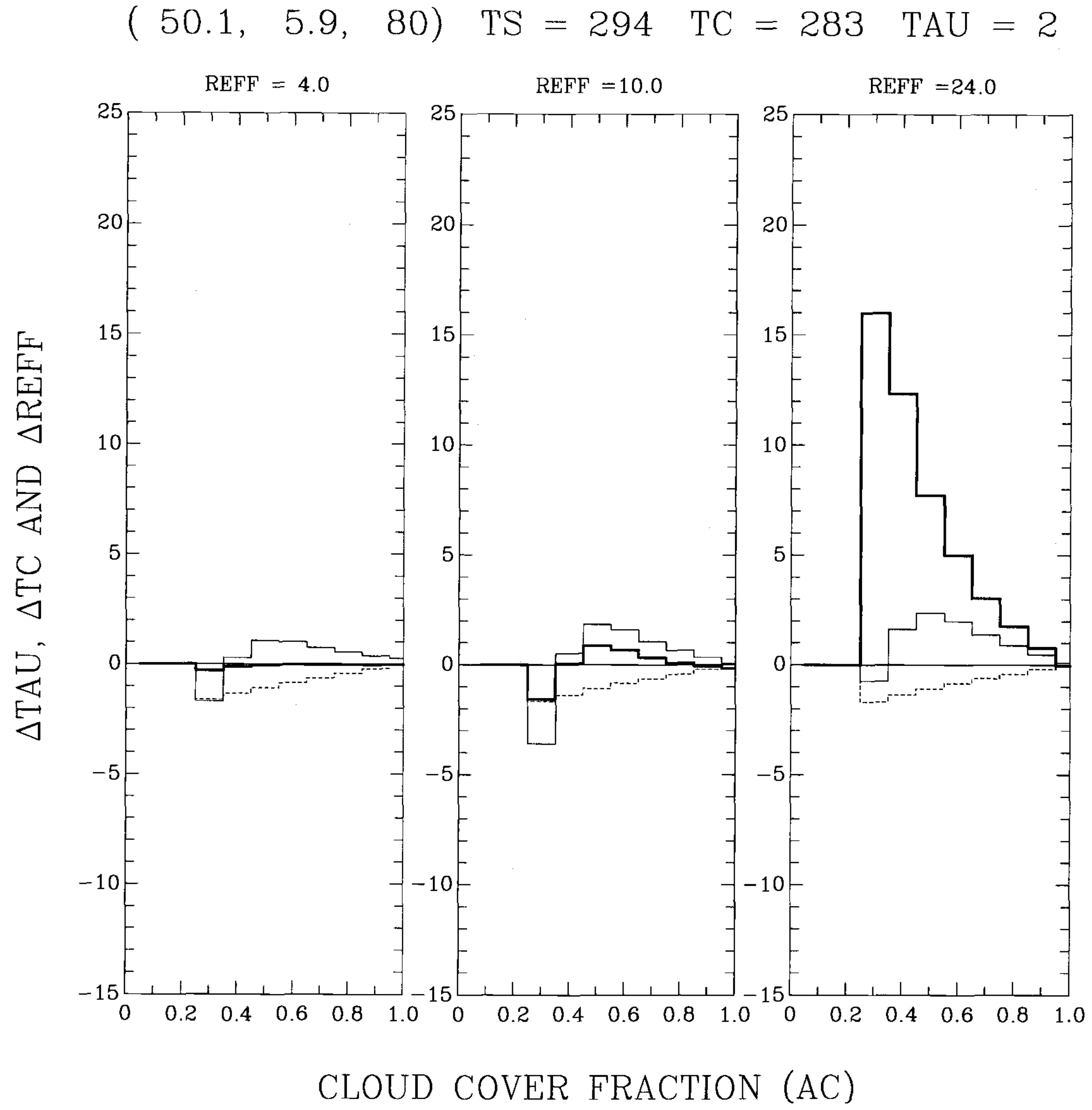

Figure 4.24(a) Differences (partly cloudy – overcast) in cloud visible optical depth (dashed), droplet effective radius (thick), and cloud top emission temperature (thin) as a function of cloud cover fraction. Results are for simulations with $(\theta_o, \theta, \phi - \phi_o) = (50.1°, 5.9°, 80°)$ and a sea surface temperature of 294K, a cloud top temperature of 283K, and a cloud visible optical depth of 2.

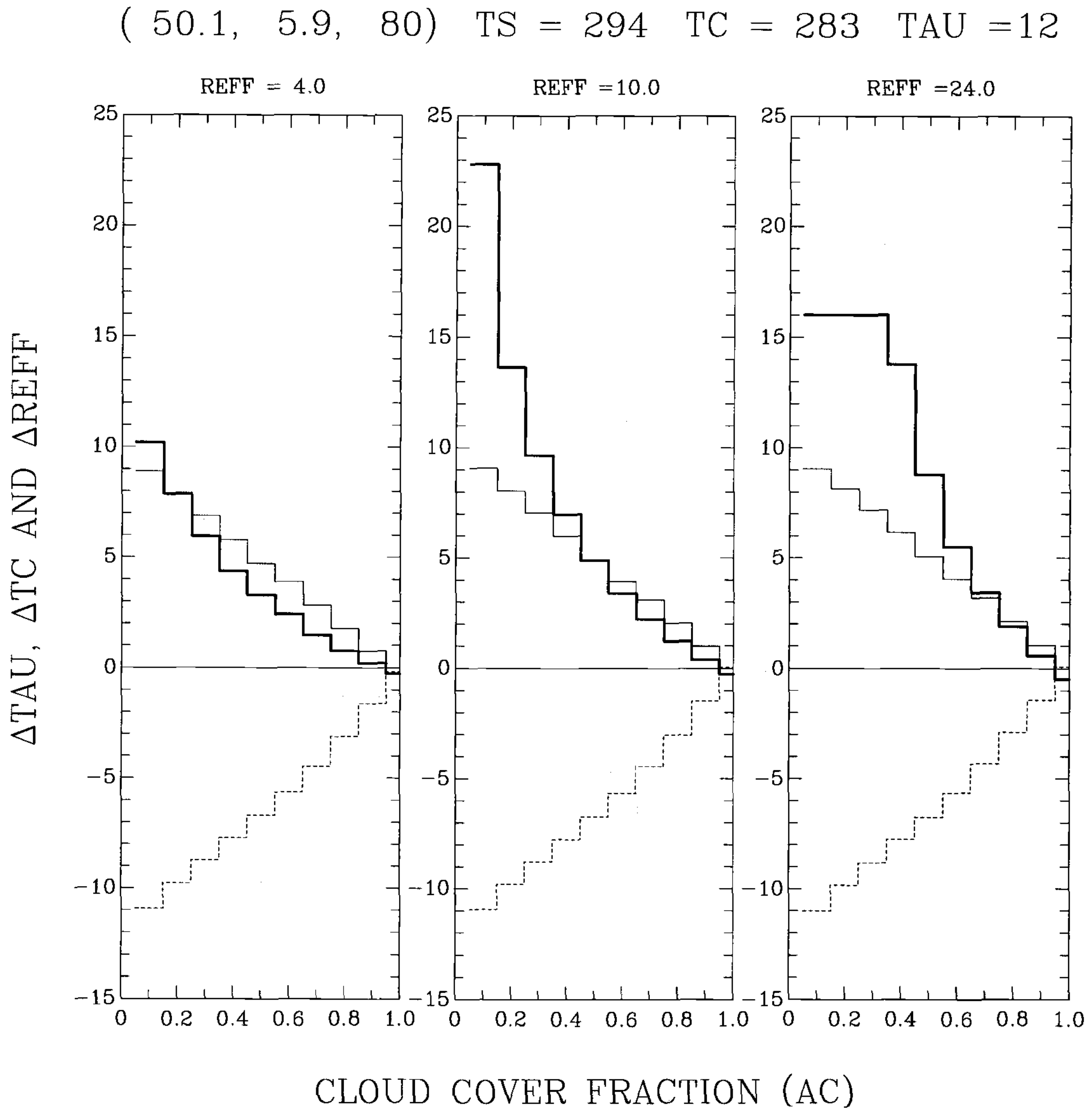

Figure 4.24(b) Same as Figure 4.24a, except for a cloud visible optical depth of 12.

channel 1 and 0.01 for channel 3 were used to calculate the cloud-free radiance. These values were also used with a plane-parallel cloud model to calculate the overcast radiances for various cloud visible optical depths, droplet effective radii, and cloud top emission temperatures. The radiance simulated for a partly cloudy pixel is calculated by using the cloud-free and overcast radiances and a specified cloud cover fraction. For a pixel-scale cloud cover fraction A_c, the radiances of AVHRR channels 1, 3, and 4 are taken to be given by

$$I_1 = [1 - A_c] \times R_{1s} + A_c \times R_{1c}(\tau_c, r_{eff}), \tag{4.5}$$

$$I_3 = [1 - A_c] \times [R_{3s} + E_{3s}] + A_c \times \left[R_{3c}(\tau_c, r_{eff}) + E_{3c}(\tau_c, r_{eff}, T_c)\right], \tag{4.6}$$

$$I_4 = [1 - A_c] \times E_{4s} + A_c \times E_{4c}(\tau_c, r_{eff}, T_c), \tag{4.7}$$

where R_s is the simulated cloud-free reflected radiance, E_s is the simulated cloud-free emission, R_c is the simulated reflected radiance for the overcast portion of the pixel, E_c is the simulated emitted radiance for the overcast portion, I is the simulated partly cloudy pixel radiance, and τ_c, r_{eff}, and T_c are, respectively, the model cloud visible optical depth, droplet effective radius, and cloud top emission temperature. In retrieving cloud properties from the partly cloudy pixel, the radiances obtained with Eqs. 4.4-4.6 are assumed to be due to overcast conditions. For overcast conditions, $A_c = 1$, Eqs. 4.4-4.6 become

$$I_1 = R'_{1c}(\tau'_c, r'_{eff}), \tag{4.8}$$

$$I_3 = R'_{3c}(\tau'_c, r'_{eff}) + E'_{3c}(\tau'_c, r'_{eff}, T'_c), \tag{4.9}$$

$$I_4 = E'_{4c}(\tau'_c, r'_{eff}, T'_c). \tag{4.10}$$

where τ_c', r_{eff}', and T_c' represent the cloud visible optical depth, droplet effective radius, and cloud top emission temperature that would be retrieved for the simulated partly cloudy radiances of I_1, I_3, and I_4.

Figure 4.24 shows differences, $\Delta\tau_c = \tau_c' - \tau_c$ (dashed), $\Delta r_{eff} = r_{eff}' - r_{eff}$ (thick), and $\Delta T_c = T_c' - T_c$ (thin), between the retrieved and input values. These differences are obtained for the sun-earth-satellite viewing geometry, $(\theta_o, \theta, \phi - \phi_o) = (50.1°, 5.9°, 80°)$ and for $\tau_c = 2$, 12, $r_{eff} = 4$, 10, 24 μm, $T_c = 280$K, and $A_c = 0.1, 0.2, \ldots, 1.0$. Figure 4.24a shows the differences for $\tau_c = 2$ and Figure 4.24b shows the differences for $\tau_c = 12$. The differences from the simulations show that, when assuming radiances observed for partly cloudy pixels are due to overcast conditions, the retrieved cloud visible optical depth, τ_c', is always smaller than the overcast cloud visible optical depth τ_c. The difference $\Delta\tau_c$ decreases with increasing A_c, as it should. For the retrieved droplet effective radius and cloud top emission temperature, $r_{eff}' > r_{eff}$ and $T_c' > T_c$ when the retrieved cloud optical depths $\tau_c' >\sim 1$. The differences, Δr_{eff} and ΔT_c, also decrease with increasing A_c. However, $r_{eff}' < r_{eff}$ and $T_c' < T_c$ when the retrieved cloud visible optical depth $\tau_c' <\sim 0.5$ which occurs when the cloud cover fraction A_c and overcast visible optical depth are small.

4.6.2 Smaller droplet sizes retrieved from observations

Figure 4.25 shows the frequency of occurrence for the fractional cloud cover for the partly cloudy pixels for the March 1989 data. The fractional cloud cover was generally larger than 0.4 and the overall mean was about 0.7. According to the fractional cloud cover for the partly cloudy pixels shown in Figure 4.25 and according to the simulation study performed in section 4.6.1, cloud droplet effective radii retrieved for partly cloudy pixels are expected to be larger than those retrieved for overcast pixels. But, the results presented in sections 4.4 and 4.5 show that cloud droplet effective radii retrieved for the partly cloudy pixels were smaller than those retrieved for their overcast counterparts.

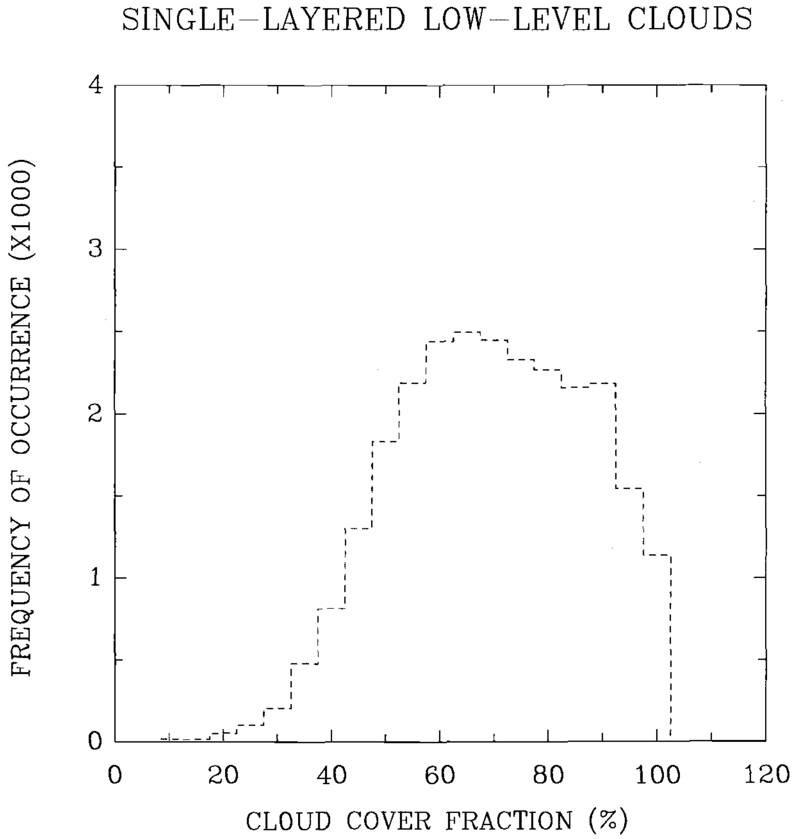

Figure 4.25 Frequency distribution of the mean cloud cover fraction (%) for partly cloudy pixels. Observations are for 60-km regions containing single-layered, low-level cloud systems for March 1989 for the Pacific ocean. The observations are restricted to near-nadir satellite zenith angles.

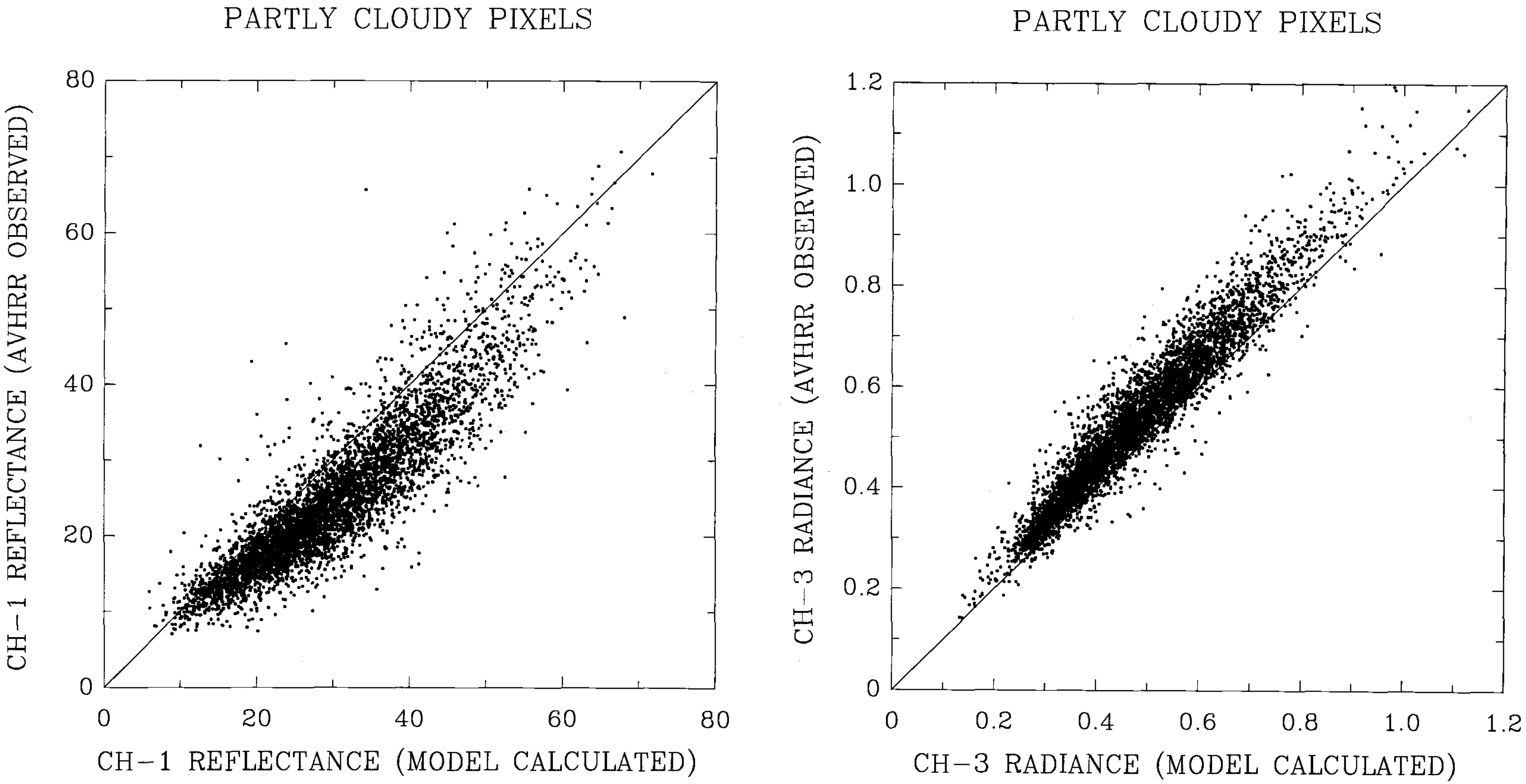

Figure 4.26 (a) 0.63-μm reflectance (%) and (b) 3.75-μm radiance (mWm^{-2}sr^{-1}cm) for partly cloudy pixels. Each point gives means obtained for a 60-km region. Results are for single-layered, low-level, partly cloudy pixels identified by the spatial coherence method for March 1989 over the Pacific ocean. Radiances for partly cloudy pixels are derived from model calculations and from AVHRR observations.

To further examine this discrepancy, for each 60-km region, the observed radiances for the partly cloudy pixels were compared to those calculated using Eqs. 4.4-4.6 for the same cloud cover fraction. In calculating the partly cloudy radiances for the March 1989 data, cloud-free and overcast radiances were obtained from the spatial coherence analysis. The 60-km mean cloud cover fraction A_c for the partly cloudy pixels was calculated using Eq. 2.1. For the data shown in Tables 4.1 and 4.2, the calculated 60-km mean radiances for the partly cloudy pixels are also shown in the right columns of each box in Table 4.2. The cloud visible optical depths, droplet effective radii, and cloud top emission temperatures retrieved using these calculated partly cloudy radiances are also shown in Table 4.2. The droplet effective radii retrieved from the calculated partly cloudy radiances (right columns) are generally larger than those retrieved for the observed partly cloudy radiances (left columns) and the calculated 3.75-μm radiances are smaller than the observed 3.75-μm radiances. Figure 4.26 shows the radiances calculated and observed for the partly cloudy pixels for the March 1989 data. Each point in the figure gives mean values for a 60-km region. The 60-km regions were restricted to near-nadir view angles ($< 25°$). Figure 4.26a shows that the observed channel-1 radiances are systematically smaller than the calculated channel-1 radiances. Figure 4.26b shows that the observed channel-3 radiances are systematically larger than the calculated channel-3 radiances. Note that, for channel 4, the observed and calculated radiances are identical. The smaller channel-1 radiances observed for partly cloudy pixels may result from broken clouds having smaller liquid water paths or they may be due to cloud 3-dimensional effects or both (Coakley, 1991). The larger channel-3 radiances observed for partly cloudy pixels may result from shifts to smaller droplets at cloud edges (Coakley and Davies, 1986; Coakley, 1991) or may be due to cloud 3-dimensional effects. The contribution of surface emission through thin cloud edges will make the 3.75-μm radiances larger, but the effect is small compared with that calculated. In any case, using a retrieval scheme similar to that described here, cloud droplet effective radii retrieved for the partly cloudy pixels, when they are assumed to be overcast, are generally smaller than those retrieved for the overcast pixels.

Chapter 5
Dependence of Cloud Visible Optical Depth on Cloud Top, Atmospheric, and Sea Surface Temperatures

5.1 Introduction

The greenhouse effect due to the buildup of trace gases is expected to warm the earth's climate (e.g., Charlson et al., 1992). As the climate warms, the "cloud radiative forcing" — the change to the earth's radiation budget brought about by the presence of clouds (Ramanathan et al., 1989) — may change due to changes in cloud optical properties. Such changes may amplify the warming and provide a positive feedback or diminish the warming and provide a negative feedback to the climate change. The cloud feedback problem is a major source of uncertainty in climate change predictions. Comparing results from 19 general circulation models, Cess et al. (1990) showed that different GCMs disagree on the magnitude and even the sign of the cloud feedback. Whether the changes in clouds will produce a positive or negative feedback depends on the changes in the cloud properties, such as cloud amount, cloud top altitude, cloud optical depth, and cloud hydrometeor size. While many climate simulation models have been used for studying the responses due to changes in cloud amount, cloud optical depth, and cloud top altitude, changes in cloud particle size have not been incorporated due to the lack of reliable, large-scale, long-term cloud observations (e.g., Roeckner et al., 1987; Mitchell et al., 1989; Le Treut and Li, 1991).

In this chapter, relationships between cloud visible optical depths and the temperatures of the cloud tops, the atmosphere, and the sea surface are examined for single-layered, low-level clouds. The study uses observations from the NOAA-11 AVHRR for March 1989 over the Pacific ocean. The identification of single-layered, low-level cloud systems and the retrieval of cloud properties were described in the proceeding chapter. The low-level cloud visible optical depth and temperature relationships are examined for both overcast and partly cloudy pixels. The effect of cloud breakup on the cloud visible optical depth-temperature relationship is demonstrated. Because the retrieved cloud visible optical depths exhibit a satellite view angle dependence, as was shown in the previous chapter, the results presented in this chapter are restricted to cloud properties retrieved at near-nadir satellite zenith angles. ISCCP C1 data for March 1989 is also analyzed for the visible optical depths and temperatures of the low-level clouds.

This study focuses on low-level clouds in order to limit variations in cloud vertical extent and effects due to changes in water phase. Low-level clouds have been shown to have a strong impact on the earth's net radiation balance (Hartmann et al., 1992). These clouds contribute a substantial fraction of planetary albedo but they have little impact on the thermal radiation emitted to space. Since their effect on the albedo dominates, the net effect of these clouds is to cool the earth. Hartmann et al. showed that low-level clouds reduce the net radiation balance at the top of the atmosphere by ~15 Wm^{-2} on a global-annual mean basis. Low-level clouds are primarily found over the subtropical, mid-latitude, and Arctic oceans. The average fraction of the earth covered by these clouds is ~29%. For oceans, the coverage is ~34% (Klein and Hartmann, 1993). Obviously, the radiation balance of the earth is expected to be sensitive to changes in the amount and optical properties of these clouds.

5.2 Cloud optical depth feedback

5.2.1 Negative or positive cloud optical depth feedback

Using more than 20,000 measurements from aircraft flights into clouds over the former Soviet Union, Feigelson (1978) concluded that cloud liquid water concentration generally increases with temperature. Based on these observations, Somerville and Remer (1984) proposed a negative cloud optical depth feedback hypothesis — cloud optical depth increases with increasing temperature, which in turn diminishes the impact of a climate warming.

Since a warmer atmosphere contains more water vapor, warm clouds will contain more condensed liquid water than the same clouds that are colder (Betts and Harshvardhan, 1987). As cloud optical depth is proportional to cloud liquid water content (Stephens, 1978), clouds having larger liquid water content would be optically thicker for the same vertical thickness. Optically thicker clouds reflect more sunlight back to space. Clouds, particularly low-level clouds, are often opaque at infrared wavelengths. Consequently, the increase in cloud liquid water would have little effect on the emitted radiation. As a result, an increase in cloud liquid water content would provide a negative feedback to a climate warming if all other cloud properties remain unchanged. Somerville and Remer (1984) also utilized the empirical relationship between cloud liquid water content and temperature to account for the changes in cloud optical depth in a radiative-convective model. They concluded that cloud optical depth, which depends strongly on cloud liquid water content, is sensitive enough to temperature to provide a substantial negative feedback to a CO_2-induced climate warming.

Satellite observations have been used for studying the cloud optical depth and cloud temperature relationship on a global scale. Tselioudis et al. (1992) used two years of ISCCP cloud data to investigate the low-level cloud visible optical depth and cloud temperature relationship. They showed that for colder, continental, low-level clouds, cloud optical depth increases with increasing temperature. This result agrees with the negative cloud optical depth hypothesis proposed by Somerville and Remer (1984) based on aircraft observations. However, for warmer continental and most marine low-level clouds, they discovered that cloud optical depth decreases with increasing temperature. Based on this finding, they suggested that in the event of a global warming there would be a decrease in global-mean, low-level cloud optical depth. Such a decrease in cloud optical depth implies a positive cloud optical depth feedback to a climate warming.

5.2.2 Effects of partly cloudy pixels on the optical depth-temperature relationship

As indicated in Chapter 2 and in earlier studies (Wielicki and Parker, 1992; Chang and Coakley, 1993), many of the satellite pixels identified by the ISCCP processing system as being overcast are in fact only partly covered by clouds. Because ISCCP treats these partly cloudy pixels as overcast and because these partly cloudy pixels are included in the ISCCP cloud optical depth and temperature retrieval scheme, the ISCCP-derived cloud optical depths are smaller than the actual optical depths of the clouds being observed and ISCCP-derived cloud temperatures are higher than the actual temperatures of the clouds. The relationship between low-level cloud optical depths and temperatures obtained by Tselioudis et al. may simply reflect cloud breakup on the regional scale where temperatures are warmer. The clouds that remain may still have larger optical depths when the temperatures are warmer, as suggested by Feigelson, Somerville and Remer, and Betts and Harshvardhan.

To illustrate the effect of cloud breakup, Figure 5.1 shows the cloud visible optical depths, cloud top emission temperatures, and cloud cover fraction retrieved for partly cloudy pixels. The data is taken from the left column in Table 4.2. Each point represents a ~(60 km)^2 portion of a (250 km)^2 region and gives cloud properties retrieved for partly cloudy pixels that are taken to be overcast. The (250 km)^2 region contains a uniform, single-layered, low-level cloud system and no evidence for upper-level clouds is found in the region. Figure 5.1a shows that, when partly cloudy pixels are assumed to be overcast, the retrieved visible optical depth decreases with decreasing fractional cloud cover. Conversely, Figure 5.1b shows that the retrieved cloud top emission temperature increases with decreasing fractional cloud cover. Clearly, variations in cloud cover fraction could easily explain the negative relationship between cloud optical depth and temperature inferred by Tselioudis et al. (1992).

5.3 ISCCP low-level cloud visible optical depths and temperatures

To examine the finding by Tselioudis et al., ISCCP C1 data (Rossow and Schiffer, 1991) for March 1989 over the Pacific ocean is used to obtain the low-level cloud optical depth and temperature relationship. The ISCCP C1 data provides cloud information for every 2.5° × 2.5° (latitude × longitude) region in space and every 3 hours in time. The ISCCP cloud properties were derived from the 0.63- and 11-μm radiances taken from four geostationary satellites and two NOAA polar orbiting satellites. The imager pixels had a spatial resolution of approximately 4-8 km at nadir.

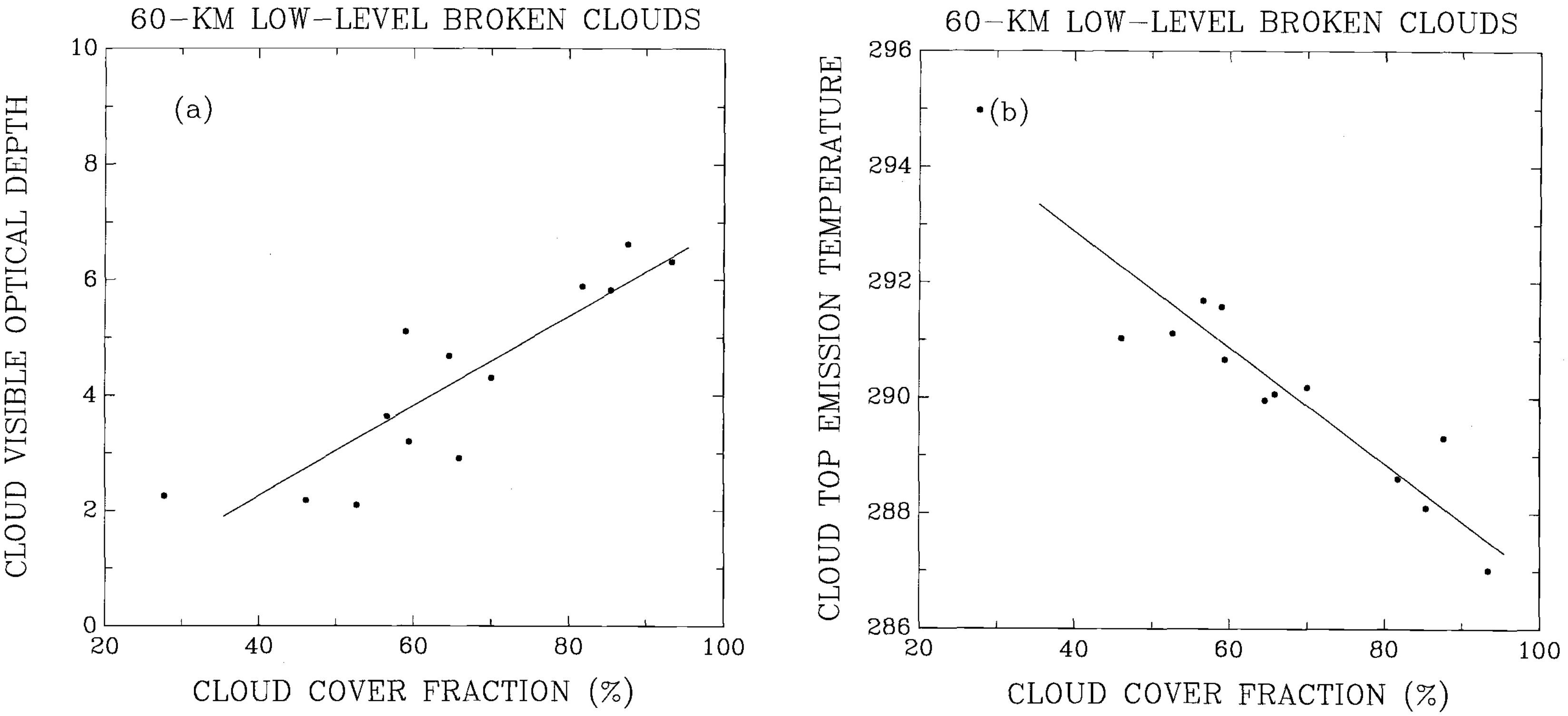

Figure 5.1 Cloud visible optical depths, cloud top emission temperatures, and cloud cover fractions for partly cloudy pixels assumed to be overcast. Each point gives the average for the partly cloudy pixels within a 60-km region. The values are given in Table 4.2. Straight lines represent least-squares fits. (a) cloud visible optical depth as a function of cloud cover fraction. (b) cloud top emission temperature as a function of cloud cover fraction.

The ISCCP cloud analysis procedure consists of two steps: cloud detection followed by radiative transfer analysis. For cloud detection, each pixel is taken to be either clear or cloudy based upon a bi-spectral threshold test applied to the 0.63 and 11-μm radiances. The cloudy pixels are those which are colder (11 μm) or brighter (0.63 μm) by pre-determined margins than the corresponding clear sky radiance. The margins represent the estimated uncertainty in the clear sky radiances. In the radiative transfer analysis, clouds are assumed to cover each cloudy pixel completely and uniformly. The 0.63- and 11-μm radiances of the cloudy pixels are then compared with calculated radiances to infer cloud visible optical depths and cloud emission temperatures. A plane-parallel model is used for the radiative transfer calculations. For low-level clouds, the droplets are assumed to be spherical, liquid water droplets with sizes specified by a gamma distribution (Hansen and Travis, 1974). An effective droplet radius of 10 μm and an effective variance of 0.15 are used in the gamma distribution.

Figure 5.2a shows the latitudinal distribution of the zonal-mean, low-level, cloud visible optical depths obtained by ISCCP for March 1989. The ISCCP cloud visible optical depths were derived from radiances taken from four geostationary and two NOAA polar orbiting satellites. The curves are the monthly averages obtained for every 2.5°-latitude band. The thin error bars indicate the standard deviations representing the variations of the daily means. The thick error bars indicate the 95% confidence intervals obtained for the monthly means and are determined by assuming that each daily mean represents an independent estimate of the monthly mean. Here, following Tselioudis et al. (1992), only pixels with retrieved 11-μm emission temperatures consistent with air temperatures occurring in the pressure interval between 680-800 mb were used. The ISCCP mean low-level cloud visible optical depths obtained for March 1989 are similar in magnitude to those obtained by Tselioudis et al. for 1984. Figure 5.2b shows the latitudinal distribution of zonal-mean cloud visible optical depths obtained for pixels overcast by single-layered, low-level clouds as identified by the spatial coherence method. Figure 5.2b is identical to Figure 4.9a. Figure 5.2c compares the means obtained in 5.2a and 5.2b and Figure 5.2d shows the differences between the means shown in 5.2c. Since many of the ISCCP cloudy pixels are only partially covered by clouds, the ISCCP mean low-level cloud optical depths are much smaller than those obtained for the overcast clouds. An interesting feature is that the magnitude of the ISCCP low-level cloud optical depths is similar to that obtained for low-level, partly cloudy pixels, as shown in Figure 4.9b.

Figure 5.3a shows the latitudinal distribution of the zonal-mean, cloud temperatures obtained by ISCCP for low-level clouds. Because ISCCP cloud retrieval procedures do not provide specific temperature information for low-level clouds, following Tselioudis et al., the 740-mb atmospheric temperature derived from TOVS (TIROS Operational Vertical Sounder) is used as an index of low-level cloud temperatures. Figure 5.3b shows the cloud top emission temperatures obtained for pixels overcast by single-layered, low-level clouds. The comparison and differences in the means are shown in Figures 5.3c and 5.3d. The distributions of the 740-mb atmospheric temperature and the cloud top emission temperature have similar features, that is, high temperatures at low latitudes and decreasing with increasing latitude. Although these latitudinal variations are expected, the low-level cloud top emission temperatures are on average 1-2 degrees higher than the associated 740-mb atmospheric temperatures. The cloud top altitudes of these single-layered, low-level clouds are on average a few hundred meters lower in altitude than the 740-mb level (Betts et al., 1992).

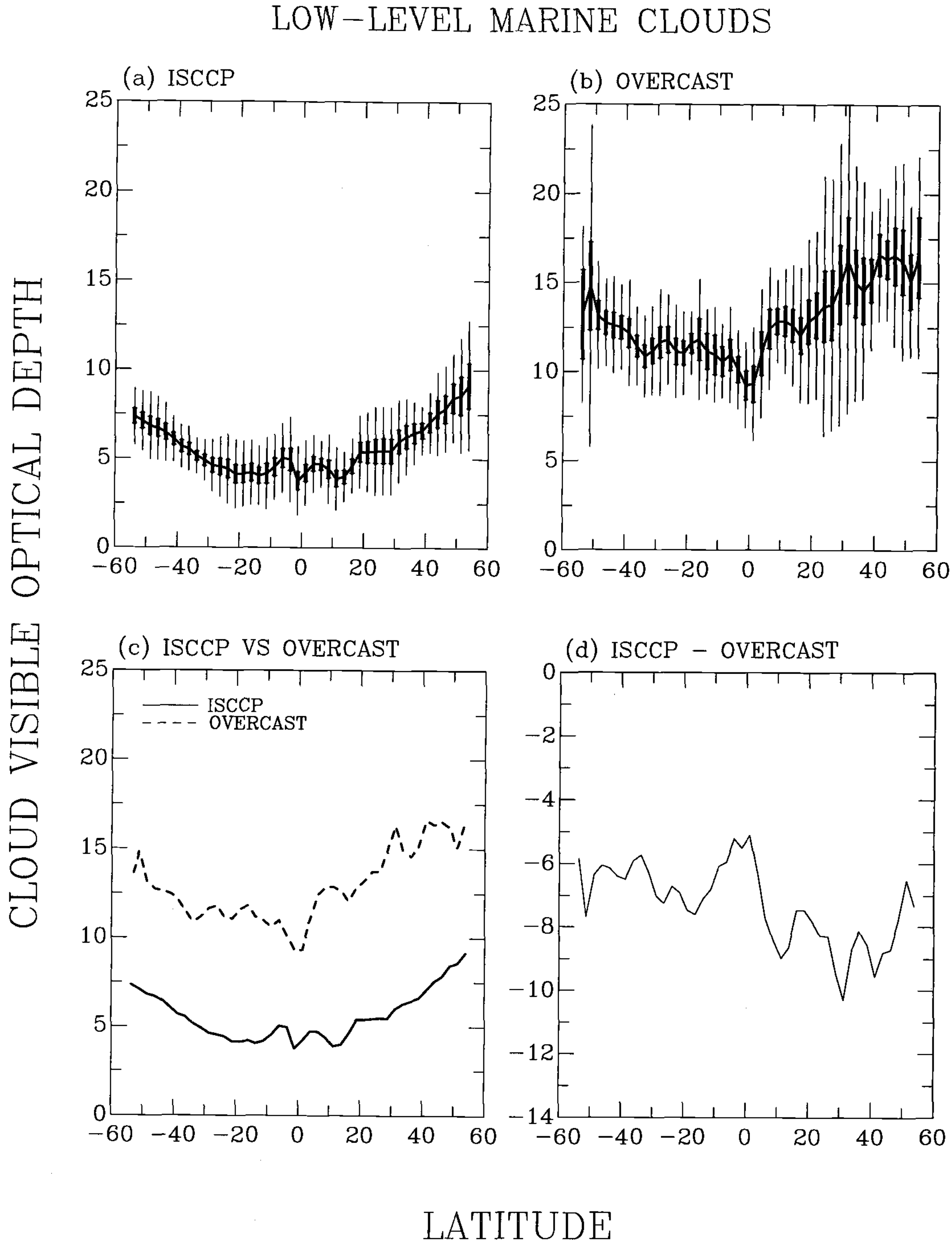

Figure 5.2 Latitudinal distribution of low-level cloud visible optical depth for ISCCP and overcast pixels. Curves are for the monthly means. Thick bars indicate the 95% confidence intervals for the means. Thin bars represent the standard deviations of the daily means. (a) ISCCP low-level clouds; (b) single-layered, low-level, overcast clouds identified by the spatial coherence method; (c) monthly means shown in (a) and (b); (d) differences between the means shown in (c).

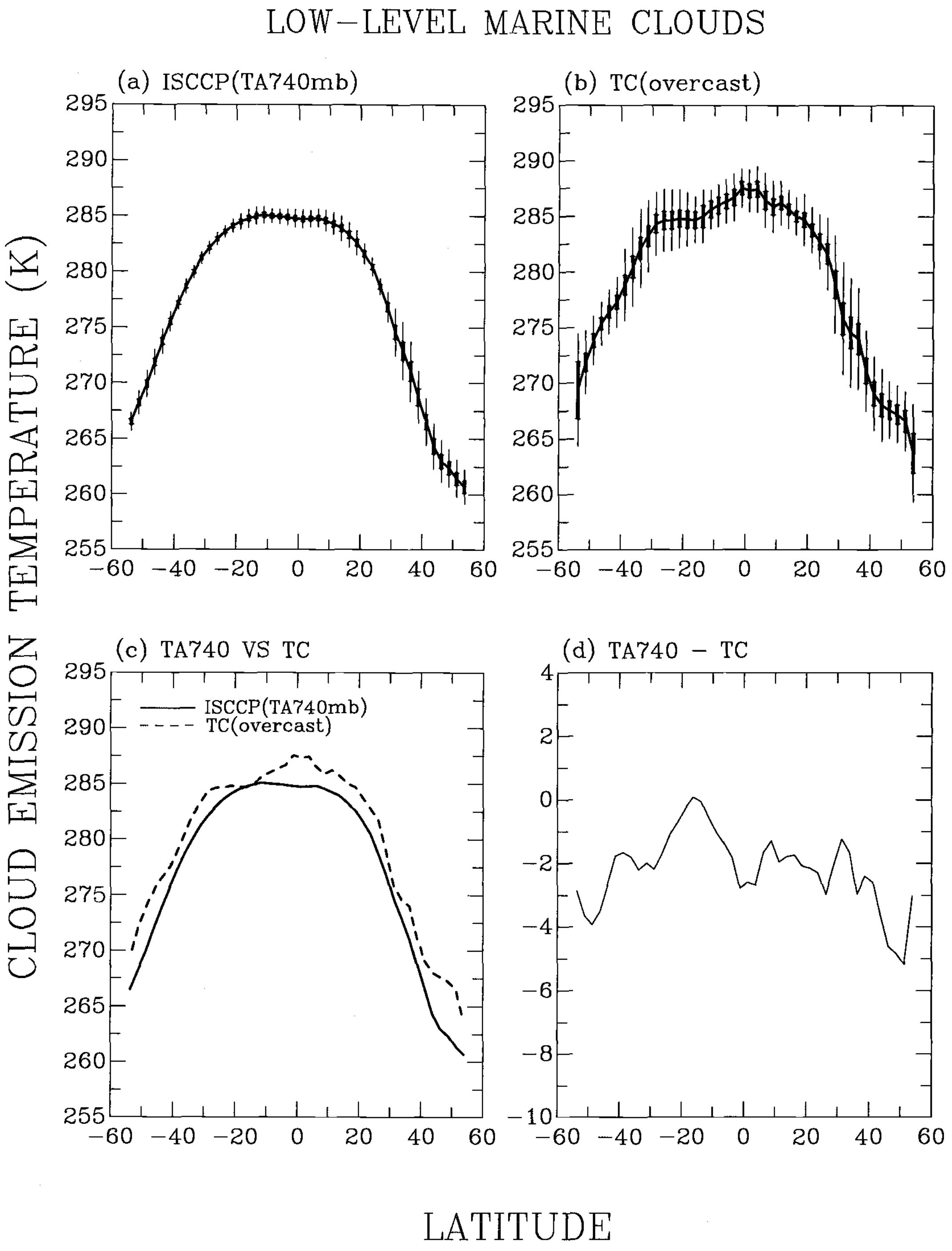

Figure 5.3 Same as Figure 5.2, except for cloud top emission temperatures (K). Note that ISCCP uses the 740–mb atmospheric temperature as an index of the cloud top emission temperature.

5.4 Variations of cloud visible optical depth with cloud top and 740-mb atmospheric temperatures

The spatial and temporal variations of the low-level cloud visible optical depths and cloud top emission temperatures obtained for the Pacific ocean for March 1989 are examined. In time, the daily-mean, low-level, cloud visible optical depths and cloud top emission temperatures are averaged for 30° × 10° (longitude × latitude) regions. Then for every 30° × 10° region (30° × 15° in the tropics), day-to-day variations of the daily-mean optical depths and emission temperatures are correlated. In space, the monthly-mean, low-level, cloud visible optical depths and cloud top emission temperatures are averaged for every 2.5° × 2.5° (longitude × latitude) region. Then for each of the 2.5°-latitude bands, the longitudinal variations of the 2.5°×2.5°-scale, monthly-mean optical depths and emission temperatures are correlated. The latitudinal correlation between cloud visible optical depths and cloud top emission temperatures is not examined here. As noted by Loeb and Davies (1996), cloud optical depths obtained with the plane-parallel theory show a strong dependence on solar zenith angle. For the AVHRR data, the latitude and solar zenith angle are tightly coupled so that the solar zenith angle dependence of the retrieved cloud optical depths leads to a latitudinal dependence of the optical depths.

5.4.1 Day-to-day correlations

Figure 5.4 shows cloud visible optical depths and cloud top emission temperatures obtained for pixels overcast by single-layered, low-level clouds. The figure shows results for fifty 30° × 10° regions covering the Pacific ocean from 55°S to 55°N.

The sub-figures associated with the fifty regions are placed such that top-to-bottom represents north-to-south and left-to-right represents west-to-east. The locations of these regions are given in Table 5.1 and indicated by the index numbers in the upper-right corners of the sub-figures. Each sub-figure represents a 30° × 10° region and each point gives the daily-mean cloud visible optical depth and cloud top emission temperature observed within that 30° × 10° region. Also, the number of days when single-layered, low-level clouds were identified by the spatial coherence method is given in Table 5.1 and the least-squares linear regression fit for the day-to-day correlation is plotted in the figure for each region. The empty sub-figures have no observations. These results show that cloud visible optical depths and cloud top emission temperatures for single-layered, low-level, overcast systems are negatively correlated on a day-to-day basis.

Table 5.1 shows the values for the slopes of the least-squares linear regression fits, the correlation coefficients ρ, and the 90% confidence level of the least-squares linear regressions for all of the 30° × 10° regions. The monthly-mean, low-level, cloud visible optical depths and cloud top emission temperatures are also listed in the table. The values for the slopes of the least-squares linear regression fits and their 90% confidence intervals are plotted in Figure 5.5, along with their corresponding monthly-mean cloud top emission temperatures. These results show that negative correlations between low-level cloud visible optical depths and cloud top emission temperatures are found in all of the regions and most of them are statistically significant at a 90% confidence level.

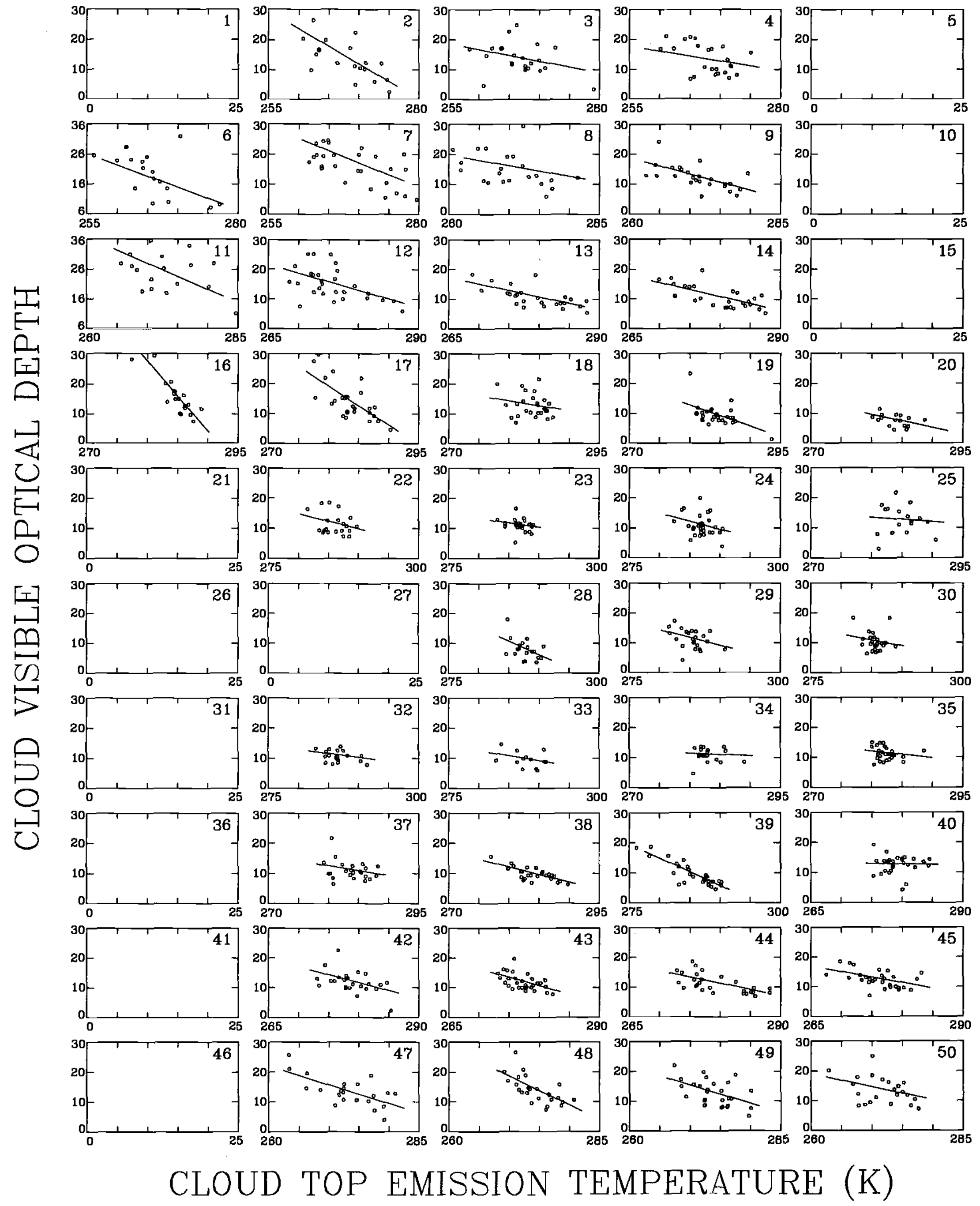

Figure 5.4 Cloud visible optical depths and cloud top emission temperatures (K) for pixels overcast by single-layered, low-level clouds. Observations are for March 1989 for the Pacific ocean. Each sub-figure is for a 30° × 10° region. The regions are given in Table 5.1. Each point gives daily means for that 30° × 10° region. Straight lines represent the least-squares fits. Empty boxes indicate sparse or no observations.

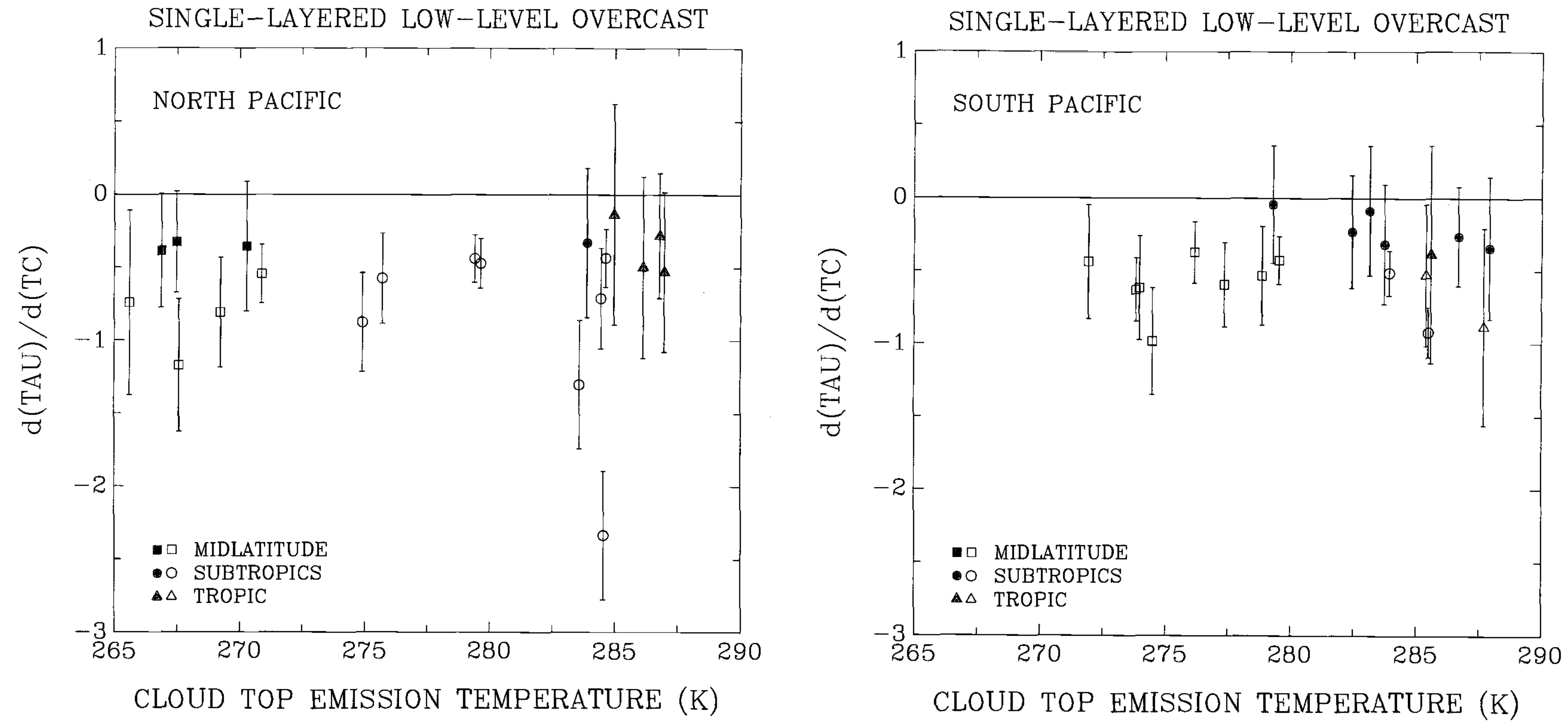

Figure 5.5 $d(TAU)/d(TC)$ and monthly-mean cloud top emission temperatures for observations shown in Figure 5.4. The values of $d(TAU)/d(TC)$ are the slopes of the least-square fits. Each data is for a 30° × 10° (longitude × latitude) region. Open symbols indicate that TAU and TC are correlated at the 90% confidence level. Error bars indicate the 90% confidence intervals.

Table 5.1 Index numbers, locations, $d(TAU)/d(TC)$, monthly-mean cloud visible optical depths, cloud top emission temperatures, numbers of days, correlation coefficients ρ, and whether the correlation is significant at the 90% confidence level. Results are shown for fifty 30°×10° (longitude × latitude) regions over the Pacific for March 1989.

Index No.	Region (latitude, longitude)	$\frac{d(TAU)}{d(TC)}$	$\overline{TAU}$	$\overline{TC}$	N	ρ	90% stat. test
1	(45°N-55°N, 120°E-150°E)				9		
2	(45°N-55°N, 150°E-180°E)	-1.172	14.7	267.6	20	-0.712	PASS
3	(45°N-55°N, 180°W-150°W)	-0.385	14.0	266.9	23	-0.338	
4	(45°N-55°N, 150°W-120°W)	-0.326	13.6	267.5	25	-0.309	
5	(45°N-55°N, 120°W- 90°W)				0		
6	(35°N-45°N, 120°E- 90°E)	-0.742	18.1	265.6	20	-0.419	PASS
7	(35°N-45°N, 150°E- 180°E)	-0.808	17.8	269.3	29	-0.562	PASS
8	(35°N-45°N, 180°W- 150°W)	-0.356	16.1	270.3	23	-0.278	
9	(35°N-45°N, 150°W- 120°W)	-0.545	12.8	270.9	26	-0.675	PASS
10	(35°N-45°N, 120°W- 90°W)				0		
11	(25°N-35°N, 120°E- 90°E)	-0.877	23.6	274.9	21	-0.703	PASS
12	(25°N-35°N, 150°E- 180°E)	-0.574	15.4	275.7	28	-0.515	PASS
13	(25°N-35°N, 180°W- 150°W)	-0.439	11.1	279.4	25	-0.679	PASS
14	(25°N-35°N, 150°W- 120°W)	-0.472	11.0	279.6	27	-0.674	PASS
15	(25°N-35°N, 120°W- 90°W)				10		
16	(15°N-25°N, 120°E- 90°E)	-2.336	17.0	284.6	21	-0.897	PASS
17	(15°N-25°N, 150°E- 180°E)	-1.303	14.6	283.6	27	-0.698	PASS
18	(15°N-25°N, 180°W- 150°W)	-0.330	13.1	283.9	27	-0.207	
19	(15°N-25°N, 150°W- 120°W)	-0.711	9.7	284.5	28	-0.554	PASS
20	(15°N-25°N, 120°W- 90°W)	-0.434	7.6	284.6	17	-0.686	PASS
21	(0°N-15°N, 120°E- 90°E)				9		
22	(0°N-15°N, 150°E- 180°E)	-0.497	11.8	286.1	20	-0.300	
23	(0°N-15°N, 180°W- 150°W)	-0.282	11.4	286.8	26	-0.216	
24	(0°N-15°N, 150°W- 120°W)	-0.531	11.1	287.0	29	-0.294	
25	(0°N-15°N, 120°W- 90°W)	-0.136	12.8	285.0	17	-0.078	
26	(0°S-15°S, 120°E- 90°E)				1		
27	(0°S-15°S, 150°E- 180°E)				5		
28	(0°S-15°S, 180°W- 150°W)	-0.883	8.3	287.7	19	-0.464	PASS
29	(0°S-15°S, 150°W- 120°W)	-0.526	11.6	285.4	23	-0.365	PASS
30	(0°S-15°S, 120°W- 90°W)	-0.384	10.6	285.6	24	-0.179	
31	(15°S-25°S, 120°E- 90°E)				4		
32	(15°S-25°S, 150°E- 180°E)	-0.262	11.2	286.7	20	-0.289	
33	(15°S-25°S, 180°W- 150°W)	-0.342	9.9	287.9	13	-0.340	
34	(15°S-25°S, 150°W- 120°W)	-0.087	11.3	283.2	19	-0.079	
35	(15°S-25°S, 120°W- 90°W)	-0.230	11.6	282.5	27	-0.193	
36	(25°S-35°S, 120°E- 90°E)				0		
37	(25°S-35°S, 150°E- 180°E)	-0.315	11.4	283.7	23	-0.266	
38	(25°S-35°S, 180°W- 150°W)	-0.513	10.2	283.9	27	-0.736	PASS
39	(25°S-35°S, 150°W- 120°W)	-0.920	9.9	285.5	28	-0.866	PASS
40	(25°S-35°S, 120°W- 90°W)	-0.043	12.9	279.3	27	-0.035	
41	(35°S-45°S, 120°E- 90°E)				8		
42	(35°S-45°S, 150°E- 180°E)	-0.532	12.3	278.9	25	-0.476	PASS
43	(35°S-45°S, 180°W- 150°W)	-0.592	12.2	277.4	30	-0.535	PASS
44	(35°S-45°S, 150°W- 120°W)	-0.426	11.4	279.6	27	-0.650	PASS
45	(35°S-45°S, 120°W- 90°W)	-0.373	12.8	276.2	29	-0.489	PASS
46	(45°S-55°S, 120°E- 90°E)				7		
47	(45°S-55°S, 150°E- 180°E)	-0.630	13.4	273.8	24	-0.716	PASS
48	(45°S-55°S, 180°W- 150°W)	-1.027	14.6	274.3	26	-0.710	PASS
49	(45°S-55°S, 150°W- 120°W)	-0.617	13.0	274.0	28	-0.489	PASS
50	(45°S-55°S, 120°W- 90°W)	-0.439	13.9	271.9	23	-0.377	PASS

Table 5.2 Index numbers, latitudes, $d(TAU)/d(TC)$, monthly-mean cloud visible optical depths and cloud top emission temperatures, numbers of 2.5°×2.5° samples, effective numbers of independent sample, and correlation coefficients, ρ, and whether the correlation is significant at the 90% confidence level. Results are shown for forty-four 2.5°-latitude bands over the Pacific for March 1989.

Index No.	Latitude	$\frac{d(TAU)}{d(TC)}$	$\overline{TAU}$	$\overline{TC}$	N	N^*	ρ	90% stat. test
1	(52.5°N-55.0°N)	-0.137	16.5	263.6	24	16.9	-0.109	
2	(50.0°N-52.5°N)	-0.880	14.9	266.9	29	24.3	-0.453	PASS
3	(47.5°N-50.0°N)	-0.914	16.1	267.4	35	25.3	-0.411	PASS
4	(45.0°N-47.5°N)	-0.633	16.5	267.6	38	18.5	-0.321	
5	(42.5°N-45.0°N)	-0.289	15.6	267.4	35	25.9	-0.298	
6	(40.0°N-42.5°N)	-0.309	16.1	268.5	34	13.0	-0.281	
7	(37.5°N-40.0°N)	-0.608	15.2	271.1	40	8.9	-0.564	PASS
8	(35.0°N-37.5°N)	-1.147	14.6	274.0	42	7.9	-0.856	PASS
9	(32.5°N-35.0°N)	-0.913	15.0	274.6	47	8.1	-0.677	PASS
10	(30.0°N-32.5°N)	-1.193	16.3	275.8	49	11.9	-0.700	PASS
11	(27.5°N-30.0°N)	-1.367	14.9	278.9	50	7.2	-0.755	PASS
12	(25.0°N-27.5°N)	-1.393	13.8	281.7	51	11.9	-0.641	PASS
13	(22.5°N-25.0°N)	-1.450	13.7	282.8	52	26.6	-0.484	PASS
14	(20.0°N-22.5°N)	-1.145	13.2	283.8	53	40.5	-0.501	PASS
15	(17.5°N-20.0°N)	-0.917	12.9	284.7	54	43.8	-0.461	PASS
16	(15.0°N-17.5°N)	0.137	12.1	285.0	53	19.8	0.061	
17	(12.5°N-15.0°N)	-0.625	12.6	285.7	55	25.4	-0.315	
18	(10.0°N-12.5°N)	-0.895	12.9	286.3	49	29.7	-0.607	PASS
19	(7.5°N-10.0°N)	-0.098	12.8	285.9	41	41.0	-0.099	
20	(5.0°N- 7.5°N)	-0.501	12.4	286.5	37	29.2	-0.355	PASS
21	(2.5°N- 5.0°N)	-0.705	11.0	287.5	34	26.5	-0.404	PASS
22	(0.0°N- 2.5°N)	0.292	9.3	287.3	38	23.5	0.172	
23	(0.0°S- 2.5°S)	-0.309	9.3	287.6	34	21.4	-0.222	
24	(2.5°S- 5.0°S)	-0.345	10.2	286.7	36	26.1	-0.329	PASS
25	(5.0°S- 7.5°S)	-0.438	11.0	286.4	37	27.9	-0.322	PASS
26	(7.5°S-10.0°S)	-0.456	10.6	286.0	25	16.8	-0.413	PASS
27	(10.0°S-12.5°S)	-1.020	11.0	285.7	22	22.0	-0.672	PASS
28	(12.5°S-15.0°S)	-0.437	11.2	285.0	22	22.0	-0.435	PASS
29	(15.0°S-17.5°S)	-0.208	11.8	284.7	32	18.9	-0.128	
30	(17.5°S-20.0°S)	0.099	11.6	284.8	41	33.9	0.137	
31	(20.0°S-22.5°S)	-0.109	11.1	284.8	47	46.5	-0.123	
32	(22.5°S-25.0°S)	-0.392	11.1	284.7	49	18.2	-0.409	PASS
33	(25.0°S-27.5°S)	-0.559	11.8	284.6	47	28.2	-0.622	PASS
34	(27.5°S-30.0°S)	-0.747	11.6	284.3	46	21.6	-0.712	PASS
35	(30.0°S-32.5°S)	-0.611	11.2	283.2	49	10.9	-0.794	PASS
36	(32.5°S-35.0°S)	-0.523	10.9	282.2	51	10.2	-0.808	PASS
37	(35.0°S-37.5°S)	-0.425	11.5	280.5	52	13.2	-0.689	PASS
38	(37.5°S-40.0°S)	-0.629	12.2	278.9	53	23.2	-0.683	PASS
39	(40.0°S-42.5°S)	-0.782	12.5	277.3	53	21.5	-0.738	PASS
40	(42.5°S-45.0°S)	-0.724	12.6	276.4	54	17.9	-0.533	PASS
41	(45.0°S-47.5°S)	-0.603	12.7	275.3	54	20.4	-0.479	PASS
42	(47.5°S-50.0°S)	-0.623	12.8	274.1	54	28.7	-0.451	PASS
43	(50.0°S-52.5°S)	-0.597	13.3	272.4	51	21.1	-0.498	PASS
44	(52.5°S-55.0°S)	-0.556	13.2	269.4	15	7.1	-0.565	

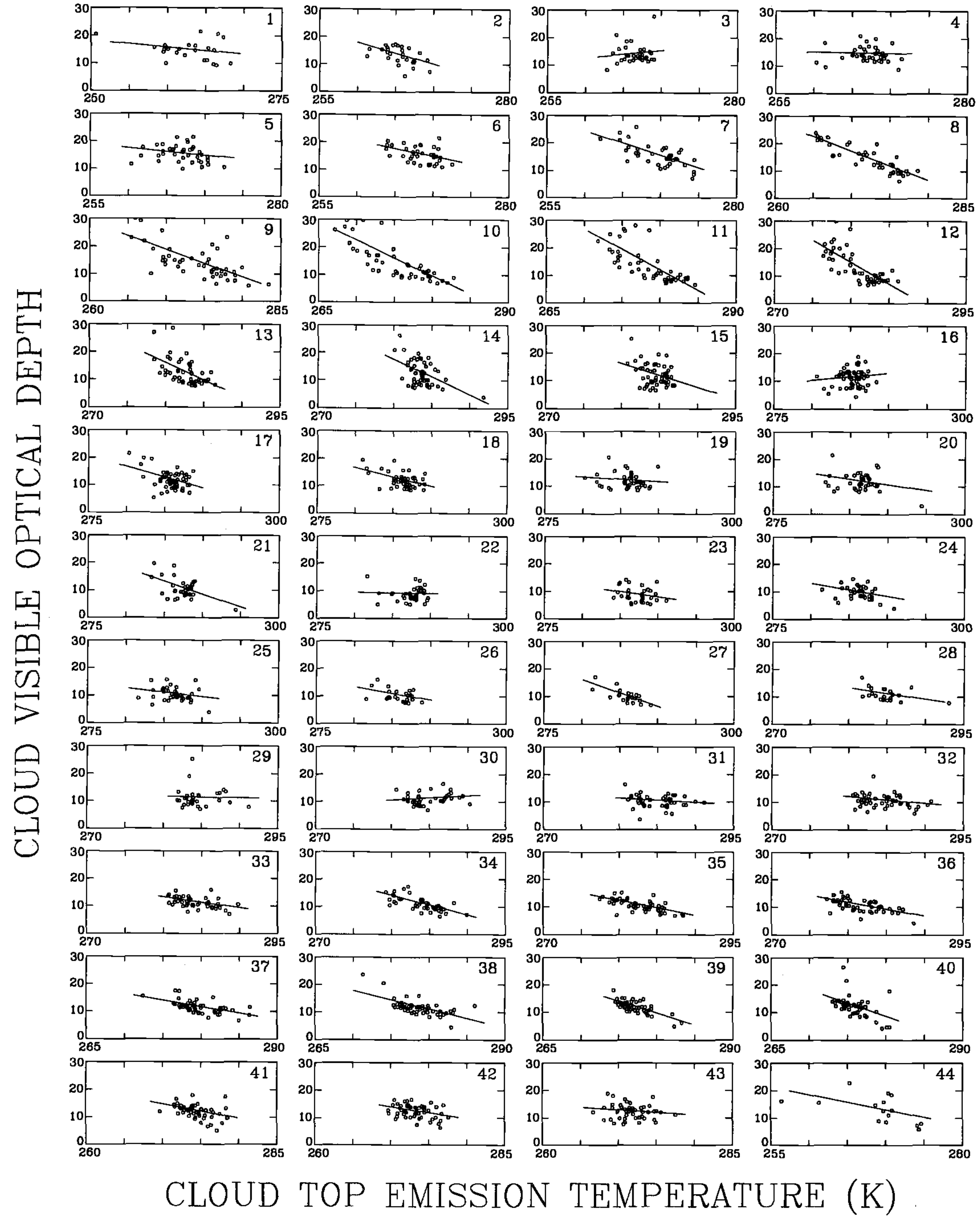

Figure 5.6 Cloud visible optical depths and cloud top emission temperatures for pixels overcast by single-layered, low-level clouds. Observations are for March 1989 for the Pacific ocean. Each sub-figure is for a 2.5°-latitude band. The latitudes are given in Table 5.2. Each point gives monthly means of a 2.5° × 2.5° region within the 2.5°-latitude band. Straight lines represent the least-squares fits.

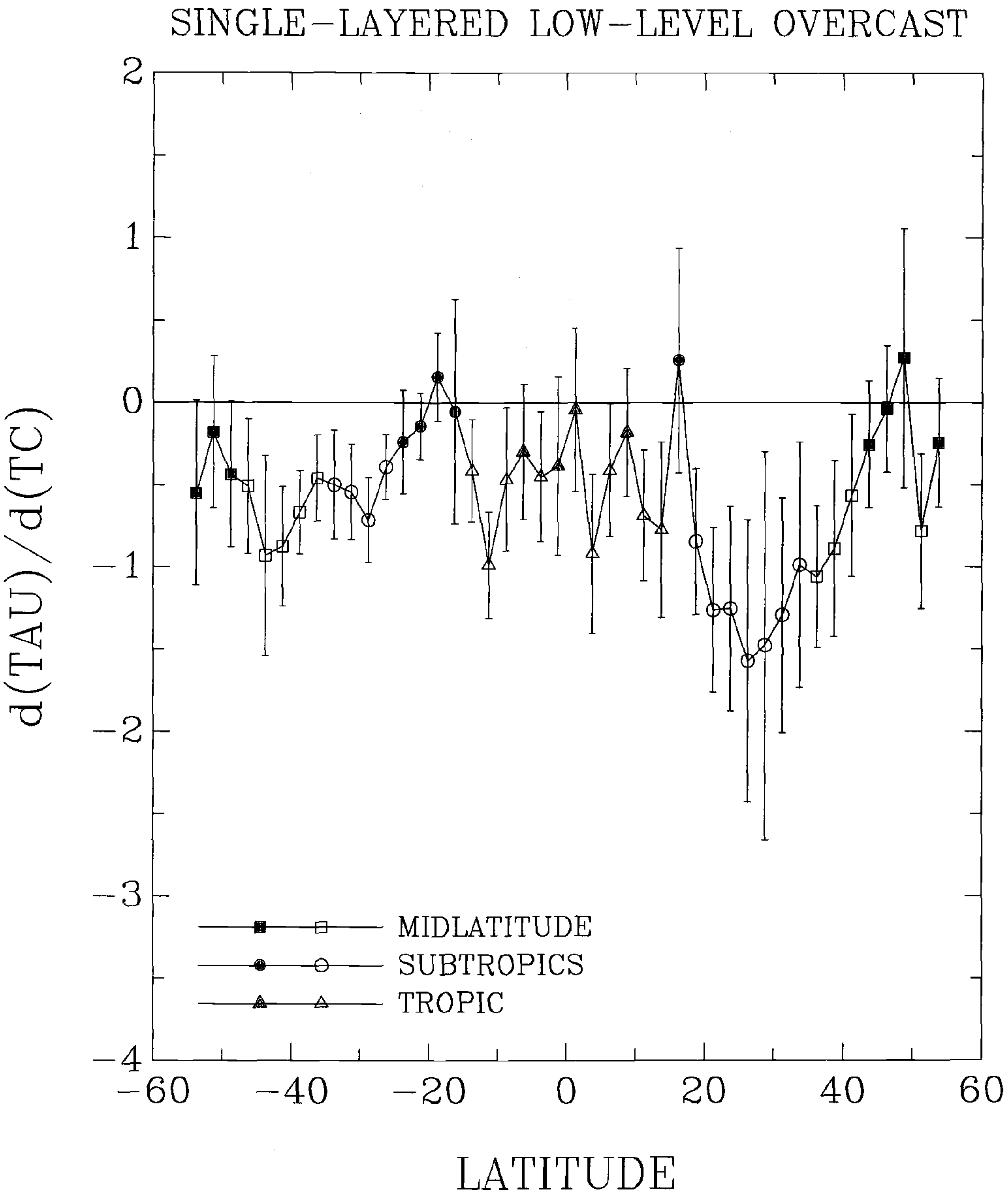

Figure 5.7 Latitudinal distribution of $d(TAU)/d(TC)$ for observations shown in Figure 5.6. The values of $d(TAU)/d(TC)$ are the slopes of the least-square fits. Each data is for a 2.5°-latitude band. Open symbols indicate that TAU and TC are correlated at the 90% confidence level. Error bars indicate the 90% confidence intervals.

5.4.2 Longitudinal correlations

Figure 5.6 shows the cloud visible optical depths and cloud top emission temperatures obtained for pixels overcast by single-layered, low-level clouds for forty-four 2.5°-latitude bands from 55°S to 55°N. Each sub-figure represents a 2.5°-latitude band. The latitudes for these sub-figures are given in Table 5.2 as indicated by the index numbers. Each point in the figure gives the monthly-mean, low-level, cloud visible optical depth and cloud top emission temperature for a 2.5° × 2.5° region. The number of 2.5° × 2.5° regions containing single-layered, low-level clouds is given in Table 5.2. The least-squares linear regression fit for the longitudinal correlation is also plotted in the figure for each latitude band. The longitudinal correlations between cloud visible optical depths and cloud top emission temperatures for single-layered, low-level clouds are generally negative.

In Section 5.4.1, when examining the day-to-day correlation between visible optical depth and cloud top emission temperature, clouds observed on different days were assumed to be independent samples. However, when examining the longitudinal correlation, the 2.5°-scale variations in the cloud properties are correlated. When the observations are not statistically independent, the number of independent samples is smaller than the total number of samples. Here an effective number of independent samples, N^*, is used in place of the number of samples, N, to determine the significance of the longitudinal correlations between low-level cloud optical depths and cloud top emission temperatures.

The effective number of independent samples, N^*, is estimated following the method of Dr. Dudley Chelton and Nathaniel Plant (personal communications). The effective number is given by

$$N^* = \nu N \tag{5.1}$$

and

$$\nu = \frac{M}{< N(\tau)\hat{S}(\tau) >}, \tag{5.2}$$

where $M = 1$ for the linear regression model, τ is the lag in the longitude domain, $\hat{S}$ is the square of the estimated value of the lag-cross-correlation coefficient between two variables, x and y. The cross-correlation coefficient for lag τ is given by

$$\hat{\rho}_{xy}(\tau) = \frac{\overline{xy} - \overline{x}\,\overline{y}}{\sigma_x \sigma_y}, \tag{5.3}$$

where σ is the standard deviation. The expected value $< N(\tau)\hat{S}(\tau) >$ can be estimated by $\left\{N(\tau)\hat{S}(\tau)\right\}$ which is the average of $N(\tau_k)\hat{S}(\tau_k)$ calculated for lags τ_k, $k = 1, 2, \ldots, K$ and $-1, -2, \ldots, -K$. The estimated effective number of independent samples, $\hat{N}^*$, is then given by

$$\hat{N} = \frac{N}{\left\{N(\tau)\hat{S}(\tau)\right\}}. \tag{5.4}$$

Table 5.2 shows the effective number of independent samples obtained for each of the 2.5°-latitude bands, along with the number of samples, the slopes of least-squares linear regression fit, the correlation coefficient, and whether the correlation is significant at the 90% confidence level. The monthly-zonal-mean cloud visible optical depths and cloud top emission temperatures are also listed. The values for the slopes of the least-squares linear regression fits and their 90% confidence intervals are plotted in Figure 5.13 as a function of the latitude. These results show that significant negative longitudinal correlations between low-level cloud optical depths and cloud top emission temperatures are found in most of the latitudes.

5.4.3 Comparisons for the overcast and partly cloudy pixels

Figures 5.8 and 5.9 show results obtained for the partly cloudy pixels that are assumed to be overcast. Figure 5.8 is plotted in the same way as Figure 5.4. Figure 5.9 is plotted in the same way as Figure 5.6. As was illustrated in Figure 5.1, for partly cloudy pixels, the retrieved cloud visible optical depth decreases and the retrieved cloud top emission temperature increases with decreasing cloud cover fraction. These negative correlations are expected for the partly cloudy pixels. However, the negative correlations are also obtained for the overcast pixels. The negative visible optical depth-emission temperature relationship obtained for the partly cloudy pixels appears to be similar to that obtained for the overcast pixels. To examine the similarity, following Tselioudis et al. (1992), Figures 5.10 and 5.11 show the values of $d\ln(TAU)/d(TC)$ obtained from the day-to-day variations shown in Figures 5.4 and 5.8. Figure 5.10 is for the overcast pixels and Figure 5.11 is for the partly cloudy pixels. Likewise, Figures 5.12 and 5.13 show the values of $d\ln(TAU)/d(TC)$ obtained from the longitudinal variations shown in Figures 5.6 and 5.9. Figure 5.12 is for the overcast pixels and Figure 5.13 is for the partly cloudy pixels. Comparing Figure 5.10 with Figure 5.11 and comparing Figure 5.12 with Figure 5.13, the cloud visible optical depths and cloud top emission temperatures for the partly cloudy pixels seem to be strongly correlated with those for the overcast pixels for the same region or latitude.

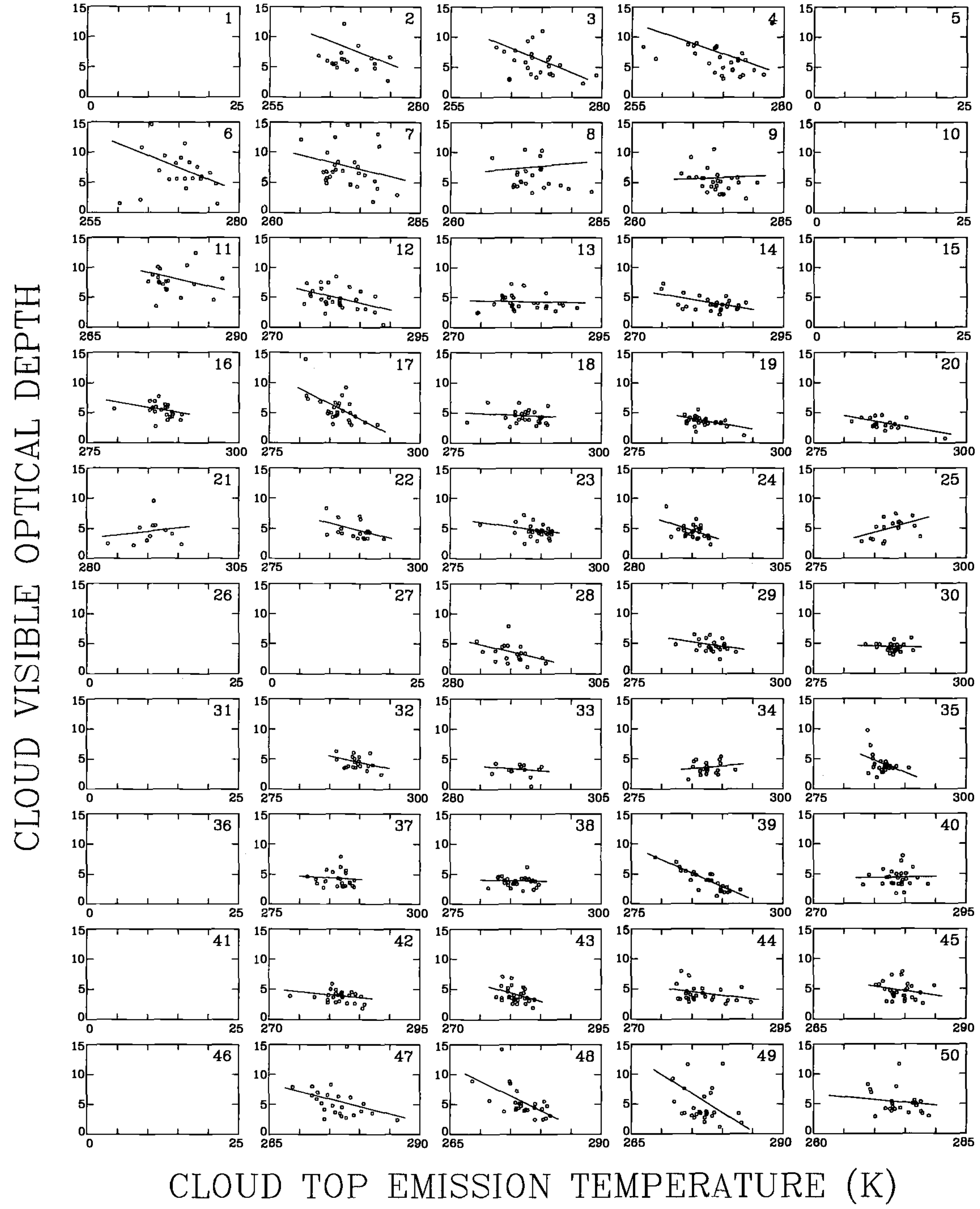

Figure 5.8 Same as Figure 5.4, except that observations are for pixels that were partly covered by the single-layered, low-level clouds. These partly cloudy pixels were assumed to be overcast.

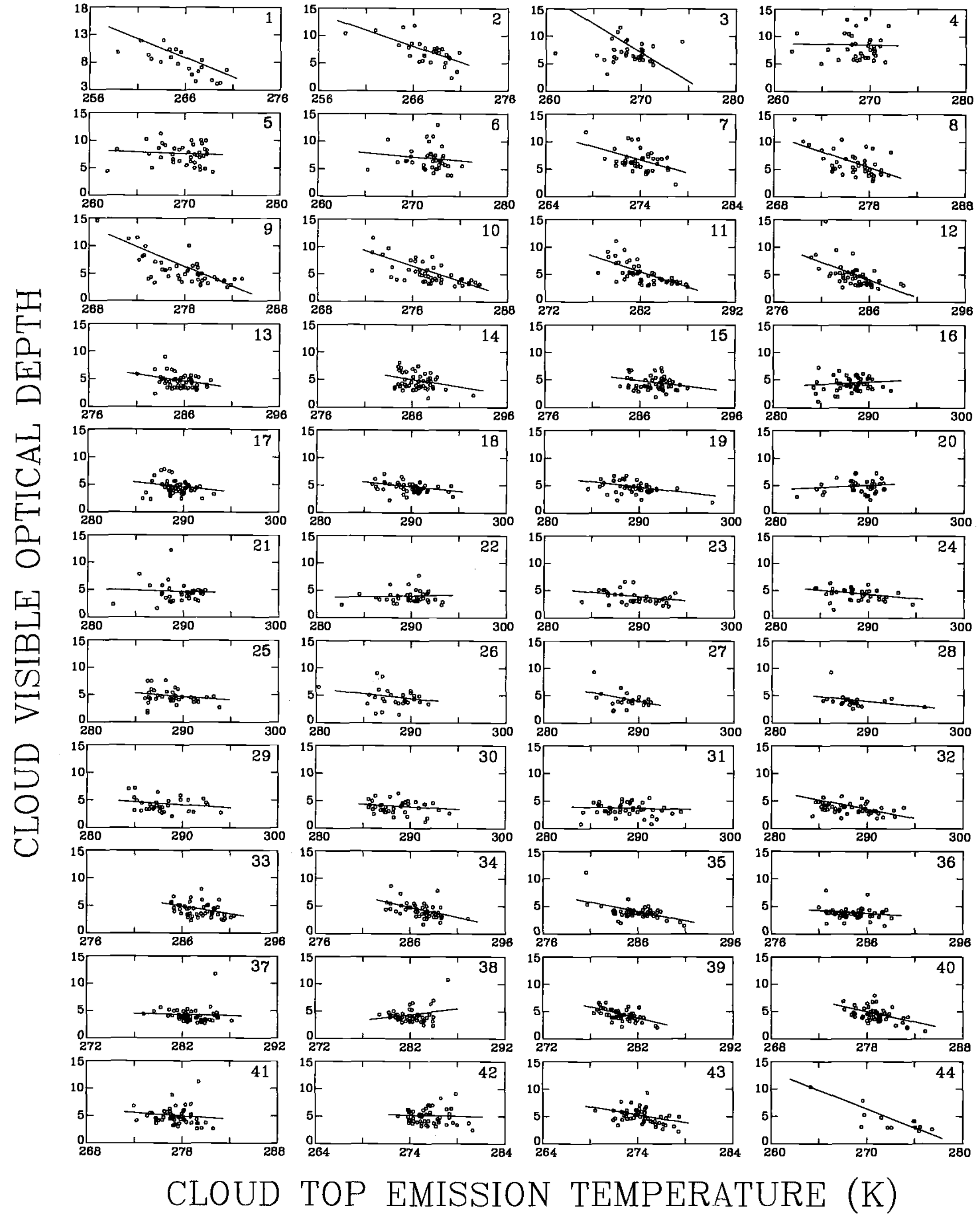

Figure 5.9 Same as Figure 5.6, except that observations are for pixels that were partly covered by the single-layered, low-level clouds. These partly cloudy pixels were assumed to be overcast.

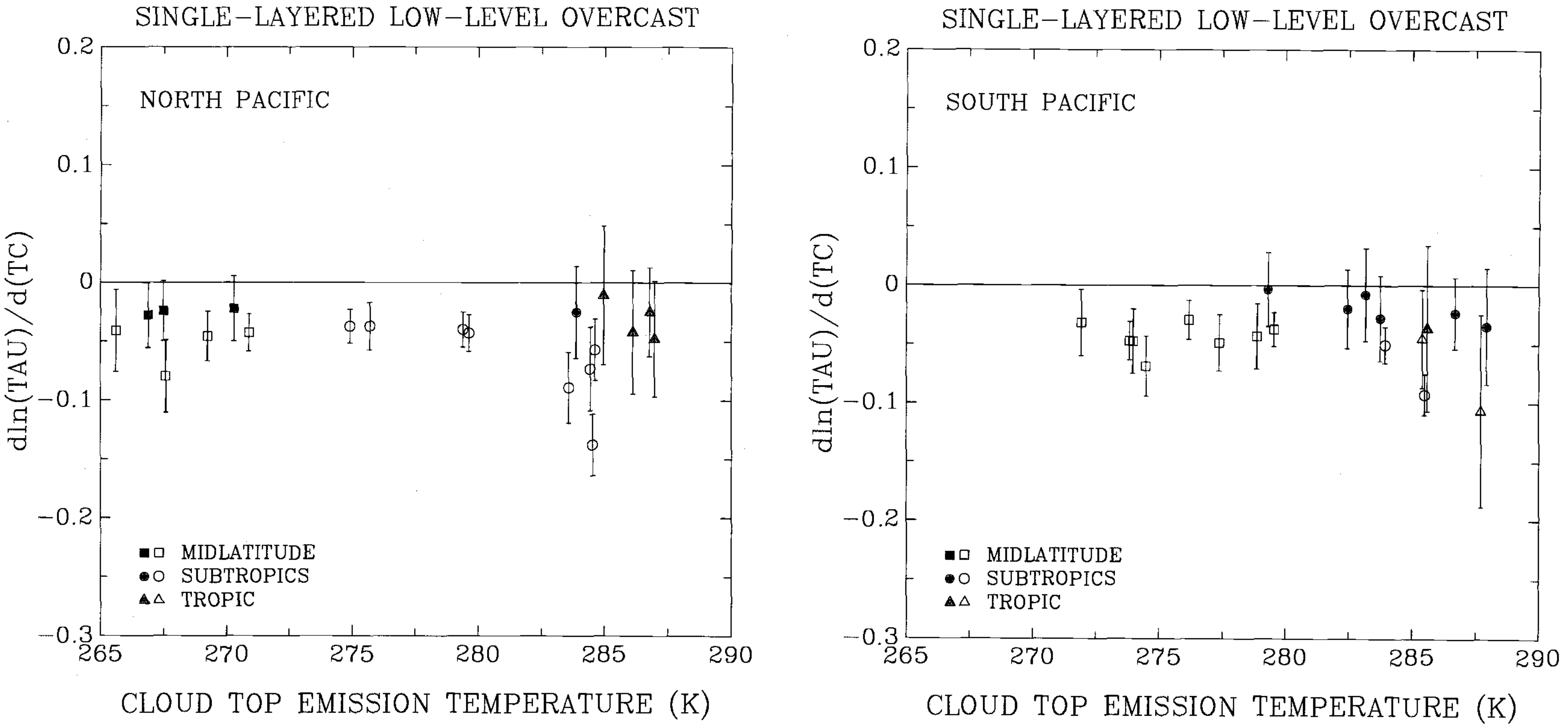

Figure 5.10 Same as Figure 5.5, except for $d\ln(TAU)/d(TC)$.

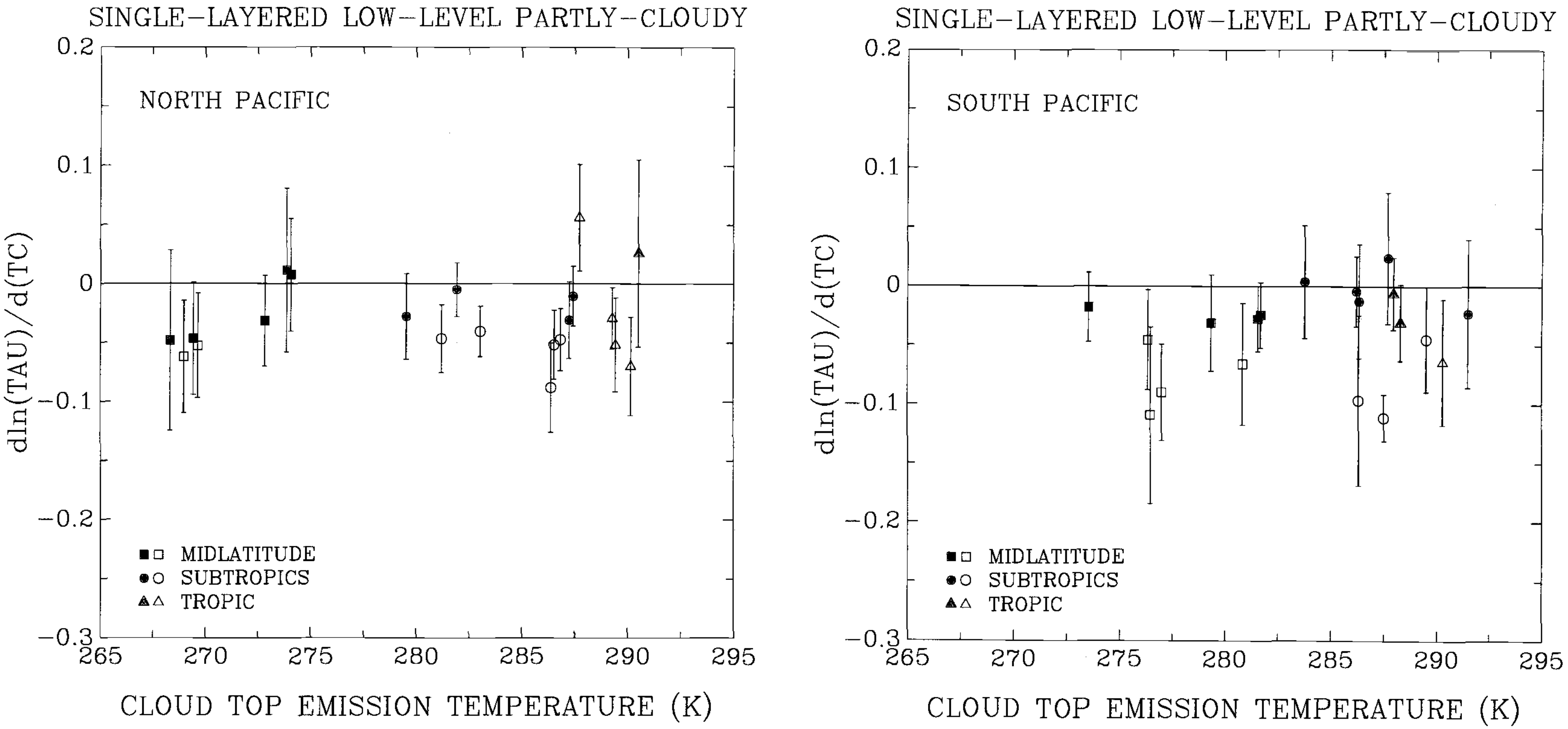

Figure 5.11 Same as Figure 5.10, except that observations are for pixels that were partly covered by the single-layered, low-level clouds. These partly cloudy pixels were assumed to be overcast.

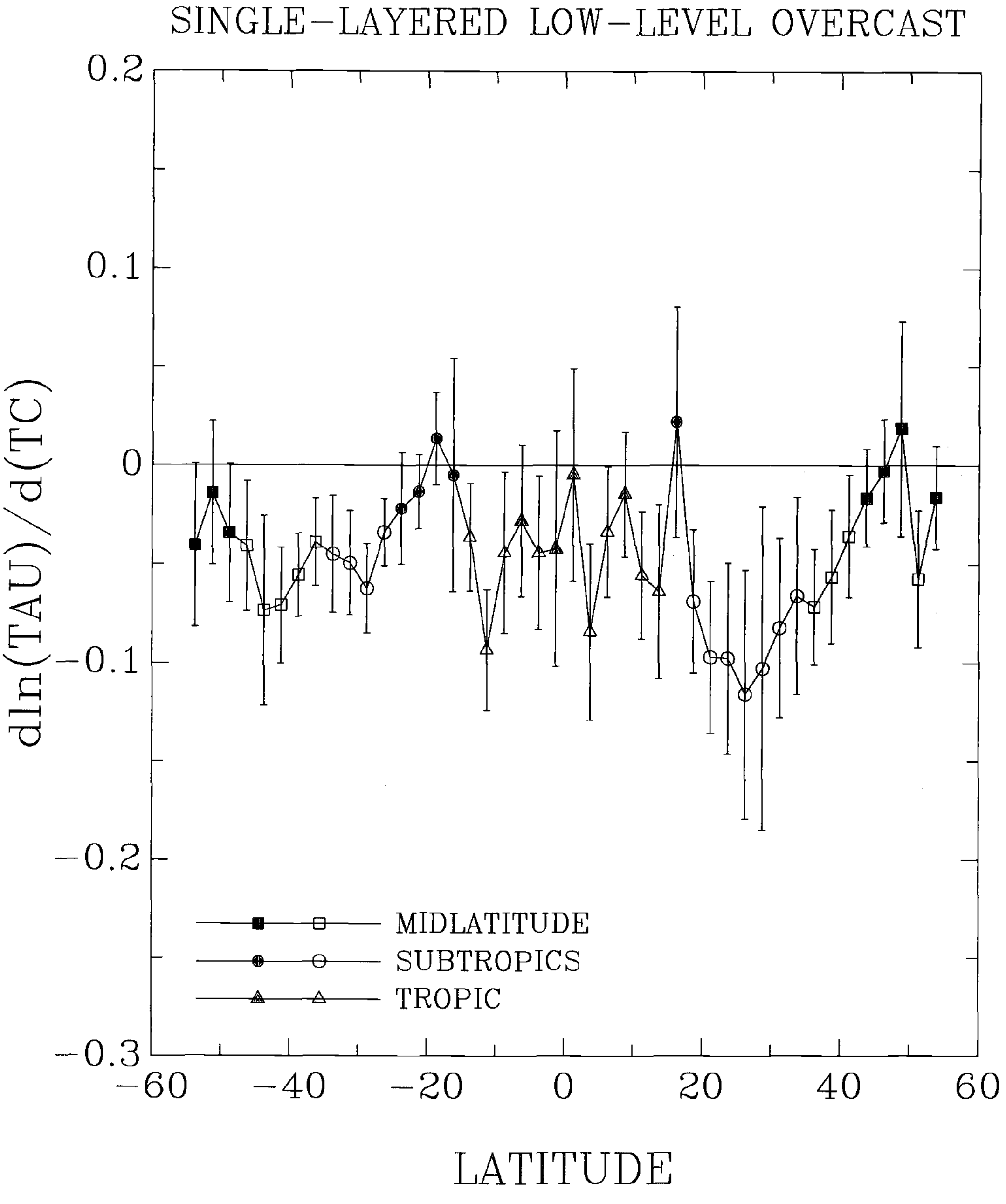

Figure 5.12 Same as Figure 5.7, except for $d\ln(TAU)/d(TC)$.

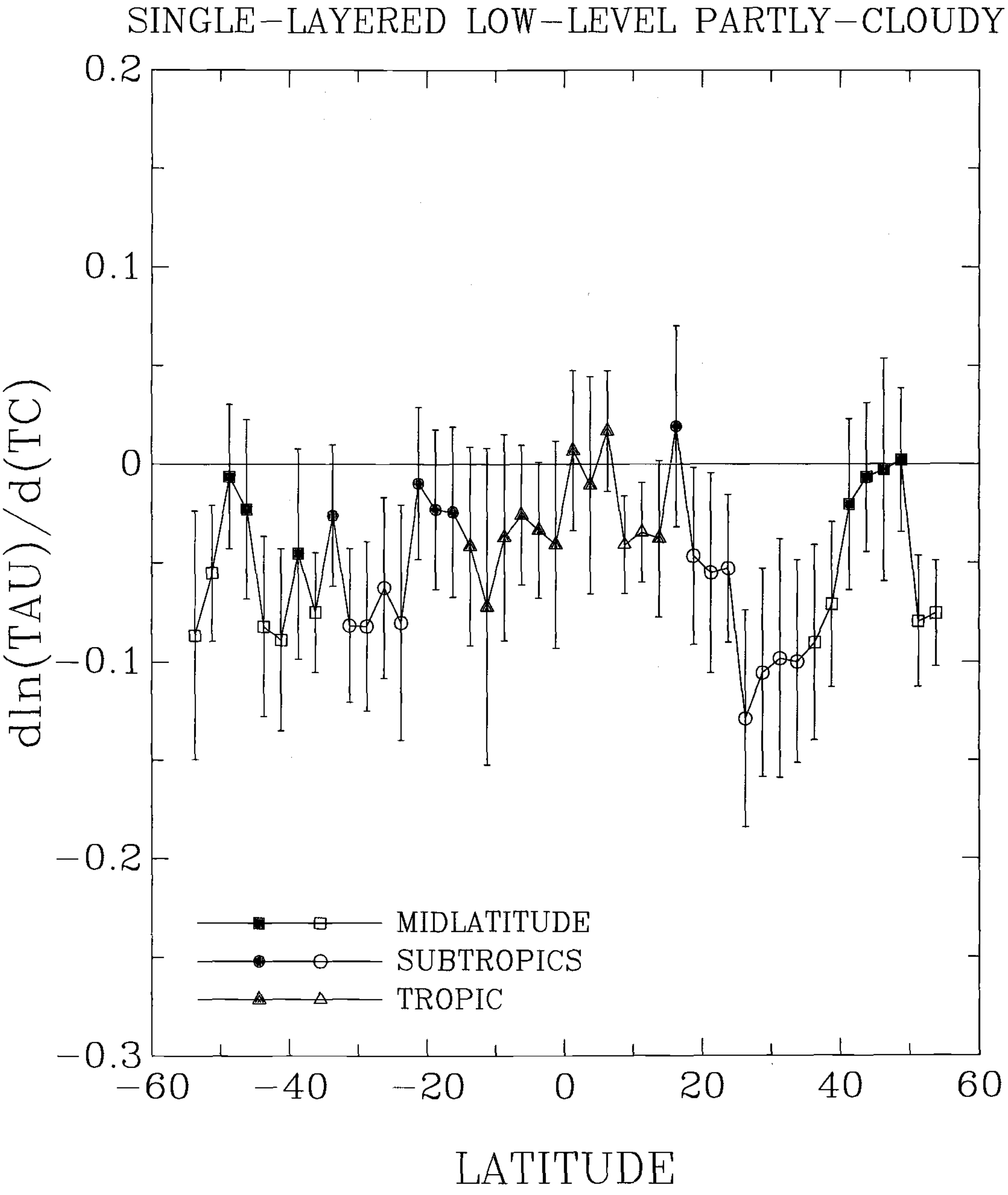

Figure 5.13 Same as Figure 5.12, except that observations are for pixels that are partly covered by the single-layered, low-level clouds. These partly cloudy pixels were assumed to be overcast.

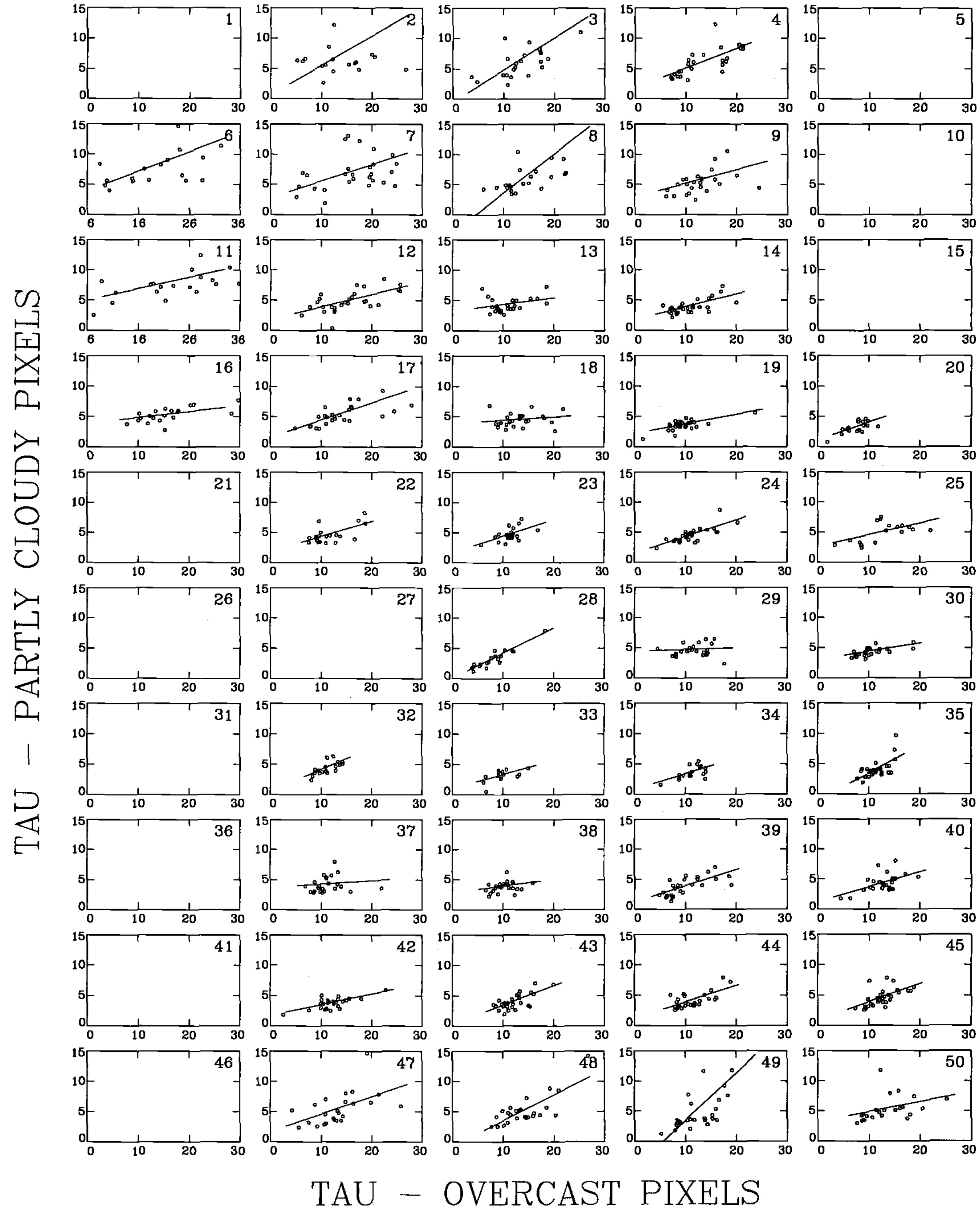

Figure 5.14 Cloud visible optical depths for pixels that were overcast and partly covered by the single-layered, low-level clouds. Observations are for March 1989 for the Pacific ocean. Each sub-figure is for a 30° × 10° region. The regions are given in Table 5.1. Each point gives daily means for that 30° × 10° region. Straight lines represent the least-squares fits. Empty boxes indicate sparse or no observations.

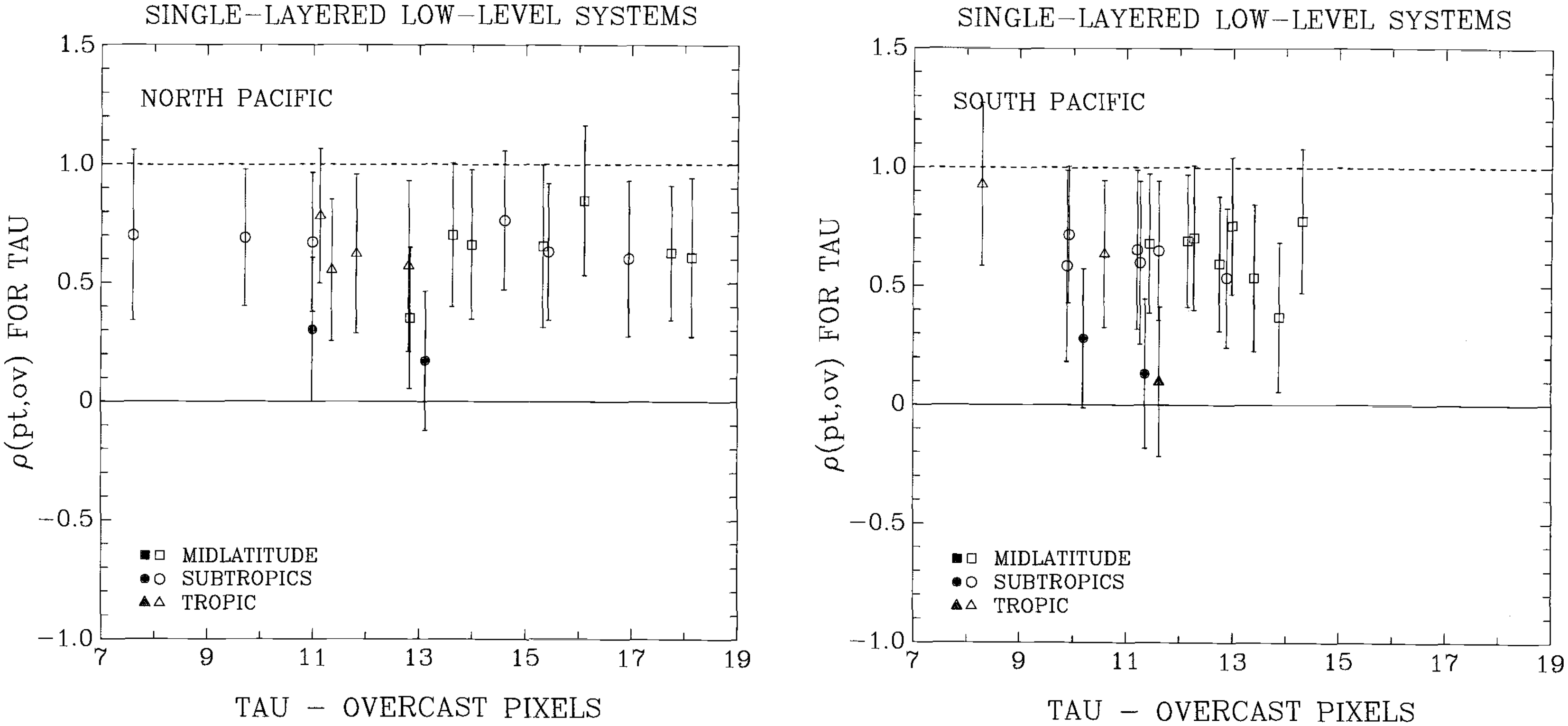

Figure 5.15 Correlation coefficients of cloud visible optical depths for the overcast and partly cloudy pixels obtained from the day-to-day variations shown in Figure 5.14. The X-axis indicates the monthly-mean visible optical depths for pixels overcast by the single-layered, low-level clouds. Each data is for a 30° × 10° (longitude × latitude) region. Open symbols indicate that the coefficients are significant at the 90% confidence level. Error bars indicate the 90% confidence intervals.

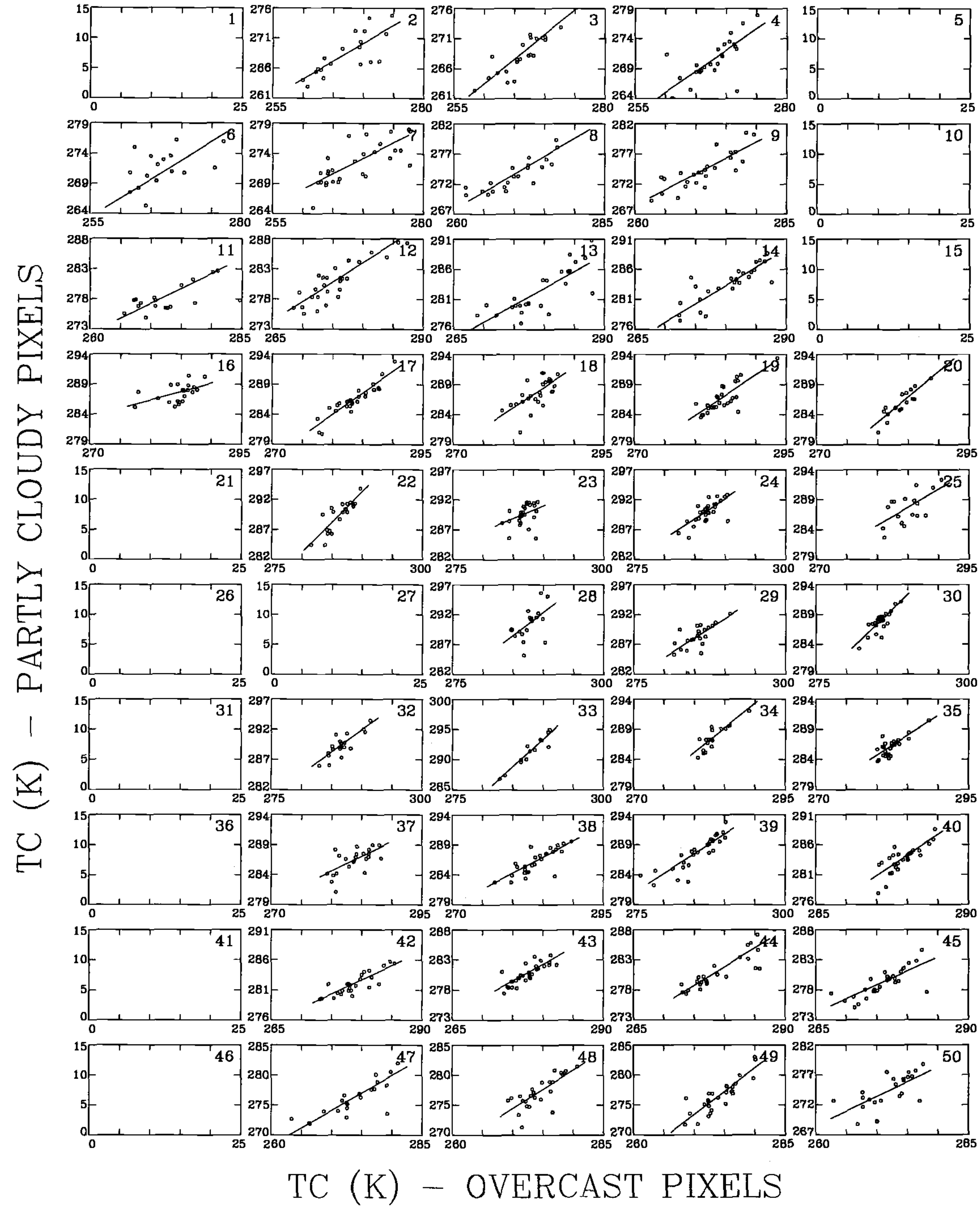

Figure 5.16 Same as Figure 5.14, except for cloud top emission temperatures (K).

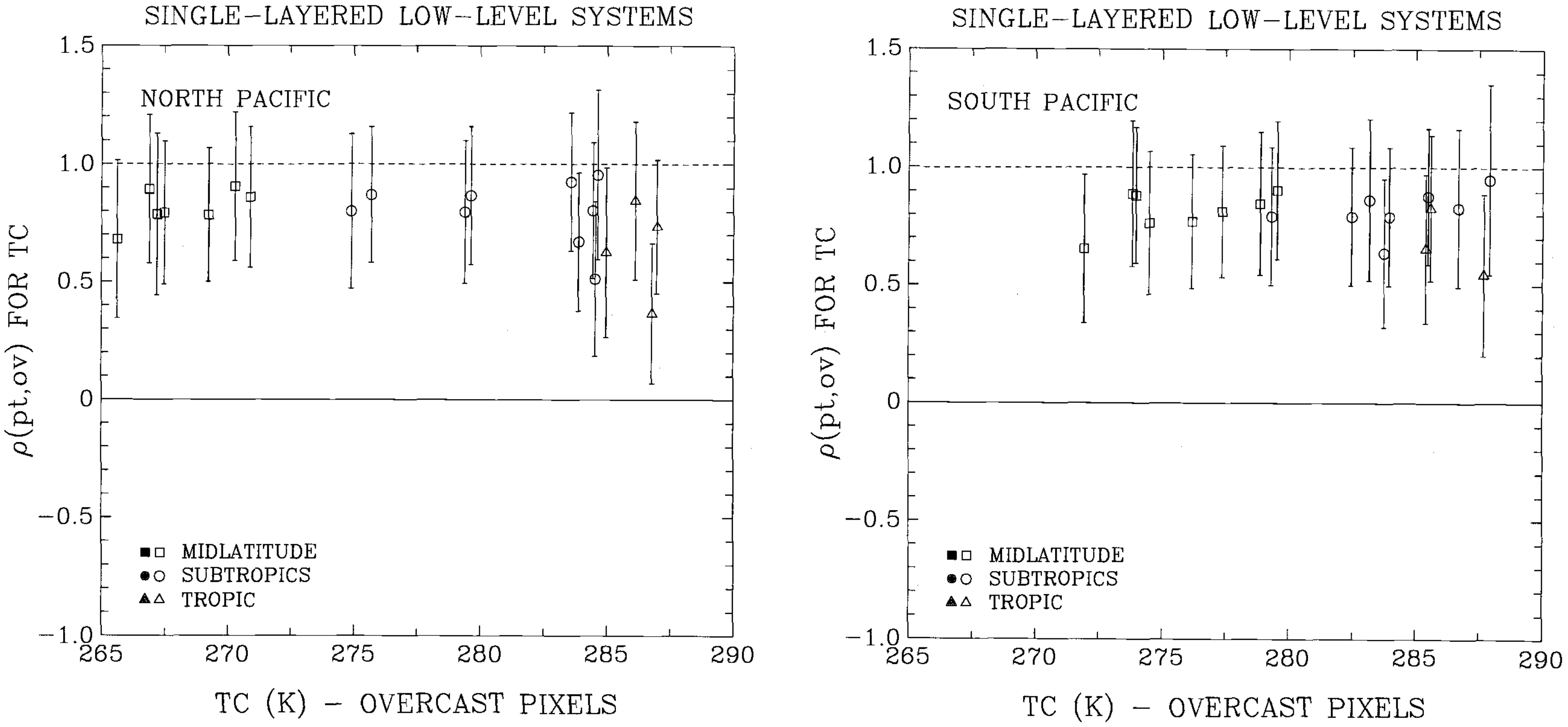

Figure 5.17 Same as Figure 5.15, except that the correlation coefficients are for the cloud top emission temperatures shown in Figure 5.16.

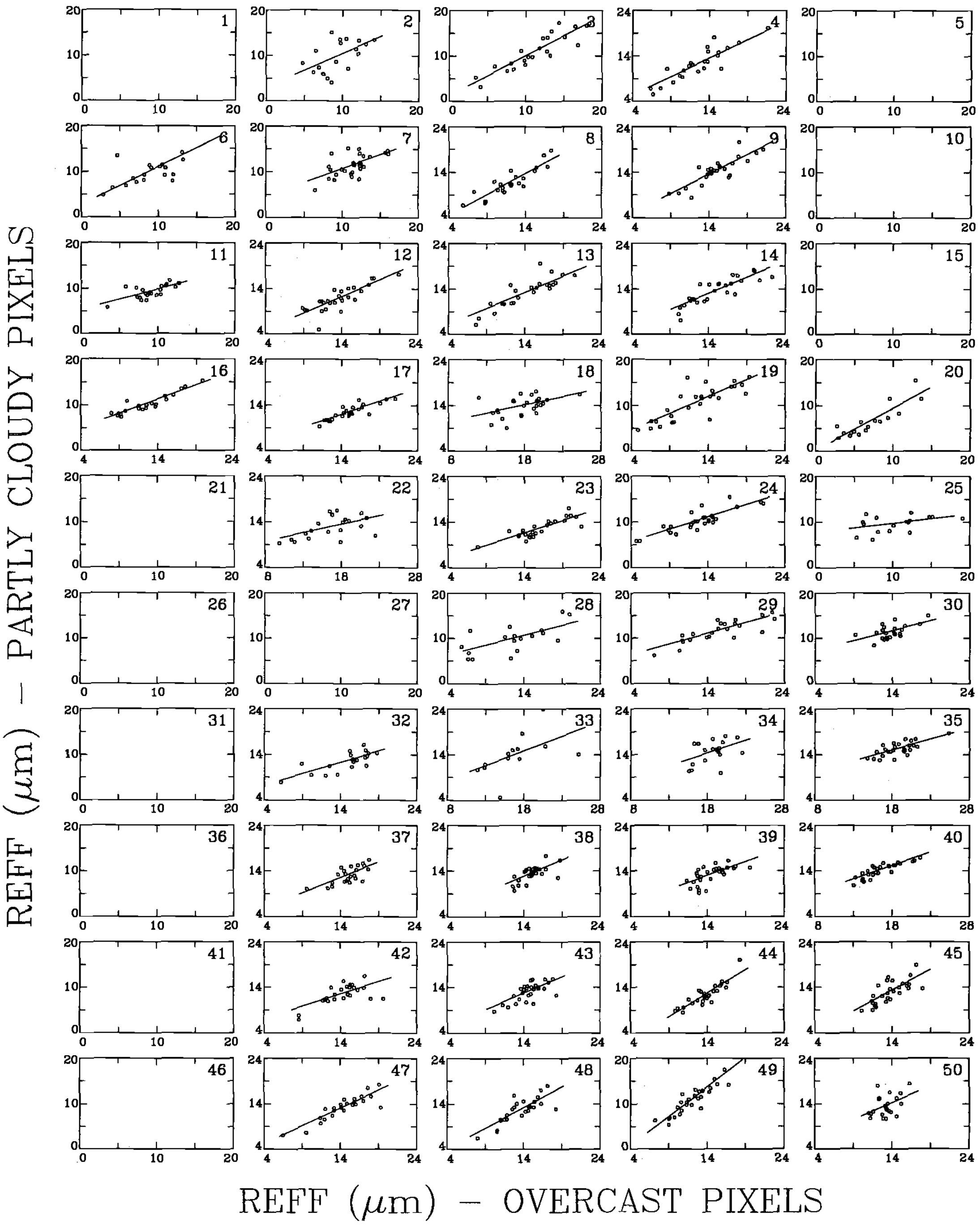

Figure 5.18 Same as Figure 5.14, except for cloud droplet effective radii (μm).

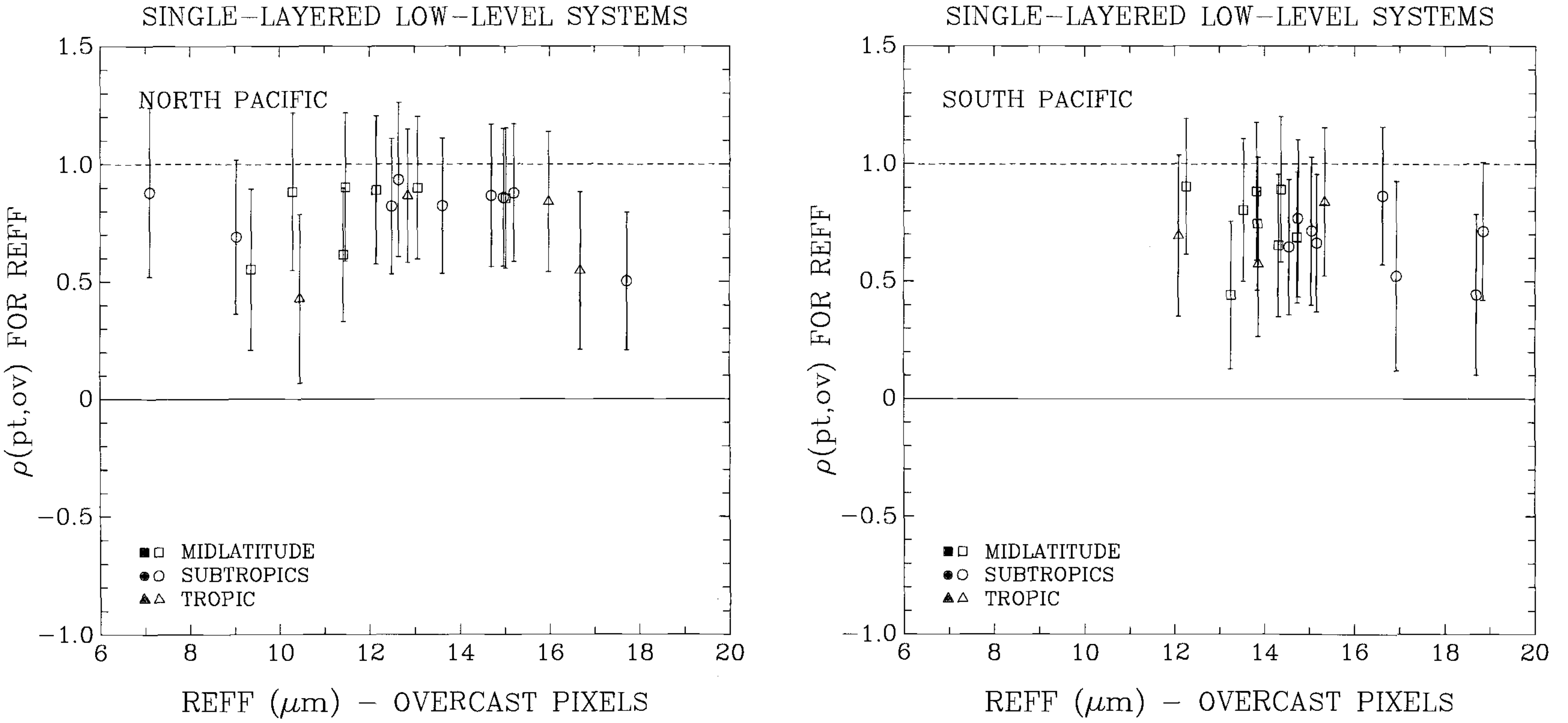

Figure 5.19 Same as Figure 5.15, except that the correlation coefficients are for the cloud droplet effective radii shown in Figure 5.18.

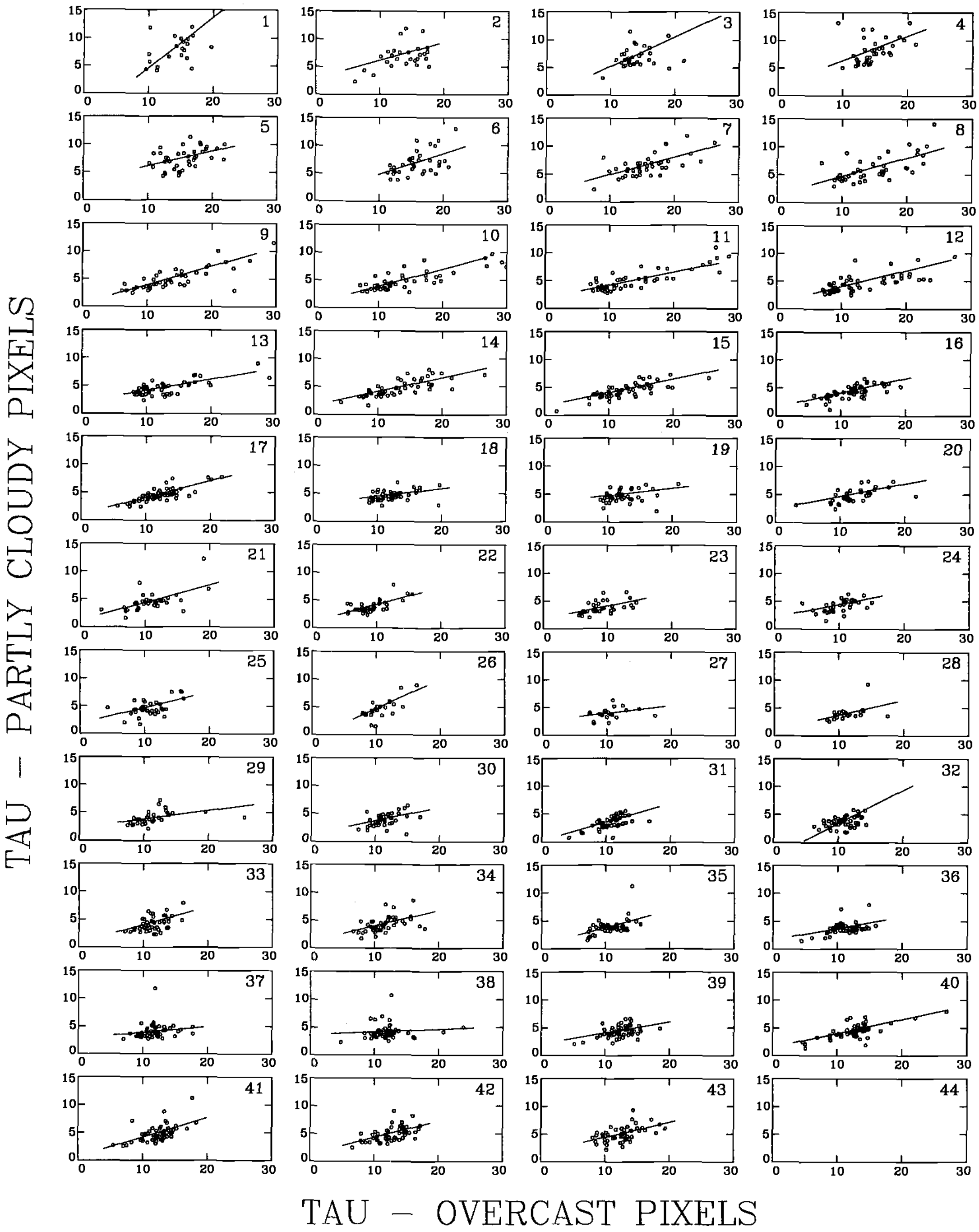

Figure 5.20 Cloud visible optical depths for pixels that were overcast and partly covered by the single-layered, low-level clouds. Observations are for March 1989 for the Pacific ocean. Each sub-figure is for a 2.5°-latitude band. The latitudes are given in Table 5.2. Each point gives monthly means of a 2.5° × 2.5° region within the 2.5°-latitude band. Straight lines represent the least-squares fits. Empty boxes indicate sparse or no observations.

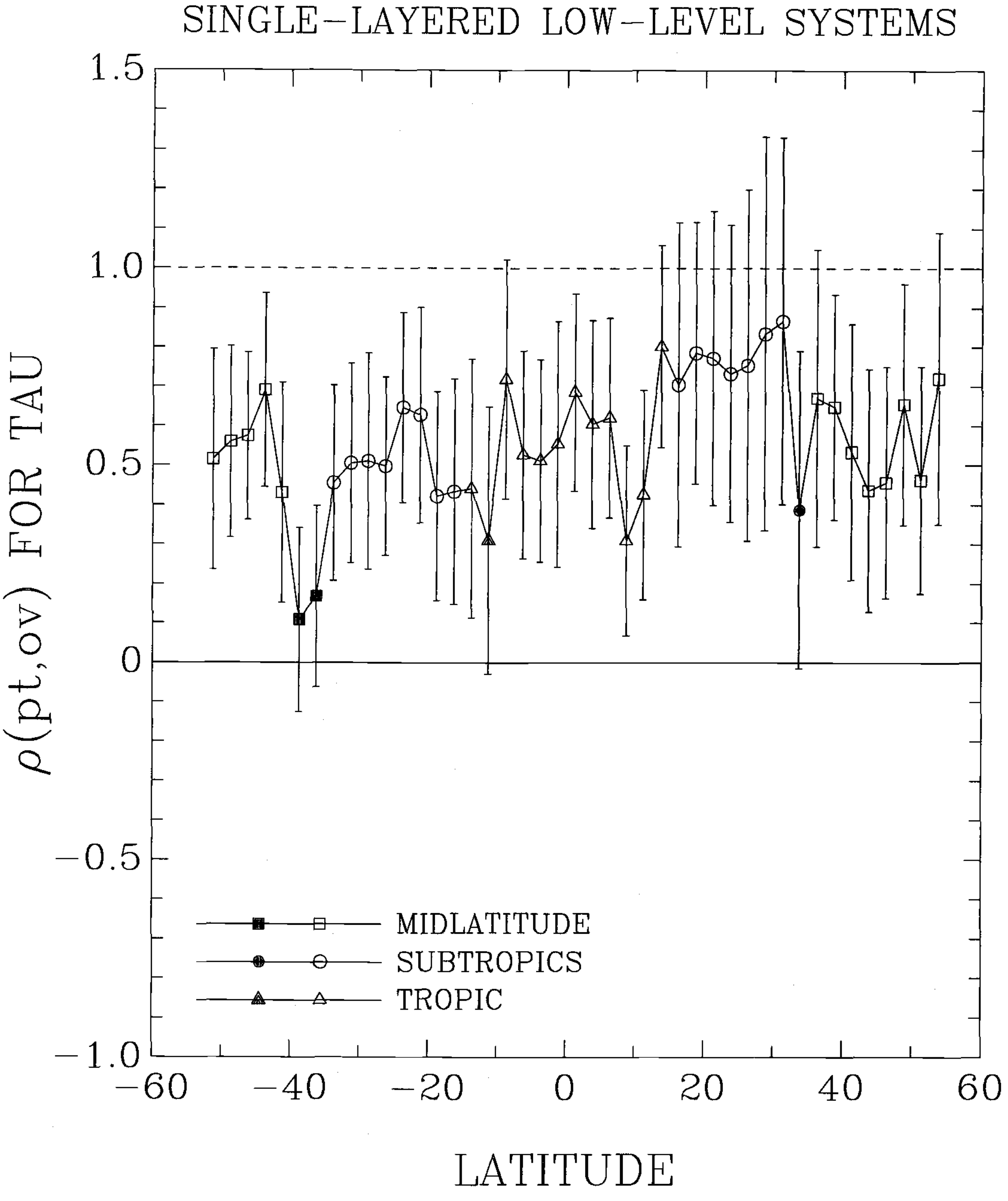

Figure 5.21 Correlation coefficients of cloud visible optical depths for the overcast and partly cloudy pixels obtained from the longitudinal variations shown in Figure 5.20. Each data is for a 2.5°-latitude band. Open symbols indicate that the coefficients are significant at the 90% confidence level. Error bars indicate the 90% confidence intervals.

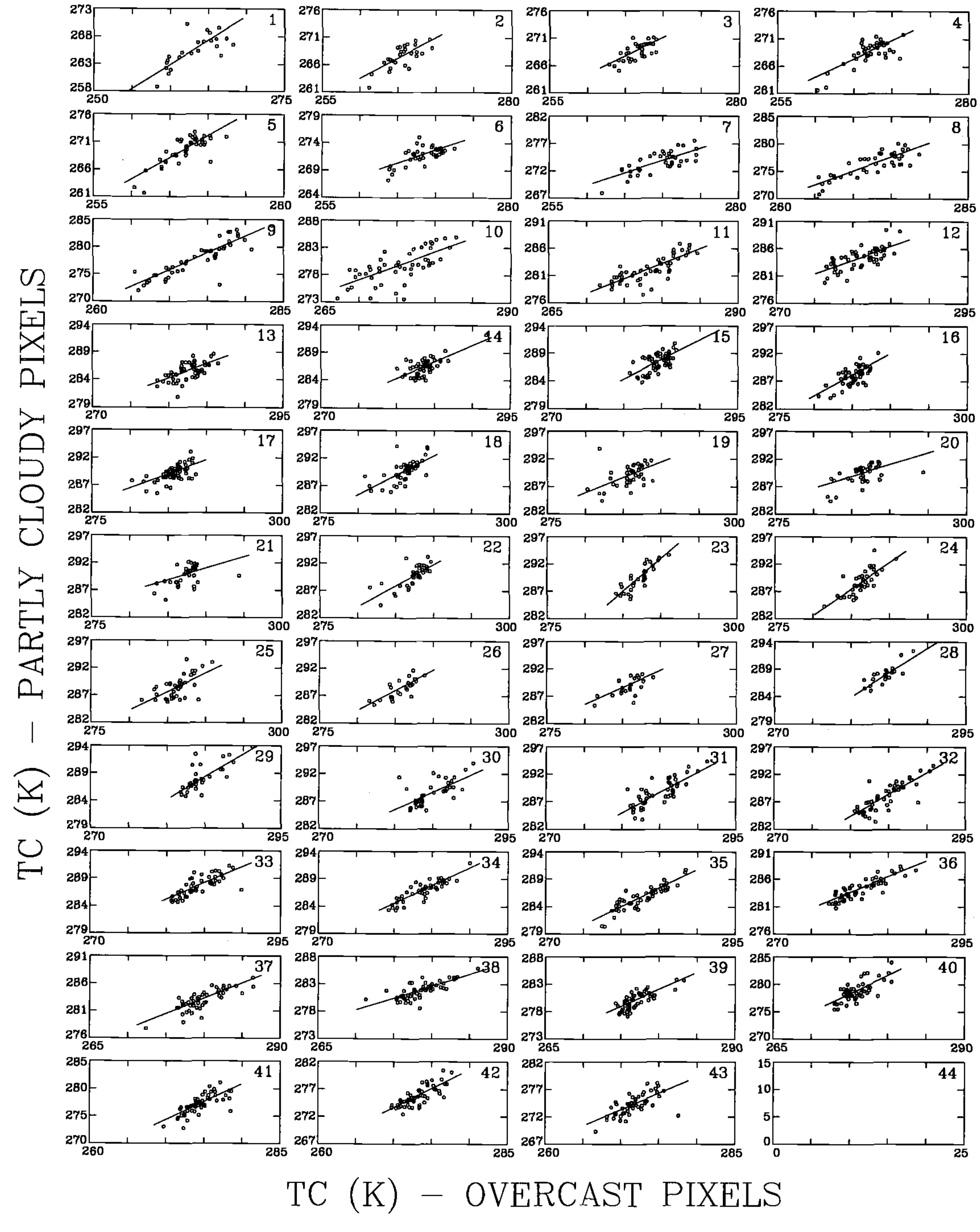

Figure 5.22 Same as Figure 5.20, except for cloud top emission temperatures (K).

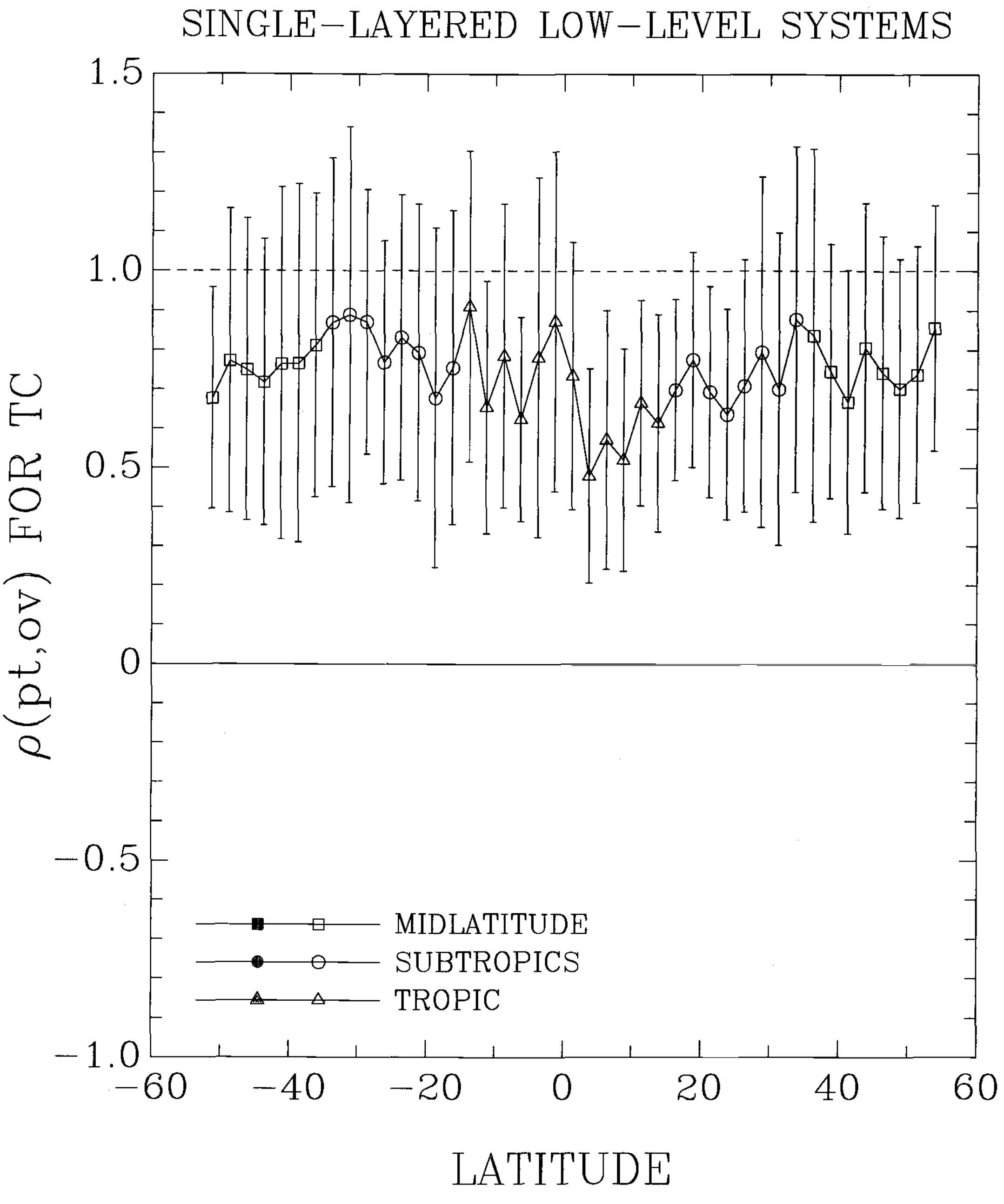

Figure 5.23 Same as Figure 5.21, except that the correlation coefficients are for the cloud top emission temperatures shown in Figure 5.22.

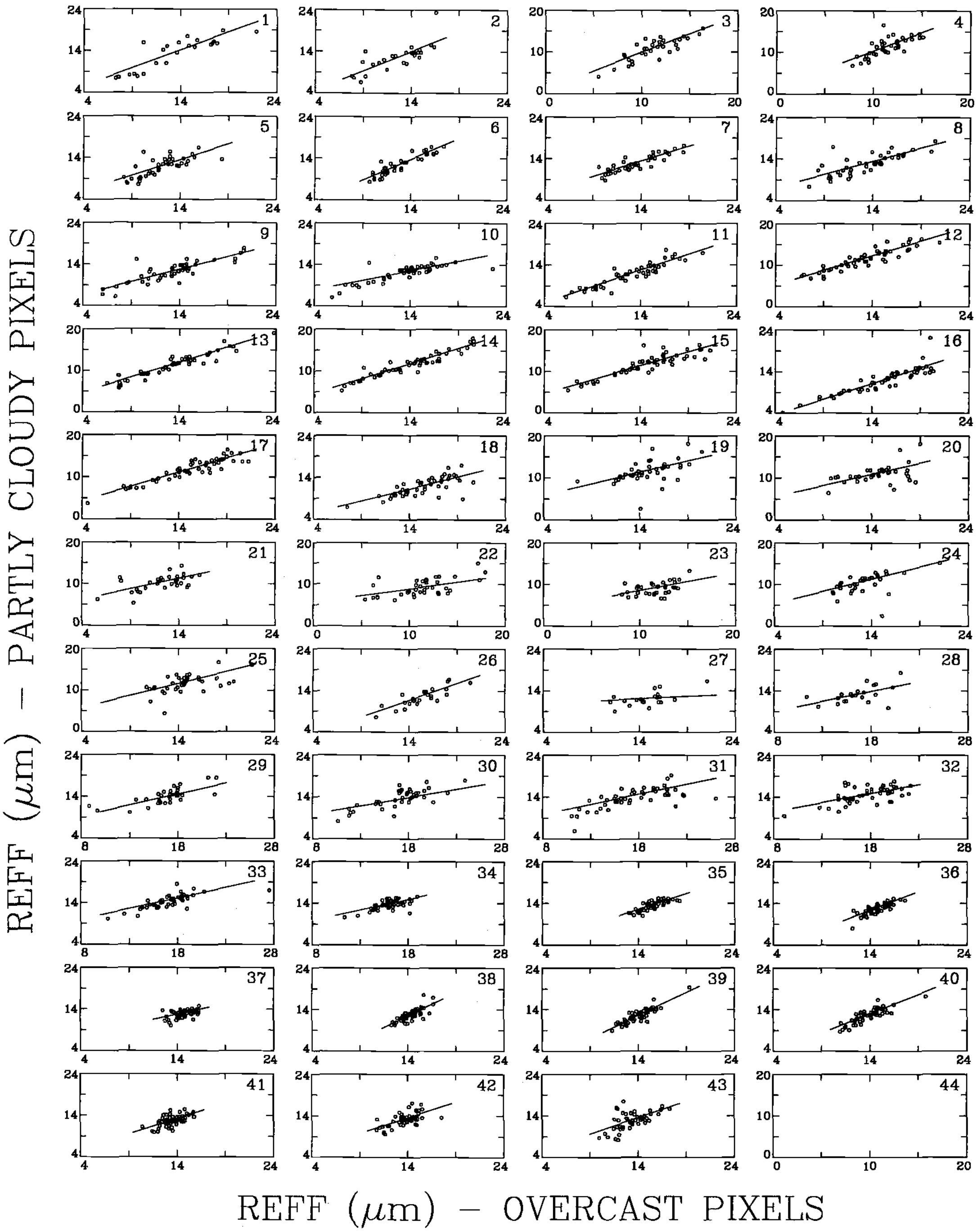

Figure 5.24 Same as Figure 5.20, except for cloud droplet effective radii (μm).

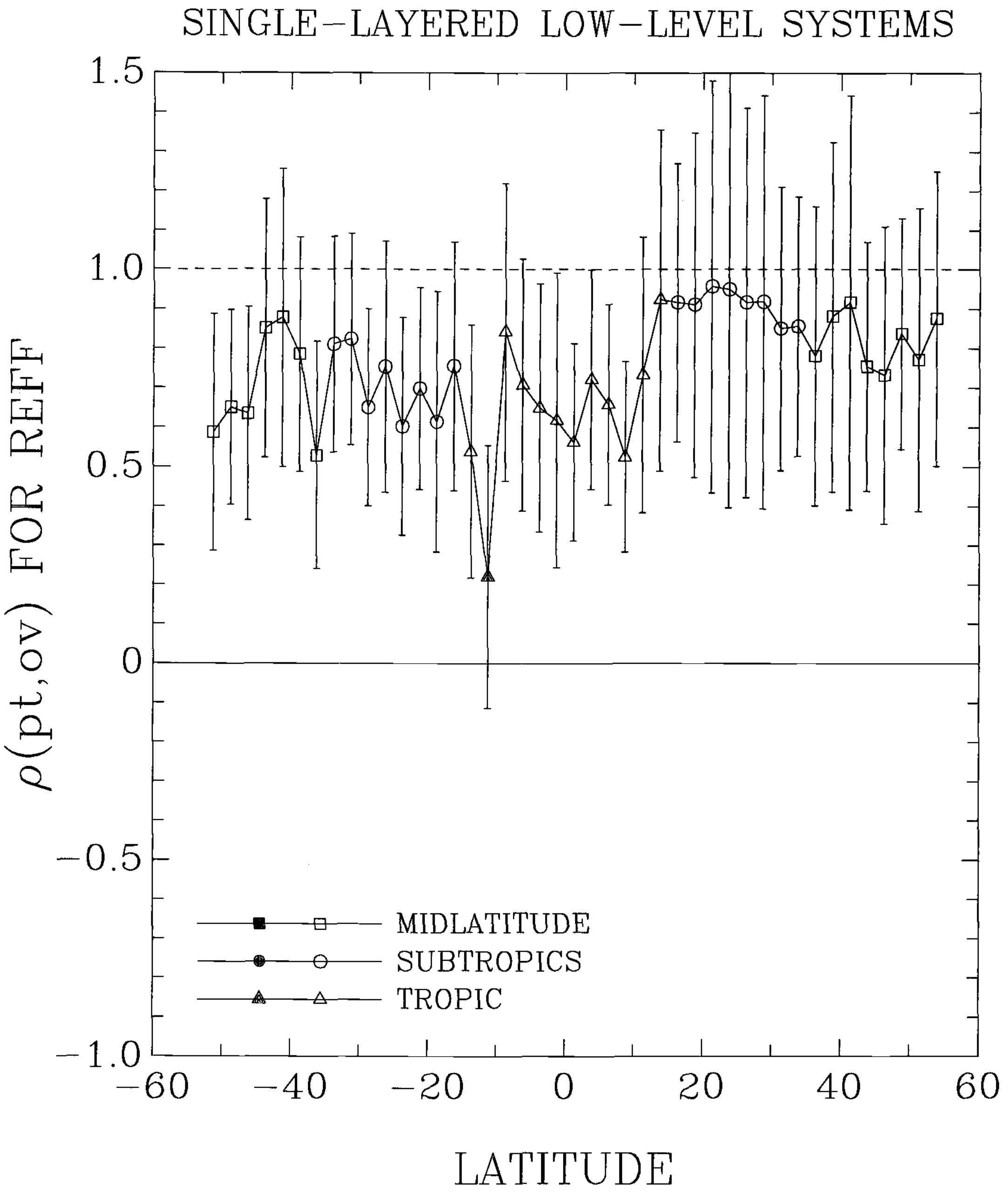

Figure 5.25 Same as Figure 5.21, except that the correlation coefficients are for the cloud droplet effective radii shown in Figure 5.24.

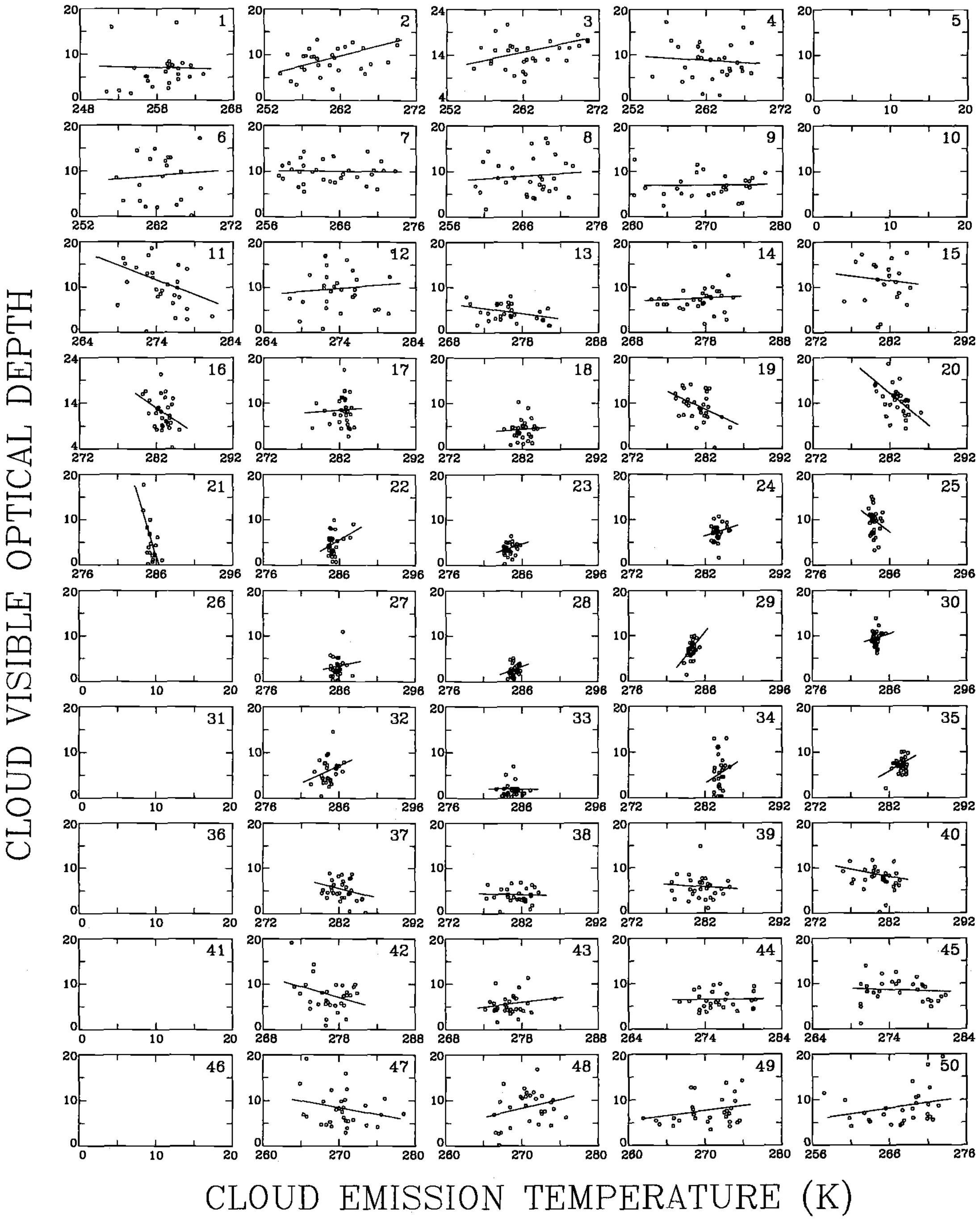

Figure 5.26 Same as Figure 5.4, except that the visible optical depths and cloud temperatures were obtained by ISCCP for low-level clouds.

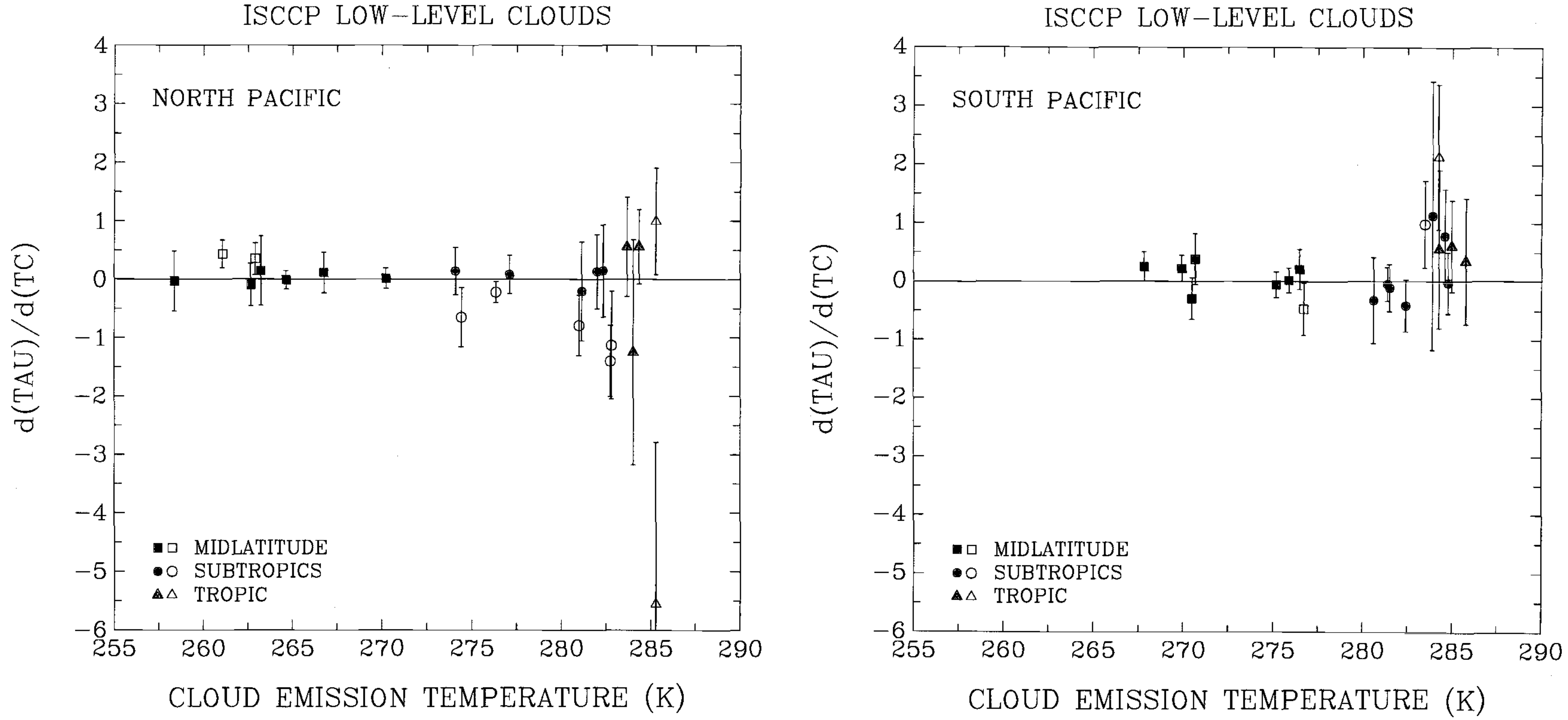

Figure 5.27 Same as Figure 5.5, except that $d(TAU)/d(TC)$ and the monthly-mean cloud temperatures are for the ISCCP low-level clouds shown in Figure 5.26.

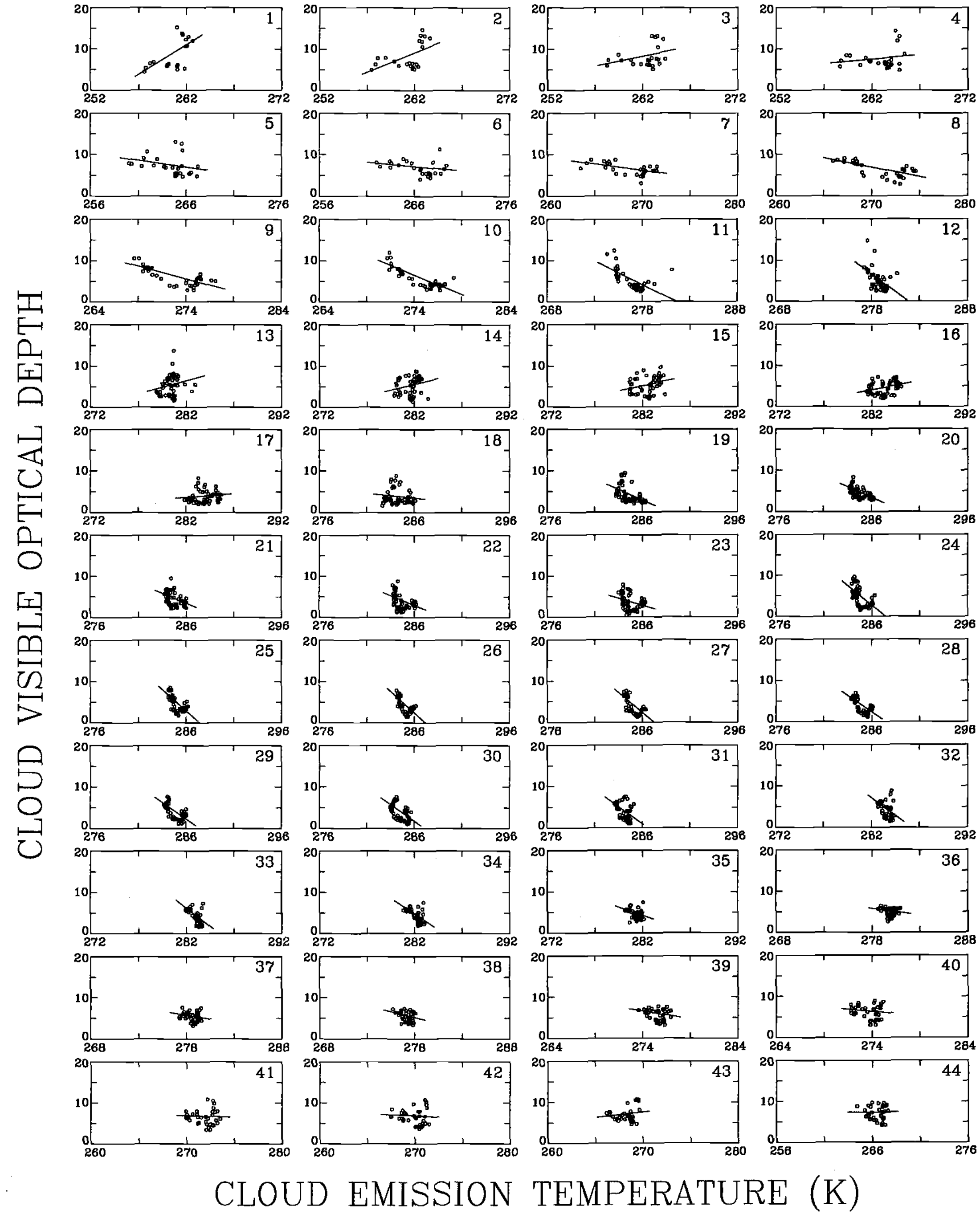

Figure 5.28 Same as Figure 5.6, except that the visible optical depths and cloud temperatures were obtained by ISCCP for low-level clouds.

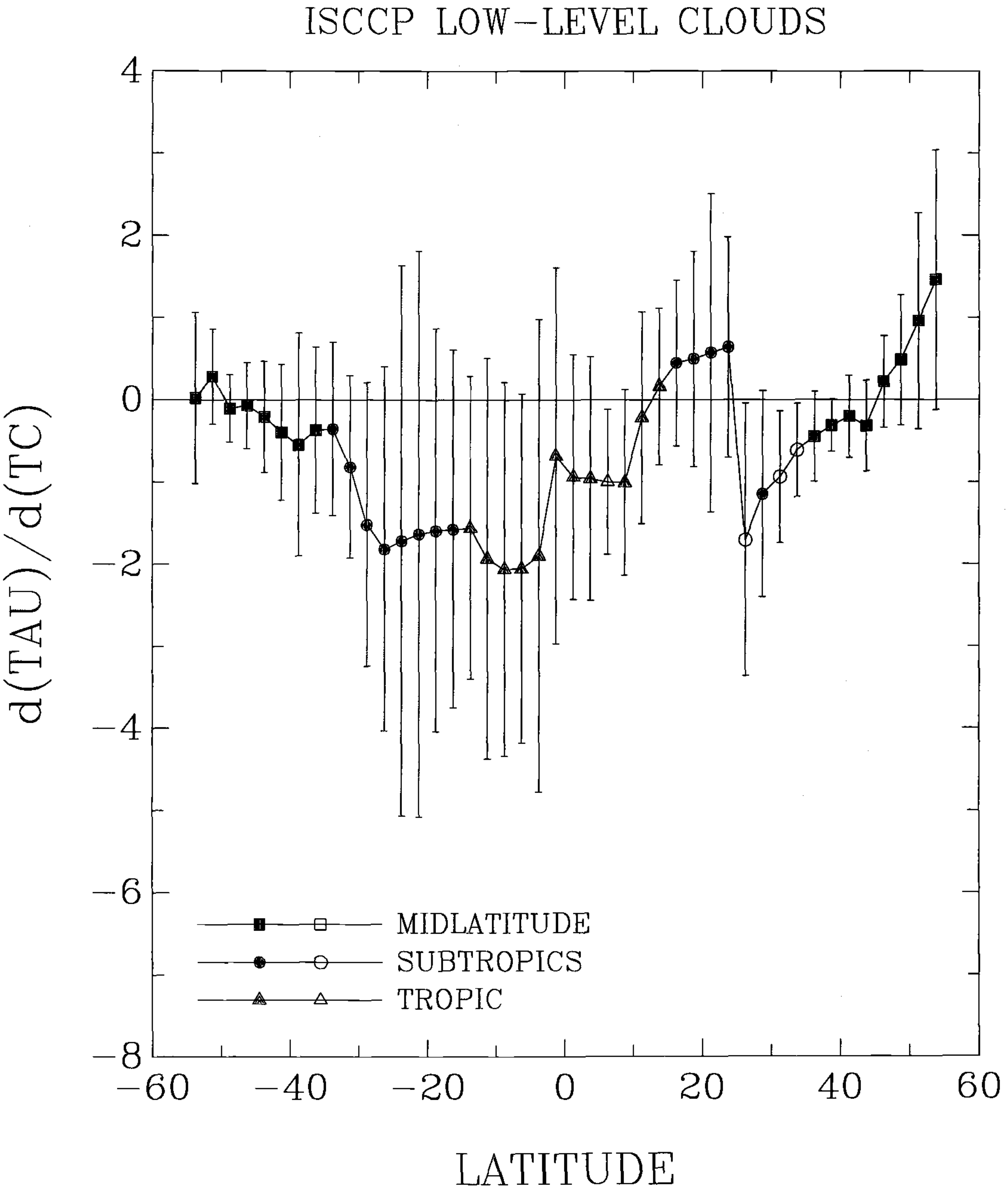

Figure 5.29 Same as Figure 5.7, except that the values of $d(TAU)/d(TC)$ are for the ISCCP low-level clouds shown in Figure 5.28.

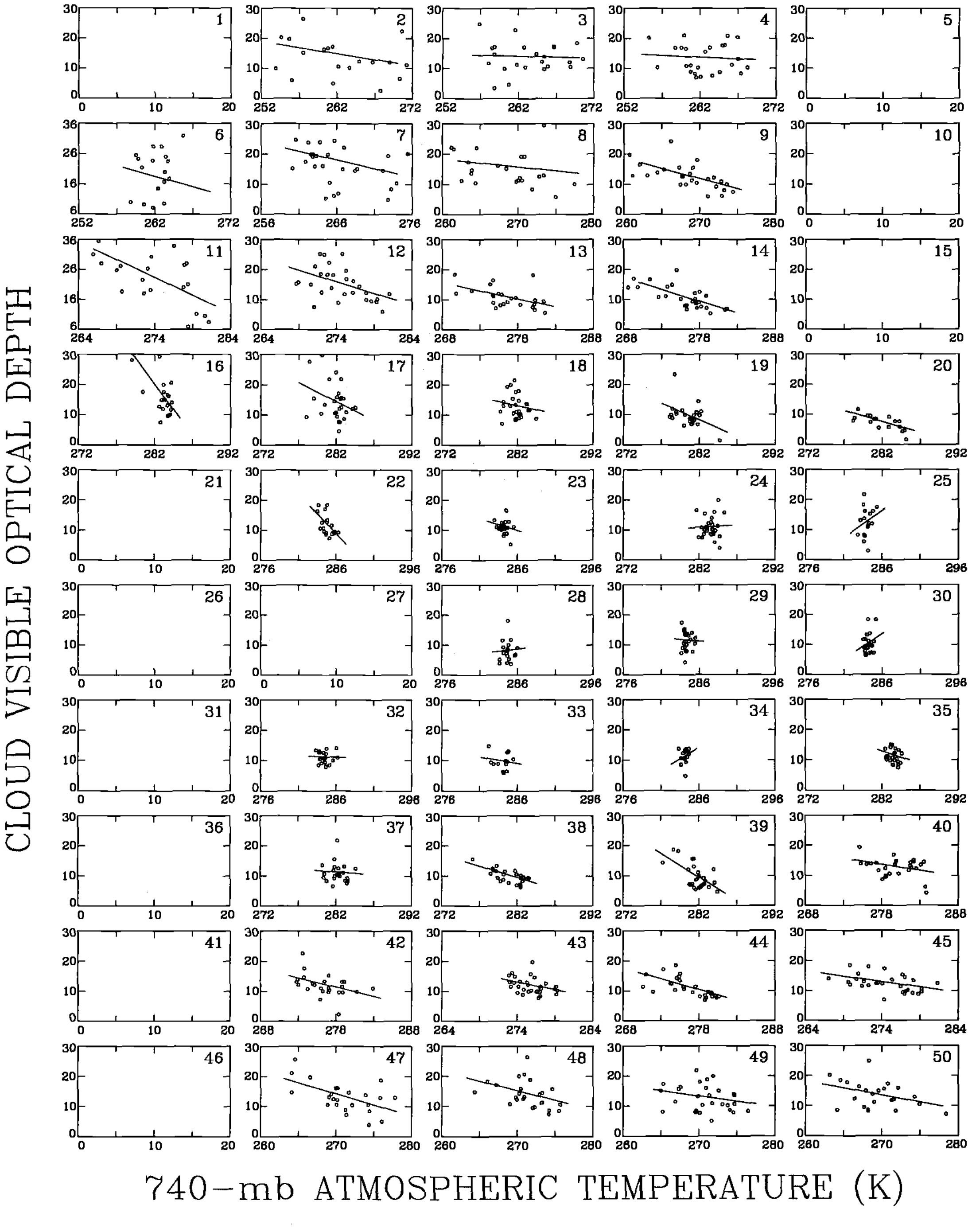

Figure 5.30 Same as Figure 5.4, except for cloud visible optical depth and 740-mb atmospheric temperature.

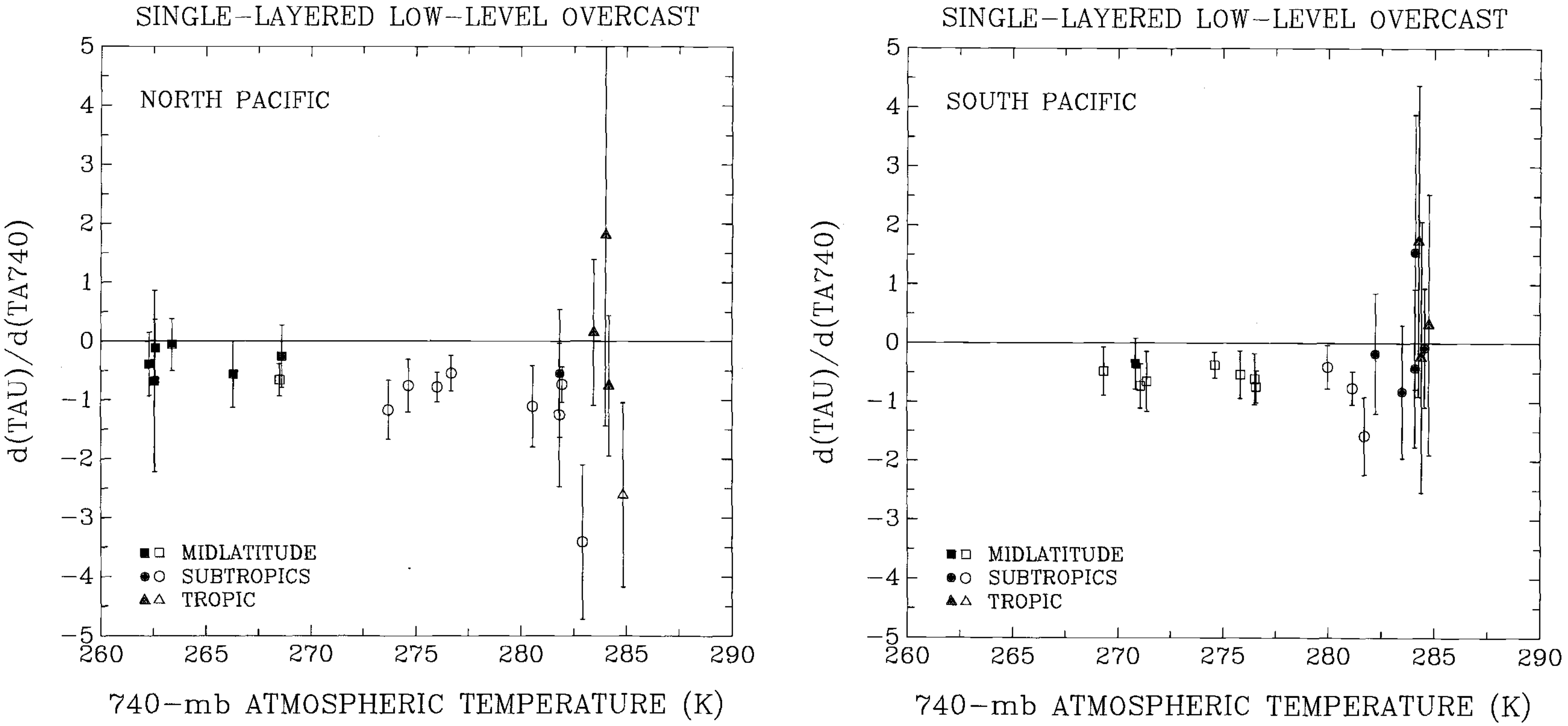

Figure 5.31 Same as Figure 5.5, except for $d(TAU)/d(TA740)$ and the monthly-mean 740-mb atmospheric temperatures shown in Figure 5.30.

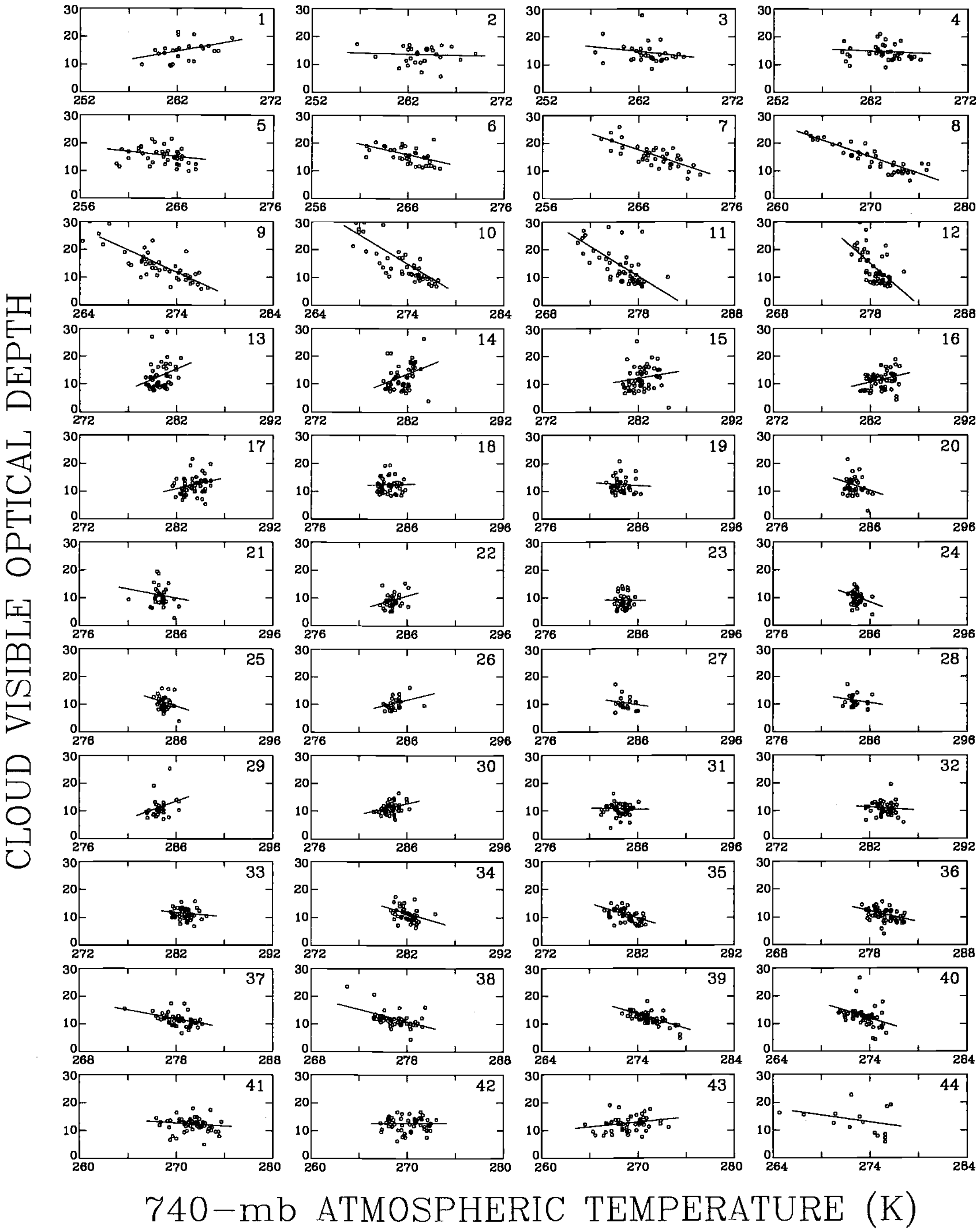

Figure 5.32 Same as Figure 5.6, except for cloud visible optical depth and 740-mb atmospheric temperature.

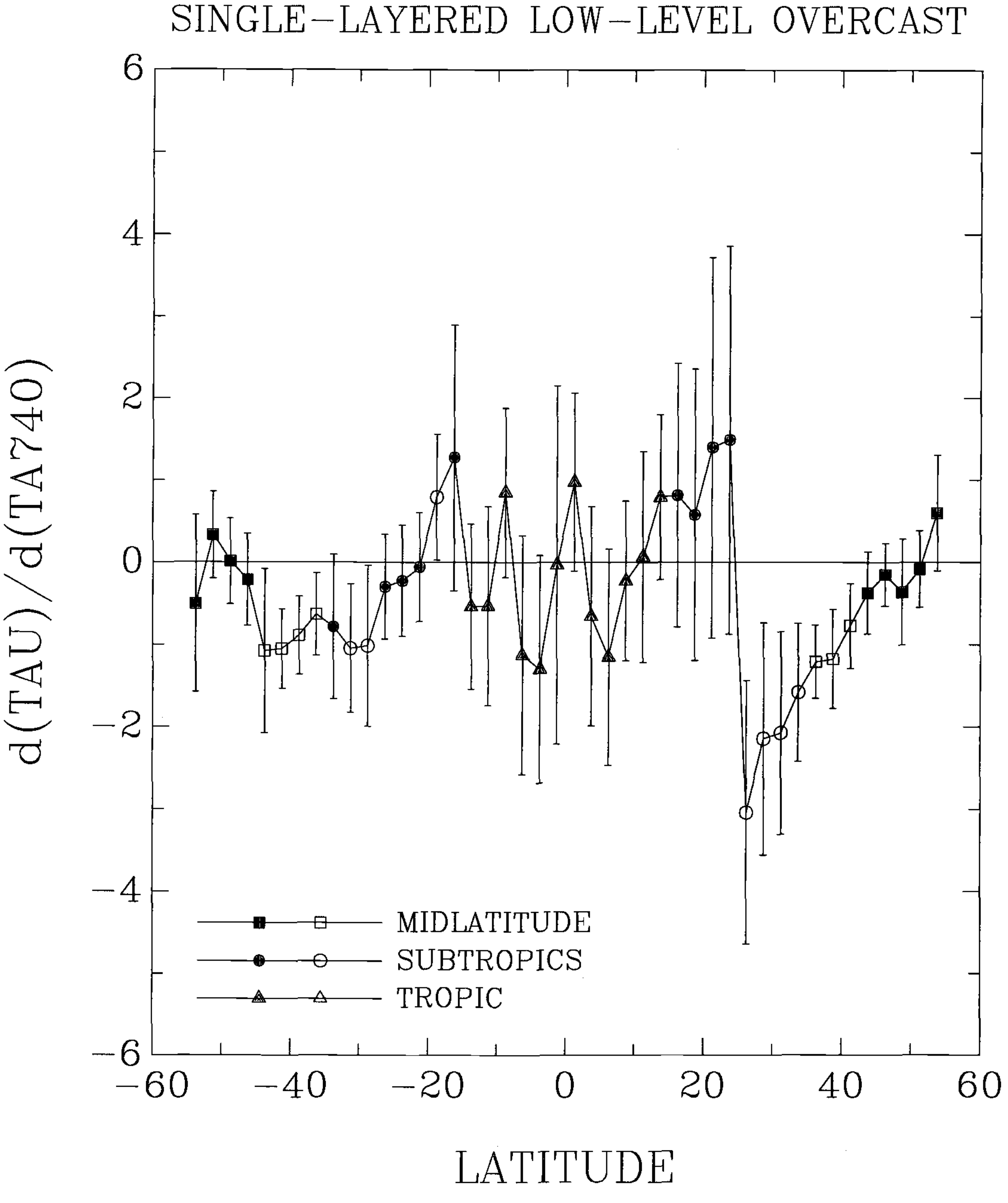

Figure 5.33 Same as Figure 5.7, except for $d(TAU)/d(TA740)$ shown in Figure 5.32.

Figure 5.14 shows the day-to-day variations of cloud visible optical depths obtained for the partly cloudy and overcast pixels. Figure 5.15 shows the correlation coefficients of the cloud visible optical depths for the partly cloudy and overcast pixels from the day-to-day variations shown in Figure 5.14. Figures 5.16 and 5.17 show the correlations of cloud top emission temperatures for the partly cloudy and overcast pixels from the day-to-day variations. Figures 5.18 and 5.19 show the correlations of cloud droplet effective radii for the partly cloudy and overcast pixels from the day-to-day variations. Likewise, Figures 5.20–5.25 show the correlations from the longitudinal variations. In conclusion, there are strong correlations between properties retrieved for partly cloudy pixels and those retrieved for overcast pixels so that, while the properties for the partly cloudy pixels are biased, the relationships between cloud visible optical depth and cloud top emission temperature are relatively unaffected.

5.4.4 ISCCP low-level clouds and 740–mb atmospheric temperature

Figure 5.26 shows the same as Figure 5.4 and Figure 5.27 shows the same as Figure 5.5, except that these results were obtained by ISCCP for low-level clouds. Although most of the regions show no significant correlation or weak correlations, negative correlations are found in northern subtropics and positive correlations are found in the southern Pacific and northern midlatitudes. These results are similar to those obtained by Tselioudis et al. for the northern hemisphere. They found significant negative correlations in most of the subtropics and part of the midlatitudes. Tselioudis et al. did not study the southern hemisphere because the variation in ISCCP cloud temperatures (the 740-mb level temperature) was often too small to obtain a statistically significant correlation between cloud visible optical depth and temperature. As shown in Figure 5.26, the variations of ISCCP cloud temperatures are small for the tropics and subtropics.

The longitudinal correlations obtained by ISCCP for low-level clouds are shown in Figures 5.28 and 5.29. Although negative correlations appear in most of the regions, they are generally weak. Negative correlations are statistically significant for latitudes $>\sim$ 25°N. These results are similar to those obtained by Tselioudis et al. (1992). For the tropical and southern Pacific oceans, ISCCP cloud temperature variations are too small to provide statistically significant correlations between the visible optical depths and the cloud temperatures.

Figures 5.30 and 5.31 show day-to-day correlations between cloud visible optical depths for pixels overcast by single-layered, low-level clouds and the 740-mb atmospheric temperatures. As with the cloud top emission temperatures, significant negative correlations exist between the cloud visible optical depths and the 740-mb atmospheric temperatures for most of the subtropics and midlatitudes in both the northern and southern Pacific ocean. The longitudinal correlations between the cloud visible optical depths for pixels overcast by single-layered, low-level clouds and the 740-mb atmospheric temperatures are shown in Figures 5.32 and 5.33. The correlations are generally negative in the subtropics and midlatitudes, but a few cases of positive correlations were also encountered.

5.5 Variations of cloud visible optical depth with sea surface temperature

The relationship between cloud visible optical depth and the sea surface temperature is also examined for pixels that were overcast by the single-layered, low-level clouds. Figures 5.34 and 5.35 show the day-to-day correlations obtained in the same way as in Figures 5.4 and 5.5. Figures 5.36 and 5.37 show the 2.5°-longitudinal correlations obtained in the same way as in Figures 5.6 and 5.7. Little correlation is found between the cloud visible optical depth and the sea surface temperature. Negative day-to-day correlations are found in a few regions and positive longitudinal correlations are found near 30°N.

5.6 Implications of the negative relationship between cloud visible optical depth and cloud top emission temperature

ISCCP C1 data for the Pacific ocean and March 1989 show negative day-to-day and longitudinal correlations between low-level cloud visible optical depths and cloud temperatures. While few statistically significant correlations are found for tropical and subtropical regions, the negative correlations obtained for the northern subtropics and midlatitudes agree with those obtained by Tselioudis et al. (1992) using ISCCP data for 1984 and 1985. The negative relationship between low-level cloud visible optical depth and cloud temperature obtained with ISCCP data is thought to be due to the breakup of clouds.

To illustrate further the role of broken clouds, Figures 5.38 and 5.39 show the day-to-day correlations between cloud visible optical depth and cloud cover fraction obtained for pixels that were partly covered by single-layered, low-level clouds as identified by the spatial coherence method. Figures 5.40 and 5.41 show the same, except for the 2.5°-longitudinal correlations. These results show that as the mean cloud cover fraction for the partly cloudy pixels decreases, i.e., clouds become more broken, the retrieved mean cloud visible optical depth also decreases. Figures 5.42-

5.45 show the same as Figures 5.38-5.41, except for the correlations between cloud top emission temperature and cloud cover fraction. These results show that cloud top emission temperature slightly increases with decreasing cloud cover fraction. Combining the decrease in cloud visible optical depth and the increase in cloud top emission temperature, a change in cloud cover fraction for the partly cloudy pixels can give rise to a negative relationship between cloud visible optical depth and cloud temperature when the partly cloudy pixels are assumed to be overcast, as was done by Tselioudis et al. (1992).

However, the cloud visible optical depths and cloud top emission temperatures retrieved for pixels that were overcast by single-layered, low-level clouds are also negatively correlated on a day-to-day and a longitudinal basis. These negative correlations were found to be statistically significant in nearly all regions. On a day-to-day and 2.5°-scale basis, the relationships between cloud visible optical depth and cloud top emission temperature obtained for partly cloudy pixels were similar to those obtained for the overcast pixels. The cloud visible optical depths and cloud top emission temperatures retrieved for partly cloudy pixels appear to be strongly correlated with those retrieved for overcast pixels. Because of the strong correlations between partly cloudy and overcast pixels, the relationships between cloud visible optical depth and cloud top emission temperature are relatively unaffected by the fractional cloud cover of the partly cloudy pixels. The effect of cloud breaks in the partly cloudy pixels had little impact on both the temporal and spatial relationships between cloud visible optical depth and cloud emission temperature.

This negative relationship between cloud visible optical depth and cloud top emission temperature is thought to result from the relationship between cloud visible optical depth and cloud vertical extent. Figures 5.46 and 5.47 show the day-to-day correlations between the cloud visible optical depth for overcast pixels and the sea surface-cloud top temperature difference. Figures 5.48 and 5.49 show the 2.5°-longitudinal correlations. Here, the sea surface-cloud top temperature difference, $\Delta T =$ sea surface temperature (SST) minus cloud top temperature (TC), is used as an index of cloud vertical thickness. Low-level cloud optical depths generally increase with an increase in the sea surface-cloud top temperature difference. Interestingly, comparing Figures 5.46–5.49 with Figures 5.4–5.7, the absolute magnitudes of $d(TAU)/d(\Delta T)$ are similar to those of $d(TAU)/d(TC)$. Since sea surface temperatures vary little within a latitude zone (see Figure 4.4), the comparisons show that clouds having a lower temperature, which is further from the sea surface temperature, are often optically thicker than those having a higher temperature, which is closer to the sea surface temperature. Since marine boundary layer clouds usually form with similar cloud base heights and since colder cloud top temperatures indicate higher cloud top altitudes (Betts and Ridgeway, 1989), the positive correlations between cloud visible optical depth and the sea surface-cloud top temperature difference imply that these low-level cloud optical depths may be strongly correlated with the vertical thickness of the cloud layer. It is unfortunate that the cloud base information for these low-level clouds cannot be retrieved using the AVHRR satellite data alone. *In situ* soundings of temperature and humidity are needed to determine the cloud vertical thickness and provide insight into the cloud optical depth and cloud vertical thickness relationship for low-level clouds.

The negative relationship between low-level cloud visible optical depth and cloud top emission temperature obtained here agrees with that obtained by Tselioudis et al. (1992). The negative relationship may simply reflect changes in cloud vertical thickness so that cloud liquid water concentration may still increase with an increase in cloud temperature (Somerville and Remer, 1984). *In situ* observations are needed to determine the relationship between cloud liquid water concentration and cloud temperature. In the next chapter, the relationships between low-level cloud visible optical depth, droplet effective radius, cloud liquid water path, and sea surface-cloud top temperature difference are examined. The role of cloud vertical thickness in determining these low-level cloud properties is explored.

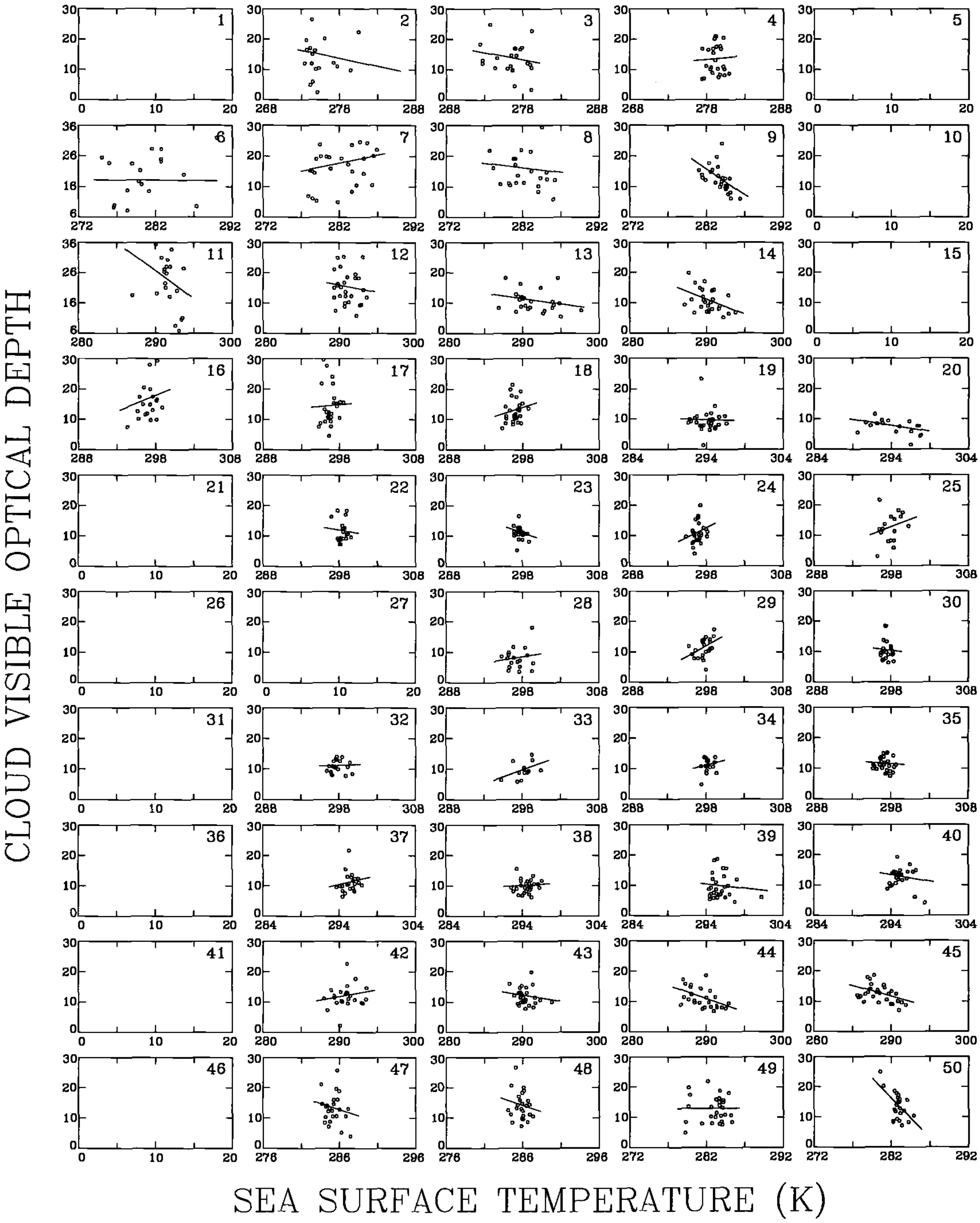

Figure 5.34 Same as Figure 5.4, except for cloud visible optical depth and sea surface temperature.

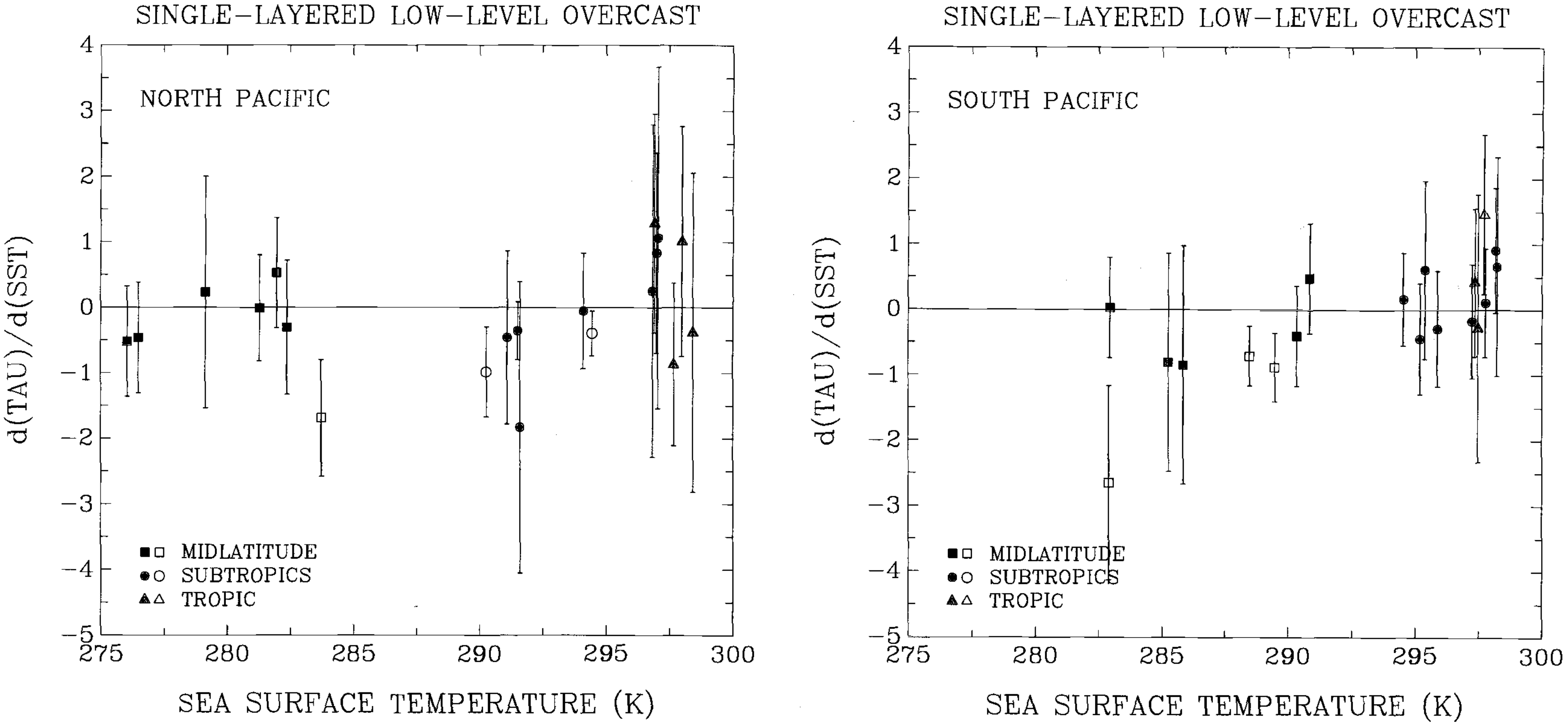

Figure 5.35 Same as Figure 5.5, except for $d(TAU)/d(SST)$ and the monthly-mean sea surface temperatures shown in Figure 5.34.

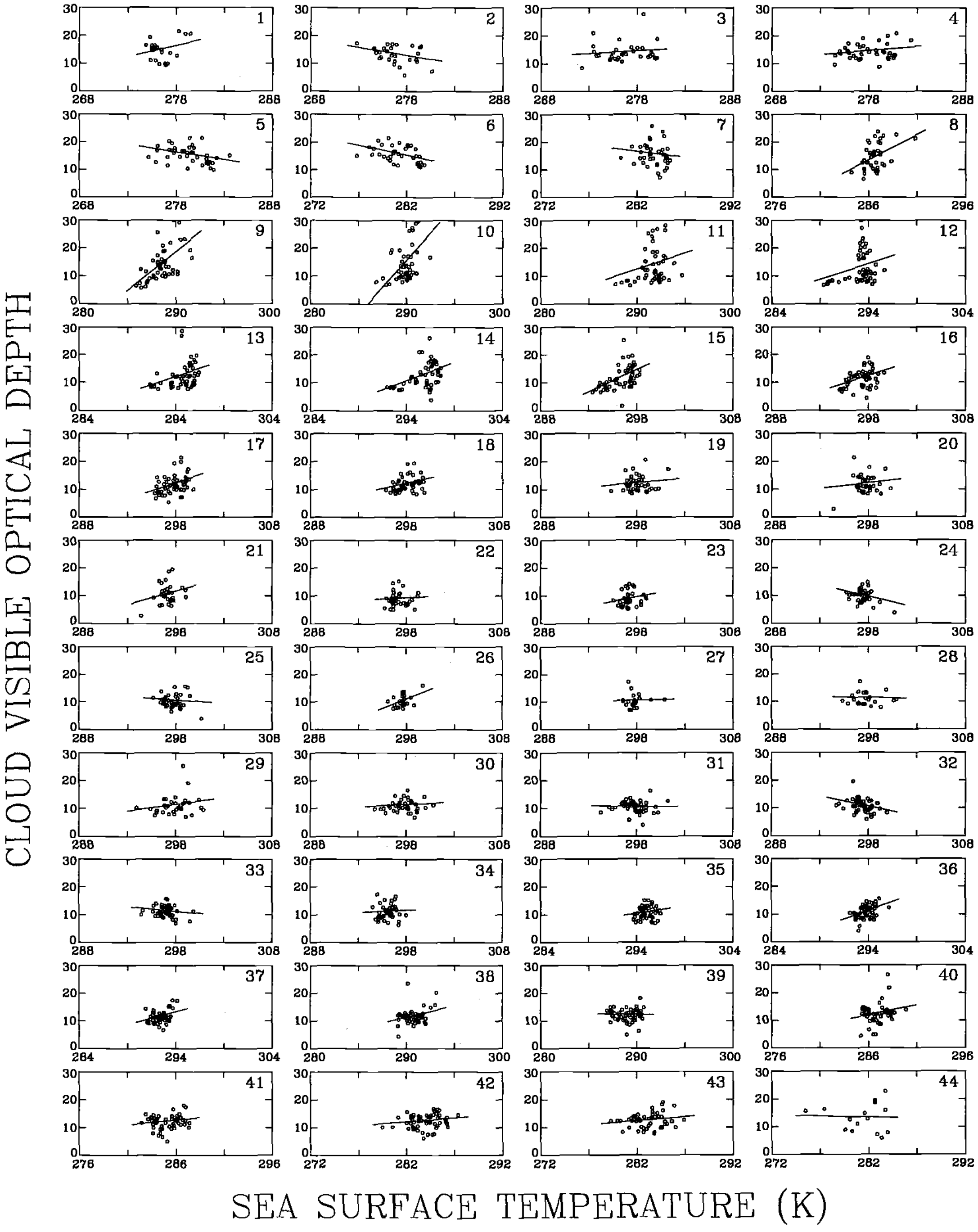

Figure 5.36 Same as Figure 5.6, except for cloud visible optical depth and sea surface temperature.

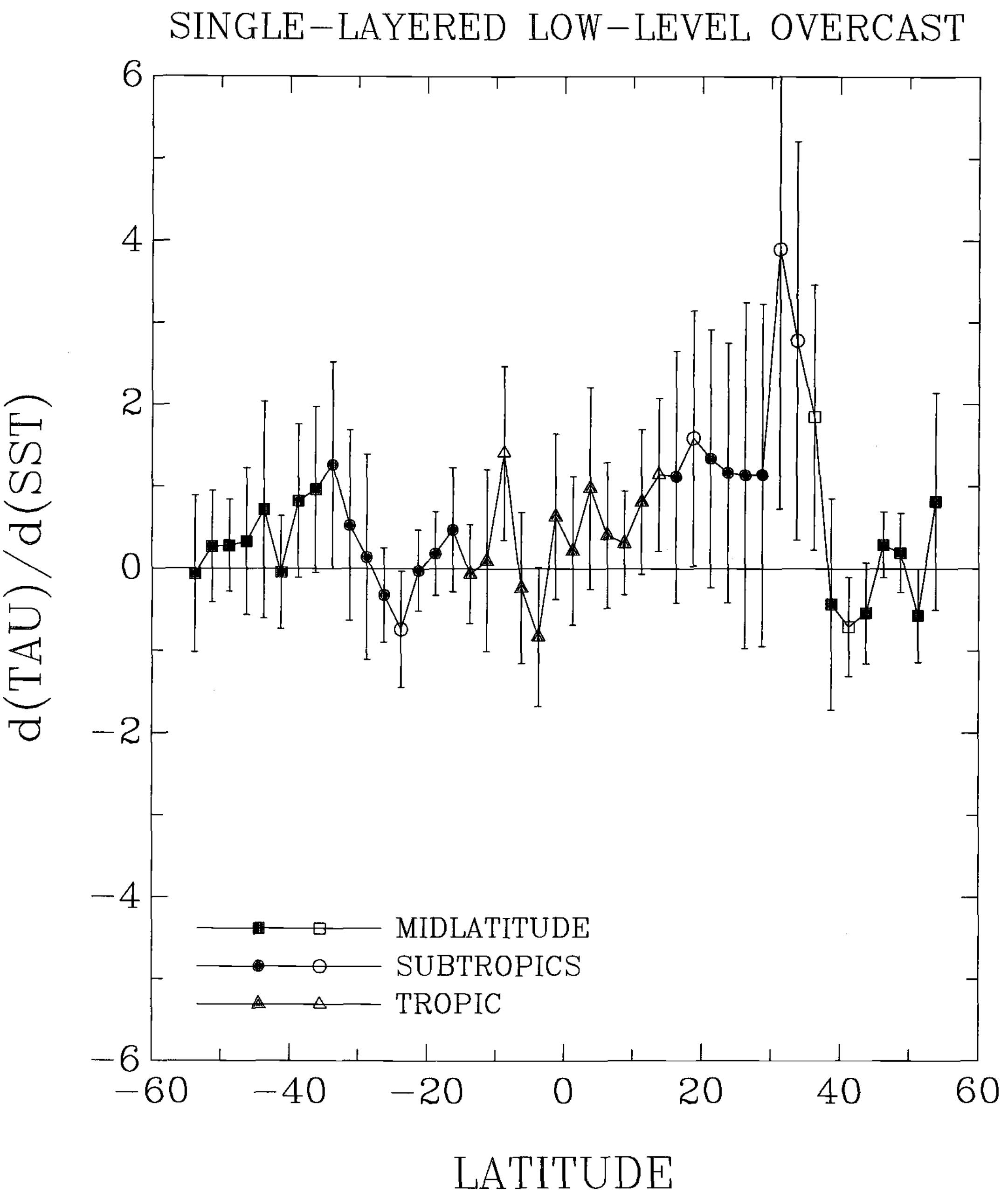

Figure 5.37 Same as Figure 5.7, except for $d(TAU)/d(SST)$ shown in FIgure 5.36.

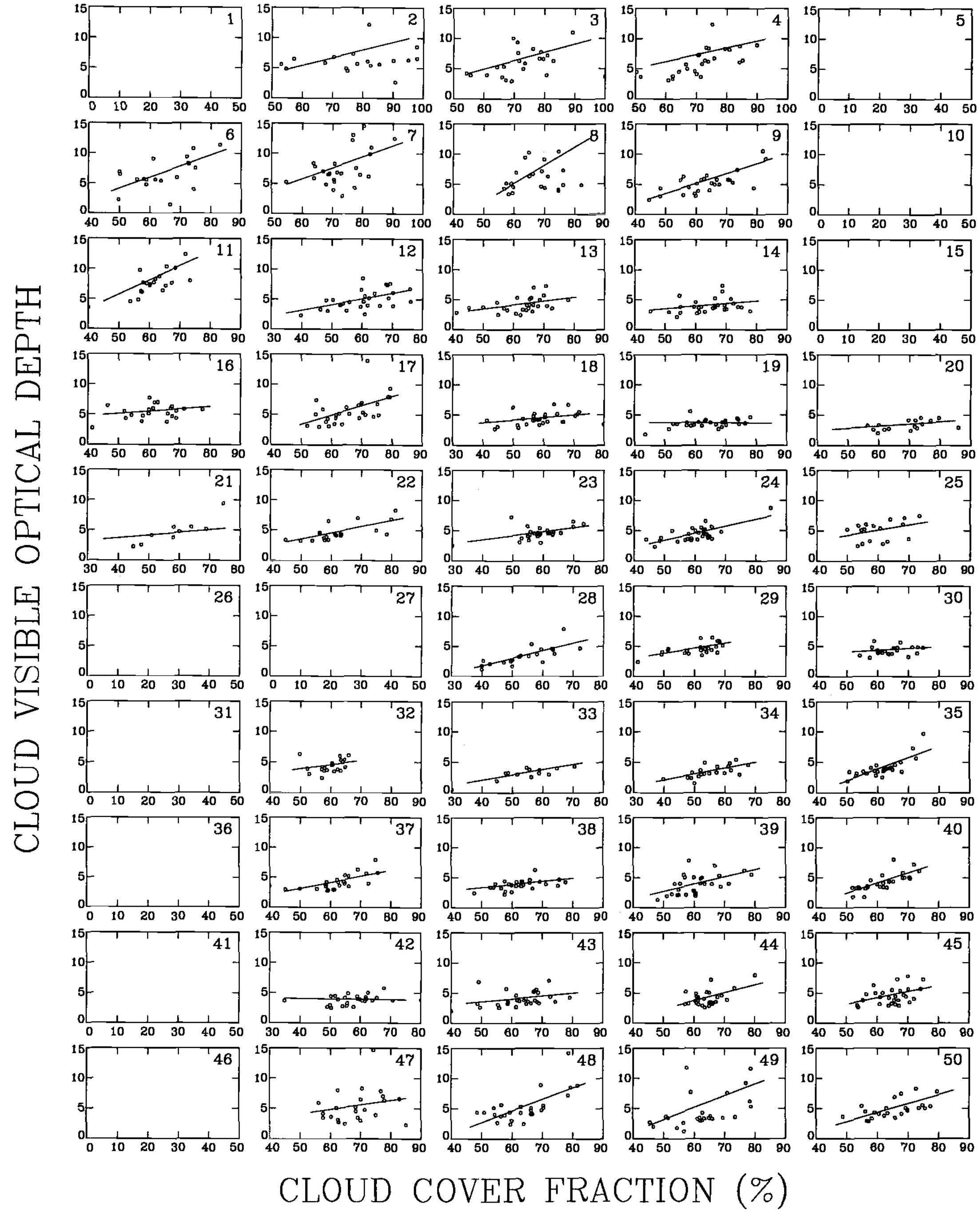

Figure 5.38 Same as Figure 5.4, except for cloud visible optical depth and cloud cover fraction for pixels that were partly covered by single-layered, low-level clouds. The cloud visible optical depths were obtained by assuming that the partly cloudy pixels were overcast.

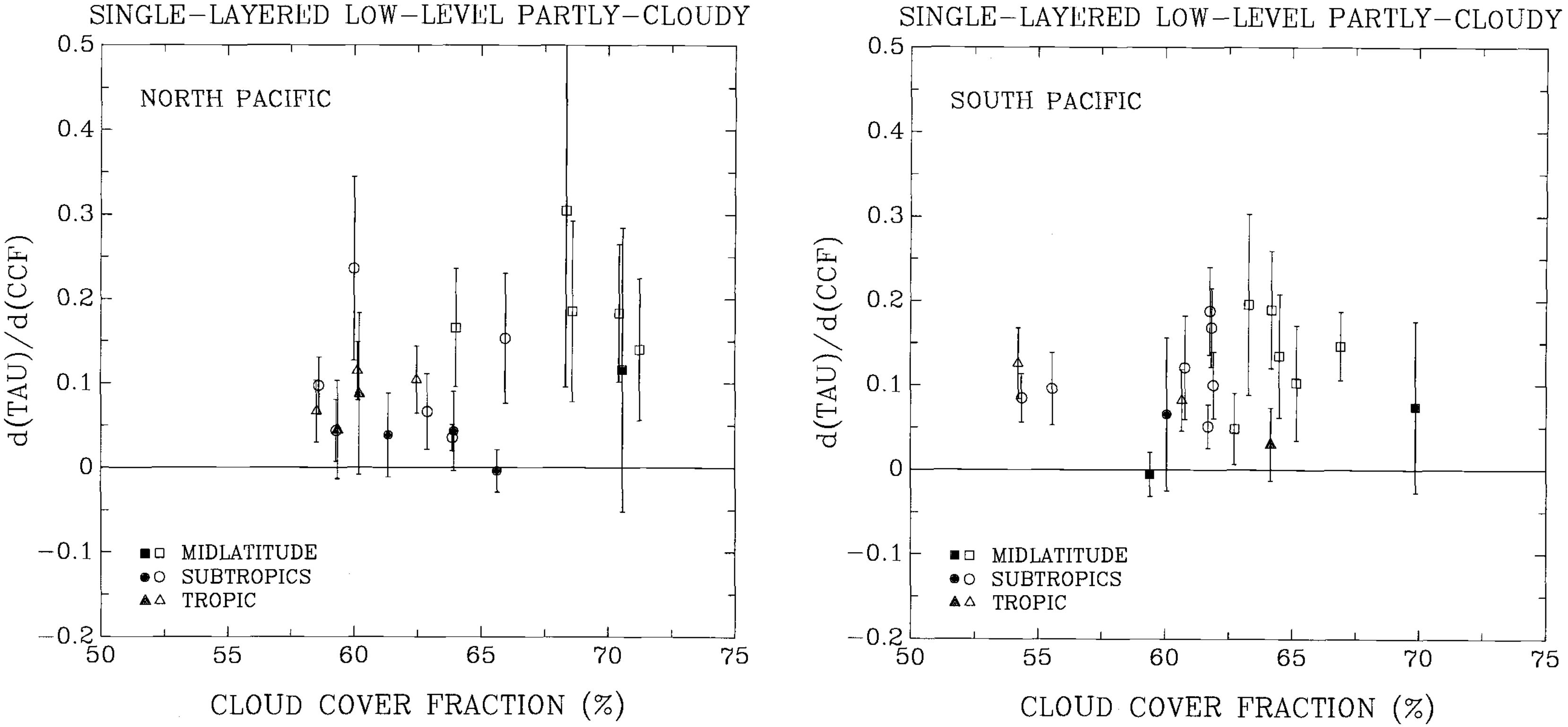

Figure 5.39 Same as Figure 5.5, except for $d(TAU)/d(CCF)$ and the monthly-mean cloud cover fraction for the partly cloudy pixels shown in Figure 5.38.

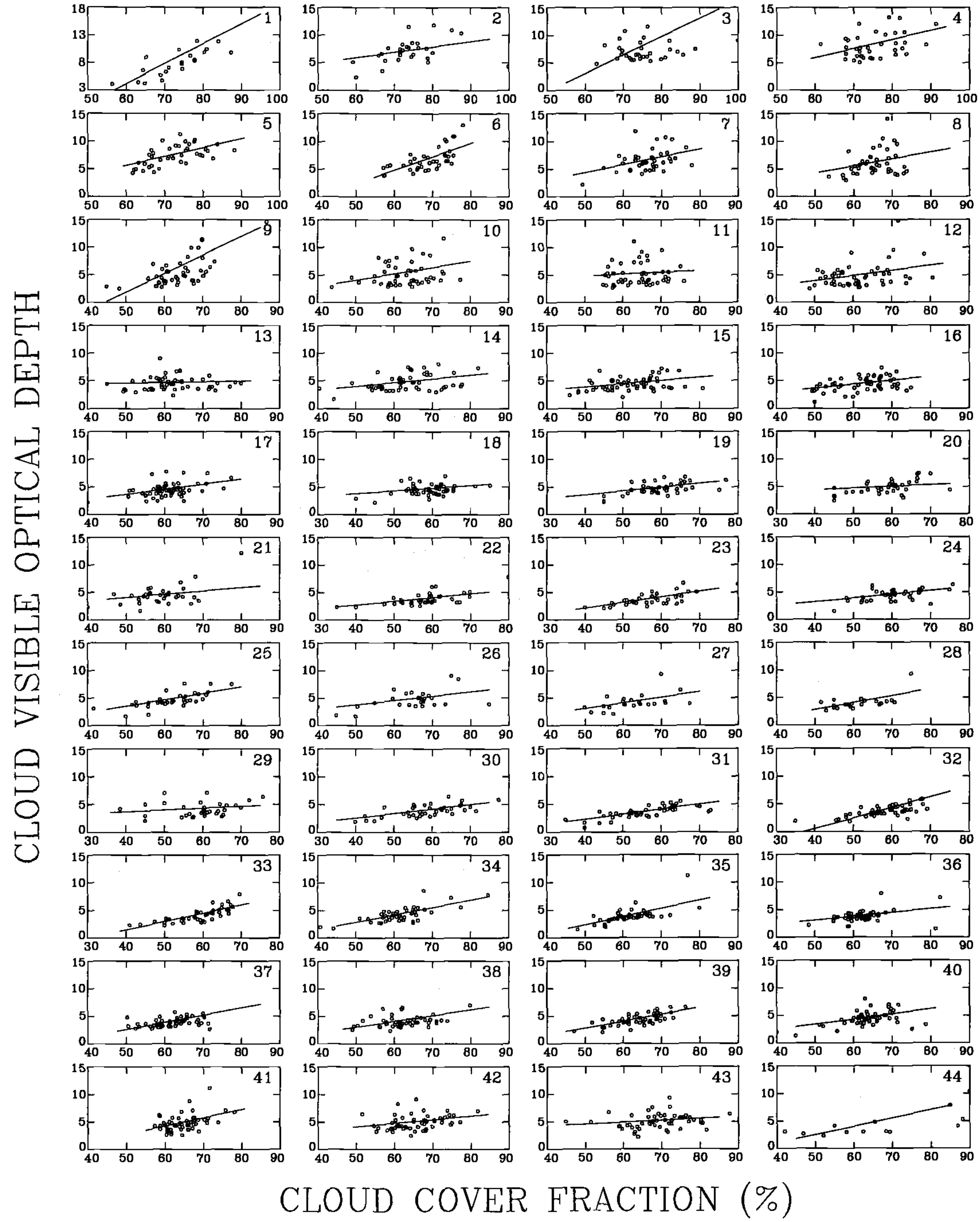

Figure 5.40 Same as Figure 5.6, except for cloud visible optical depth and cloud cover fraction for pixels that were partly covered by single-layered, low-level clouds. The cloud visible optical depths were obtained by assuming that the partly cloudy pixels were overcast.

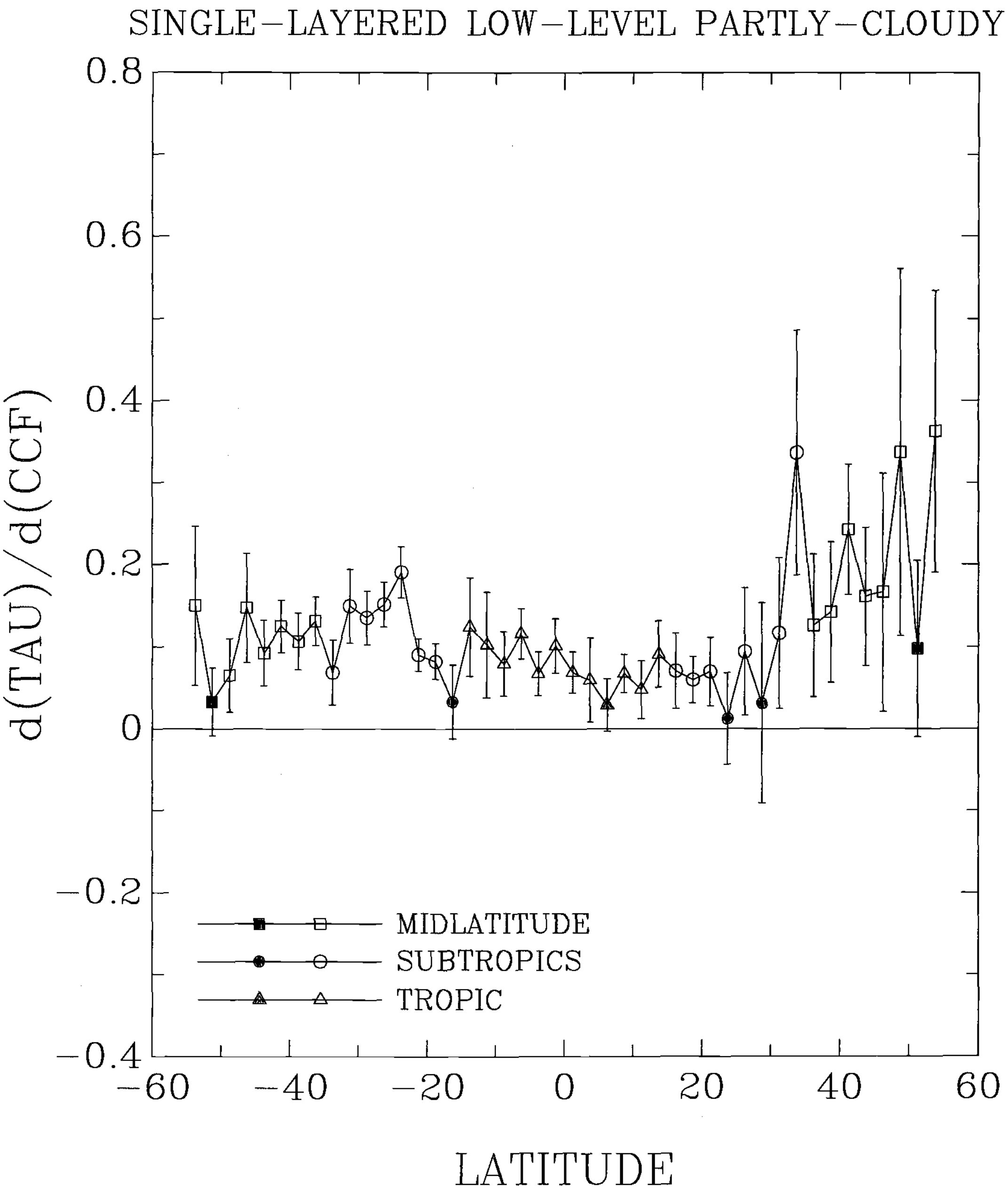

Figure 5.41 Same as Figure 5.7, except for $d(TAU)/d(CCF)$ for the partly cloudy pixels shown in Figure 5.40.

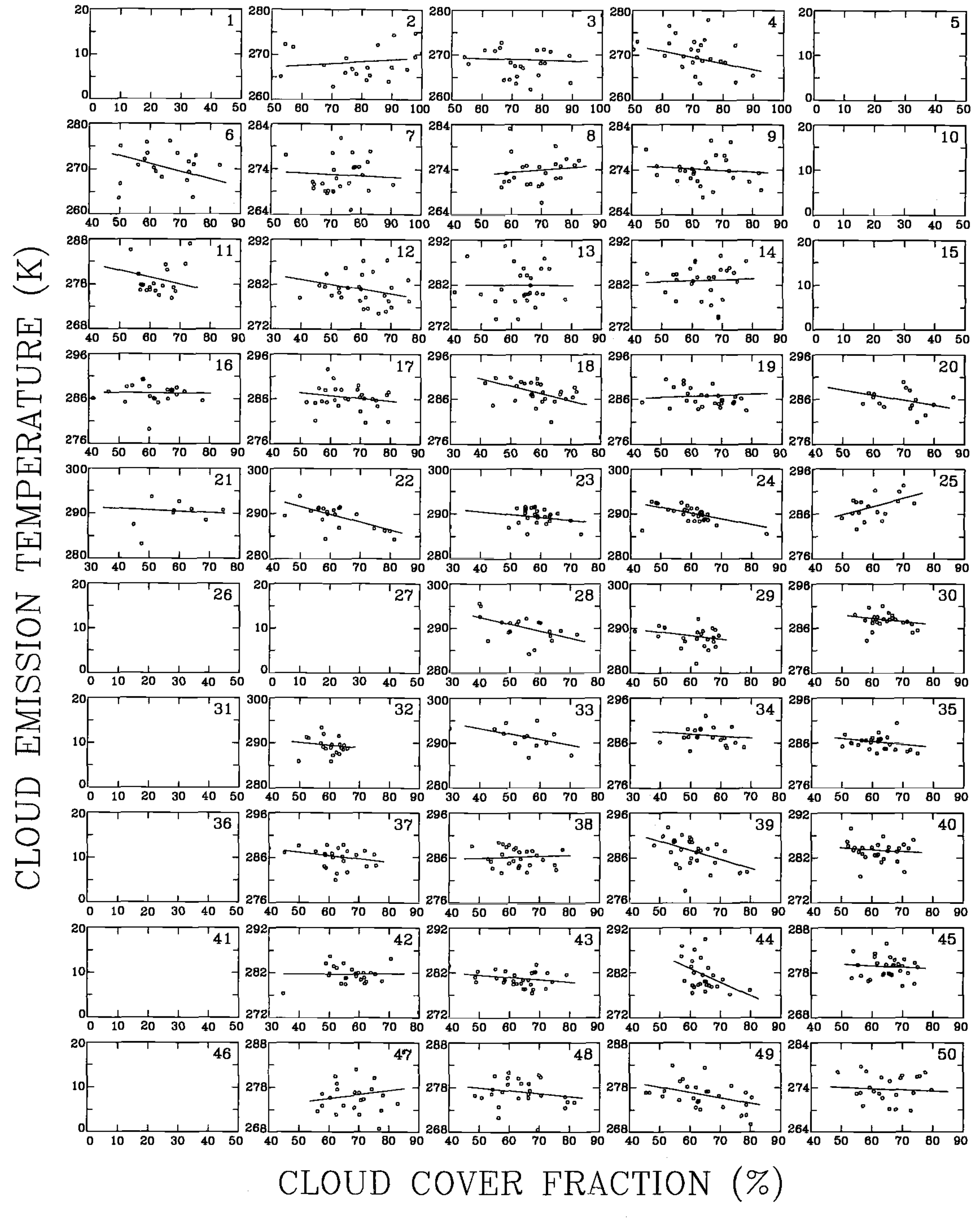

Figure 5.42 Same as Figure 5.4, except for cloud top emission temperature and cloud cover fraction for pixels that were partly covered by single-layered, low-level clouds. The cloud top emission temperatures were obtained by assuming that the partly cloudy pixels were overcast.

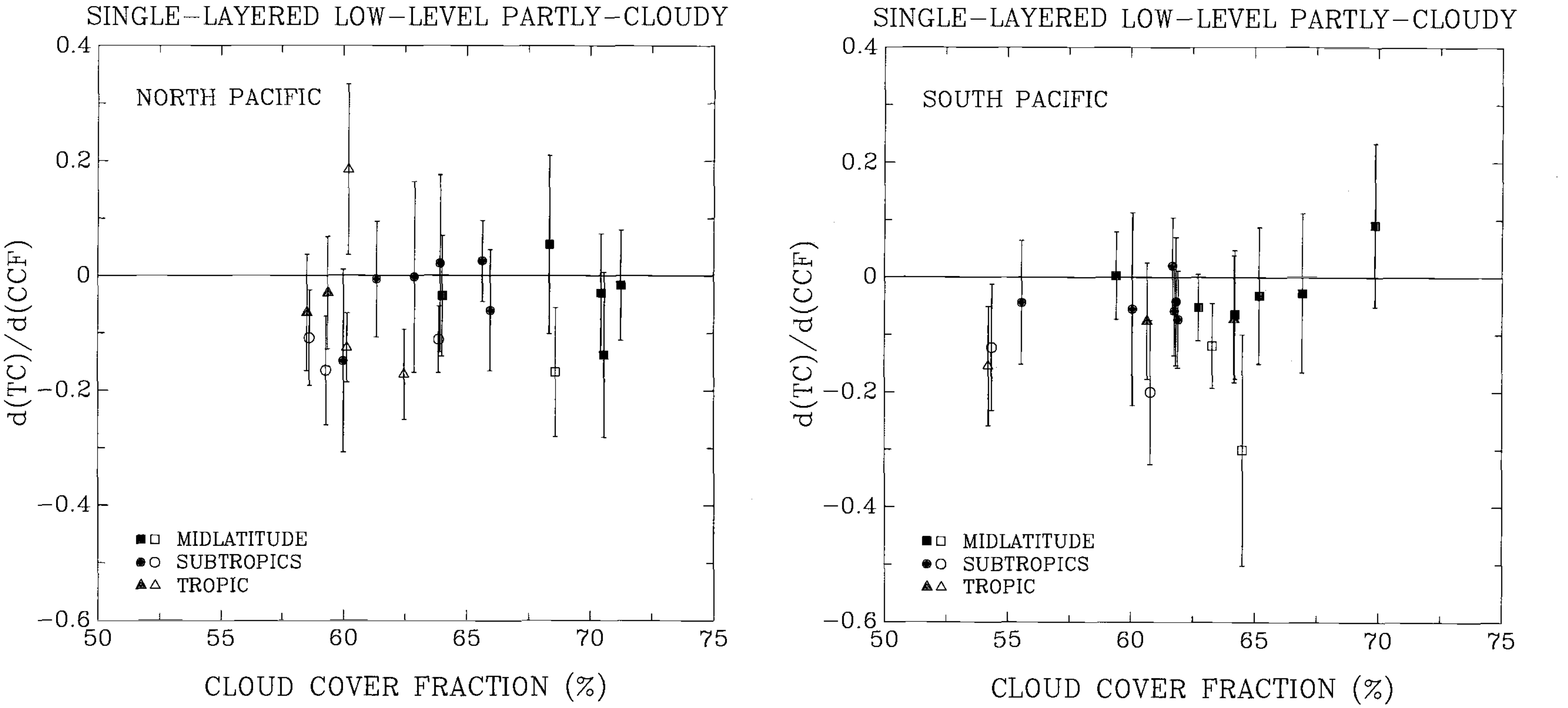

Figure 5.43 Same as Figure 5.5, except for $d(TC)/d(CCF)$ and the monthly-mean cloud cover fraction for the partly cloudy pixels shown in Figure 5.42.

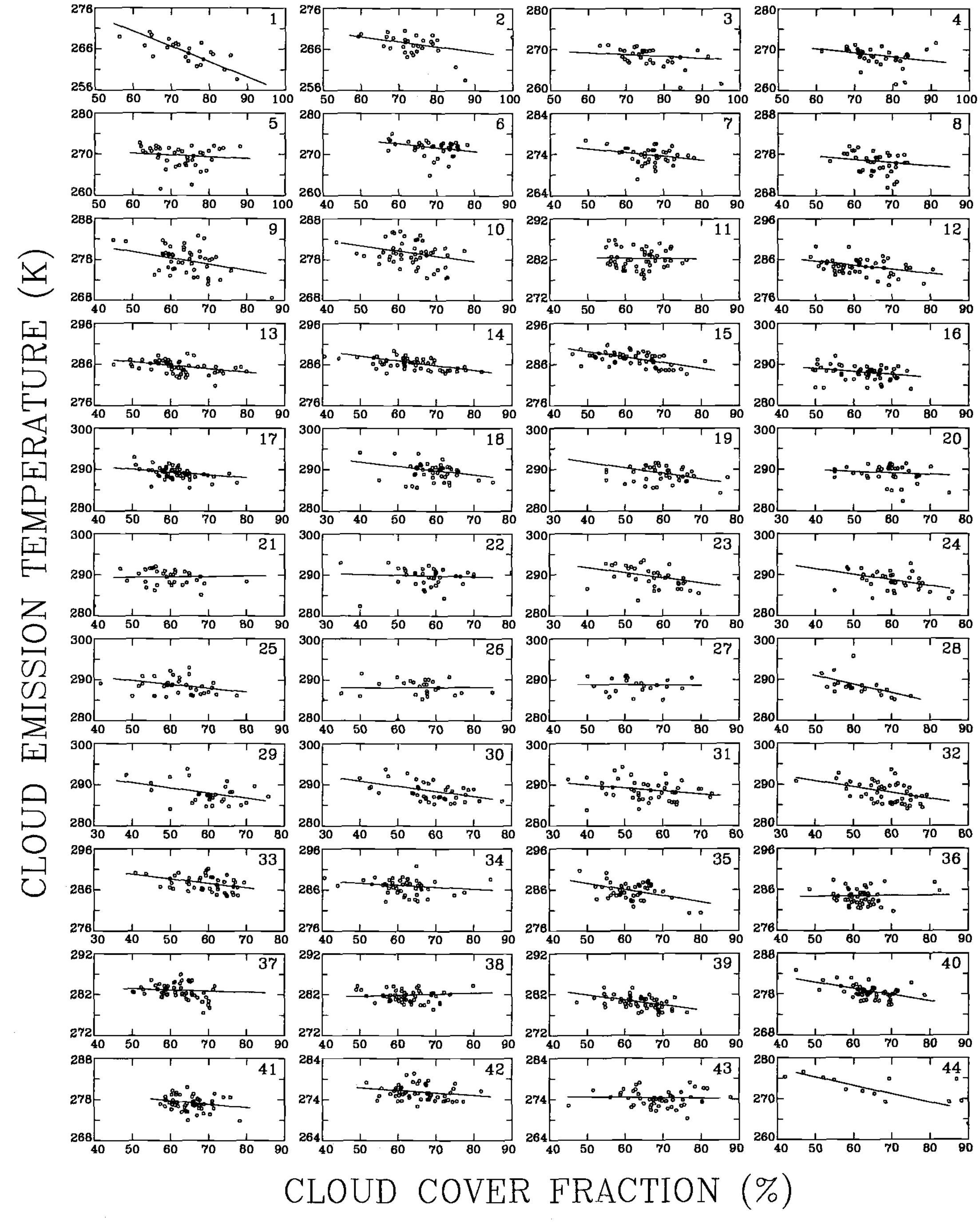

Figure 5.44 Same as Figure 5.6, except for cloud top emission temperature and cloud cover fraction for pixels that were partly covered by single-layered, low-level clouds. The cloud top emission temperatures were obtained by assuming that the partly cloudy pixels were overcast.

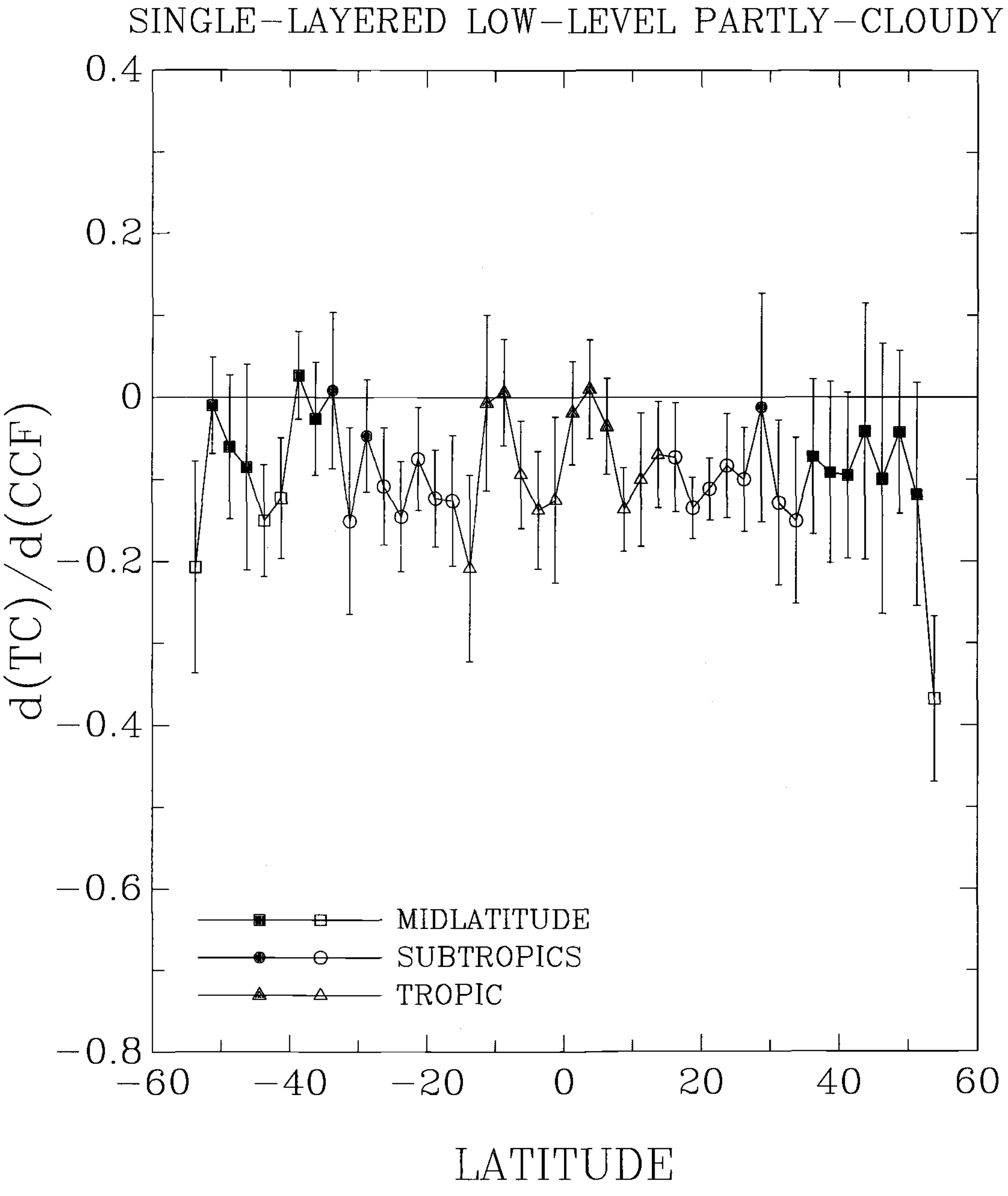

Figure 5.45 Same as Figure 5.7, except for $d(TC)/d(CCF)$ for the partly cloudy pixels shown in Figure 5.44.

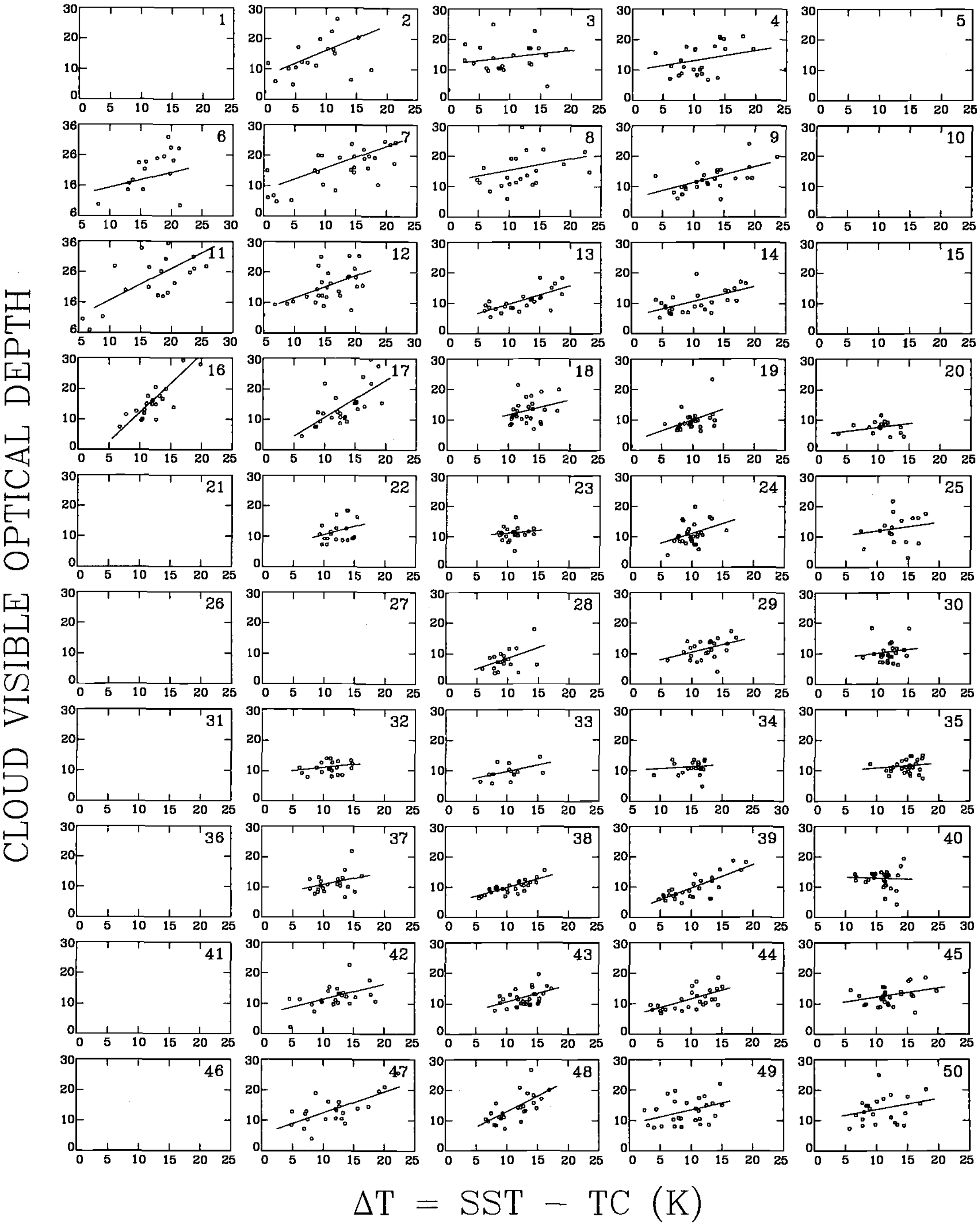

Figure 5.46 Same as Figure 5.4, except for cloud visible optical depth and sea surface-cloud top temperature difference.

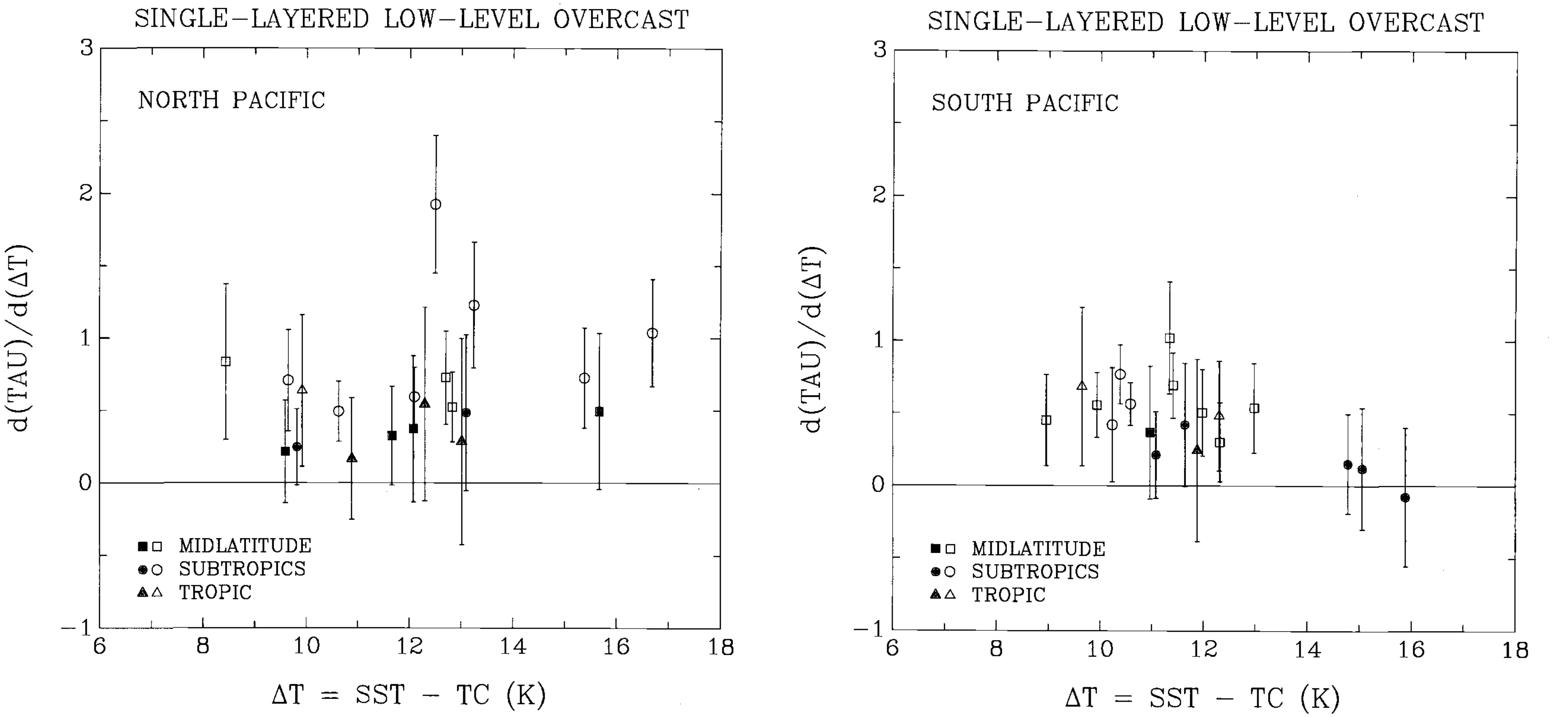

Figure 5.47 Same as Figure 5.5, except for $d(TAU)/d(\Delta T)$ and the monthly-mean sea surface-cloud top temperature differences shown in Figure 5.46.

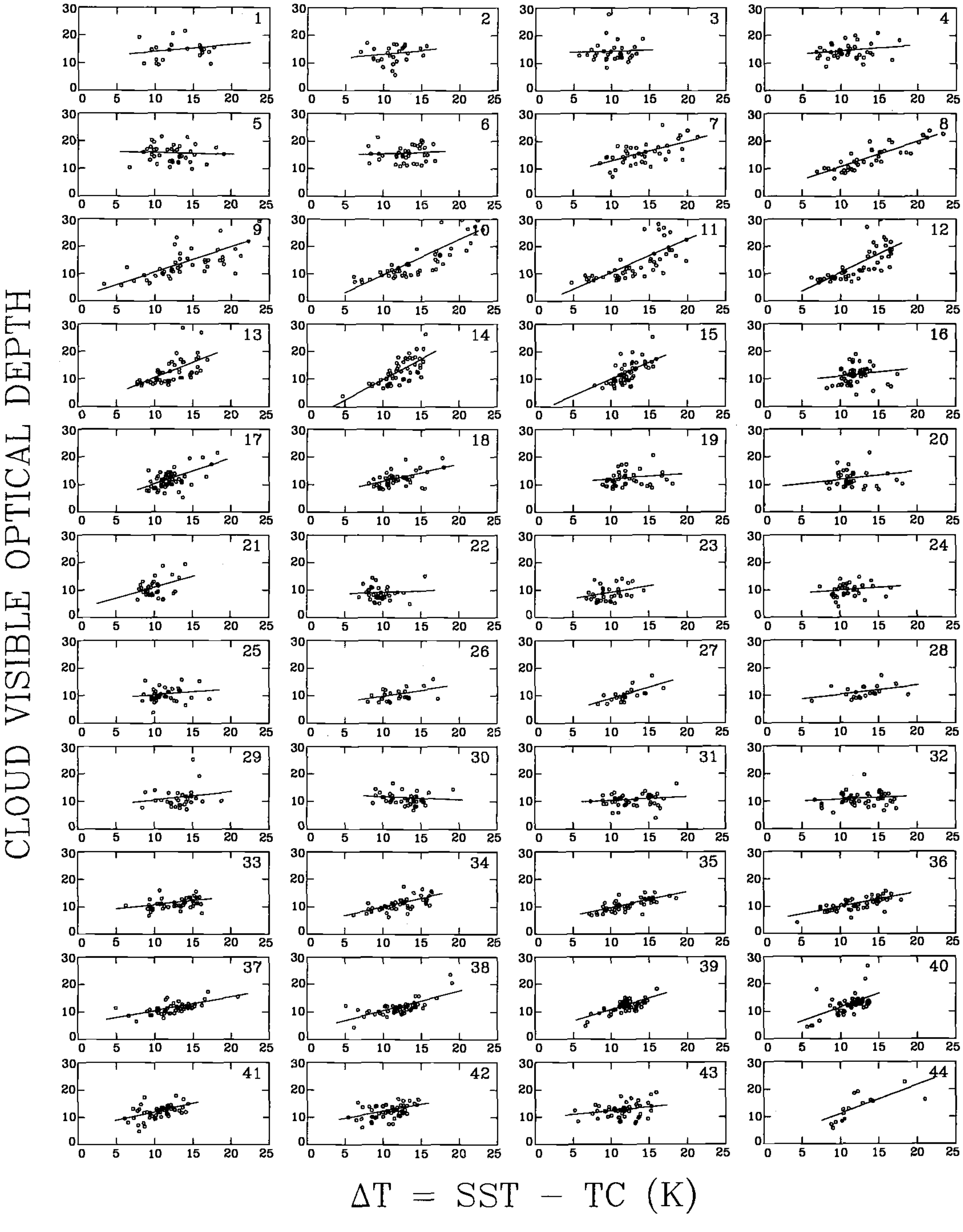

Figure 5.48 Same as Figure 5.6, except for cloud visible optical depth and sea surface-cloud top temperature difference.

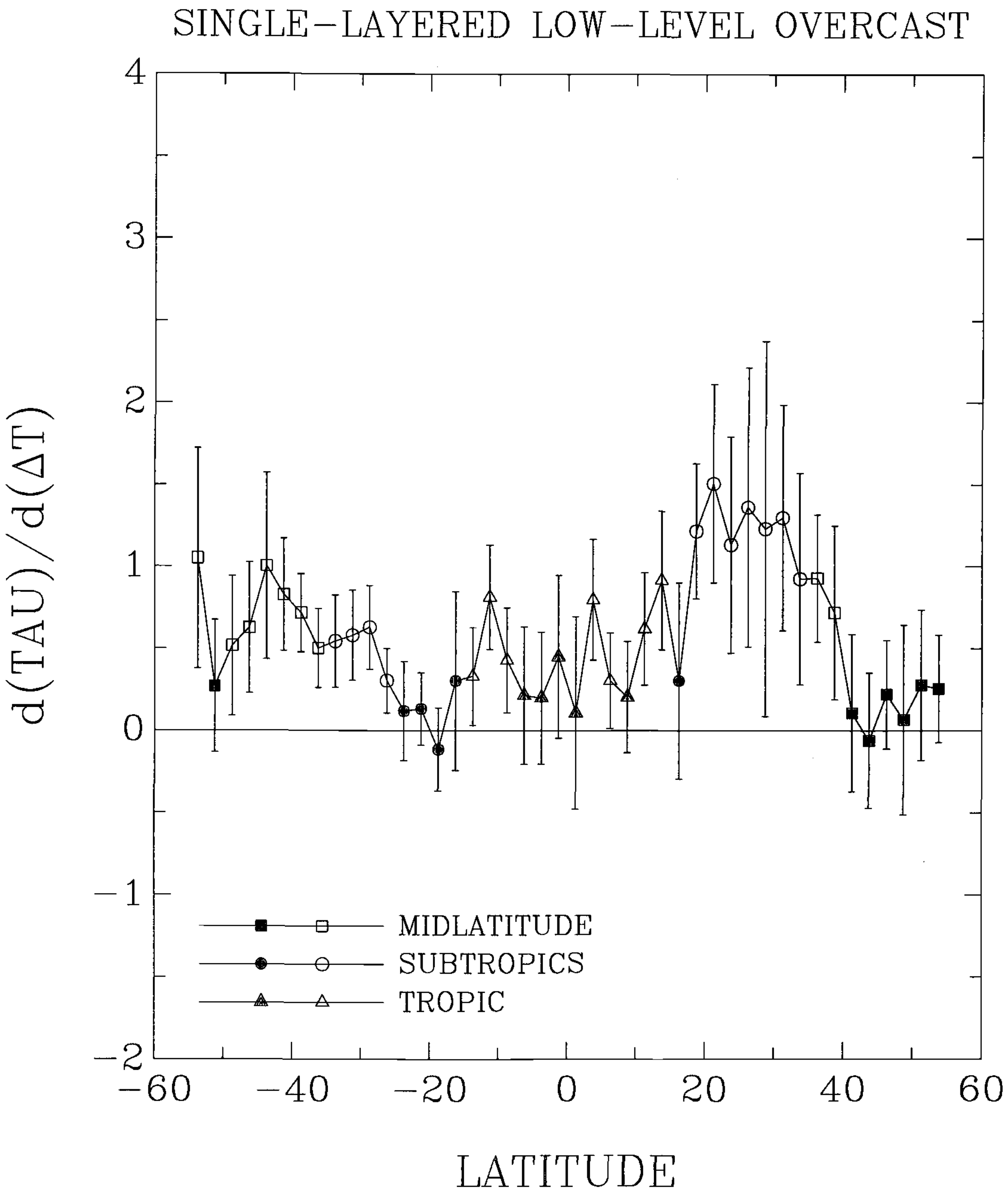

Figure 5.49 Same as Figure 5.7, except for $d(TAU)/d(\Delta T)$ shown in Figure 5.48.

Chapter 6

Relationships between Cloud Liquid Water Path, Cloud Visible Optical Depth, Cloud Droplet Effective Radius, and Sea Surface-Cloud Top Temperature Difference

6.1 Introduction

The earth's radiation balance is sensitive to changes in cloud properties. Actually, how clouds would respond to a climate change is poorly understood. Cess et al. (1990) compared 19 general circulation models (GCMs) and found that the response in the radiation budgets of these models to a fixed change in sea surface temperature differed by a factor of three. They attributed most of these differences to differences in the cloud parameterizations used in the models. These differences suggest that reliable, large-scale, longterm observations of cloud properties are needed. For cloud properties that affect the earth's radiation budget, the climate modeling community has focused on cloud amount, cloud top altitude, and cloud optical depth (e.g., Roeckner et al., 1987; Mitchell et al., 1989; Randall et al., 1992). It is hoped that by incorporating information on cloud microphysics, namely, cloud droplet size and cloud liquid water path, climate modelers can improve the parameterizations of cloud properties.

As the concentration of anthropogenic aerosols increases, variations in cloud optical depth and cloud droplet size due to interaction between the clouds and aerosols have recently received considerable attention (King et al., 1993; Platnick and Twomey, 1994; Twohy et al., 1995; Han et al., 1997; Coakley et al., 1997). The interactions, referred to as the aerosol indirect effect, result from an increase in the number of cloud condensation nuclei (CCN) (Twomey et al., 1984). Higher concentrations of CCN generally produce higher concentrations of cloud droplets, but the droplets are smaller (Twomey, 1974; Charlson et al., 1987; Coakley et al., 1987). For similar liquid water content and vertical thickness, clouds with small droplets reflect more sunlight than those with larger droplets (Twomey, 1977). Since anthropogenic aerosols contain soluble sulfate and nitrate compounds, they are likely to be a source for CCN. Polluted clouds are likely to have higher concentrations of small droplets and, consequently, larger reflectivities than unpolluted clouds. The larger reflectivities counteract somewhat the warming caused by the increase of greenhouse gases. The global average value for the indirect radiative cooling was estimated to be about -1 Wm^{-2} for the present atmosphere, which is equivalent in sign and magnitude to that for the direct radiative cooling due to the backscattering of sunlight by aerosol particles (Charlson et al., 1992). But, the uncertainty in this estimate is as large as the estimate. Combining both direct and indirect effects, the total net cooling is comparable to the current $\sim$ 3 Wm^{-2} warming due to the buildup of the greenhouse gases (IPCC, 1994).

Effects of ship effluents on cloud droplet radius, droplet numbers, and therefore cloud reflectivities have long been used to demonstrate the aerosol indirect effect (Coakley et al., 1987; Radke et al., 1989). Coakley et al. (1987) showed that ship tracks are found as lines of augmented reflectivity in the overlying low-level marine stratus and stratocumulus. Higher CCN concentrations may also lead to larger cloud liquid water paths because a decrease in droplet size may reduce precipitation efficiency thereby reducing the sink of cloud water and possibly increasing cloud lifetime (Albrecht, 1989; Radke et al., 1989). For marine boundary layer clouds, Charlson et al. (1987) also proposed that increased production of dimethylsulfide, a natural precursor of sulfate aerosols over ocean, by phytoplankton would lead to an increase in cloud droplet number, a decrease in droplet radius, and an increase in cloud reflectivity.

Han et al. (1997) used four years of ISCCP data to study the global-scale, spatial and temporal relationships between cloud droplet radius and cloud albedo. They found positive correlations between low-level cloud droplet radius and albedo for most of the globe. They proposed that variations in cloud liquid water path were responsible for these positive correlations. However, ISCCP takes many pixels that are partly cloudy and analyzes their radiances as if they were overcast. The smaller cloud droplet radii and smaller cloud optical depths obtained for partly cloudy pixels, as shown in Chapter 4, may lead to incorrect inferences concerning cloud albedo, cloud droplet size, and cloud liquid water path.

As in previous chapters, NOAA-11 AVHRR 4-km GAC data for March 1989 was used to study the 60-km-scale, single-layered, low-level, cloud liquid water paths, cloud visible optical depths, droplet effective radii, and cloud top altitudes for the Pacific ocean. Cloud liquid water paths were compared for overcast and partly cloudy pixels, as determined with the spatial coherence method. The satellite zenith angle dependence in the retrieved cloud liquid water paths was also examined. In addition, day-to-day correlations and longitudinal correlations between cloud liquid water paths, cloud visible optical depths, droplet effective radii, and sea surface-cloud top temperature differences were examined. Variations in cloud layer vertical thickness were suggested to be the primary mechanism for the relationship observed between cloud visible optical depth, cloud liquid water path, droplet effective radius, and cloud top emission temperature.

6.2 Low-level cloud liquid water paths

Figure 6.1a shows the latitudinal distribution of the zonal-mean cloud liquid water paths obtained for pixels overcast by single-layered, low-level clouds for March 1989. The cloud liquid water path (g/m^2) is given by

$$LWP = \frac{4}{3}\frac{\rho_{liq} r_{eff} \tau_c\left(\lambda, r_{eff}\right)}{Q_{ext}\left(\lambda, r_{eff}\right)}, \tag{6.1}$$

where ρ_{liq} (g/m^3) is the density of water, r_{eff} (μm) is the droplet effective radius, τ_c is the cloud optical depth, Q_{ext} is the extinction coefficient, and λ (μm) is the wavelength. (For the definitions of these variables, see section 3.2.1.) In the figure, thick error bars indicate the 95% confidence intervals of the monthly means and thin error bars indicate the standard deviations of the daily averages. Relatively small cloud liquid water paths of $\sim$ 75 g/m^2 are obtained for equatorial regions. For the rest of the latitudes, the cloud liquid water path ranges between about 100-130 g/m^2. These results were obtained for near-nadir satellite zenith angles ($< 25°$). The mean cloud liquid water path for the pixels overcast by single-layered, low-level clouds is 117.8 g/m^2 for the northern Pacific and 115.7 g/m^2 for the southern Pacific. These mean values are larger than the annual mean of 87.4 g/m^2 for global oceans obtained by Han et al. (1994) using ISCCP data. The smaller value obtained by Han et al. is attributable to the effect of partly cloudy pixels in the ISCCP data.

Figure 6.1b shows the same as Figure 6.1a, except that results are obtained for partly cloudy pixels that were assumed to be overcast. The mean cloud liquid water path for these partly cloudy pixels is 44.3 g/m^2 for the north Pacific and 40.0 g/m^2 for the south Pacific. The comparison for the means obtained in Figure 6.1a and 6.1b are shown in Figure 6.1c and the differences between the means are shown in Figure 6.1d. Cloud liquid water paths obtained for the partly cloudy pixels were on average 30-50% of those obtained for the overcast pixels. Figure 6.2a shows cloud liquid water paths for the overcast and partly cloudy pixels drawn from the same 60-km region. The frequency of occurrence of the cloud liquid water paths are shown in Figure 6.2b. Again, these observations were restricted to near-nadir satellite zenith angles. Clearly, cloud liquid water paths derived for partly cloudy pixels were significantly smaller than those derived for overcast pixels.

Figure 6.3 shows cloud liquid water paths for the overcast pixels as a function of satellite zenith angle. As in Figure 4.15, the monthly means, 95% confidence intervals (thick error bars), and the standard deviations (thin error bars) of the daily means are shown for both the northern and southern midlatitudes, subtropics, and tropics. In both the forward and backward scattering directions, a decrease of ~20-30% in the mean cloud liquid water path was obtained for a change from nadir to 60° oblique satellite zenith angles. Figure 6.4 shows the monthly-mean cloud liquid water paths for overcast (solid curves) and partly cloudy pixels (dashed curves). Large differences were found at all satellite zenith angles. The satellite zenith angle dependence of cloud liquid water paths for partly cloudy pixels was smaller than that for the overcast pixels.

Table 6.1 shows the average low-level cloud liquid water paths obtained for overcast and partly cloudy pixels at near-nadir satellite zenith angles. The near-global mean, low-level, oceanic cloud liquid water path obtained by Han et al. (1994) using ISCCP data is also listed in the table. Their mean cloud liquid water path lies between the mean cloud liquid water paths obtained for overcast and partly cloudy pixels.

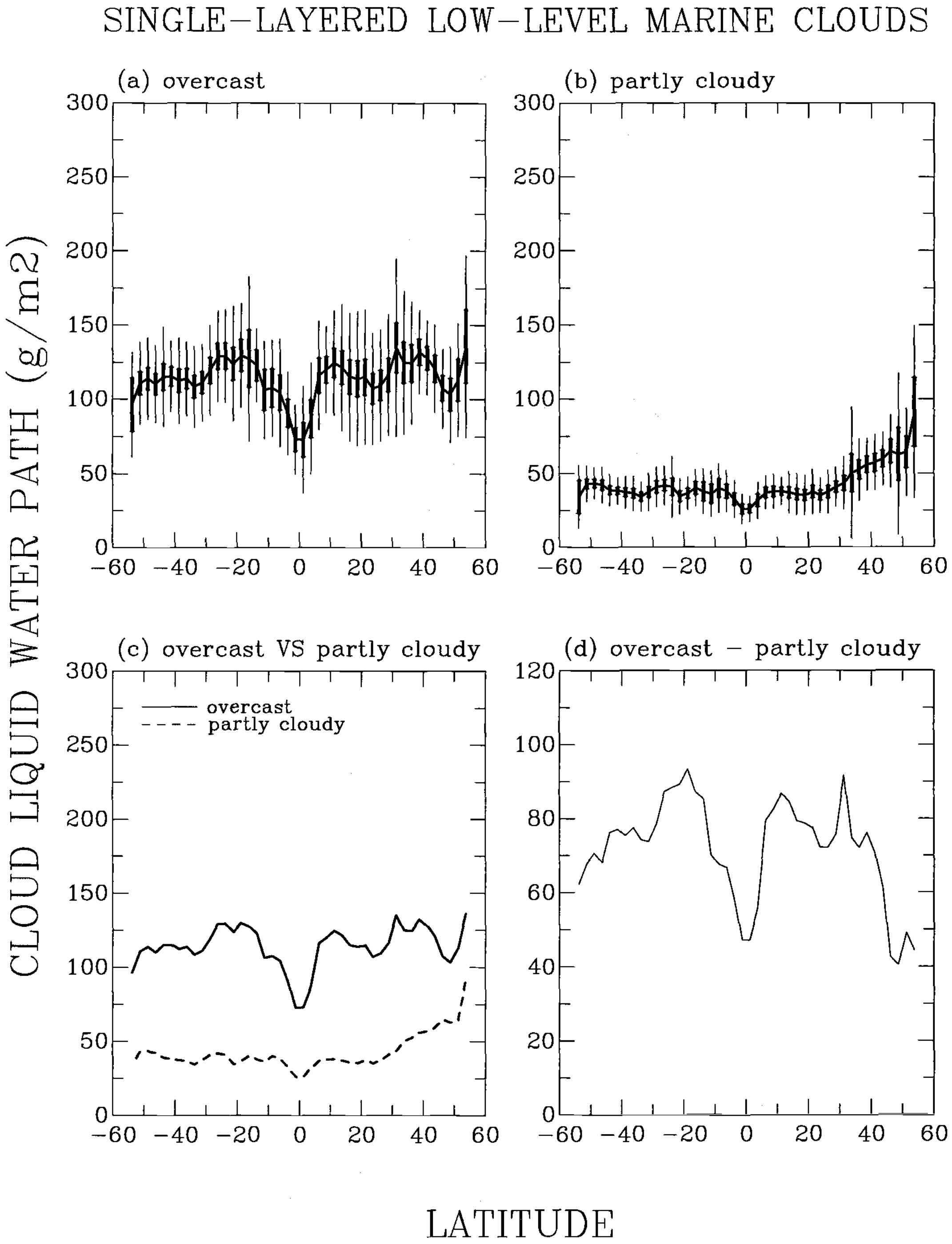

Figure 6.1 Cloud liquid water paths for single-layered, low-level clouds for March 1989 over the Pacific ocean. Observations were restricted to near-nadir satellite view angles. Curves show the monthly means. Thick bars indicate the 95% confidence intervals for the means and thin bars indicate the standard deviations of the daily means. (a) overcast; (b) partly cloudy; (c) means shown in (a) and (b); (d) differences between the means shown in (c). Negative latitudes are for the south Pacific.

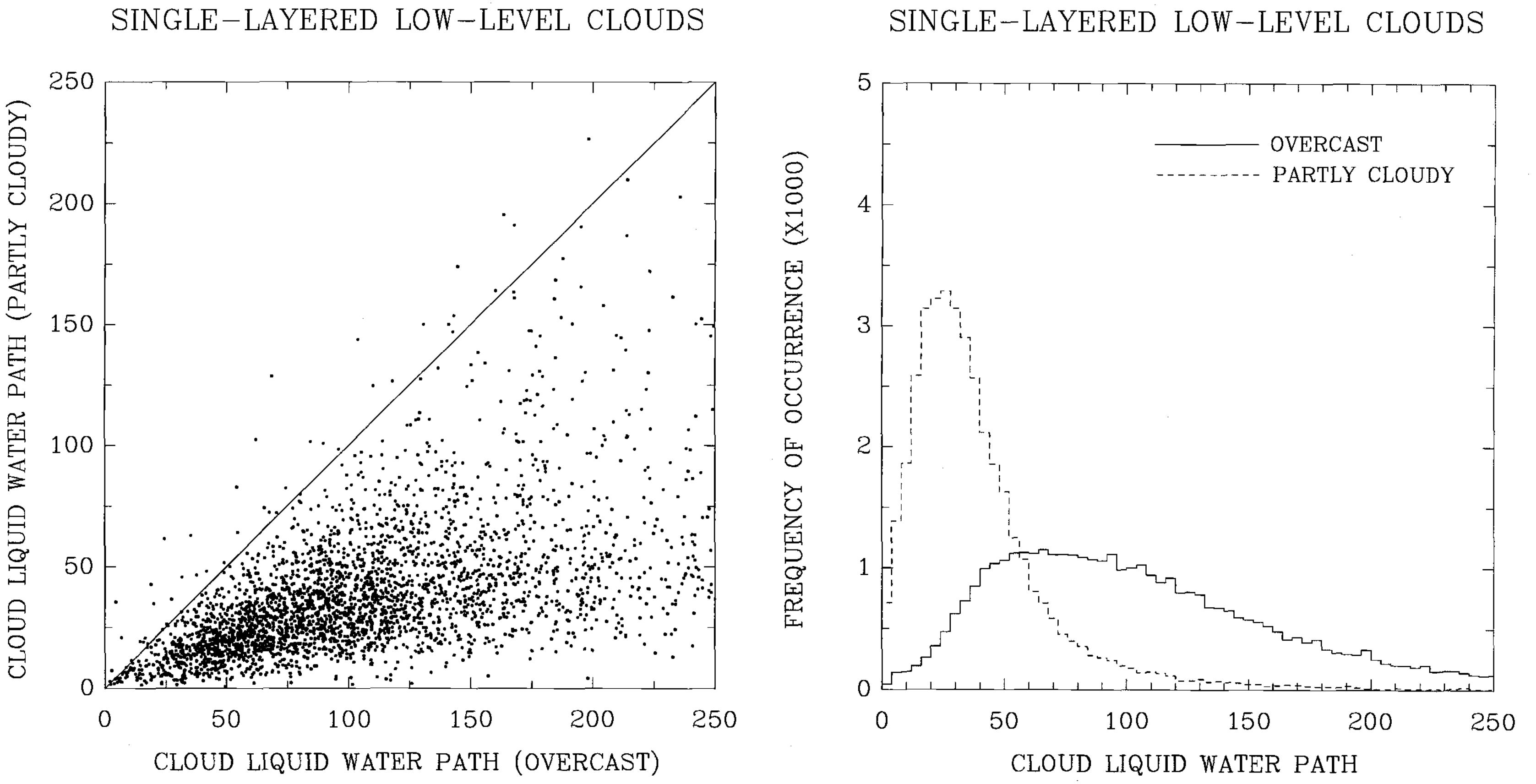

Figure 6.2 Cloud liquid water paths (g/m^2) for overcast and partly cloudy pixels drawn from the same 60-km region. Observations are for single-layered, low-level clouds identified by the spatial coherence method for March 1989 over the Pacific ocean. The observations were restricted to near-nadir satellite view angles. (a) overcast and partly cloudy pixels. (b) frequency distributions.

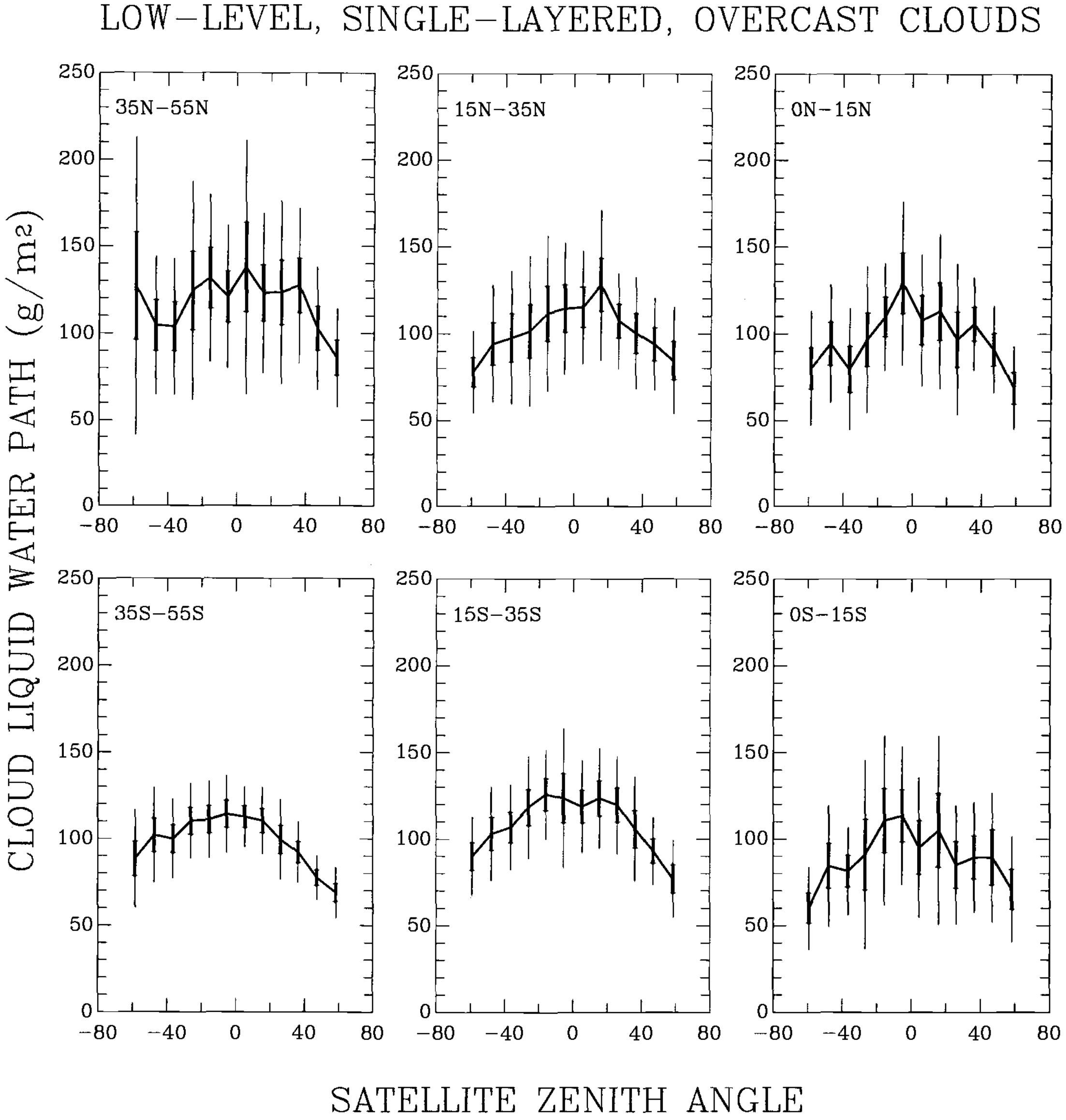

Figure 6.3 Cloud liquid water paths as a function of satellite zenith angle. Observations are for pixels overcast by single-layered, low-level clouds identified by the spatial coherence method for March 1989 for both northern and southern midlatitudes (35°–55°), subtropics (15°–35°), and tropics (0°–15°). Curves are for the monthly means. Thick bars indicate the 95% confidence intervals for the means. Thin bars represent the standard deviations of the daily means. Negative view angles indicate the backward scattering direction.

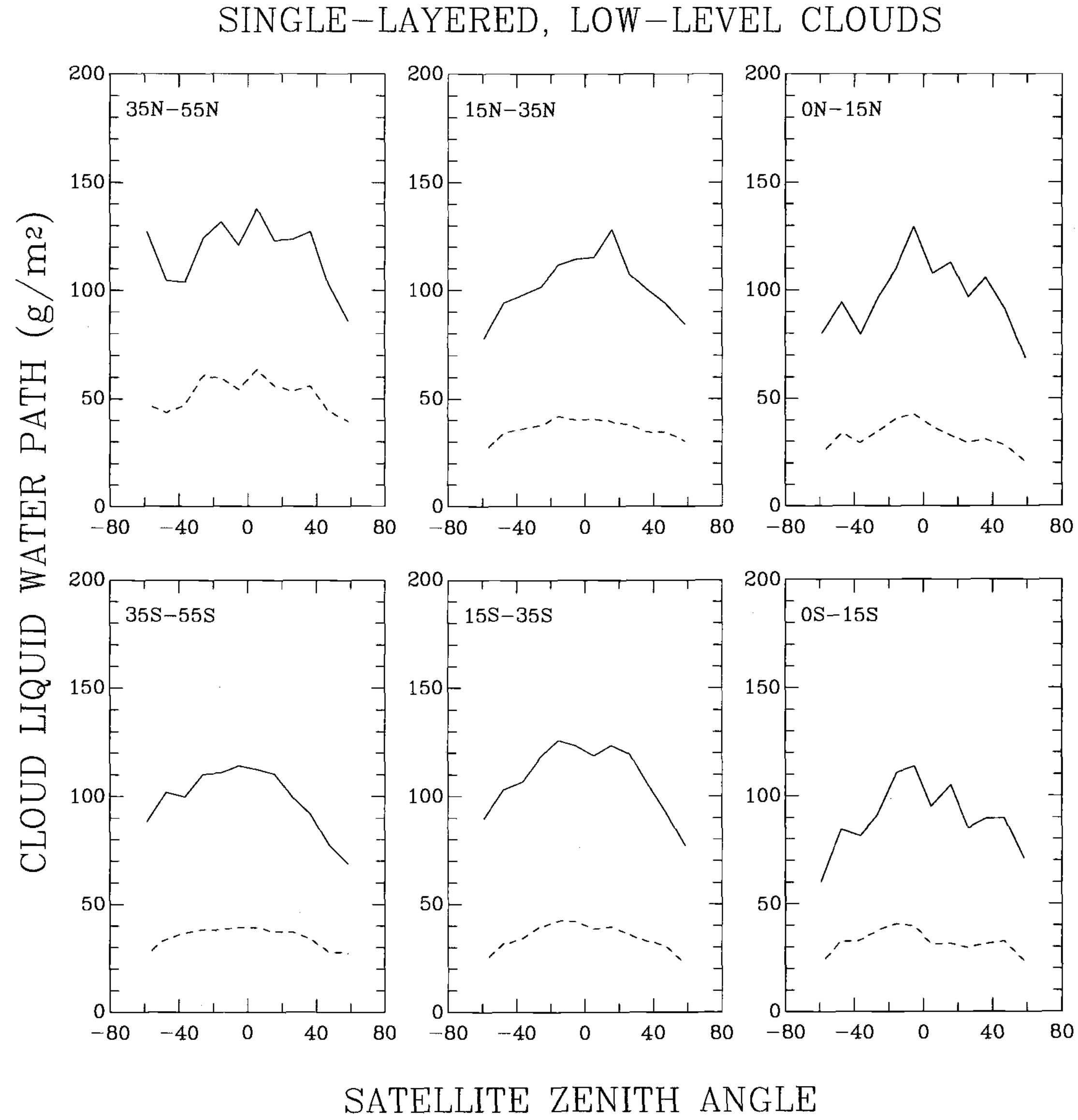

Figure 6.4 Monthly-mean cloud liquid water paths (g/m^2) for pixels overcast and partly covered by single-layered, low-level clouds. Observations are for March 1989 for both northern and southern midlatitudes (35°–55°), subtropics (15°–35°), and tropics (0°–15°). Solid curves are for overcast pixels; dashed curves are for partly cloudy pixels which were assumed to be overcast.

Table 6.1 Monthly-mean cloud liquid water paths (g/m^2). Results are for pixels overcast by single-layered, low-level clouds for March 1989 over the Pacific. The observations were restricted to near-nadir view angles. Numbers in the parentheses are for partly cloudy pixels assumed to be overcast. Results obtained by Han et al. (1994) (Table 9) are also listed for comparisons.

<table>
<tr><th></th><th>35°N-55°N</th><th>15°N-35°N</th><th>0°N-15°N</th><th>0°S-15°S</th><th>15°S-35°S</th><th>35°S-55°S</th></tr>
<tr><td rowspan="4">Cloud liquid water path (g/m^2)</td><td>126.3
(58.4)</td><td>116.4
(40.5)</td><td>115.0
(38.3)</td><td>106.1
(36.0)</td><td>122.9
(40.8)</td><td>112.0
(38.6)</td></tr>
<tr><td colspan="3">117.8 (44.3)</td><td colspan="3">115.7 (40.0)</td></tr>
<tr><td colspan="6">116.8 (42.2)</td></tr>
<tr><td colspan="6">Han et al.: 80.2 (April), 87.4 (annual)</td></tr>
</table>

6.3 Effects of partly cloudy pixels on cloud liquid water path and droplet effective radius

Figure 6.5 shows cloud liquid water paths and cloud cover fractions obtained for the pixels that were partly covered by single-layered, low-level clouds, as identified by the spatial coherence method for March 1989 over the Pacific ocean. Figure 6.5a, which is similar to Figure 5.24, illustrates the day-to-day variations of cloud liquid water path and cloud cover fraction for fifty 30° × 10° regions. The locations of these regions are given in Table 5.1. Figure 6.5b, which is similar to Figure 5.26, illustrates the 2.5°-scale longitudinal variations for forty-four 2.5°-latitude bands. The latitudes for these 2.5°-latitude bands are given in Table 5.2. Figure 6.5 shows that as the mean cloud cover fraction of the partly cloudy pixels decreases, i.e., clouds become more broken, the retrieved mean cloud liquid water path also decreases.

Figure 6.6 shows the same as Figure 6.5, except for the cloud droplet effective radii and cloud cover fractions for the partly cloudy pixels. Figure 6.6a shows the day-to-day variations and Figure 6.6b shows the 2.5°-scale longitudinal variations. Cloud droplet effective radius shows no discernible trends with a change in the cloud cover fraction of the partly cloudy pixels. The lack of a trend with cloud cover fraction may result from the small differences of the droplet effective radii retrieved for overcast and partly cloudy pixels. As was shown in Figure 4.11, the differences were on average only $\sim$1-2 μm.

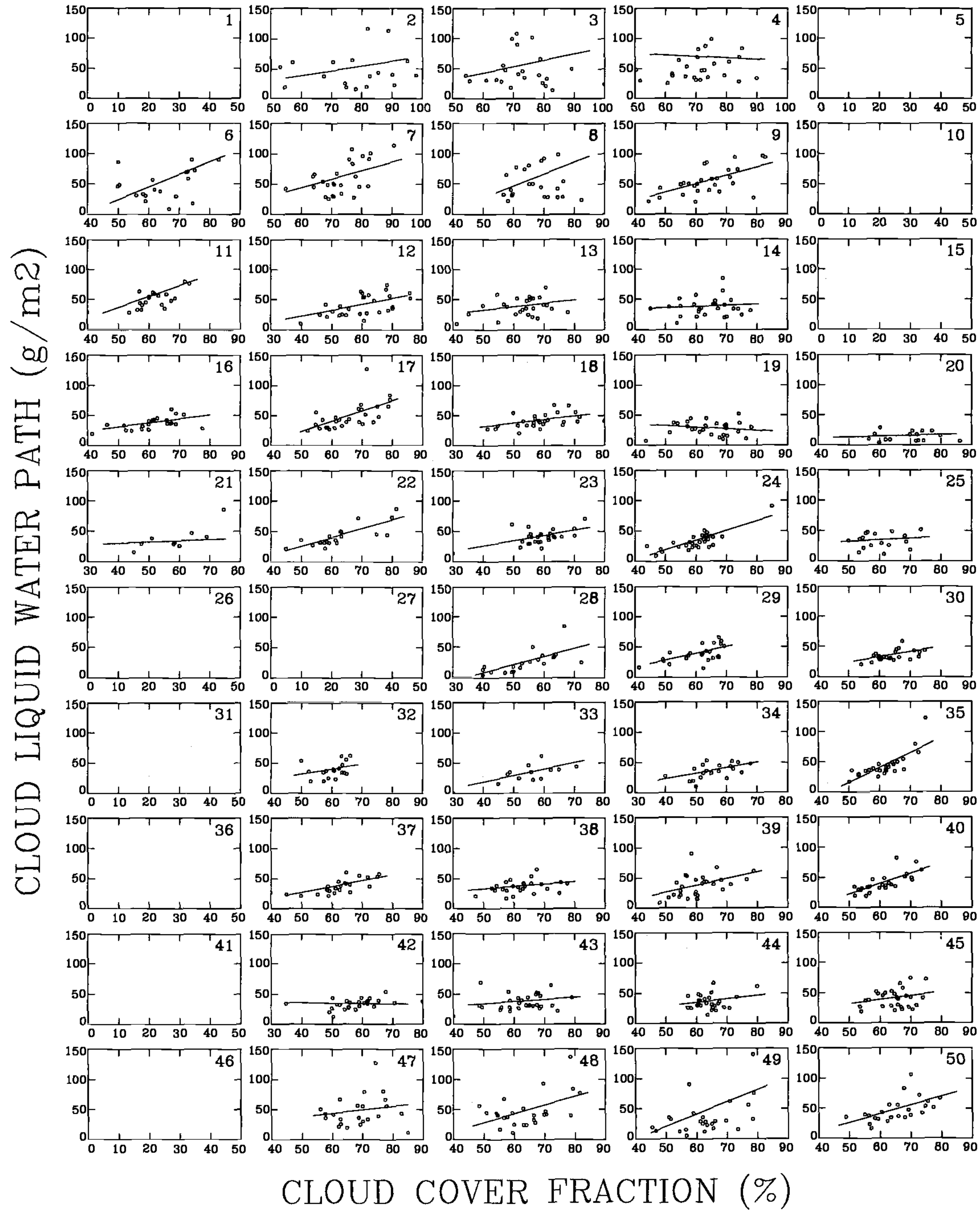

Figure 6.5(a) Same as Figure 5.4, except for cloud liquid water path and cloud cover fraction for pixels that were partly covered by single-layered, low-level clouds. The cloud liquid water paths were obtained by assuming that the partly cloudy pixels were overcast.

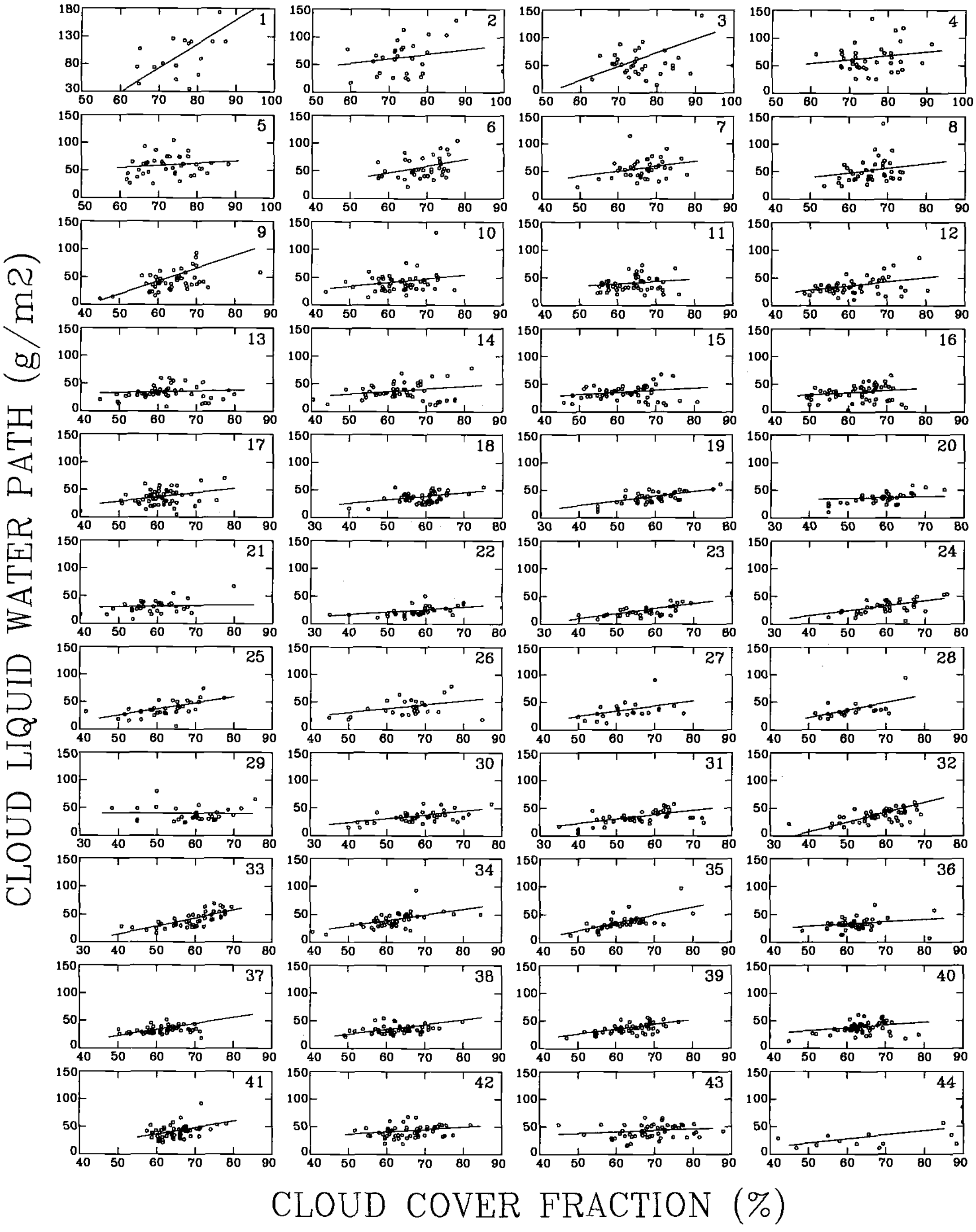

Figure 6.5(b) Same as Figure 5.6, except for cloud liquid water path and cloud cover fraction for pixels that were partly covered by single-layered, low-level clouds. The cloud liquid water paths were obtained by assuming that the partly cloudy pixels were overcast.

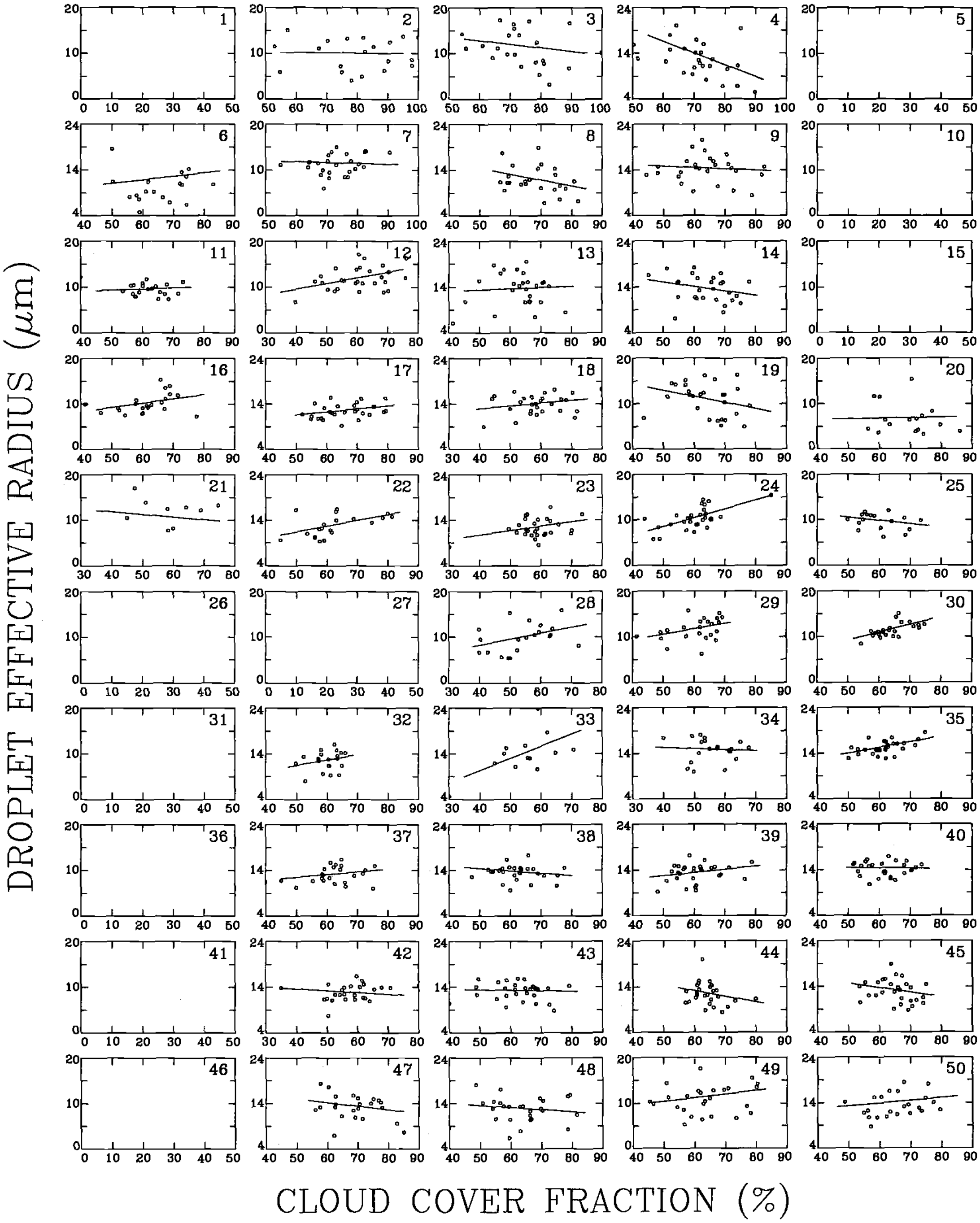

Figure 6.6(a) Same as Figure 5.4, except for cloud droplet effective radius and cloud cover fraction for pixels that were partly covered by single-layered, low-level clouds. The droplet effective radii were obtained by assuming that the partly cloudy pixels were overcast.

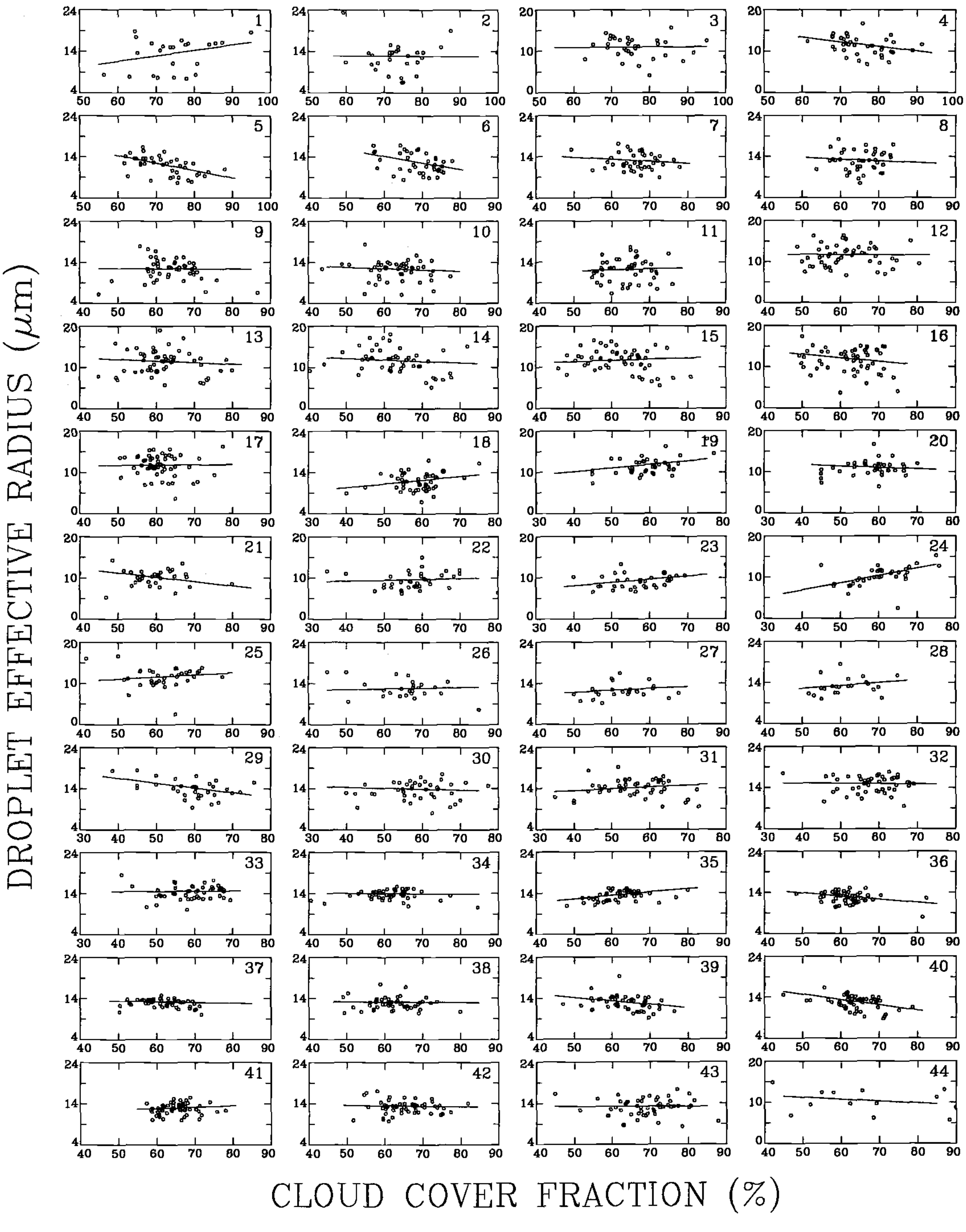

Figure 6.6(b) Same as Figure 5.6, except for cloud droplet effective radius and cloud cover fraction for pixels that were partly covered by single-layered, low-level clouds. The droplet effective radii were obtained by assuming that the partly cloudy pixels were overcast.

6.4 Relationships between cloud visible optical depth, droplet effective radius, and cloud liquid water path

6.4.1 Cloud visible optical depth and droplet effective radius

The relationship between cloud visible optical depth and droplet effective radius is examined for pixels that were overcast by the single-layered, low-level clouds. Figures 6.7 and 6.8 show the day-to-day correlations obtained in the same way as in Figures 5.4 and 5.5. These day-to-day correlations show that either cloud visible optical depths increased with droplet effective radius or showed no significant correlation with the droplet effective radius. Only one region, 15°N-25°N and 120°E-150°E, (index number 16, see Table 5.1) off the coast of southeast China showed a strong negative correlation between cloud optical depth and droplet effective radius.

Figures 6.9 and 6.10 show the longitudinal correlations obtained in the same way as in Figures 5.12 and 5.13. These figures show very little correlation between cloud visible optical depth and droplet effective radius for the tropics and for relatively high latitudes. However, it is interesting that positive correlations are found in the south Pacific between 30°S-40°S and negative correlations are found in the north Pacific between 20°N-45°N. These findings would be consistent with the effects anticipated for the different aerosol loadings expected for the northern and southern Pacific.

To further examine the cloud visible optical depth and droplet effective radius distributions, Figure 6.11 shows the longitudinal variations of the monthly-mean, low-level cloud visible optical depths (dashed) and droplet effective radii (solid) across the Pacific ocean. The observations were restricted to near-nadir pixels that were overcast by single-layered, low-level clouds, as determined with the spatial coherence method. The monthly-mean longitudinal variations are shown for every 2.5°-latitude band. In the northern Pacific, as is shown in Figure 6.11a, cloud droplet effective radii generally decreased when approaching the continents (both sides of solid curves). Such a decrease is most obvious in the subtropics and is stronger in the west Pacific than in the east Pacific. Also, a large increase in cloud visible optical depth with decreasing droplet effective radius was found in the western subtropical Pacific. The negative longitudinal correlations found between 20°N-45°N shown in Figure 6.9, were primarily due to the strong negative correlations in the western Pacific ocean, as shown in Figure 6.11a. For the east Pacific, cloud visible optical depths generally showed in-phase variation with droplet effective radii. In Figure 6.11b, the cloud visible optical depths and droplet effective radii for the southern Pacific showed little variation across the Pacific.

6.4.2 Cloud visible optical depth and cloud liquid water path

Figures 6.12 and 6.13 show the day-to-day correlations between cloud visible optical depths and cloud liquid water paths for pixels overcast by single-layered, low-level clouds. Figures 6.14 and 6.15 show the longitudinal correlations. These figures show strong positive correlations between cloud visible optical depths and cloud liquid water paths. These positive correlations were found in all regions and all latitudes. On average, an increase of $\sim$ 10 g/m^2 in the low-level cloud liquid water path corresponded to an increase of one unit in the cloud visible optical depth. The variation in cloud visible optical depth with cloud liquid water path is smaller for the tropics and larger for the northern subtropics around 25°N.

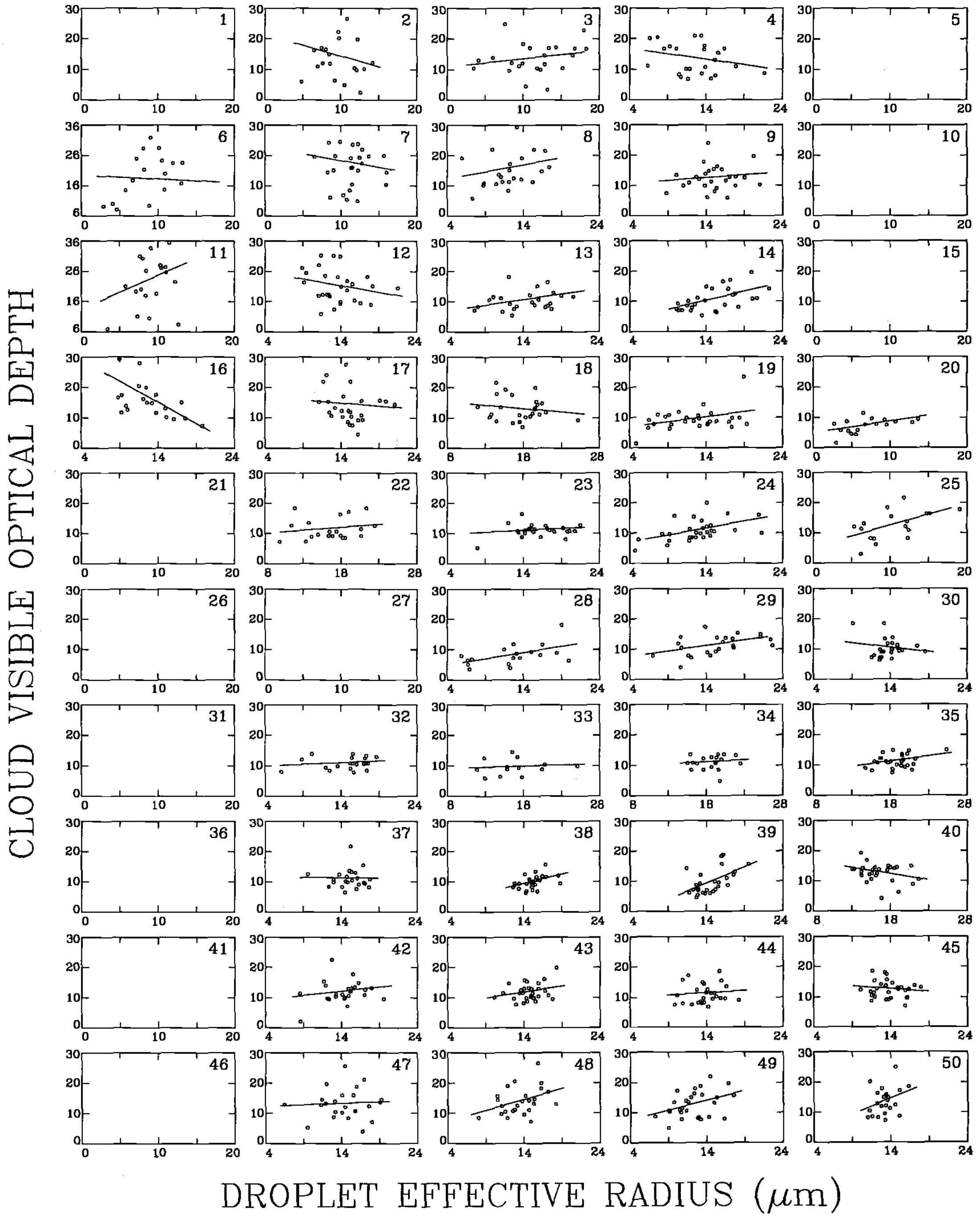

Figure 6.7 Same as Figure 5.4, except for cloud visible optical depth and cloud droplet effective radius.

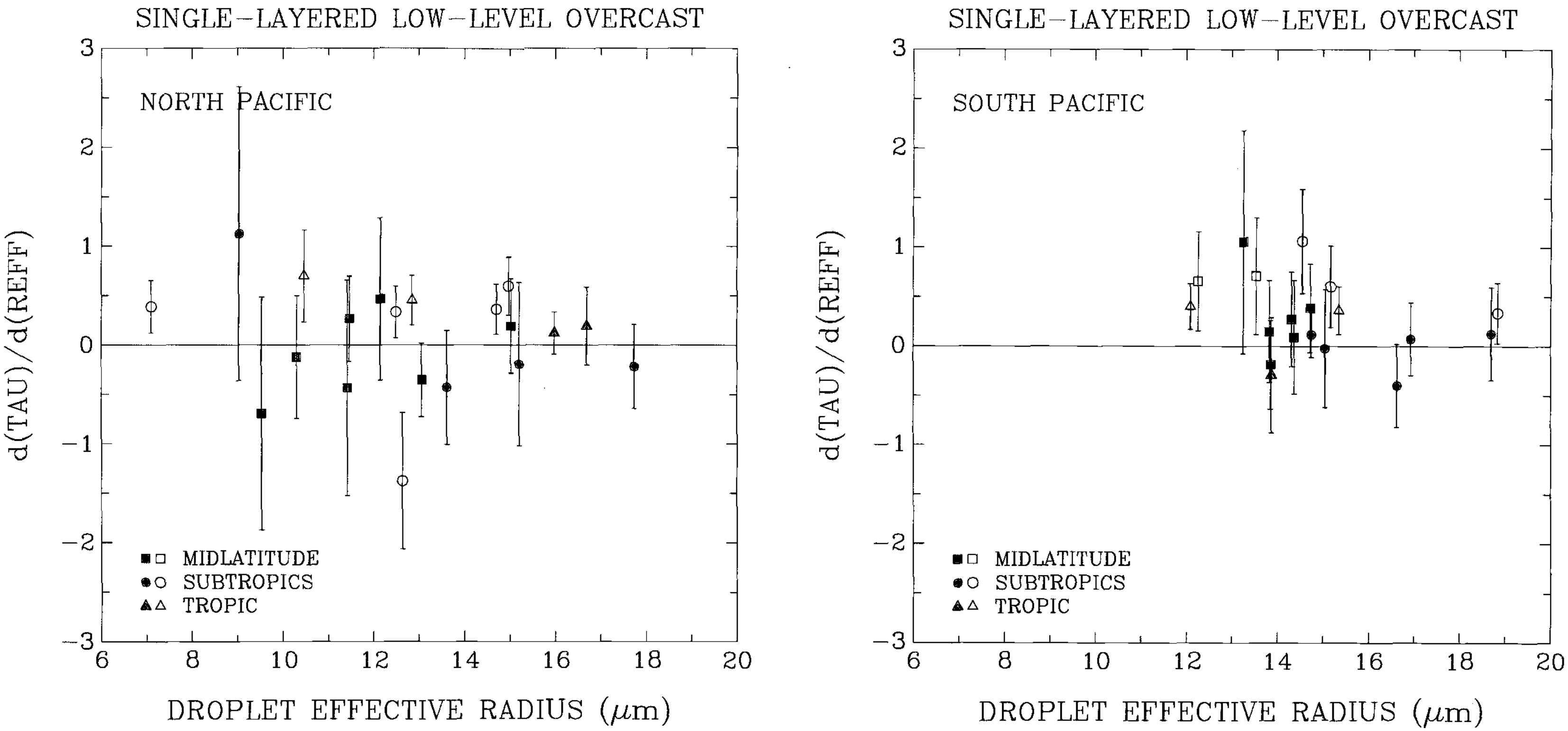

Figure 6.8 Same as Figure 5.5, except for $d(TAU)/d(REFF)$ and the monthly-mean cloud droplet effective radius shown in Figure 6.7.

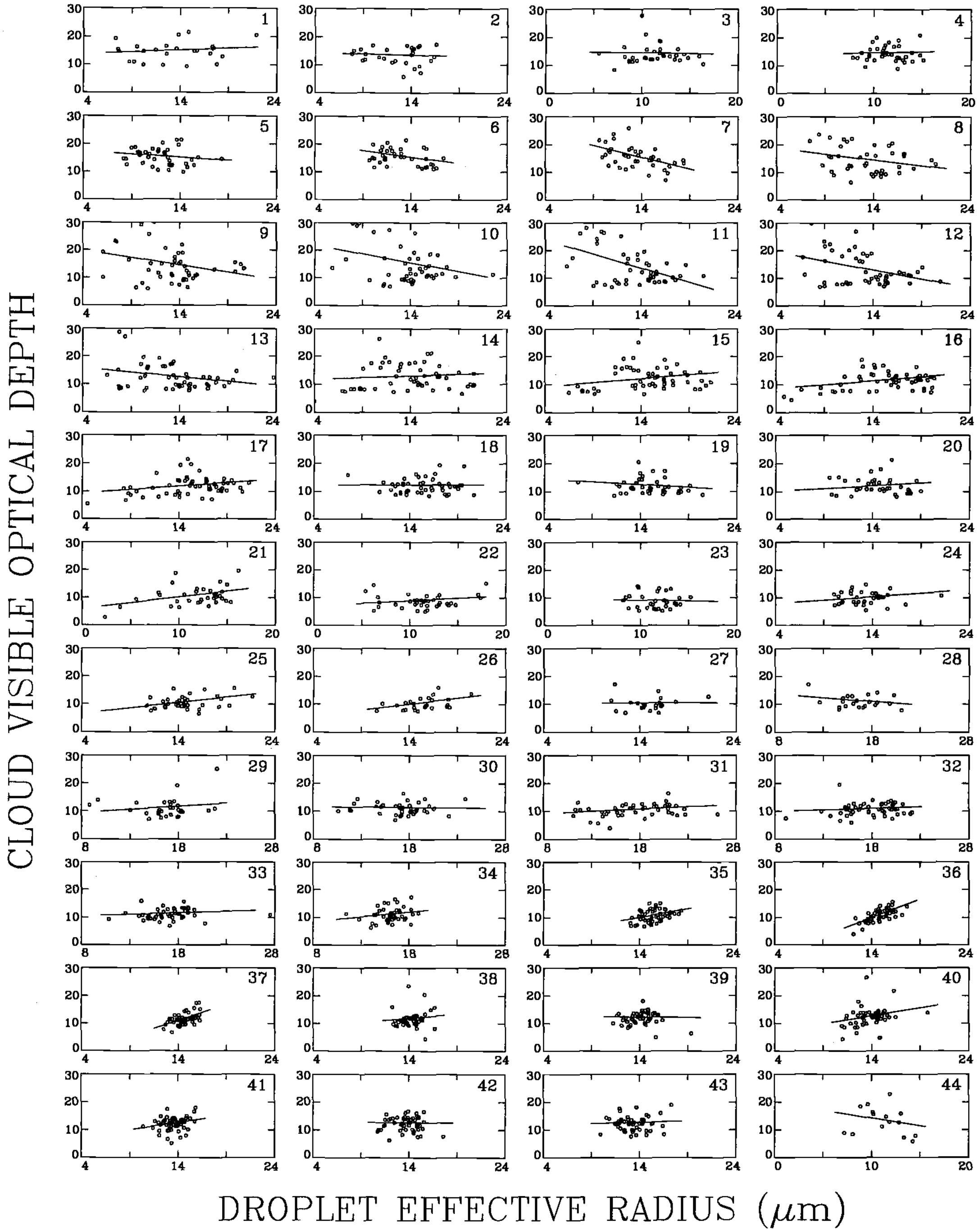

Figure 6.9 Same as Figure 5.6, except for cloud visible optical depth and cloud droplet effective radius.

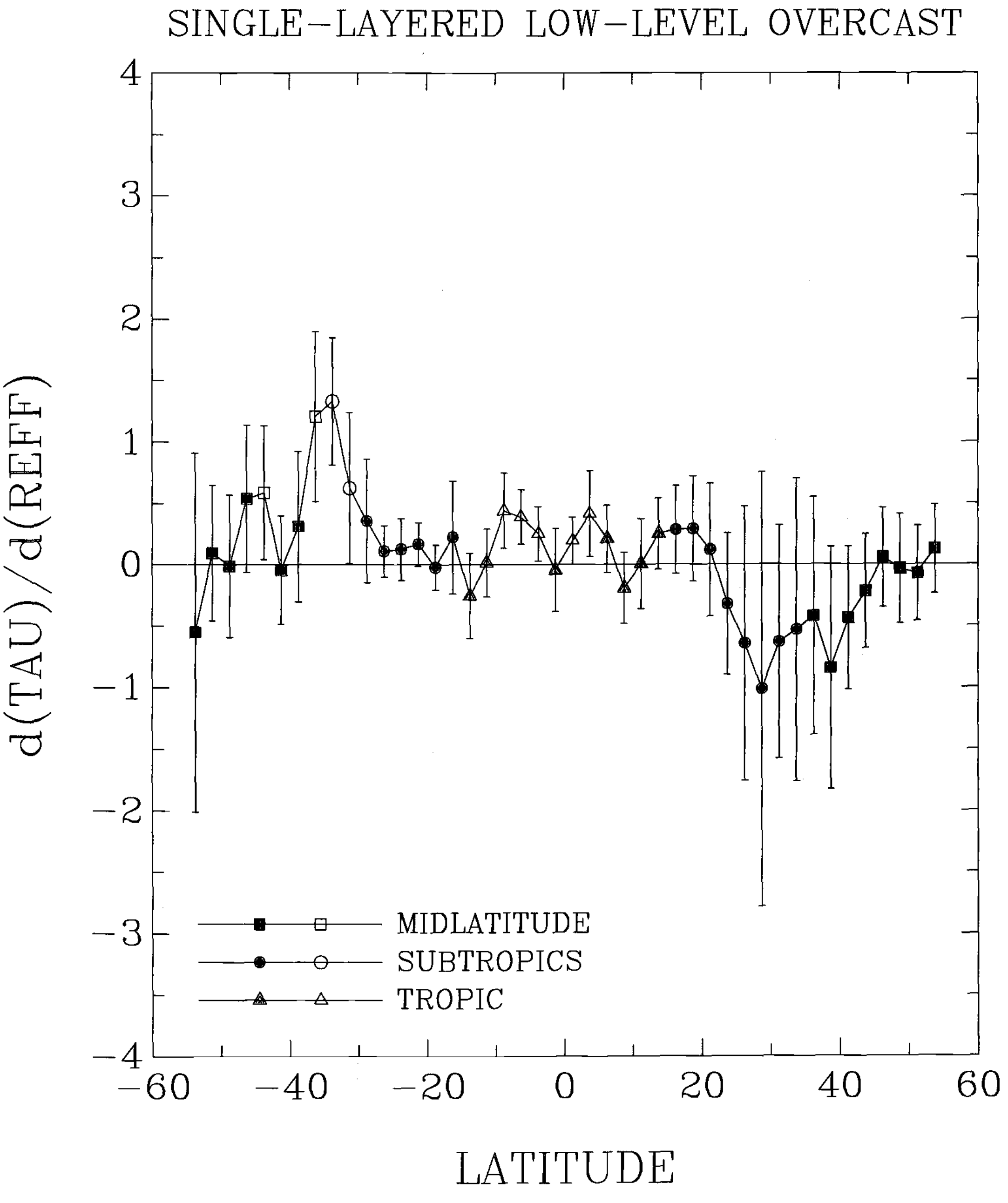

Figure 6.10 Same as Figure 5.7, except for $d(TAU)/d(REFF)$ shown in Figure 6.9. $REFF$ is in μm.

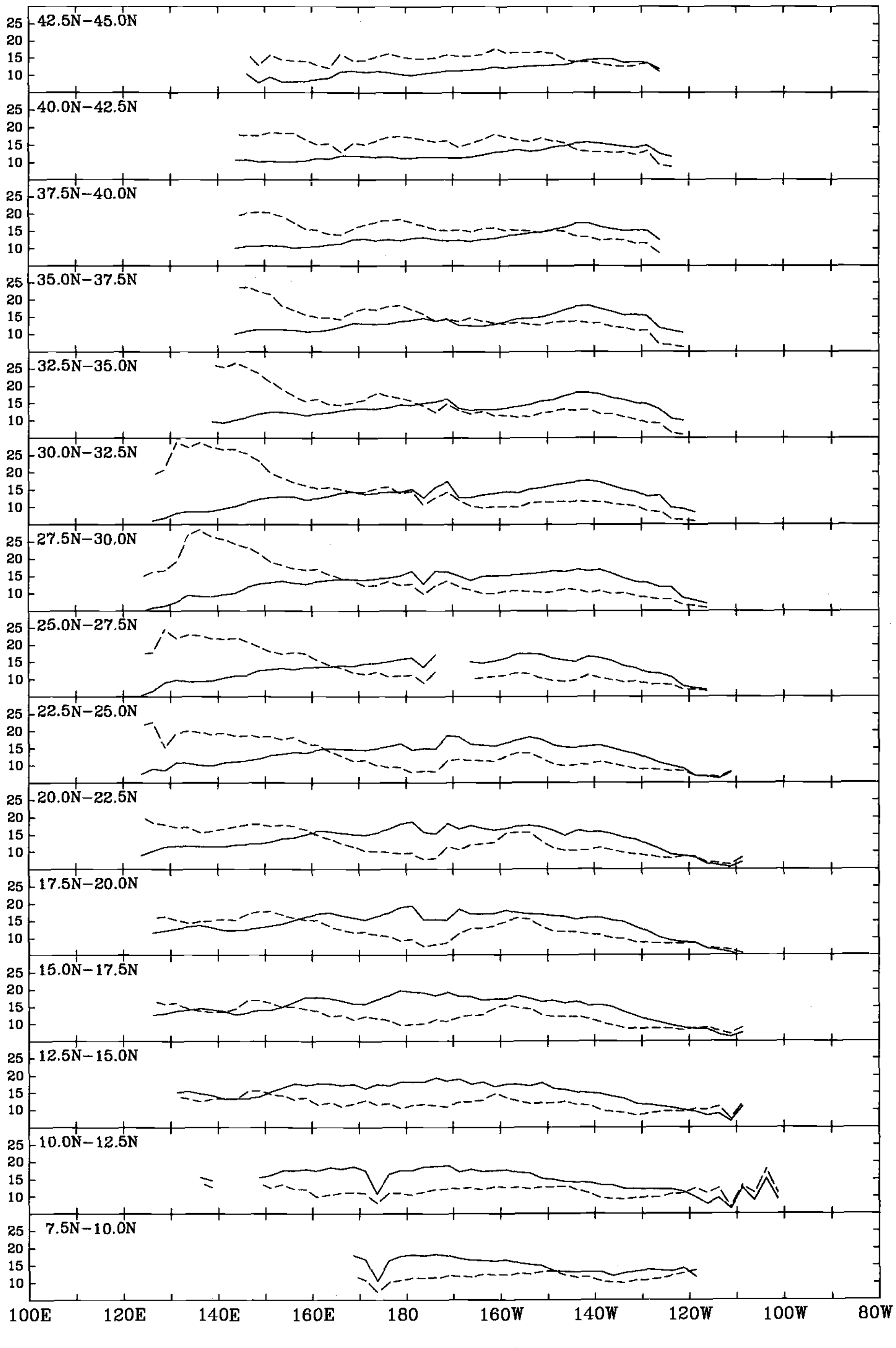

Figure 6.11(a) Longitudinal variations of monthly-mean cloud visible optical depth (dashed) and cloud droplet effective radius (solid) for the north Pacific between 7.5°N and 45°N. Results obtained for pixels overcast by single-layered, low-level clouds identified by the spatial coherence method for March 1989. The observations were restricted to near-nadir satellite view angles. Numbers for the vertical axis are for both the cloud visible optical depth and droplet effective radius (μm).

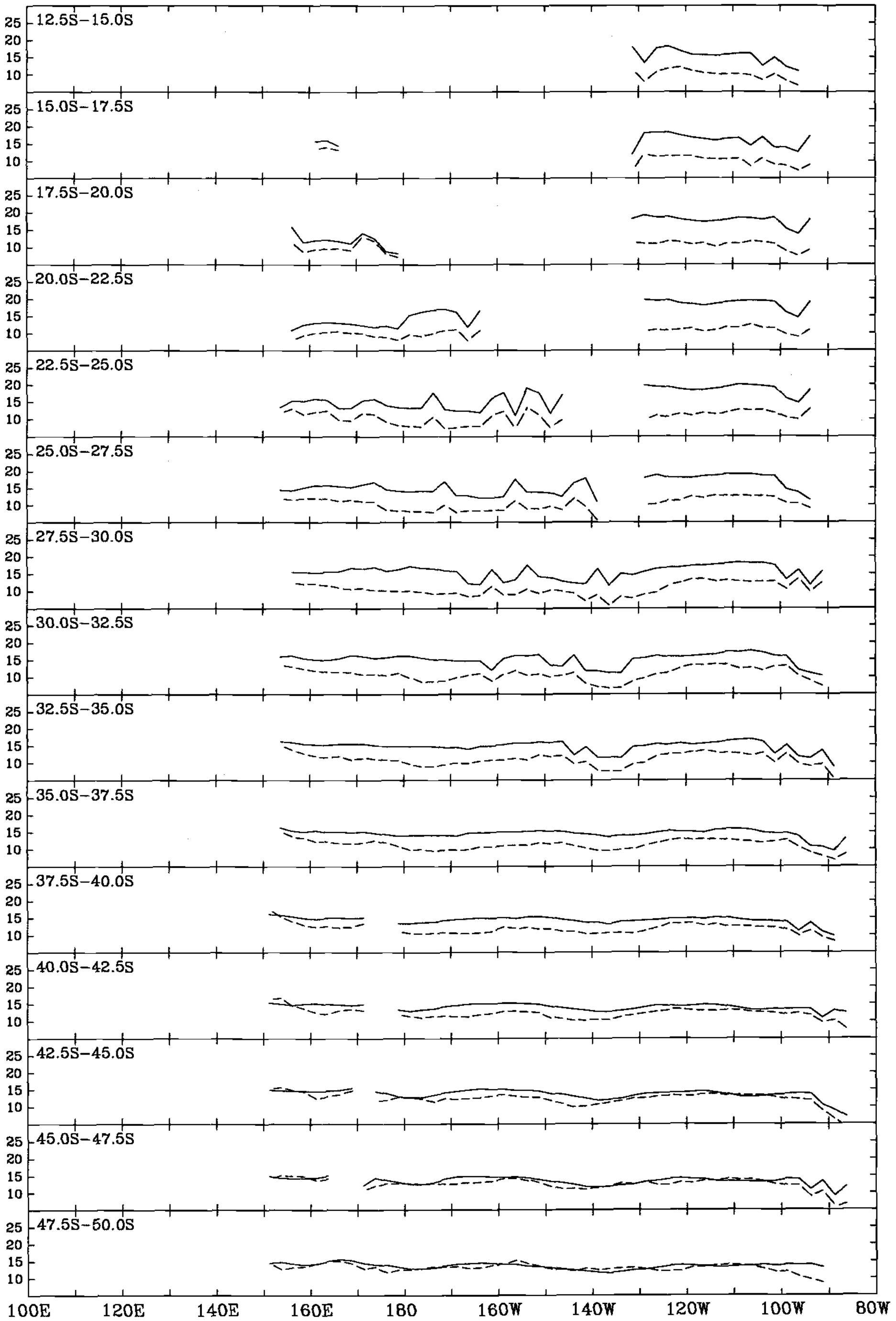

Figure 6.11(b) Same as Figure 6.11a, except for the south Pacific ocean between 12.5°S and 50°S.

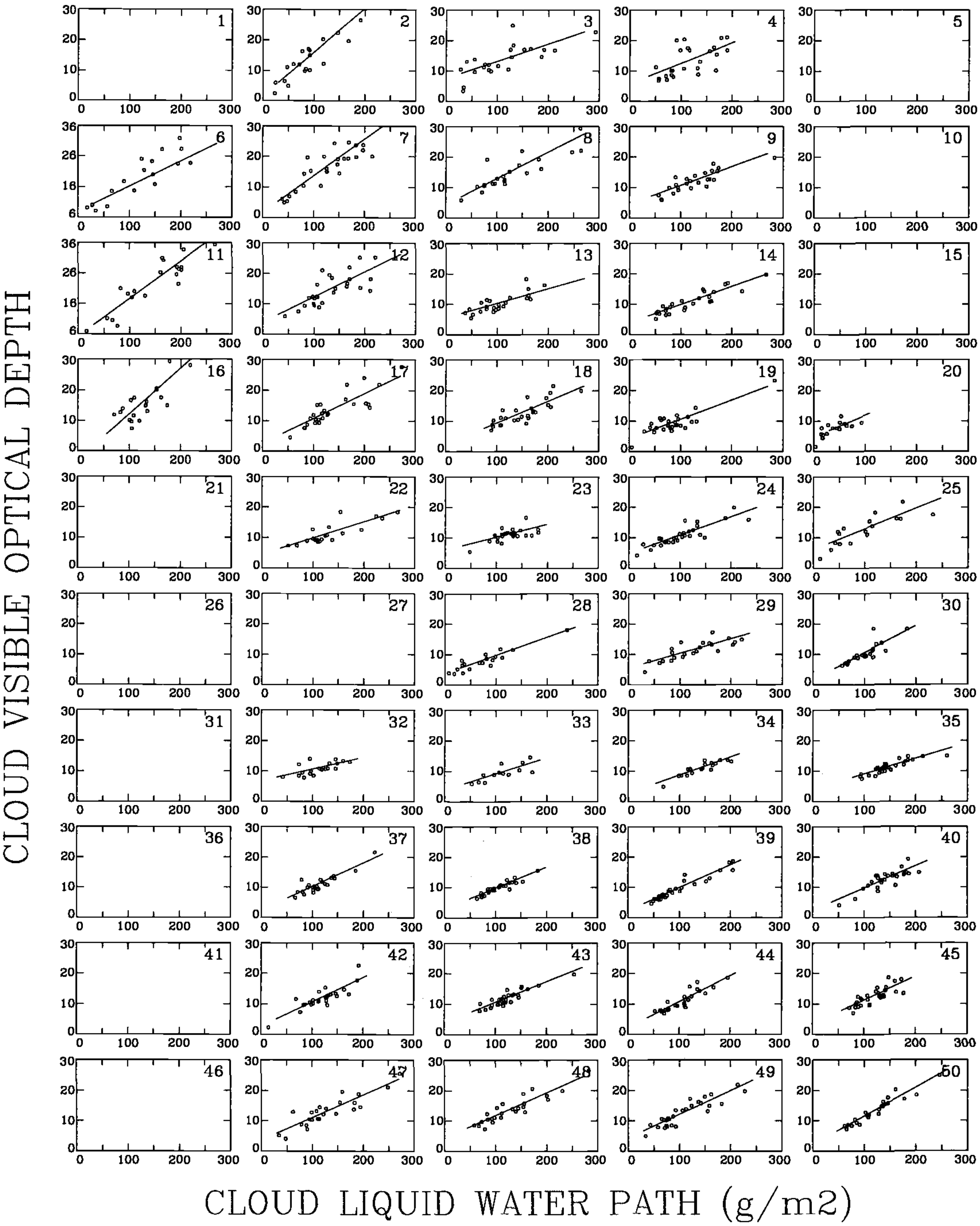

Figure 6.12 Same as Figure 5.4, except for cloud visible optical depth and cloud liquid water path.

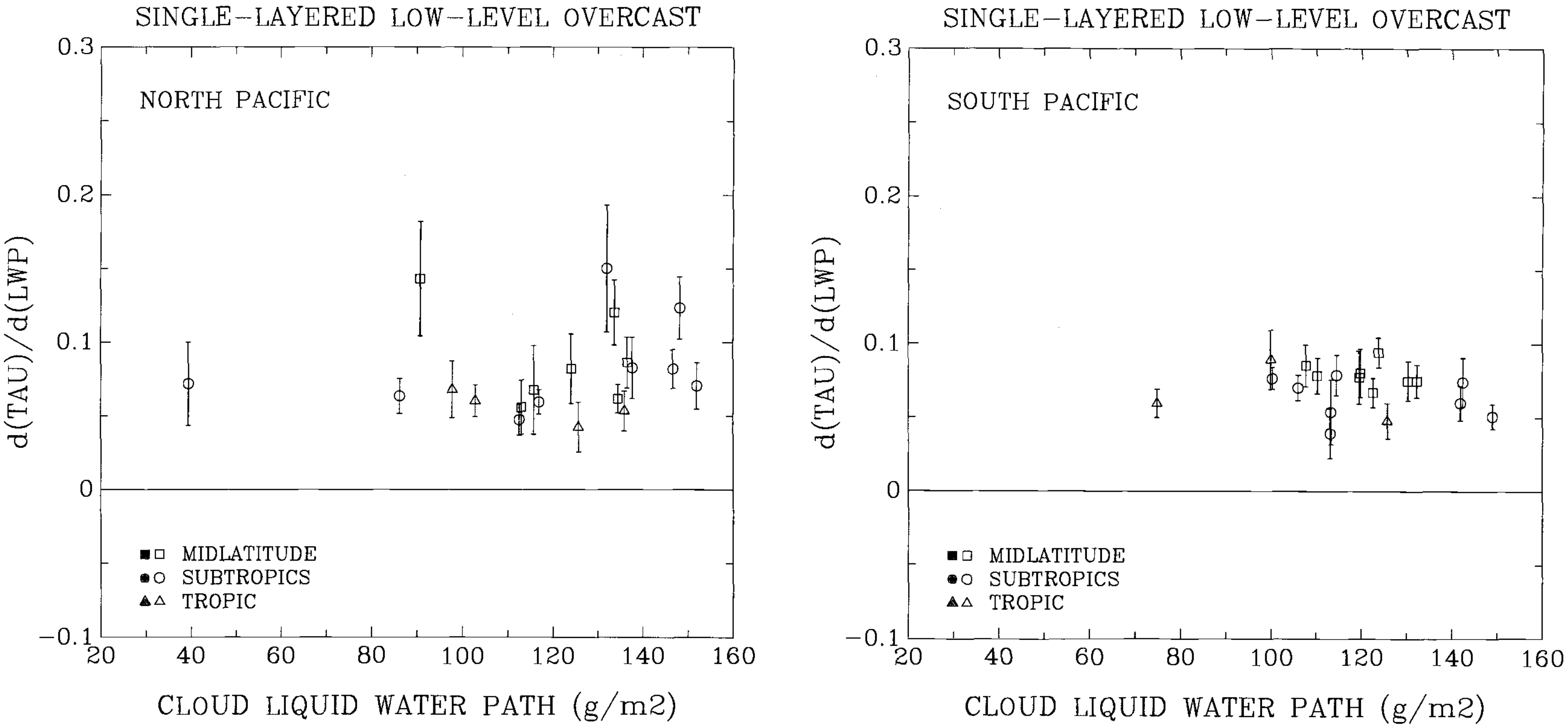

Figure 6.13 Same as Figure 5.5, except for $d(TAU)/d(LWP)$ and the monthly-mean cloud liquid water path shown in Figure 6.12.

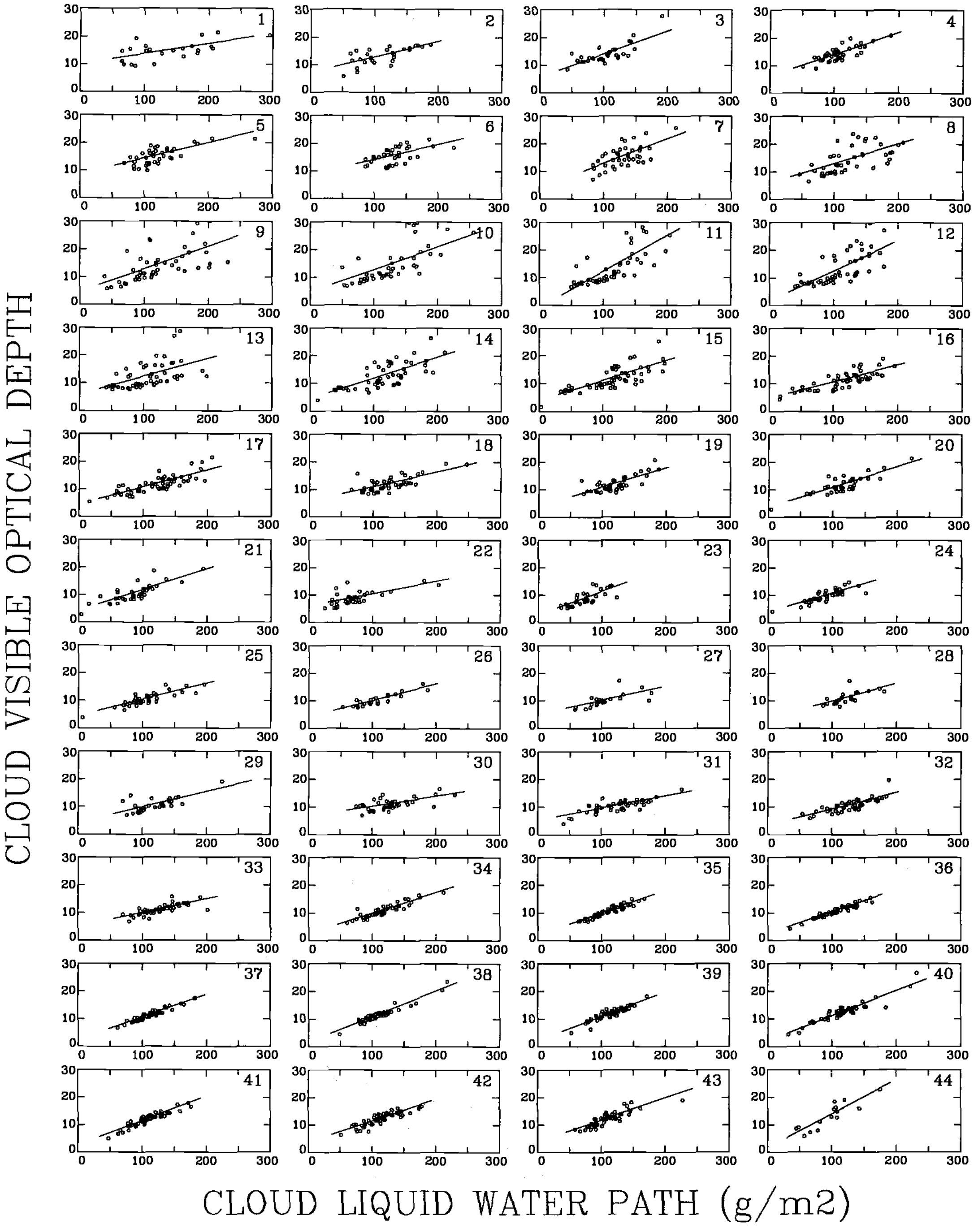

Figure 6.14 Same as Figure 5.6, except for cloud visible optical depth and cloud liquid water path.

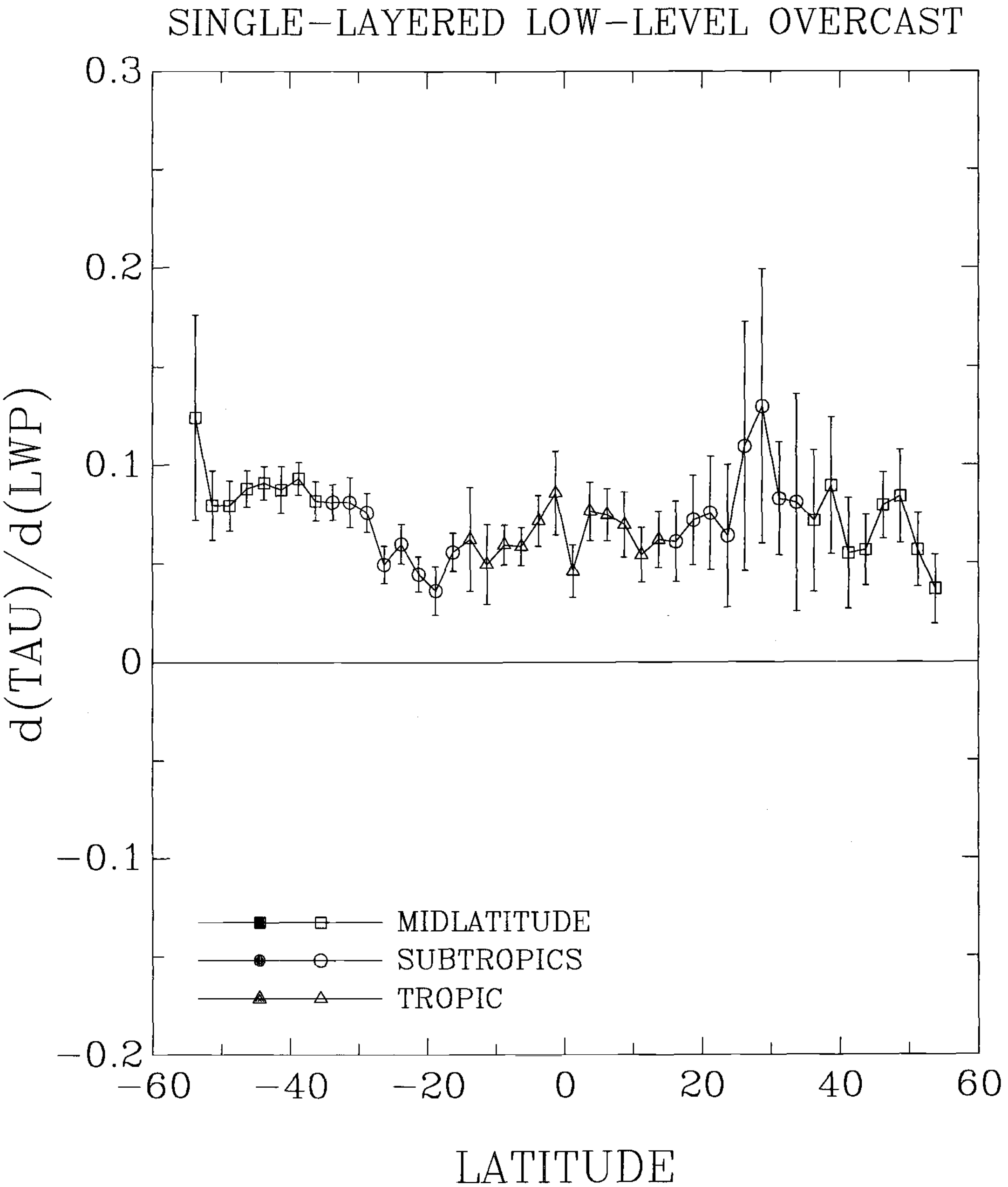

Figure 6.15 Same as Figure 5.7, except for $d(TAU)/d(LWP)$ shown in Figure 6.14. LWP is in g/m^2.

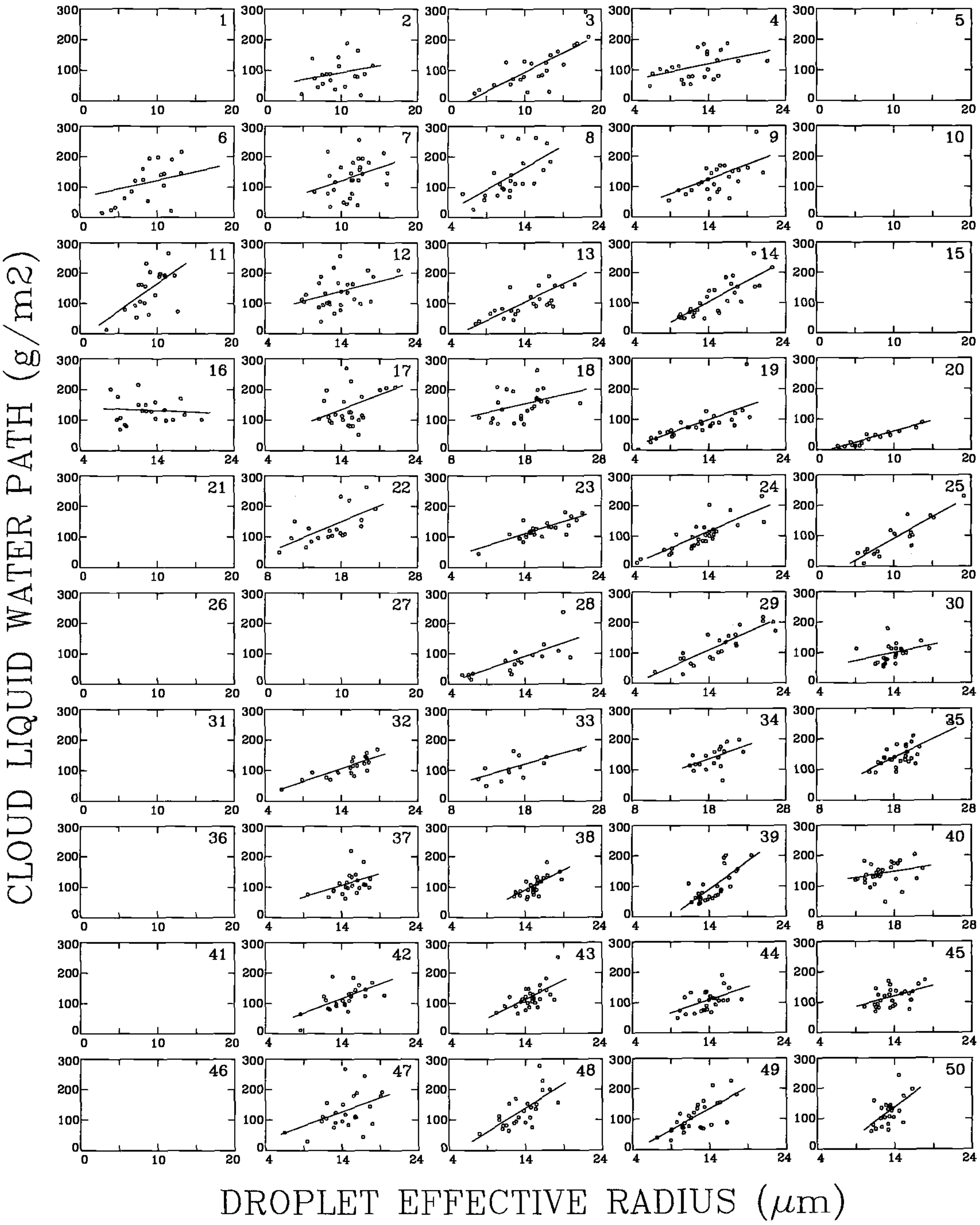

Figure 6.16 Same as Figure 5.4, except for cloud liquid water path and cloud droplet effective radius.

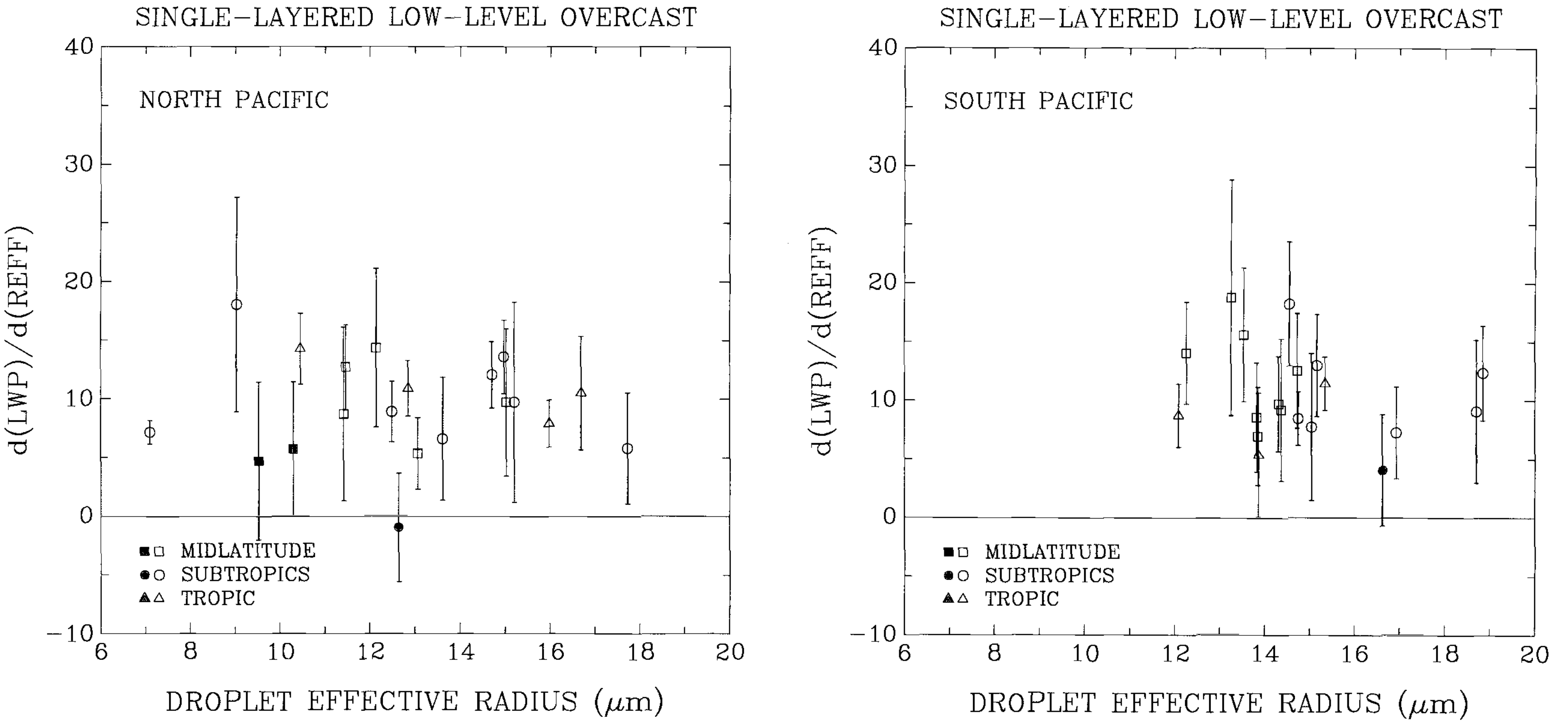

Figure 6.17 Same as Figure 5.5, except for $d(LWP)/d(REFF)$ and the monthly-mean cloud droplet effective radii shown in Figure 6.16. LWP is in g/m^2.

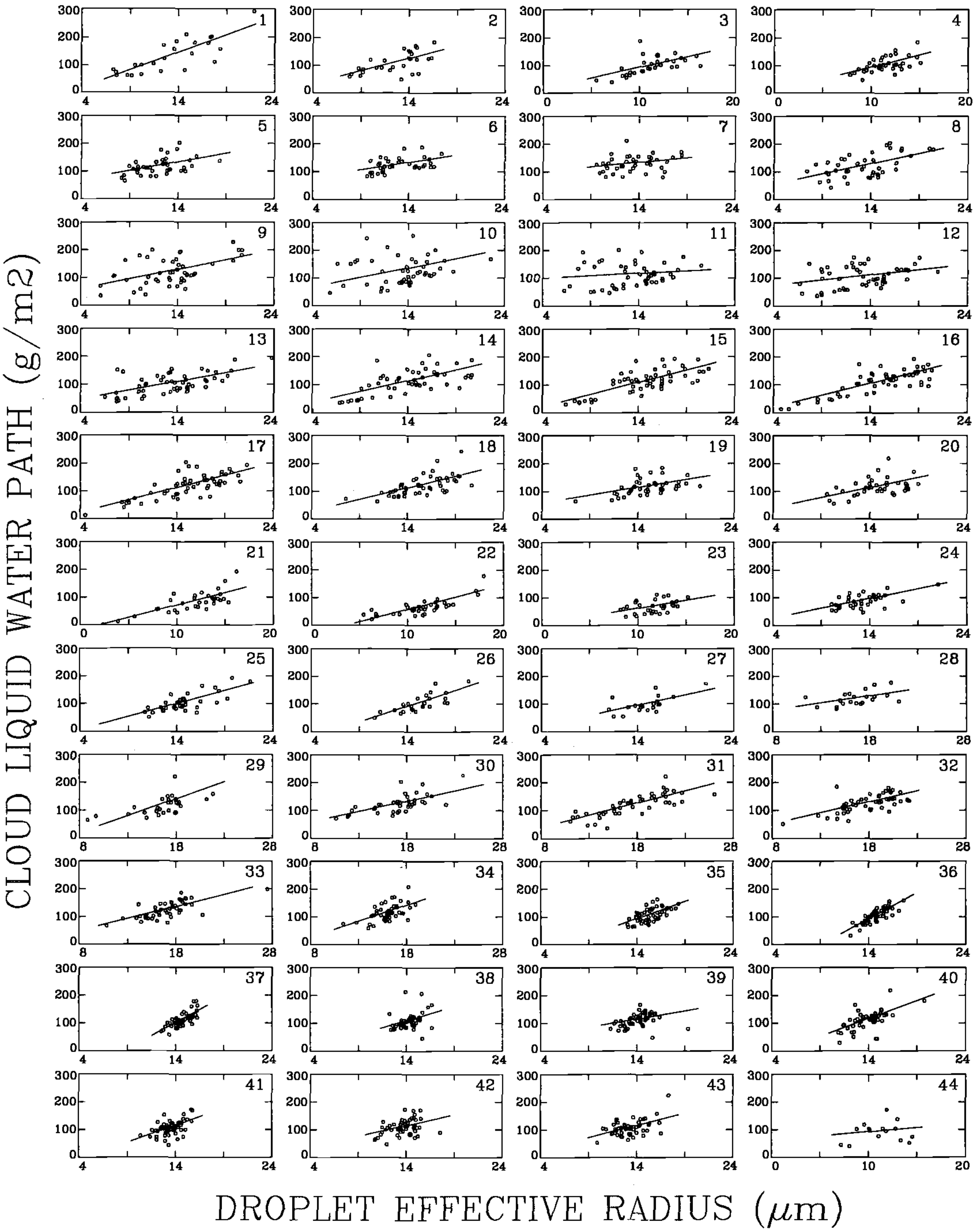

Figure 6.18 Same as Figure 5.6, except for cloud liquid water path and cloud droplet effective radius.

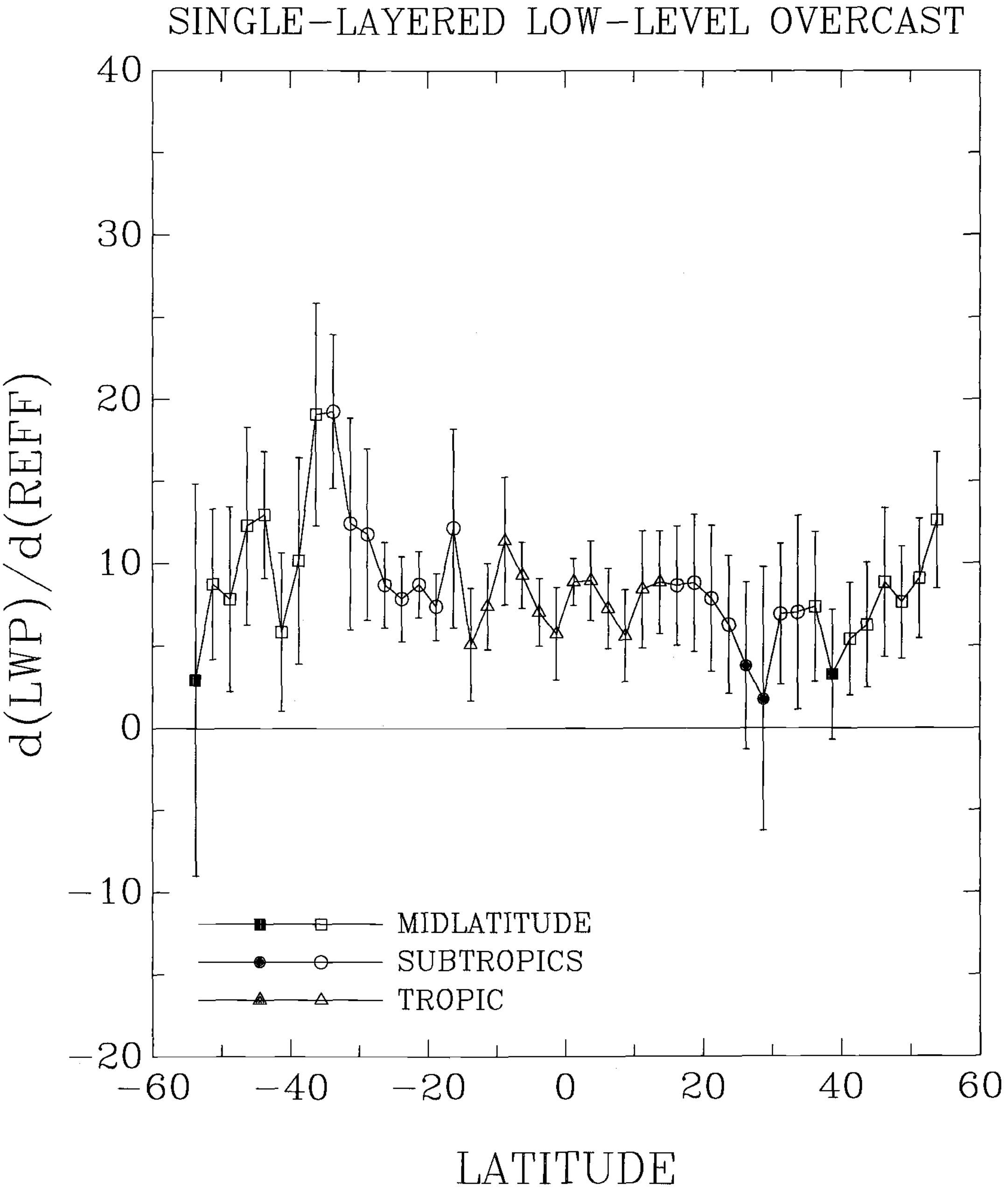

Figure 6.19 Same as Figure 5.7, except for $d(LWP)/d(REFF)$ shown in Figure 6.18. LWP is in g/m^2 and $REFF$ is in μm.

6.4.3 Cloud liquid water path and droplet effective radius

Figures 6.16 and 6.17 show the day-to-day correlations between cloud liquid water paths and droplet effective radii for pixels overcast by single-layered, low-level clouds. The longitudinal correlations are shown in Figures 6.18 and 6.19. These figures show that cloud liquid water paths were positively correlated with cloud droplet effective radii. However, exceptions were found near 25°N. These exceptions are shown in region 16 of Figure 6.16 and in latitude bands 11 and 12 of Figure 6.18. The exceptions showed no significant correlations between cloud liquid water path and droplet effective radius. These regions, as shown previously in Figures 6.7 and 6.9, displayed an increase in cloud visible optical depth with decreasing droplet effective radius. In general, for the single-layered, low-level clouds, large cloud liquid water paths were associated with large cloud droplets; small cloud liquid water paths were associated with small cloud droplets. The low-level cloud visible optical depth, cloud liquid water path, and droplet effective radius were all positively correlated.

6.5 Variations of cloud liquid water path and droplet effective radius with cloud top emission temperature

Figures 6.20 and 6.21 show the day-to-day correlations between low-level cloud liquid water path and cloud top emission temperature. Figures 6.22 and 6.23 show the longitudinal correlations for the two. These figures show that cloud liquid water path generally decreased with increasing cloud top emission temperature. The negative correlations obtained here are similar to those obtained for cloud visible optical depth and cloud top emission temperature. These negative correlations are thought to be due to variations in the cloud vertical thickness. As cloud vertical thickness decreases, cloud visible optical depth, cloud liquid water path, and cloud top altitude all decrease. As cloud top altitude decreases, cloud top temperature increases.

The relationships between cloud droplet effective radii and cloud top emission temperatures for these low-level clouds are illustrated in Figures 6.24 and 6.25 for the day-to-day correlations and in Figures 6.26 and 6.27 for the longitudinal correlations. In the day-to-day correlations, cloud droplet effective radius generally decreased with increasing cloud top emission temperature. As warmer cloud top temperatures often mean lower cloud top altitudes or smaller cloud vertical thickness, smaller droplets found in clouds having lower altitudes on a day-to-day basis may be due to the low-level clouds coupling with marine boundary layer (Coakley et al., 1997). Since the marine boundary layer is thought to be more polluted (e.g., ship effluents, sea salt, sulfate aerosols), such a coupling between the low-level cloud layer and the marine boundary layer may give rise to smaller cloud droplets. For the longitudinal correlations, cloud droplet effective radius and cloud top emission temperature show very little correlation, except for the tropics. For most of the southern Pacific ocean, the droplet effective radii for the low-level, overcast pixels were constant across the ocean in each of the 2.5°-latitude bands.

For most of the tropical regions, the correlations between cloud droplet effective radius and cloud top emission temperature were negative for both day-to-day and longitudinal correlations. The larger droplet effective radii at colder cloud top emission temperatures may result from the vertically thicker clouds being accompanied by stronger, long-lasting vertical motions which tend to produce larger droplets near cloud top (Rodger and Yau, 1980). Thicker clouds are expected to have larger droplets.

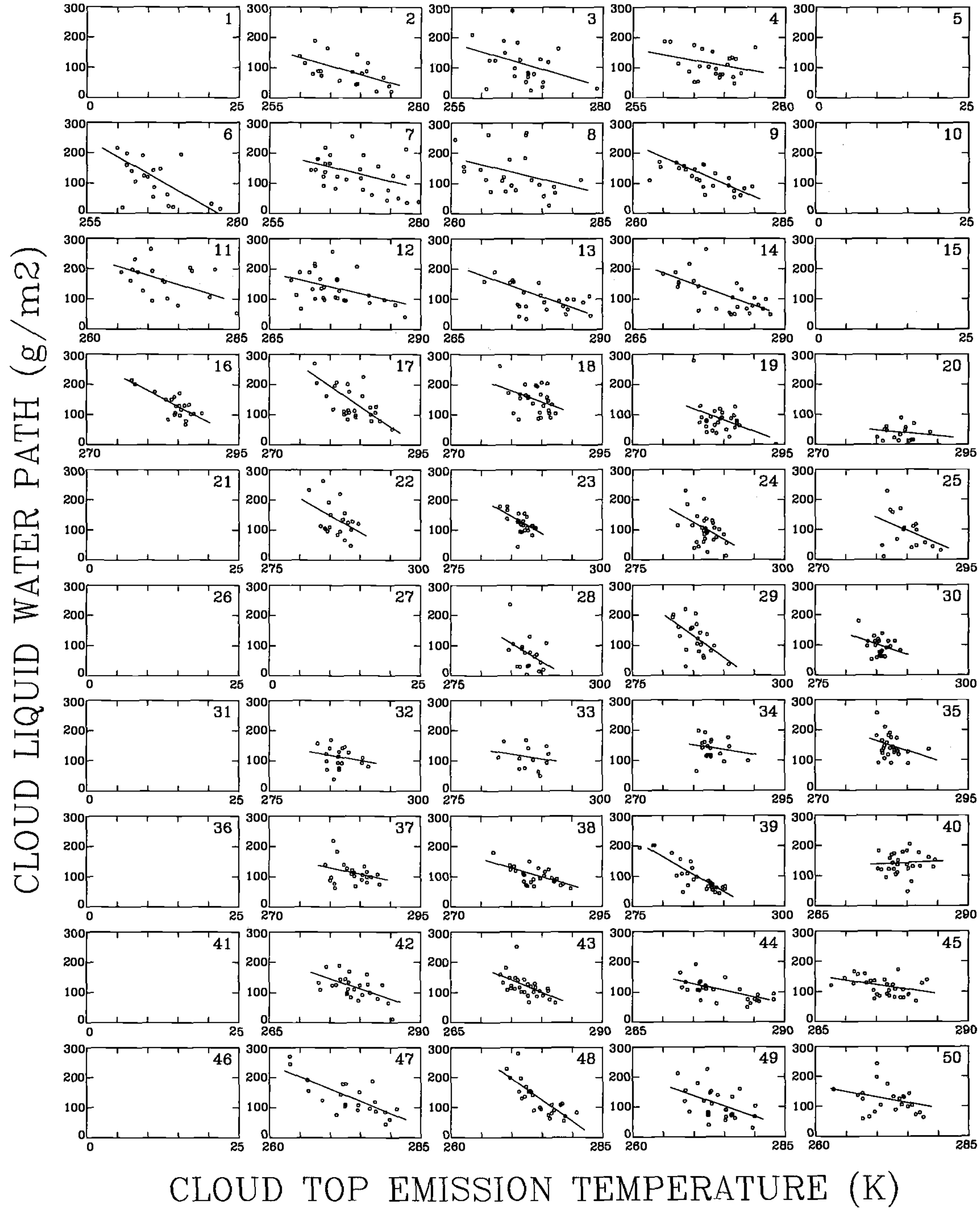

Figure 6.20 Same as Figure 5.4, except for cloud liquid water path and cloud top emission temperature.

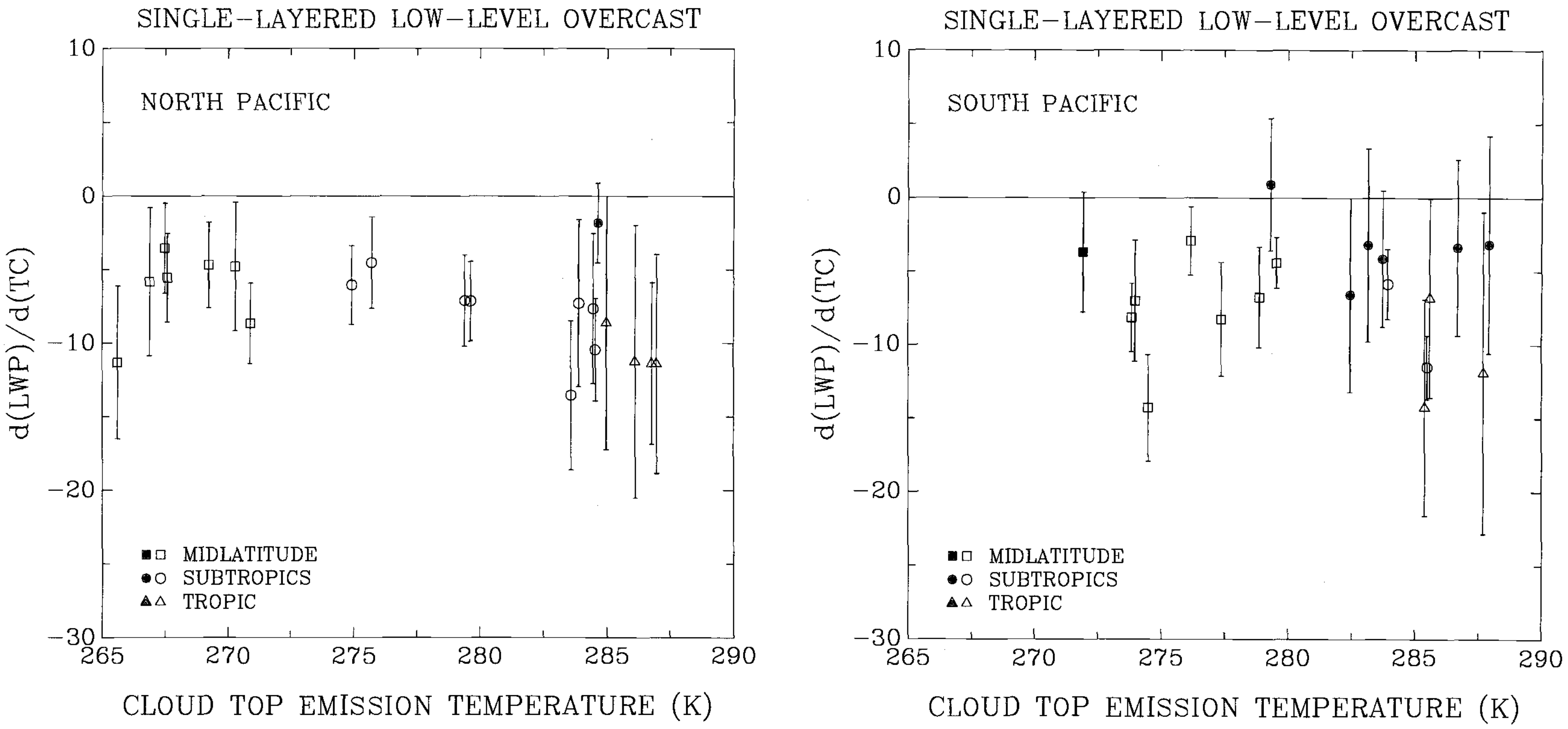

Figure 6.21 Same as Figure 5.5, except for $d(LWP)/d(TC)$ and the monthly-mean cloud top emission temperatures shown in Figure 6.20. LWP is in g/m^2.

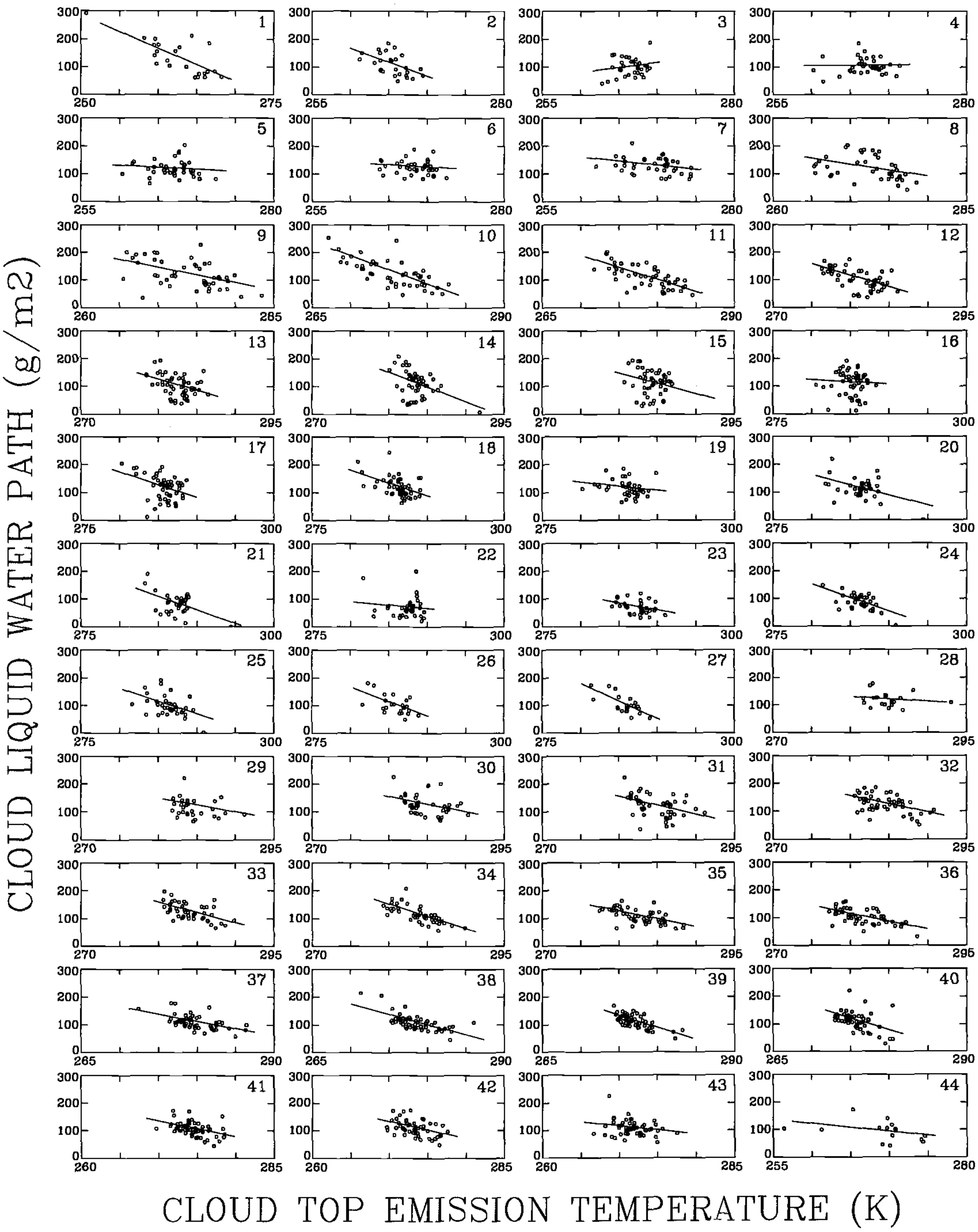

Figure 6.22 Same as Figure 5.6, except for cloud liquid water path and cloud top emission temperature.

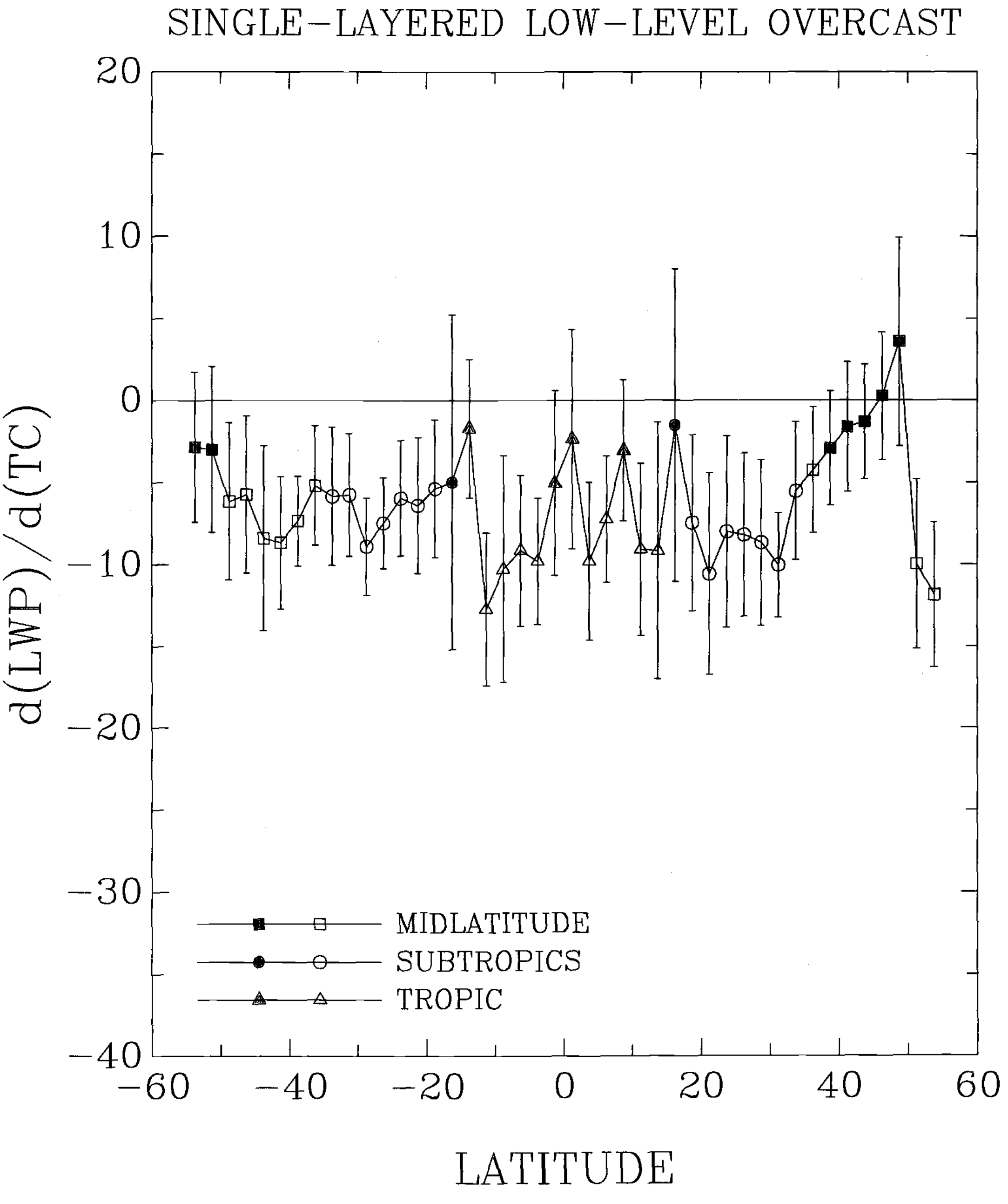

Figure 6.23 Same as Figure 5.7, except for $d(LWP)/d(TC)$ shown in Figure 6.22. LWP is in g/m^2 and TC is in K.

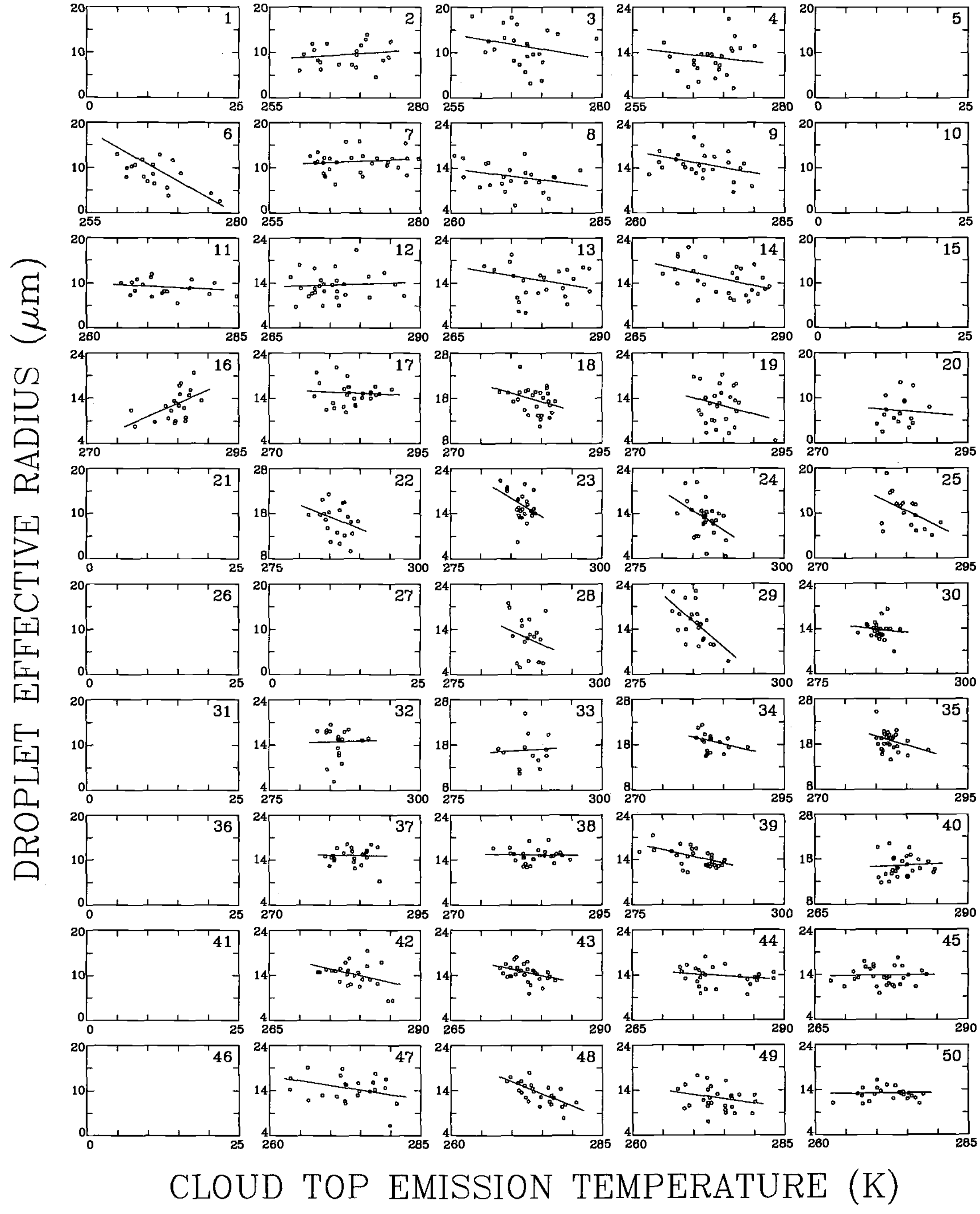

Figure 6.24 Same as Figure 5.4, except for cloud droplet effective radius and cloud top emission temperature.

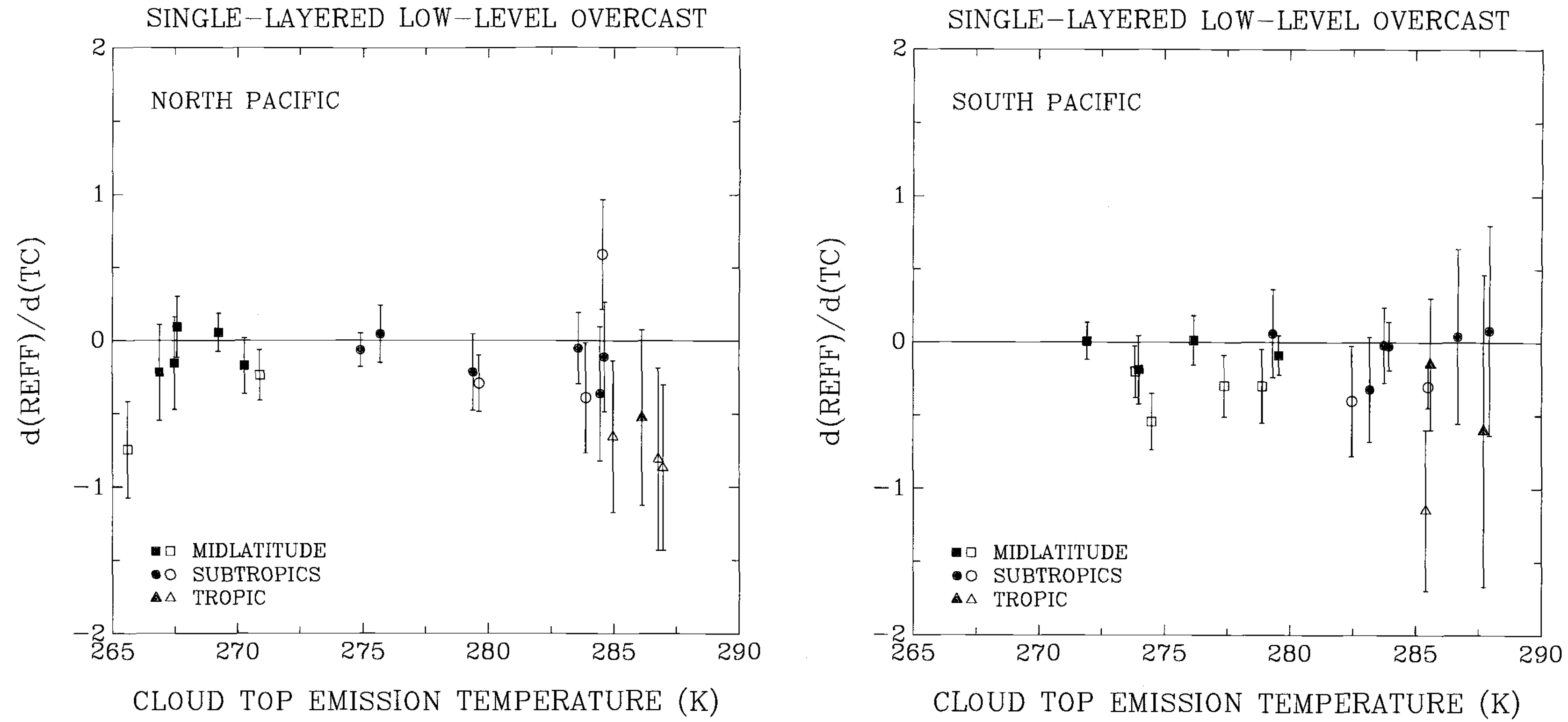

Figure 6.25 Same as Figure 5.5, except for $d(REFF)/d(TC)$ and the monthly-mean cloud top emission temperatures shown in Figure 6.24. $REFF$ is in μm.

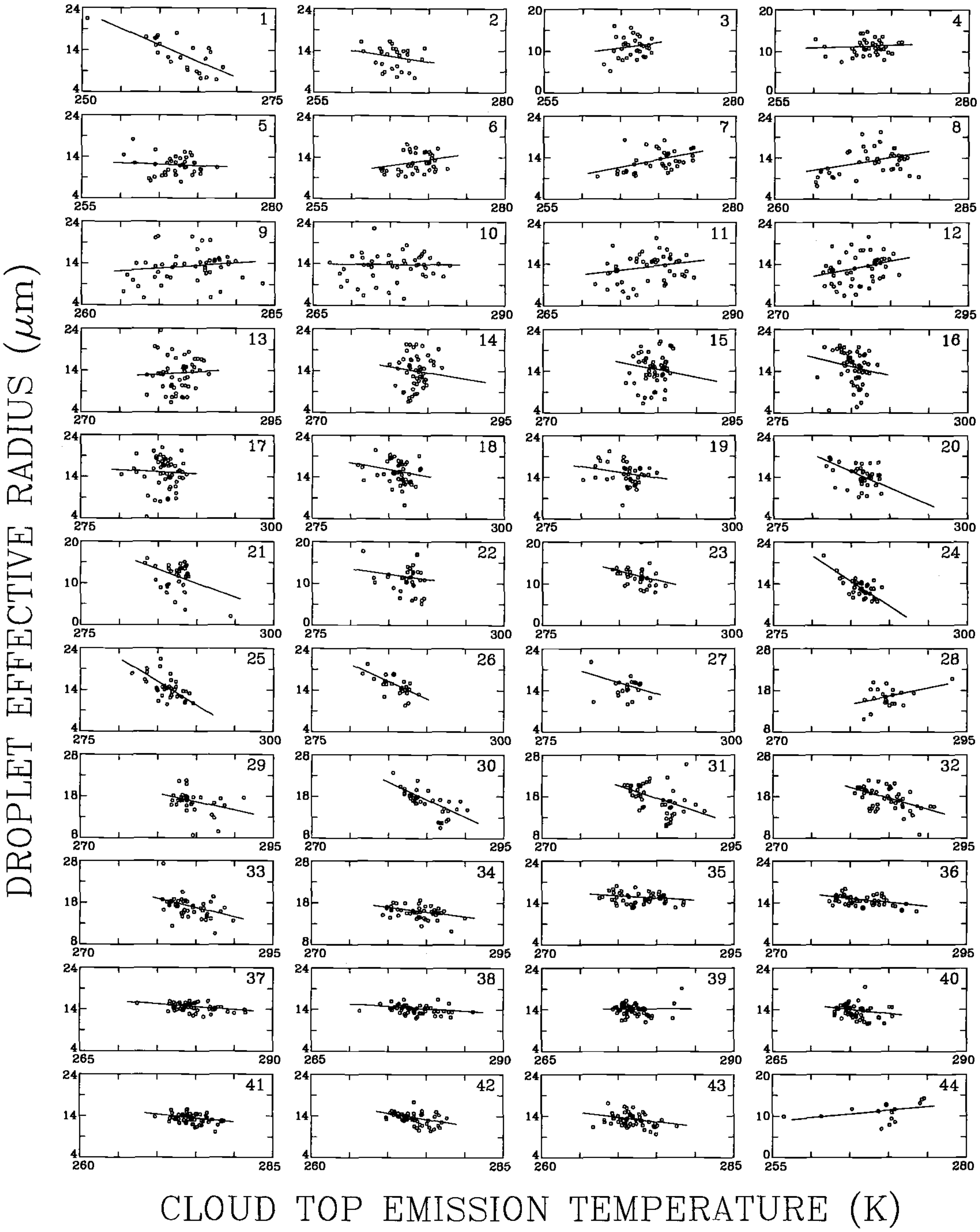

Figure 6.26 Same as Figure 5.6, except for cloud droplet effective radius and cloud top emission temperature.

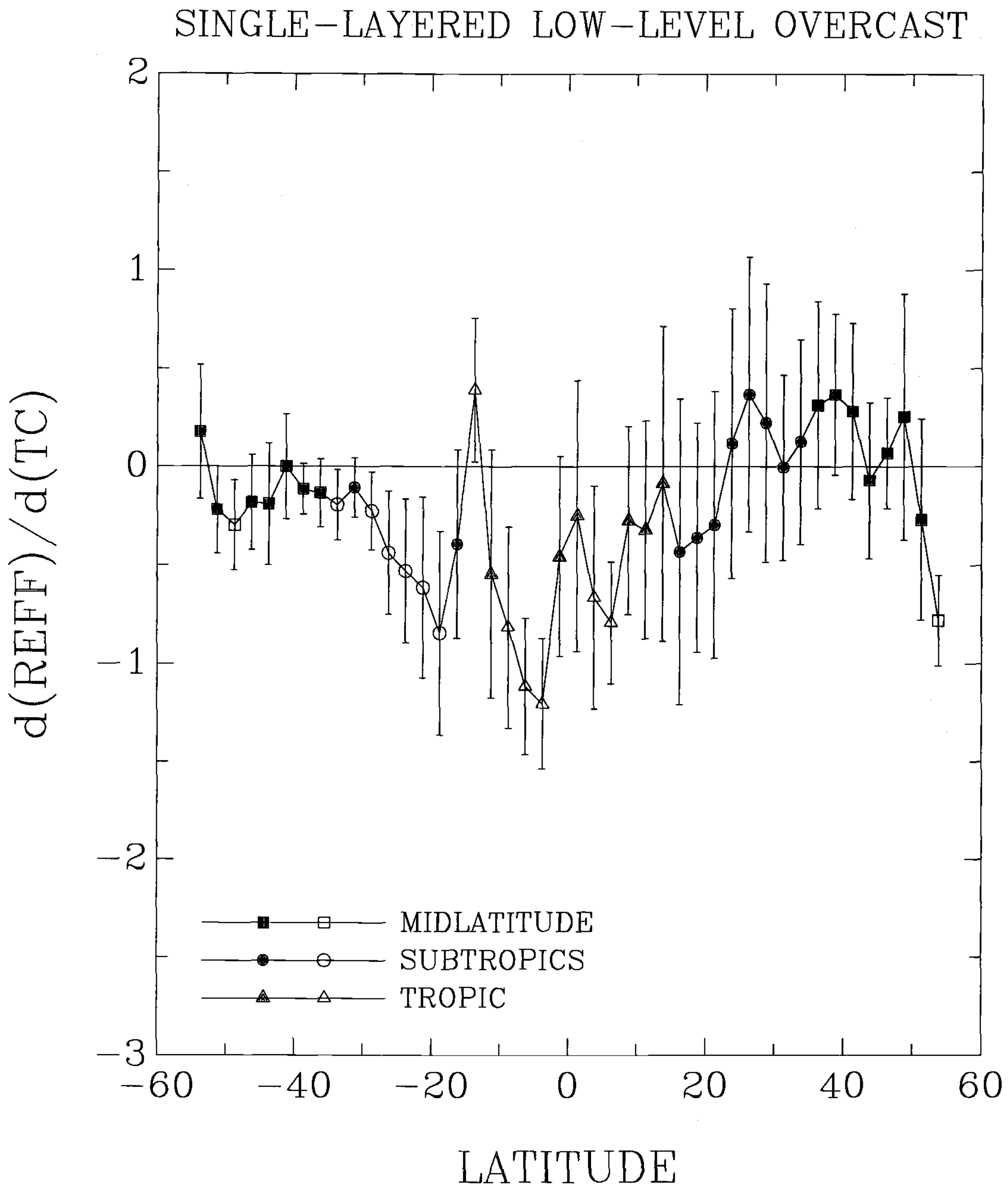

Figure 6.27 Same as Figure 5.7, except for $d(REFF)/d(TC)$ shown in Figure 6.26. $REFF$ is in μm and TC is in K.

6.6 Variations of cloud liquid water path and droplet effective radius with sea surface-cloud top temperature difference

To study the role of cloud vertical thickness, the sea surface-cloud top temperature difference, $\Delta T = SST - TC$, was used here as an index of cloud vertical thickness. The latitudinal distributions of the sea surface-cloud top temperature differences were shown in Figure 4.15. The monthly-mean, sea surface-cloud top temperature differences for pixels overcast by the single-layered, low-level clouds were about 8-14K. For a lapse rate of 7 K/km (Betts et al., 1992), the 8–14K, sea surface-cloud top temperature differences correspond to a $\sim$1–2 km range in cloud top altitude. The sea surface-cloud top temperature differences obtained for partly cloudy pixels were about 2-4K smaller than those obtained for the overcast pixels. This difference is due to the higher cloud top emission temperatures obtained for the partly cloudy pixels when they were assumed to be overcast. An interesting result shown in the figure is that the sea surface-cloud top temperature differences for the overcast and partly cloudy pixels were similar at the higher latitudes ($>\sim$ 45°N). This finding may be explained by the relatively large cloud optical depths and cloud cover fractions obtained for the partly cloudy pixels at these latitudes. These large optical depths and cloud cover fractions make the partly cloudy pixels appear as if they were opaque, like their overcast counterparts, at 11 μm.

Figures 6.28 and 6.29 show the day-to-day correlations between low-level cloud liquid water paths and the sea surface-cloud top temperature differences. Figures 6.30 and 6.31 show the longitudinal correlations. Cloud liquid water paths and sea surface-cloud top temperature differences were positively correlated. The values of $d(LWP)/d(\Delta T)$ for the pixels overcast by single-layered, low-level clouds for March

1989 over the Pacific ocean were ~5-10 g/m^2/K. Some values between 10-15 g/m^2/K were also found in the tropics and subtropics.

Figures 6.32-6.35 show the same as Figures 6.28-6.31, except for cloud droplet effective radius and the sea surface-cloud top temperature difference. In the day-to-day variations, droplet effective radii generally increased with increasing sea surface-cloud top temperature differences. The increase was relatively large in the tropics. Again, the only significant decrease in droplet effective radius with increasing sea surface-cloud top temperature difference was found in region 16 (15°N-25°N, 120°E-150°E). Positive correlations were common between cloud droplet effective radius and sea surface-cloud top temperature difference and would appear to be consistent with expectations for droplet growth with increasing cloud vertical thickness. The longitudinal correlations, as shown in Figures 6.34 and 6.35, were also positive in most of the tropics, the southern subtropics, and northern midlatitudes. Low-level cloud droplet effective radii in the southern subtropics and southern midlatitudes appeared to vary little, whereas relatively large variations were found in the northern Pacific.

6.7 The role of cloud vertical thickness in determining cloud liquid water path, optical depth, and droplet radius

It has been shown that low-level cloud liquid water path generally increased with an increase in the sea surface-cloud top temperature difference. Since the change in the difference between sea surface and cloud top temperature often indicates a change in cloud top altitude (Betts et al., 1992) and since the maritime, single-layered, low-level cloud base is assumed to vary little in altitude, it is proposed that the increase in low-level cloud liquid water path is mainly due to an increase in the vertical thickness

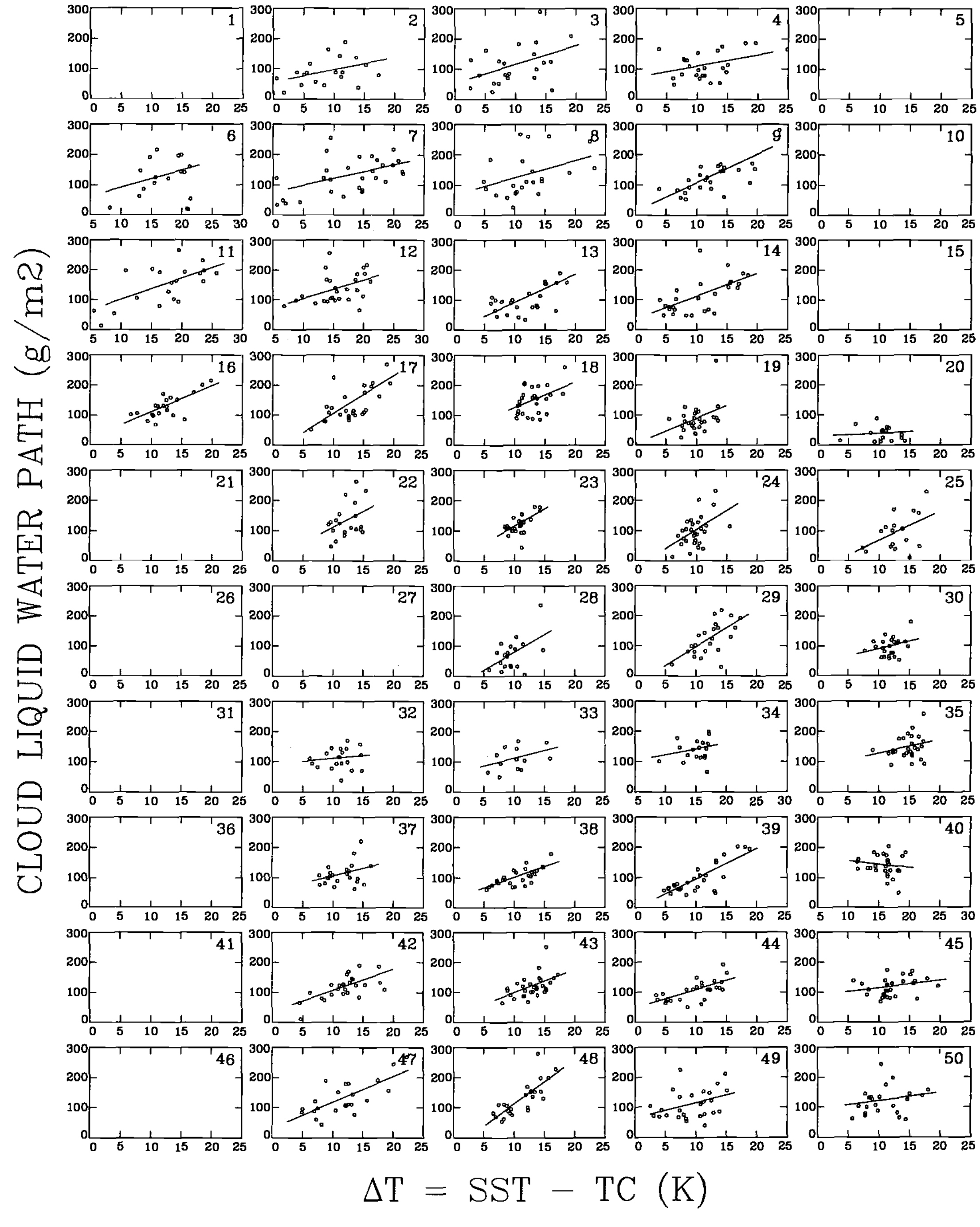

Figure 6.28 Same as Figure 5.4, except for cloud liquid water path and sea surface-cloud top temperature difference.

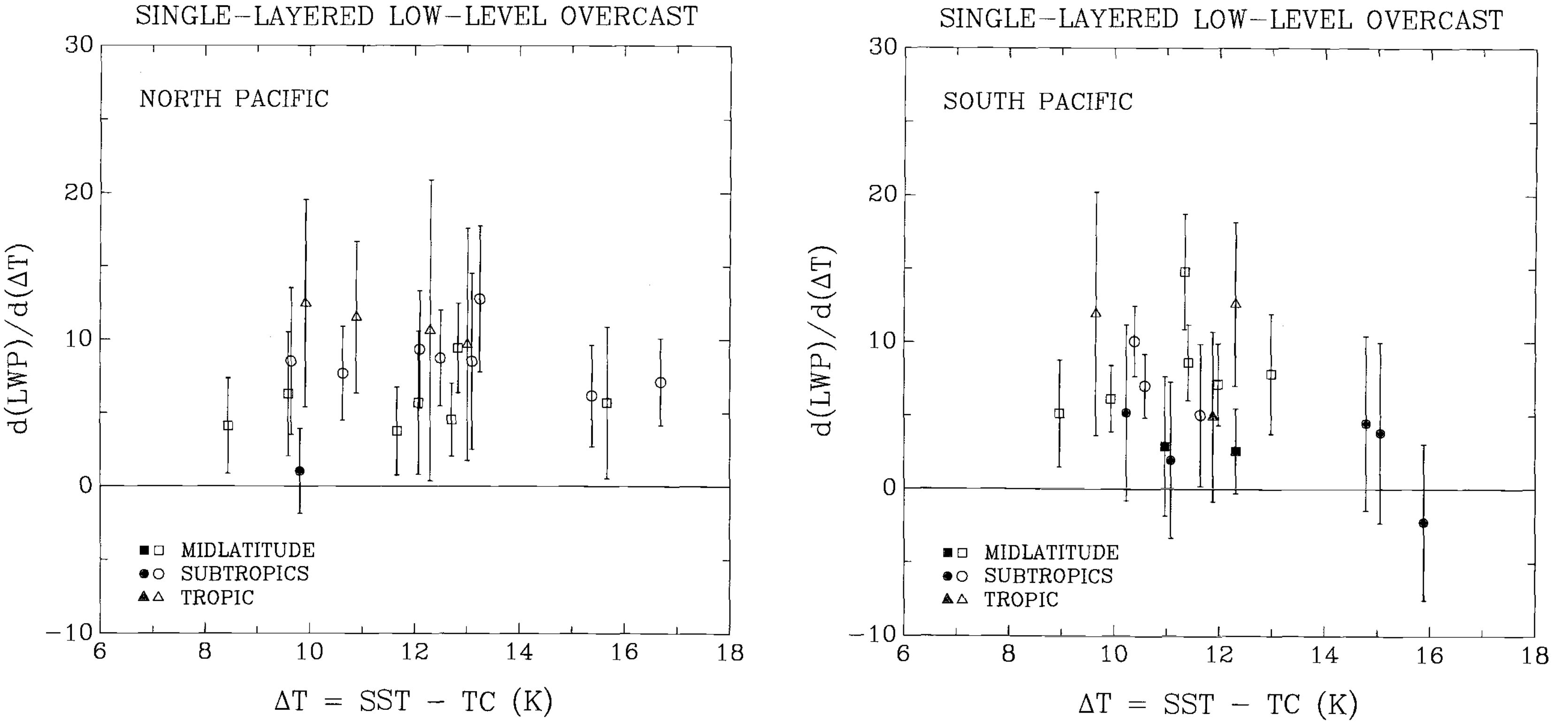

Figure 6.29 Same as Figure 5.5, except for $d(LWP)/d(\Delta T)$ and the monthly-mean sea surface-cloud top temperature differences shown in Figure 6.28. LWP is in g/m^2.

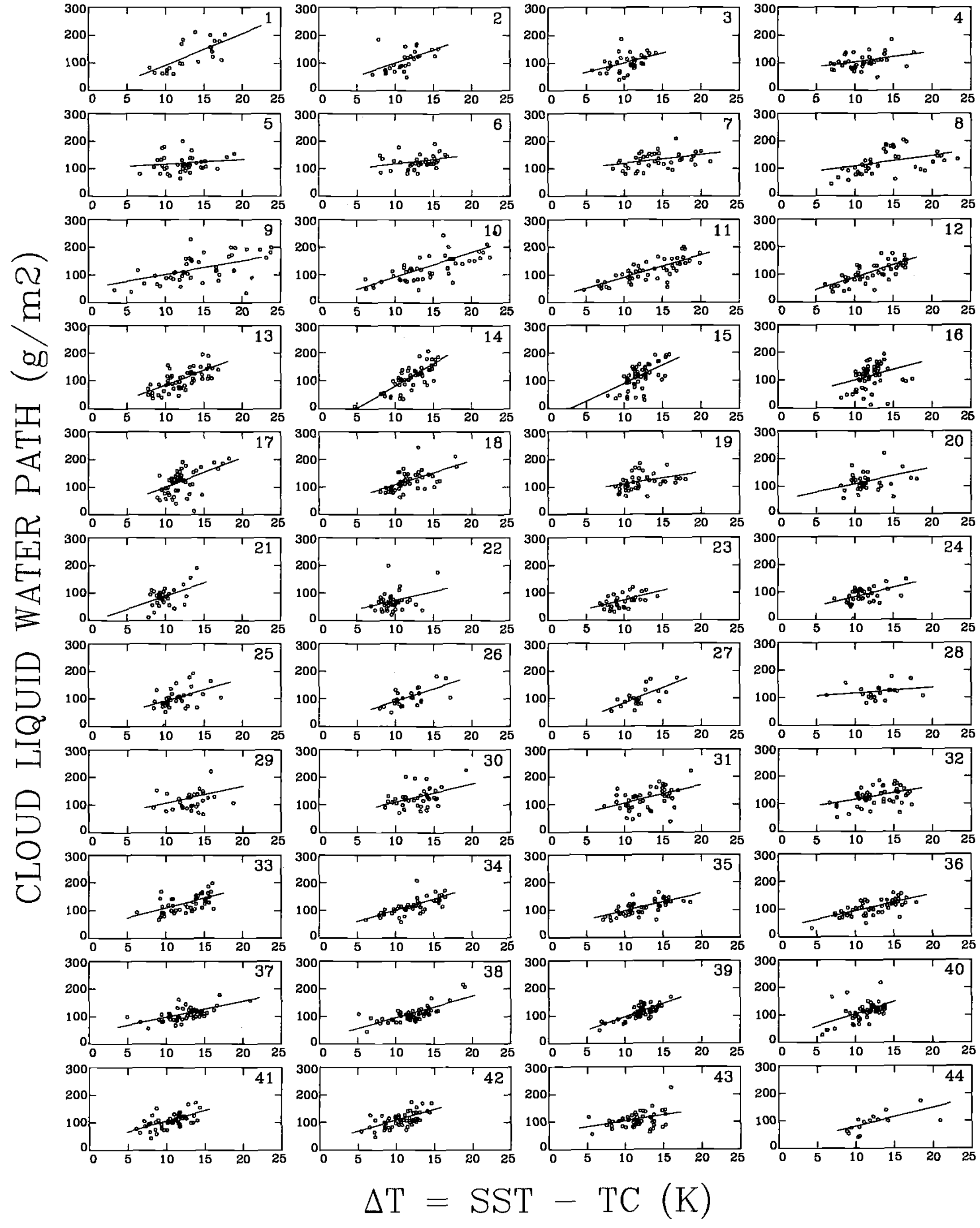

Figure 6.30 Same as Figure 5.6, except for cloud liquid water path and sea surface-cloud top temperature difference.

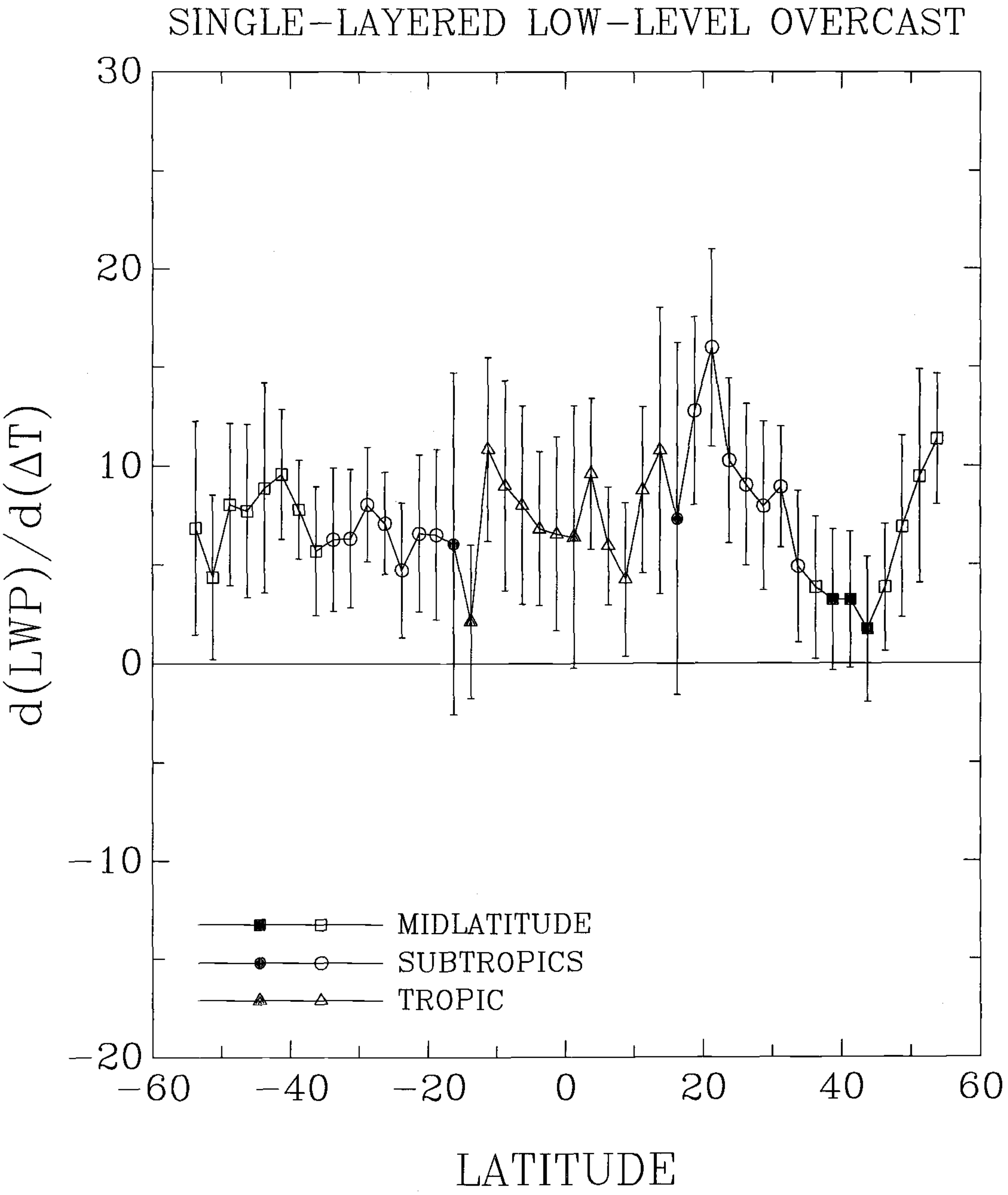

Figure 6.31 Same as Figure 5.7, except for $d(LWP)/d(\Delta T)$ shown in Figure 6.30. LWP is in g/m^2 and ΔT is in K.

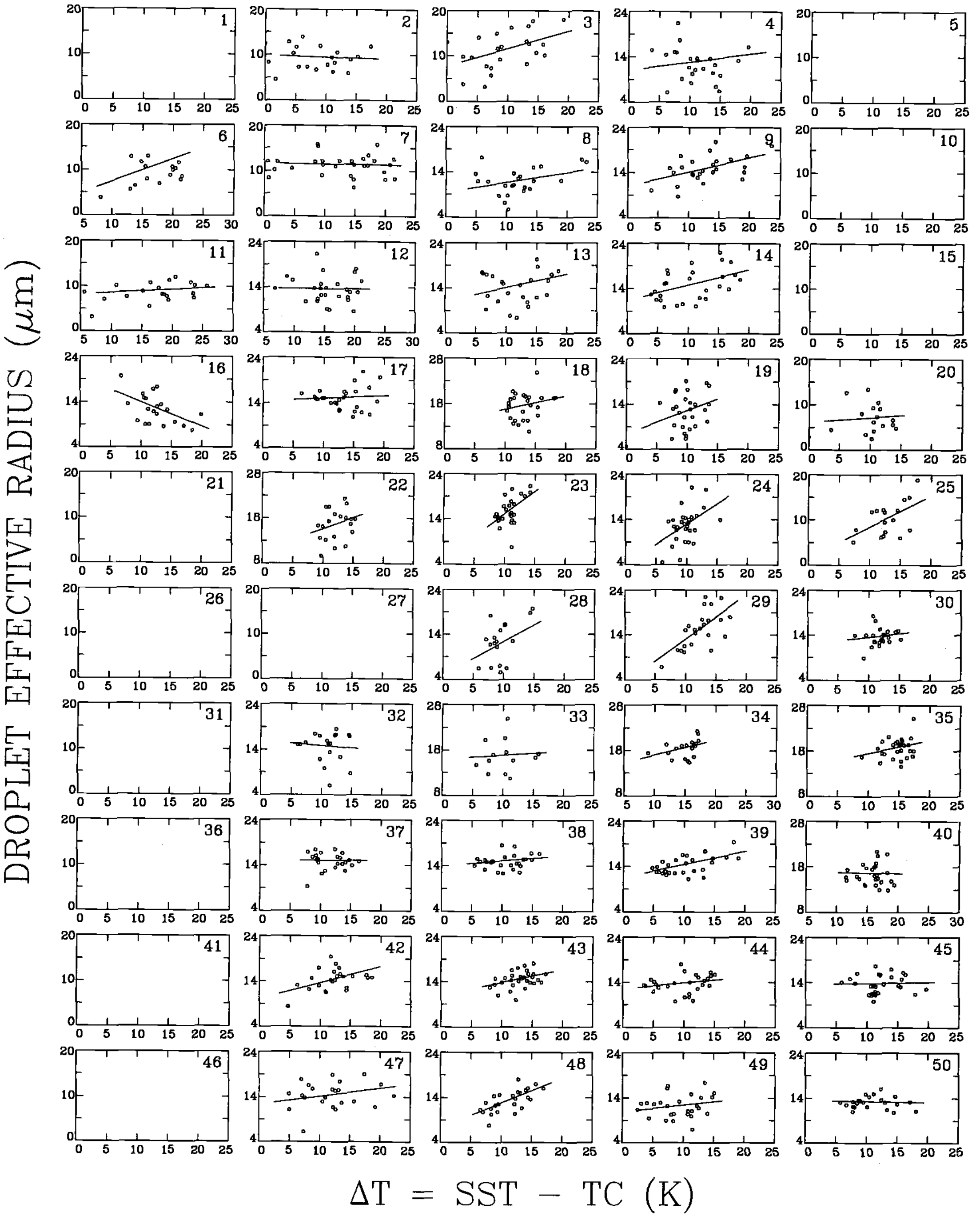

Figure 6.32 Same as Figure 5.4, except for cloud droplet effective radius and sea surface-cloud top temperature difference.

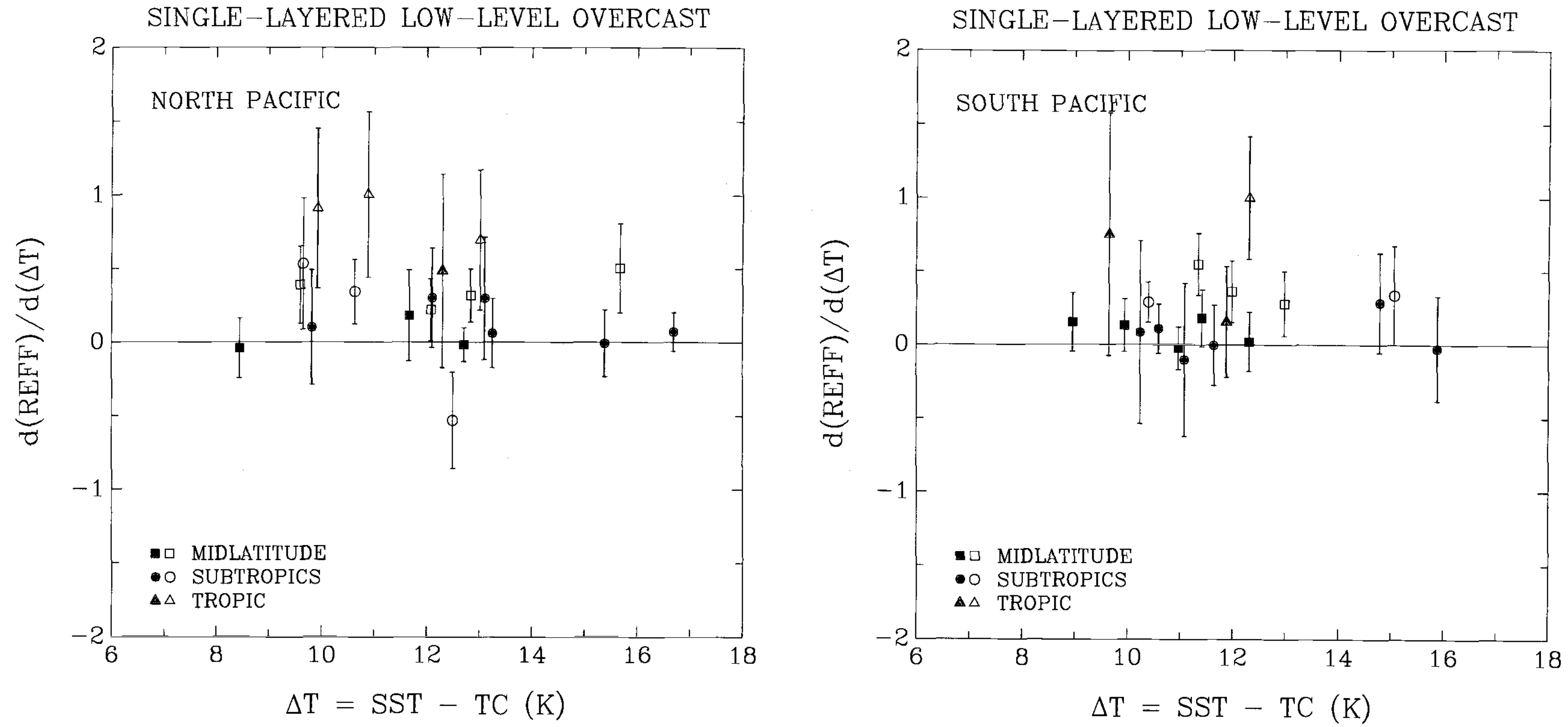

Figure 6.33 Same as Figure 5.5, except for $d(REFF)/d(\Delta T)$ and the monthly-mean sea surface-cloud top temperature differences shown in Figure 6.32. $REFF$ is in μm.

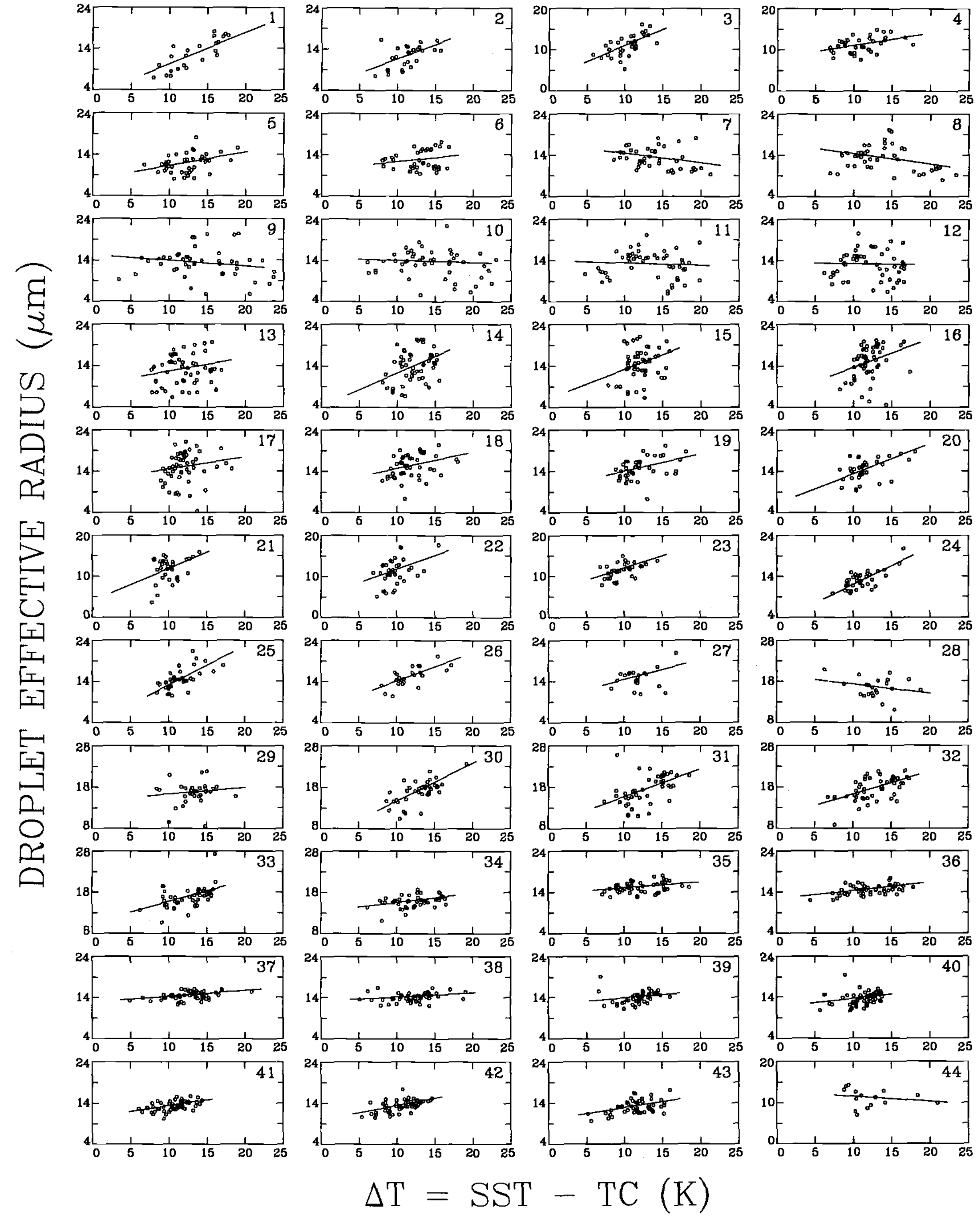

Figure 6.34 Same as Figure 5.6, except for cloud droplet effective radius and sea surface-cloud top temperature difference.

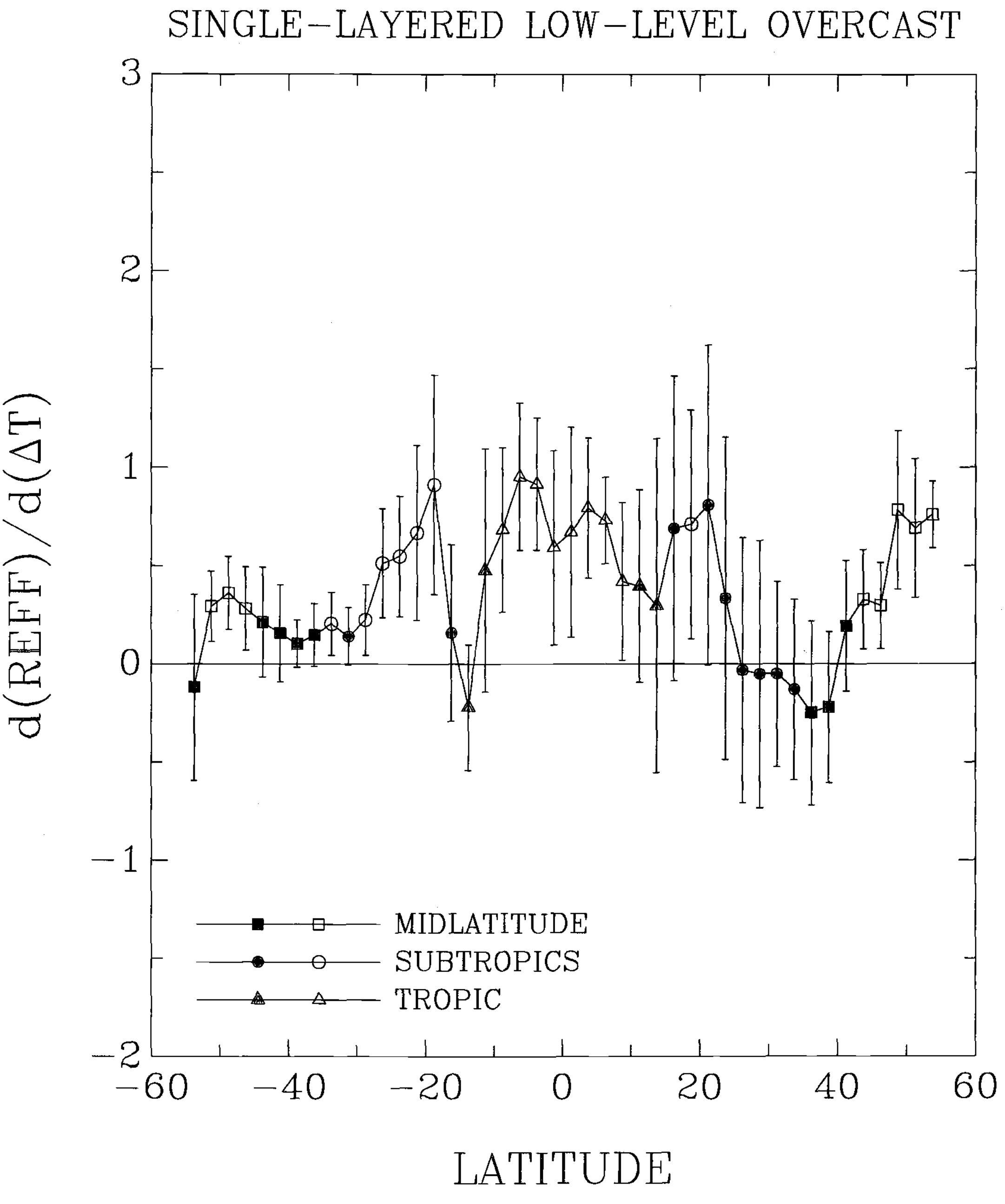

Figure 6.35 Same as Figure 5.7, except for $d(REFF)/d(\Delta T)$ shown in Figure 6.34. $REFF$ is in μm.

of these layered clouds. The cloud liquid water path is given by

$$LWP = \frac{4}{3}\,\rho_{liq} \int_{Z_1}^{Z_2} \int_{0}^{\infty} \pi r^3 n(r)\, dr\, dz \,, \tag{6.2}$$

where Z_1 is the altitude of the cloud base and Z_2 is the cloud top altitude. Based on the definition, cloud liquid water path is governed by cloud vertical thickness and the cloud droplet size distribution, which in turn is characterized by the droplet effective radius (see Eq. 3.4). Figures 6.16-6.19 show that cloud liquid water path is a strong function of droplet effective radius. Figures 6.28-6.31 show that cloud liquid water path is a strong function of the sea surface-cloud top temperature difference.

The spatial distributions of the monthly-mean, low-level cloud properties for pixels overcast by the single-layered, low-level clouds for March 1989 are shown in Figure 6.36. The observations were restricted to near-nadir satellite zenith angles and to 2.5°-regions for which single-layered, low-level clouds were identified on more than three of the thirty-one days. Figure 6.36a shows the sea surface and the cloud top temperature differences. Figure 6.36b shows the cloud liquid water paths. The sea surface-cloud top temperature differences and cloud liquid water paths appear to be nicely correlated over the Pacific ocean. Large cloud liquid water paths and large sea surface-cloud top temperature differences were found east of Japan, southeast of Australia, in the central north Pacific, and south eastern subtropics. Small cloud liquid water paths and small sea surface-cloud top temperature differences were found in the central tropics and off the coast of Baja California.

Figure 6.36c shows the low-level cloud visible optical depths; Figure 6.36d shows the low-level cloud droplet effective radii; and Figure 6.36e shows the low-level cloud top emission temperatures. Large cloud visible optical depths were found southeast of Japan. Small cloud visible optical depths were found in the central tropics and off the coast of Baja California. Large cloud droplet effective radii were found in the north central subtropics and south eastern subtropics. Small cloud droplet effective radii were found along the coast of Asia and off the coast of Baja California. Cloud visible optical depths and sea surface-cloud top temperature differences appeared to be more correlated in the northern Pacific than in the southern Pacific. Cloud droplet effective radii and sea surface-cloud top temperature differences were more correlated in the southern Pacific than in the northern Pacific. Further observations on seasonal, interannual, and diurnal time scales and on other portions of the globe, both ocean and land, are necessary for a better understanding of the large time- and space-scale relationships between low-level cloud liquid water path, cloud optical depth, cloud droplet radius, cloud top temperature, and cloud vertical thickness.

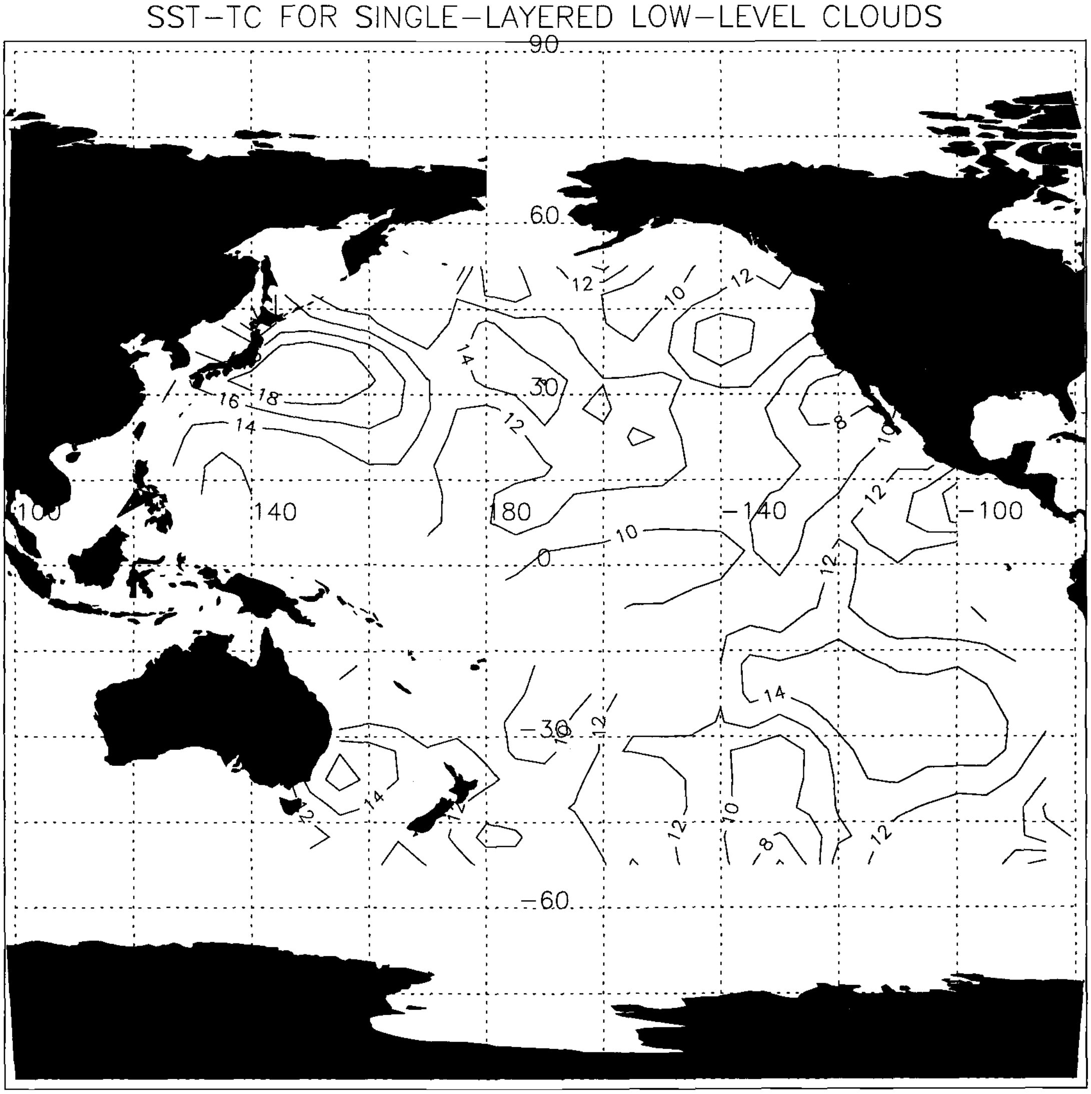

SST-TC FOR SINGLE-LAYERED LOW-LEVEL CLOUDS

90
60
30
0
-30
-60
100
140
180
-140
-100
18
16
14
12
10
8

Figure 6.36(a) Monthly-mean sea surface-cloud top temperature differences (K) for March 1989 for the Pacific ocean. Observations are for pixels overcast by single-layered, low-level clouds identified by the spatial coherence method. The observations were restricted to near-nadir satellite view angles. The contour interval is every 2K.

LOW-LEVEL CLOUD LIQUID WATER PATHS

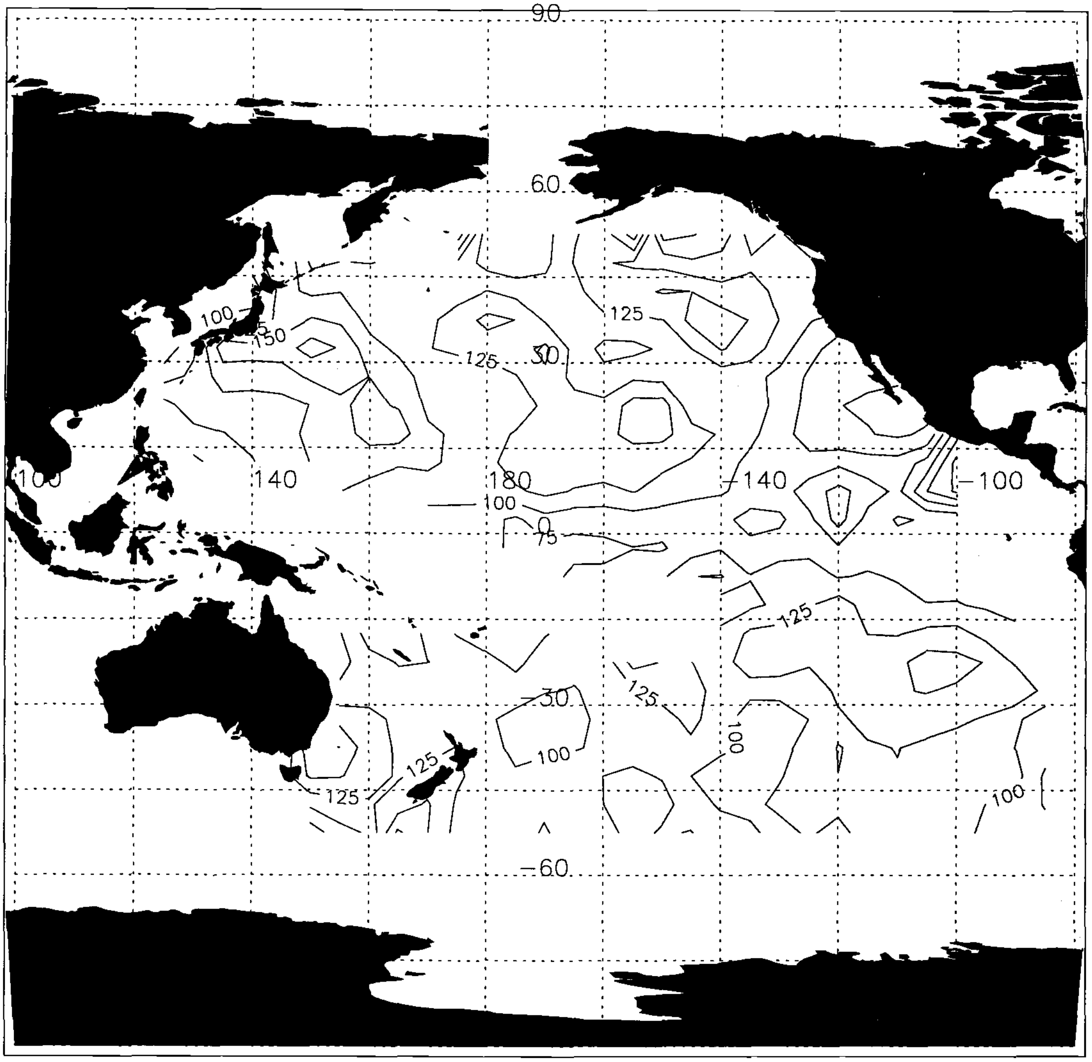
90
60
-60
100
140
180
-140
-100
100
125
150
75
50
30
-30
100
125
125
100
100
125
100

Figure 6.36(b) Same as Figure 6.36a, except for cloud liquid water path (g/m^2). The contour interval is every 25 g/m^2.

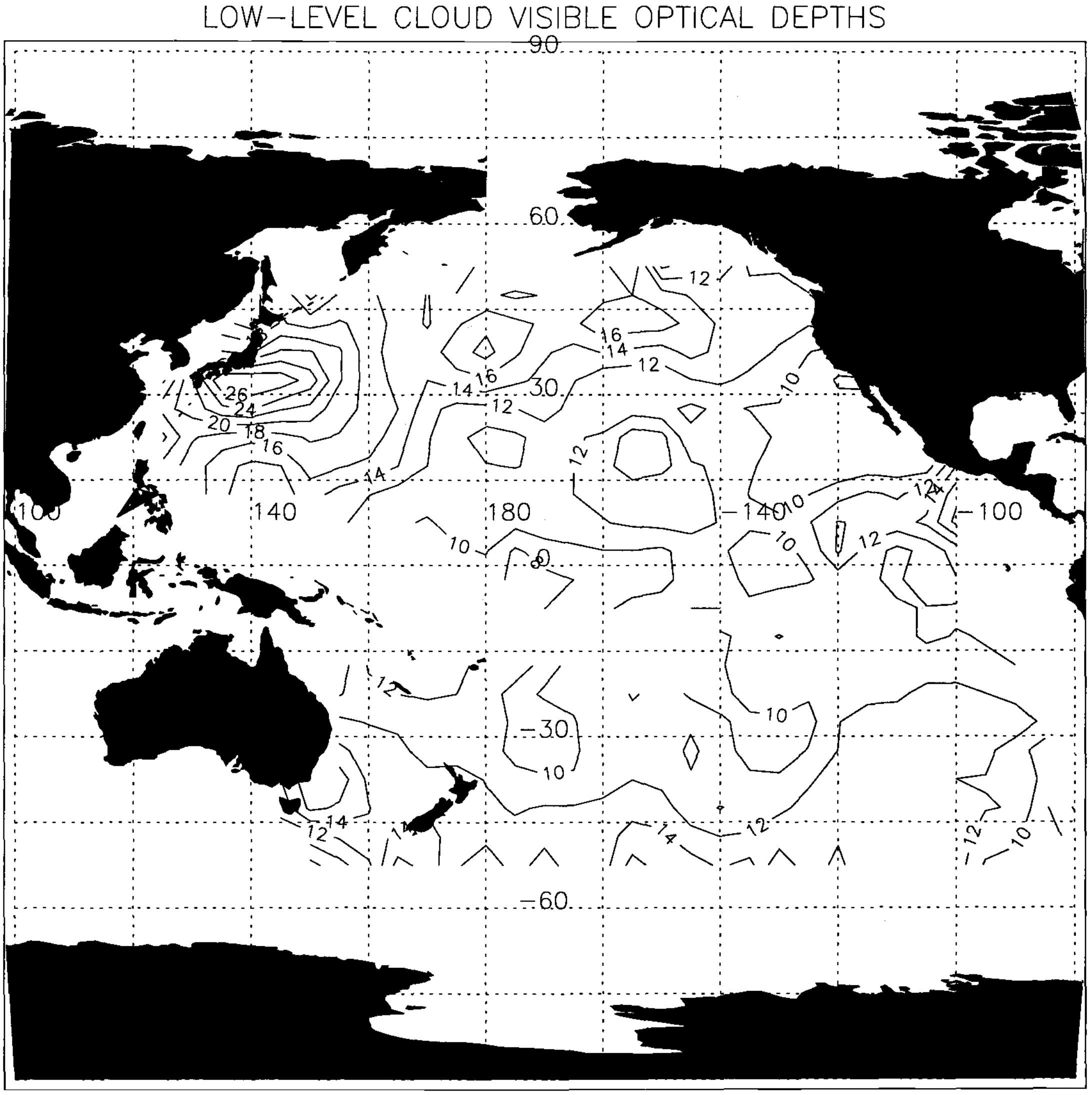
LOW-LEVEL CLOUD VISIBLE OPTICAL DEPTHS
90
60
30
100
140
180
-140
-100
-30
-60
26
24
20
18
16
14
12
10

Figure 6.36(c) Same as Figure 6.36a, except for cloud visible optical depth. The contour interval is 2.

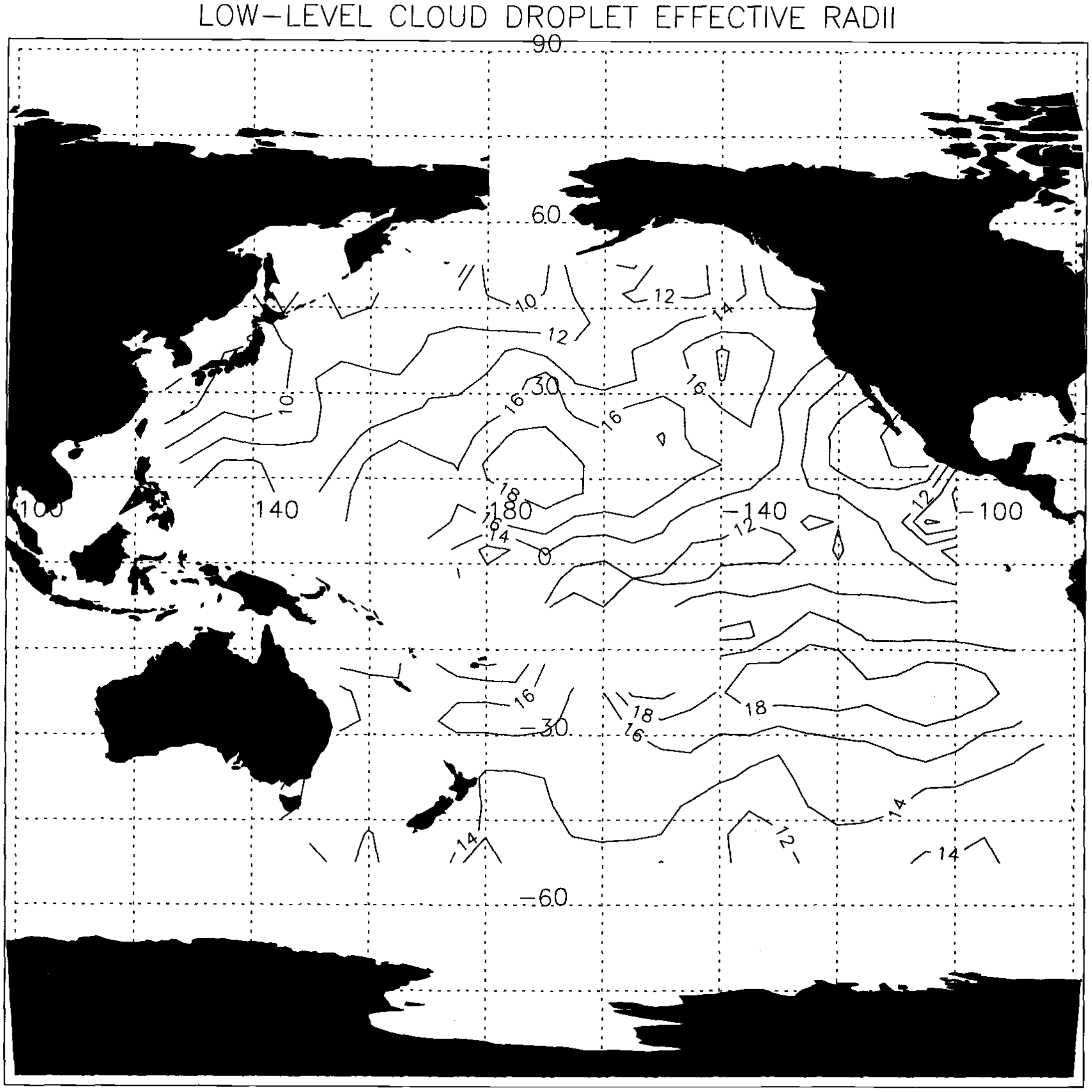

LOW-LEVEL CLOUD DROPLET EFFECTIVE RADII

90
60
100
140
180
-140
-100
30
-30
-60
10
12
14
16
18

Figure 6.36(d) Same as Figure 6.36a, except for cloud droplet effective radius (μm). The contour interval is every 2 μm.

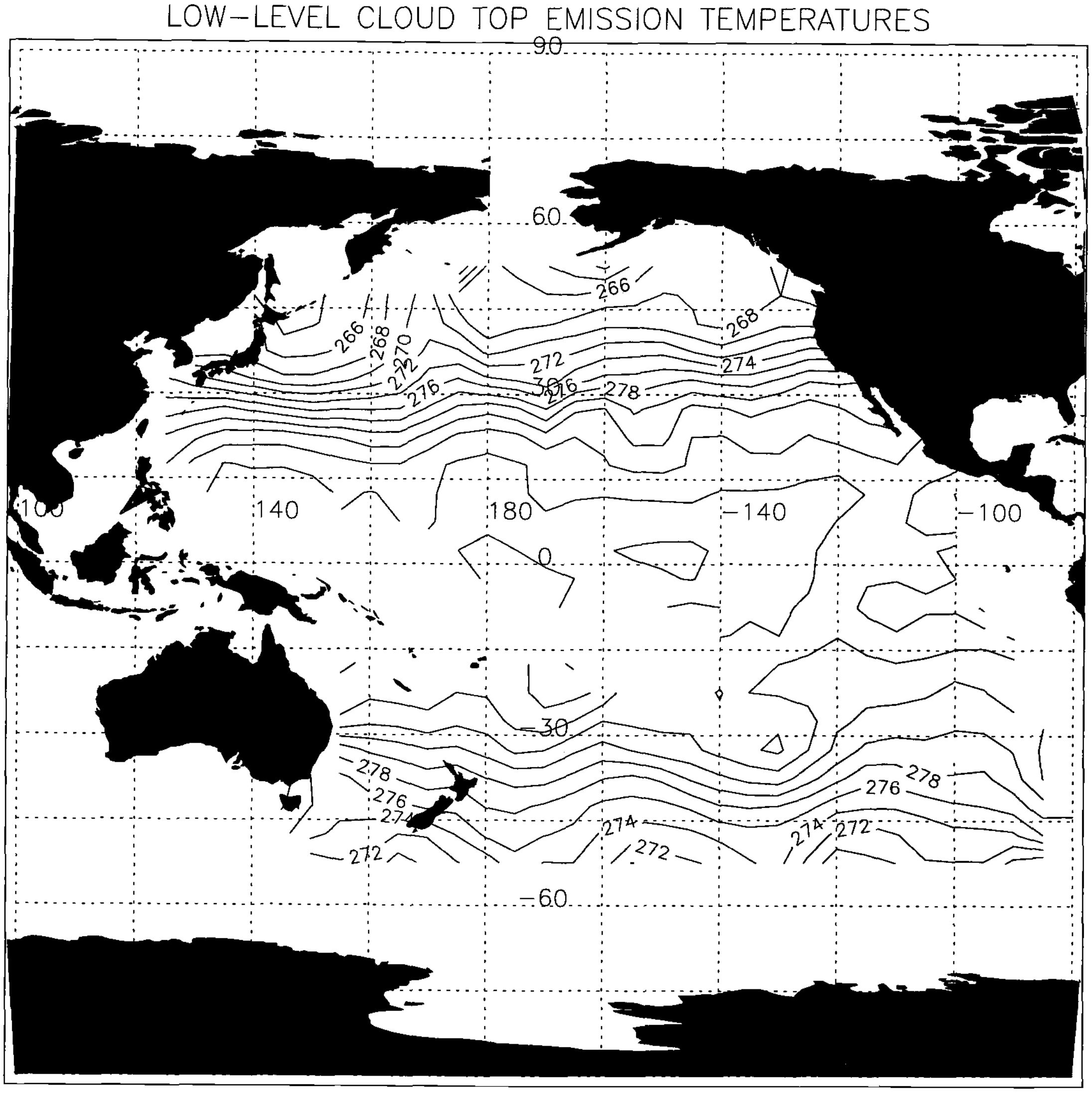
LOW–LEVEL CLOUD TOP EMISSION TEMPERATURES
90
60
266
268
270
272
274
276
278
100
140
180
–140
–100
0
–30
–60

Figure 6.36(e) Same as Figure 6.36a, except for cloud top emission temperature (K). The contour interval is every 2K.

Chapter 7
Concluding Remarks: Summary and Future Studies

7.1 Cloud detection

In Chapter 2, three cloud detection methods, the spatial coherence, CLAVR, and an ISCCP-like threshold method, were applied to September 6, 1989, NOAA-11 AVHRR 4-km GAC data to identify pixels that were either cloud-free, overcast, or partly cloud-covered. Comparisons between the three methods were performed for well-defined, single-layered cloud systems as identified by the spatial coherence method over oceans. The comparisons relied on the performance of the spatial coherence method which has been a reliable method for the identification of single-layered cloud systems and the identification of cloud-free, overcast, and partly cloud-covered pixels. The three methods employed distinct algorithms for cloud detection. The primary objective of the comparison was to investigate differences in the cloud physical properties derived by the three methods.

The ISCCP-like threshold method identified far more pixels as cloudy and overcast than were identified as overcast by either CLAVR or the spatial coherence method. Many pixels that are identified by threshold methods as being cloudy or overcast are only partly cloud-covered. Taking these partly cloud-covered pixels to be overcast leads to an overestimate in fractional cloud cover, an underestimate in cloud reflectivity, and an overestimate in cloud emission temperature. As shown in Chapter 2, the 250-km and 60-km-scale cloud cover fractions produced by applying the ISCCP-like threshold method were systematically larger than those produced by the spatial coherence method. Likewise, the mean 0.63-μm cloud reflectivities were systematically smaller and the mean 11-μm cloud brightness temperatures were systematically larger than those produced by the spatial coherence method.

Unlike ISCCP, both the spatial coherence method and CLAVR allow for partly cloud-covered pixels. However, the different cloud detecting algorithms employed by the two methods lead to the selection of different pixels as cloud-free, overcast, and partly cloud-covered. Consequently, the methods produce different cloud properties. For the September 6, 1989 data, CLAVR identified fewer cloud-free and overcast pixels than did the spatial coherence method. This result was attributed to the restrictive criteria employed by the CLAVR cloud detection algorithm. The restrictive criteria led to a large fraction of pixels being identified as partly cloud-covered by CLAVR. Despite the restrictive criteria, the mean 0.63-μm cloud reflectivities and mean 11-μm cloud brightness temperatures produced by CLAVR on a 250- or a 60-km-scale basis were generally similar to those produced by the spatial coherence method. Occasionally, the mean 0.63-μm cloud reflectivities produced by CLAVR were smaller than those for the spatial coherence method and the mean 11-μm cloud brightness temperatures produced by CLAVR were larger than those produced by the spatial coherence method. These differences were attributed to a gross cloud-reflectivity threshold employed by CLAVR. When the reflectivity for a pixel was larger than the CLAVR gross cloud-reflectivity threshold, the pixel was taken to be overcast regardless of the actual cloud cover, which was often substantially less than unity. The smaller reflectivities and larger brightness temperatures associated with these partly cloud-covered pixels caused the smaller mean cloud reflectivities and larger mean cloud brightness temperatures for CLAVR.

In determining the fractional cloud cover, pixels identified by ISCCP as being cloudy or overcast were all assigned a cloud cover fraction of 100%. Since the ISCCP threshold method takes many pixels that are only partly cloud-covered as overcast, an overestimate in fractional cloud cover would be expected. For the 250-km-scale regions containing single-layered cloud systems obtained on September 6, 1989 over oceans, the total fractional cloud cover derived by ISCCP (~0.70) was about 0.25 larger than that derived by the spatial coherence method (~0.45). CLAVR has been developed to allow for partly cloud-covered pixels. However, all partly cloud-covered pixels identified by CLAVR were assigned a cloud cover fraction of 0.5. With such an assignment for all partly cloud-covered pixels, CLAVR underestimates the fractional cloud cover for areas that have large cloud cover fractions and overestimates the fractional cloud cover for areas that have little cloud cover. For the 250-km-scale, single-layered cloud systems over oceans on September 6, 1989, the total fractional cloud cover derived by CLAVR was ~0.54.

The performance of ISCCP and CLAVR cloud detecting algorithms needs to be justified for other more complex cloud systems and for continental clouds. The justification will rely on the quality of the "truth" data. The spatial coherence method only produces reliable results for well-defined, single-layered cloud systems, but it fails, like all other currently available methods, when more complex clouds occur. It is hoped that future comparisons between satellite observations and *in situ* or LIDAR data can help to characterize the performance of ISCCP, CLAVR, and the spatial coherence method as well as provide guidance for other cloud detecting algorithms.

7.2 Cloud property retrievals

In Chapter 3, a cloud property retrieval scheme was developed for extracting cloud visible optical depths, cloud droplet effective radii, and cloud top emission temperatures from AVHRR satellite observations. The scheme incorporated a radiative transfer model which adopted Mie theory to account for the light scattering by cloud droplets, the adding-doubling method to perform the radiative transfer calculations, the correlated *k*-distribution model to account for the atmospheric gaseous absorption, Rayleigh theory to account for atmospheric molecular scattering, and a Lambertian surface to account for the surface reflectance. The model was used to calculate cloud bidirectional reflectivities for various cloud visible optical depths and droplet effective radii by employing 148-stream and 16-stream adding-doubling radiative transfer calculations. For both the visible (AVHRR channel 1) and near-infrared (AVHRR channel 3) wavelengths, the cloud bidirectional reflectivities obtained with the 16-stream scheme were generally within ±5% of those obtained with the 148-stream scheme when the satellite zenith angle and the solar zenith angle were both less than $\sim 70^\circ$ and cloud visible optical depths were larger than ~ 4. The ±5% differences caused differences of the same magnitude in the retrieved cloud visible optical depths and droplet effective radii when using the 16-stream retrieval scheme to approximate the 148-stream retrieval scheme. Larger differences were sometimes found when satellite or solar zenith angles were greater than 70° or when cloud visible optical depths were smaller than 4.

The model was also employed to study the performance of the double Henyey-Greenstein phase function when used to approximate the Mie phase function. Cloud bidirectional reflectivities obtained with the double Henyey-Greenstein phase functions were generally within ±10% of those obtained with the Mie phase functions when the satellite zenith angle and the solar zenith angle were both less than $\sim 70^\circ$ and cloud visible optical depths were larger than ~ 4. Differences larger than ±10% were found when satellite or solar zenith angles were greater than 70° or when cloud visible optical depths were smaller than 4.

The model was applied to March 1989, NOAA-11 AVHRR GAC 0.63-, 3.75-, and 11-μm radiances that were observed for completely overcast pixels to retrieve cloud visible optical depths, droplet effective radii, and cloud top emission temperatures. These overcast pixels were identified by the spatial coherence method and were taken from 60-km-scale regions which contained horizontally uniform, single-layered, low-level cloud systems over the Pacific ocean. The sensitivity studies showed that: The retrieved cloud droplet effective radii and cloud top emission temperatures were sensitive to the retrieved cloud optical depths, the instrument calibration, and the atmospheric absorption above the cloud, which in turn was governed by the atmospheric temperature and humidity profiles. They were insensitive to the sea surface temperature, the surface reflectance, and the atmospheric absorption inside clouds. The retrieved cloud visible optical depths were rather sensitive to the instrument calibration, but relatively insensitive to the atmospheric absorption and scattering, the surface reflectance, the cloud altitude, and the cloud droplet size.

In Chapter 4, the satellite zenith angle dependence of the retrieved cloud properties was examined. The satellite zenith angle dependence suggested either a failure of the plane-parallel assumption that was employed in the radiative transfer calculations or an angular dependence in the performance of the spatial coherence method.

The study focused only on low-level cloud systems that were horizontally uniform and formed a single layer over the Pacific ocean. These uniform single-layered cloud systems are the closest in nature to being plane-parallel. For the March 1989 data, the retrieved cloud visible optical depths were on average smaller at larger satellite zenith angles. The cloud visible optical depths retrieved at oblique satellite zenith angles of 60° were $\sim$60–70% of those retrieved at nadir. Likewise, cloud liquid water paths were $\sim$70–80%. This dependence was found for both the forward and backward scattering directions. The retrieved cloud droplet effective radii showed no significant dependence on satellite zenith angle, except that the overall mean droplet effective radius in the forward scattering direction was ~ 1 μm larger than that in the backward scattering direction. The retrieved cloud top emission temperatures also showed no angular dependence for satellite zenith angles $< 40°$. But, for satellite zenith angles $> 50°$, the emission temperatures were on average 1–2K larger than the near-nadir values. As a result of the satellite zenith angle dependence, retrievals were restricted to near-nadir satellite zenith angles, where at least the pixels identified as being overcast were more likely to be overcast. The solar zenith angle dependence of the cloud properties retrieved for near-nadir satellite zenith angles remains to be studied. Biases in the retrieved cloud properties due to variations in the solar zenith angle have been presented by Loeb and Davies (1996) and Loeb and Coakley (1997). Comparisons between plane-parallel and Monte Carlo simulations of radiative transfer would also help to understand the failures of the plane-parallel radiative transfer model (Loeb et al., 1997).

7.3 Properties of low-level marine clouds

In Chapters 4 and 6, NOAA-11 AVHRR GAC pixels observed at near-nadir satellite view angles ($< 25^\circ$) and identified by the spatial coherence method as being overcast by single-layered, low-level cloud systems were used to retrieve low-level cloud properties. For the March 1989 data, the mean cloud visible optical depths derived for overcast pixels was 13.9 for the northern Pacific and 11.9 for the southern Pacific. Likewise, the mean cloud liquid water path was 117.8 g/m^2 for the north Pacific and 115.7 g/m^2 for the south Pacific and the mean cloud droplet effective radius was 13.1 μm for the north Pacific and 14.7 μm for the south Pacific. The mean cloud top altitude was estimated to be 1.5–1.8 km for both the north and south Pacific.

These cloud properties were also retrieved for the near-nadir pixels that were identified by the spatial coherence method as being partly covered by the same single-layered, low-level cloud systems. These partly cloudy pixels had cloud cover fractions ranging between 0.0 and 1.0 and had a total mean cloud cover fraction of $\sim$0.75. In the retrievals, the partly cloudy pixels were taken to be overcast. The resulting cloud properties were compared with those retrieved for the overcast pixels in the same 60-km region. For the single-layered, low-level cloud systems over the Pacific ocean during March 1989, cloud visible optical depths retrieved from the partly cloudy pixels were on average $\sim$40–60% of those for the overcast pixels. Likewise, cloud liquid water paths were $\sim$30–50%, cloud droplet effective radii were $\sim 1 - 2$ μm smaller, and cloud top emission temperatures were 2–4K larger. Clearly, cloud properties retrieved from partly cloudy pixels, when assumed to be overcast, differ significantly from those retrieved for their overcast counterparts. Such findings have suggested that the cloud properties produced in the ISCCP data stream are biased because many pixels identified by ISCCP as being overcast are only partly cloudy.

In Chapters 5 and 6, temporal (day-to-day) and spatial (longitudinal) variations of the cloud visible optical depth, cloud droplet effective radius, cloud liquid water path, cloud top emission temperature, and sea surface-cloud top temperature difference were examined for pixels overcast by the single-layered, low-level clouds obtained over the Pacific ocean during March 1989. The sea surface-cloud top temperature difference was used as an index of cloud vertical thickness. As shown in Chapter 5, the cloud visible optical depths and cloud top emission temperatures were negatively correlated. The negative correlations were obtained for both the temporal and spatial variations and were often statistically significant at a 90% confidence level. The negative correlations were thought to be due mainly to the dependence of cloud visible optical depth on cloud vertical thickness. The negative correlations between cloud visible optical depth and cloud temperature obtained by Tselioudis et al. (1992) using ISCCP data for low-level clouds were attributed in part to the breakup of clouds, i.e., ISCCP takes partly cloudy pixels as being overcast, and in part to the effect of cloud optical depth increasing with cloud vertical thickness.

In Chapter 6, cloud visible optical depths and cloud droplet effective radii were often positively correlated for both temporal and spatial variations. Positive correlations were also obtained between cloud liquid water paths and cloud visible optical depths and between cloud liquid water paths and cloud droplet effective radii. These correlations were attributed mainly to the effects of changes in cloud vertical thickness. The cloud visible optical depths, droplet effective radii, and cloud liquid water paths were all shown to be positively correlated with sea surface-cloud top temperature differences.

Evidently, cloud vertical thickness plays a major role in governing the properties of low-level marine clouds. The sea surface-cloud top temperature difference may be a useful variable for the parameterization of low-level marine clouds in climate models. As shown in Chapters 5 and 6, a change of 1K in sea surface-cloud top temperature difference brought about a change of ~4–12 g/m^2 in cloud liquid water path and a change in cloud visible optical depth of ~1.2–1.6 for the northern subtropics and ~0.2–0.8 for other latitude zones. The change in cloud droplet effective radius was generally small, ~0–1 μm.

To summarize, for the March 1989, single-layered, low-level clouds for the Pacific ocean, cloud liquid water paths were strongly and positively correlated with the sea surface-cloud top temperature differences. Cloud visible optical depths and droplet effective radii were also positively correlated with the sea surface-cloud top temperature differences, except that the correlations between cloud visible optical depth and sea surface-cloud top temperature difference were weaker in the south Pacific and the correlations between cloud droplet effective radius and sea surface-cloud top temperature difference were weaker in the north Pacific. These correlations were attributed to the role that cloud vertical thickness plays in governing the properties of low-level marine clouds. Unfortunately, cloud vertical thickness cannot be directly retrieved from satellite observations. Future studies should examine these correlations using data obtained for different seasons, years, and locations, and in particular over land. At last, it is worth noting that the low-level cloud properties retrieved here rely on the quality of the overcast pixels as were determined by the spatial coherence method. If the spatial coherence method has errors, thin "overcast" clouds may be caused by breaks in the clouds. So, the positive correlations obtained here between cloud visible optical depth, cloud liquid water path, cloud droplet effective radius, and sea surface-cloud top temperature difference may be caused by breakdowns of the spatial coherence method.

Bibliography

Albrecht, B. A., 1989: Aerosols, cloud microphysics, and fractional cloudiness. *Science*, **245**, 1227-1230.

Arking, A., 1991: The radiative effects of clouds and their impact on climate. *Bull. Amer. Meteorol. Soc.*, **71**, 795–813.

Arking, A., and J. D. Childs, 1985: The retrieval of cloud cover parameters from multispectral satellite images. *J. Climate Appl. Meteorol.*, **24**, 322-333.

Betts, A. K., P. Minnis, W. Ridgway, and D. F. Young, 1992: Integration of satellite and surface data using a radiative-convective oceanic boundary-layer model. *J. Appl. Meteorol.*, **31**, 340-350.

Betts, A. K. and W. Ridgeway, 1989: Climatic equilibrium of the atmospheric convective boundary layer over a tropical ocean. *J. Atmos. Sci.*, **46**, 2621-2641.

Betts, A. K. and Harshvardhan, 1987: Thermodynamic constraint on the cloud liquid water feedback in climate models. *J. Geophys. Res.*, **92**, 8483–8485.

Bohren, C. F. and D. R. Huffman, 1983: *Absorption and Scattering of Light by Small Particles.* Wiley.

Cahalan, R. F., W. Ridgeway, W. J. Wiscombe, T. L. Bell, and J. B. Snider, 1994: The albedo of fractal stratocumulus clouds. *J. Atmos. Sci.*, **51**, 2434-2455.

Cess, R. D. and co-authors, 1990: Intercomparison and interpretation of climate feedback processes in 19 atmospheric global circulation models. *J. Geophys. Res.*, **95**, 16,601-16,615.

Cess, R. D. and co-authors, 1989: Interpretation of cloud-climate feedback as produced by 14 atmospheric general circulation models. *Science*, **245**, 513-516.

Chang, F-L., and J. A. Coakley, Jr., 1993: Estimating errors in fractional cloud cover obtained with infrared threshold methods. *J. Geophys. Res.*, **98**, 8825-8839.

Chang, F-L., 1991: Toward the estimation of errors in cloud cover derived by threshold methods. M.S. thesis, Oregon State University, 67 pp.

Charlson, R. J., J. E. Lovelock, M. O. Andrae and S. G. Warren, 1987: Oceanic phytoplankton, atmospheric sulphur, cloud albedo and climate. *Nature*, **326**, 655-661.

Charlson, R. J., S. E. Schwartz, J. M. Hales, R. D. Cess, J. A. Coakley, Jr., J. E. Hansen, and D. J. Hofmann, 1992: Climate forcing by anthropogenic aerosols. *Science*, **255**, 423-430.

Coakley, J. A., Jr. P. A. Durkee, K. Nielsen, J. P. Taylor, S. Platnick, B. A. Albrecht, D. Badd, F-L. Chang, W. R. Tahnk, C. S. Bretherton, and P. V. Hobbs, 1997: The appearance and disappearance of ship tracks on large spatial scales. *J. Atmos. Sci.*, (accepted).

Coakley, J. A., Jr., 1993: Remote sensing of cloud microphysics. *NCAR Summer Colloquium on Clouds and Climate*, 73–106.

Coakley, J. A., Jr., 1991: Reflectivities of uniform and broken layered clouds. *Tellus*, **43B**, 420-433.

Coakley, J. A., Jr., and T. Kobayashi, 1989: Broken cloud biases in albedo and surface insolation derived from satellite imagery data. *J. Climate*, **2**, 721-730.

Coakley, J. A., Jr., R. L. Bernstein, and P. A. Durkee, 1987: Effect of ship-stack effluents on cloud reflectivity. *Science*, **237**, 1020-1022.

Coakley, J. A., Jr., 1987: A dynamic threshold method for obtaining cloud cover from satellite imagery data. *J. Geophys. Res.*, **92**, 3985-3990.

Coakley, J. A., Jr. and R. Davies, 1986: The effect of cloud sides on reflected solar radiation as deduced from satellite observations. *J. Atmos. Sci.*, **43**, 1025-1035.

Coakley, J. A., Jr., and D. G. Baldwin, 1984: Towards the objective analysis of clouds from satellite imagery data. *J. Climate and Appl. Meteor.*, **23**, 1065-1099.

Coakley, J. A., Jr. and F. P. Bretherton, 1982: Cloud cover from high-resolution scanner data: Detecting and allowing for partially filled fields of view. *J. Geophys. Res.*, **87**, 4917-4932.

Curran, R. J. and M. L. C. Wu, 1982: Skylab near-infrared observations of clouds indicating supercooled liquid water droplets. *J. Atmos. Sci.*, **39**, 635-647.

Davies, R., 1978: The effect of finite geometry on the three-dimensional transfer of solar irradiance in clouds. *J. Atmos. Sci.*, **35**, 1712-1725.

Downing, H. D. and D. Williams, 1975: Optical Constants of Water in the Infrared. *J. Geophys. Res.*, **80**, 1656-1661.

Elden, B., 1953: The dispersion of standard air. *J. Opt. Soc. Amer.*, **43**, 339–344.

Feigelson, E. M., 1978: Preliminary radiation model of a cloudy atmosphere, 1, Structure of clouds and solar radiation. *Contrib. Atmos. Phys.*, **51**, 203–229.

Gallegos, S. C., J. D. Hawkins and C. F. Cheng, 1993: A new automated method of cloud masking for AVHRR full-resolution data over the ocean. *J. Geophys. Res.*, **98**, 8505-8516.

Goody, R. M. and Y. L. Yung, 1989: *Atmospheric Radiation.* Oxford University Press.

Grant, I. P. and G. E. Hunt, 1969: Discrete space theory of radiative transfer. I. Fundamentals. *Proc. Roy. Soc. London Ser.*, **A313**, 183–197.

Hale, G. M. and M. R. Querry, 1973: Optical constants of water in the 200 nm to 200 mm wavelength region. *Appl. Opt.*, **12**, 555-563.

Han, Q., W. B. Rossow, J. Chou, and R. M. Welch, 1997: Global survey of the relationship between cloud droplet size and albedo using ISCCP. *AMS 9th Conference on Atmospheric Radiation.* 426–430.

Han, Q., W. B. Rossow, and A. A. Lacis, 1994: Near-global survey of effective droplet radii in liquid water clouds using ISCCP data. *J. Climate*, **7**, 465-497.

Hansen, J. E. and L. D. Travis, 1974: Light scattering in planetary atmospheres. *Space Sci. Rev.*, **16**, 527-610.

Hansen, J. E., 1971: Multiple scattering of polarized light in planetary atmospheres. Part II: Sunlight reflected by terrestrial water clouds. *J. Atmos. Sci.*, **28**, 1400-1426.

Harrison, E. F., P. Minnis, B. R. Barkstrom, V. Ramanathan, R. D. Cess, and G. G. Gibson, 1990: Seasonal variation of cloud radiative forcing derived from the Earth Radiation Budget Experiment. *J. Geophys. Res.*, **95**, 18,687–18,703.

Hartmann, D. L., M. E. Ockert-Bell and M. L. Michelsen, 1992: The effect of cloud type on earth's radiation balance: Global analysis. *J. Climate*, **5**, 1281-1304.

Hartmann, D. L. and D. A. Short., 1980: Use of earth radiation budget statistics for studies of clouds and climate. *J. Atmos. Sci.*, **37**, 1233–1250.

Henyey, L. C. and J. L. Greenstein, 1941: Diffuse radiation in the galaxy. *Astrophys. J.*, **93**, 70-83.

Heymsfield, A. J. and L. M. Miloshevich, 1993: Overview of microphysical state parameter measurements from FIRE II. *FIRE Cirrus Science Conference*, Breckenridge, Colorado, June 14–17, 1–4.

IPCC, Climate Change, 1994: Radiative Forcing of Climate Change and an Evaluation of the IPCC IS92 Emission Scenarios. *Cambridge University Press*, 339 pp. ed., John T. Houghton, 1995.

Kidwell, K. B., 1991: *NOAA Polar Orbiter Data Users Guide*, NOAA National Climate Data Center, Satellite Data Services Division, Washington, D.C.

King, M. D., 1983: Number of terms required in the Fourier expansion of the reflection function for optically thick atmospheres. *J. Quant. Spectrosc. Radiat. Transfer*, **30**, 143-161.

King, M. D., L. F. Radke, and P. V. Hobbs, 1993: Optical properties of marine stratocumulus clouds modified by ships. *J. Geophys. Res.*, **98D**, 2729-2739.

Klein, S. A., and D. L. Hartmann, 1993: The seasonal cycle of low stratiform clouds. *J. Climate*, **6**, 1578-1606.

Kratz, D. P., 1995: The correlated -distribution technique as applied to the AVHRR channels. *J. Quant. Spectrosc. Radiat. Transfer*, **53**, 501-517.

Le Treut, H. and Z.-X. Li, 1991: Sensitivity of an atmospheric general circulation model to prescribed SST changes: Feedback effects associated with the simulation of cloud optical properties. *Climate Dyn.*, **5**, 175–187.

Lin, X. and J. A. Coakley, Jr., 1993: Retrieval of properties for semitransparent clouds from multispectral infrared imagery data. *J. Geophys. Res.*, **98**, 18,501-18,514.

Liou, K. N., 1980: *An Introduction to Atmospheric Radiation.* International Geophysics Series. Vol. 25, Academic Press, 392 pp.

Loeb, N. G. and J. A. Coakley, Jr., 1997: Consistency of satellite cloud property retrievals from layered marine clouds: Does 1D theory apply? *J. Climate*, (accepted).

Loeb, N. G., T. Vάrnai and R. Davies, 1997: Effect of cloud inhomogeneities on the solar zenith angle dependence of nadir reflectance. *J. Geophys. Res.*, **102**, 9387-9395.

Loeb, N. G. and R. Davies, 1996: Observational evidence of plane parallel model biases: The apparent dependence of cloud optical depth on solar zenith angle. *J. Geophys. Res.*, **101**, 1621-1634.

Luo, G., X. Lin, and J. A. Coakley, Jr., 1994: 11-μm emissivities and droplet radii for marine stratocumulus. *J. Geophys. Res.*, **99**, 3685-3698.

Macke, A., 1993: Scattering of light by polyhedral ice crystals. *Appl. Opt.*, **32**, 2780–2788.

Macke, A., J. Mueller and E. Raschke, 1996: Single scattering properties of atmospheric ice crystals. *J. Atmos. Sci.*, **53**, 2813–2825.

Mclain, E. P., W. G. Pichel and C. C. Walton, 1985: Comparative performance of AVHRR-based multichannel sea surface temperature. *J. Geophys. Res.*, **90**, 11,587-11,601.

McClatchey, R. A., R. W. Fenn, J. E. Selby, F. E. Volz, and J. S. Garing, 1972: *Optical Properties of the Atmosphere.* Air Force Cambridge Research Laboratories. AFCRL-72-0497, Environmental Research Paper No. 411, 108 pp.

McMillin, L. M, and D. S. Crosby, 1984: Theory and Validation of the Multiple Window Sea Surface Temperature Technique. *J. Geophys. Res.*, **89**, 3655-3661.

Minnis, P., P. W. Heck, D. F. Young, C. W. Fairall, and J. B. Snider, 1992: Stratocumulus cloud properties derived from simultaneous satellite and island-based instrumentation during FIRE. *J. Appl. Meteorol.*, **31**, 317-339.

Mitchell, J. F. B., C. A. Senior, and W. J. Ingram, 1989: CO2 and climate: A missing feedback? *Nature*, **341**, 132-134.

Nakajima, T. and M. D. King, 1990: Determination of the optical thickness and effective particle radius of clouds from reflected solar radiation measurements. Part I: Theory. *J. Atmos. Sci.*, **47**, 1878-1893.

Nakajima, T. Y. and T. Nakajima, 1995: Wide-area determination of cloud microphysical properties from NOAA AVHRR measurements for FIRE and ASTEX regions. *J. Atmos. Sci.*, **52**, 4043-4059.

Platnick, S. and F. P. J. Valero, 1995: A validation of a satellite cloud retrieval during ASTEX. *J. Atmos. Sci.*, **52**, 2985-3001.

Platnick, S. and S. Twomey, 1994: Determining the susceptibility of cloud albedo to changes in droplet concentration with the Advanced Very High Resolution Radiometer. *J. Appl. Meteorol.*, **33**, 334-347.

Radke, L. F., and J. A. Coakley, Jr., M. D. King, 1989: Direct and remote sensing observations of the effects of ships on clouds. *Science*, **246**, 1146-1149.

Ramanathan, V., R. D. Cess, E. F. Harrison, P. Minnis, B. R. Barkstrom, E. Ahmad and D. Hartmann, 1989: Cloud-radiative forcing and climate: Results from the Earth Radiation Budget Experiment. *Science*, **243**, 57-63.

Ramanathan, V., E. J. Pitcher, R. C. Malone, and M. L. Blackmon, 1983: The response of a spectral general circulation model to refinements in radiative processes. *J. Atmos. Sci.*, **40**, 605-630.

Ramanathan and Coakley, 1978: Climate modeling through radiative-convective models. *Rev. Geophys. Space Phys.*, **16**, 465–489.

Ramaswamy, V., and V. Ramanathan, 1989: Solar absorption by cirrus clouds and maintenance of the tropical upper tropospheric thermal structure. *J. Atmos. Sci.*, **46**, 2293-2310.

Randall, D. A. and co-authors, 1992: Intercomparison and interpretation of surface energy fluxes in atmospheric general circulation models. *J. Geophys. Res.*, **97**, 3711-3724.

Rao, C. R. N. and J. Chen, 1995: Inter satellite calibration linkages for the visible and near-infrared channels of the Advanced Very High Resolution Radiometer on the NOAA-7, -9, and -11 spacecraft. *Int. J. Remote Sens*, **16**, 1931-1942.

Rao, C. R. N., L. L. Stowe and E. P. Mclain, 1989: Remote sensing of aerosols over the ocean using AVHRR data: Theory, practice and applications. *Int. J. Remote Sens.*, **5**, 743-749.

Rawlins, F. and J. S. Foot, 1990: Remotely sensed measurements of stratocumulus properties during FIRE using the C130 aircraft multi-channel radiometer. *J. Atmos. Sci.*, **47**, 2488-2503.

Roeckner, E., U. Schlese, J. Biercamp, and P. Loewe, 1987: Cloud optical depth feedbacks and climate modeling. *Nature*, **329**, 138-140.

Rogers, R. R. and M. K. Yau, 1989: *A Short Course in Cloud Physics.* 3rd Edn. Pergamon Press. 293 pp.

Rossow, W. B. and L. C. Garder, 1993: Cloud detection using satellite measurements of infrared and visible radiances for ISCCP. *J. Climate*, **6**, 2341-2369.

Rossow, W. B. and R. A. Schiffer, 1991: ISCCP cloud data products. *Bull. Amer. Meteorol. Soc.*, **72**, 2-20.

Rossow, W. B., 1989: Measuring cloud properties from space: A review. *J. Climate*, **2**, 201-213.

Rossow, W. B., F. Mosher, E. Kinsella, A. Arking, M. Desbois, E. Harrison, P. Minnis, E. Ruprecht, G. Seze, C. Simmer and E. Smith, 1985: ISCCP cloud algorithm intercomparison. *J. Climate and Appl. Meteor.*, **24**, 877-903.

Schiffer, R. A. and W. B. Rossow, 1983: The International Satellite Cloud Climatology Project (ISCCP): The first project of the World Climate Research Programme. *Bull. Amer. Meteorol. Sci.*, **64**, 779-784.

Slingo, A. and J. M. Slingo, 1991: Response of the National Center for Atmospheric Research Community Climate Model to improvements in representation of clouds. *J. Geophys. Res.*, **96**, 15,341–15,357.

Slingo, A., 1989: A GCM parameterization for the shortwave radiative properties of water clouds. *J. Atmos. Sci.*, **46**, 1419-1427.

Somerville, R. C. J. and L. A. Remer, 1984: Cloud optical thickness feedbacks in the CO_2 climate problem. *J. Geophys. Res.*, **89**, 9668–9672.

Stephens, G. L. and S.-C. Tsay, 1990: On the cloud absorption anomaly. *Quart. J. Roy. Meteorol. Soc.*, **116**, 671-704.

Stevermer, A. J., J. A. Coakley, Jr. and D. M. Winker, 1997: Identification of layered cloud systems from satellite imagery and LITE. *AMS 9th Conference on Atmospheric Radiation.* 418-421.

Stowe, L. L., P. A. Davis and E. P. McClain, 1997: Global cloud cover from NOAA/AVHRR data. Part I: Development and case study evaluation of the CLAVR-1 classification algorithm. *J. Atmos. Ocean. Tech.* (submitted).

Stowe, L. L., E. P. Mclain, R. Carey, P. Pellegrino, G. Gutman, P. Davis, C. Long and S. Hart, 1991: Global distribution of cloud cover derived from NOAA/AVHRR operational satellite data. *Adv. Space Res.*, **11**, 51-54.

Taylor, J. P., 1992: Sensitivity of remotely sensed effective radius of cloud droplets to changes in LOWTRAN version. *J. Atmos. Sci.*, **49**, 2564-2569.

Thekaekara, M. P., 1974: Extraterrestrial solar spectrum, 3000-6100$\dot{A}$ at 1-$\dot{A}$ intervals. *Appl. Opt.*, **13**, 518-522.

Tselioudis, G., W. B. Rossow and D. Rind, 1992: Global patterns of cloud optical thickness variation with temperature. *J. Climate*, **5**, 1484-1495.

Twohy, C. H., P. A. Durkee, R. J. Huebert, and R. J. Charlson, 1995: Effects of aerosol particles on the microphysics of coastal stratiform clouds. *J. Climate*, **8**, 773-783.

Twomey, S., 1991: Aerosols, clouds and radiation. *Atmos. Environ.*, **254**, 2435-2442.

Twomey, S., M. Piepgrass, and T. L. Wolfe, 1984: An assessment of the impact of pollution on global cloud albedo. *Tellus*, **36B**, 356-366.

Twomey, S. and T. Cocks, 1982: Spectral reflectance of clouds in the near-infrared: Comparison of measurements and calculations. *J. Meteorol. Soc. Japan*, **60**, 583-592.

Twomey, S., 1977: The influence of pollution on the shortwave albedo of clouds. *J. Atmos. Sci.*, **34**, 1149-1152.

Twomey, S., 1974: Pollution and the planetary albedo. *Atmos. Environ.*, **8**, 1251-1256.

Welch, R. M. and B. A. Wielicki, 1984: Stratocumulus cloud field reflected fluxes: The effect of cloud shape. *J. Atmos. Sci.*, **41**, 3085–3103.

Wetherald, R. T. and S. Manabe, 1988: Cloud feedback processes in a general circulation model. *J. Atmos. Sci.*, **45**, 1397–1415.

Wielicki, B. A., and L. Parker, 1992: On the determination of cloud cover from satellite sensors: The effect of sensor spatial resolution. *J. Geophys. Res.*, **97**, 12799-12823.

Wiscombe, W. J., 1977: The Delta-M method: Rapid yet accurate radiative flux calculations for strongly asymmetric phase functions. *J. Atmos. Sci.*, **34**, 1408–1422.

Ye, Q. and J. A. Coakley, Jr., 1996: Biases in earth radiation budget observations. Part II: Consistent scene identification and anisotropic factors. *J. Geophys. Res.*

APPENDIX

Procedures for Constructing the Spatial Coherence Cloud Mask

Color coded images of pixel-scale cloud cover and cloud layer emission are designed to convey the fractional cloud cover within a pixel and the layered structure associated with the clouds in the region from which the pixel is drawn. The color code ranges from 1 to 255. The images are created as follows:

1. Cloud-free pixels

Cloud-free pixels are obtained from the spatial coherence analysis (Coakley and Bretherton, 1982) as being exhibiting spatially uniform emission and reflection.

$$\begin{aligned} &\mathit{cloud\ \ cover}: \ A_c = 0.0 \\ &\mathit{pixel\ \ code} = \begin{cases} 251\ (\mathit{blue}), & \mathit{over\ ocean} \\ 252\ (\mathit{brown}), & \mathit{over\ land} \end{cases} \end{aligned}$$

2. Overcast pixels

Overcast pixels are also obtained from the spatial coherence analysis as being exhibiting spatially uniform emission.

$$\begin{aligned} &\mathit{cloud\ \ cover}: \ \ A_c = 1.0 \\ &\mathit{pixel\ \ code} = 5 \times \mathit{int}\left(\frac{I_{max} - I}{2}\right), \end{aligned}$$

where I is the pixel–scale 11–μm emission (in mWm^{-2}sr^{-1}cm) and I_{max} is the maximum 11–μm emission allowed for individual overcast pixel. $I_{max} = 109$.

3. Partially cloud-covered pixels

Pixels that are neither cloud-free nor overcast are decided to be partially cloud-covered. The coding procedures are as follows:

1. Collect subframe-scale cloud layer information (retrieved by spatial coherence technique) of a region of 9 subframes × 9 subframes with the subframe containing the pixel of interest at the center.
2. Classify all cloud layers collected in step 1 into clusters. Each of these clusters is now determined to be one cloud layer representitive for the region.
3. Calculate a mean radiance, $\overline{I_c(i)}$, and a standard deviation, $\Delta I_c(i)$, for each cloud cluster i, where $i = 1$ refers to the warmest cloud cluster.
4. Calculate the pixel-scale cloud cover fraction. Calculation is essentially based on the formula, $A_c(i) = \dfrac{I - I_s}{\overline{I_c(i)} - I_s}$, where I_s is the subframe cloud-free radiance and I is the pixel radiance. For the calculation there are three circumstances may occur:

1) Single-layered cloud system (only one cloud cluster is present):

$$cloud\ \ cover: \quad A_c = \frac{I - I_s}{\overline{I_c(1)} - I_s}$$

$$pixel\ \ code = \begin{cases} 5 \times int\left(\dfrac{I_{max} - \overline{I_c(1)}}{2}\right) - k, & I \geq \overline{I_c(1)} - \Delta I_c(1) \\ 5 \times int\left(\dfrac{I_{max} - I}{2}\right) - k, & I < \overline{I_c(1)} - \Delta I_c(1) \end{cases},$$

$$\text{where } k = \begin{cases} 1, & A_c > 0.9\ (overcast) \\ 2, & 0.9 \geq A_c > 0.5\ (mostly\ cloudy) \\ 3, & 0.5 \geq A_c \geq 0.1\ (partly\ cloudy) \\ 4, & A_c < 0.1\ (clear) \end{cases}$$

2) No layered cloud system (no cloud cluster is present):

$$\mathit{cloud\ cover}: \quad A_c = \frac{I - I_s}{\overline{I_c(0)} - I_s}\text{, where } \overline{I_c(0)} = I_s - \Delta \text{ and } \Delta = \begin{cases} 20, & \mathit{over\ ocean} \\ 40, & \mathit{over\ land} \end{cases}$$

$$\mathit{pixel\ \ code} = \begin{cases} 5 \times int\left(\dfrac{I_{max} - \overline{I_c(0)}}{2}\right) - k, & I \geq \overline{I_c(0)} \\ 5 \times int\left(\dfrac{I_{max} - I}{2}\right) - k, & I < \overline{I_c(0)} \end{cases}$$

3) Multi-layered cloud system (N cloud clusters): The pixel-scale cloud cover is determined to be the average value of cloud cover calculated for each cluster.

$$\mathit{cloud\ \ cover}: \quad A_c = \frac{A_c(1) + A_c(2) + \ldots + A_c(j)}{j}$$

where $j \leq N$ and $\overline{I_c(j)} < I_{10th} < \overline{I_c(j-1)}$. I_{10th} is the 10th percentile radiance value of the 11–μm pixel-scale radiance probability distribution for the subframe of interest.

$$\mathit{code} = \begin{cases} 5 \times int\left(\dfrac{I_{max} - \overline{I_c(1)}}{2}\right) - k, & I \geq \overline{I_c(1)} - \Delta I_c(1) \\ 5 \times int\left(\dfrac{I_{max} - \overline{I_c(i)}}{2}\right) - k, & \overline{I_c(i)} - \Delta I_c(i) \leq I < \overline{I_c(i-1)} - \Delta I_c(i-1) \\ 5 \times int\left(\dfrac{I_{max} - I}{2}\right) - k, & I < \overline{I_c(N)} - \Delta I_c(N) \end{cases}$$